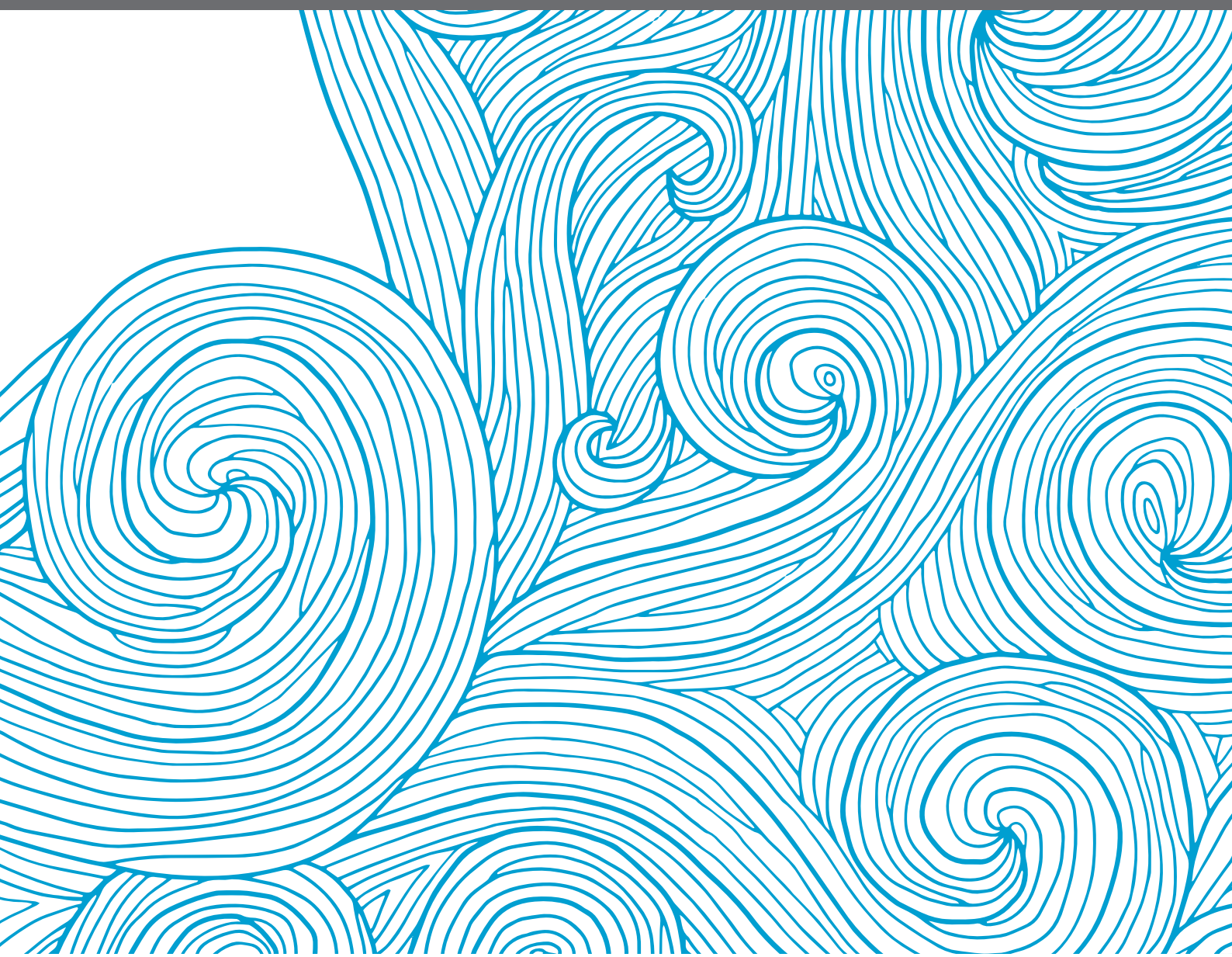
PHYSICAL DRIVERS OF BIOGEOGRAPHICAL SHIFTS IN THE NORTHEASTERN ATLANTIC – AND ADJACENT SHELVES

EDITED BY: Hjálmar Hátún, Oeystein Skagseth and Teresa Sofia Giesta da Silva
PUBLISHED IN: Frontiers in Marine Science



frontiers Research Topics

Frontiers eBook Copyright Statement

The copyright in the text of individual articles in this eBook is the property of their respective authors or their respective institutions or funders. The copyright in graphics and images within each article may be subject to copyright of other parties. In both cases this is subject to a license granted to Frontiers.

The compilation of articles constituting this eBook is the property of Frontiers.

Each article within this eBook, and the eBook itself, are published under the most recent version of the Creative Commons CC-BY licence. The version current at the date of publication of this eBook is CC-BY 4.0. If the CC-BY licence is updated, the licence granted by Frontiers is automatically updated to the new version.

When exercising any right under the CC-BY licence, Frontiers must be attributed as the original publisher of the article or eBook, as applicable.

Authors have the responsibility of ensuring that any graphics or other materials which are the property of others may be included in the CC-BY licence, but this should be checked before relying on the CC-BY licence to reproduce those materials. Any copyright notices relating to those materials must be complied with.

Copyright and source acknowledgement notices may not be removed and must be displayed in any copy, derivative work or partial copy which includes the elements in question.

All copyright, and all rights therein, are protected by national and international copyright laws. The above represents a summary only. For further information please read Frontiers' Conditions for Website Use and Copyright Statement, and the applicable CC-BY licence.

ISSN 1664-8714
ISBN 978-2-83250-742-1
DOI 10.3389/978-2-83250-742-1

About Frontiers

Frontiers is more than just an open-access publisher of scholarly articles: it is a pioneering approach to the world of academia, radically improving the way scholarly research is managed. The grand vision of Frontiers is a world where all people have an equal opportunity to seek, share and generate knowledge. Frontiers provides immediate and permanent online open access to all its publications, but this alone is not enough to realize our grand goals.

Frontiers Journal Series

The Frontiers Journal Series is a multi-tier and interdisciplinary set of open-access, online journals, promising a paradigm shift from the current review, selection and dissemination processes in academic publishing. All Frontiers journals are driven by researchers for researchers; therefore, they constitute a service to the scholarly community. At the same time, the Frontiers Journal Series operates on a revolutionary invention, the tiered publishing system, initially addressing specific communities of scholars, and gradually climbing up to broader public understanding, thus serving the interests of the lay society, too.

Dedication to Quality

Each Frontiers article is a landmark of the highest quality, thanks to genuinely collaborative interactions between authors and review editors, who include some of the world's best academicians. Research must be certified by peers before entering a stream of knowledge that may eventually reach the public - and shape society; therefore, Frontiers only applies the most rigorous and unbiased reviews.
Frontiers revolutionizes research publishing by freely delivering the most outstanding research, evaluated with no bias from both the academic and social point of view. By applying the most advanced information technologies, Frontiers is catapulting scholarly publishing into a new generation.

What are Frontiers Research Topics?

Frontiers Research Topics are very popular trademarks of the Frontiers Journals Series: they are collections of at least ten articles, all centered on a particular subject. With their unique mix of varied contributions from Original Research to Review Articles, Frontiers Research Topics unify the most influential researchers, the latest key findings and historical advances in a hot research area! Find out more on how to host your own Frontiers Research Topic or contribute to one as an author by contacting the Frontiers Editorial Office: frontiersin.org/about/contact

PHYSICAL DRIVERS OF BIOGEOGRAPHICAL SHIFTS IN THE NORTHEASTERN ATLANTIC – AND ADJACENT SHELVES

Topic Editors:
Hjálmar Hátún, Faroe Marine Research Institute (FAMRI), Faroe Islands
Oeystein Skagseth, Norwegian Institute of Marine Research (IMR), Norway
Teresa Sofia Giesta da Silva, Marine and Freshwater Research Institute, Iceland
Peter Grønkjær, Aarhus University, Denmark

Citation: Hátún, H., Skagseth, O., da Silva, T. S. G., Grønkjær, P., eds. (2022). Physical Drivers of Biogeographical Shifts in the Northeastern Atlantic – and Adjacent Shelves. Lausanne: Frontiers Media SA. doi: 10.3389/978-2-83250-742-1

Table of Contents

05 ***Editorial: Physical Drivers of Biogeographical Shifts in the Northeastern Atlantic – and Adjacent Shelves***
Hjálmar Hátún, Teresa Sofia Giesta da Silva, Øystein Skagseth and Peter Grønkjær

09 ***The Norwegian Sea Gyre – A Regulator of Iceland-Scotland Ridge Exchanges***
Hjálmar Hátún, Léon Chafik and Karin Margretha Húsgarð Larsen

24 ***Darkening of the Svalbard Fjords Waters Observed With Satellite Ocean Color Imagery in 1997–2019***
Marta Konik, Mirosław Darecki, Alexey K. Pavlov, Sławomir Sagan and Piotr Kowalczuk

41 ***Twenty-One Years of Phytoplankton Bloom Phenology in the Barents, Norwegian, and North Seas***
Edson Silva, François Counillon, Julien Brajard, Anton Korosov, Lasse H. Pettersson, Annette Samuelsen and Noel Keenlyside

57 ***Distinct Seasonal Primary Production Patterns in the Sub-Polar Gyre and Surrounding Seas***
Katherine Richardson and Jørgen Bendtsen

71 ***Spatial Distribution of Different Age Groups of Herring in Norwegian Sea, May 1996–2020***
Sólvá Káradóttir Eliasen, Eydna Í. Homrum, Jan Arge Jacobsen, Inga Kristiansen, Guðmundur J. Óskarsson, Are Salthaug and Erling Kåre Stenevik

84 ***Impact of Decadal Trends in the Surface Climate of the North Atlantic Subpolar Gyre on the Marine Environment of the Barents Sea***
Vimal Koul, Sebastian Brune, Johanna Baehr and Corinna Schrum

98 ***Exploring the Potential of Forecasting Fish Distributions in the North East Atlantic With a Dynamic Earth System Model, Exemplified by the Suitable Spawning Habitat of Blue Whiting***
Anna K. Miesner, Sebastian Brune, Patrick Pieper, Vimal Koul, Johanna Baehr and Corinna Schrum

121 ***Planktic Foraminiferal Assemblages in Surface Sediments From the Subpolar North Atlantic Ocean***
Nibedita Sahoo, Syed Mohammad Saalim, Alexander Matul, Rahul Mohan, Anna Tikhonova and Nina Kozina

140 ***Declining Pre-bloom* Calanus finmarchicus *Egg Production Adjacent to Two Major Overwintering Regions in the Northeastern Atlantic***
Sólvá Jacobsen, Eilif Gaard and Hjálmar Hátún

151 ***Comparison Between Trophic Positions in the Barents Sea Estimated From Stable Isotope Data and a Mass Balance Model***
Torstein Pedersen

169 *Horizontal and Vertical Migration of Anglerfish* **Lophius piscatorius** *in Relation to Hydrography in Faroese Waters*
Lise Helen Ofstad, Hjálmar Hátún, Torstein Pedersen, Petur Steingrund and Bjarni Mikkelsen

186 *Spatial Variability of the Feeding Conditions for the Norwegian Spring Spawning Herring in May*
Inga Kristiansen, Hjálmar Hátún, Jan Arge Jacobsen, Sólvá K. Eliasen, Hildur Petursdottir and Eilif Gaard

200 *Impacts of a Changing Ecosystem on the Feeding and Feeding Conditions for Atlantic Salmon During the First Months at Sea*
Kjell Rong Utne, Øystein Skagseth, Vidar Wennevik, Cecilie Thorsen Broms, Webjørn Melle and Eva B. Thorstad

213 *Arctic and Atlantic Waters in the Norwegian Basin, Between Year Variability and Potential Ecosystem Implications*
Øystein Skagseth, Cecilie Broms, Kjell Gundersen, Hjálmar Hátún, Inga Kristiansen, Karin Margretha H. Larsen, Kjell Arne Mork, Hildur Petursdottir and Henrik Søiland

227 *Temporal Variability of Co-Occurring* **Calanus finmarchicus** *and* **C. helgolandicus** *in Skagerrak*
Tone Falkenhaug, Cecilie Broms, Espen Bagøien and Nikolaos Nikolioudakis

244 *Prevalence of* **Kudoa thyrsites** *(Myxozoa, Multivalvulida) in Atlantic Mackerel,* **Scomber scombrus** *L., in the Vicinity of the Faroe Islands*
Dánjal Petur Højgaard, Eydna í Homrum and Ian Salter

254 *Relationship Between Plankton Dynamics and Growth of the Long-Lived Clam* **Arctica islandica** *on the Faroe Shelf*
Una Matras, Ian Salter, Karin Margretha H. Larsen, Eilif Gaard and Petur Steingrund

273 *Changes Towards Stable Good Somatic Condition and Increased Gonad Investment of Norwegian Spring-Spawning Herring (***Clupea harengus***) After 2005 are Linked to Extended Feeding Period*
Eydna í Homrum, Guðmundur J. Óskarsson, Kotaro Ono, Sondre Hølleland and Aril Slotte

frontiers | Frontiers in Marine Science

TYPE Editorial
PUBLISHED 26 October 2022
DOI 10.3389/fmars.2022.1062204

Check for updates

OPEN ACCESS

EDITED AND REVIEWED BY
Ming Li,
University of Maryland, College Park, United States

*CORRESPONDENCE
Hjálmar Hátún
hjalmarh@hav.fo

SPECIALTY SECTION
This article was submitted to Physical Oceanography, a section of the journal Frontiers in Marine Science

RECEIVED 05 October 2022
ACCEPTED 11 October 2022
PUBLISHED 26 October 2022

CITATION
Hátún H, Silva TSG, Skagseth Ø and Grønkjær P (2022) Editorial: Physical drivers of biogeographical shifts in the Northeastern Atlantic – and adjacent shelves.
Front. Mar. Sci. 9:1062204.
doi: 10.3389/fmars.2022.1062204

COPYRIGHT
© 2022 Hátún, Silva, Skagseth and Grønkjær. This is an open-access article distributed under the terms of the Creative Commons Attribution License (CC BY). The use, distribution or reproduction in other forums is permitted, provided the original author(s) and the copyright owner(s) are credited and that the original publication in this journal is cited, in accordance with accepted academic practice. No use, distribution or reproduction is permitted which does not comply with these terms.

Editorial: Physical drivers of biogeographical shifts in the Northeastern Atlantic – and adjacent shelves

Hjálmar Hátún[1]*, Teresa Sofia Giesta da Silva[2], Øystein Skagseth[3] and Peter Grønkjær[4]

[1]Faroe Marine Research Institute (FAMRI), Environmental Division, Tórshavn, Faroe Islands, [2]Marine and Freshwater Research Institute (MFRI), Pelagic Division, Reykjavik, Iceland, [3]Institute of Marine Research (IMR), Oceanography and Climate Division, Bergen, Norway, [4]Department of Aquatic Biology/Arctic Research Centre, Aarhus University, Århus, Denmark

KEYWORDS

ecological indicators, physical drivers, biogeography, climate, North Atlantic

Editorial on the Research Topic

Physical drivers of biogeographical shifts in the Northeastern Atlantic – and adjacent shelves

Climate change is affecting ecosystems, both marine and terrestrial, and this makes it critically important to improve our understanding of couplings between environmental change – natural or human-induced - and the biology and ecology of marine organisms. As illustrated in the logo associated with the present Research Topic (RT), this theme is inspired by the dynamics of the North Atlantic subpolar gyre (SPG) and its interaction with the Atlantic inflow (poleward arrow) and the returning cold subarctic water masses (equatorward arrow) - collectively referred to as the Atlantic Meridional Overturning Circulation (AMOC). During the last ~15 years, research has shed light on the importance key physical drivers, such as the SPG, on the dynamics of all trophic levels in the subpolar North Atlantic (SPNA). The present RT elaborates on linkages between the changing physical and biogeochemical environment and the organisms inhabiting this mid- to high latitude area.

The concept of biogeographical zones and ecoregions with large areas sharing similar physical, biogeochemical and biological characteristics is presently making a come-back in marine science. When two different water masses rest against each other they create frontal zones delineating biogeographic boundaries across which the physical properties and biological assemblages change rapidly over short distances. The outlines of oceanic gyres are determined by such water mass boundaries, and therefore constitute frontal zones and biogeographical boundaries. Changes in gyre size and circulation strength warp the biogeographic morphology directly, as well as regulating the transport of water between biomes. This justifies our inclusion of the word 'biogeography' in the title of this RT.

The 19 papers compiled in this RT cover the entire SPNA, from the Labrador Sea in southwest, the North Sea and Skagerrak in southeast to the Barents Sea, Svalbard and the

Iceland Sea in the north. All trophic levels are represented, with *physical oceanography and biogeochemistry* here referred to as the 0-th level, *primary producers* (e.g. phytoplankton, 1st level), *secondary producers* (e.g. zooplankton, 2nd level) and *fish/predators* (3rd level). Unfortunately, no contribution has addressed sea mammals or seabirds. In this editorial, we will introduce each paper by a categorization into the following five recurrent themes: *1) Phenology, 2) Spatial segregation, 3) Biological hotspots, 4) Regime shifts and 5) Long-term trends*. The papers generally discuss more than one of these themes, and after their initial introduction, this will be referred to by in-text citations. The trophic levels addressed will also be noted, with several papers addressing more than one level.

Phenological change

Phenology is the study of periodic events in a biological life cycle, and the timing of these events are influenced by seasonal and interannual variations. This RT clearly documents the phenological changes occurring in the SPNA and its potential effects on the linkages between trophic levels.

Using two models based on satellite observations of surface chlorophyll-a, light and temperature, Richardson and Bendtsen (level 1) show that the seasonal pattern and distribution of primary production differ in the SPG south of the Greenland-Scotland ridge and surrounding water masses probably due to differences in mixed layer depth. Silva et al. (levels 0 and 1) segregate the Barents Sea, Norwegian Sea and the North Sea into smaller regions with similar climatological and interannual trends in phytoplankton bloom onset, peak day and duration based on remote sensing data. Moving one trophic level up to zooplankton, Falkenhaug et al. (level 2) show that the annual abundance peak in the copepod species *Calanus finmarchicus* and *Calanus helgolandicus* in Skagerrak have advanced by about a month since 1994. In addition, the seasonal pattern of *C. helgolandicus* switched from a unimodal to a bimodal pattern, around the year 2002, with a small additional peak also appearing in spring. While these key copepods have advanced their phenological cycle, the Norwegian spring spawning herring has prolonged their feeding period into the late autumn, especially in a feeding hotspot east of Iceland (Homrum et al., level 3). This clear shift after 2005, could be caused by the emergence of a second generation of their preferred prey, *C. finmarchicus*, appearing in the autumn.

Biogeographical segregation within the SPNA

Using sediment samples along a zonal transect along 59.50°N, from the Labrador Sea to the Faroe-Shetland Channel, Sahoo et al. (level 1) were able to assign planktonic foraminifera assemblages into three main groups: A cold/polar group in the Labrador Sea, a mixed (both cold and warm) group in the Irminger Sea, and a warmer temperate group in the eastern part of the transect. Spatial segregation of phytoplankton groups and traits is also discussed by the already introduced studies by Richardson and Bendtsen, and Silva et al. Sharp lateral contrasts in zooplankton abundances and species composition are observed east of Iceland (Kristiansen et al. levels 0,2,3), with high biomass composed of overwintering stages of *C. finmarchicus* and *Calanus hyperboreus* in subarctic waters, contrasted with smaller stages of *C. finmarchicus* and absence of *C. hyperboreus* in the Atlantic water immediately south of the Iceland-Faroe Front. This segregation is also evident in the stomach content of herring in this region.

Water mass boundaries similarly govern the spawning distribution of blue whiting west of the British Isles (Miesner et al. levels 0, 3), as this boreal species has an affinity for the relatively warm Atlantic waters and avoids the subarctic waters, which can flush the Rockall-Hatton Plateau during periods when the SPG is strong.

As well as being separated laterally, water masses are also 'stacked' upon each other. The biomes are therefore structured in three dimensions; latitude, longitude and depth. Around the Faroe Plateau, Atlantic waters are overlying both Arctic intermediate waters deriving from the Iceland and Greenland Seas, and very cold overflow waters – the deep branch of the AMOC. This sharp 3-D biogeographical structure is utilized by e.g. anglerfish, which seek the main interface between warm and cold waters during the winter/spring spawning period, and migrate to central parts of the Faroe shelf during the summer/fall feeding period (Ofstad et al. levels 0 and 3).

Connectivity and predictability

The biogeographic boundaries are associated with large current systems, which induce down-stream connectivity, advective time lags and thus potential predictability as evidenced by Miesner et al. They show that shifting water mass distribution and water mass advection induce predictability of the environmental conditions in the spawning are of blue whiting in the Rockall Region by about one year ahead (Miesner et al.).

The major currents systems in SPNA create a broad, but spatially variable, boreal biome and pelagic fish species like blue whiting and mackerel migrate from the Rockall region towards the down-stream fringes of this biome. Strong hydrographic anomalies, recurrently manifesting in the Rockall region, can impact sea-ice coverage and primary production in the Barents Sea after a time lag of 4-5 years (Koul et al. levels 0, 1 and 3), which subsequently impacts the biomass of cod in this northerly region.

Like water masses and biogeographic zones, connectivity also has a depth dimension. The cold, low-saline and nutrient and zooplankton rich subarctic waters from the Iceland/

Greenland Seas slide iso-pycnally eastwards under the Atlantic inflow. This transports nutrients and large and energy-rich zooplankton (*C. finmarchicus* and *C. hyperboreus*) species to intermediate depths along the north Faroe slope (Kristiansen et al.), and east towards the Norwegian slope (Skagseth et al. levels, 0 and 2). Skagseth et al. suggest that that the amount of Arctic waters and its concentration of nutrients and zooplankton are more important for the Norwegian Basin ecosystem functioning than the - more frequently discussed - temperature of the Atlantic waters. The connectivity from the East Iceland Current might even reach south into the Norwegian Trench, and thus have an impact on the zooplankton composition on the south Norwegian shelf (Falkenhaug et al.). There is, furthermore, a tight correlation between the oceanic conditions just downstream from the East Icelandic Current (proxied by the sea surface height) and the overflow transport through the Faroe Bank Channel (Hátun et al. level 0).

Biological hotspots

Elevated primary production and the confluence of water masses at ocean fronts collectively lead to increased abundances of zooplankton, and this attracts higher trophic level predators. Using a spatio-temporally comprehensive plankton production dataset (phytoplankton and spawning activity and egg production rates of *C. finmarchicus*) covering the Faroe shelf (1997-2020), Jacobsen et al. (levels 0, 1 and 2) demonstrate that the highest production takes place in the main inflow branch of oceanic water onto the permanently well mixed inner shelf. The confluence of subarctic and Atlantic waters east of Iceland also creates a feeding hotspot, where – before 1999 and after 2004 - older year-classes of herring did tightly congregate during the early seasonal feeding period (Eliasen et al., 2021, level 3). Into the late autumn months, the herring have shifted their main feeding area closer to the East Iceland shelf, into the main inflow branch of Atlantic water (Homrum et al.). A similar confluence of water masses with contrasting properties likely induced a biological hotspot west of Ireland, which can explain why large fish stocks such as blue whiting and mackerel select this region as their main spawning domain (Miesner et al.).

Regime shifts in the SPNA

Oceanic regime shifts are large, sudden changes in the marine climate that entails changes in the internal dynamics and feedbacks of an ecosystem and last substantial periods of time. Previous research described major shifts in the SPNA during the mid-1990s (e.g. Hátún et al., 2009). Many papers in the present RT report on similar marked changes during the early 2000s. During this period, the subpolar gyre circulation became historically weak, which led to high temperatures and salinities in the spawning region of blue whiting (Miesner et al.). This translated downstream to a temperature increase in the waters on the Iceland-Faroe Ridge (Hátún et al.) and all the way to the Barents Sea (Koul et al.). In concert, the Norwegian Sea gyre weakened abruptly during 2002-2003, which caused the Atlantic inflow/boreal zone to widen and led to a transport peak in the Faroe-Bank Channel overflow (Hátún et al.). The influx of western waters (both Arctic Intermediate Water and Modified East Icelandic Water) into the southern Norwegian Sea weakened (Hátún et al.; Skagseth et al.), and the abundance of the Arctic calanoid *C. hyperboreus* decreased both north of the Faroes (Kristiansen et al.) and along the Norwegian slope (Skagseth et al.). Skagseth et al. therefore refer to the post-2003 years as an *Atlantic period*. The abundances of *C. finmarchicus* and *C. helgolandicus* changed on the south Norway shelf, and the seasonality of *C. helgolandicus* shifted from a unimodal fall peak to a bimodal pattern, with an emerging spring peak around 2002 (Falkenhaug et al.). As mentioned, herring started to congregate near the East Iceland Current during May (Eliasen et al.) and prolonged their feeding activity near the east Icelandic slope after 2003 (Homrum et al.). Whether this is a sign of food deprivation during the early feeding season or increased food abundance later in the season remains an unresolved question. The feeding of Atlantic salmon post smolts also changed dramatically after the early 2000s shift, whereafter the stomach fullness of this species, consisting primarily of copepods, amphipods and fish larvae, was considerably reduced (Utne et al. levels 1,3)

On the Faroe shelf, the growth of the long-lived clam *Arctica islandica* decreased after 2003 (Matras et al. levels 0-3), which the authors ascribe to reduced advection of zooplankton from the East Icelandic Current – a hypothesis that involves trophic interaction with the on-shelf bloom and grazing pressure from juvenile fish. Oppositely there was a major boom in the abundance of the boreal anglerfish on the Faroe shelf during the warm early 2000s (Ofstad et al.). The *early 2000s shift* is so broad and consistent, that it justifies the term regime shift. However, while many of the mentioned ecological changes have persisted since around 2003, some merely portrayed a peak around this time.

After 2016, the southern Norwegian Sea has shifted back from the Atlantic period to a more (sub)Arctic period, with stronger influx of Icelandic waters (Skagseth et al.), more subarctic zooplankton species (Kristiansen et al.) and improved feeding conditions for Atlantic salmon (Utne et al.). However, while salinity indeed has decreased much, temperatures have remained high since 2016.

Long-term trends

Observations of uni-directional trends can be due to relatively short records of natural cycles with long periodicities (e.g. the Atlantic Multi-decadal Oscillation) or real trends in the system, potentially caused by anthropogenic influence (e.g. climate change). Based on satellite data series, Konik et al. (level 1), find that the

Svalbard fjords have become darker (reduced light availability) during the last two decades, and suggest that this likely is a symptom of transformations in the environment. Also based on remote sensing data, Silva et al. report on a rapid delay in the onset and increased biomass of the summer blooms during the past 21 years throughout most of the Barents, Norwegian and North Seas. Regarding zooplankton, individual egg production rates and the fraction of spawning females of *C. finmarchicus* have declined throughout the Faroe shelf since 1997 (Jacobsen et al.). Since this last finding is based solely on zooplankton data from late April, it is uncertain whether this reflects a change in phenology or if this represents the annual reproduction of this species.

Two papers do not fit into our categorization above. Northward shifts in host-parasite related infectious diseases, with human health and socio-economic impacts, have been linked to climate warming stress. Højgaard et al. (level 2) describe infection of Atlantic mackerel (*Scomber scombrus*) for the years 2017 and 2018 by the myxozoan parasite *Kudoa thyrsites*, leading to myoliquefaction that renders this fish commercially unviable. It is hypothesized that the infection has occurred in the southern spawning areas, and that infected fish migrate north. Pedersen (levels 1-4) presents a comparison of trophic position estimates from stable-isotopes and an Ecopath mass-balance food web model for the Barents Sea. This study, based on a broad selection of animal species, generally shows good correspondences between the two analysis approaches.

This RT on physical drivers in the SPNA provides a 'bottom-up' perspective on observed marked ecosystem changes in this biologically productive region. This is a limitation because commercial fisheries and other human-induced 'top-down' effects do also play major roles. However, since the projected climate changes are expected to primarily disturb bottom-up processes, we find it urgently important to expand our knowledge on this interplay.

Author contributions

HH composed the first version of this Editorial, which TS, ØS and PG have commented on, and contributed to. All authors contributed to the article and approved the submitted version.

Funding

HH was supported by the Faroese Research Council, project number 8013 and ØS was supported by the Research Council of Norway, (grant no. 299554). We wish to thank Dr. Guðmundur Óskarsson, head of the pelagic division at the MFRI, for his support to this Research Topic.

Conflict of interest

The authors declare that the research was conducted in the absence of any commercial or financial relationships that could be construed as a potential conflict of interest.

Publisher's note

All claims expressed in this article are solely those of the authors and do not necessarily represent those of their affiliated organizations, or those of the publisher, the editors and the reviewers. Any product that may be evaluated in this article, or claim that may be made by its manufacturer, is not guaranteed or endorsed by the publisher.

Reference

Hátún, H., Payne, M. R., Beaugrand, G., Reid, P. C., and Sandø, A. B. Drange, H. (2009). Large bio-geographical shifts in the north-eastern Atlantic Ocean: From the subpolar gyre, via plankton, to blue whiting and pilot whales. *Progress in Oceanography* 80 (3-4), 149–162. doi: 10.1016/j.pocean.2009.03.001

frontiers in Marine Science

ORIGINAL RESEARCH
published: 29 July 2021
doi: 10.3389/fmars.2021.694614

The Norwegian Sea Gyre – A Regulator of Iceland-Scotland Ridge Exchanges

Hjálmar Hátún[1], Léon Chafik[2] and Karin Margretha Húsgarð Larsen[1]*

[1] Faroe Marine Research Institute, Tórshavn, Faroe Islands, [2] Department of Meteorology and Bolin Centre for Climate Research, Stockholm University, Stockholm, Sweden

The Norwegian Sea gyre (NSG) is a large body of Arctic intermediate water and deep dense overflow waters, which circulate counterclockwise within the Norwegian Sea. Argo float trajectories presented in this study suggest that the NSG attains its strongest and most focused flow downstream of a confluence of subarctic waters from the Iceland Sea and the Jan Mayen Ridge at steep bathymetry north of the Faroe slope. Based on hydrographic data from a meridional standard section across this flow (1988 to present), the first baroclinic estimate of the NSG circulation strength is provided. We, furthermore, show that the NSG circulation regulates key aspects of both the poleward Atlantic Water (AW) currents and the equatorward near-bottom and mid-depth flows in the Norwegian Sea – the main arteries of the Meridional Overturning Circulation. More specifically, we demonstrate close links between the NSG circulation and (i) the observed Faroe Bank Channel Overflow (FBCO) transport, (ii) variable depth of the main thermocline separating AW from the underlying colder and denser subarctic water masses, and (iii) satellite-derived sea-surface heights (SSHs) in the southern Nordic Seas. In general, a strong NSG and weak FBCO transport are associated with an uplifted thermocline and depressed SSH. Along a narrow band near the Norwegian and Shetland slopes, a strong NSG – oppositely – links to a depressed interface. Daily records of the FBCO transport, and satellite altimetry in a sensitive region north of the Iceland-Faroe Ridge, complement our hydrographic monitoring of the NSG strength. Together these records constitute valuable indicators for aspects of the Norwegian Sea physical oceanography, which likely have an impact on regional climate, ecology and biological productivity.

Keywords: overflow, Atlantic inflows, main thermocline, Norwegian Sea Gyre, ecological indicator

OPEN ACCESS

Edited by:
Benjamin Rabe, Alfred Wegener Institute, Helmholtz Centre for Polar and Marine Research (AWI), Germany

Reviewed by:
Andreas Macrander, Marine and Freshwater Research Institute, Iceland
Robert Pickart, Woods Hole Oceanographic Institution, United States

****Correspondence:***
Hjálmar Hátún
hjalmarh@hav.fo

Specialty section:
This article was submitted to Physical Oceanography, a section of the journal Frontiers in Marine Science

Received: *13 April 2021*
Accepted: *02 July 2021*
Published: *29 July 2021*

Citation:
Hátún H, Chafik L and Larsen KMH (2021) The Norwegian Sea Gyre – A Regulator of Iceland-Scotland Ridge Exchanges. Front. Mar. Sci. 8:694614. doi: 10.3389/fmars.2021.694614

INTRODUCTION

Total volume and heat transports from the North Atlantic to the Nordic Seas are estimated from observations along monitoring arrays at the Greenland-Scotland Ridge (Hansen and Østerhus, 2000; Hansen et al., 2015). Whether these heat anomalies actually reach the high Arctic is, however, strongly determined by the flow dynamics within the Nordic Seas – especially in the eastern part. Realistic prediction of such anomalies in model systems requires proper representation of critical regional oceanic processes.

In the northeastern Atlantic, variable eastward extent and circulation intensity of the subpolar gyre (SPG – abbreviations are provided in **Table 1** and **Figure 1**) determines the relative contribution of Atlantic and subarctic source water masses to the resulting Modified North Atlantic Water (MNAW, and here referred to as just AW – **Table 2**), which subsequently feeds the Atlantic inflows toward the Arctic (Hátún et al., 2005a). AW enters the Nordic Seas as a new source water mass, where it interacts with the subarctic water masses of the Norwegian Sea Gyre (NSG; **Figure 1**), producing even more modified waters in this region (Read and Pollard, 1992). Source AW also enters the Nordic Seas through the Faroe-Shetland Channel, where it encounters a limb of the NSG extending into this channel (Hátún, 2004; Hansen et al., 2017; **Figure 1**). In this way, AW flows cyclonically around the southeastern Norwegian Sea, wedged between the continental slopes [north of the Iceland-Faroe Ridge (IFR), Faroe Plateau and west of Norway] and the body of the NSG.

Although the NSG is less flexible for lateral shifts compared to the SPG, its southward and eastward extent does also shift. As such, we here hypothesize that the NSG is a regulator of the main water masses in the southeastern Nordic Seas. That is, the NSG might play a mediating role within the Nordic Seas, comparable to the SPG regulation of the oceanography in the northeastern North Atlantic (Hátún et al., 2005a; Hátún and Chafik, 2018).

Variable westward AW extent is synonymous with the zonal position of the subarctic front in the eastern Norwegian Basin, and this issue has been observed and discussed over decades (Blindheim et al., 2000; Mork and Blindheim, 2000). The dynamics of this subarctic front – which north of the Faroes is called the Iceland-Faroe front – is directly linked to undulations in the main thermocline between the warm AW and the underlying subarctic water masse. This *interface*, as it hereafter will be referred to, is suggested to respond to the large-scale wind field, i.e., the North Atlantic Oscillation (NAO). Weak/strong NAO periods (denoted NAO− and NAO+, respectively) lead depressed/uplifted states, respectively, of the interface along the Faroe and Norwegian slopes (Mork and Blindheim, 2000; Richter and Maus, 2011).

Using a two-layer reduced gravity model, Orvik (2004) proposed a link between the flow directionality of the lower layer and the width and depth of the AW wedge. More specifically, he pointed out that when the deep topographically steered flow follows (opposes) that of the AW, the wedge area is reduced (expanded) and the interface separating the two main water masses deepens (shoals) as a result of a convergence (divergence) of AW locally. The link between the wind forcing in the Nordic Seas, the AW width and the interface depth must therefore involve changes in the deep currents.

Deep waters from the NSG and/or its immediate surroundings are funneled out through the narrow Faroe Bank Channel (FBC; **Figure 1**), and continuous observations of the Faroe Bank Channel Overflow (FBCO) transport are available since the mid-1990s (Hansen et al., 2016). Model experiments (Köhl, 2010; Serra et al., 2010) and a recent study combining both a high-resolution ocean general circulation model and observations from multiple platforms (Chafik et al., 2020) show that the FBCO is fed *via* two pathways – a western source from along the Faroe slope and an eastern source along the Norwegian slope region. Both branches converge into the newly discovered southwestward directed deep Faroe-Shetland Channel jet (FSCJ), located at the base of the Shetland slope (Chafik et al., 2020; **Figure 1**), before feeding the FBCO.

These three key aspects of the Norwegian Sea – the NSG, the interface depth and the FBCO – have all previously been separately linked to changes in sea-surface height (SSH). A wind-driven barotropic model by Nøst and Isachsen (2003) suggests a close link between the deep NSG-related flow and the SSH over the central Norwegian Sea. The most pronounced SSH variability is, however, observed over the AW wedge in the southeastern Norwegian Sea (Richter et al., 2012). It has been linked to undulations of the interface and to the hydrographic properties (density) of the AW – both through the steric relation (Siegismund et al., 2007; Richter et al., 2012). Variability in the FBCO is shown to correlate with the simulated SSH in the central Norwegian Basin (Olsen et al., 2008), and with satellite altimetry data integrated over a broad region farther north (Bringedal et al., 2018). It is, however, not clear where the most plausible drivers of FBCO variability (pressure, interface height, and SSH) have their center-of-action.

Since only water associated with the boundary current around the Norwegian basin can be in direct contact with the FBCO (Yang and Pratt, 2013) direct causal linkages between the overflow and SSH must be found within a bottom depth range comparable to the FBC sill depth (840 m).

The FBCO is likely driven by the southward pressure gradient between the Norwegian Sea and the northeast Atlantic pressure at the FBC sill depth (Olsen et al., 2008). This is, in turn, regulated by the height of the interface above the sill depth. Model studies confirm this expected link between stronger FBCO and a higher upstream interface (Sandø et al., 2012), but this link is only identifiable to the Shetland slope, and thus to the overflow-feeding FSCJ (Chafik et al., 2020). Also based on adjoint sensitivity calculations (a tool that helps to determine mechanisms of a chosen variable), Köhl, 2010 used the sensitivities $\partial \mathrm{FBCO}/\partial h_{27.8}$ to describe at which location perturbations of the local height of the $\sigma_\theta = 27.8$ surface ($h_{27.8}$) changes the FBCO most. This analysis showed that the interface height just north of the IFR is particularly sensitive to the FBCO transport variability (Köhl, 2010, their Figure 11B). This "negative sensitivity" between the overflow and the interface came as a surprise to these authors, who

TABLE 1 | List of abbreviations, arranged in alphabetical order.

Acronym	Name
FBCO	Faroe Bank Channel Overflow
FSCJ	Faroe-Shetland Channel Jet
IFSJ	Iceland-Faroe Slope Jet
NAO	North Atlantic Oscillation
NSG	Norwegian Sea Gyre
SPG	Subpolar Gyre
SSH	Sea-surface height

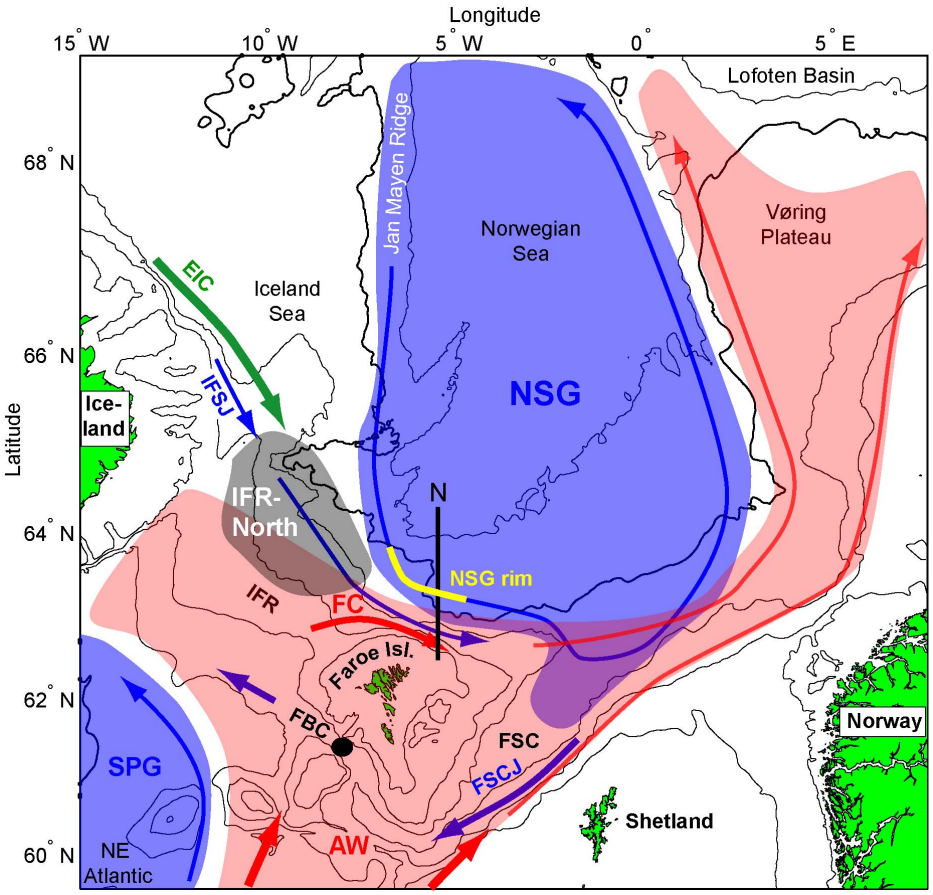


FIGURE 1 | Overview over the study region. The counterclockwise circulating Norwegian Sea Gyre (NSG) and the subpolar gyre (SPG) – composed of cold and dense subarctic waters – are highlighted in blue color. The *NSG rim* is outlined in yellow color and the IFR-North region is illustrated in gray. Poleward flowing AW are shown in red. The location of monitoring Section N is illustrated with a black line. FBC, Faroe Bank Channel; IFR, Iceland-Faroe Ridge; FSC, Faroe-Shetland Channel; FSCJ, Faroe-Shetland Channel Jet; IFSJ, Iceland-Faroe Slope Jet; FC, Faroe Current; and EIC, East Icelandic Current. The following depth contours are plotted: 200, 500, 1000, 2000 (heavy contour line), and 3000 m.

TABLE 2 | List of water mass abbreviations.

Acronym	Name	Temperature range	Salinity range
(MN)AW	(Modified North) Atlantic Water	>7°C	35.00 → 35.35
MEIW	Modified East Icelandic Water	1 → 3°C	<34.90
NNAW	Norwegian North Atlantic Water	2.5 → 3.2°C	34.96 → 34.99
NSAIW	Norwegian Sea Arctic Intermediate Water	−0.5 → 0.5°C	34.87 → 34.91
NSDW	Norwegian Sea Deep Water	<−0.5°C	34.90 → 34.92

could not provide a satisfactory explanation thereof. The present article presents a possible explanation of this apparent conundrum (see section "Contrasting NSG+/NSG− States and Possible Drivers").

Direct observations of the NSG intensity are not available, and only general aspects of this gyre system have been illustrated, e.g., using Lagrangian data sources – Argo floats (Voet et al., 2010), RAFOS floats (Søiland et al., 2008), and surface drifters (Jakobsen, 2003). Spatial structures are, however, lost in such studies due to the mapping of data onto relatively coarse grids. The idealized model by Nøst and Isachsen (2003) predicts strong bottom-intensified flows where the seabed topography is steep. At the steep bathymetry along the shallow part of the north Faroe slope (∼700–1100 m), Semper et al. (2020) have recently discovered the presence of the so-called Iceland-Faroe Slope Jet (IFSJ; **Figure 1**). This jet brings intermediate depth waters from the Iceland Sea toward the southeastern Norwegian Sea. Numerical model outputs suggest the presence of an even stronger deep flow farther north, where the seabed deepens from about 2000 to 3000 m (Dale, 2019). A standard meridional monitoring section (Section N, **Figure 1**) cuts across these two deep flow cores (Hansen and Østerhus, 2000). These observations have hitherto primarily been used to estimate transports of the Atlantic inflow, although recent studies have also focused on

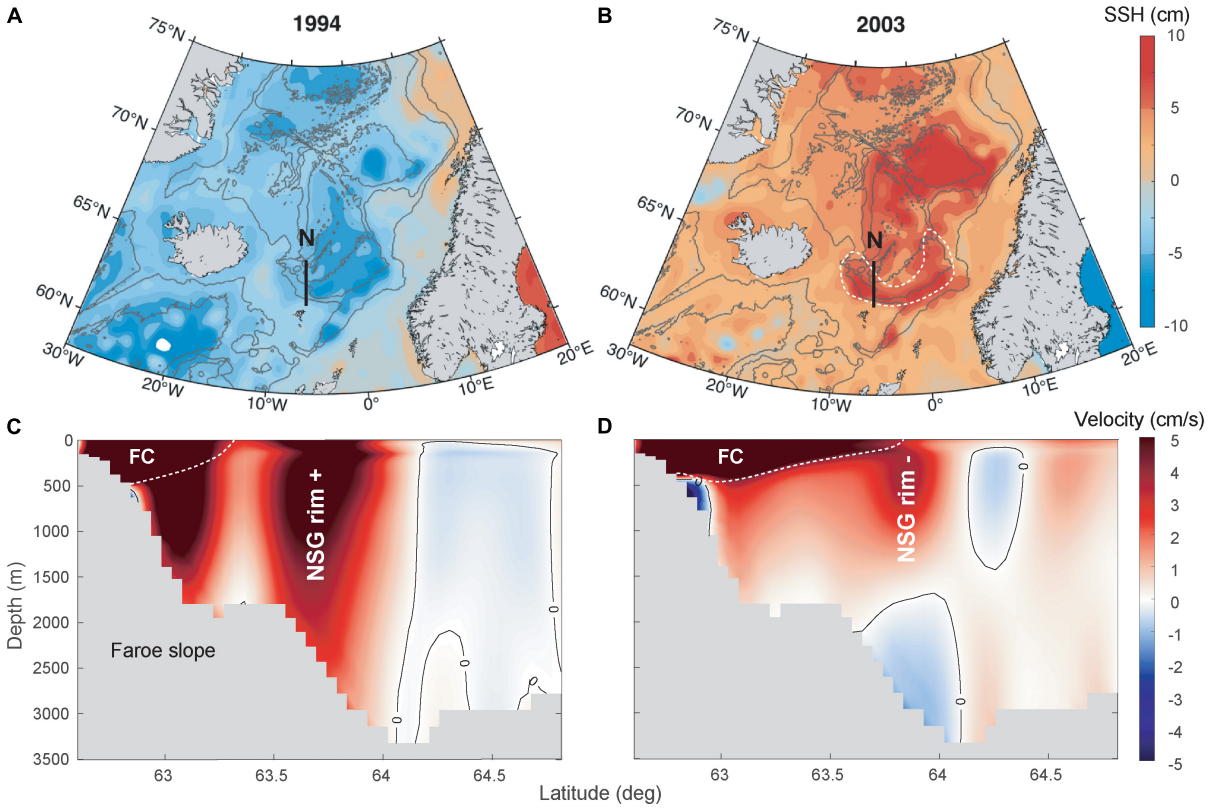


FIGURE 2 | Contrasting states of the NAO and the Norwegian Sea Gyre. Left panels show a NAO+/NSG rim+ state (year 1994) and the right a NAO−/NSG rim− state (year 2003). The upper panels show annually averaged SSH anomalies (deseasonalized and detrended satellite altimetry data) and the lower panels show annually averaged simulated eastward current velocities through Section N (black lines in **A,B**). The approximate position of the interface (dashed white curves in **C,D**) marks the lower boundary of the Faroe Current (FC). The horseshoe-shaped band is illustrated in **(B)** with the dashed white outline.

the influence of the deeper IFSJ (Semper et al., 2020), and the eastward flow of Modified East Icelandic Water (MEIW) (Kristiansen et al., 2016, 2019). Dynamics of the deep flow core (between the 2000 and 3000 m isobaths), which likely carries the highest transport through Section N, has not been studied previously.

Climatic changes are expected to have strong impacts on high latitude oceans, and this calls for continuous and comprehensive monitoring of key aspect of these waters. The recent results by Chafik et al. (2020) and Semper et al. (2020) warrant an updated understanding of the deep flows in the southern Nordic Seas, and modern ocean science aims at a thorough integration of physical, biogeochemical and biological characteristics of such systems. Our motivation with the present study is to start meeting these challenging demands.

By combining hydrographic data from the northern part of Section N, spatio-temporally comprehensive satellite altimetry, updated inventories of Lagrangian Argo data, and model simulations we show that the fundamental aspects of the Norwegian Sea – the NSG, the interface height and the FBCO – are actually interlinked. This provides a new perspective on the Norwegian Sea and its surroundings, which could enable a more holistic understanding of climatic, oceanographic, and ecological aspects of this biologically rich region. Based on this new knowledge, we want to construct key indicator records, which could guide interdisciplinary work in this complex northern region, in a similar way as the SPG index has successfully done for the North Atlantic. The article is organized as follows. Data and methods are presented in section "Data and Methods," results in section "Results" before these are discussed in section "Discussion." The section "Conclusion and Outlook" ends the article.

DATA AND METHODS

Numerical Simulations – NEMO

We use the three-dimensional velocity, temperature, and salinity fields from a simulation of the global ocean using the NEMO ocean model, version 3.6. The simulation, ORCA0083-N001, uses a global grid of nominally 1/12° horizontal resolution and 75 vertical z-star levels. We choose to use a relatively high-resolution model since it is able to explicitly resolve much of the mesoscale eddy–eddy and ocean–atmosphere interactions but also the narrow boundary currents. This is unlike lower resolution models, where such processes are not well represented. The ocean model is forced by the DRAKKAR forcing set v5.2, which is based on the ERA-40 and ERA-interim reanalysis for the

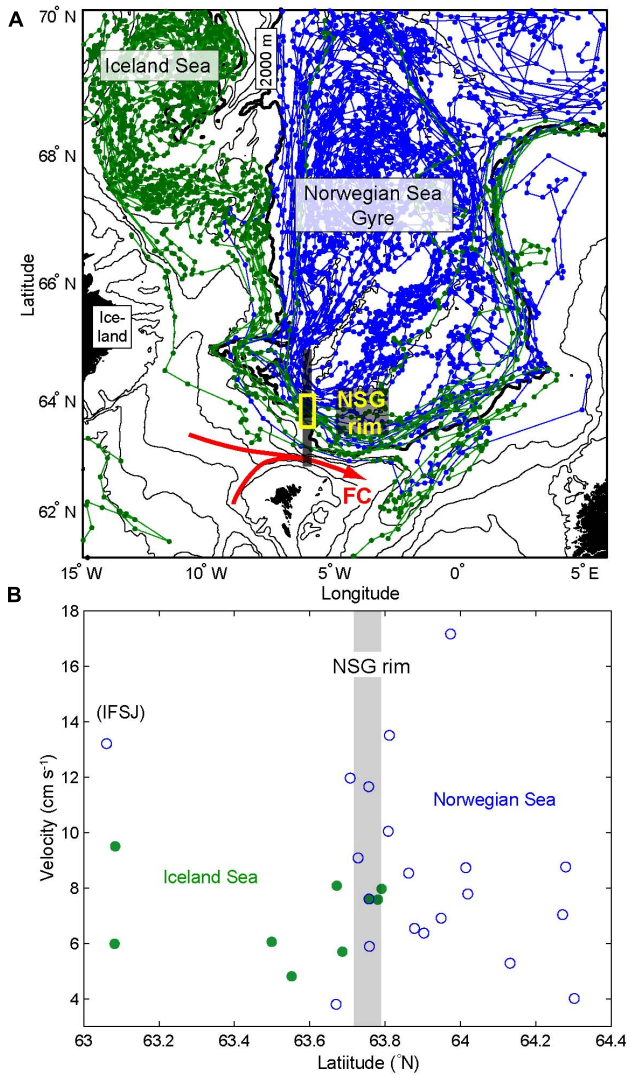


FIGURE 3 | Argo floats. **(A)** Drift trajectories of all available floats which have occupied the Iceland Sea (green) and the Norwegian Sea (blue), respectively. The semi-transparent black line represents Section N, the yellow rectangle shows the location of the NSG rim and the red arrow outlines the Faroe Current (FC). **(B)** Current velocities (*y*-axis) of all the floats crossing Section N, from the Iceland Sea (green) and the Norwegian Sea (blue), respectively. The drift velocities are obtained by interpolating spatially onto this section.

1958–1978 and 1979–2010 period, respectively. The simulation is free-running except for a restoring of sea-surface salinity toward climatology. The model was started from rest in 1958 and run until 2010 (the model output before 1979 is discarded as a model spin-up). In the present work, we only use annual mean zonal velocities along Section N.

Float Trajectories

Float trajectory data are obtained from an Argo-based deep displacement dataset named ANDRO (Ollitrault et al., 2020). The ANDRO atlas ASCII file[1] contains the float parking pressure and temperature, deep and surface displacements, and associated times and deep and surface-associated velocities with their (roughly) estimated errors. From the NetCDF public Argo files, ANDRO first generate a dataset, called DEP (for déplacement, meaning displacement in French) that comprises all the useful information given by the various floats (Ollitrault and Rannou, 2013). Then, the data are checked, corrected, and improved with information gathered outside or through a decoding of the original raw data files. From the final DEP files, the ANDRO atlas is generated. A deep displacement is defined as the distance between the last Argos (or GPS) fix and the first Argos (or GPS) fix of two consecutive cycles.

Hydrographic Data

Section N

Standard Section N consists of 14 stations, labeled N01 to N14, that extend northwards from the Faroe Islands (62.30°N, 6.08°W) into the Norwegian Sea (64.5°N, 6.00°W) (**Figures 1–4**). Since 1988, there have been up to five CTD cruises each year covering this standard section with casts down to the seafloor, or to 1300 m where the bottom depths exceed this value. The maximum bottom depth is 3300 m (at station N14). Typically, cruises have been made in late February, mid-May, late August/early September and early November. After 2011, the monitoring effort was reduced to three cruises each year (the November cruise was terminated).

Large-Scale Data Collection

We use a high-resolution regional (Nordic and Barents Seas) hydrographic database produced by the National Oceanographic Data Center (Korablev et al., 2014) and previously used by e.g., Chafik et al. (2015). It is a compilation of all available data (37 different) sources for the area bounded by 60–82°N, 40°W–70°E (Korablev et al., 2014). This database merges all available oceanographic measurements into one single gridded product. The spatial resolution is 0.25° × 0.25° and annual means have been analyzed. The data have been extensively checked for quality and biases, arising from instruments, were eliminated from the data used in this hydrographic Atlas. Between 1992 and 2012, which is the time period under consideration here, about 60,000 temperature profiles have been compiled in the Nordic Seas. The position of the interface is estimated by the depth of the 3°C isotherm.

Satellite Altimetry

We utilize daily multi-mission satellite altimetry (Pujol et al., 2016) to study the SSH spatial patterns associated with the FBCO transport, the NSG and vertical undulations of the interface. The grid resolution is 0.25° × 0.25° and the period under investigation is between January 1993 and April 2016.

Geostrophic Velocities

Since no direct current observations are available north of the Faroe Current (FC; between stations N08 and N11, described

[1]https://www.seanoe.org/data/00360/47077/#66657

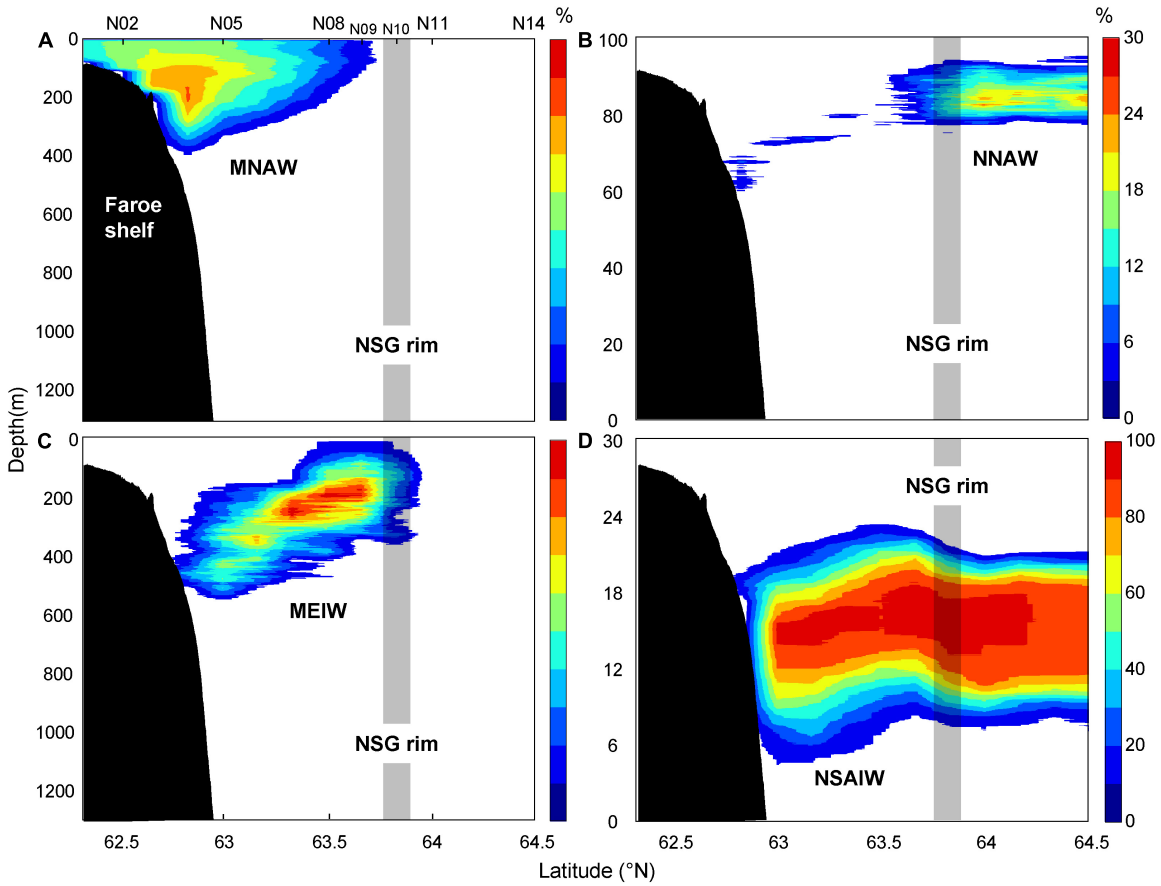


FIGURE 4 | Distribution of the main water masses at Section N (percentages of 103 complete transects between 1988 and 2019 that each latitude-depth data pixel meets the source water mass temperature and salinity criteria in **Table 2**). **(A)** MNAW, **(B)** NNAW, **(C)** MEIW and **(D)** NSAIW. Water mass abbreviations are written in full in **Table 2**. The approximate location of the NSG rim is emphasized with gray bars, and the position of selected standard hydrographic stations are shown in **(A)**.

below), we have to rely on hydrographic data there. By using the thermal wind relation (Cushman-Roisin, 1994), vertical changes in current velocity are proportional to lateral changes in seawater density

$$\frac{\partial u(y,\ z,\ t)}{\partial z} = \frac{g}{\rho_0 f}\frac{\partial \rho(y,\ z,\ t)}{\partial y} \tag{1}$$

where y is lateral (here meridional) distance, z is depth, t is time, g is the gravitational acceleration, ρ_0 is an average density, and f is the Coriolis parameter. Semper et al. (2020) calculated current velocities in the IFSJ region, referenced to the depth of the σ_θ = 27.8 isopycnal ($h_{27.8}$). This isopycnal separates AW from underlying potential overflow water sources. The same approach is used here, but for the deeper current core. Velocity profiles, relative to a reference depth z_0, are in general terms given by

$$u\,(y,\ z,\ t) = \frac{g}{\rho_0 f}\int_{z_0}^{z}\frac{\partial \rho(y,\ z,\ t)}{\partial y}dz \tag{2}$$

here estimated by

$$u_{N,n}\,(y_N,\ z,\ t_n) = \frac{g}{D\,\rho_0 f}\sum_{z_0}^{z}\Delta\rho_{N,n} \tag{3}$$

where N refers to the station numbers (1,…,14), n refers to section number (1,…,103), D = 18.52 km is the distance between the standard stations (10 nautical miles), and $\Delta\rho_{N,n}$ is the density difference between adjacent stations: $\rho\,(y_N,\ z,\ t_n) - \rho\,(y_{N-1},\ z,\ t_n)$. In this study, z_0 is chosen at $h_{27.8}$, and is therefore different for each hydrographic station.

Statistics

Pearson's linear correlation coefficients are calculated using the Matlab® function "corr.m." The presented p-value is the probability of getting a correlation as large as the observed value by random chance, when the true correlation is zero.

RESULTS

Contrasting NAO+ and NAO− States

Annual average conditions during years following particularly NAO high (1994) and NAO low (2003) winters, respectively, are illustrated using altimetry data and simulated current velocities through Section N (**Figure 2**). SSH is depressed/elevated

throughout the NE Atlantic and the Nordic Seas during 1994/2003 (**Figures 2A,B**).

This contrast is particularly pronounced along a horseshoe-shaped band extending from east of Iceland, through Section N and farther eastward along the Norwegian slope. The simulations clearly show two deep flow cores north of the Faroe slope (**Figures 2C,D**). These are resting against steep segments of the Faroe slope roughly between 1000 and 2000 m depths and between 2000 and 3000 m, separated by a region (63.2–63.6°N) with a gentler meridional topographic slope. And the model shows that both cores are much weaker during 2003 (NAO−, **Figure 2D**) as compared to 1994 (NAO+, **Figure 2C**). It should be noted that weakened or even reversal (westward) of the deep flows under the FC core during weak atmospheric forcing such as during 2003 (blue region in **Figure 2D**) have previously been verified by direct current observations (Chafik et al., 2020). No Eulerian current observations are available from the deeper jet. It should also be noted that AW flow in the FC appears to be narrower when the deep jet is strong (1994, dashed curve in **Figure 2C**) and wider when the deep jet relaxes (2003, **Figure 2D**). These results suggest a link between wind forcing, deep flow as well as the main interface between the overlying AW and the underlying denser subarctic waters. And that these processes, furthermore, induce a clear imprint on the SSH field.

Mid-Depth Circulation and Temperatures From Argo Floats

Trajectories of Argo floats show that deep flows from the Iceland Sea (green tracks in **Figure 3A**, all floats parked at 1000 m) and southward deep flows along the Jan Mayen Ridge (floats from 1000, 1200, and 1500 m, blue tracks) merge upstream of Section N. After this confluence, the mid-depth flow concentrates and accelerates along the relatively steep topography north of the Faroe slope (2000–3000 m), whereafter the flow again fans out into 2–3 eastward slower current branches (**Figure 3**). The latitude and speed of the floats, where they cross Section N, is estimated by linear interpolation. Three floats passed under the core of the FC (63.0–63.2°N) – two from the Iceland Sea likely associated with the IFSJ (green dots, **Figure 3B**) – and one from the Norwegian Sea (blue circles). However, the bulk of the floats crossed the section between 63.6 and 64.0°N (**Figure 3B**), with those from the Iceland Sea generally aligning on the southern/shallower side of the jet, and those from the Norwegian Sea congregating on the northern/deeper flank. The 10-days averaged Argo drift velocities in this deeper jet vary between 4 and 17 cm s^{-1} (**Figure 3B**), with an average of 9 cm s^{-1}. Only floats that are parked at 1000 m depths experience drift velocities faster than 10 cm s^{-1}, while those at 1200 and 1500 m did not reach this velocity (depth not shown). The float data thus indicate a mid-depth intensified flow.

We will hereafter refer to the deep jet as the *NSG rim*. Since most floats within the NSG complex are sooner or later being transported by the NSG rim, we postulate that the transport within this narrow and intensified flow represents the circulation strength of the NSG as a whole. We also suggest that this might be an ideal location for monitoring the NSG.

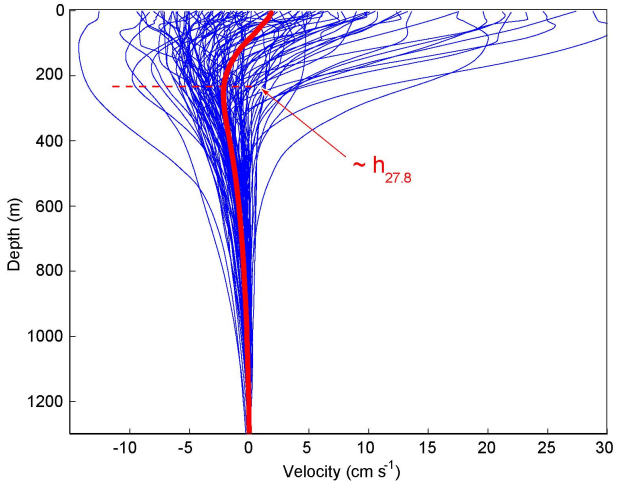


FIGURE 5 | Geostrophic eastward velocity calculations in the NSG rim (between standard stations N09 and N10), relative to z = 1300 m (deepest available data). The blue profiles represent individual occupations of Section N and the averaged of these is shown with the red profile. The average depth of the σ_θ = 27.8 surface ($h_{27.8}$) at this locations, is highlighted.

The NSG Rim at Section N

A Water Mass Boundary

Water mass distributions along Section N (**Figure 4**), are illustrated as percentages (out of 103 complete transects between 1988 and 2019) that each latitude-depth data pixel meets the source water mass temperature and salinity criteria in **Table 2** – adjusted from Hansen and Østerhus (2000). This shows that the NSG rim represents a division zone between the main water masses observed along Section N. It is: (i) the northern limit of the (MN)AW wedge (**Figure 4A**), (ii) the southern limit of the Norwegian North Atlantic Water (NNAW; **Figure 4B**), and (iii) the northern limit of the MEIW tongue (Read and Pollard, 1992; **Figure 4C**). Influence of the NSG rim is also evident at depth by the northward deepening vertical boundaries of the Norwegian Sea Arctic Intermediate Water (NSAIW; 400–800 m, **Figure 4D**). Norwegian Sea Deep Water (NSDW) resides below NSAIW and these two constitute the main overflow source waters (Hansen and Østerhus, 2000).

Limitation Using Satellite Altimetry

Several studies have used satellite altimetry data (SSH) for estimating transports in surface currents (Chafik et al., 2015) – an approach also used for estimating AW transports in the FC (Hátún and McClimans, 2003; Hansen et al., 2015). However, strong near-surface variability (depths > $h_{27.8}$), associated with the variable northward extension of AW (Hansen et al., 2020), prevents us from utilizing altimetry to estimate the deep current variability in the NSG rim. The noise in the upper water above $h_{27.8}$ is much larger than the signal below. It is, however, worth mentioning that the highest correlations between the geostrophic surface current velocities based on the thermal wind relation (referenced to 1300 m) and the SSH gradient from satellite altimetry are indeed identified in

the NSG rim (**Supplementary Figure 2A**). Here, the water column density profile leads the SSH by about a week (**Supplementary Figure 2B**).

A Baroclinic NSG Rim Transport – ψ_{NSG}

Because of the limitation with satellite altimetry, we adopt the approach by Semper et al. (2020), and calculate geostrophic velocities relative the 27.8 kg m^{-3}, and thus to the $h_{27.8}$ depth level. Velocity profiles (relative to 1300 m) in the core of NSG rim (between stations N09 and N10) show that the eastward flows on average weaken up to 200–300 m depths, above which they tend to intensify again (**Figure 5**). This local velocity minimum is generally co-located with $h_{27.8}$. The increase in average velocity from $h_{27.8}$ to 1300 m – a feature unique to the NSG rim (see **Supplementary Figure 1**) – reflects the mid-depth intensification of this deep current jet.

An estimate of the baroclinic NSG rim transport (ψ_{NSG}) is constructed by vertically integrating the geostrophic velocity profiles (see section "Geostrophic Velocities") from $h_{27.8}$ and downwards. From each individual transect (n), we select the highest obtained value within the meridional window between hydrographic stations N08 to N11 (see **Figure 4A**), in order to account for lateral shifts of the NSG rim. This is given as:

$$\psi_{\mathrm{NSG}}(t_n) = W \cdot \max_{N\in\{N08,\ldots,N11\}} \left[\int_{h_{27.8}}^{D} u_{N,n} dz \right] \quad (4)$$

Where $u_{N,n}$ is given by eq. 3 down to 1300 m depth, and where we extrapolate the estimated baroclinic velocity at 1300 m down to the seafloor (see also **Figure 5**). This might be a slight overestimation, since the NSG rim seems to be mid-depth intensified. D and W are unknown representative depths and widths of the NSG rim. The latitudinal position of the NSG rim core shifts between stations N08–N09 (11%), N09–N10 (49%), and N10–N11 (40%). Although the averaged signature of the NSG rim might therefore influence a ∼ 60 km wide swath, synoptic CTD sections reveal a narrower jet, often localized between two hydrographic stations (18.52 km apart). We thus estimate the representative width to 20–30 km. A representative depth, from $h_{27.8}$ to an average bottom depth at these stations, must lie in the range 2–2.5 km.

Statistics of an upper and a lower estimate of ψ_{NSG}, respectively, are provided in **Table 3**. The median value is in the range 1.5–2.4 Sv (relative to $h_{27.8}$), and there is a seasonal variation with the strongest relative transport during February (1.9–3.5 Sv) and the weakest transport during late summer cruises, August/early September, (−0.8 to −1.6 Sv, westward transport relative to $h_{27.8}$). The transport was high around 1999–2000, but 2–3 years after (2002–2003) the low-passed ψ_{NSG} had weakened by about 4–7 Sv (**Table 3** and see **Figure 7**) – given no velocity changes at the $h_{27.8}$ depth level. Differences between individual extreme transects, however, exceed ten Sverdrups (not shown).

The wind stress curl driven barotropic component of the NSG circulation is strong (e.g., Nøst and Isachsen, 2003), and the current velocities at $h_{27.8}$ are therefore not zero. This obvious limitation in the baroclinic ψ_{NSG} can probably not be overcome with the presently available observational material. The barotropic flow is, however, in phase with ψ_{NSG}, with maximum cyclonic circulation during winter and NAO+ years (e.g., 1999–2000), and much weaker circulation during summer and NAO− years (e.g., 2002–2003) (Jakobsen, 2003). ψ_{NSG} should not be regarded as an absolute measure, but rather a conservative (underestimated) metric of the NSG circulation intensity.

Contrast Between Strong and Weak ψ_{NSG}

A composite analysis is made by contrasting averages of sections with the ten highest values of ψ_{NSG} (out of 103) (NSG+ state) against averages of the ten lowest ψ_{NSG} values (NSG− state). This reveals the following: A strong NSG rim (**Figures 6A,B**) entails a generally uplifted $h_{27.8}$ and thus a narrow AW wedge, increased volume of MEIW (visible as a low salinity wedge between AW above and NSAIW below, **Figure 6B**), and a fresh top (0–100 m) funneled over the NSG rim (63.5–64.0°N). A weak NSG, on the other hand (**Figures 6C,D**), relates to an additional AW core in the 63–63.6°N latitudinal band (particularly visible in the salinity field, **Figure 6D**), and a northward shift of the surface front to around 63.8°N. The fresh top layer is laterally spread out north of the front during this state.

ψ_{NSG} is significantly correlated to the interface height averaged over the region with a variable northern AW core (63–63.6°N), both when comparing individual transects and after applying the five-transect low pass filter (R ∼ −0.7). In this region, the interface is about 150 m higher during NSG+ states, compared to NSG− states (cf. **Figures 6A,C**). This contraction/spreading of the AW wedge is in general agreement with the simulations (**Figures 2C,D**).

As illustrated with the contrasting years 1994 vs. 2003, this interface undulation also influences the SSH (**Figures 2A,B**). On a more local scale strong station-by-station correlations are found between the steric height (relative to 800 m) in this region, and the SSH at the nearest satellite altimetry grid-point (**Table 4**).

A Broader View

Links Between ψ_{NSG}, FBCO, and SSH

The NSG rim baroclinic transport ψ_{NSG} is linked to both the FBCO (**Figure 7B**, $R = 0.85$, $p < 10^{-18}$, $N = 86$) and SSH north of the IFR (**Figure 7A**, $R = 0.74$, $p < 10^{-11}$,

TABLE 3 | Statistics of the NSG rim transport (ψ_{NSG}), provided as a lower estimate (width W = 30 km and average depth D = 2 km, see eq. 4) and as an upper estimate (W = 30 km and average depth D = 2.5 km).

ψ_{NSG}	Median	Standard error (SE)	February	September	NSG+ (1999–2000)	NSG− (2002–2003)
Lower	1.3 Sv	0.3 Sv	1.9 Sv	−0.8 Sv	3.2 Sv	−0.7 Sv
Upper	2.5 Sv	0.6 Sv	3.5 Sv	−1.6 Sv	6.0 Sv	−1.4 Sv

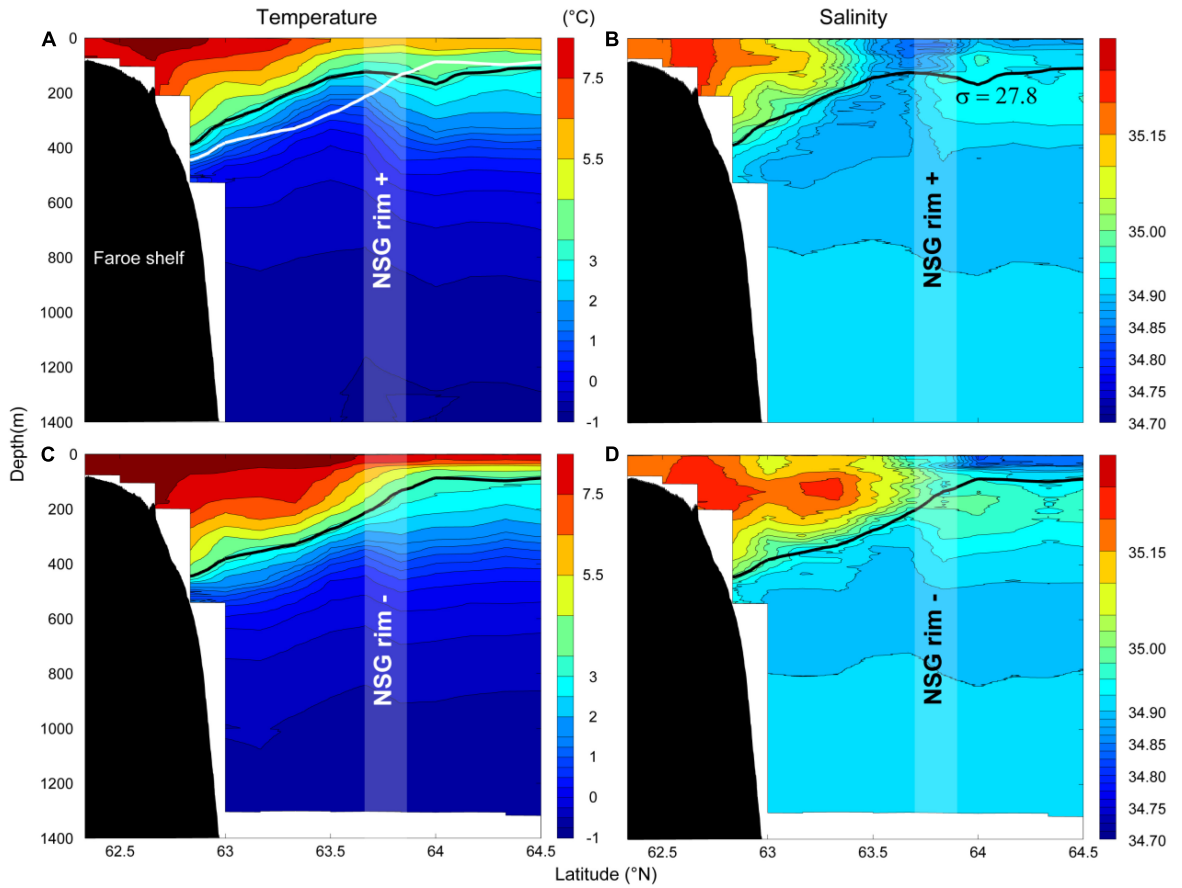


FIGURE 6 | Hydrographic composite sections, contrasting periods with a strong NSG rim **(A,B)** against periods with a weak NSG rim **(C,D)**. The states are represented by an average over ten sections with the highest and lowest value of ψ_{NSG}, respectively. Black lines show the position of the σ_θ = 27.8 isopycnal ($h_{27.8}$) during NSG rim+ and NSG rim– states, respectively. The white line in **(A)** shows $h_{27.8}$ from **(C)**.

N = 86), where the interface height is tightly linked to the FBCO (Köhl, 2010) and where strong SSH variability is observed (**Figures 2A,B**). This region is hereafter referred to as *IFR-North*. In order to smooth out the seasonal signal, the FBCO and the SSH series were low-pass filtered using a running mean (over 360 days), while ψ_{NSG} was low-passed using a Butterworth filter (width of four data points, corresponding to one year). The monitoring of Section N was reduced in 2011 from 4–5 annual transects to three transects, which has made the extraction of a reliable inter-annual signal less reliable (Hátún et al., 2005b). The years after 2011 have therefore been omitted from this correlation analysis and from **Figure 7**.

The extreme shift from a strong NSG rim in 1999–2000 to a weak NSG rim in 2002–2003 (**Table 3** and **Figure 7**) concurred with both a shift from weak FBCO to the highest FBCO transport on record (**Figure 7B**), and a marked increase in SSH in the IFR-North region (**Figure 7A**). Having established a link between ψ_{NSG} and the FBCO, we use the latter record (which is represented by daily sampling) to explore linkages between the NSG/FBCO system and the interface/SSH fields.

Links Between FBCO and the Interface

The FBCO is negatively correlated to the interface height along the horseshoe shaped band mentioned in section "Contrasting NAO+ and NAO− states" (**Figures 2**, **8A**). Particularly strong and statistically significant correlations (blue color) are evident in the IFR-North region and along the edge of the Vøring Plateau. That is, strong/weak overflow relates to depressed/shoaled interface in these regions. The interface position was represented as the depth of the 3°C isotherm, obtained from the gridded hydrographic data set (see section "Large-Scale Data Collection").

In contrast, the FBCO variability is positively correlated with the interface height along a narrow band following the Norwegian and Shetland slopes (red colors in **Figure 8A**), which generally overlays the deep FSCJ (**Figure 1**; Chafik et al., 2020). Thus strong overflow concurs with a higher interface over the FSCJ – and thus a banking up of cold and dense water along the continental slope.

Links Between FBCO and SSH

Correlation analysis between the daily records of FBCO transport and the gridded altimetry data reveals a close link between the

TABLE 4 | Correlation analysis between the steric height (relative to 800 m) and SSH.

Station	*N*	Standard	R_0	a_0	Significant
N05	87	6.74	0.77	0.85	$p < 0.001$
N06	79	7.48	0.77	0.78	$p < 0.001$
N07	82	7.72	0.84	0.78	$p < 0.001$
N08	80	7.47	0.83	0.68	$p < 0.001$
N09	79	7.10	0.80	0.48	$p < 0.001$
N10	79	6.69	0.67	0.33	$p < 0.001$

*Data from six standard hydrographic stations along the central part of Section N (see **Figure 4A**) and the nearest satellite altimetry grid-points are used. N is number of data points and R_0 and a_0 are the correlation and the regression coefficients, respectively.*

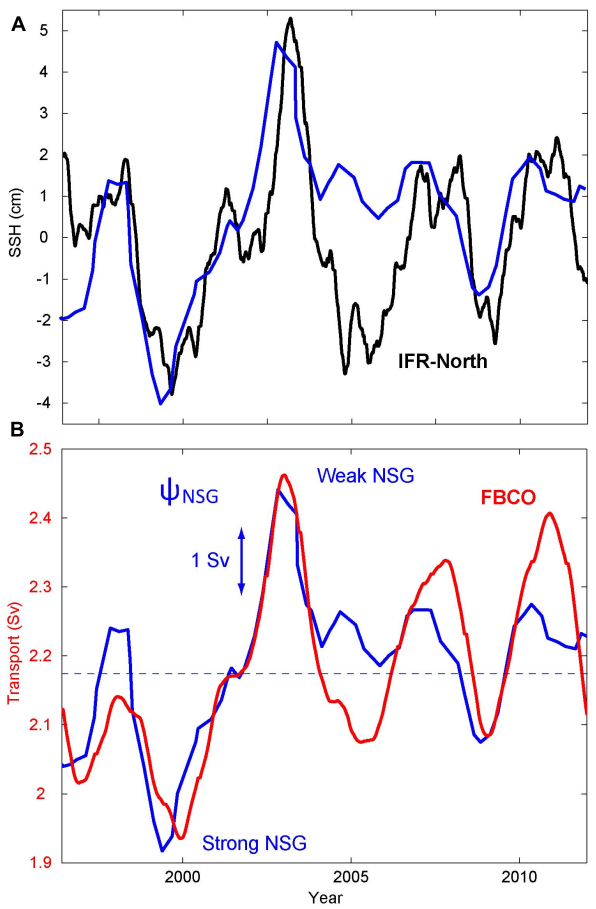


FIGURE 7 | Time series of the baroclinic NSG rim transport ψ_{NSG} (blue), compared to **(A)** sea-surface height north of the Iceland-Faroe ridge (IFR-North, black), and **(B)** the FBCO transport (red). ψ_{NSG} is here estimated using representative depth and width of D = 2 km and W = 30 km, respectively (**Table 3**). ψ_{NSG} is not an absolute measure of transport (therefore no values are provided on the y-axis), and the magnitude of inter-annual changes is illustrated by the blue double arrow in **(B)**.

FBCO transport and SSH in the IFR-North region, even on weekly time scales (**Figures 8B**, **9**, $R > 0.8$). The series are high-pass filtered by subtracting the 360-days running mean, in order to remove the pronounced annual cycle. Our observations thus support those previous model results. High FBCO vs. SSH correlations also appear east of the Vøring Plateau – where strong negative FBCO vs. interface correlations were found (**Figure 8B**).

This close coupling between FBCO and both interface heights and SSH in the IFR-North region points to the action of a common and direct driver. In the discussion, we propose the NSG circulation, and ultimately the action of the wind stress curl (Nøst and Isachsen, 2003), as this driver.

DISCUSSION

The NSG Rim

The here presented Argo floats trajectories show that intermediate source waters from the Iceland Sea and the southward flow along the Jan Mayen Ridge converge north of the Faroe slope, where the seafloor steeply deepens from 2000 to 3000 m depths (**Figures 2**, **3**). This region is here referred to as the NSG rim.

A meridional monitoring section, Section N, crosses both the Atlantic inflow in the FC and the NSG rim (**Figures 1**, **4A**), and we provide the first utilization of data from the deeper parts, i.e., away from the slope, of this valuable monitoring section. Direct current observations are not available from the NSG rim (hydrographic standard stations N09–N10, see **Figure 4A**), but Argo trajectory data reveal relatively strong mid-depth (1000–1500 m) currents in the NSG rim. Furthermore, there is a congregation of surface drifters[2] in the NSG rim, and their eastward drift velocity is appreciable (not shown).

We show that the NSG rim is a transition zone between the main upper ocean water masses north of the Faroe slope. It forms the northern boundary of the AW wedge, the northern extent of the subducted MEIW tongue, and the southern limit of NNAW (**Figure 4**). Acknowledging the deep-reaching flow in the NSG rim is therefore a prerequisite for understanding the physical oceanography in this important region.

Transport Variability in the NSG Rim

Lacking direct current observations in the NSG rim, we have relied on geostrophic calculations. Thermal wind shear shows that current velocities in the NSG rim generally increases with depth in the more quiescent waters below $h_{27.8}$ (**Figure 5**). Increasing velocities with depth can also occur in the IFSJ (bottom depths 700–1100 m) (Semper et al., 2020), while at all other locations, current velocities decrease with depth (**Supplementary Figure 1**) – which is the more typical condition in the ocean. As a proxy for the intensity of the NSG rim current (ψ_{NSG}), we calculate the eastward transport below $h_{27.8}$ and 1300 m (deepest hydrographic data). Although ψ_{NSG} is temporally coarse (based on only 4–5 data points each year), we can substantiate a close inverse correlation between this proxy record and the temporally well resolved FBCO record. ψ_{NSG} is strong when the overflow is weak and vice versa. Particularly evident is the major change from weak overflow around 1999–2000 (∼1.95 Sv) to the strongest overflow on

[2]http://www.aoml.noaa.gov/envids/gld/dirkrig/parttrk_spatial_temporal.php

record during 2002–2003 (∼2.45 Sv). This event was associated with a decreasing ψ_{NSG} by more than 6 Sv – relative to $h_{27.8}$ (**Table 3** and **Figure 7**). The general near-surface circulation in the NSG likely also decreased from the around 2000 (NAO+) to the latter period, which was characterized by a low NAO (Jakobsen, 2003). The barotropic contribution therefore adds to the presented baroclinic proxy record, and together this is clear evidence of a weakening NSG circulation between these extreme periods. Based on this, we propose the following hypothesis: *The FBCO variability is linked inversely to the strength of the NSG circulation.*

Contrasting NSG+/NSG− States and Possible Drivers

According to Yang and Pratt (2013), our hypothesized link between the NSG circulation and the FBCO must involve sill-level pressures in near-slope regions (at near sill-level depths), and not within the central parts of the Norwegian Sea.

A summary of key elements during contrasting NSG+ and NSG− states is provided in the schematic in **Figure 10**. A NSG− state, and high FBCO transport, are associated with generally elevated SSH in the Nordic Seas, especially along the horseshoe-shaped swath along the boundary current system (**Figures 2A,B**, **8**, **10**). NSG– and strong overflow also links to a depressed interface in this region (red **Figures 8A**, **10**). This latter fact appears to contradict the generally accepted view, that an uplifted interface is required to establish a Norwegian Sea-to-North Atlantic sill-level pressure gradient – and thus strong overflow. The depressed interface reduces the pressure increase from the elevated SSH, but it remains uncertain whether this 'baroclinic compensation' is complete at sill-level-depths (Olsen et al., 2008).

We have, on the other hand, identified a narrower band along the Norwegian and Shetland slopes with positive correlations between the FBCO transport and the interface heights (**Figures 8A**, **10**). Along this band, strong overflow transports (NSG−) are linked to both an uplifted interface and higher SSH, which thus both contribute to increased sill-level pressure. This suggests that collaborative influence of SSH and interface height on the near-bottom pressure along the European continental slope could drive the FBCO transport variability (at least on relatively short barotropic time scales). In this way, cyclonic/anti-cyclonic wind circulation anomalies could directly/regionally impact the poleward AW boundary current and the interface depth along the European continental shelf, which, in turn, regulates sill-level pressures in the FSCJ and the variability in the FBCO (Sandø et al., 2012; Bringedal et al., 2018). That implies that the FBCO is driven by shifting wind regimes, which concurrently drives both the AW boundary current, and the NSG circulation.

However, a release of dense overflow water from the gyre to the adjacent slopes is required to continuously feed the FSCJ and subsequently the FBCO. And these NSG-to-slope exchange processes are likely linked to both the wind stress curl field and the NSG circulation (Yang and Pratt, 2013). A complete description of this system is beyond the scope of the present work, and just a few tentative statements will be provided here. The fact that strong FBCO is associated with weaker eastward flow north of the Faroe slope, both in the shallower IFSJ region (Chafik et al., 2020), and further north in the deeper NSG rim (**Figures 7A**, **9**) remains a conundrum, which warrants further study.

Variable FBCO can exert an upstream feedback effect on both the interface height and SSH over a dense water reservoir just off the Norwegian slope (part of the horseshoe-shaped region between the Faroes and Norway). Anomalies in the FBCO transport can reach 0.5 Sv for extended periods (**Figure 9**), and such a drainage anomaly flux would cause the interface

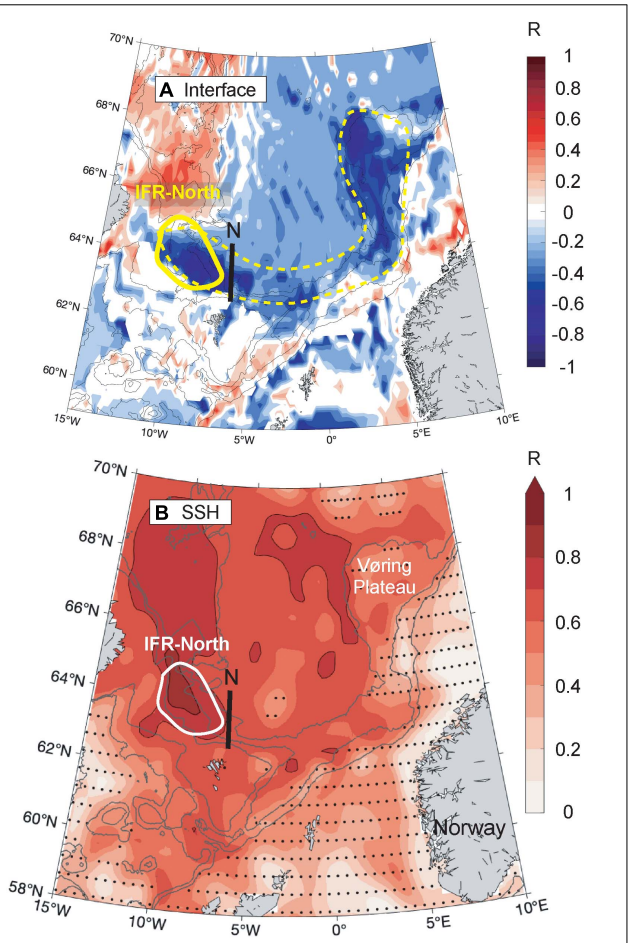


FIGURE 8 | A broader view. Correlation maps between the FBCO transport and **(A)** the height of the 3°C isotherm (see section "Large-Scale Data Collection") and **(B)** the sea-surface height field (SSH) from satellite altimetry. The correlation of the interface in the upper panel is based on annual mean data, while a 360-day running mean is used for the SSHs in the lower panel. Because of the time smoothing, the dotted regions in the lower panel indicate non-significant correlations based on the number of effective degrees of freedom (Pyper and Peterman, 1998). The position of standard hydrographic section N is shown with black lines, and the yellow/white outline in **(A,B)** marks the IFR-North region, from where the SSH time series in **Figure 9** is extracted. The horseshoe-shaped band is illustrated with the dashed yellow outline in **(A)**.

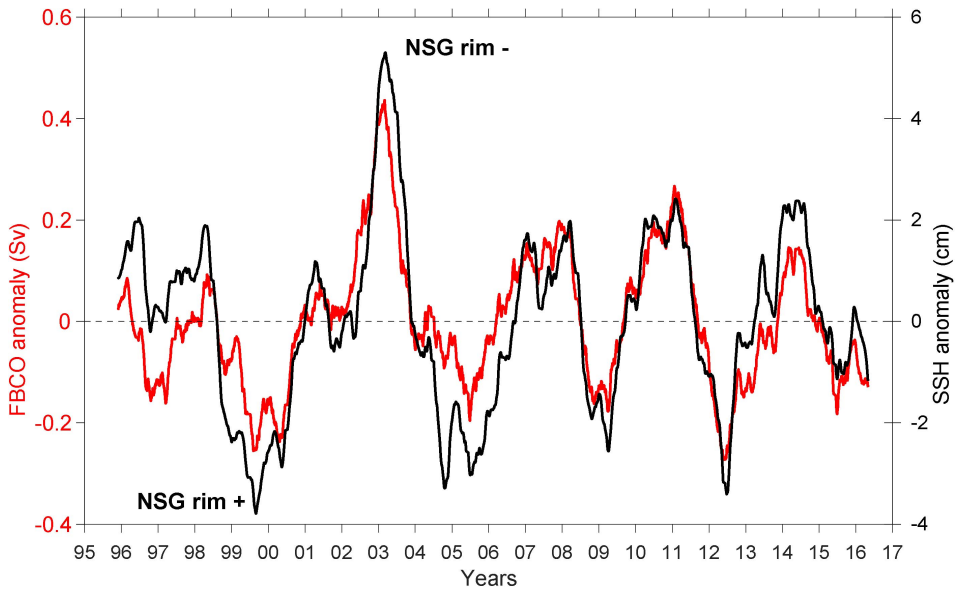


FIGURE 9 | Time series of the FBCO (red) and the sea-surface height (SSH) in the IFR-North region (yellow/white outline in **Figure 8**). The series have been detrended and running mean filtered over 360 days, in order to remove the seasonal signal.

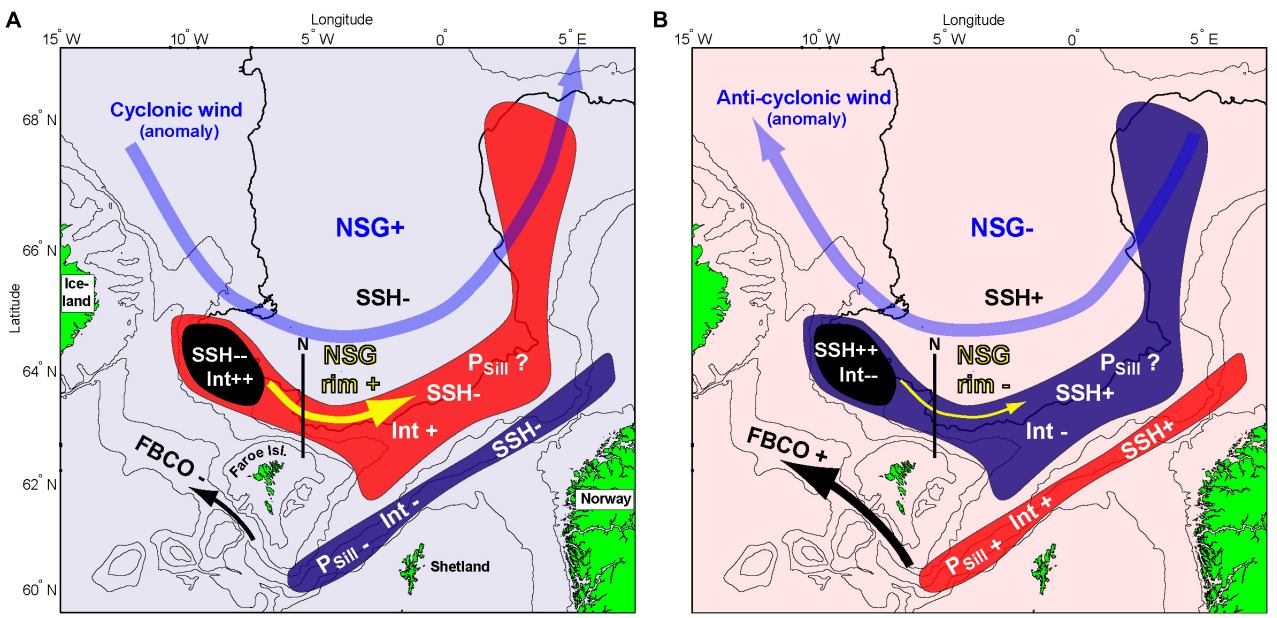


FIGURE 10 | A schematic of key element under contrasting **(A)** NSG+ and **(B)** NSG– states. "Int" refers to the interface height and P_{Sill} refers to the pressure at depth levels of the Faroe Bank Channel sill (~850 m). The other abbreviations are provided in **Table 1**. A "+" refers to a strong value, cyclonic anomaly or elevated level of both the interface and SSH, and opposite for a "–." The weak background colors refer to the broad SSH contrasts, while the more strongly colored regions show the additional imprint of vertical interface movement.

over a realistic source region (~1000 km long and ~100 km wide) to move vertically – about 1 m per day. Persistent FBCO+ periods could therefore notably lower the interface and elevate SSH over parts of the horse-shoe shaped region (blue in **Figure 10B**), while FBCO– states have the opposite effect (red in **Figure 10A**).

The fact that the highest FBCO vs. SSH correlations are identified in the IFR-North region (**Figure 8B**) – and not near the plausible source pathway along the European Continental slope – is likely related to the variable deep currents under the FC, through the mechanisms discussed in Orvik (2004). Weak eastward flows, and even reversals to westward deep flows

(Chafik et al., 2020) during NSG−/FBCO+ states (**Figure 2**) oppose the Atlantic inflow through the Iceland-Faroe gap, causing convergence of AW, deepening of the interface and elevation of the sea surface in the IFR-North region (**Figure 10**). We conclude that SSH changes over the IFR-North do not drive the FBCO changes, but are merely a result of the variable NSG circulation. We suggest that this mechanism can explain the puzzling negative sensitivity between the IFR-North interface height and the FBCO variability, as reported by Köhl (2010).

Other Implications of the Sensitive IFR-North Region

The vertical interface motion in the IFR-North region is in itself of profound oceanographic importance, since it likely relates to Atlantic inflow through the Iceland-Faroe gap (Blindheim, 1990), substantiated by negative correlations between the FC AW inflow and the IFR-North SSH (Hansen et al., 2010). These dynamical linkages might also impact both the IFR overflows as well as water mass contribution from the Iceland Sea (e.g., *via* the IFSJ; Semper et al., 2020) – although these last mechanisms have not yet been demonstrated with observations.

The very close correlation between these two remotely located, and important in its own right, processes (FBCO and IFR-North SSH; **Figure 9**), holds promise for a firmer understanding of the oceanographic variability within and around the Norwegian Sea. Furthermore, the freely available altimetry data can be used to complement the observational record of the FBCO, e.g., in case of instrument failure. The satellite data can, however, not replace the *in situ* current data since the directly observed FBCO contains high frequency variability (less than a week) and long-term trends, which are not captured by the satellites.

Ecological Implications

Contrasting periods with a strong NSG rim (e.g., 1999–2000) against periods with a weak gyre (e.g., 2002–2003) reveals fundamental oceanographic changes in the southern Norwegian Sea, which likely reverberate in ecosystems.

A strong NSG draws large amounts of MEIW and likely also of Arctic intermediate water masses from the Iceland Sea (**Figure 6B**), and these contain high concentrations of large and lipid-rich zooplankton types (*Calanus hyperboreus* and large overwintering stages of *Calanus finmarchicus*) (Kristiansen et al., 2016, 2019). The marked NSG weakening after 2002 resulted in a wider (northward extended) AW wedge, and a deeper interface at the northern flank of the FC. This increased AW influence entailed phenological changes as, e.g., the numbers of the younger stages in the *C. finmarchicus* population markedly increased, while the abundance of both overwintering *C. finmarchicus* and *C. hyperboreus*, sampled in May, decreased (Kristiansen et al., 2016).

Furthermore, large mesopelagic biomass congregates along the AW/subarctic water interface, which by acoustic monitoring is identified as the so-called Deep Scattering Layer (Hays, 2003). A depressed interface extends the range of the Daily Vertical Migration of mesopelagic biomass – from the interface during day to the near-surface feeding zone during night (Cisewski et al., 2021).

Herring (*Clupea harengus*) selectively prey on the mentioned relatively large zooplankton species (Dalpadado et al., 2000). This fish species does also perform Diel vertical migrations and during the May feeding season, it congregates in the confluence region between Iceland Sea and Norwegian Sea water masses, which exhibits contrasting changes in the 3°C isotherm depth (65–66°N, 6–8°W; **Figures 3**, **8A**). This is just north of the highest FBCO vs. SSH correlations, which underscores the likely ecological significance of the records presented here.

CONCLUSION AND OUTLOOK

While inflowing warm AW into the Nordic Seas toward the Arctic and returning dense overflow water at depth are typically studied separately, we here show that the variability in these key flows is intrinsically coupled. The connections involve both vertical undulations of the main interface – which separates the warm and cold waters – and the circulation strength of the NSG. We provide the first record of baroclinic transport variability in this gyre, based on hydrographic data from a standard section (Section N), which crosses the strongest and most focused flow of the NSG. This NSG rim is guided by the steep bathymetry between 2000 and 3000 m bottom depths and its presences divides the main water masses in the southwestern Norwegian Sea. During periods with strong NSG (and weak FBCO), the wedge of AW is narrow, and the interface around the southern and eastern rim of the Norwegian Sea is generally elevated – and vice versa for weak NSG/strong FBCO. These linkages are, however, opposite in shallower waters close to the Norwegian and Shetland slopes, where strong NSG/weak FBCO is associated with a depressed interface. The sea level topography in the biologically rich confluence region north of the IFR is highly sensitive to variability in the NSG/FBCO system. The low temporal resolution of standard hydrographic sections is at the detection limit of the herein discussed dynamics. In order to improve the spatial resolution of the NSG region, the Faroe Marine Research Institute (FAMRI) has already added an extra hydrographic standard station between standard station N09 and N10. We furthermore recommend that hydrographic Section N should be occupied at least four times a year, distributed evenly over the seasons. And presently, FAMRI has deployed an upward looking Acoustic Doppler Current Profiler (ADCP) in the NSG rim, in an attempt to increase the vertical and temporal sampling resolution, as well as capturing the barotropic component of this flow. And as demonstrated, high spatio-temporal resolution data provided by satellite altimetry can complement the monitoring of the FBCO transport and, by inference, the NSG strength. The demonstrated connectedness provides a basis for improved understanding of

physical, climatic, and ecological aspects of this dynamic and biologically productive system.

DATA AVAILABILITY STATEMENT

The original contributions presented in the study are included in the article/**Supplementary Material**, further inquiries can be directed to the corresponding author/s.

AUTHOR CONTRIBUTIONS

HH developed the main ideas and did most of the analysis and the writing, in correspondence with LC. LC provided analysis of altimetry data, numerical model output, and hydrographic database. KMHL provided *in situ* data (hydrography and current observations) and supported with the writing. All authors contributed to the article and approved the submitted version.

FUNDING

This study was supported by the European Union's Horizon 2020 Research and Innovation Program under grant agreement no. 727852 (Blue-Action). Data collection along Section N received support from the European Framework Programs under grant agreement numbers GA212643 (THOR), and 308299 (NACLIM) and from the Danish Ministry of Climate, Energy and Utilities through its climate support program to the Arctic (FARMON and FARMON2). LC acknowledges support from the Swedish National Space Agency through the FiNNESS project (Dnr: 133/17).

SUPPLEMENTARY MATERIAL

The Supplementary Material for this article can be found online at: https://www.frontiersin.org/articles/10.3389/fmars.2021.694614/full#supplementary-material

Supplementary Figure 1 | Averaged (over 103 complete transects) geostrophic current velocities, relative to 1300 m depths. Dark red color shows that velocities increase up through the water column, while the other colors demonstrate that velocities decrease up through the water column in the NSG rim. (The tick marks on the *x*-axis are the same as in **Figure 4**).

Supplementary Figure 2 | (a) Correlation coefficients between surface geostrophic currents based on hydrography (relative to 1300 m), SSH gradient (altimetry), respectively. Both are calculated between the standard hydrographic stations, and a daily satellite altimetry product is used. **(b)** Time lags between hydrography and altimetry, where the highest correlation coefficient is obtained (positive values show that hydrography leads). In the NSG rim, the water column density profile leads the SSH by about a week **(b)**. We interpret this curious fact as follows: the vorticity input from winds is efficiently transmitted to the bottom, where the local slope of the *f*/*H* field, through bottom Ekman dynamics, set up near-bottom currents (Nøst and Isachsen, 2003) which subsequently translate up through the NSG after an inertial time lag – which appears to be about a week.

REFERENCES

Blindheim, J. (1990). Arctic intermediate water in the Norwegian Sea. *Deep Res. A Oceanogr. Res. Pap.* 37, 1475–1489. doi: 10.1016/0198-0149(90)90138-l

Blindheim, J., Borovkov, V., Hansen, B., Malmberg, S. A., Turrell, W. R., and Østerhus, S. (2000). Upper layer cooling and freshening in the Norwegian Sea in relation to atmosphere forcing. *Deep Res.* 47, 655–680. doi: 10.1016/s0967-0637(99)00070-9

Bringedal, C., Eldevik, T., Skagseth, Ø, Spall, M. A., and Østerhus, S. (2018). Structure and forcing of observed exchanges across the greenland–scotland ridge. *J. Clim.* 31, 9881–9901. doi: 10.1175/JCLI-D-17-0889.1

Chafik, L., Hátún, H., Kjellsson, J., Larsen, K. M. H., Rossby, T., and Berx, B. (2020). Discovery of an unrecognized pathway carrying overflow waters toward the Faroe Bank Channel. *Nat. Commun.* 11:3721. doi: 10.1038/s41467-020-17426-8

Chafik, L., Nilsson, J., Skagseth, Ø, and Lundberg, P. (2015). On the flow of Atlantic water and temperature anomalies in the Nordic Seas toward the Arctic Ocean. *J. Geophys. Res.* 120, 7897–7918.

Cisewski, B., Hátún, H., Kristiansen, I., Hansen, B., Larsen, K. M. H., Eliasen, S. K., et al. (2021). Vertical migration of pelagic and mesopelagic scatterers from ADCP backscatter data in the Southern Norwegian Sea. *Front. Mar. Sci.* 7:542386. doi: 10.3389/fmars.2020.542386

Cushman-Roisin, B. (1994). *Introduction to Geophysical Fluid Dynamics*. New Jersey: Prentice-Hall, Inc, 1–320.

Dale, A. (2019). *Variabilité Saisonnière de L'écoulement D'eau Dense Dans le Passage du Banc des Féroé*. Thesis. Paris: Laboratoire d'Océanographie et du Climat (LOCEAN), 1–27.

Dalpadado, P., Ellertsen, B., Melle, W., and Dommasnes, A. (2000). Food and feeding conditions of Norwegian spring-spawning herring (*Clupea harengus*) through its feeding migrations. *ICES J. Mar. Sci.* 57, 843–857. doi: 10.1006/jmsc.2000.0573

Hansen, B., Hátún, H., Kristiansen, R., Olsen, S. M., and Østerhus, S. (2010). Stability and forcing of the Iceland-Faroe inflow of water, heat, and salt to the Arctic. *Ocean Sci.* 6, 1013–1026. doi: 10.5194/os-6-1013-2010

Hansen, B., Larsen, K. M. H., and Hátún, H. (2020). *Atlantic water extent on the Faroe Current monitoring section. Havstovan NR.: 20-03 Technical Report*. Faroe Islands: Tórshavn, 1–103.

Hansen, B., Larsen, K. M. H., Hátún, H., Kristiansen, R., Mortensen, E., and Østerhus, S. (2015). Transport of volume, heat, and salt towards the Arctic in the Faroe Current 1993-2013. *Ocean Sci.* 11, 743–757. doi: 10.5194/os-11-743-2015

Hansen, B., Larsen, K. M. H., Hátún, H., and Østerhus, S. (2016). A stable Faroe Bank Channel overflow 1995-2015. *Ocean Sci.* 12, 1205–1220. doi: 10.5194/os-12-1205-2016

Hansen, B., and Østerhus, S. (2000). North Atlantic–Nordic Seas exchanges. *Prog. Oceanogr.* 45, 109–208. doi: 10.1016/S0079-6611(99)00052-X

Hansen, B., Poulsen, T., Húsgarð Larsen, K. M., Hátún, H., Østerhus, S., Darelius, E., et al. (2017). Atlantic water flow through the Faroese Channels. *Ocean Sci.* 13, 873–888. doi: 10.5194/os-13-873-2017

Hátún, H. (2004). *The Faroe Current*. Norway: University of Bergen, 1–113.

Hátún, H., and Chafik, L. (2018). On the recent ambiguity of the North Atlantic subpolar gyre index. *J. Geophys. Res. Ocean.* 2014, 1–5. doi: 10.1029/2018JC014101

Hátún, H., and McClimans, T. A. (2003). *Cont. Shelf Res.* 23, 859–868.

Hátún, H., Sandø, A. B., Drange, H., Hansen, B., and Valdimarsson, H. (2005a). Influence of the Atlantic subpolar gyre on the thermohaline circulation. *Science* 309, 1841–1844. doi: 10.1126/science.1114777

Hátún, H., Sandø, A. B., Drange, H., and Bentsen, M. (2005b). "The Nordic Seas: An Integrated Perspective," in *Geophysical Monograph series*, eds H. Drange, T. Dokken, T. Furevik, R. Gerdes, W. Berger, (American Geophysical Union, Washington, DC, 2005), 158, 239–250.

Hays, G. C. (2003). A review of the adaptive significance and ecosystem consequences of zooplankton diel vertical migrations. *Hydrobiologia* 503, 163–170. doi: 10.1023/B:HYDR.0000008476.23617.b0

Jakobsen, P. K. (2003). Near-surface circulation in the northern North Atlantic as inferred from lagrangian drifters: variability from the mesoscale to interannual. *J. Geophys. Res.* 108:3251. doi: 10.1029/2002JC001554

Köhl, A. (2010). Variable source regions of Denmark Strait and Faroe Bank Channel overflow waters. *Tellus A* 62, 551–568. doi: 10.1111/j.1600-0870.2010.00454.x

Korablev, A. A., Smirnov, A. V., and Baranova, O. K. (2014). *Climatological atlas of the Nordic Seas and Northern North Atlantic. NOAA Atlas NESDIS 77*. Washington, DC: NOAA.

Kristiansen, I., Gaard, E., Hátún, H., Jónasdóttir, S., and Ferreira, A. S. A. (2016). Persistent shift of *Calanus* spp. in the southwestern Norwegian Sea since 2003, linked to ocean climate. *ICES J. Mar. Sci.* 73, 1319–1329. doi: 10.1093/icesjms/fsv222

Kristiansen, I., Hátún, H., Petursdóttir, H., Gislason, A., Broms, C., Melle, W., et al. (2019). Decreased influx of *Calanus* spp. into the south-western Norwegian Sea since 2003. *Deep Sea Res. I Oceanogr. Res. Pap.* 149:103048. doi: 10.1016/j.dsr.2019.05.008

Mork, K. A., and Blindheim, J. (2000). Variations in the Atlantic inflow to the Nordic Seas, 1955-1996. *Deep Res.* 47, 1035–1057. doi: 10.1016/s0967-0637(99)00091-6

Nøst, O. A., and Isachsen, P. E. (2003). The large-scale time-mean ocean circulation in the Nordic Seas and Arctic Ocean estimated from simplified dynamics. *J. Mar. Res.* 61, 175–210. doi: 10.1357/002224003322005069

Ollitrault, M., and Rannou, J. P. (2013). ANDRO: an argo-based deep displacement dataset. *J. Atmos. Ocean. Technol.* 1, 759–788. doi: 10.1175/JTECH-D-12-00073.1

Ollitrault, M., Rannou, J. P., Brion, E., Cabanes, C., Piron, A., Reverdin, G., et al. (2020). *ANDRO: An Argo-Based Deep Displacement Dataset*. London: SEANOE.

Olsen, S. M., Hansen, B., Quadfasel, D., and Østerhus, S. (2008). Observed and modelled stability of overflow across the Greenland–Scotland ridge. *Nature* 455, 519–522. doi: 10.1038/nature07302

Orvik, K. A. (2004). The deepening of the Atlantic water in the Lofoten Basin of the Norwegian Sea, demonstrated by using an active reduced gravity model. *Geophys. Res. Lett.* 31, 1–5. doi: 10.1029/2003GL018687

Pujol, M. I., Faugère, Y., Taburet, G., Dupuy, S., Pelloquin, C., Ablain, M., et al. (2016). DUACS DT2014: the new multi-mission altimeter data set reprocessed over 20 years. *Ocean Sci.* 12, 1067–1090. doi: 10.5194/os-12-1067-2016

Pyper, B. J., and Peterman, R. M. (1998). Comparison of methods to account for autocorrelation in correlation analyses of fish data. *Can. J. Fish. Aquat. Sci.* 55, 2127–2140. doi: 10.1139/cjfas-55-9-2127

Read, J. F., and Pollard, R. T. (1992). Water masses in the region of the Iceland faeroes front. *J. Phys. Oceanogr.* 22, 1365–1378. doi: 10.1175/1520-0485(1992)022<1365:wmitro>2.0.co;2

Richter, K., and Maus, S. (2011). Interannual variability in the hydrography of the Norwegian Atlantic current: frontal versus advective response to atmospheric forcing. *J. Geophys. Res.* 116:C12031. doi: 10.1029/2011JC007311

Richter, K., Segtnan, O. H., and Furevik, T. (2012). Variability of the Atlantic inflow to the Nordic Seas and its causes inferred from observations of sea surface height. *J. Geophys. Res. Ocean.* 117:C04004. doi: 10.1029/2011JC007719

Sandø, A. B., Nilsen, J. E. Ø, Eldevik, T., and Bentsen, M. (2012). Mechanisms for variable North Atlantic-Nordic seas exchanges. *J. Geophys. Res. Ocean.* 117, 1–14. doi: 10.1029/2012JC008177

Semper, S., Pickart, R. S., Våge, K., Larsen, K. M. H., Hátún, H., and Hansen, B. (2020). The Iceland-Faroe Slope Jet: a conduit for dense water toward the Faroe Bank Channel overflow. *Nat. Commun.* 11, 1–10. doi: 10.1038/s41467-020-19049-5

Serra, N., Käse, R. H., Köhl, A., Stammer, D., and Quadfasel, D. (2010). On the low-frequency phase relation between the Denmark Strait and the Faroe-Bank Channel overflows. *Tellus A* 62, 530–550. doi: 10.1111/j.1600-0870.2010.00445.x

Siegismund, F., Johannessen, J., Drange, H., Mork, K. A., and Korablev, A. (2007). Steric height variability in the Nordic Seas. *J. Geophys. Res.* 112:C12010. doi: 10.1029/2007JC004221

Søiland, H., Prater, M. D., and Rossby, T. (2008). Rigid topographic control of currents in the Nordic Seas. *Geophys. Res. Lett.* 35, 1–5. doi: 10.1029/2008GL034846

Voet, G., Quadfasel, D., Mork, K. A., and Søiland, H. (2010). The mid-depth circulation of the Nordic Seas derived from profiling float observations. *Tellus Ser. A Dyn. Meteorol. Oceanogr.* 62, 516–529. doi: 10.1111/j.1600-0870.2010.00444.x

Yang, J., and Pratt, L. J. (2013). On the effective capacity of the dense-water reservoir for the Nordic Seas overflow: some effects of topography and wind stress. *J. Phys. Oceanogr.* 43, 418–431. doi: 10.1175/JPO-D-12-087.1

Conflict of Interest: The authors declare that the research was conducted in the absence of any commercial or financial relationships that could be construed as a potential conflict of interest.

The reviewer RP declared a past co-authorship with several of the authors HH and KMHL to the handling editor.

Publisher's Note: All claims expressed in this article are solely those of the authors and do not necessarily represent those of their affiliated organizations, or those of the publisher, the editors and the reviewers. Any product that may be evaluated in this article, or claim that may be made by its manufacturer, is not guaranteed or endorsed by the publisher.

Copyright © 2021 Hátún, Chafik and Larsen. This is an open-access article distributed under the terms of the Creative Commons Attribution License (CC BY). The use, distribution or reproduction in other forums is permitted, provided the original author(s) and the copyright owner(s) are credited and that the original publication in this journal is cited, in accordance with accepted academic practice. No use, distribution or reproduction is permitted which does not comply with these terms.

frontiers in Marine Science

ORIGINAL RESEARCH
published: 27 October 2021
doi: 10.3389/fmars.2021.699318

Darkening of the Svalbard Fjords Waters Observed With Satellite Ocean Color Imagery in 1997–2019

Marta Konik[1,2]†, Mirosław Darecki[1]†, Alexey K. Pavlov[1]†, Sławomir Sagan[1]† and Piotr Kowalczuk[1]†*

[1] Remote Sensing Laboratory, Institute of Oceanology, Polish Academy of Sciences, Sopot, Poland, [2] Department of Geography, University of Victoria, Victoria, BC, Canada

OPEN ACCESS

Edited by:
Hjálmar Hátún,
Faroe Marine Research Institute (FAMRI), Faroe Islands

Reviewed by:
Solva Karadottir Eliasen,
Faroe Marine Research Institute (FAMRI), Faroe Islands
Michelle Jillian Devlin,
Centre for Environment, Fisheries and Aquaculture Science (CEFAS), United Kingdom

***Correspondence:**
Marta Konik
mk@iopan.gda.pl

†ORCID:
Marta Konik
orcid.org/0000-0003-1145-9127
Mirosław Darecki
orcid.org/0000-0003-4326-5212
Alexey K. Pavlov
orcid.org/0000-0002-1978-5368
Sławomir Sagan
orcid.org/0000-0003-4183-0337
Piotr Kowalczuk
orcid.org/0000-0001-6016-0610

Specialty section:
This article was submitted to Ocean Observation, a section of the journal Frontiers in Marine Science

Received: 23 April 2021
Accepted: 04 October 2021
Published: 27 October 2021

Citation:
Konik M, Darecki M, Pavlov AK, Sagan S and Kowalczuk P (2021) Darkening of the Svalbard Fjords Waters Observed With Satellite Ocean Color Imagery in 1997–2019. Front. Mar. Sci. 8:699318. doi: 10.3389/fmars.2021.699318

Global warming is not often discussed in the context of light availability within the water column. However, the light regimes in the Arctic Ocean are controlled by three factors that are influenced by climate changes which are the sea ice *albedo* feedback, glacial meltwater runoff and marine primary production. Based on a satellite data series acquired during time period 1997 – 2019, we inspected long-term changes of the three commonly used optical characteristics *Chla*, $a_{tot}(443)$, and $K_d(490)$ within the Svalbard fjords and on the West Spitsbergen Shelf. We revealed evident positive trends in summer (July – September) in the Isfjorden, the Kongsfjorden, the Hornsund fjord, and the Bellsund. Moreover, between 1997 and 2019 at the majority of locations we observed a regime shift toward darker waters. We showed that light availability has changed in the Svalbard fjords since 1997, which may be a symptom of transformations in the environment that should be further investigated and monitored.

Keywords: Svalbard fjords, IOPs, remote sensing, coastal darkening, phytoplankton

INTRODUCTION

In the mid-1970s a significant change in the Arctic Ocean system began. Since then, systematic satellite observations have proved that the Arctic Ocean ice cover is shrinking, and in the following decades the trend has continued with a rate of -13.3% dec^{-1} (Serreze and Stroeve, 2015). The main driving force for the decline of the Arctic Sea ice area and its thickness was an increase in global mean temperature, which in the Arctic is two times stronger than elsewhere (Weller, 2005; Cohen et al., 2014). Sea ice forms a boundary layer in polar and sub-polar marine basins, that reduces the heat, mass, and momentum exchange between the ocean and atmosphere (McPhee, 2017), alters the surface *albedo* and reduces radiative energy transfer to the underlying water, which affects the heating rate and primary production (Arrigo, 2017). Sea ice, especially in the Arctic, regulates global climatic processes-, because its *albedo* is drastically higher than the open water surface or ice-free land areas. Therefore, enhanced melting and ice cover retreat results in higher doses of radiation reaching sea waters which when absorbed, additionally enhances water temperatures accelerating the heating rate that is the so-called sea ice *albedo* feedback (Curry et al., 1995; Kashiwase et al., 2017). The consequences of global warming have impacted the whole Arctic Ocean and its terrestrial watershed leading to a cascade of changes in the physical environment, biogeochemical process, and its ecosystems and their functions (Smedsrud et al., 2016). The sea-ice decline in the Arctic Ocean has been accompanied by an increase of its productivity (Ardyna and Arrigo, 2020) that has been observed in eutrophic shelf area, oligotrophic Central Arctic Basin and exchange gateways in Bering and Fram Straits (Kohler et al., 2007) and Canadian Archipelago (Hill et al., 2018). Terrestrial systems in the vast watersheds surrounding the Arctic Ocean are subject to

changes too (Parmentier et al., 2017). Increased precipitation and accelerating permafrost thawing affected coastal erosion and water runoff from land (Kipp et al., 2018). Terrestrial fluxes of heat, dissolved, and particulate material through melt-water discharge and riverine inflow contributed to an increase of productivity in continental shelf margins. Through the exchange gateways, particularly, the Fram Strait, the Arctic Ocean received steadily increased advection of heat and salt from mid-latitudes with inflowing Atlantic Water (Walczowski, 2014; Polyakov et al., 2017). Together with the inflow of warm and salty Atlantic Water a significant northward advance of temperate phytoplankton and changes of the planktonic organism size distribution toward smaller organisms, i.e., pico- and nanoplankton have been observed (Oziel et al., 2017; Neukermans et al., 2018).

Changes in the light availability in the ocean are not often discussed as one of the consequences of global climatic changes. The light regimes in the surface waters of the Arctic Ocean are controlled mainly by the sea ice *albedo* feedback, terrestrial fluxes, and marine primary production. As those three processes are strongly affected by global warming, the light availability in the Arctic Ocean has been significantly altered across the whole ocean basin. The amount of light at various wavelengths reaching the ocean surface through the atmosphere is regulated by the Sun's activity, the Earth's orbit geometry, and transmission through the atmosphere, which depends on cloud cover, the concentration of water vapor and other gasses, and concentration of scattering and absorbing aerosols (Dera, 1992). In the water column, the transmission of solar energy into deeper layers depends mainly on the spectral optical properties of water and optically significant water constituents. In the simplified model, the optical properties of seawater are a superposition of spectral scattering and absorption coefficients of water molecules themselves, suspended organic and inorganic particles, colored dissolved organic matter (CDOM), dissolved inorganic salts, and dissolved inorganic gasses (Woźniak and Dera, 2007). Spectral absorption properties of each of them are additive and combined constitute inherent optical properties of the water (IOPs). In the Nordic Seas, the IOPs variability is driven by sea ice and glacier ice-melt processes (Noël et al., 2020; Schuler et al., 2020), phytoplankton dynamics in spring and summer (Winter et al., 2014; Pavlov et al., 2015; Kowalczuk et al., 2019), and mixing of multiple water masses that contain different CDOM concentrations (Granskog et al., 2015; Pavlov et al., 2015; Makarewicz et al., 2018). Melting ice provides input of fresh water, but also inorganic suspended matter (Bélanger et al., 2013) which sub-glacial melt is particularly rich in (Holinde and Zielinski, 2016). Plankton communities are a primary source of organic particles and are tightly related to particulate carbon stocks in Fram Strait (Engel et al., 2019). Phytoplankton also contributes to the autochthonous production of dissolved organic matter in the West Spitsbergen Current (Makarewicz et al., 2018). Therefore, this is a region of particular environmental significance, but the remoteness, ice cover, and harsh meteorological conditions drastically limit the amount of *in situ* data on inherent (IOPs) and apparent optical properties (AOPs). Most of the papers have been published in recent years (see citations above) and only few in the first decade of 21st century (Stramska et al., 2003, 2006). Long-term changes and evolution of IOPs and AOPs is largely unknown in the Arctic Ocean, especially in the European sector. The scarcity of the long-term records could be partially addressed using available ocean color data time-series for this region.

In general, a typical Svalbard fjord would consist of three water layers: Surface Waters at the top (local), Intermediate Waters at intermediate depths (advected), and Winter Water at the bottom of the water column (Cottier et al., 2010). The near-surface, relatively fresh layer is formed mostly by sea ice and glacial-melt, and freshwater runoff discharged in the spring and early summer months. A gradual formation of the density gradient reduces vertical mixing and particle sedimentation. Particulate suspended and dissolved matter trapped in the surface layer accelerate water heating in the months when insolation is the most intense. A warmer surface layer may provide optimal temperature conditions for various organisms over a season that would support primary production. Although photosynthetically available radiation, "PAR," intensity values reach a maximum in June, the highest air temperatures are lagged by about a month, and water temperatures are usually the highest in late July and early August (Calleja et al., 2017; Payne and Roesler, 2019). The vertical stratification stabilizes in summer, which is accompanied by shallowing of the mixed layer and accumulation of the *Chla* near the sea surface, which was clearly demonstrated in the results of Calleja et al. (2017). Calleja et al. (2017) compared vertical profiles of T, S, *Chla* measured at locations in the inner, middle and outer part of the Kongsfjorden in May, August, and October. They found that in the central part of the fjord in August, the thermo- and pycnocline were only several meters deep. Variability of the depth of the top mixed layer is a key-aspect regarding remote sensing.

Spectral IOPs and AOPs, and the relationships between them served as theoretical foundations of the ocean color remote sensing (OCRS). The first so-called "blue-green ratio" algorithms were developed for retrieval of chlorophyll *a* concentration (Morel and Prieur, 1977; Gordon et al., 1980; Gordon and Morel, 1983) during the "proof of concept" of the Coastal Zone Color Scanner (CZCS) mission launched in 1979. Since then, OCRS has evolved and has been used successfully for studying spatial and temporal dynamics of phytoplankton abundance, IOPs and AOPs, and oceanic primary production across a range of spatial and temporal scales (Blondeau-Patissier et al., 2014). After the outstanding scientific and operational success of the CZCS mission, a number of the next generation of ocean color sensors have been launched into the Earth's orbit: Sea-viewing Wide Field-of-View Sensor (SeaWiFS), placed in orbit in 1997, was followed by the Moderate-Resolution Imaging Spectroradiometer (MODIS) deployed on the AQUA satellite, launched in 2002 and operated by United States NASA (Emberton et al., 2016). In 2002, the European Space Agency (ESA) also launched an Earth observation satellite. The Medium-Resolution Imaging Spectrometer (MERIS), in operation until 2012, was highly successful. The successor of MERIS is the Ocean and Land Color Instrument (OLCI). In 2010, the Climate Change Initiative (CCI) with the special Ocean Color section (OC-CCI) was launched to create data series of

climate-quality by combining all available satellite measurements (Sathyendranath et al., 2012, 2019). A set of common spectral bands derived from the ocean color sensors with overlapping operation periods provided after merging a time series of coherent satellite observations spanned more than two decades (Mélin et al., 2016). We have used available data sets to analyze temporal changes in chlorophyll *a* and selected IOP and AOP values in West Spitsbergen fjords and adjacent oceanic shelf waters.

Fjords have been defined as aquatic critical zones (ACZs) (Bianchi et al., 2020) as these environments have been recognized as important carbon burial hot-spots sequestering the largest amount of organic carbon per unit of area (Smith et al., 2015). In those specific environments, especially in boreal and polar zones, integrated and accumulated effects of interactions between atmosphere, ocean, cryosphere, and surrounding landmass could be observed, which make those geomorphological units very sensitive to climatic changes (Bianchi et al., 2020). Effects of environmental changes could be observed visually as a progressive decline of water transparency in fjords, as the increase in terrestrial flux and autochthonous production of optically significant water constituents decreases water transparency and limits the amount of light in the water column, which is commonly called 'darkening.' This term was introduced about a decade ago when this effect was described for the first time along the Norwegian coast and has come to be used too, especially beyond the marine optics community (Aksnes et al., 2009). It was associated with enhanced riverine input of the CDOM and suspended particles due to increasing precipitation over terrestrial watersheds. The impact of climatic changes on water transparency in specific fjords in Norway and Greenland has been the subject of recent studies by Mascarenhas et al. (2017) and Mascarenhas and Zielinski (2018, 2019). To this day, very few papers have been published on seawater optical properties in Svalbard fjords and adjacent waters. Sagan and Darecki (2017) reported differences in IOPs distribution between the Hornsund and the Kongsfjorden and Pavlova et al. (2019) reviewed impacts of climatic changes on the light field in Kongsfjorden based on the existing data record. The local bio-optical and remote sensing algorithms for retrieval of chlorophyll *a* and suspended matter concentrations were developed for Kongsfjorden by Son and Kim (2018) and in adjacent coastal waters by Konik et al. (2020). The only long-term remote sensing study was published on the changes of IOPs in the Kongsfjorden (Payne and Roesler, 2019) in the context of modeling light availability for phytoplankton distribution in this fjord. No other studies of long-term changes in seawater optical properties have been conducted in the other fjords of the Svalbard Archipelago or the Nordic Seas. Despite the lack of direct observations, there are multiple lines of indirect evidence of ongoing long-term darkening of fjords. Among those is an already observed increased occurrence of the jellyfish *Periphylla periphylla* in Svalbard waters (Geoffroy et al., 2018), and shifts of kelp forest to shallower depths in Kongsfjorden likely associated with light limitation (Bartsch et al., 2016). Besides, the following manifestations of climate change are expected to contribute to the further darkening of coastal waters on Svalbard: accelerated melting of glaciers (Kohler et al., 2007), the anticipated increase in precipitations (Førland et al., 2011) in combination with accelerated thawing of permafrost (Isaksen et al., 2007) and greening of terrestrial vegetation (Vickers et al., 2016) will likely further elevate inputs of suspended particles and CDOM into fjords, thus making surface waters less transparent.

In this work, we aimed to fill the knowledge gap on the long-term changes of the water transparency in West Spitsbergen fjords and adjacent oceanic shelf, using ocean color data archive and developed locally optimized algorithms for retrieval of IOPs, AOPs, and chlorophyll *a* concentration. The long term assessment in fjord waters in Spitsbergen is important due to the high value of ecosystem services provided by the coastal areas, and presumable adverse effects of darkening and importance of this effect for the environmental management in Norwegian coastal waters (Tiller et al., 2017) and from the ecological and scientific standpoint for the global community.

DATA AND METHODS

Study Area

We have conducted our analyses in the coastal waters of West Spitsbergen, the biggest island of the Svalbard Archipelago. We have focused on the fjords directly connected with the Greenland Sea: the Hornsund Fjord, the Van Mijenfjord with the Bellsund, the Isfjorden, and the Kongsfjorden (**Figure 1**). Water temperature and salinity within these fjords are controlled by the interaction of several water masses, typically dominated by the Atlantic Waters (AW) with modification of terrestrial and meltwater input as well as the contribution of cold and fresh Arctic Water (ArW) carried by the Sørkapp Current (SC). The AW carried by the West Spitsbergen Current (WSC) is the major heat source in the area that accelerates the ice melting and has a significant effect on the biogeochemical cycles and nutrient loads (Hegseth et al., 2019). The composition of water masses in the Hornsund fjord is strongly regulated by the SC that flows around the southern tip of Spitsbergen, bringing cold and fresh ArW from the Barents Sea. It propagates northward along the West Spitsbergen Shelf (WSS) parallel to the coast and the WSC, which results in reduced advection of AW into the fjord (Promińska et al., 2017). The other fjords on the west coast of Spitsbergen are more impacted by the WSC and AW. In particular, the seabed topography of the Isfjorden and the Kongsfjorden allows for easier penetration of AW into these fjords (Cottier et al., 2010; Skogseth et al., 2020; Bloshkina et al., 2021). In contrast, the Van Mijenfjord is a semi-enclosed water basin, separated from the Bellsund that connects it with the Greenland Sea by two elongated islands Akseløya and Mariaholmen positioned across the entrance of the fjord. It is an example of a fjord controlled by semi-diurnal tidal forcing with a strong vertical stratification. Relatively fresh and warm water, formed by runoff from glaciers, resides near the surface, whereas salt and cold water that flow into the fjord, remain in deeper layer (Støylen and Fer, 2014).

Satellite Data

As the main indicators describing quantitative changes in water transparency, we selected the variables routinely retrieved by

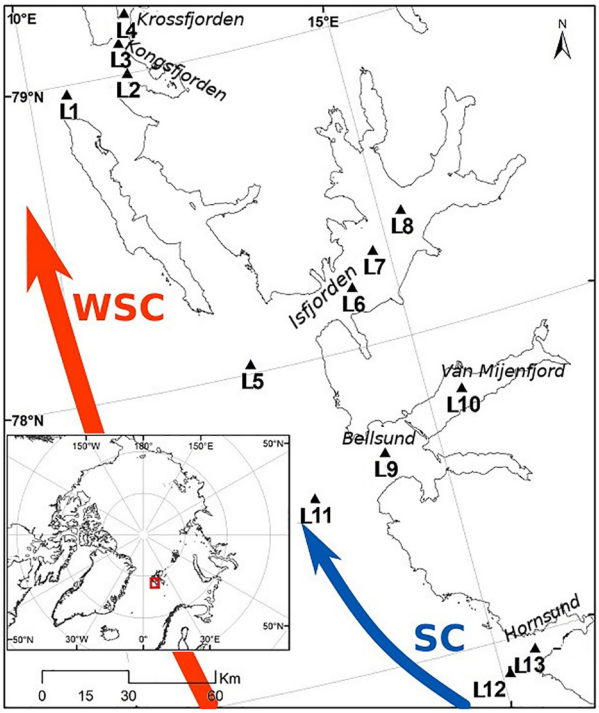


FIGURE 1 | All of the considered study locations (also excluded L4) within Svalbard Fjords with the cold Sørkapp Current (SC) marked in blue and the warm West Spitsbergen Current (WSC) marked in red (shoreline: Wessel and Smith, 1996).

OCRS and directly linked with the notion of 'darkening.' Of the three analyzed variables, chlorophyll *a* concentration, *Chla*, is a proxy for phytoplankton biomass. The total absorption coefficient at 443 nm, $a_{tot}(443)$, overlaps with the main maximum of phytoplankton pigments absorption spectra and contains the contribution of other absorbing constituents in natural water: CDOM and suspended particles. The solar downward irradiance diffuse attenuation coefficient at 490 nm, $K_d(490)$, describes the transmission of solar energy through the water column as the rate at which the solar downward irradiance is attenuated with increasing depth. It is one of the standard AOPs of the water column retrieved from satellite data. However, we based our analyses on the local algorithms and we used only remote sensing reflectance products at several wavelengths.

The satellite data used for the analysis were obtained from the EU Copernicus Marine Environment Monitoring Service (CMEMS[1]). This was a long time series of daily mosaics merged from multiple optical satellite sensors (MODIS, VIIRS, SeaWiFS, MERIS, and OLCI). The merged product had been developed in the framework of the ESA Climate Change Initiative (ESA-CCI/C3S project) (Sathyendranath et al., 2012, 2019). We exploited the remote sensing reflectance, R_{rs} [sr^{-1}], product at six spectral bands: 412, 443, 490, 510, 555, and 670 nm from the Arctic region in a form of Level-3 OPTICS product of 1-km ground resolution (CMEMS id: OCEANCOLOUR_ARC_OPTICS_L3_REP_OBSERVATIONS_009_068) that covered years 1997 – 2019. These data set had been provided to CMEMS by Plymouth Marine Laboratory (McClain et al., 1995; CMEMS, 2020).

Remote Sensing Algorithms for Determination of Chlorophyll *a* Concentration and Total Absorption Coefficient

Available spectral remote sensing reflectance values were used to derive *Chla*, $K_d(490)$, and $a_{tot}(443)$ values at selected locations, and assess the darkening effects. We have used the empirical band ratio algorithms developed and validated in the Greenland Sea and the West Spitsbergen Shelf based on the *in situ* radiometric measurements conducted in the study area in summer seasons between 2013 and 2015 (Konik et al., 2020). Details of field work, methodologies of measurements and analytical methods that were used for determination of values of optically significant constituents and radiometric quantities needed for algorithm development and validation have been given in detail in studies by Makarewicz et al. (2018), Kowalczuk et al. (2019), and Konik et al. (2020). In brief, chlorophyll *a* concentration values were determined in collected water samples using the spectrophotometric method by Lorenzen (1967) and the formula by Strickland and Parsons (1972). The total absorption coefficient $a_{tot}(\lambda)$ is the superposition of the spectral values of light absorption coefficient by CDOM $a_{CDOM}(\lambda)$ and the light absorption coefficient by suspended particles $a_p(\lambda)$. We omitted the influence of the light absorption coefficient after subtracting the pure water contribution to the light absorption coefficient, because it is almost constant in the natural waters and in typical for natural waters temperature ranges (Pope and Fry, 1997). The absorption coefficients by suspended particles were determined using Perkin-Elmer Lambda 650 double-beam spectrophotometer equipped with an integrating sphere. Details on sample handling, measurements protocol, and data processing have been included in Kowalczuk et al. (2017, 2019). The CDOM sample handling, measurements protocol, and data processing were described by Makarewicz et al. (2018). The OCRS algorithms, mathematical equations for determination of *Chla* and $a_{tot}(443)$ in the Greenland Sea, validation details, and uncertainty assessments have been presented in detail by Konik et al. (2020).

Remote Sensing Algorithm for the Calculation of Solar Downward Irradiance Diffuse Attenuation Coefficient at 490 nm $K_d(490)$

The often-used spectral band, centered at 490 nm is located in the spectral range of maximum transmission (least attenuation) of solar energy in clear oceanic waters. At 490 nm, impact of phytoplankton is the least pronounced and it is possible to detect there more prominent signals by the other particles. In turbid coastal waters that are typical for the Arctic fjords, the spectral

[1]http://marine.copernicus.eu/

region of maximum transmission of solar energy can often be shifted toward the longer wavelengths, even to 560–580 nm. For this reason, the region-specific algorithm for retrieval of $K_d(490)$ should be developed and applied in the Svalbard fjords.

We developed a locally optimized algorithm for retrieving the $K_d(490)$ values based on four field campaigns conducted in the Svalbard fjords, mainly in the Hornsund fjord and the Kongsfjorden in 2009, 2010, 2016, and 2017 (**Figure 2A**). More than one hundred profiles of spectral downward irradiance $E_d(\lambda)$ and upward radiance $L_u(\lambda)$ have been made with the use of the high-performance free-fall aquatic profiler C-OPS (Compact Optical Profiling Systems, Biospherical Instruments, Inc.). C-OPS radiometer equipped with 19 wavebands (from 305 to 765 nm) was mounted in a free-fall backplane, allowing deployment far from the ship's shadow. The instrument was equipped with a reference irradiance sensor mounted on the deck to measure incident irradiance and to control the stability of ambient light during deployment. The remote sensing reflectance, $R_{rs}(\lambda)$, was calculated as a ratio of the upwelling radiance just above the water surface, $L_w(\lambda)$, to downwelling irradiance measured above the water, $E_s(\lambda)$. The water-leaving radiance $L_w(\lambda)$ was obtained from the upwelling radiance estimated just below the water surface, $L_u(z = 0^-,\lambda)$, and propagated through the water-air interface according to standard procedures described in the literature (Mueller et al., 2003). The $K_d(490)$ for the subsurface layer was calculated as the local slope of $\ln[E_d(z,490)]$ measured within a depth interval spanning a few meters within the surface layer, depending on the extent to which the surface layer was homogeneous:

$$K_d\,(490)\left[m^{-1}\right] = 10^{0.2084-1.133\log_{10}(R_{rs}(490)/R_{rs}(670))} \quad (1)$$

The optimal regression between $K_d(490)$ and R_{rs} band ratio ($R^2 = 0.85$) has been found for $R_{rs}(490)/R_{rs}(670)$ ratio, as presented in **Figure 2B** and Equation 1. The algorithm has been validated based on *in situ* radiometric measurements. The calculated mean normalized bias MNB (systematic error) and the normalized root-mean-square RMS error (random error) were 9 and 52%, respectively. We used this algorithm in our study to assess the long-term changes of the $K_d(490)$ in the Svalbard fjords.

Statistical Analyzes

To assess the long-term variability of selected IOPs and AOPs in the fjords, we selected several locations labeled from L1 to L13 (**Figure 1**). The choice of locations allowed for capturing: open waters, the mouths of the fjords and the central parts of the fjords. There was at least one location placed within the fjord and one location on the West Spitsbergen Shelf near the mouth of a fjord. In order to minimize the noise influence we used median values of remotely sensed *Chla*, $K_d(490)$, and $a_{tot}(443)$ that were extracted from each processed map at 12 selected locations from a window of 3 pixels × 3 pixels (9 km^2 area) (**Figure 1**). We used values where at least 5 out of 9 pixels were valid. Only results from locations with characteristic patterns or trends are presented in the paper. Results from all locations are included in the **Supplementary Figures 1–6**. The L4 location was excluded. Since this position had no valid data in relatively long periods, we feared that this could potentially bias our trend analysis. The full picture of the amount of valid data may be found in the **Supplementary Figure 7**.

Regarding the log-normal distribution of *Chla*, $a_{tot}(443)$ and the $K_d(490)$ (Campbell, 1995), all statistical analyses were performed using median metrics for all parameters. Statistical analyses were performed using R-CRAN software [libraries: ggplot2 (Wickham et al., 2020), ggformula (Kaplan and Pruim, 2020)]. Boxplots depict median values with lower and upper hinges corresponding to the first and third quartiles, and

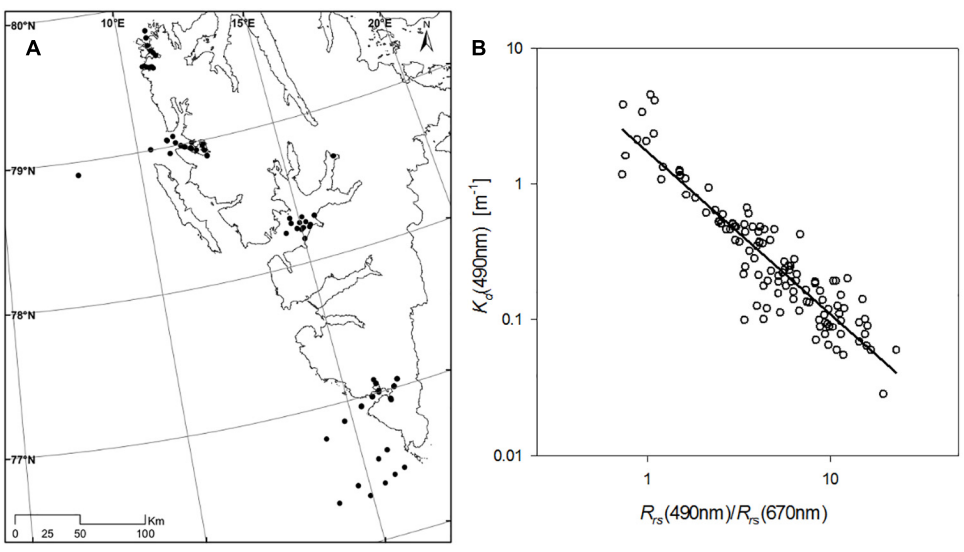


FIGURE 2 | Location of the *in situ* measurements of $K_d(490)$ used to develop a formula for satellite $K_d(490)$ computation **(A)** and the relationship between the $K_d(490)$ and the $R_{rs}(490)/R_{rs}(670)$ band ratio with the regression applied in this study (line marked in black) **(B)**.

whiskers extend to 1.5 * Inter-Quartile Range (IQR). The trend significance was assessed based on the *lm* fitting function (R Core Team, 2020). The regime shifts in the summer levels of *Chla* and $K_d(490)$ values were identified using the *changepoint* library (Killick and Eckley, 2014; Killick et al., 2016). It identifies points within a data set where the statistical properties of a time-series change, and it is used in a variety of fields like finances or genetics, but it has been gaining recognition also in the climatology and oceanography (Giamalaki et al., 2018; Nordli et al., 2020). A time series is partitioned into smaller segments where data distribution remains homogeneous, and the beginnings and ends of these segments are characterized by an abrupt change of the mean value, which are sometimes called "tipping points" (Jackson et al., 2005). The algorithm used here is a combination of an optimal partitioning and pruning algorithm denoted "PELT the Pruned Exact Linear Time" (Jackson et al., 2005; Killick et al., 2012).

RESULTS

Monthly Variability

The dark polar night and almost permanent cloud cover limit the number of available and usable satellite images to the period between March and September. Throughout the whole data series spanning 1997–2019, the broadest range of *Chla* concentration values were recorded mostly in April when phytoplankton blooms start in this region. It was visible particularly in the open waters at locations L1, L5, and L9 (**Figure 3** and **Supplementary Figure 1**). In the Hornsund fjord at locations L12 and L13, there was also a substantial variability in March (**Supplementary Figure 1**). The spring bloom peaked in May when the local maxima of *Chla* were observed at most locations. It was followed by a slight *Chla* decrease in June and another increase with a stationary phytoplankton growth phase until the end of summer, sometimes sloping down in the last summer month (September). It is worth noting that at the locations outside the fjords, maximum *Chla* values were observed in May (L1, L5, and L11). On the contrary, in the central parts of the fjords, *Chla* reached maximum concentrations later in the year, usually around July – August (L2, L3, L6, L7, L8, L12, and L13) (**Figure 3** and **Supplementary Figure 1**). The exception is L10, where both global and local maxima were noted only in July and August.

Differences between median values of $K_d(490)$ for a given month were around two orders of magnitude and were the smallest among analyzed parameters. In most cases, the strongest variability was observed in April except L10 in the Van Mijenfjord and L12 and L13 at the Hornsund (**Figure 3** and **Supplementary Figure 3**). At the first location, $K_d(490)$ values increased gradually until July and started sloping downward in August. The latter two locations in the Hornsund fjord are the most interesting due to the fact that the highest variability was observed there in March when there were also observed the highest median values of $K_d(490)$ during analyzed months (March–September). The seasonal changes at other locations in the Isfjorden and the Kongsfjorden depend on whether they are outside or inside the fjords. At the West Spitsbergen Shelf locations (L1, L5, and L11) (**Figure 3** and **Supplementary Figure 2**) or the ones open to enhanced water exchange with the shelf, like L9, the highest medians of $K_d(490)$ were observed in May, whereas at L2, L3, and L10 they were noted in July – August. In the Isfjorden and the Hornsund fjord the July – August local maximum is less visible, but in the inner parts of these two fjords, the higher $K_d(490)$ values were noted later in the year (L6 – L8 and L12 – L13) (**Figure 3** and **Supplementary Figure 3**).

The $a_{tot}(443)$ changes partly follow the patterns of *Chla* with the high variability of values in April, local maxima in May, and a rather unimodal variability with the maximum values in August at L10. However, the local maxima in May could be clearly identified mainly at the open water locations (L1, L5, L9, and L11) or with higher exchange of water with the Greenland Sea (L3). In the inner parts of the Isfjorden, the Kongsfjorden or the Hornsund fjord no maximum in May was observed (L6 – L8 and L12 – L13) (**Figure 3** and **Supplementary Figure 2**). The $a_{tot}(443)$ gradually increased there until September (L6, L7, and L12) or slightly sloped downward in September (L2, L8, and L13) (**Figure 3** and **Supplementary Figure 2**).

Due to the presence of the two local maxima in most analyzed cases – the one around May and the other in July – August, we decided to divide trend analyses and conduct them for the two seasons, separately. The low number of data points in March and April and very high variability of values of considered parameters would significantly disturb the multiyear trend analysis. Therefore, we decided to limit long-term trend analysis only to the period from the beginning of May until the end of September. We estimated separately multiyear trends in spring that covered May – June and in the summer that covered the months of July – September.

Long-Term Trends

Results of trend analysis for all selected locations for all considered optical parameters, *Chla,* $K_d(490)$, and $a_{tot}(443)$ are presented in **Table 1**. We have only included the trend estimates that were statistically significant at p-values < 0.05. The trend analysis revealed a clear seasonal differentiation (**Figure 4**). It should be noted that for the majority of selected locations, the trends estimates for *Chla* and $a_{tot}(443)$ were statistically insignificant. Negative trends for *Chla,* $K_d(490)$, and $a_{tot}(443)$ in spring were identified at the mouth of the Kongsfjorden (L3) and in the Van Mijen Fjord (L10) (**Figures 1**, **4**). The negative $K_d(490)$ trends were also calculated in the Isfjorden (L6 – L8), at the northernmost location on the shelf (L1) and near the mouth of the Hornsund fjord (L12). The only positive trend in spring was observed for $a_{tot}(443)$ in the central Isfjorden at L8 (**Table 1** and **Figure 4**). The opposite pattern was observed in summer. Clearly, the positive trends in the Isfjorden, the Bellsund area and Hornsund fjord were identified. In total, an increase was confirmed at 10 and 9 out of 12 selected locations in the case of *Chla* and $a_{tot}(443)$, respectively (**Figure 4**). At the locations on the shelf (L1, L5, and L11), significant positive trends for *Chla* and $a_{tot}(443)$ were identified, and a positive trend of $K_d(490)$ was confirmed at L1. In the case of the $K_d(490)$, we identified positive

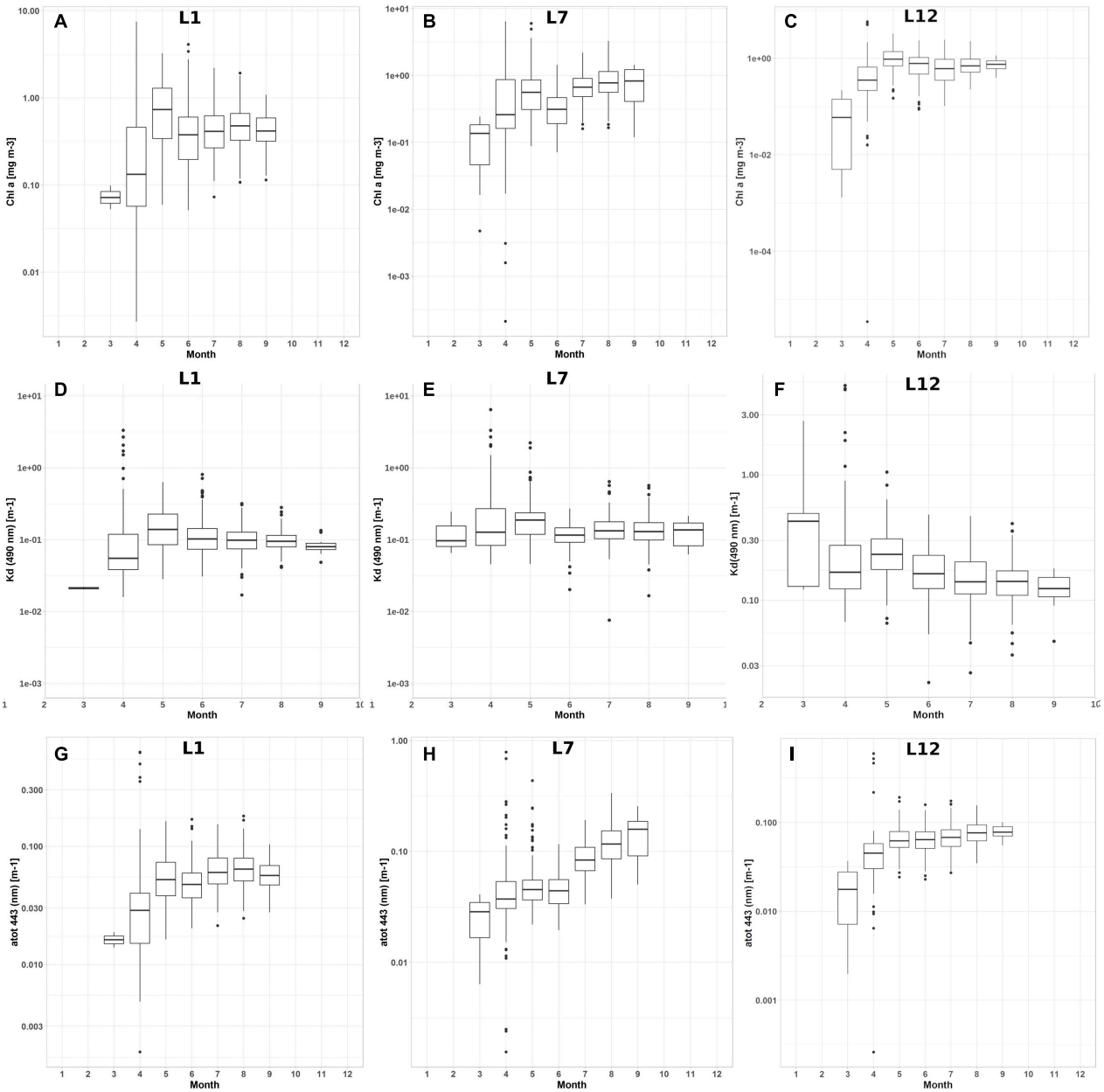


FIGURE 3 | Distribution of the *Chla* **(A–C)**, $K_d(490)$ **(D–F)**, and $a_{tot}(443\ nm)$ **(G–I)** in each month for the whole data series 1997 – 2019 at locations: L1 (on the shelf near the entrance to the Kongsfjorden) **(A,D,G)** – 1st column, L7 (in the central Isfjorden) **(B,E,H)** – 2nd column and L12 (in the outer Hornsund fjord) **(C,F,I)** – 3rd column.

and statistically significant trends at 4 out of 12 locations. Positive summer trends had weaker statistical significance compared to those calculated for *Chla* and $a_{tot}(443)$, and were found at the northern location L1 on the shelf, in the inner part of Isfjorden (L7), in the Bellsund (L9), and the outer part of the Hornsund fjord (L12) with p-values < 0.01 for all of them (**Table 1**). In the inner part of the Hornsund fjord (L13) and on the shelf (L5), no statistically significant trends for $K_d(490)$ were identified. However, in the recent years at L13, we have observed evidently higher variability of $K_d(490)$ values what might indicate beginning of some regime shifts on the long term. Examples of trends calculated for *Chla* and $a_{tot}(443)$ are characterized by the highest value of determination coefficient, R^2, that clearly present positive trend of linearly increasing parameter values within the inner part of the Hornsund (L13) and on the shelf adjacent to the entrance to the Isfjorden (L5) were presented on (**Figure 5**).

To expand information gained with trend analysis, we computed temporal distribution of anomalies of selected optical parameters. The anomalies were calculated as the difference between the median value of each month and the median

TABLE 1 | Identified trends based on the changes of the *Chla* [mg m^{-3}], $\underline{K}_d(490)$ [m^{-1}], and $a_{tot}(443)$ [m^{-1}] during spring (V–VI) and summer months (VII – IX) in the years 1997 – 2019.

Spring (V–VI)	**Lon**	**Lat**	**log(*Chla*)**					**log(a_{tot}(443))**					**log(K_d(490))**				
ID	**°E**	**°N**	***N***	***n***	***a***	***R*^{2}**	***p***	***N***	***n***	***a***	***R*^{2}**	***p***	***N***	***n***	***a***	***R*^{2}**	***p***
1	10.6143	78.9739	1338	401				1338	401				**1338**	**401**	**0.0001**	**0.009**	**0.050**
2	11.6432	79.0034	1341	389				1341	389				1341	389			
3	11.6046	79.1005	1342	246	−0.0004	0.047	0.001	1342	246	−0.0002	0.051	0.001	**1342**	**246**	**0.0004**	**0.123**	**0.001**
5	12.5689	78.0312	1339	387				1339	387				1339	387			
6	14.3210	78.1920	1340	425				1340	425				**1340**	**425**	**0.0001**	**0.017**	**0.100**
7	14.7662	78.2892	1342	441				1342	441				**1342**	**441**	**0.0001**	**0.014**	**0.100**
8	15.3439	78.3892	1342	424				**1342**	**424**	**0.0003**	**0.008**	**0.050**	**1342**	**424**	**0.0001**	**0.024**	**0.001**
9	14.1914	77.6653	1341	361				1341	361				1341	361			
10	15.5140	77.8013	1341	111	−0.0002	0.060	0.010	1341	111	−0.0002	0.106	0.001	**1341**	**111**	**0.0002**	**0.056**	**0.050**
11	13.0515	77.5770	1338	337				1338	337				1338	337			
12	15.1121	76.8992	1342	321				1342	321				**1342**	**321**	**0.0001**	**0.015**	**0.050**
13	15.5281	76.9528	1342	268				1342	268				1342	268			
Summer (V–VI)	**Lon**	**Lat**	**log(*Chla*)**					**log(a_{tot}(443))**					**log(K_d(490))**				
ID	**°E**	**°N**	***N***	***n***	***a***	***R*^{2}**	***p***	***N***	***n***	***a***	***R*^{2}**	***p***	***N***	***n***	***a***	***R*^{2}**	***p***
1	10.6143	78.9739	**2039**	**306**	**0.0001**	**0.061**	**0.001**	**2039**	**306**	**0.0001**	**0.028**	**0.010**	**2039**	**306**	**0.0001**	**0.023**	**0.010**
2	11.6432	79.0034	2041	294				2041	294				2041	294			
3	11.6046	79.1005	2041	224	−0.0001	0.033	0.010	**2041**	**224**	**0.0001**	**0.019**	**0.050**	2041	224			
5	12.5689	78.0312	**2041**	**303**	**0.0001**	**0.022**	**0.010**	**2041**	**303**	**0.0001**	**0.020**	**0.010**	2041	303			
6	14.3210	78.1920	**2040**	**337**	**0.0001**	**0.065**	**0.001**	**2040**	**337**	**0.0001**	**0.050**	**0.001**	2040	337			
7	14.7662	78.2892	**2040**	**342**	**0.0001**	**0.082**	**0.001**	**2040**	**342**	**0.0001**	**0.073**	**0.001**	**2040**	**342**	**0.0001**	**0.027**	**0.010**
8	15.3439	78.3892	**2039**	**340**	**0.0001**	**0.072**	**0.001**	**2039**	**340**	**0.0001**	**0.081**	**0.001**	2039	340			
9	14.1914	77.6653	**2039**	**282**	**0.0001**	**0.064**	**0.001**	**2039**	**282**	**0.0001**	**0.067**	**0.001**	**2039**	**282**	**0.0001**	**0.035**	**0.001**
10	15.5140	77.8013	2041	300				2041	300				2041	300			
11	13.0515	77.5770	**2040**	**274**	**0.0001**	**0.032**	**0.010**	**2040**	**274**	**0.0001**	**0.069**	**0.001**	2040	274			
12	15.1121	76.8992	**2041**	**281**	**0.0001**	**0.052**	**0.001**	**2041**	**281**	**0.0001**	**0.061**	**0.001**	**2041**	**281**	**0.0001**	**0.033**	**0.010**
13	15.5281	76.9528	**2041**	**200**	**0.0001**	**0.031**	**0.010**	**2041**	**200**	**0.0001**	**0.041**	**0.010**	2041	200			

Where N is the total number of data, n is the number of valid values (after excluding e.g., cloud cover), a is the slope of the trend line, R^2 is the determination coefficient and p is p-value. Significant positive trends are marked in bold.

value of all available data in given spring or summer season in the period between 1997 and 2019. At all locations, the amplitudes of $K_d(490)$ anomalies were the smallest, which is consistent with the smallest variability of $K_d(490)$ in the time series dataset (**Figure 3**). Positive anomalies were stronger than negative. The exceptionally high values were noted in the Isfjorden in 2013 and the Hornsund fjord in 2014 (**Figure 6** and **Supplementary Figure 3**). Since 2010, we have observed at most of the analyzed locations the predominance of positive anomalies with higher amplitudes at the majority of locations, especially in the Kongsfjorden (L2), in the outer part of Isfjorden (L6 and L7), and in the Hornsund fjord (L12 and L13). A similar pattern was identified at the West Spitsbergen Shelf locations like L1, L5, and L9, except L11, where strong year-to-year changes from positive to negative anomalies occurred (**Figure 6**).

The trend analysis applied to the whole data series in years 1997 – 2019 gives us an overall view on the long-term changes in the Svalbard area. In order to get a more detailed view on the processes and changes throughout the analyzed time period, we plotted year-to-year anomalies and applied the changepoint detection PELT algorithm. Positive anomalies were predominant for both *Chla* and $a_{tot}(443)$, especially in the Kongsfjorden (L2), the Isfjorden (L6 – L8), the Hornsund fjord (L12 and L13) and even in the Van Mijen fjord (L10). However, within the latter fjord, positive *Chla* anomalies were present along with negative $a_{tot}(443)$ anomalies, all of higher amplitudes. This unusual situation could be explained by greater contributions of other constituents than phytoplankton pigments to the total absorption coefficient. On the shelf (L1, L5, and L11) also positive anomalies persisted after 2010, but at the northernmost shelf locations (L1 and L5), negative anomaly in 2019 was spotted (**Figure 6** and **Supplementary Figures 4,6**).

The change-point method introduces some generalization to the anomalies view by determining some patterns and regimes observed throughout the time of the analyzes (**Figure 7**). Moreover, identified segments follow the anomalies groups and show broader patterns. In the central Isfjorden (L7) the first shift of the mean *Chla* values was in 1998, at the beginning

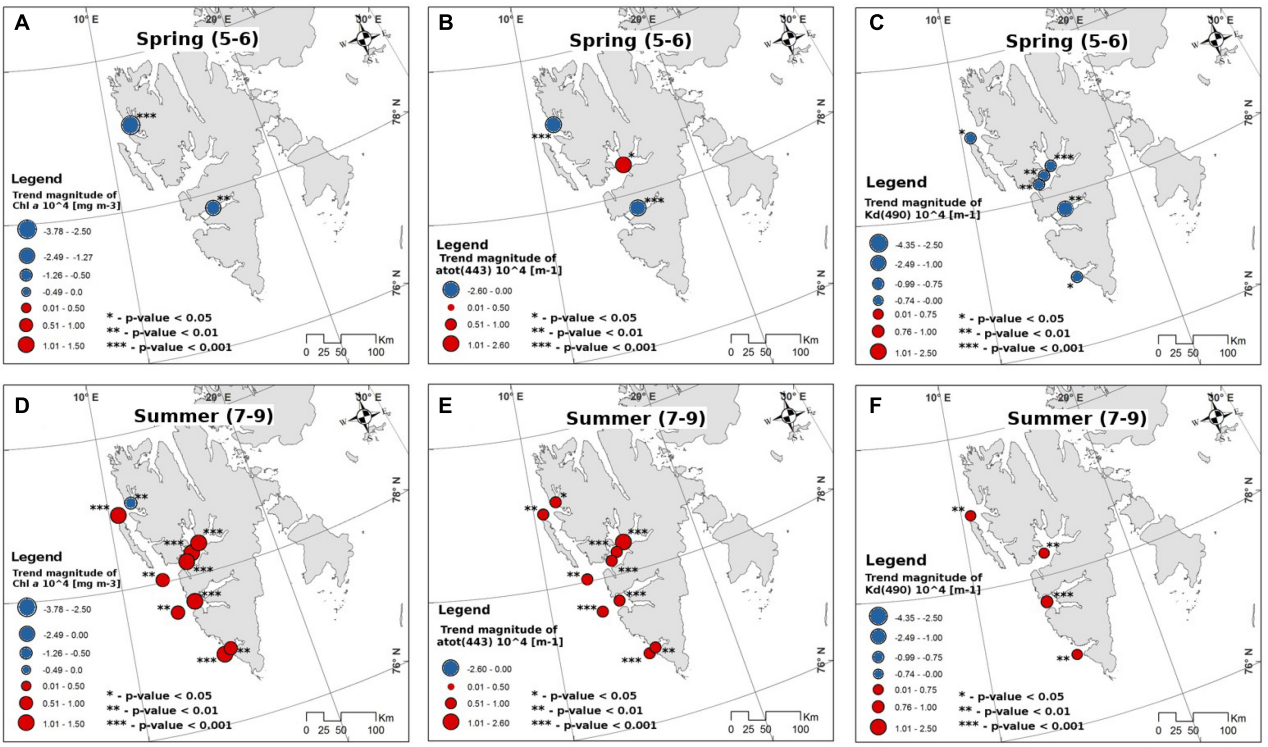


FIGURE 4 | Trends estimates of *Chla* **(A,D)**, a_{tot}(443 nm) **(B,E)**, and K_d(490) **(C,F)** changes throughout the years 1997 – 2019 divided into spring (May – June) and summer (July – September) seasons. *p-value < 0.05; **p-value < 0.01; ***p-value < 0.001.

of our data series, when the mean *Chla* increased from about 0.3 to 0.8 mg m^{-3}. It was followed by a long stationary period. Since 2017, there was another abrupt change to mean values reaching 1.4 mg m^{-3}, which is supported by 4 years characterized by clearly positive *Chla* anomalies (**Figure 6**). The negative *Chla* anomalies in the Bellsund (L9) contributed to the first segment of relatively low mean *Chla* levels around 0.4 mg m^{-3} until 2001 when an evident increase to the level of 1 mg m^{-3} was detected and has persisted since then. Larger variability was observed in the Hornsund fjord (L12) and at L1, the northernmost shelf location. At L1, the *Chla* values were about 0.3 mg m^{-3}, similar to concentrations at L7. In 2002, the mean concentrations increased to about 0.6 mg m^{-3}, but in 2006 *Chla* concentrations dropped to about 0.4 mg m^{-3}. However, it remained higher than at the beginning of the time series. In 2012, another shift took place and the mean *Chla* values around 0.7 mg m^{-3} have persisted since then, despite some negative anomalies in 2015 and 2019 (**Figures 6**, **7**). In the Hornsund fjord (L12), we observed a stepwise increase in *Chla* values from around 0.5 mg m^{-3} to over 1 mg m^{-3} reached in 2012 and persisting since then. However, a particular drop was revealed in the years 2008–2012, notably pronounced in the 2008 – 2009, which are also years of certain negative *Chla* anomalies (**Figure 6**).

The mean values of K_d(490) varied less in time than *Chla* and mostly in the second half of the analyzed period of time (2012–2019). The one exception was a peak observed in 2006 at L1, which was extreme. The K_d(490) doubled in comparison to the mean value in the years 1997–2012 (**Figure 7B**). Since 2012 the mean K_d(490) has been about 20% higher than at the beginning of the time series with the mean values around 1.2 m^{-1}, but within that last period, numerous strong positive anomalies were observed (**Supplementary Figure 6**). In the Hornsund fjord, despite clearly negative anomaly in 2009, situation seemed to be balanced until 2013, followed by a number of positive anomalies which are reflected in the results of change-point analysis since 2013. The last 2 years 2018–2019, especially a decrease of K_d(490) values in 2019 was detected as a downward shift, but depending on the next years it might turn out to be only short-term like the one in 2015 (**Figures 6**, **7**). In the Isfjorden (L7), the average K_d(490) was 0.15 m^{-1} with evident reduction of K_d(490) values in years 2008–2009 and 2014–2015, and a peak in 2013. Since 2015, the average K_d(490) has remained at the higher level of 0.2 m^{-1}. An upward shift of K_d(490) average by 0.1 m^{-1} was first observed in the Bellsund (L9) in 2010. Since then, the average has remained above 0.2 m^{-1}, except for the years 2014 and 2015.

DISCUSSION

Monthly variability in most cases showed two local maxima of the analyzed water characteristics during each year. The first maximum was typically observed in May, and it was particularly pronounced at the shelf locations and in the outer parts of the fjords. The other peak, was observed in late July – early August.

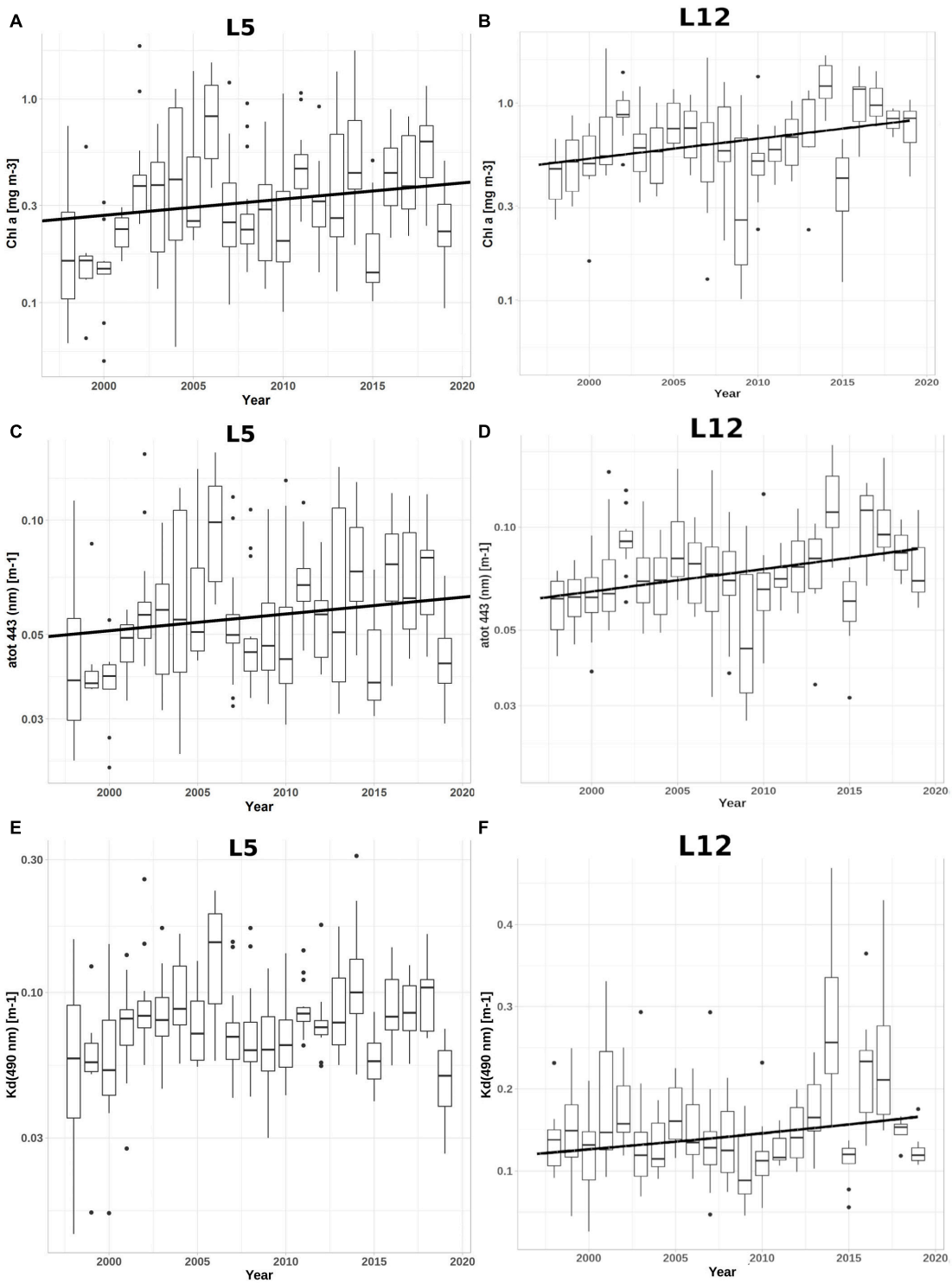


FIGURE 5 | Boxplots of *Chla* **(A,B)** – 1st row, a_{tot} (443) **(C,D)** – 2nd row, and K_d(490) **(E,F)** – 3rd row values during summer season in years 1997 – 2019 with increasing trends (p-value < 0.01) marked with black lines at locations L5 **(A,C,E)** and L12 **(B,D,F)** (**Figure 1**).

This peak was particularly distinct in the central parts of the fjords. The increase of *Chla* and a_{tot}(443) in the Svalbard fjords during analyzed years (1997 – 2019), in particular, is associated with the spring phytoplankton bloom that is additionally stimulated by the advection of the warm AW inflow. The only positive trend in the spring (May – June) months was identified

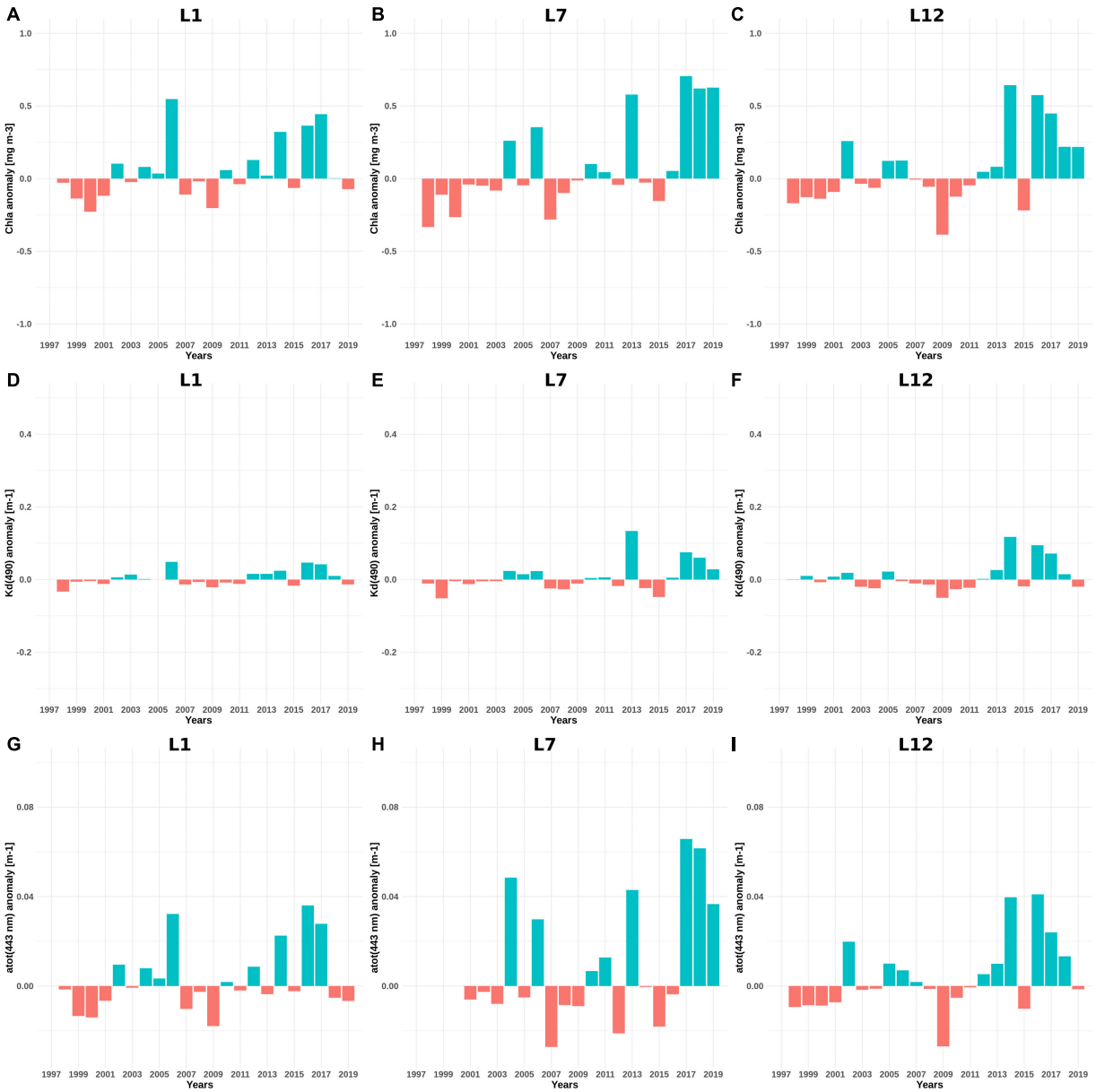


FIGURE 6 | Anomalies of the summer median values of *Chla* (**A–C** – 1st row), $K_d(490)$ (**D–F** – 2nd row), and $a_{tot}(443)$ (**G–I** – 3rd row) each year in reference to the median value for all summer months 1997 – 2019 at locations: L1 (on the shelf at the similar latitude as the Kongsfjorden) (**A,D,G** – left column), L7 (the central Isfjorden) (**B,E,H** – middle column), and L12 (the entrance to the Hornsund fjord) (**C,F,I** – right column).

in the Isfjorden, where there is the strongest influence of the AW due to favoring seabed topography (Cottier et al., 2010). In previous publications, regarding phytoplankton blooms timing in the open waters of Fram Strait, it was acknowledged that blooms started in this region in May, reached maxima in June, and lasted through July (Cherkasheva et al., 2014). Satellite observations in this paper revealed that phytoplankton blooms within the Svalbard fjords start, in general, a month earlier – in April and peak in May. Although we do not have *in situ* measurements collected in April – June, the timing of the identified blooms in May is consistent with the findings of other studies conducted in the Svalbard fjords, e.g., the Kongsfjorden (Calleja et al., 2017; Ericson et al., 2019; Hegseth et al., 2019). The late summer maximum is probably of a more complex nature that will be further discussed. Anyway, this clear division combined with the awareness of the seasonal differences in the water column structure was a basis for analyzing available time series in the two separate seasons – spring (May – June) and summer (July – September).

A shallow mixed layer is typically favorable for accumulation of particulate matter within it. Payne and Roesler (2019) reported a systematic increase of the backscattering coefficient

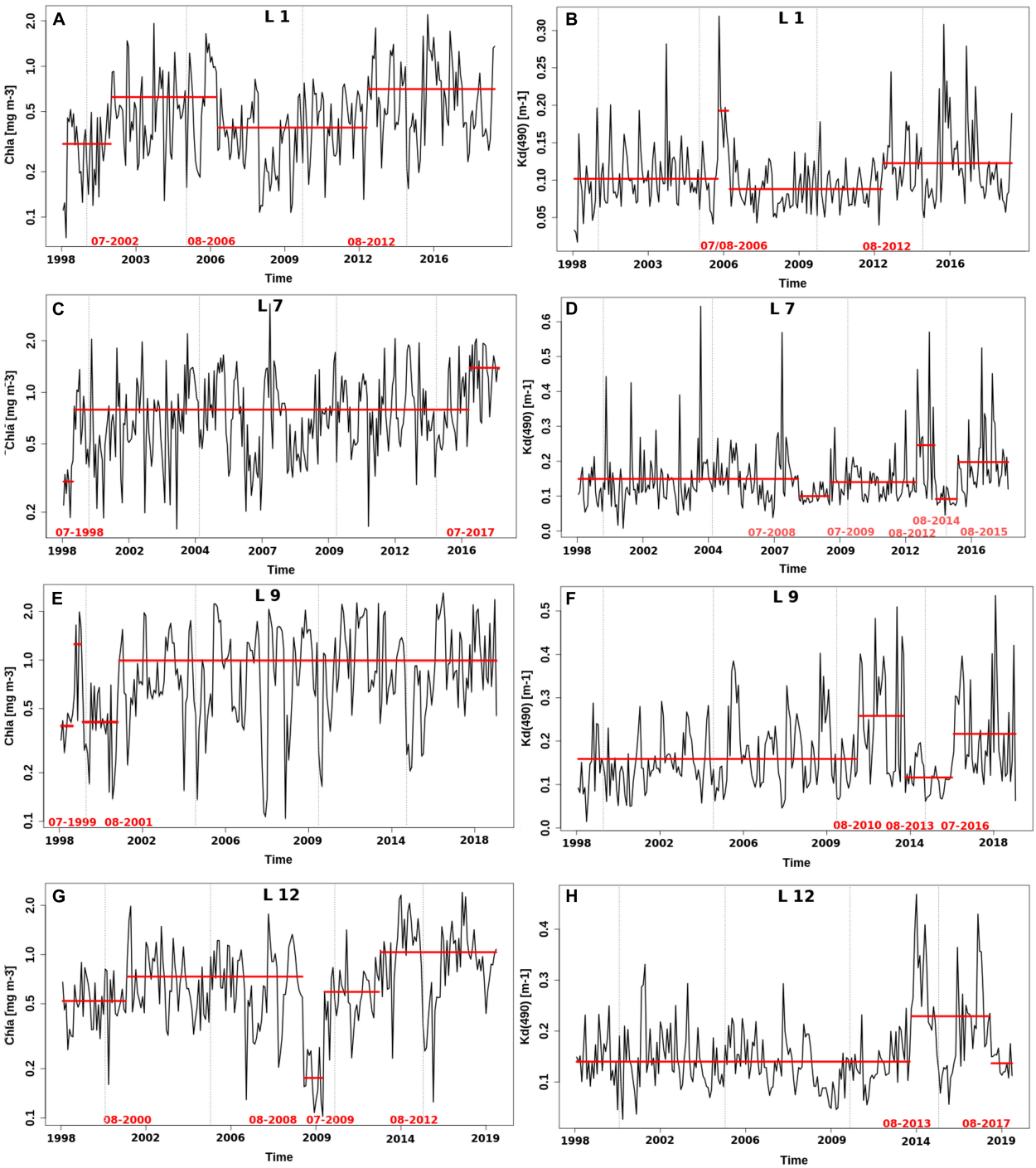


FIGURE 7 | Data series of *Chla* **(A,C,E,G)** – left row and $K_d(490)$ **(B,D,F,H)** – right row – stacked values from the summer months at the locations L1 (the shelf near the Kongsfjorden), L7 (the central Isfjorden), L9 (the Bellsund) and L12 (the entrance to the Hornsund fjord) with the segments of consistent water characteristics split at the shift points marked in red line. The turning points were determined based on the PELT changepoint detection method (Killick et al., 2012). Additional vertical gray lines mark the beginnings of the years 2000, 2005, 2010, and 2015.

$b_b(440)$ and absorption coefficient by colored detrital material (particulate and dissolved) $a_{dg}(440)$ values from May to August in the Kongsfjorden, which was attributed to an increase in stratification. Higher quantities of optically active sea-water constituents become trapped in a confined mixed layer, i.e., within light penetration depth and satellite sensors detection range. It was estimated back in the 1970s that ocean color satellite sensors measure light that penetrates water column to the depth

above which 90% of the diffusely reflected irradiance originates z_{90} (except specular reflectance) (Gordon and McCluney, 1975). According to Jerlov (1976) in coastal waters light penetration depth z_{90} usually does not exceed 10 m and in homogeneous water bodies such as the top mixed layer of oceanic waters, e.g., near the mouth of the fjord, the z_{90} may range up to around 20 m (Gordon and McCluney, 1975; Szeligowska et al., 2020). This means that within the fjords analyzed here, only changes of the IOPs in the maximum top 20 m would be visible in the satellite images. Therefore, the summer season is a time when the probability of obtaining the most complete picture of the primary productivity is the highest. Thus, in order to observe and identify any long-term changes we focused on the summertime when strong stratification ensures accumulation of the optically significant sea water constituents within the z_{90}.

The most interesting result was the consistent increase of all analyzed parameters in July – August in the long-term at numerous locations (**Figure 4**). On the one hand, a high correlation between $K_d(490)$, *Chla,* and $a_{tot}(443)$ implies that the phytoplankton (with C*hla* as a proxy) controls the IOPs variability to a large extent in the area of study. Our observations seem to coincide with the positive trends in long-term AW inflow and glacier-melt runoff during the analyzed period (1997 – 2019) which are the two possible reasons, potentially explaining the positive trends in IOPs. The increase of the AW impact on the water masses within the Svalbard fjords, phytoplankton bloom dynamics, and acceleration of the melting processes were reported in some of the recent publications (Pavlov et al., 2013; Promińska et al., 2017; Hegseth et al., 2019; Bloshkina et al., 2021). The presence of the warmer AW may cause faster ice-melting from the bottom and higher heat content at the starting point which means that the temperature optima of the planktonic organisms may be reached or exceeded earlier in the year. It may result in earlier blooms onset or phenology shifts, or both. On the other hand, nutrients are the limiting factor for primary productivity, and nutrient levels remain low during summer, starting from June (Calleja et al., 2017; Ericson et al., 2019). However, particular attention should be given to glacier meltwaters considered an important local nutrient source (Stachnik et al., 2019). Microbial activity at the glacier surfaces and within the cryoconite holes where even nitrogen-fixing cyanobacteria are found, can provide a substantial source of nutrients into fjords (Telling et al., 2011; Anesio et al., 2017). Despite the fact that composition of the glacier and fjord bacterial communities are entirely distinct, a significant relationship between nutrients (NO_3^- and SiO_4^{2-}) and glacier melt-water bacterial communities within the fjords was already confirmed (Thomas et al., 2020). This suggests that acceleration of the glacier retreat may bring excess loads of nutrients and photosynthetic microbes that stimulate primary productivity, and may be responsible for the higher values of *Chla* and $a_{tot}(443)$ observed here in July – August. Previous research also revealed that, in the Hornsund fjord, the contribution of the total precipitation over land (excluding winter snowfall), total precipitation over the fjord area, and melting of the snow cover over unglaciated areas are roughly less than 36% of the total freshwater input. In contrast, glacier melt-water runoff and frontal ablation of tidewater glaciers are predominant in the area (Błaszczyk et al., 2013). A coupled energy balance–subsurface model also confirmed this tendency for the whole of Svalbard and predicted a further increase of the glacier-melt runoff in the coming years (van Pelt et al., 2019). This means that the nutrient pool may rise for some time in the Svalbard area, it supports our observations of positive *Chla* and $a_{tot}(443)$ trends and forecasts further possible increases at least as long as the glaciers are still present.

In spring, we mainly observed negative trends in the Svalbard area during 1997 – 2019 (**Figure 3**). However, *Chla* and $a_{tot}(443)$ seemed to decrease only in the Van Mijen Fjord (L10) and around the mouth of the Kongsfjorden (L3). The negative trends of $K_d(490)$ are visible also within the fjords or the entrance of the fjords. Due to higher year-to-year variability and more possible sources of satellite data contamination, conclusions should be drawn more carefully for this season. Firstly, we should consider the role of adjacency effects. Their impact may be twofold, and in both cases, they are closely related to the *albedo*. Typically, at locations where *albedo* is high, particularly due to the presence of snow or ice, photons are scattered into the atmosphere and contaminate registered radiance. It often results in overestimating water-leaving radiance in the neighboring areas (Bélanger et al., 2005). Analogical effects are observed near the clouds, because of their high *albedo*. It was proved that during the melting season cloud cover above the Arctic intensifies (He et al., 2019). Even though the snow and ice cover have decreased in the Kongsfjorden, a significant increase in humidity and the cloud cover in that area were confirmed with the highest variability in May – July (Maturilli et al., 2019). The impact of land topography may also play a role here. The narrow, elongated shape and steep walls of the fjords enhance scattering and multiply the adjacency effects (Rozwadowska and Górecka, 2017). The other aspect is the high year-to-year variability that in spring may stem from the fact that dynamics of the three factors controlling the environment in this area which are the AW inflow, the snow and ice cover, and glacier melt-water discharge, has been changing recently (Hegseth et al., 2019). In the Kongsfjorden, ice cover has been declining in the last 10 years (Pavlova et al., 2019). The estimated first snow-free day at Svalbard as a whole is around 29th of June, so both the sea ice and land snowmelt may intensify around April – June (Vickers et al., 2020). Except for winter, spring was the season when the fastest increase of air temperatures was identified based on the observations at Ny-Ålesund BSRN site at a rate of 1K $\pm$ 1.4K per decade (Maturilli et al., 2019). Processes in the water column cannot be analyzed separately from the atmospheric conditions and land influence. The air temperatures govern the pace of the ice and snowmelt in the whole area, and therefore govern the amount of the meltwater runoff from the land into the fjords. In spring, fresh meltwater forms a thin near-surface layer due to the low salinity. This is a relatively transparent layer (0–10 m) which is optically clear in comparison to the underlying water masses (Granskog et al., 2015), because meltwater effectively dilutes the CDOM (Kowalczuk et al., 2017, 2019). Although the meltwater could contain higher loads of

the suspended particulate material (Bélanger et al., 2013), this does not contribute significantly to the decreased transparency, especially at the beginning of the melting time. Approximately half of the ice-free area in Svalbard falls beyond the vegetation season (Vickers et al., 2016). The ice and snow water themselves contains a depleted level of nutrients (Ardyna et al., 2011) which does not allow for intense phytoplankton growth. When it predominates the water column above the first optical depth, it leads to underestimating values of remotely sensed *Chla*, $a_{tot}(443)$ or $K_d(490)$, because subsurface chlorophyll *a* maxima usually form below ocean color sensor detection depth (Ardyna et al., 2013; Kowalczuk et al., 2019). This may be the main reason why we observe negative trends in spring. Smaller amounts of the sea ice combined with intense melting of it may result in earlier and more pronounced near-surface diluted layer observed from the satellites.

With the start of the vegetative season the water composition may change. Land vegetation is a potential source of CDOM, suspended particulate material or nutrients, especially in summer months when flora thrives. The previous analyses revealed an increasing trend of the vegetation growth in Svalbard during the last decades (Vickers et al., 2016). It is particularly worth noting that the previous studies conducted by Vickers et al. (2020) on the timing of the snow disappearance is consistent with the inter-annual anomalies of all three analyzed water properties. In the years when the first snow-free days were observed earlier, in most cases negative anomalies in spring and positive anomalies in summer were observed, whereas later snow cover retreat resulted in the opposite patterns. This may imply that earlier start of the melting period may cause intensified ice and snow melt resulting in formation of a deeper or more diluted top layer in spring which may be followed by enhanced vegetation growth and glacier melt that provide extra nutrients inputs. It is reflected in negative anomalies in spring, followed by positive anomalies in summer. The long-term increasing trends of the glacier melt and vegetation growth in summer by the other researchers support this explanation, as well as justify the increasing summer trends observed here in the long term (Vickers et al., 2016; van Pelt et al., 2019).

Apart from air temperatures the AW water is also a huge heat store that gives up its heat and stimulates the melting processes of the sea ice as well as near-shore snow and ice cover. An evident manifestation of the AW impact was the extreme inflow to the Kongsfjorden (L2 and L1 on the shelf in the fjord vicinity) in 2006 (Głuchowska et al., 2016). Positive summer anomalies of all analyzed water characteristics were observed in that year at the locations L2 and L1, with a particularly strong anomaly of $K_d(490)$ on the shelf at L1 (**Supplementary Figure 6**) which was detected using change-point analysis as an exceptional year (**Figure 7**). In the inner Hornsund fjord the AW was recognized for the first time in summer of 2014 and has been observed there with varied frequency and intensity since then (Promińska et al., 2017). The year 2014 was suggested to be a breakthrough year for the Hornsund fjord (Głuchowska et al., 2016) and it was identified as such here based on the change-point analysis of $K_d(490)$ where we may see a regime shift between 2013 and 2014 (**Figure 7**). The other years with some AW intrusions that turned both the Hornsund fjord and the Kongsfjorden into the 'warmer' mode were 2002, 2006, and 2013 when we observed positive anomalies (**Supplementary Figures 4–6**) (Promińska et al., 2017). On the other hand, strong influence of the SC current on the Hornsund environment (L12) was reflected in our research. In the years when the SC inflow into the Hornsund was indicated by Promińska et al. (2017) such as 2001, 2004, 2008, and 2011 we observed negative summer anomalies of *Chla*, $a_{tot}(443)$ and $K_d(490)$ values (**Supplementary Figures 4–6**). A general message of the comparison of anomalies and time patterns at various locations around Svalbard is the clear upward shift of the *Chla* starting from the open-water locations at the beginning of 2000s, and an even more pronounced increase of all three parameters *Chla*, $a_{tot}(443)$ and $K_d(490)$ around 2012 – 2013 that manifested in strong positive anomalies in summer months and significant changes of the regimes that probably contributed the most to the increasing trends identified on the long term (**Figures 6**, **7** and **Supplementary Figures 4–6**).

CONCLUSION

Based on the analysis of the time series of satellite images in years 1997 – 2019, evident positive trends were revealed in the Kongsfjorden, the Isfjorden, the Hornsund fjord and the Bellsund. Even though there were differences between the trend estimates and their significance, we confirmed positive summer trends (July – September) of $a_{tot}(443)$, *Chla* and $K_d(490)$ at 10, 9, and 4 locations out of 12 consequently. We hypothesize that these changes can be attributed to changes and interplay in other environmental factors, such as hydrography, glacier and river runoff, precipitations, and atmospheric warming. It also should be noted that the enhanced amplitudes of anomalies observed in recent years are in line with observations and models showing that growing variability in the system can precede its regime shift (Spanbauer et al., 2014; Bury et al., 2021). Moreover, between 1997 and 2019 at the majority of locations we observed a regime shift toward darker waters. Our work provides the first documented record of 'darkening' in Svalbard fjords and adjacent shelf waters, and call for further investigation of these potentially profound environmental and ecosystem changes in the area. This work sets the baseline for consideration of the coastal darkening in the environmental management plans on Svalbard. It should be also considered in ecological modeling aiming at prediction of environmental changes related to global warming.

DATA AVAILABILITY STATEMENT

The original contributions presented in the study are included in the article/**Supplementary Material**, further inquiries can be directed to the corresponding author.

AUTHOR CONTRIBUTIONS

MK, PK, AP, MD, and SS: conceptualization, formal analysis, and writing–review and editing. MK and MD: methodology and

data curation. MK: software and visualization. MK, PK, AP, and MD: investigation. PK, MD, and SS: resources. MK, PK, and MD: writing–original draft preparation. PK: project administration. PK, AP, MD, and SS: funding acquisition. All authors contributed to the article and approved the submitted version.

FUNDING

This study was supported by the Svalbard Environmental Protection Fund (Svalbards miljøvernfond), project nr. 19/21 - Monitoring Darkening of Svalbard Fjords from space.

ACKNOWLEDGMENTS

We thank the crews of R/V Lance and R/V Oceania and colleagues for the help on board during collecting the sea-truth data.

SUPPLEMENTARY MATERIAL

The Supplementary Material for this article can be found online at: https://www.frontiersin.org/articles/10.3389/fmars.2021.699318/full#supplementary-material

REFERENCES

Aksnes, D. L., Dupont, N., Staby, A., Fiksen, Ø, Kaartvedt, S., and Aure, J. (2009). Coastal water darkening and implications for mesopelagic regime shifts in Norwegian fjords. *Mar. Ecol. Prog. Ser.* 387, 39–49. doi: 10.3354/meps08120

Anesio, A. M., Lutz, S., Chrismas, N. A. M., and Benning, L. G. (2017). The microbiome of glaciers and ice sheets. *Bio. Microb.* 3:10. doi: 10.1038/s41522-017-0019-0

Ardyna, M., and Arrigo, K. R. (2020). Phytoplankton dynamics in a changing Arctic Ocean. *Nat. Clim. Change* 10, 892–903. doi: 10.1038/s41558-020-0905-y

Ardyna, M., Babin, M., Gosselin, M., Devred, E., Bélanger, S., Matsuoka, A., et al. (2013). Parameterization of vertical chlorophyll a in the Arctic Ocean: impact of the subsurface chlorophyll maximum on regional, seasonal, and annual primary production estimates. *Biogeosciences* 10, 4383–4404. doi: 10.5194/bg-10-4383-2013

Ardyna, M., Gosselin, M., Michel, C., Poulin, M., and Tremblay, J. E. (2011). Environmental forcing of phytoplankton community structure and function in the Canadian High Arctic: Contrasting oligotrophic and eutrophic regions. *Mar. Ecol. Prog. Ser.* 442, 37–57. doi: 10.3354/meps09378

Arrigo, K. R. (2017). "Sea ice as a habitat for primary producers," in *Sea Ice*, ed. D. N. Thomas (Chichester: John Wiley & Sons, Ltd).

Bartsch, I., Paar, M., Fredriksen, S., Schwanitz, M., Daniel, C., Hop, H., et al. (2016). Changes in kelp forest biomass and depth distribution in kongsfjorden, svalbard, between 1996–1998 and 2012–2014 reflect Arctic warming. *Polar Biol.* 39, 2021–2036. doi: 10.1007/s00300-015-1870-1

Bélanger, S., Cizmeli, S. A., Ehn, J., Matsuoka, A., Doxaran, D., Hooker, S., et al. (2013). Light absorption and partitioning in Arctic Ocean surface waters: impact of multiyear ice melting. *Biogeosciences* 10, 6433–6452. doi: 10.5194/bg-10-6433-2013

Bélanger, S., Ehn, J., and Babin, M. (2005). "Impact of sea ice on ocean color remote sensing," in *Proceeding of the SPIE 5885, Remote Sensing of the Coastal Oceanic Environment, 588509* (San Diego, CA).

Bianchi, T. S., Arndt, S., Austin, W. E. N., Benn, D. I., Bertrand, S., Cui, X., et al. (2020). Fjords as aquatic critical zones (ACZs). *Earth Sci. Rev.* 203:103145. doi: 10.1016/j.earscirev.2020.103145

Błaszczyk, M., Jania, J. A., and Kolondra, L. (2013). Fluctuations of tidewater glaciers in hornsund fjord (Southern Svalbard) since the beginning of the 20th century Pol. *Polar Res.* 34, 327–352. doi: 10.2478/popore-2013-0024

Blondeau-Patissier, D., Gower, J., Dekker, A., Phinn, S., and Brando, V. (2014). A review of ocean color remote sensing methods and statistical techniques for the detection, mapping and analysis of phytoplankton blooms in coastal and open oceans. *Prog. Oceanogr.* 123, 123–144. doi: 10.1016/j.pocean.2013.12.008

Bloshkina, E., Pavlov, A. K., and Filchuk, K. (2021). Warming of Atlantic water in three west spitsbergen fjords: recent patterns and century-long trends. *Polar Research* 40:5392. doi: 10.33265/polar.v40.5392

Bury, T. M., Sujith, R. I., Pavithran, I., Scheffer, M., Lenton, T. M., Anand, M., et al. (2021). Deep learning for early warning signals of regime shifts. *bioRxiv* [preprint]. doi: 10.1101/2021.03.28.437429

Calleja, M. L., Kerhervé, P., Bourgeois, S., Kędra, M., Leynaert, A., Devred, E., et al. (2017). Effects of increase glacier discharge on phytoplanktonbloom dynamics and pelagic geochemistry in a high Arctic fjord. *Prog. Oceanogr.* 159, 195–210. doi: 10.1016/j.pocean.2017.07.005

Campbell, J. W. (1995). The log-normal distribution as a model for bio-optical variability in the sea. *J. Geophys. Res. Atmospheres* 100, 13237–13254. doi: 10.1029/95JC00458

Cherkasheva, A., Bracher, A., Melsheimer, C., Köberle, C., Gerdes, R., Nöthig, E. M., et al. (2014). Influence of the physical environment on polar phytoplankton blooms: a case study in the fram strait. *J. Mar. Syst.* 132, 196–207. doi: 10.1016/j.jmarsys.2013.11.008

CMEMS (2020). *Product User Manual for All Ocean Colour Products. Ref: CMEMS-OC-PUM-009-ALL.* PUM. Available online at: marine.copernicus.eu/documents/PUM/CMEMS-OC-PUM-009-ALL.pdf, QUID: marine.copernicus.eu/documents/QUID/CMEMS-OC-QUID-009-066-067-068-069-088-091.pdf doi: 10.1016/j.jmarsys.2013.11.008 (accessed March 11, 2020).

Cohen, J., Screen, J. A., Furtado, J. C., Barlow, M., Whittleston, D., Coumou, D., et al. (2014). Recent Arctic amplification and extreme mid-latitude weather. *Nat. Geosci.* 7, 627–637. doi: 10.1038/ngeo2234

Cottier, F. R., Nilsen, F., Skogseth, R., Tverberg, V., Skarđhamar, J., and Svendsen, H. (2010). Arctic fjords: a review of the oceanographic environment and dominant physical processes. *Geolog. Soc. London Special Publi.* 344, 35–50. doi: 10.1144/SP344.4

Curry, J. A., Schramm, J. L., and Ebert, E. E. (1995). Sea ice-albedo climate feedback mechanism. *J. Clim.* 8, 240–247.

Dera, J. (1992). *Marine Physics*. Amsterdam: Elsevier.

Emberton, S., Chittka, L., Cavallaro, A., and Wang, M. (2016). Sensor capability and atmospheric correction in ocean colour remote sensing. *Remote Sens.* 8. doi: 10.3390/rs8010001

Engel, A., Bracher, A., Dinter, T., Endres, S., Grosse, J., Metfies, K., et al. (2019). Inter-annual variability of organic carbon concentration in the eastern fram strait during summer (2009–2017). *Front. Mar. Sci.* 6:187. doi: 10.3389/fmars.2019.00187

Ericson, Y., Chierici, M., Falck, E., Fransson, A., Jones, E., and Kristiansen, S. (2019). Seasonal dynamics of the marine CO2 system in adventfjorden, a west spitsbergen fjord. *Polar Res.* 38:3345. doi: 10.33265/polar.v38.3345

Førland, E. J., Benestad, R., Hanssen-Bauer, I., Haugen, J. E., and Skaugen, T. E. (2011). Temperature and precipitation development at svalbard 1900–2100. *Adv. Meteorol.* 2011:893790. doi: 10.1155/2011/893790

Geoffroy, M., Berge, J., Majaneva, S., Johnsen, G., Langbehn, T. J., Cottier, F., et al. (2018). Increased occurrence of the jellyfish periphylla periphylla in the European high Arctic. *Polar Biol.* 41, 2615–2619.

Giamalaki, K., Beaulieu, C., Faranda, D., Henson, S. A., Josey, S. A., and Martin, A. P. (2018). Signatures of the 1976–1977 regime shift in the North Pacific revealed by statistical analysis. *J. Geophys. Res. Oceans* 123, 4388–4397. doi: 10.1029/2017JC013718

Głuchowska, M., Kwaśniewski, S., Promińska, A., Olszewska, A., Goszczko, I., Falk-Petersen, S., et al. (2016). Zooplankton in Svalbard fjords on the Atlantic–Arctic boundary. *Polar Biol.* 39, 1785–1802. doi: 10.1007/s00300-016-1991-1

Gordon, H. R., and McCluney, W. R. (1975). Estimation of the depth of sunlight penetration in the seafor remote sensing. *Appl. Optics* 14, 413–416.

Gordon, H. R., and Morel, A. Y. (1983). *Remote Assessment of Ocean Colour for Interpretation of Satellite Visible Imagery: A Review*. New York, NY: Springer.

Gordon, H. R., Clark, D. K., Mueller, J. L., and Hovis, W. A. (1980). Phytoplankton pigments from the Nimbus-7 coastal zone color scanner: comparisons with surface measurements. *Science* 210, 63–66.

Granskog, M. A., Pavlov, A. K., Sagan, S., Kowalczuk, P., Raczkowska, A., and Stedmon, C. A. (2015). Effect of sea-ice melt on inherent optical properties and vertical distribution of solar radiant heating in Arctic surface waters. *J. Geophys. Res. Oceans* 120, 7028–7039. doi: 10.1002/2015JC011087

He, M., Hu, Y., Chen, N., Wang, D., Huang, J., and Stamnes, K. (2019). High cloud coverage over melted areas dominates the impact of clouds on the albedo feedback in the Arctic. *Sci. Rep.* 9:9529. doi: 10.1038/s41598-019-44155-w

Hegseth, E. N., Assmy, P., Wiktor, J. M., JWiktor, J. Jr., Kristiansen, S., Leu, E., et al. (2019). "Phytoplankton seasonal dynamics in kongsfjorden, Svalbard and the adjacent shelf," in *The Ecosystem of Kongsfjorden, Svalbard, Advances in Polar Ecology 2*, eds H. Hop and C. Wiencke (Springer).

Hill, V., Ardyna, M., Lee, S. H., and Varela, D. E. (2018). Decadal trends in phytoplankton production in the Pacific Arctic region from 1950 to 2012. *Deep Sea Res. Part II Top. Stud. Oceanogr.* 152, 82–94. doi: 10.1016/j.dsr2.2016.12.015

Holinde, L., and Zielinski, O. (2016). Bio-optical characterization and light availability parameterization in Uummannaq fjord and vaigat–disko bay (West Greenland). *Ocean Sci.* 12, 117–128. doi: 10.5194/os-12-117-2016

Isaksen, K., Benestad, R. E., Harris, C., and Sollid, J. L. (2007). Recent extreme near-surface permafrost temperatures on Svalbard in relation to future climate scenarios. *Geophys. Res. Lett.* 34:L17502. doi: 10.1029/2007GL031002

Jackson, B., Sargle, J. D., Barnes, D., Arabhi, S., Alt, A., Gioumousis, P., et al. (2005). An algorithm for optimal partitioning of data on an interval. *IEEE Signal Proc. Lett.* 12, 105–108.

Jerlov, N. G. (1976). *Marine Optics*. Amsterdam: Elsevier.

Kaplan, D., and Pruim, R. (2020). *ggformula: Formula Interface to the Grammar of Graphics. R Package Version 0.9.4*.

Kashiwase, H., Ohshima, K. I., Nihashi, S., and Eicken, H. (2017). Evidence for ice-ocean albedo feedback in the Arctic Ocean shifting to a seasonal ice zone. *Sci. Rep.* 7:8170. doi: 10.1038/s41598-017-08467-z

Killick, R., and Eckley, I. A. (2014). Changepoint: an R package for changepoint analysis. *J. Statist. Softw.* 58:i03.

Killick, R., Fearnhead, P., and Eckley, I. A. (2012). Optimal detection of changepoints with a linear computational cost. *J. Am. Statist. Assoc.* 107, 1590–1598.

Killick, R., Haynes, K., Eckley, I., Fearnhead, P., and Lee, J. (2016). *Changepoint: Methods for Changepoint Detection. R Package Version 2.2.2*.

Kipp, L. E., Charette, M. A., Moore, W. S., Henderson, P. B., and Rigor, I. G. (2018). Increased fluxes of shelf-derived materials to the central Arctic Ocean. *Sci. Adv.* 4:eaao1302. doi: 10.1126/sciadv.aao1302

Kohler, J., James, T. D., Murray, T., Nuth, C., Brandt, O., Barrand N. E., et al. (2007). Acceleration in thinning rate on western Svalbard glaciers. *Geophys Res. Lett.* 34:L18502. doi: 10.1029/2007GL030681

Konik, M., Kowalczuk, P., Zabłocka, M., Makarewicz, A., Meler, J., Zdun, A., et al. (2020). Empirical relationships between remote-sensing reflectance and selected inherent optical properties in nordic sea surfacewaters for the MODIS and OLCI Ocean colour sensors. *Remote Sens.* 12:2774. doi: 10.3390/rs12172774

Kowalczuk, P., Meler, J., Kauko, H. M., Pavlov, A. K., Zabłocka, M., Peeken I., et al. (2017). Bio-optical properties of Arctic drift ice and surface waters north of Svalbard from winter to spring. *J. Geophys. Res. Oceans,* 122, 4634–4660. doi: 10.1002/2016JC012589

Kowalczuk, P., Sagan, S., Makarewicz, A., Meler, J., Borzycka, K., Zabłocka, M., et al. (2019). Bio-optical properties of surface waters in the Atlanticwater inflow region off Spitsbergen (Arctic Ocean). *J. Geophys. Res. Oceans* 124, 1964–1987. doi: 10.1029/2018JC014529

Lorenzen, C. L. (1967). Determination of chlorophyll and pheo-pigments: spectrophotometric equations. *Limnol. Oceanogr.* 12, 343–346.

Makarewicz, A., Kowalczuk, P., Sagan, S., Granskog, M., Pavlov, A., Zdun, A., et al. (2018). Characteristics of chromophoric and fluorescent dissolved organic matter in the Nordic Seas. *Ocean Sci.* 14, 543–562. doi: 10.5194/os-14-543-2018

Mascarenhas, V. J., and Zielinski, O. (2018). Parameterization of spectral particulate and phytoplankton absorption coefficients in sognefjord and trondheimsfjord, two contrasting norwegian fjord ecosystems. *Remote Sens.* 10:977. doi: 10.3390/rs10060977

Mascarenhas, V. J., and Zielinski, O. (2019). Hydrography-driven optical domains in the vaigat-disko bay and godthabsfjord: effects of glacial meltwater discharge. *Front. Mar. Sci.* 6:335. doi: 10.3389/fmars.2019.00335

Mascarenhas, V. J., Voß, D., Wollschlaeger, J., and Zielinski, O. (2017). Fjord light regime: bio-optical variability, absorption budget, and hyperspectral light availability in sognefjord and trondheimsfjord, norway. *J. Geophys. Res. Oceans* 122, 3828–3847. doi: 10.1002/2016JC012610

Maturilli, M., Hanssen-Bauer, I., Neuber, R., Rex, M., and Edvardsen, K. (2019). "The atmosphere above ny-ålesund: climate and global warming, ozone and surface UV radiation," in *The Ecosystem of Kongsfjorden, Svalbard, Advances in Polar Ecology 2*, eds H. Hop and C. Wiencke (Springer).

McClain, C. R., Arrigo, K. R., Esaias, W., Darzi, M., Patt, F. S., Evans, R. H., et al. (1995). "SeaWiFS algorithms, part 1," in *SeaWiFS Technical Report Series*, eds S. B. Hooker, E. R. Firestone, and J. G. Acker (Maryland: NASA Goddard Space Flight Center, Greenbelt).

McPhee, M. G. (2017). "The sea ice–ocean boundary layer," in. *Sea Ice*, Vol. 5, ed. D. N. Thomas (John Wiley & Sons), 138–159. doi: 10.1002/9781118778371.ch5

Mélin, F., Vantrepotte, V., Chuprin, A., Grant, M., Jackson, T., and Sathyendranath, S. (2016). "Global trends in chlorophyll concentration observed with the satellite ocean colour data record," in *Proceeding of the European Space Agency, Special Publication*, ed. L. Ouwehand (ESA), 740.

Morel, A., and Prieur, L. (1977). Analysis of variations in ocean color. *Limnol. Oceanogr.* 22, 709–722.

Mueller, J. L., Austin, R. W., Morel, A., Fargion, G. S., and McClain, C. R. (2003). *Ocean Optics Protocols For Satellite Ocean Color Sensor Validation, Revision 4*.

Neukermans, G., Oziel, L., and Babin, M. (2018). Increased intrusion of warming Atlantic water leads to rapidexpansion of temperate phytoplankton in the Arctic. *Global Change Biol.* 24:14075. doi: 10.1111/gcb.14075

Noël, B., Jakobs, C. L., van Pelt, W. J. J., Lhermitte, S., Wouters, B., Kohler, J., et al. (2020). Low elevation of Svalbard glaciers drives high mass loss variability. *Nat. Commun.* 11:4597. doi: 10.1038/s41467-020-18356-1

Nordli, Ø, Wyszyński, P., Gjelten, H. M., Isaksen, K., Łupikasza, E., Niedźwiedź, T., et al. (2020). Revisiting the extended Svalbard airport monthly temperature series, and the compiled corresponding daily series 1898–2018. *Polar Res.* 39:3614. doi: 10.33265/polar.v39.3614

Oziel, L., Neukermans, G., Ardyna, M., Lancelot, C., Tison, J.-L., Wassman, P., et al. (2017). Role for Atlantic inflows and sea ice loss on shifting phytoplankton blooms in the barents sea. *J. Geophys. Res. Oceans Wiley Blackwell* 122, 5121–5139. doi: 10.1002/2016JC012582

Parmentier, F.-J. W., Christensen, T. R., Rysgaard, S., Bendtsen, J., Glud, R. N., Else, B., et al. (2017). A synthesis of the arctic terrestrial and marine carbon cycles under pressure from a dwindling cryosphere. *Ambio* 46, S53–S69.

Pavlov, A. K., Granskog, M. A., Stedmon, C. A., Ivanov, B. V., Hudson, S. R., and Falk-Petersen, S. (2015). Contrasting optical properties of surface waters across the fram strait and its potential biological implications. *J. Mar. Syst.* 143, 62–72. doi: 10.1016/j.jmarsys.2014.11.001

Pavlov, A. K., Tverberg, V., Ivanov, B. V., Nilsen, F., Falk-Petersen, S., and Granskog, M. A. (2013). Warming of Atlantic water in two west Spitsbergen fjords over the last century (1912 – 2009). *Polar Res.* 32:11206. doi: 10.3402/polar.v32i0.11206

Pavlova, O., Gerland, S., and Hop, H. (2019). "Changes in sea-ice extent and thickness in Kongsfjorden, Svalbard (2003–2016)," in *The Ecosystem of Kongsfjorden, Svalbard, Advances in Polar Ecology 2*, eds H. Hop and C. Wiencke (Springer).

Payne, C. M., and Roesler, C. S. (2019). Characterizing the influence of Atlantic water intrusion on water mass formation and phytoplankton distribution in Kongsfjorden, Svalbard. *Continental Shelf Res.* 191:104005. doi: 10.1016/j.csr.2019.104005

Polyakov, I. V., Pnyushkov, A. V., Alkire, M. B., Ashik, I. M., Baumann, T. M., Carmack, E. C., et al. (2017). Greater role for Atlantic inflows on sea ice loss in the Eurasian Basin of the Arctic Ocean. *Science* 356, 285–291. doi: 10.1126/science.aai8204

Pope, R., and Fry, E. (1997). Absorption spectrum (380-700 nm) of pure water. II. integrating cavity measurements. *Appl. Optics* 36, 8710–8723. doi: 10.1364/AO.36.008710

Promińska, A., Cisek, M., and Walczowski, W. (2017). Kongsfjorden and hornsund hydrographycomparative study based on a multiyear survey in fjords

of west Spitsbergen. *Oceanologia* 59, 397–412. doi: 10.1016/j.oceano.2017.07.003

R Core Team (2020). *R: A Language and Environment for Statistical Computing*. Vienna: R Foundation for Statistical Computing.

Rozwadowska, A., and Górecka, I. (2017). Impact of reflecting land surface on radiation environment over Hornsund, Spitsbergen – a model study for cloudless skies. *Polish Polar Res.* 38, 149–174. doi: 10.1515/popore-2017-0008

Sagan, S., and Darecki, M. (2017). Inherent optical properties and particulate matter distribution in summer season in waters of Hornsund and Kongsfjordenen, Spitsbergen. *Oceanologia* 60, 65–75. doi: 10.1016/j.oceano.2017.07.006

Sathyendranath, S., Brewin, R. J. W., Brockmann, C., Brotas, V., Calton, B., Chuprin, A., et al. (2019). An ocean-colour time series for use in climate studies: the experience of the ocean-colour climate change initiative (OC-CCI). *Sensors* 19:4285. doi: 10.3390/s19194285

Sathyendranath, S., Brewin, R. J. W., Müeller, D., Brockmann, C., Deschamps, P.-Y., Doerffer, R., et al. (2012). "Ocean colour climate change initiative: approach and initial results," in *Proceeding of the Geoscience and Remote Sensing Symposium (IGARSS), 2012 IEEE International*, doi: 10.1109/IGARSS.2012.6350979

Schuler, T. V., Kohler, J., Elagina, N., Hagen, J. O. M., Hodson, A. J., Jania, J. A., et al. (2020). Reconciling Svalbard glacier mass balance. *Front. Earth Sci.* 8:156. doi: 10.3389/feart.2020.00156

Serreze, M. C., and Stroeve, J. (2015). Arctic sea ice trends, variability and implications for seasonal ice forecasting. *Philos. Trans. A Math Phys. Eng. Sci.* 373:20140159. doi: 10.1098/rsta.2014.0159

Skogseth, R., Olivier, L. L., Nilsen, F., Falck, E., Fraser, N., Tverberg, V., et al. (2020). Variability and decadal trends in the Isfjorden (Svalbard) ocean climate and circulation–an indicator for climate change in the European Arctic. *Prog. Oceanogr.* 187:102394. doi: 10.1016/j.pocean.2020.102394

Smedsrud, L. H., Halvorsen, M. H., Stroeve, J. C., Zhang, R., and Kloster, K. (2016). Fram strait sea ice export variability and september Arctic sea ice extent over the last 80 years. *Cryosphere* 11, 65–79. doi: 10.5194/tc-11-65-2017

Smith, R. W., Bianchi, T., Allison, M. A., Savage, C., and Galy, V. (2015). High rates of organic carbon burial in fjord sediments globally. *Nat. Geosci.* 8:2421. doi: 10.1038/ngeo2421

Son, Y.-S., and Kim, H.-C. (2018). Empirical ocean color algorithms and bio-optical properties of the western coastal waters of Svalbard, Arctic. *ISPRS J. Photogr. Remote Sen.* 139, 272–283. doi: 10.1016/j.isprsjprs.2018.03.024

Spanbauer, T. L., Allen, C. R., Angeler, D. G., Eason, T., Fritz, S. C., Garmestani, A. S., et al. (2014). Prolonged instability prior to a regime shift. *PLoS One* 9:e108936. doi: 10.1371/journal.pone.0108936

Stachnik, Ł, Yde, J. C., Nawrot, A., Uzarowicz, Ł, Łepkowska, E., and Kozak, K. (2019). Aluminium in glacial meltwater demonstrates an association with nutrient export (Werenskiöldbreen, Svalbard). *Hydrol. Process.* 33, 1638–1657. doi: 10.1002/hyp.1342

Støylen, E., and Fer, I. (2014). Tidally induced internal motion in an Arctic fjord. *Nonlin. Processes Geophys.* 21, 87–100. doi: 10.5194/npg-21-87-2014

Stramska, M., Stramski, D., Hapter, R., Kaczmarek, S., and Stoń, J. (2003). Bio-optical relationships and ocean color algorithms for the northpolar region of the Atlantic. *J. Geophys. Res.* 108:3143. doi: 10.1029/2001JC001195

Stramska, M., Stramski, D., Kaczmarek, S., Allison, D. B., and Schwarz, J. (2006). Seasonal and regional differentiation of bio-optical properties within the north polar Atlantic. *J. Geophys. Res.* 111:3293. doi: 10.1029/2005JC003293

Strickland, J. D. H., and Parsons, T. R. (1972). *A Practical Handbook of Seawater Analyses*. Ottawa, ON: Fisheries Research Board of Canada.

Szeligowska, M., Trudnowska, E., Boehnke, R., Dąbrowska, A. M., Wiktor, J. M., Sagan, S., et al. (2020). Spatial patterns of particles and plankton in the warming Arctic fjord (Isfjorden, west Spitsbergen) in seven consecutive mid-summers (2013–2019). *Front. Mar. Sci.* 7:584. doi: 10.3389/fmars.2020.00584

Telling, J., Anesio, A. M., Tranter, M., Fynn, T. I., Hodson, A., Butler, C., et al. (2011). Nitrogen fixation on Arctic glaciers, Svalbard. *J. Geophys. Res.* 116:G03039. doi: 10.1029/2010JG001632

Thomas, F. A., Sinha, R. K., and Krishnan, K. P. (2020). Bacterial community structure of a glacio-marine system in the Arctic (Ny-Ålesund, Svalbard). *Sci. Total Environ.* 718:135264. doi: 10.1016/j.scitotenv.2019.135264

Tiller, R. G., De Kok, J.-L., Vermeiren, K., and Thorvaldsen, T. (2017). Accountability as a governance paradox in the norwegian salmon aquaculture. industry. *Front. Mar. Sci.* 4:71. doi: 10.3389/fmars.2017.00071

van Pelt, W., Pohjola, V., Pettersson, R., Marchenko, S., Kohler, J., Luks, B., et al. (2019). A long-term dataset of climatic mass balance, snow conditions, and runoff in Svalbard (1957–2018). *Cryosphere* 13, 2259–2280. doi: 10.5194/tc-13-2259-2019

Vickers, H., Høgda, K. A., Solbø, S., Karlsen, S. R., Tømmervik, H., Aanes, R., et al. (2016). Changes in greening in the high Arctic: insights from a 30 year AVHRR max NDVI dataset for Svalbard. *Environ. Res. Lett.* 11:105004. doi: 10.1088/1748-9326/11/10/105004

Vickers, H., Karlsen, S. R., and Malnes, E. (2020). A 20-year MODIS-based snow cover dataset forsvalbard and its link to phenological timing and seaice variability. *Remote Sens.* 12:1123. doi: 10.3390/rs12071123

Walczowski, W. (2014). *Atlantic Water in the Nordic Seas*. Heidelberg, N.Y: Springer.

Weller, G. (2005). "Summary and synthesis of the Arctic Climate Impact Assessment (ACIA)," in *Arctic Climate Impact AssessmentScientific Report*, eds C. Symon, L. Arris, and B. Heal (Cambridge: Cambridge University Press).

Wessel, P., and Smith, W. H. F. (1996). A global self-consistent, hierarchical, high-resolution shoreline database. *J. Geophys. Res.* 101, 8741–8743.

Wickham, H., Chang, W., Henry, L., Pedersen, T. L., Takahashi, K., Wilke, C., et al. (2020). *ggplot2: Create Elegant Data Visualisations Using the Grammar of Graphics. R package version 3.3.0*.

Winter, A., Henderiks, J., Beaufort, L., Rickaby, R. E. M., and Brown, C. W. (2014). Poleward expansion of the coccolithophore *Emiliania huxleyi*. *J. Plankton Res.* 36, 316–325. doi: 10.5194/os-2016-13

Woźniak, B., and Dera, J. (2007). *Light Absorption in Sea Water*. New York: Springer.

Conflict of Interest: The authors declare that the research was conducted in the absence of any commercial or financial relationships that could be construed as a potential conflict of interest.

Publisher's Note: All claims expressed in this article are solely those of the authors and do not necessarily represent those of their affiliated organizations, or those of the publisher, the editors and the reviewers. Any product that may be evaluated in this article, or claim that may be made by its manufacturer, is not guaranteed or endorsed by the publisher.

Copyright © 2021 Konik, Darecki, Pavlov, Sagan and Kowalczuk. This is an open-access article distributed under the terms of the Creative Commons Attribution License (CC BY). The use, distribution or reproduction in other forums is permitted, provided the original author(s) and the copyright owner(s) are credited and that the original publication in this journal is cited, in accordance with accepted academic practice. No use, distribution or reproduction is permitted which does not comply with these terms.

frontiers in Marine Science

ORIGINAL RESEARCH
published: 10 November 2021
doi: 10.3389/fmars.2021.746327

Twenty-One Years of Phytoplankton Bloom Phenology in the Barents, Norwegian, and North Seas

Edson Silva[1], François Counillon[2], Julien Brajard[1], Anton Korosov[1], Lasse H. Pettersson[1], Annette Samuelsen[2] and Noel Keenlyside[2,3]*

[1] Nansen Environmental and Remote Sensing Center, Bergen, Norway, [2] Nansen Environmental and Remote Sensing Center, and Bjerknes Centre for Climate Research, Bergen, Norway, [3] Geophysical Institute, University of Bergen, Bergen, Norway

Phytoplankton blooms provide biomass to the marine trophic web, contribute to the carbon removal from the atmosphere and can be deadly when associated with harmful species. This points to the need to understand the phenology of the blooms in the Barents, Norwegian, and North seas. We use satellite chlorophyll-a from 2000 to 2020 to assess robust climatological and the interannual trends of spring and summer blooms onset, peak day, duration and intensity. Further, we also correlate the interannual variability of the blooms with mixed layer depth (MLD), sea surface temperature (SST), wind speed and suspended particulate matter (SPM) retrieved from models and remote sensing. The climatological spring blooms start on March 10th and end on June 19th. The climatological summer blooms begin on July 13th and end on September 17th. In the Barents Sea, years of shallower mixed layer (ML) driven by both calm waters and higher freshwaters input keeps the phytoplankton in the euphotic zone, causing the spring bloom to start earlier and reach higher biomass but end sooner due to the lack of nutrients upwelling from the deep. In the Norwegian Sea, a correlation between SST and the spring blooms is found. Here, warmer waters are correlated to earlier and stronger blooms in most regions but with later and weaker blooms in the eastern Norwegian Sea. In the North Sea, years of shallower ML reduces the phytoplankton sinking below the euphotic zone and limits the SPM increase from the bed shear stress, creating an ideal environment of stratified and clear waters to develop stronger spring blooms. Last, the summer blooms onset, peak day and duration have been rapidly delaying at a rate of 1.25-day year^{-1}, but with inconclusive causes based on the parameters assessed in this study.

Keywords: phytoplankton, bloom phenology, Barents Sea, Norwegian Sea, North Sea, remote sensing, spring algae bloom, summer algae bloom

OPEN ACCESS

Edited by:
Hjálmar Hátún, Faroe Marine Research Institute (FAMRI), Faroe Islands

Reviewed by:
Rajdeep Roy, Indian Space Research Organisation, India
Tomonori Isada, Hokkaido University, Japan

****Correspondence:***
Edson Silva
edson.silva@nersc.no

Specialty section:
This article was submitted to Marine Biogeochemistry, a section of the journal Frontiers in Marine Science

Received: *23 July 2021*
Accepted: *12 October 2021*
Published: *10 November 2021*

Citation:
Silva E, Counillon F, Brajard J, Korosov A, Pettersson LH, Samuelsen A and Keenlyside N (2021) Twenty-One Years of Phytoplankton Bloom Phenology in the Barents, Norwegian, and North Seas. Front. Mar. Sci. 8:746327. doi: 10.3389/fmars.2021.746327

INTRODUCTION

Phytoplankton blooms play a crucial role in the marine trophic web and global climate. By assimilating the sunlight, carbon dioxide and nutrients, the algae produce high biomass concentration blooms that feed zooplankton and the higher trophic levels or sink below the euphotic zone. Thus, the algae blooms can support the development of fish larvae

(Townsend and Cammen, 1987; Platt et al., 2003; Vikebø et al., 2012; Asch et al., 2019), provide biomass to the benthic fauna (Zhang et al., 2015) and also contribute to the carbon removal from the atmosphere (Legendre, 1990; Leblanc et al., 2018). Conversely, harmful algae blooms (HABs) can be devastating and lethal (Pettersson and Pozdnyakov, 2013; Gobler, 2020). The high organic matter concentration generated during the bloom can damage or clog fish gills (Chang et al., 1990; Kent et al., 1995) and increase bacteria activity, depleting the dissolved oxygen and causing hypoxia in fishes (Harrison et al., 2017; Mohd-Din et al., 2020). Besides, some algal species can produce toxins, leading to the mortality of fish or even humans when contaminated mussels are consumed (Tangen, 1977; Kaartvedt et al., 1991; Landsberg et al., 2020). The influence of algae blooms on natural living resources and global climate points to the need of assessing the phenology of algae blooms, such as the date of onset, duration, date of the bloom reaching its maximum biomass and the maximum biomass (intensity).

In the Barents, Norwegian, and North seas, two well-known seasonal blooms are the spring and later summer/autumn blooms. During the spring, the sunlight increases and allows the phytoplankton to consume the nutrients upwelled to the upper layers during the winter storms and through terrestrial river discharges (in the coastal waters). At the same time, the mixed layer (ML) shallows above the Sverdrup critical depth and makes the phytoplankton biomass production exceed respiration losses, triggering the spring bloom (Sverdrup, 1953). During summer or autumn, the surface waters are depleted of nutrients due to the algae consumption during the spring bloom. Remineralization, upwelling and river runoff refresh the surface waters with nutrients again, leading to a secondary bloom called summer or autumn bloom (Sverdrup, 1953; Glen Harrison et al., 2013; Sundby et al., 2016).

Although the main processes of spring and summer blooms are well understood in the Barents, Norwegian, and North seas, there is a need to understand mechanisms that can influence the phytoplankton bloom phenology on interannual variability as well as its response to climate change. During a survey campaign in 2013 in the North Atlantic, Naustvoll et al. (2020) observed that regions with earlier shallowing of ML are related to earlier spring blooms. Using satellite data from 2003 to 2017 along the Norwegian coast, Vikebø et al. (2019) found that years with strong winds delay the spring bloom onset. Using a water column model, Opdal et al. (2019) suggested that reducing the water transparency could delay the spring bloom onset in the North Sea. While these studies provided valuable insight on the variability of spring blooms onset and its potential driving mechanisms, still little is known about the duration, date of the peak and intensity of the spring bloom. Besides, the phenology of summer blooms has not been addressed to our knowledge in this region. Thanks to the available extended period of optical remote sensing data (from 1998 to present), one can now more robustly assess the spatial distribution, climatology, trend and potential drivers of interannual variability of both spring and summer blooms.

Here we take advantage of ocean color remote sensing data to provide a comprehensive assessment of both spring and summer blooms phenology in the Barents, Norwegian, and North seas. We use pattern recognition tools to cluster the bloom phenology in regions of comparable statistical behavior, which reduces small-scale noise and allows for a coherent visualization of the properties of the blooms phenology–onset, duration, peak day and intensity. Furthermore, the extended data set used (2000–2020) allows for providing a primary analysis of the trend of the property of the bloom phenology and of potential drivers that can influence the interannual variability.

MATERIALS AND METHODS

Study Region

This study focuses on the Norwegian shelf seas, including the North Sea, the Norwegian Sea, and the Barents Sea entrance (**Figure 1**). The North Sea is shallow, with depth varying from 20 m in the southern region to 700 m in the south of Norway (Eisma et al., 1987). In the Norwegian Sea, the shallowest waters are on the Norwegian Continental Shelf, varying from 100 to 400 m, and the deepest waters are in the Norway Basin, ranging from 3600 to 3800 m. The Barents Sea has a wide continental shelf varying from 100 to 300 m deep (Perry, 1986).

Two significant currents dominate the circulation in the study region, the Norwegian Atlantic Current (NwAC) and the Norwegian Coastal Current (NCC). The NwAC originates from the North Atlantic Current as it flows between the Faroe Islands and Scotland and continues northward along with the Norwegian Continental Shelf break. The NwAC splits into two branches close to the Barents Sea. One branch flows eastward into the Barents Sea, while the other flows northward into the Fram Strait (Furevik et al., 2002; Eldevik et al., 2009). The NCC flows from the south of Norway and along the Norwegian coast up the Barents Sea. It is substantially fresher than the Atlantic Water as it transports fresh waters from the land inflow, the Baltic Sea and the North Sea (Mork, 1981).

Satellite Chlorophyll-a Measurements

Chlorophyll-a concentration (mg m^{-3}) is used as a proxy to phytoplankton biomass and has been retrieved regularly by satellite remote sensing since 1998. We accessed satellite data from the European Space Agency (ESA) Ocean Colour Climate Change Initiative (OC-CCI) project (Sathyendranath et al., 2019), product version 5, which has a spatial resolution of 4 km at a fixed geographical grid and binned in an 8-day average between 1998 and 2020 (**Table 1**). The OC-CCI data is intended for climate studies and merges Chl-a concentration estimated from MODIS, MERIS, OLCI, SeaWiFS, and VIIRS sensors. We have used the data set in the 8-day average bin so that cloud contaminated grid cells are reduced and allow a continuous estimation of the Chl-a time series. From 1998 to 1999, there is only SeaWiFS data available and many grid cells with gaps in the high latitudes of the Norwegian Sea. Thus, we have excluded these 2 years from our analysis.

Global validation of the OC-CCI satellite data with *in situ* Chl-a measurements (n = 17901) showed good agreements between the two data sets–with a correlation coefficient (R)

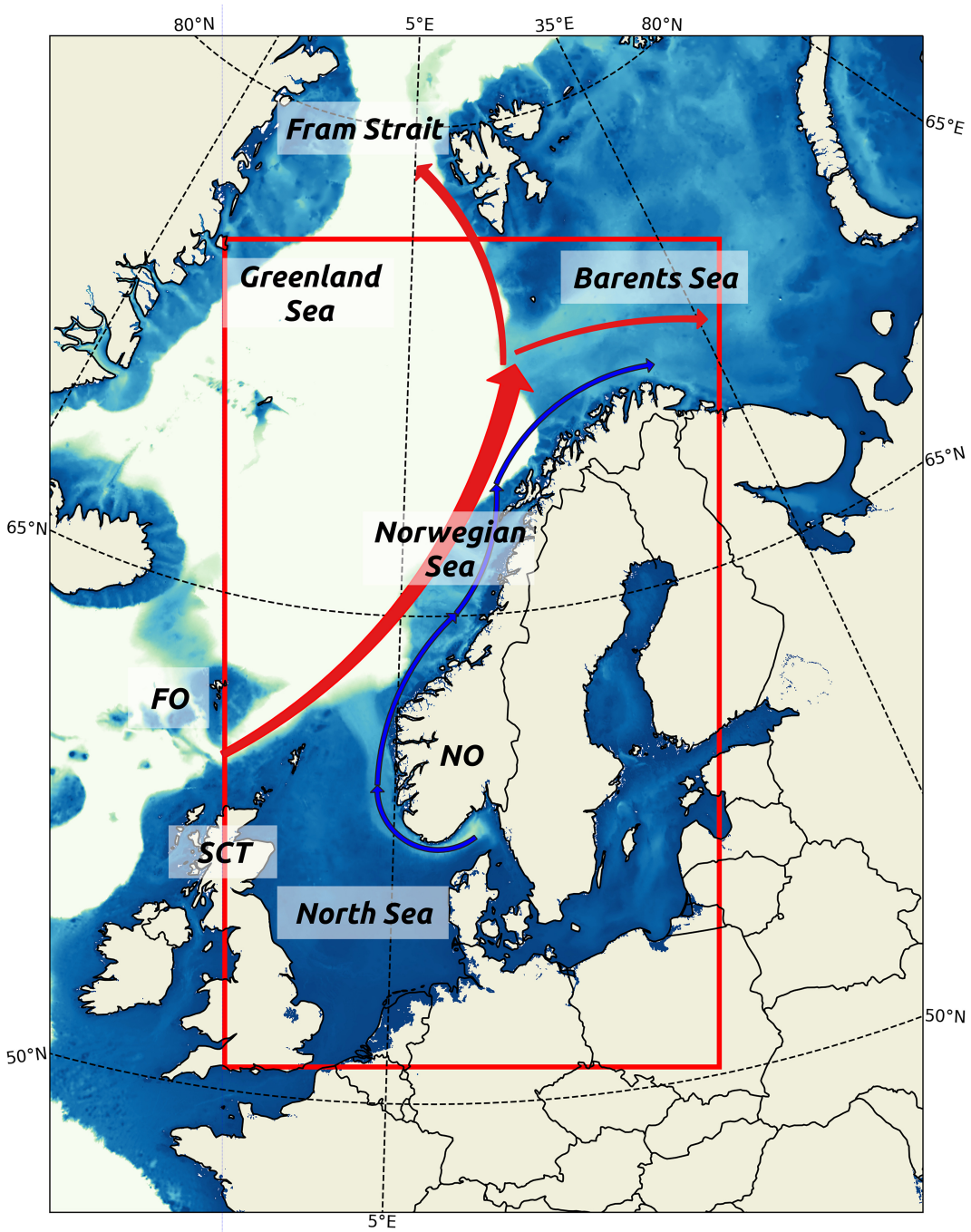


FIGURE 1 | The study region. The red box delimits the area where the blooms phenology is assessed. Red arrow is a coarse representation of the NwAC and blue arrow is the NCC. Abbreviations are Faroe Islands (FO), Norway (NO), and Scotland (SCT).

of 0.78, a root mean square difference of 0.3 mg m^{-3} and a bias of 0.003 mg m^{-3} (Calton, 2020). Note that the OC-CCI product uses an algorithm tuned to perform best in open ocean case-1 waters, where the phytoplankton abundance controls both direct and indirect the optical properties of water (Morel and Prieur, 1977). The OC-CCI Chl-a product has limited validity for coastal case-2 waters where the land input or resuspension of suspended particulate matter (SPM) and yellow substance contributes significantly to the optical properties. Since case-2 waters occur mainly close to the coastline and standard case-1 water algorithms perform poorly in such regions (Blondeau-Patissier et al., 2004; Folkestad et al., 2007), we have discarded grid cells within 30 km off the coastline from the analysis.

TABLE 1 | Summary of the data used in this study.

Source	Variables	Spatial resolution	Temporal resolution	Temporal range
OC-CCI	Chl-a (mg m^{-3})	4 km	8 days	2000–2020
	Chl-a (mg m^{-3})	4 km	Daily	2000–2020
CCI/C3S	SST (°K)	0.05°	Daily	2000–2020
GlobColour	SPM (g m^{-3})	4 km	8 days	2000–2020
TOPAZ	MLD (m)	12.5 km	Daily	2000–2020
IFREMER CERSAT	Wind Speed (m s^{-1})	0.25°	6 h	2000–2019
NMDC	*In situ* Chl-a (mg m^{-3})	–	–	2000–2017
PRG	*In situ* Chl-a (mg m^{-3})	–	–	2000–2016
NVE	River flow (m^3 s^{-1})	–	Daily	2000–2020

This study relies entirely on exploiting information on the phytoplankton dynamics derived from satellite remote sensing sensors. Since passive sensors depend on the solar light scattering, there is no optical satellite data in the winter darkness. Reliable data are only available from February to November in the southern region of the study region and from March to October in the northern region. Although the low sun angle and light availability during the winter may not be sufficient to trigger algae blooms, the bloom onset may occur just before the satellite measurements have sufficient quality when the light starts increasing. This issue was observed in the North Sea (see section "Sub-regions and Chlorophyll-a Validation").

Auxiliary Data

Auxiliary data is used to correlate the interannual variability of bloom phenology (onset, peak day, duration, and intensity) with potential key drivers. The parameters assessed are the mixed layer depth (MLD), sea surface temperature (SST), wind speed, SPM concentration, and river runoff (**Table 1**).

We accessed SST (K) from the ESA SST CCI and C3S global SST Reprocessed product level 4, available on the Copernicus Marine Environment Monitoring Service (CMEMS)[1]. The product is created by running the Operational Sea Surface Temperature and Sea Ice Analysis (OSTIA) system (Good et al., 2020), which combines satellite (AATSR, ATSR, SLSTR, and AVHRR) and *in situ* observations to produce gap-free maps of daily average SST at 0.05° of spatial resolution (Merchant et al., 2019).

Suspended particulate matter (g m^{-3}) data was obtained by satellite observations and accessed from the GlobColour project[2]. SPM is estimated using Gohin (2011) algorithm on MODIS, MERIS, OLCI, SeaWiFS, and VIIRS sensors, and binned at an 8-day interval at a 4 km of spatial resolution. Note that SPM is estimated by radiometric measurements from the same optical sensors used for estimating Chl-a concentration, and they may share a common bias.

The MLD (m) is provided by the CMEMS Arctic MFC TOPAZ system (Sakov et al., 2012; Xie et al., 2017). The TOPAZ system is a coupled ocean–sea ice data assimilation system for the North Atlantic and the Arctic Ocean. The model couples a Hybrid Coordinate Ocean Model (Bleck, 2002) with an elasto-viscous-plastic sea ice model (Hunke and Dukowicz, 1997). TOPAZ assimilates available ocean and sea ice data with the Ensemble Kalman filter (Evensen, 2003) every week. The MLD is calculated using a density criterion with a threshold of 0.01 kg m^{-1}, as in Petrenko et al. (2013) and Ferreira et al. (2015).

Surface wind speed (m s^{-1}) was obtained from the IFREMER CERSAT Global Blended Mean Wind Fields reprocessed product accessed from the CMEMS. Wind speed is derived from scatterometers (ASCAT-A and ASCAT-B satellites), the SSMIS radiometers (F16, F17, F18, and F19 satellites) and the WindSat radiometer onboard the Coriolis satellite. All satellite observations are binned into a single product with a 6-hourly wind field at a 0.25° of spatial resolution.

We use the daily flow data from the Tana (70.070°N, 28.016°E) and Målselva (69.035°N, 18.658°E) rivers accessed from The Norwegian Water Resources and Energy Directorate[3]. The river flow was used as a proxy of coastal waters freshening to discuss the MLD variability in sections "Barents Sea: Stronger, Earlier and Shorter Spring Blooms Driven by Shallower Mixed Layer" and "Mixed Layer Depth and Sea Surface Temperature Influence on the Spring Bloom Phenology in the Norwegian Sea."

Clustering Sub-Regions

We have used cluster analysis to objectively identify 20 sub-regions of similar bloom phenology using the 21 years of Chl-a time series. In the pre-processing, we subset the time series between the Julian days 60 and 300 to exclude the winter when there is a lack of data. Although we have accessed Chl-a data binned in 8-day average, 30.8% of the data cube (latitude × longitude × time) is still missing–mainly in the Greenland Sea–due to the cloud contamination. We interpolate those missing values as we need them for clustering the sub-regions. For each year, we use linear interpolation (limit = 10-time intervals) for filling the missing values over time, reducing the missing data to 5.2%. The remaining missing values are in the beginning and end of the time series in the higher latitudes. Since we cannot interpolate values in the time series borders, we filled them with 0.01, assuming that the Chl-a concentration is virtually null but still present during the beginning and end of the winter. We emphasize that the filling value with 0.01 was only used for clustering and not further used to assess the blooms phenology.

We use principal component analysis to reduce the dimension of 630-time intervals to 300 components, accounting for 95% of the Chl-a time variability. Then, we use the k-means algorithm (MacQueen, 1967) fed with the components as features and the grid cells as observations. We chose the optimal number of sub-regions (k) as the maximum value where coherent (spatially continuous) sub-regions were still obtained. With more than 20 clusters, we got noisy sub-regions composed of a few grid cells. We use the k-means++ algorithm (Arthur and Vassilvitskii, 2007) to define the initial seeds and avoid changing the sub-regions areas each time the k-means is reproduced.

[1]https://marine.copernicus.eu/

[2]https://www.globcolour.info/

[3]https://www.nve.no/

In the post-processing, we observed that four sub-regions in the Greenland Sea were heavily contaminated by clouds and probably sea ice. We set a high interpolation limit of 10-time intervals in the pre-processing to address this issue during the clustering. However, this wide range of interpolation made the Chl-a time series in the Greenland Sea too linear and unrealistic to assess the blooms phenology. For this reason, we have excluded those four sub-regions, resulting in 16 sub-regions. Furthermore, a few grid cells along the sub-regions boundaries were overlapping each other sub-region. We have smoothed the boundaries by removing those grid cells and interpolating with the nearest sub-region.

For assessing the clustering performance, we computed the Silhouette score (Rousseeuw, 1987) using the 300 components of every grid cell:

$$S(i) = \frac{b(i) - a(i)}{max\left(a(i), b(i)\right)} \quad (1)$$

where S is the Silhouette score for a given grid cell i, b is the mean nearest-cluster Euclidean distance, and a is the mean intra-cluster Euclidean distance. A Silhouette score higher than 0 means that the Chl-a time series of one individual grid cell is more similar–in the Euclidean space–to the cells of the same sub-region than the remaining regions.

Satellite Chlorophyll-a Validation

We assess the performance of the OC-CCI Chl-a product in the 16 sub-regions by comparing the daily OC-CCI Chl-a with *in situ* Chl-a collected on the same day (**Table 1**). The *in situ* Chl-a data was provided by the Norwegian Institute of Marine Research (IMR) from two different sources. One was retrieved from the Norwegian Marine Data Centre[4] with the registered id imr_11. The other was provided by the Plankton Research Group (PRG) (courtesy of Dr. Kjell Gundersen) and was analyzed by the Plankton Chemistry Laboratory at IMR. For measuring *in situ* Chl-a, a standard volume (265 mL) is collected and filtered onto a 25 mm GFF filter and stored frozen (−20°C) until analysis in the land-based laboratory. Samples are transported in specially designed coolers, with an internal temperature recorder rated for −20°C for a minimum of 3 days. The samples are thawed in 90% acetone in the laboratory and stored at +4°C overnight before analysis on a Turner Design 10AU fluorometer. The fluorometer is regularly calibrated using a solid standard with known fluorescence following Holm-Hansen and Riemann (1978). Measurements of the top 10 m have been averaged to compare well with the remote sensing data. Note that the satellite data is calibrated with Chl-a estimated by high-performance liquid chromatography (HPLC), which slightly differs from Chl-a estimated by fluorometers available in this study (Neveux et al., 1990; Reynolds et al., 2001; Giannini et al., 2021).

To match the *in situ* and satellite Chl-a data, we followed the protocols described by Bailey and Werdell (2006) with some slight adjustments. As the satellite product is a merged output of different sensors and has more than one measurement time, we matched the satellite data with *in situ* data collected on the same day and between 09:00 and 15:00 UTC+2. For each match-up, we extracted the average of a 3 × 3 window from the satellite product and compared it with the *in situ* measurements. Besides, we computed the coefficient of variation in the same window for assessing spatial homogeneity in the satellite product. Windows with a coefficient of variation higher than 30% were considered spatial heterogeneous and unsuitable for assessing the satellite data accuracy, so we removed them. Last, we removed a few *in situ* samples with values lower than 0.1 mg m^{-3}, which were substantially overestimating the mean absolute percentage error (MAPE).

The satellite Chl-a validation includes linear correlation (R), MAPE, and the root mean squared error (RMSE):

$$R_{x,y} = \frac{cov(X, Y)}{\sigma X \sigma Y} \quad (2)$$

$$MAPE(\%) = \frac{100}{n} \sum_{t=1}^{n} \left| \frac{X_t - Y_t}{X_t} \right| \quad (3)$$

$$RMSE\left(mg\ m^{-3}\right) = \sqrt{\frac{\sum_{t=1}^{n} (X_t - Y_t)^2}{n}} \quad (4)$$

where X and Y are the independent and dependent variables, respectively; cov is the covariance function; σ is the standard deviation; n is the number of samples; t is the sample. For the satellite and *in situ* match-ups, X is the *in situ* Chl-a, and Y is the satellite Chl-a. Furthermore, we also fit a linear regression between satellite and *in situ* match-ups.

Bloom Phenology Estimates

This study only focuses on the seasonal spring and summer blooms that last a couple of weeks. As mentioned in section "Satellite Chlorophyll-a Measurements," the Chl-a ocean color data is averaged into 8-day bins with the frequency of Chl-a variations in each bin reaching as high as 1/8 day^{-1}. We use functional data analysis (Ramsay and Silverman, 2005) to smooth the seasonal Chl-a time series and remove high frequencies from Chl-a variability. We smooth each year time series of each grid cell using a Fourier series with five basis coefficients. The number of basis coefficients can significantly impact the smoothness of the time series. On one hand, having too many basis coefficients will fail to smooth the time series enough and contains the high frequencies of Chl-a variability. On the other hand, too few basis coefficients can exaggeratedly smooth the time series and miss the phytoplankton blooms. We tested the number of basis coefficients varying from 3 to 10 on 1 year of data, and five basis coefficients were found to be the most suitable for representing the seasonality of spring and summer blooms (not shown). With less than four basis coefficients, some summer blooms in the Barents Sea were not detected, and with more than six basis coefficients, the weekly variability of Chl-a was included for spring bloom in the North Sea.

We estimate the bloom onset, peak day, duration and intensity using the smoothed Chl-a time series. The peak day corresponds

[4]https://nmdc.no/

to the local Chl-a maxima, and the bloom intensity is the Chl-a concentration at the peak. Since there is high uncertainty in the ocean color derived Chl-a concentration estimate below 0.5 mg m^{-3} (see section "Sub-regions and Chlorophyll-a Validation"), the local Chl-a maximum is only computed when values reach more than 0.5 mg m^{-3}.

Several methods were considered for estimating the bloom onset from the time series of Chl-a observations, such as the threshold method, the rate of change method and the cumulative sum method (Brody et al., 2013). The threshold method computes the climatological median of a Chl-a time series, defines a threshold value above the median, and the onset is estimated when the Chl-a concentration reaches this threshold. The rate of change method estimates the onset as the date with the highest increase of Chl-a before the peak. The cumulative sum method computes the cumulative sum from the beginning of the time series to the peak, and the onset is estimated when the sum reaches a percentual threshold of the cumulative sum (e.g., 15%). The threshold method cannot be applied in our case because there is no data available during the winter, and the climatological median of the Chl-a time series cannot be estimated. We found the rate of change method to delay the onset by a few weeks for blooms of longer duration (not shown). The cumulative sum method estimates the onset when the Chl-a starts to increase and can be applied despite the lack of winter data, and it is retained for the following analysis. We use the 15% threshold to estimate the bloom onset as recommended in Brody et al. (2013) for subpolar regions.

Since the annual Chl-a time series usually has two peaks of bloom intensity, in spring and summer, and the ocean color data is not available at the beginning of the year during the winter, we had to define the beginning of the time series for computing each bloom onset. For the spring bloom onset, the beginning of the time series was defined as the first local minima of the annual Chl-a time series. For estimating the summer bloom onset, the beginning of the time series was defined as the first local minima between the first and second peaks. Last, the bloom duration is estimated as the time between the onset and peak day.

Climatology, Trends and Detrended Correlation Assessment

We estimate the spring and summer blooms phenology for each grid cell of each year. The climatological spring and summer blooms onset, peak day, duration and intensity are estimated by averaging the grid cells belonging to each of the 16 sub-regions over the entire period. We also estimate the average value of the auxiliary parameters during the climatological bloom period (from onset to peak day) of each sub-region and year. For computing the trends of all parameters assessed, we use the sub-regions averaged values of each year and fit a linear least-squares regression. In order to relate the interannual variability of blooms phenology characteristics with key potential drivers, we subtract the trends from the interannual variability. Then, we use the Pearson correlation between the blooms phenology and the auxiliary parameters.

The correlation significance level is estimated using a probability density function (Student, 1908). For a given two random datasets with zero correlation, a probability density function of R is drawn for a given n (number of years). Then, we use a two-sided Wald test between the estimated R and the probability density function, and the null hypothesis is that the R is zero for an α threshold of 0.05. In practical terms, for a given $n = 21$ the $-0.42 < R < 0.42$ is insignificant. Note that it was ensured that there is no autocorrelation in the interannual variability. To estimate the trend significance, we test the slope of the linear least-squares regression using a two-sided Wald test with an α threshold of 0.05.

RESULTS

Sub-Regions and Chlorophyll-a Validation

The Barents, Norwegian, and North seas have been clustered into 16 sub-regions using the Chl-a time series (**Figure 2**). Four sub-regions (1–4) are in the Barents Sea, six sub-regions are in the Norwegian Sea (5–10), and the other six regions are in the North Sea (11–16). All 16 sub-regions are well localized in specific geographical regions except for sub-region 11, which starts in the central North Sea, extends throughout Skagerrak and covers the southern part of the NCC. Based on earlier investigations (Pozdnyakov et al., 2017), we initially intended to split the sub-region 11. However, all further clustering analyses gave nearly identical results for splitting the sub-region further, so we decided to keep it as one sub-region.

The 16 sub-regions showed heterogeneous annual Chl-a time series patterns and, consequently, different spring and summer blooms phenology (**Figure 2**). The sub-regions heterogeneity is also supported by the Silhouette score, where 84% of the grid cells showed values higher than 0 (**Supplementary Figure 1**). Most grid cells with a Silhouette score lower than 0 are concentrated on the sub-regions boundaries. The Chl-a time-series patterns are expected to vary among the sub-regions smoothly rather abruptly. Thus, Silhouette scores lower than 0 in the boundaries represent transitional areas among the Chl-a time-series patterns shown in **Figure 2**.

As explained in section "Satellite Chlorophyll-a Measurements," satellite data is only of sufficient quality after the beginning of February to the end of October, and there is no data available during the winter. This restriction limited the assessment of the spring bloom phenology in the southernmost sub-regions 11 and 14. There, Chl-a concentration only decreases after the middle of February, and there is no spring peak. Besides, the secondary bloom seems to reach its peak after October. Without detecting the bloom peaks, it is not possible to assess the bloom phenology in those regions. Another limitation occurs in sub-region 2 and 10, where the summer bloom developed only in a few grid cells and in some years. Since summer blooms seem rare in those sub-regions, it is unfeasible to compute a robust summer bloom climatology based on the 21 years dataset.

The OC-CCI product shows a fair agreement with *in situ* Chl-a concentration in sub-regions from 1 to 12 (**Figure 3**). The

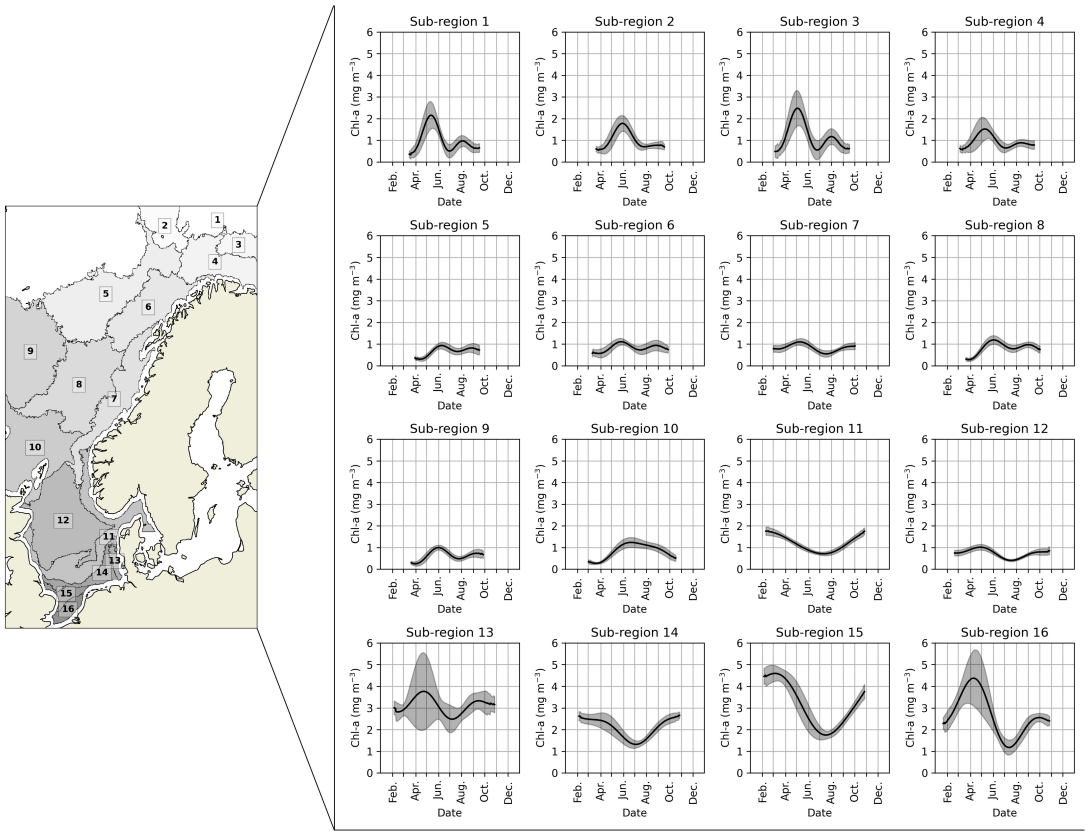


FIGURE 2 | The clustered sub-regions (left) and their annual Chl-a time series (right). The solid black line is the average over the period 2000–2020 and the shaded area is one standard deviation of the interannual variability.

R varies from 0.37 to 0.77, MAPE varies from 33 to 63% and RMSE varies from 0.3 to 0.8 mg m^{-3}. Most regions show results comparable to the OC-CCI overall validation for case-1 waters, which showed an R of 0.78 and RMSE of 0.23 for Chl-a logged data (Calton, 2020). Besides, the match-up also shows that the main source of the misfits relates to a satellite overestimation of Chl-a concentrations for values lower than 0.5 mg m^{-3}. This overestimation for the lower-level concentrations is not of great concern for assessing the seasonal bloom phenology because the bloom is only computed when the peak reaches values above 0.5 mg m^{-3}. Furthermore, we do not have access to enough *in situ* samples ($n < 8$) matching satellite data in sub-regions from 13 to 16. Since other studies show a need to use case-2 water algorithms for retrieving Chl-a concentration in the south of the North Sea (De Cauwer et al., 2004; Tilstone et al., 2012), we decided to exclude those sub-regions in the assessment of bloom phenology.

Bloom Climatology

The average spring bloom in the North Sea (sub-region 12) starts on March 10th and lasts until April 26th for 46 days (**Figure 4**), reaching 1.2 mg m^{-3} at the peak during the studied period. In the Norwegian Sea (sub-regions 6–10), the timing (onset, peak day, and duration) of the spring blooms has high longitudinal variability. The average bloom starts on March 30th in the eastern side and on May 3rd in the western sub-regions, reaching its peak between May 10th and June 19th, respectively. The spring bloom lasts between 39 and 45 days in most sub-regions. However, the bloom lasts for 58 days in the sub-region 10 in the southern Norwegian Sea, which is the longest spring bloom in the study region. The spring bloom intensity varies from 1.1 to 1.4 mg m^{-3} in the Norwegian Sea. In the Barents Sea (sub-regions 1–4), the spring bloom starts between April 11th and 27th and ends between May 7th and 28th, lasting for up to 33 days, which is the shortest spring bloom of the study region. Nevertheless, the Barents Sea shows the strongest intensity of the spring blooms that vary on average from 1.8 to 2.7 mg m^{-3}.

The timing and intensity of summer blooms have lower spatial discrepancies than for the spring blooms. The summer bloom begins on average from July 8th in the Barents Sea to August 1st in the Norwegian Sea and it ends from August 3rd in the Barents Sea to September 17th in the North Sea. The blooms last from 23 days in the Barents Sea to 48 days in the North Sea. Finally, the summer blooms intensity varies between 0.9 and 1.2 mg m^{-3}.

Bloom Phenology Trends

The spring bloom timing does not significantly change in the North and the Norwegian seas over the 21 years study period, but the spring bloom onset advances and the duration increases

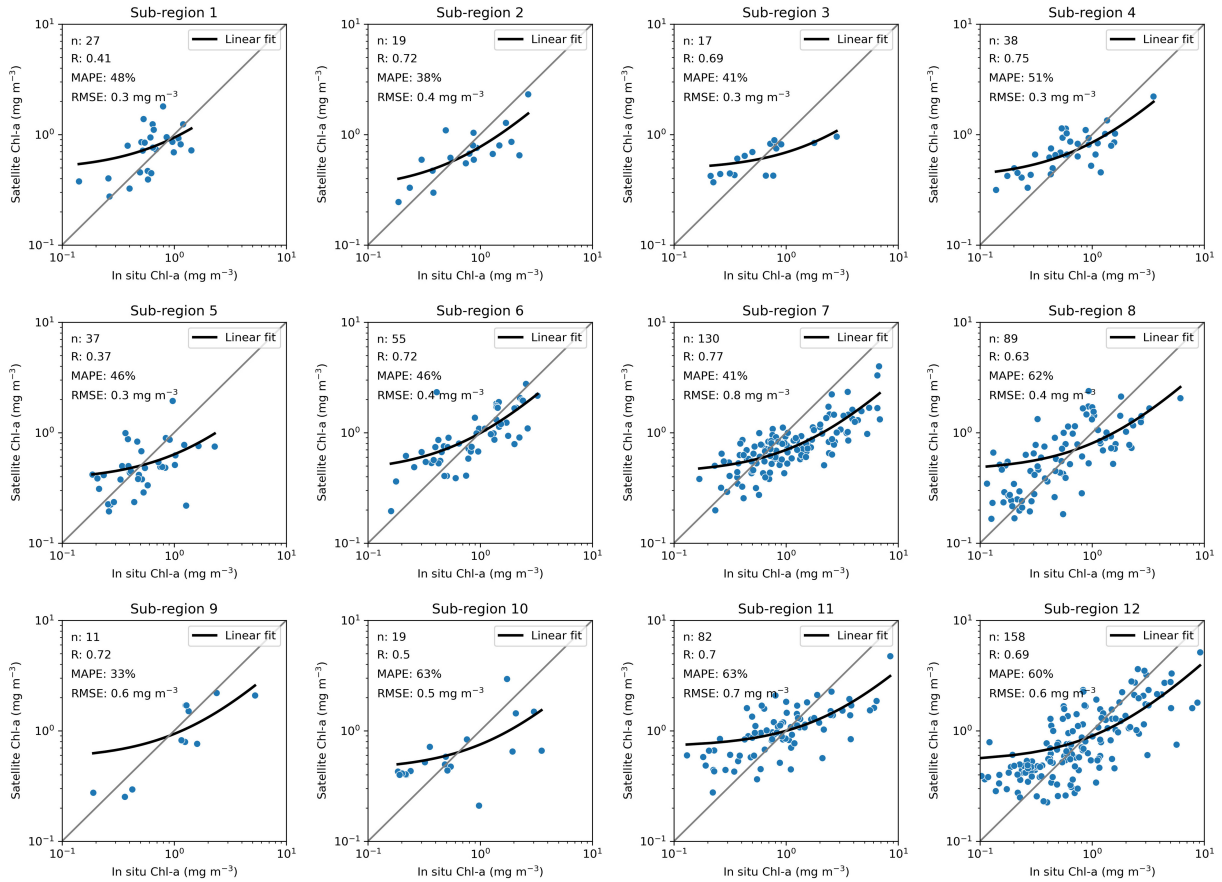


FIGURE 3 | Comparison between *in situ* and satellite Chl-a concentration for each sub-region. The black line is a linear model fitted using least squared regression, and it is curved due to the axes log scale.

in the Barents Sea (**Figure 5** and **Supplementary Figure 2**). In sub-regions 1 and 3, the blooms onset advances by −0.74-day year^{-1}, and in sub-regions 3 and 4, the blooms duration increases by 0.49-day year^{-1}. Furthermore, the intensity of spring blooms increases in the Norwegian Sea (**Supplementary Figure 3**) in sub-regions 5 and 7, with a rate of 0.02 and 0.01 mg m^{-3} year^{-1}, respectively.

The summer blooms significantly change from the North Sea and the Barents Sea. The summer blooms onset and peak day is delayed by 1.25-day year^{-1} in sub-regions 5, 6, 7, 8, 9, and 11. The duration of the blooms also increases at a rate up to 0.35-day year^{-1} in sub-regions 4, 6, 7, 8, 9, and 12. Last, the intensity of blooms increases in sub-regions 7, 9, and 12 with a rate of 0.025 mg m^{-3} year^{-1}.

Interannual Detrended Correlation

The MLD interannual variability correlates with the spring bloom timing and intensity in the North, Norwegian, and Barents seas (**Figure 6**). The correlation varies between 0.51 and 0.74 with the bloom onset and peak day and between −0.54 and −0.62 with the intensity. Thus, despite a study arguing that the spring bloom is not triggered by the shallowing of the ML and it starts in winter when the MLD is maximum (Behrenfeld, 2010), our results show that MLD seems to regulate the timing of spring blooms. The only exceptions are in sub-regions 2, 7, and 10, where MLD does not correlate with the spring bloom phenology.

Sea surface temperature correlates with the spring blooms timing and intensity in the Norwegian Sea but with inverse relationships depending on the region. On one hand, warmer waters are correlated with later and weaker spring blooms in sub-region 7. On the other hand, warmer waters are correlated with earlier spring blooms in sub-regions 5, 8, and 9, and stronger spring blooms in sub-region 10. Wind speed and SPM are correlated with the spring blooms just in a few regions. Wind speed is significantly correlated with the Barents Sea spring bloom timing and intensity, where weaker winds relate to earlier onsets and peak days and more intense blooms. SPM is correlated to spring bloom timing in sub-regions 2, 8, and 9, and with the intensity only in the North Sea, where low SPM concentrations relate to stronger spring blooms.

The summer bloom correlates with physical and biogeochemical parameters only in a few sub-regions (**Figure 7**). Shallower MLD correlates with the earlier summer blooms onset and peak day in sub-regions 8 and 9. Warmer SST correlates with later and longer summer blooms in sub-regions 6, 7, 8, and 12, and with less intense

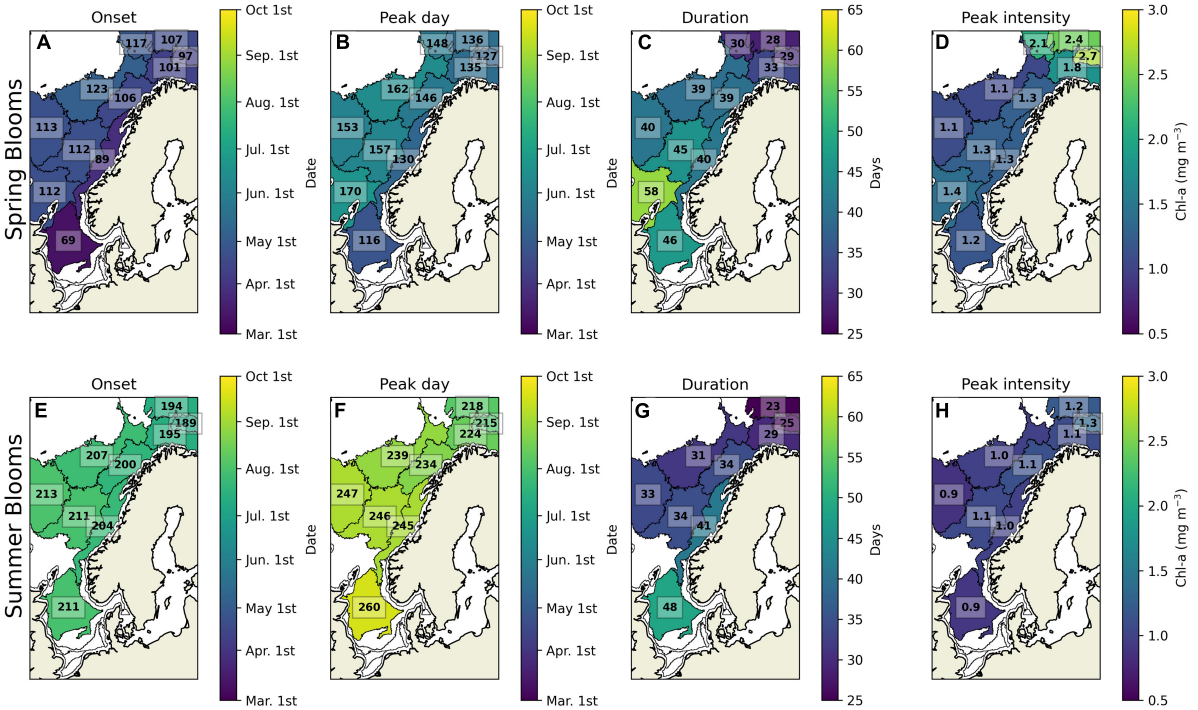


FIGURE 4 | Climatology of spring and summer blooms phenology. The subplots are the spring bloom **(A)** onset, **(B)** peak day, **(C)** duration, and **(D)** intensity; the summer blooms **(E)** onset, **(F)** peak day, **(G)** duration, and **(H)** intensity. The numbers in the onset and peak day are Julian days; in the duration are in days; in the peak intensity are in Chl-a (mg m^{-3}). Sub-regions where quantity is untrustworthy are masked in white.

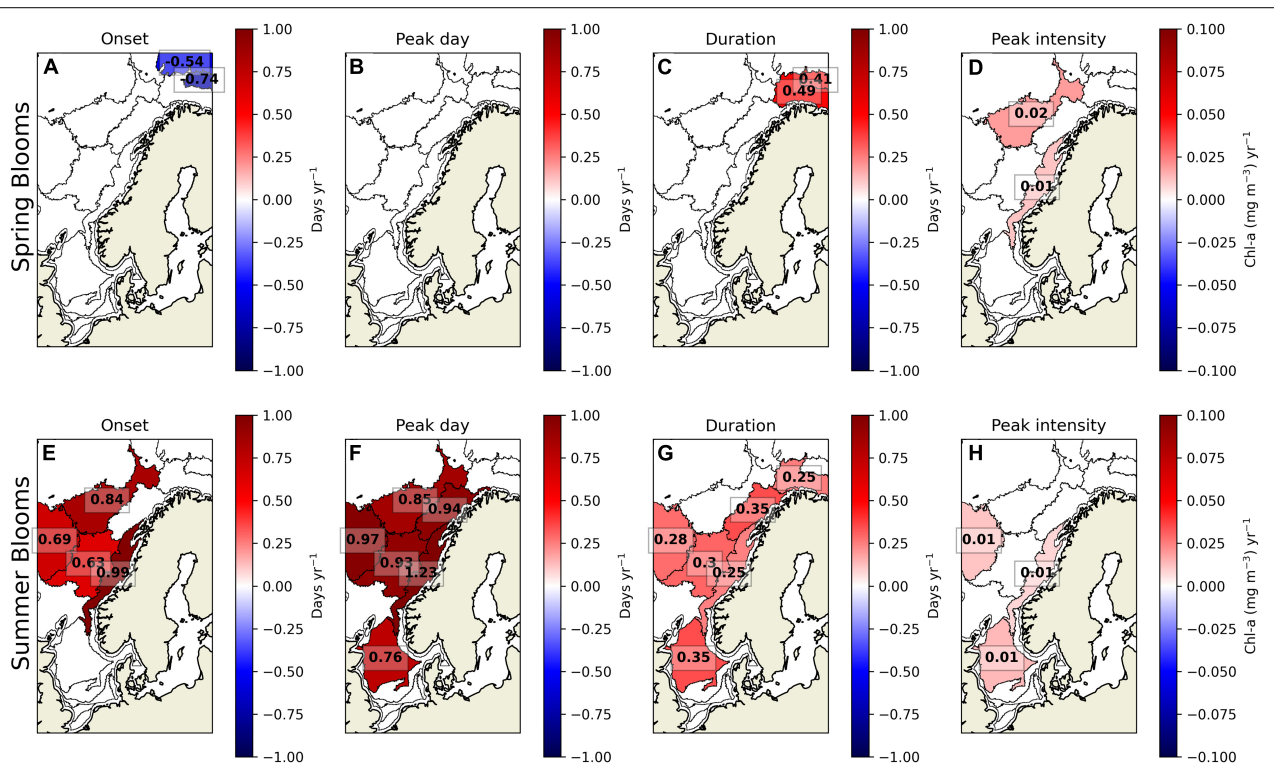


FIGURE 5 | The trends of spring and summer blooms phenology from 2000 to 2020. The subplots are the spring bloom **(A)** onset, **(B)** peak day, **(C)** duration, and **(D)** intensity; the summer blooms **(E)** onset, **(F)** peak day, **(G)** duration, and **(H)** intensity. Sub-regions where trends are insignificant ($\alpha > 0.05$) are masked in white.

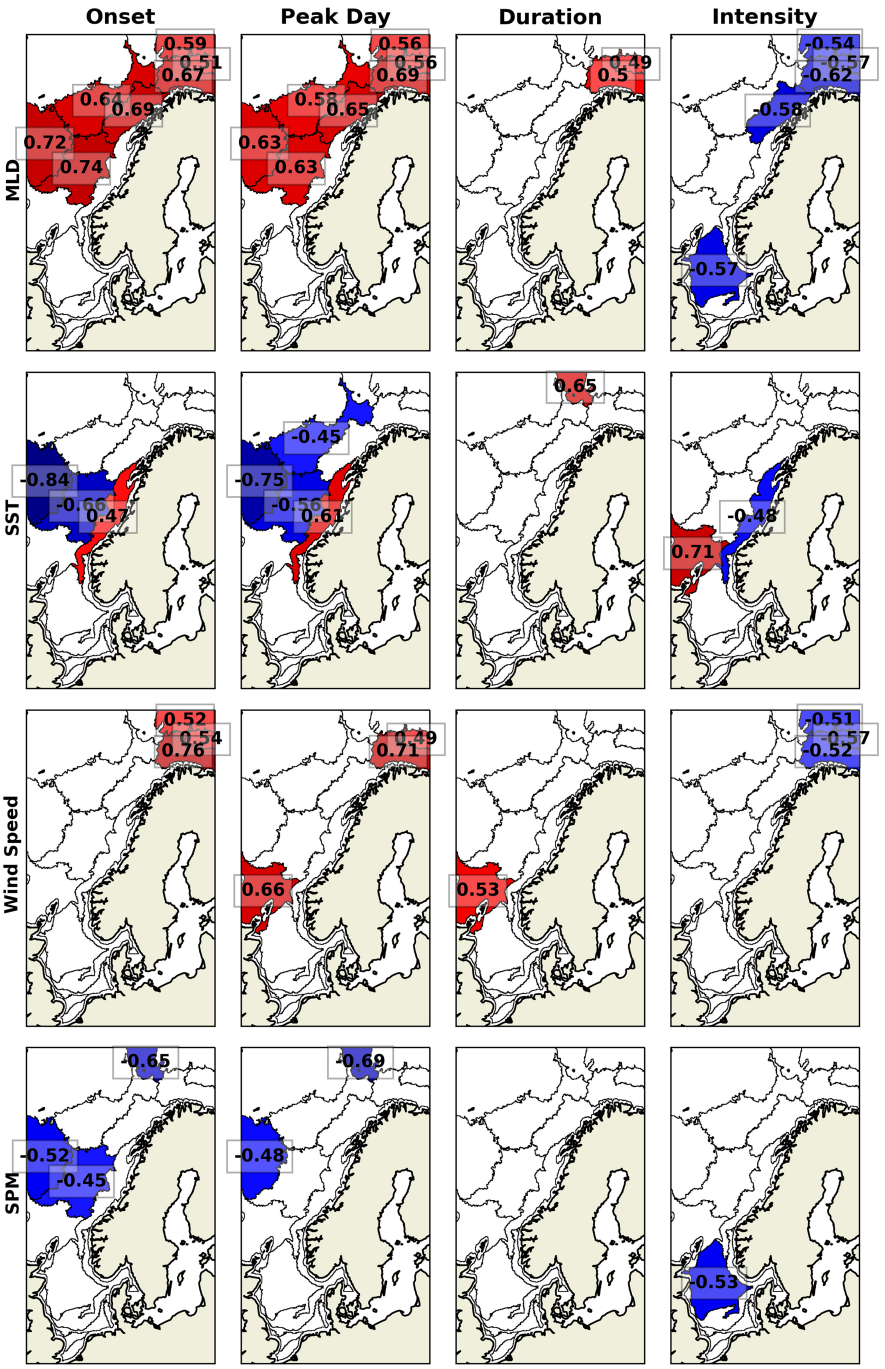


FIGURE 6 | Detrended interannual correlation between the spring bloom phenology and MLD, SST, wind speed, and SPM. Red colors are positive correlations, blue colors are negative correlations and white colors are used for insignificant correlations ($\alpha > 0.05$).

blooms in sub-regions 3 and 8. Last, wind speed only correlates with summer blooms intensity in sub-region 6, and SPM only correlates with summer blooms intensity in sub-regions 4, 5, and 6.

It should be noted that other remotely sensed and modeled parameters have been considered but were not presented to keep the paper concise. For spring bloom, photosynthetically available radiation (PAR) has significant correlations in sub-region 4 in a similar manner to MLD–albeit weaker. For summer blooms, the correlations with PAR are at the edge of significance and somewhat counter-intuitive–with higher PAR linked to shorter and weaker summer blooms. Euphotic depth (Z_{eu}) and light attenuation coefficient (K_d) were also considered. These are inherently related to the algae blooms–i.e.,

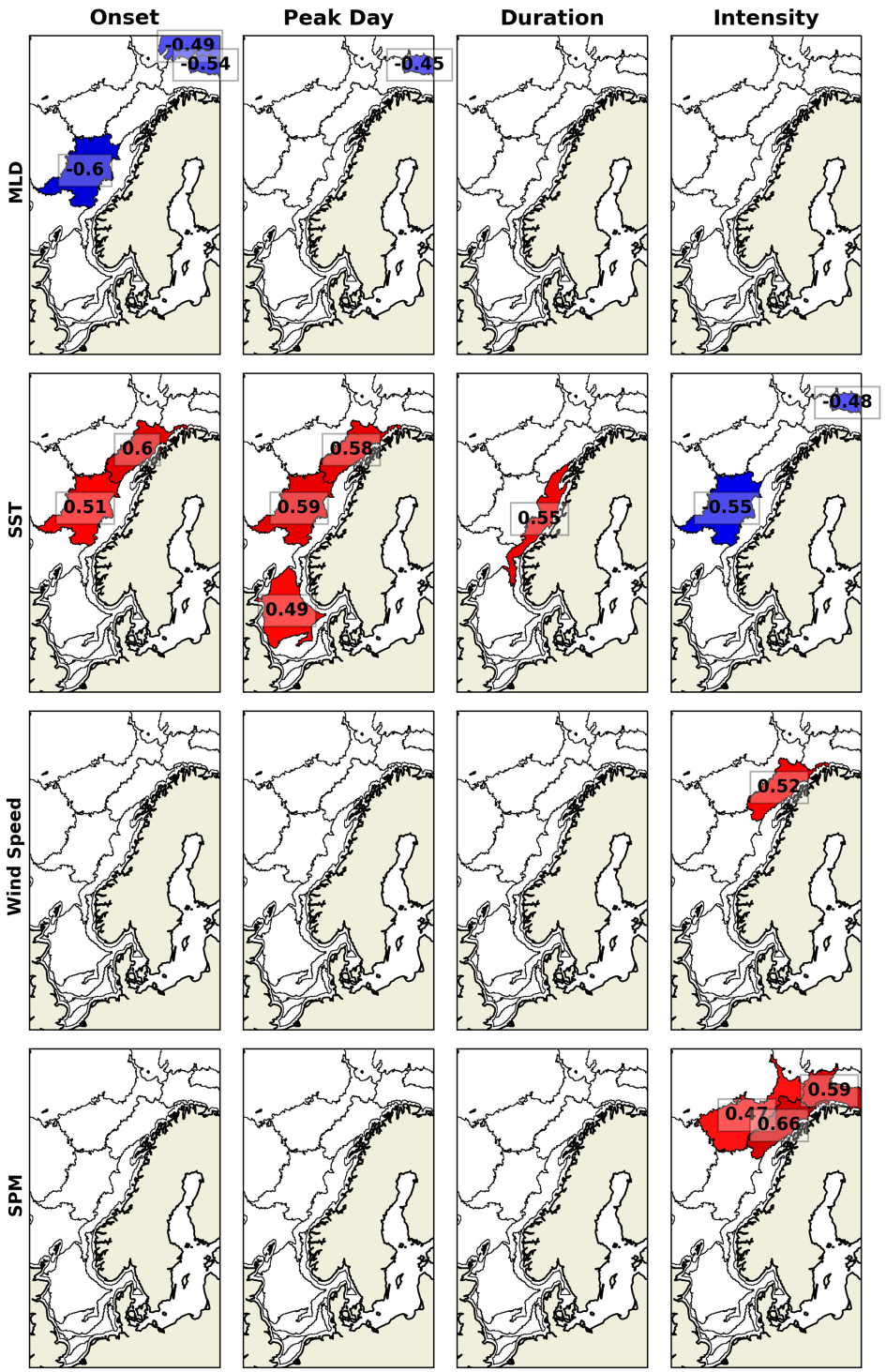


FIGURE 7 | Detrended interannual correlation between the summer bloom phenology and MLD, SST, wind speed, and SPM. Red colors are positive correlations, blue colors are negative correlations and white colors are used for insignificant correlations ($\alpha > 0.05$).

Z_{eu} and K_d change the blooms (Sverdrup, 1953) at the same time the Chl-a change the Z_{eu} and K_d (Kirk, 2011). Thus, we retrieved high correlations. However, the correlations showed that higher biomass blooms are correlated to higher K_d and lower Z_{eu}, meaning that the blooms probably control the interannual variability of K_d and Z_{eu} during the bloom rather than the contrary. For this reason, PAR, K_d, and Z_{eu} are not presented in this study.

DISCUSSION

Summer Bloom Delay

In the trends analysis, it appears that summer blooms are getting delayed from 2000 to 2020. However, the possible causes of this delay are unclear to us. The spring bloom exhausts the nutrients on the surface, and associated with other factors such as zooplankton grazing, leads to the ending of spring bloom. In the poor nutrient waters of summer, the increase of MLD results in an upwell of nutrients required for a summer or autumn bloom (Glen Harrison et al., 2013; Wihsgott et al., 2019). Therefore, we would expect that changes in the summer bloom phenology are related to the MLD. For example, Martinez et al. (2011) suggested that a possible cause for the weaker autumn bloom in the North Atlantic (30–50°N) was a delayed increase of MLD during the autumn of the 2000s. We computed the MLD trend during the summer bloom and down to 4 weeks before the onset. Our results showed that there had been no significant trend in the MLD from 2000 to 2020. Besides, we also computed the trends of SST, SPM and wind speed, and none showed a significant trend.

The lack of trends in MLD, SST, SPM and wind speed suggests that other factors that are not assessed in this study may be influencing the delay of summer blooms. For example, bio-advection of phytoplankton and zooplankton pressure. A recent study showed that bio-advection caused by a faster intrusion of the North Atlantic Current is causing the phytoplankton *Emiliania huxleyi* to increase in the Barents Sea (Oziel et al., 2020). In the North Atlantic, the predominant zooplankton species has been changing (Beaugrand, 2002), and the new species biomass increases during autumn (Planque and Fromentin, 1996). Martinez et al. (2011) suggested that the new predominant zooplankton species increased the grazing pressure in the autumn, probably leading to a weaker bloom in the 2000s. Likewise, the delay of summer blooms found in this study could be related to the bio-advection of phytoplankton or changes in the zooplankton community structure. Still, no firm conclusion can be held yet on the reason of the delayed summer blooms. This will be the topic of a follow-up study.

Barents Sea: Stronger, Earlier and Shorter Spring Blooms Driven by Shallower Mixed Layer

The intensity of spring blooms in the Barents Sea (sub-regions 1, 3, and 4) showed the highest interannual variability of the study area (**Supplementary Figure 3**). For example, varying from 1.2 mg m^{-3} in 2008 to 4.1 mg m^{-3} in 2002 in sub-region 3. Besides, the intensity of spring blooms is negatively correlated with the onset, peak day and duration ($R < -0.44$), meaning that the spring blooms in the Barents Sea are typically either early, short and strong or late, long and weak.

Two dynamical processes contribute to the nutrient loads in the surface waters of the southern and central Barents Sea: the lateral inflow of Atlantic waters that come from NwAC and the vertical mixing when the ML is deeper during winter (Wassmann et al., 2006). In March, the deep ML makes the phosphate, nitrate and silicate evenly distributed in the water column, reaching 0.85, 11.2, and 4.5 μM, respectively (Reigstad et al., 2002). It was shown that springs with a deeper ML are correlated with higher nitrate concentrations (Olsen et al., 2003). However, deep ML and high nitrate concentrations do not necessarily lead to stronger spring blooms. Our results suggest that a shallower ML is correlated to stronger spring blooms. Stratified waters reduce the phytoplankton sinking below the euphotic zone, which may be critical in the Barents Sea, where one of the predominant phytoplankton taxa is Diatom that quickly sinks due to its dense cell walls of silica (Degerlund and Eilertsen, 2010). The high concentration of nutrients available at the beginning of the bloom in March (Reigstad et al., 2002) could be sufficient for developing the spring blooms, while interannual variability of MLD would control the intensity and the timing of the blooms. Nevertheless, a reduced level of nutrients available in years of shallower ML can explain why stronger spring blooms end sooner.

The seasonal ML shallowing during spring is driven by the SST increase from solar radiation and the freshening of water coming from sea ice melting, interactions with the fresher fjord water systems and inflow of the NCC (Drinkwater et al., 2003; Olsen et al., 2003; Loeng and Drinkwater, 2007). In the sub-regions 1, 3, and 4, we found that the interannual variability of MLD is significantly correlated with wind speed ($R = 0.58$) and freshwaters discharge of Tana River ($R = -0.65$) during the bloom. This indicates that calm waters and high discharge of freshwaters may lead to shallower ML, resulting in stronger spring blooms. This also explains why weaker winds correlate with earlier and stronger spring blooms in the Barents Sea.

Mixed Layer Depth and Sea Surface Temperature Influence on the Spring Bloom Phenology in the Norwegian Sea

Surface heating from solar radiation and freshening of the coastal waters leads to the shallowing ML during the spring in the Norwegian Sea, and the spring bloom starts when the MLD reaches a lower depth than the Sverdrup critical depth (Sverdrup, 1953). The MLD has been shown to influence the spatial variability of spring blooms onset (Naustvoll et al., 2020). Our results show that MLD is also a possible driver of the interannual variability of bloom onset and peak day. The positive correlation between MLD and the spring blooms onset and peak day in the sub-regions 5, 6, 8, and 9 ($R > 0.58$) suggests that a shallower ML favor earlier spring blooms. In sub-regions 5, 8, and 9, interannual SST is correlated with MLD ($R < -0.46$), and consequently, SST is also correlated with the spring bloom timing. In sub-region 6, only the Målselva River inflow has a significant correlation with MLD ($R = -0.55$). Therefore, warmer years during the spring could lead to shallower ML and earlier blooms from the middle to the northwestern Norwegian Sea, while the spring bloom in sub-region 6 behaves similarly to spring blooms in the Barents Sea.

The SST is correlated with the spring blooms in sub-regions 7 and 10 without the influence of MLD. In both sub-regions, MLD has not correlated with SST and the spring blooms as observed in the remaining Norwegian Sea. Besides, the spring bloom intensity of both sub-regions shows an inverse relationship with SST. Warmer waters are correlated with stronger blooms in sub-region 10, whereas colder waters are correlated with earlier and stronger blooms in sub-region 7. Without the influence of SST on MLD interannual variability, two hypotheses could explain why warmer waters are correlated with stronger spring blooms in sub-region 10. First, warmer waters increase the growth rate of phytoplankton (Eppley, 1972; Moisan et al., 2002; Bissinger et al., 2008), and during the spring bloom, a higher growth rate could support the bloom to reach higher Chl-a biomass. Second, warmer waters could indicate a higher intrusion of Atlantic waters from the North Atlantic Current. If Atlantic waters are associated with the input of nutrients in sub-region 10, more nutrients could lead the spring bloom to higher Chl-a biomass.

Regarding sub-region 7, warm Atlantic waters trapped in mesoscale anticyclonic eddies were found to delay the spring blooms in the Norwegian Shelf (Hansen et al., 2010). However, the spring bloom delay in the eddy was probably caused by the delayed shallowing of the ML, and our results have not shown a relationship between SST and MLD in sub-region 7. Thus, we have not found a plausible explanation why colder waters could relate to earlier and stronger spring blooms in this region.

Shallower Mixed Layer Drives Clearer Waters and Stronger Spring Blooms in the North Sea

The average spring bloom intensity in the sub-region 12 ranges from 0.9 to 1.5 mg m^{-3}, and it is significant correlated with MLD and SPM. A shallower ML reduces the phytoplankton sinking to deeper waters, and a lower SPM concentration increases the euphotic zone and the light available to the algae photosynthesis. Moreover, we also found that SPM is correlated with MLD during the spring bloom ($R = -0.44$). A previous study showed that surface SPM variability in the North Sea is correlated with the bed shear stress caused by oceanic waves, but only for months with a deep ML (Wilson and Heath, 2019). In March, deep ML allows the bed shear stress to increase the surface SPM concentration ($R^2 = 0.47$). In April, the MLD decreases and the bead shear stress is no longer correlated with the surface SPM variability. The climatological spring bloom in sub-region 12 starts on March 10th and ends on April 26th, and this implies that the relation between MLD, bed shear stress and SPM are strongly correlated for almost half of the bloom period. Therefore, the compound influence of SPM and MLD was found to explain the intensity of spring blooms. Years of shallower ML reduces the phytoplankton sinking and could lead to more transparent waters, resulting in more sunlight available to photosynthesis and, hence, stronger spring blooms.

CONCLUSION

This study presents an exhaustive analysis of the regional spring and summer blooms phenology for a region that extends from the Barents, Norwegian to the North seas using an extended and novel clustering analysis. The regional climatology and trend of the phytoplankton blooms phenology, as well as a primary analysis of the co-variability of potential drivers with interannual variability, are presented and discussed. In the Barents Sea, we found that low wind amplitude and increased freshening lead to springs with shallower ML, and more stratified waters are related to spring blooms starting earlier and reaching higher biomass during the peak. In the Norwegian Sea, we found that SST has an opposed correlation with spring blooms. There, warmer waters are correlated with earlier and higher biomass blooms from the north of Scotland to the off-shore central parts of the Norwegian Sea, but lower temperatures are correlated with earlier and higher biomass blooms in the eastern Norwegian Sea. In the North Sea, springs with shallower ML limits the SPM increase by bottom shear stress, favoring an environment of more stratified and clearer waters, correlating well with blooms of higher biomass. Last, we also found a rapid delay in the onset and increased biomass of the summer blooms during the past 21 years in almost the entire study region. The summer blooms are starting later, ending later, getting longer and reaching higher Chl-a concentrations.

DATA AVAILABILITY STATEMENT

Publicly available datasets were analyzed in this study. This data can be found here: OC:CCI: https://www.oceancolour.org/, CMEMS: https://marine.copernicus.eu/, GlobColour: https://www.globcolour.info/, and NMDC: https://nmdc.no/.

AUTHOR CONTRIBUTIONS

ES, FC, JB, AK, and LP contributed to the conception and design of the study. ES organized the database, performed the statistical analysis, and wrote the first draft of the manuscript. ES and FC performed the data processing. FC and JB supervised the data processing and statistical analysis. All authors contributed to the interpretation of the results of this work, manuscript revision, read, and approved the submitted version.

FUNDING

ES is a holder of an institute research fellowship (INSTSTIP) funded by the basic institutional funding through Norwegian Research Council (#318085). FC acknowledges the Trond Mohn Foundation under project number: BFS2018TMT01. JB acknowledges the NFR Climate Futures (309562). NK acknowledges the Nansen Legacy project (276730). This work has also received a grant for computer time from the Norwegian

Program for super computing (NOTUR2, project number nn9039k) and a storage grant (NORSTORE, NS9039k).

ACKNOWLEDGMENTS

We want to thank Jiping Xie for making the TOPAZ4 MLD data available to us. We also want to thank the Norwegian Institute of Marine Research for making the *in situ* Chl-a data available. JB is member of Sorbonne University as associate professor.

SUPPLEMENTARY MATERIAL

The Supplementary Material for this article can be found online at: https://www.frontiersin.org/articles/10.3389/fmars.2021.746327/full#supplementary-material

REFERENCES

Arthur, D., and Vassilvitskii, S. (2007). "k-means++: the advantages of careful seeding," in *Proceedings of the Eighteenth Annual ACM-SIAM Symposium on Discrete Algorithms, SODA*, (New Orleans), 11.

Asch, R. G., Stock, C. A., and Sarmiento, J. L. (2019). Climate change impacts on mismatches between phytoplankton blooms and fish spawning phenology. *Glob. Chang. Biol.* 25, 2544–2559. doi: 10.1111/gcb.14650

Bailey, S. W., and Werdell, P. J. (2006). A multi-sensor approach for the on-orbit validation of ocean color satellite data products. *Remote Sens. Environ.* 102, 12–23. doi: 10.1016/j.rse.2006.01.015

Beaugrand, G. (2002). Reorganization of North Atlantic marine copepod biodiversity and climate. *Science (80-.).* 296, 1692–1694. doi: 10.1126/science.1071329

Behrenfeld, M. J. (2010). Abandoning sverdrup's critical depth hypothesis on phytoplankton blooms. *Ecology* 91, 977–989. doi: 10.1890/09-1207.1

Bissinger, J. E., Montagnes, D. J. S., Sharples, J., and Atkinson, D. (2008). Predicting marine phytoplankton maximum growth rates from temperature: improving on the Eppley curve using quantile regression. *Limnol. Oceanogr.* 53, 487–493. doi: 10.4319/lo.2008.53.2.0487

Bleck, R. (2002). An oceanic general circulation model framed in hybrid isopycnic-Cartesian coordinates. *Ocean Model.* 4, 55–88. doi: 10.1016/S1463-5003(01)00012-9

Blondeau-Patissier, D., Tilstone, G. H., Martinez-Vicente, V., and Moore, G. F. (2004). Comparison of bio-physical marine products from SeaWiFS, MODIS and a bio-optical model with in situ measurements from Northern European waters. *J. Opt. A Pure Appl. Opt.* 6, 875–889. doi: 10.1088/1464-4258/6/9/010

Brody, S. R., Lozier, M. S., and Dunne, J. P. (2013). A comparison of methods to determine phytoplankton bloom initiation. *J. Geophys. Res. Ocean.* 118, 2345–2357. doi: 10.1002/jgrc.20167

Calton, B. (2020). *ESA Ocean Colour Climate Change Initiative – Phase 3 Product User Guide for v5*. 0 Dataset. Paris: ESA.

Chang, F. H., Anderson, C., and Boustead, N. C. (1990). First record of a Heterosigma (Raphidophyceae) bloom with associated mortality of cage-reared salmon in Big Glory Bay, New Zealand. *New Zeal. J. Mar. Freshw. Res.* 24, 461–469. doi: 10.1080/00288330.1990.9516437

De Cauwer, V., Ruddick, K., Park, Y.-J., Nechad, B., and Kyramarios, M. (2004). *Optical Remote Sensing in Support of Eutrophication Monitoring in the Southern North Sea*. European Association of Remote Sensing Laboratories (EARSeL), 208–221.

Degerlund, M., and Eilertsen, H. C. (2010). Main species characteristics of Phytoplankton spring blooms in NE Atlantic and Arctic Waters (68–80° N). *Estuaries Coasts* 33, 242–269. doi: 10.1007/s12237-009-9167-7

Drinkwater, K. F., Belgrano, A., Borja, A., Conversi, A., Edwards, M., Greene, C. H., et al. (2003). "The response of marine ecosystems to climate variability associated with the north atlantic oscillation," in *The North Atlantic Oscillation: Climatic Significance and Environmental Impact*, eds J. W. Hurrell, Y. Kushnir, G. Ottersen, and M. Visbeck (Washington, DC: American Geophysical Union), 211–234.

Eisma, D., Johnston, R., and Cadogan, J. I. G. (1987). The North Sea: an overview. *Philos. Trans. R. Soc. London. B, Biol. Sci.* 316, 461–485. doi: 10.1098/rstb.1987.0032

Eldevik, T., Nilsen, J. E., Iovino, D., Anders Olsson, K., Sandø, A. B., and Drange, H. (2009). Observed sources and variability of Nordic seas overflow. *Nat. Geosci.* 2, 406–410. doi: 10.1038/ngeo518

Eppley, R. W. (1972). Temperature and Phytoplankton Growth in the Sea. *Fish. Bull.* 70, 1063–1085.

Evensen, G. (2003). The Ensemble Kalman Filter: theoretical formulation and practical implementation. *Ocean Dyn.* 53, 343–367. doi: 10.1007/s10236-003-0036-9

Ferreira, A. S. A., Hátún, H., Counillon, F., Payne, M. R., and Visser, A. W. (2015). Synoptic-scale analysis of mechanisms driving surface chlorophyll dynamics in the North Atlantic. *Biogeosciences* 12, 3641–3653. doi: 10.5194/bg-12-3641-2015

Folkestad, A., Pettersson, L. H., and Durand, D. D. (2007). Inter-comparison of ocean colour data products during algal blooms in the Skagerrak. *Int. J. Remote Sens.* 28, 569–592. doi: 10.1080/01431160600821044

Furevik, T., Bentsen, M., Drange, H., Johannessen, J. A., and Korablev, A. (2002). Temporal and spatial variability of the sea surface salinity in the Nordic Seas. *J. Geophys. Res. Ocean.* 107, 1–16. doi: 10.1029/2001jc001118

Giannini, F., Hunt, B. P. V., Jacoby, D., and Costa, M. (2021). Performance of OLCI Sentinel-3A satellite in the Northeast Pacific coastal waters. *Remote Sens. Environ.* 256:112317. doi: 10.1016/j.rse.2021.112317

Glen Harrison, W., Yngve Børsheim, K., Li, W. K. W., Maillet, G. L., Pepin, P., Sakshaug, E., et al. (2013). Phytoplankton production and growth regulation in the Subarctic North Atlantic: a comparative study of the Labrador Sea-Labrador/Newfoundland shelves and Barents/Norwegian/Greenland seas and shelves. *Prog. Oceanogr.* 114, 26–45. doi: 10.1016/j.pocean.2013.05.003

Gobler, C. J. (2020). Climate change and harmful algal blooms: insights and perspective. *Harmful Algae* 91:101731. doi: 10.1016/j.hal.2019.101731

Gohin, F. (2011). Annual cycles of chlorophyll-a, non-algal suspended particulate matter, and turbidity observed from space and in-situ in coastal waters. *Ocean Sci.* 7, 705–732. doi: 10.5194/os-7-705-2011

Good, S., Fiedler, E., Mao, C., Martin, M. J., Maycock, A., Reid, R., et al. (2020). The current configuration of the OSTIA system for operational production of foundation sea surface temperature and ice concentration analyses. *Remote Sens.* 12, 1–20. doi: 10.3390/rs12040720

Hansen, C., Kvaleberg, E., and Samuelsen, A. (2010). Anticyclonic eddies in the Norwegian Sea; their generation, evolution and impact on primary production. *Deep Sea Res. Part I Oceanogr. Res. Pap.* 57, 1079–1091. doi: 10.1016/j.dsr.2010.05.013

Harrison, P. J., Piontkovski, S., and Al-Hashmi, K. (2017). Understanding how physical-biological coupling influences harmful algal blooms, low oxygen and fish kills in the Sea of Oman and the Western Arabian Sea. *Mar. Pollut. Bull.* 114, 25–34. doi: 10.1016/j.marpolbul.2016.11.008

Holm-Hansen, O., and Riemann, B. (1978). Chlorophyll a Determination: improvements in Methodology. *Oikos* 30:438. doi: 10.2307/3543338

Hunke, E. C., and Dukowicz, J. K. (1997). An Elastic–Viscous–Plastic model for sea ice dynamics. *J. Phys. Oceanogr.* 27, 1849–1867. doi: 10.1175/1520-04851997027<1849:AEVPMF<2.0.CO;2

Kaartvedt, S., Johnsen, T. M., Aksnes, D. L., Lie, U., and Svendsen, H. (1991). Occurrence of the toxic phytoflagellate Prymnesium parvum and associated fish mortality in a Norwegian fjord system. *Can. J. Fish. Aquat. Sci.* 48, 2316–2323. doi: 10.1139/f91-272

Kent, M., Whyte, J., and LaTrace, C. (1995). Gill lesions and mortality in seawater pen-reared Atlantic salmon Salmo salar associated with a dense bloom of Skeletonema costatum and Thalassiosira species. *Dis. Aquat. Organ.* 22, 77–81. doi: 10.3354/dao022077

Kirk, J. T. O. (2011). *Light and Photosynthesis in Aquatic Ecosystems*. Cambridge: Cambridge University Press.

Landsberg, J. H., Hendrickson, J., Tabuchi, M., Kiryu, Y., Williams, B. J., and Tomlinson, M. C. (2020). A large-scale sustained fish kill in the St. Johns River, Florida: a complex consequence of cyanobacteria blooms. *Harmful Algae* 92:101771. doi: 10.1016/j.hal.2020.101771

Leblanc, K., Quéguiner, B., Diaz, F., Cornet, V., Michel-Rodriguez, M., Durrieu de Madron, X., et al. (2018). Nanoplanktonic diatoms are globally overlooked but play a role in spring blooms and carbon export. *Nat. Commun.* 9:953. doi: 10.1038/s41467-018-03376-9

Legendre, L. (1990). The significance of microalgal blooms for fisheries and for the export of particulate organic carbon in oceans. *J. Plankton Res.* 12, 681–699. doi: 10.1093/plankt/12.4.681

Loeng, H., and Drinkwater, K. (2007). An overview of the ecosystems of the Barents and Norwegian Seas and their response to climate variability. *Deep. Res. Part II Top. Stud. Oceanogr.* 54, 2478–2500. doi: 10.1016/j.dsr2.2007.08.013

MacQueen, J. (1967). "Some methods for classification and analysis of multivariate observations," in *Proceeding of the Fifth Berkeley Symposium* (Berkeley), 281–297.

Martinez, E., Antoine, D., D'Ortenzio, F., and De Boyer Montégut, C. (2011). Phytoplankton spring and fall blooms in the North Atlantic in the 1980s and 2000s. *J. Geophys. Res. Ocean.* 116, 1–11. doi: 10.1029/2010JC006836

Merchant, C. J., Embury, O., Bulgin, C. E., Block, T., Corlett, G. K., Fiedler, E., et al. (2019). Satellite-based time-series of sea-surface temperature since 1981 for climate applications. *Sci. Data* 6, 1–18. doi: 10.1038/s41597-019-0236-x

Mohd-Din, M., Abdul-Wahab, F., Mohamad, S. E., Jamaluddin, H., Shahir, S., Ibrahim, Z., et al. (2020). Prolonged high biomass diatom blooms induced formation of hypoxic-anoxic zones in the inner part of Johor Strait. *Environ. Sci. Pollut. Res.* 27, 42948–42959. doi: 10.1007/s11356-020-10184-6

Moisan, J. R., Moisan, T. A., and Abbott, M. R. (2002). Modelling the effect of temperature on the maximum growth rates of phytoplankton populations. *Ecol. Modell.* 153, 197–215. doi: 10.1016/S0304-3800(02)00008-X

Morel, A., and Prieur, L. (1977). Analysis of variations in ocean color1. *Limnol. Oceanogr.* 22, 709–722. doi: 10.4319/lo.1977.22.4.0709

Mork, M. (1981). Circulation phenomena and frontal dynamics of the Norwegian coastal current. *Philos. Trans. R. Soc. London. Ser. A, Math. Phys. Sci.* 302, 635–647. doi: 10.1098/rsta.1981.0188

Naustvoll, L. J., Melle, W., Klevjer, T., Drinkwater, K. F., Strand, E., and Knutsen, T. (2020). Dynamics of phytoplankton species composition, biomass and nutrients in the North Atlantic during spring and summer - A trans-Atlantic study. *Deep Sea Res. Part II Top. Stud. Oceanogr.* 180:104890. doi: 10.1016/j.dsr2.2020.104890

Neveux, J., Delmas, D., Romano, J., Algarra, P., Ignatiades, L., Herbland, A., et al. (1990). Comparison of chlorophyll and phaeopigment determinations by spectrophotometric, fluorometric, spectrofluorometric and HPLC methods. *Mar. Microb. Food Webs* 4, 217–238.

Olsen, A., Johannessen, T., and Rey, F. (2003). On the nature of the factors that control spring bloom development at the entrance to the Barents Sea and their interannual variability. *Sarsia* 88, 379–393. doi: 10.1080/00364820310003145

Opdal, A. F., Lindemann, C., and Aksnes, D. L. (2019). Centennial decline in North Sea water clarity causes strong delay in phytoplankton bloom timing. *Glob. Chang. Biol.* 25, 3946–3953. doi: 10.1111/gcb.14810

Oziel, L., Baudena, A., Ardyna, M., Massicotte, P., Randelhoff, A., Sallée, J. B., et al. (2020). Faster Atlantic currents drive poleward expansion of temperate phytoplankton in the Arctic Ocean. *Nat. Commun.* 11, 1–8. doi: 10.1038/s41467-020-15485-5

Perry, R. K. (1986). "Bathymetry," in *The Nordic Seas*, ed. B. G. Hurdle (New York, NY: Springer New York), 211–236.

Petrenko, D., Pozdnyakov, D., Johannessen, J., Counillon, F., and Sychov, V. (2013). Satellite-derived multi-year trend in primary production in the Arctic Ocean. *Int. J. Remote Sens.* 34, 3903–3937. doi: 10.1080/01431161.2012.762698

Pettersson, L. H., and Pozdnyakov, D. (2013). *Monitoring of Harmful Algal Blooms*. Berlin: Springer Berlin Heidelberg.

Planque, B., and Fromentin, J. (1996). Calanus and environment in the eastern North Atlantic. I. Spatial and temporal patterns of C. finmarchicus and C. helgolandicus. *Mar. Ecol. Prog. Ser.* 134, 101–109. doi: 10.3354/meps134101

Platt, T., Fuentes-Yaco, C., and Frank, K. T. (2003). Spring algal bloom and larval fish survival off Nova Scotia. *Nature* 423, 398–399.

Pozdnyakov, D. V., Pettersson, L. H., and Korosov, A. A. (2017). *Exploring the Marine Ecology From Space*. Cham: Springer International Publishing.

Ramsay, J. O., and Silverman, B. W. (2005). *Functional Data Analysis*. New York, NY: Springer New York.

Reigstad, M., Wassmann, P., Wexels Riser, C., Øygarden, S., and Rey, F. (2002). Variations in hydrography, nutrients and chlorophyll a in the marginal ice-zone and the central Barents Sea. *J. Mar. Syst.* 38, 9–29. doi: 10.1016/S0924-7963(02)00167-7

Reynolds, R. A., Stramski, D., and Mitchell, B. G. (2001). A chlorophyll-dependent semianalytical reflectance model derived from field measurements of absorption and backscattering coefficients within the Southern Ocean. *J. Geophys. Res. Ocean.* 106, 7125–7138. doi: 10.1029/1999JC000311

Rousseeuw, P. J. (1987). Silhouettes: a graphical aid to the interpretation and validation of cluster analysis. *J. Comput. Appl. Math.* 20, 53–65. doi: 10.1016/0377-0427(87)90125-7

Sakov, P., Counillon, F., Bertino, L., Lisæter, K. A., Oke, P. R., and Korablev, A. (2012). TOPAZ4: an ocean-sea ice data assimilation system for the North Atlantic and Arctic. *Ocean Sci.* 8, 633–656. doi: 10.5194/os-8-633-2012

Sathyendranath, S., Brewin, R. J. W., Brockmann, C., Brotas, V., Calton, B., Chuprin, A., et al. (2019). An ocean-colour time series for use in climate studies: the experience of the ocean-colour climate change initiative (OC-CCI). *Sensors (Switzerland)* 19:4285. doi: 10.3390/s19194285

Student. (1908). Probable error of a Correlation Coefficient. *Biometrika* 6, 302–310. doi: 10.2307/2331474

Sundby, S., Drinkwater, K. F., and Kjesbu, O. S. (2016). The North Atlantic spring-bloom system-where the changing climate meets the winter dark. *Front. Mar. Sci.* 3:28. doi: 10.3389/fmars.2016.00028

Sverdrup, H. U. (1953). On conditions for the vernal blooming of phytoplankton. *ICES J. Mar. Sci.* 18, 287–295. doi: 10.1093/icesjms/18.3.287

Tangen, K. (1977). Blooms of gyrodinium aureolum (dinophygeae) in north european waters, accompanied by mortality in marine organisms. *Sarsia* 63, 123–133. doi: 10.1080/00364827.1977.10411330

Tilstone, G. H., Peters, S. W. M., van der Woerd, H. J., Eleveld, M. A., Ruddick, K., Schönfeld, W., et al. (2012). Variability in specific-absorption properties and their use in a semi-analytical ocean colour algorithm for MERIS in North Sea and Western English Channel Coastal Waters. *Remote Sens. Environ.* 118, 320–338. doi: 10.1016/j.rse.2011.11.019

Townsend, D. W., and Cammen, L. M. (1987). Potential importance of the timing of spring plankton blooms to benthic-pelagic coupling and recruitment of juvenile demersal fishes. *Biol. Oceanogr.* 5, 215–228. doi: 10.1080/01965581.1987.10749514

Vikebø, F. B., Korosov, A., Stenevik, E. K., Husebø, A., and Slotte, A. (2012). Spatio-temporal overlap of hatching in Norwegian spring-spawning herring and the spring phytoplankton bloom at available spawning substrata. *ICES J. Mar. Sci.* 69, 1298–1302. doi: 10.1038/278097a0

Vikebø, F. B., Strand, K. O., and Sundby, S. (2019). Wind intensity is key to phytoplankton spring bloom under climate change. *Front. Mar. Sci.* 6:518. doi: 10.3389/fmars.2019.00518

Wassmann, P., Reigstad, M., Haug, T., Rudels, B., Carroll, M. L., Hop, H., et al. (2006). Food webs and carbon flux in the Barents Sea. *Prog. Oceanogr.* 71, 232–287. doi: 10.1016/j.pocean.2006.10.003

Wihsgott, J. U., Sharples, J., Hopkins, J. E., Woodward, E. M. S., Hull, T., Greenwood, N., et al. (2019). Observations of vertical mixing in autumn and its effect on the autumn phytoplankton bloom. *Prog. Oceanogr.* 177:102059. doi: 10.1016/j.pocean.2019.01.001

Wilson, R. J., and Heath, M. R. (2019). Increasing turbidity in the North Sea during the 20th century due to changing wave climate. *Ocean Sci.* 15, 1615–1625. doi: 10.5194/os-15-1615-2019

Xie, J., Bertino, L., Counillon, F., Lisæter, K. A., and Sakov, P. (2017). Quality assessment of the TOPAZ4 reanalysis in the Arctic over the period 1991–2013. *Ocean Sci.* 13, 123–144. doi: 10.5194/os-13-123-2017

Zhang, Q., Warwick, R. M., McNeill, C. L., Widdicombe, C. E., Sheehan, A., and Widdicombe, S. (2015). An unusually large phytoplankton spring bloom drives rapid changes in benthic diversity and ecosystem function. *Prog. Oceanogr.* 137, 533–545. doi: 10.1016/j.pocean.2015.04.029

Conflict of Interest: The authors declare that the research was conducted in the absence of any commercial or financial relationships that could be construed as a potential conflict of interest.

Publisher's Note: All claims expressed in this article are solely those of the authors and do not necessarily represent those of their affiliated organizations, or those of the publisher, the editors and the reviewers. Any product that may be evaluated in this article, or claim that may be made by its manufacturer, is not guaranteed or endorsed by the publisher.

Copyright © 2021 Silva, Counillon, Brajard, Korosov, Pettersson, Samuelsen and Keenlyside. This is an open-access article distributed under the terms of the Creative Commons Attribution License (CC BY). The use, distribution or reproduction in other forums is permitted, provided the original author(s) and the copyright owner(s) are credited and that the original publication in this journal is cited, in accordance with accepted academic practice. No use, distribution or reproduction is permitted which does not comply with these terms.

frontiers in Marine Science

ORIGINAL RESEARCH
published: 09 December 2021
doi: 10.3389/fmars.2021.785685

Distinct Seasonal Primary Production Patterns in the Sub-Polar Gyre and Surrounding Seas

Katherine Richardson[1†] and Jørgen Bendtsen[2,3†]*

[1] Center for Macroecology, Evolution and Climate, Globe Institute, University of Copenhagen, Copenhagen, Denmark, [2] Norwegian Institute for Water Research, NIVA Denmark, Copenhagen, Denmark, [3] ClimateLab, Copenhagen, Denmark

Primary production (PP) in the sub-polar region appears to be important for ocean carbon uptake but how the different water masses contribute to the PP occurring here has not yet been described. Using two models based on satellite observations of surface chlorophyll, light and temperature, seasonal patterns in the distribution of PP are shown here to differ in the sub-polar gyre south of the Greenland-Scotland Ridge (GSR) and surrounding water masses. Monthly averages of PP (2003–2013) were determined. Total and seasonal PP were similar in both models. Average PP in five of the domains (0.47–0.77 g C m^{-2} d^{-1}) was well above the global average (0.37 g C m^{-2} d^{-1}). Over the East Greenland shelf, however, total annual PP was estimated to be only 0.19 g C m^{-2} d^{-1}. The Norwegian shelf was the most productive of the regions studied. "Spring blooms" appear sporadically as spikes in the annual distribution of PP in some regions/years, but do not emerge as a dominant feature in the average annual development of PP in any of the domains. For all regions, ∼25% of the annual PP takes place in the period January-May. PP peaked over most of the study area at or around maximum insolation or temperature. PP in the study region as a whole appears to be more related to latitude or water masses than to bathymetry. In waters over the East Greenland shelf, the Norwegian shelf, and north of the GSR up to 50% of annual PP had taken place when ∼50% of the annual flux of light has reached the surface. In contrast, only about 35% of annual PP had taken place in the sub-polar gyre and waters over the southern open shelf by this time. Light-use efficiency differences may be explained by differences in mixed layer depth (MLD). Multi-model Earth System model studies have indicated that climate change may decrease the MLD in the sub-polar gyre and suggest this may lead to a decrease in the PP occurring here. The results presented here, however, suggest that a shallower MLD could lead to an increase in PP.

Keywords: spring bloom, North Atlantic, primary production, light, temperature, primary production model

OPEN ACCESS

Edited by:
Teresa Sofia Giesta da Silva, Marine and Freshwater Research Institute, Iceland

Reviewed by:
A. Sofia A. Ferreira, University of Oslo, Norway
Karin Margretha Húsgarð Larsen, Faroe Marine Research Institute (FAMRI), Faroe Islands

****Correspondence:***
Katherine Richardson
kari@sund.ku.dk

† These authors have contributed equally to this work

Specialty section:
This article was submitted to Physical Oceanography, a section of the journal Frontiers in Marine Science

Received: *29 September 2021*
Accepted: *17 November 2021*
Published: *09 December 2021*

Citation:
Richardson K and Bendtsen J (2021) Distinct Seasonal Primary Production Patterns in the Sub-Polar Gyre and Surrounding Seas. Front. Mar. Sci. 8:785685. doi: 10.3389/fmars.2021.785685

INTRODUCTION

The waters in and surrounding the North Atlantic sub-polar gyre are recognized as being important in atmospheric CO_2 drawdown. Chemical-physical processes alone, however, cannot completely explain observed distribution patterns in surface water CO_2 (Takahashi et al., 2009) and it is therefore assumed that removal of CO_2 from surface waters by phytoplankton photosynthesis

[primary production (PP)] is an important driver in the development of the seasonal distribution of CO_2 in these waters (Takahashi et al., 2002). Nevertheless, a detailed understanding of the seasonal patterns in PP in different water masses found in this region is still lacking.

The region is large and characterized by varied bathymetric conditions with shelves along East Greenland, Norway and the shallow Greenland-Scotland Ridge (GSR) that separate the open sea areas in the Nordic Seas and the sub-polar Gyre. In addition, regional-scale currents affecting both nutrient distributions and stratification characteristics pass through the area. Several studies have suggested that PP characteristics of these different water masses may differ (e.g., Astthorsson et al., 2007) and inter-annual variability has been shown to correlate with the North Atlantic Oscillation, i.e., the principal mode explaining atmospheric variability in the region (e.g., Skogen et al., 2007; Henson et al., 2009; Harrison et al., 2013). Linkages between PP and water mass distributions are also indicated from the timing and distribution of phytoplankton blooms (Friedland et al., 2016), and differences in the timing of the spring bloom across the GSR have been explained by water mass characteristics, e.g., mixed layer depth (Zhai et al., 2012) or iron-depletion (Nielsdóttir et al., 2009).

Climate change scenarios show significant changes in the sub-polar North Atlantic by the end of the 21st century where reduction in sea ice cover, increased stratification and changes in water mass distributions will affect PP in the area. PP in the sub-polar gyre is expected to decrease significantly whereas PP in areas north of the GSR shows a mixed response (Laufkötter et al., 2015; Kwiatkowski et al., 2020). Predictions of PP are, however, associated with large uncertainties and a better understanding of local drivers for PP, e.g., light, nutrients, grazing and stratification, is required for making robust future assessments.

The aim of the current study is to examine seasonal distribution patterns in PP in the sub-polar gyre and adjacent waters and to relate these patterns to physical conditions. As there are insufficient *in situ* data to address this question, we employ models estimating PP from surface optical water characteristics remotely determined from satellite observation (chlorophyll, light and temperature). Satellite sensors can only provide direct observations from the surface layer of the ocean and PP is well known to also occur below the surface layer. Thus, the validity of the estimates resulting from the models converting surface ocean characteristics to PP is highly dependent upon the model's approach to estimating PP in the water column as a whole. We chose, therefore, two different model approaches for estimating PP, where the principle difference between the models is the strategies employed for estimating total water column PP.

In the first, the commonly employed VGPM model (vertically generalized production model; Behrenfeld and Falkowski, 1997), sub-surface PP is estimated based on statistical analyses of archived chlorophyll profiles. In the other, VPP (vertically integrated primary production model; Richardson and Bendtsen, 2019), a universal pattern in the vertical distribution of PP in relation to nutricline depth is used to estimate sub-surface PP. In the study area, the nutricline is generally located close to the surface (Garcia et al., 2010). Thus, we argue that most of the water column PP will occur near the surface layer and can be accurately estimated from surface water characteristics.

Models estimating PP are also highly sensitive to the photosynthetic parameters used (Behrenfeld and Falkowski, 1997). The same (temperature sensitive) maximum rates of photosynthesis (P^B_{max}) are used in both model approaches employed here. The parameterization of P^B_{max} used in the models was that used in VGPM and, thus, not based on data collected in the study region. We, therefore, evaluate the global VGPM parameterization against measurements of P^B_{max}-values from the North Atlantic.

The study area is divided into six regions, representing open sea and shelf areas and seasonal PP is analyzed in relation to light, photosynthetic parameters and mixed layer depth. The study suggests that changes in water column stratification characteristics in the sub-polar gyre can be expected to change the seasonal distribution and magnitude of PP here. A reduction of sea-ice along the East Greenland shelf would likely lead to an increase in the PP occurring in that region.

MATERIALS AND METHODS

Calculation of Primary Production

Primary production is calculated from observations of surface fields of chlorophyll, sea surface temperature (SST), photosynthetically active radiation (PAR, i.e., the fraction of incident light between 400–700 nm at the ocean surface) and from climatology of nutrient concentrations in the upper ocean. Two PP-models, VPP and VGPM, are applied in the analysis. In the VGPM-model, PP estimates are based on surface fields and empirical relations of the vertical distribution of chlorophyll a (Behrenfeld and Falkowski, 1997). In the VPP-model (described in section "Modeling PP"), water column PP is estimated based on a calculation of PP in the upper 10 m of the surface layer and empirical relations of the total water column PP determined by the distribution of nutrients in the upper ocean (Richardson and Bendtsen, 2019). On a global scale, the geographical distribution of PP differs significantly between the two models (Richardson and Bendtsen, 2019) and this motivates the use of both models in this study. A comparison is made between the regional PP estimates from the two models and the VPP-model is applied in the subsequent analysis of seasonal PP in the area.

Satellite Observations and Nutricline Climatology

Satellite observations (MODIS data provided by NASA) were obtained from the Ocean Productivity site[1] where global fields ($1/12° \times 1/12°$ spherical grid) averaged for 8 day periods between 2003–2013 are applied as input to the PP-models. Satellite data included fields of SST, PAR, surface chlorophyll a (chl) and the diffuse attenuation coefficient in the 490 nm band. Nutrient concentrations are estimated from the monthly climatology of nitrate in the World Ocean Atlas (Garcia et al., 2010). The nutricline depth (DNO_3) is defined as the depth where the nitrate

[1] www.science.oregonstate.edu/ocean.productivity

concentration is 1 μmol kg^{-1} (found by linear interpolation of the vertical profile of nitrate).

Photosynthetic Parameters

Calculation of PP depends on the photosynthetic parameters P^B_{max} (in VGPM and VPP) and α^B (in VPP), representing the chlorophyll a normalized maximum rate of photosynthesis and the initial slope of the PE-curve [i.e., PP (P) vs. irradiance (E) describing the light-dependent photosynthesis], respectively. The VGPM-model applies a temperature dependent parameterization of P^B_{max} that varies between 1.1 μg C (μg chl h) $^{-1}$ at low temperatures and a maximum value at 20°C of ∼7 μg C (μg chl h) $^{-1}$ (Behrenfeld and Falkowski, 1997). Temperature-dependence represents both the physiological response in phytoplankton to temperature and correlation between temperature and the geographical variation of phytoplankton community composition. A global analysis showed relatively large scatter of P^B_{max} as a function of temperature and also a significant dependence on the characteristic size of the phytoplankton community (Richardson et al., 2016) and nutrient concentration (Richardson and Bendtsen, 2019). However, variation of P^B_{max} is relatively small in cold water (<5°C) where it typically varies between 1–3 μg C (μg chl h) $^{-1}$. We apply the same parameterization for P^B_{max}, suggested by Behrenfeld and Falkowski (1997), in the two models. The influence of P^B_{max} on PP is considered by comparing the applied parameterization with P^B_{max}-values obtained from PP-incubation experiments on water samples from the area. The value of α^B is applied in the VPP-model and it is parameterized in three nutricline depth intervals; (1) DNO_3 < 20 m, (2) 20–90 m and (3) >90 m, as (1) 3.57, (2) 2.68, and (3) 1.59 $\{10^{-2}$ [μg C (μg chl h μE m^{-2} s^{-1}) $^{-1}$]}, respectively (Richardson and Bendtsen, 2019).

Modeling PP

Primary production is calculated from the VGPM-model where it depends on P^B_{max}, surface concentration of chlorophyll a, the daily PAR and the depth of the euphotic zone estimated from the surface concentration of chlorophyll a (Behrenfeld and Falkowski, 1997).

Primary production calculated in the VPP-model assumes that the surface production in the upper 10 m, i.e., the approximate depth range visible from satellites, can be related to the total PP via a relation to D_{NO3} (Richardson and Bendtsen, 2019). PP in the upper 10 m is calculated according to Webb et al. (1974):

$$PP_{10m} = \int_0^{24h} \int_{-10m}^{0} P^B_{\max} chl\,(z) \left(1 - \exp\left(-PAR\,(t, z)\,\frac{\alpha^B}{P^B_{\max}}\right)\right) dzdt \quad (1)$$

where t is time, z is the vertical coordinate, and chl(z) and PAR(t, z) represent the vertical distribution of chlorophyll and PAR, respectively. The vertical distribution of light is considered by calculating the light-attenuation coefficient from the satellite-derived attenuation coefficient at 490 nm, and the temporal variation of PAR is considered by integrating Eq. (1) with a time step of one hour during a 24-hour period. In principle, the integrals in Eq. (1) provide the total PP if the inner integral is integrated to the bottom of the euphotic zone. However, variations in chlorophyll and the photosynthetic parameters are poorly known and cannot be directly inferred from satellite data and, therefore, it only integrates the upper 10 m visible from space.

Richardson and Bendtsen (2019) analyzed global *in situ* PP in the surface layer and showed a significant nutricline depth dependence of PP_{10m} and the total PP; PP_{10m} = γ PP, i.e., γ represents the fraction of total PP occurring in the upper 10 m. The fraction is defined in three nutricline depth intervals: (1) D_{NO3} less than 20 m, γ = 31.0%, (2) between 20 and 90 m, γ = 19.0%, and (3) deeper than 90 m, γ = 10.7%, respectively. This implies, for example, that only 10.7% of total PP takes place in the upper 10 m in oligotrophic areas where the nutricline depth is below 90 m depth, and that PP can be calculated as: PP = PP_{10m}/γ. Correspondingly, in areas with a shallow nutricline (i.e., $D_{NO3} \leq 20$ m), as in the sub-polar region, a total of 31% of the vertically integrated PP is estimated to take place in the upper 10 m.

Measurements of Photosynthetic Parameters

Measurements of P^B_{max} in the study area were obtained from primary production incubation experiments from surface (5 m) water samples collected in August 2006 on the Galathea 3 expedition (on board R/V Vædderen) and from two cruises with R/V Dana in the North Atlantic in August 2008 and September 2012, respectively (Richardson and Bendtsen, 2019). Primary production was measured according to a modified carbon-14 method (Steemann Nielsen, 1952), and photosynthetic parameters were determined by fitting a PP vs. light intensity curve to data (Hilligsøe et al., 2011). Samples were collected south of the GSR along approximately 62.5°N from the East Greenland shelf and into the Iceland basin, and in an area north of the Denmark Strait at ∼67.5°N (**Figure 1**).

Mixed Layer Depth

We calculated mixed layer depth (MLD) from the climatology of de Boyer Montégut et al. (2004). The mixed layer depth was interpolated from the climatological 2° latitude by 2° longitude grid onto the 1/12° x 1/12° degree grid applied by the PP-models and monthly averaged values were calculated for each of the six domains. A comparison of several MLD-climatologies has shown that differences can be large where stratification is weak due to different MLD-detection algorithms and observational data sets (Holte et al., 2017). However, here we only apply the MLD-climatology for comparing the relative seasonal difference between the six areas.

Shelf and Open Sea Areas

Shelf areas in the Arctic are relatively wide and deep, with mean depths of more than 300 m (Paris et al., 2016), and are confined within the shelf break from where a relatively steep slope (∼>3%, e.g., Heezen et al., 1959) leads to the bottom of the ocean basins.

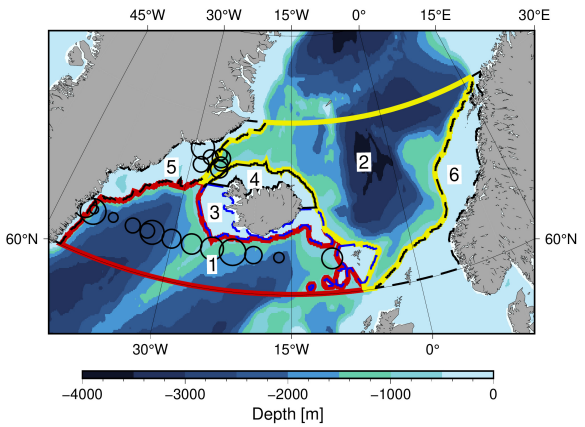


FIGURE 1 | Lambert azimuthal equal-area map of the sub-polar north-eastern North Atlantic with six subdomains between 60–70°N and divided between shelf-areas (depths less than 500 m) and open ocean areas: (1) Sub-polar gyre south of GSR (red), (2) Nordic Seas north of GSR (yellow), (3) Southern open shelf south of Iceland and including shelf and shallow areas around the Faroes (blue dashed), (4) Northern open shelf area north of Iceland (black), (5) Eastern shelf along Greenland (dashed), and (6) Western shelf along Norway (dashed). Circles show location and the relative size of P^B_{max}-values shown in **Figure 7**.

We define the shelf area as being where the bottom depth is less than 500 m, i.e., containing the shallow continental shelf as well as deeper areas within, typically, ∼10 km of the 2–400 m iso-depth.

We consider the sub-polar area between 60–70°N (**Figure 1**), located between Greenland and Norway. We refer to the open sea areas south and north of the GSR and within the latitude limits as the sub-polar gyre and the Nordic Seas, respectively, although they geographically only cover part of these areas. Shelf area is shallower than 500 m, except for two deep (>500 m) and relatively narrow troughs across the East Greenland shelf (∼66°N) which are categorized as shelf areas.

Previous studies have shown that biological production differs in timing between the shelf north and south of Iceland (e.g., Zhai et al., 2012; Friedland et al., 2016), and this motivates the separation of the shelf area north of Iceland as a separate domain. Correspondingly, Friedland et al. (2016) showed that the entire shelf area around the Faroes (located south of Iceland) shares some similarity in terms of frequency and start of the spring bloom with conditions in the Iceland basin. Therefore, this area is considered together with the shelf south of Iceland. The sub-polar north-eastern North Atlantic is thereby divided into six subdomains representing either shelf or open sea areas; (1) Sub-polar Gyre south of GSR, (2) Nordic Seas north of GSR, (3) Southern open shelf south of Iceland and including shelf and shallow areas around the Faroes, (4) Northern open shelf area north of Iceland, (5) Eastern shelf along Greenland, and (6) Western shelf along Norway.

Statistical Tests

Comparison of average values from different domains and the two models are based on Welch modified two-sample *t*-test. Statistical *p*-values are calculated in R (R Core Team, 2021) using the BSDA-package (Arnholt and Evans, 2021) (low *p*-values indicate significantly different mean values). Correlations between time-series from different domains are calculated from Pearson's r (Press et al., 1992).

RESULTS

Annual PP in the Sub-Polar Region

The average global PP estimate in the period 2003–2013 by the VPP-model is 49 Pg C yr^{-1} (**Table 1**). This is comparable to the global PP of 48 Pg C yr^{-1} estimated by the VGPM model ($p < 0.004$). The spatial distribution of the averaged regional PP in the period 2003–2013 is shown in **Figure 2**. The largest annual PP (0.5–1 g C m^{-2} d^{-1}) is located in a belt around the GSR from Iceland toward the Faroes and along the Norwegian coast (**Figure 2A**). Slightly lower values (0.3–0.5 g C m^{-2} d^{-1}) characterize the southern part of the sub-polar subdomain in the Irminger Sea and parts of the Iceland basin. Similar values are found north of the GSR in the Nordic Seas with a gradual decrease toward the shelf along east Greenland. The associated standard deviations show that the largest variability of the annual PP (± 0.3–0.5 g C m^{-2} d^{-1}) is seen above the shelf south of Iceland and in the southern part of the Norwegian shelf (**Figure 2B**). However, relatively large variability (± 0.2–0.3 g C m^{-2} d^{-1}) is also seen north and south of the Faroe Islands and above the Reykjanes ridge (the Reykjanes ridge is shown in **Figure 1** as the shallow area directly southwest of Iceland).

The corresponding PP estimated by the VGPM-model shows a similar distribution in the study area. The ratio of the VPP and the VGPM-estimates indicates higher PP estimated by the VPP-model along the GSR and south of the Faroes, whereas there is a tendency toward a lower production in the southern part of the sub-polar domain and northern part of the Nordic Seas, respectively (**Figure 2C**). The difference between the two estimates is, however, relatively small and VGPM-values averaged in the six areas (not shown) is only 1–12% lower than in the VPP-model (differences are only significant in area 3, 4, and 6 where $p < 0.05$). In total, the study area in the sub-polar region covers an area of $2.4{\cdot}10^{12}$ m^2 and accounts for an annual averaged PP of 0.46 Pg C yr^{-1}, i.e., an average production of 0.53 g C m^{-2} d^{-1} (**Table 1**).

PP Above Shelves vs. Open Ocean

Shelf areas, i.e., domains 3–6, cover a total area of $0.70{\cdot}10^{12}$ m^2, corresponding to 29% of the area in the study region (domains 1–6). The corresponding PP above the shelves accounts for 0.15 Pg C yr^{-1}, or 32% of PP in the area (**Table 1**). Thus, the area-normalized PP from shelf areas, in general, approximately corresponds to the average PP in the area. However, PP above the shelves spans a relatively large interval from the low values along east Greenland of 0.19 g C m^{-2} d^{-1} to the highest value along the Norwegian coast of 0.77 g C m^{-2} d^{-1}. The annual average PP above the southern shelves in the sub-polar gyre of 0.72 g C m^{-2} d^{-1} was higher than that estimated for the surrounding open sea ($p <$ 1e-6). Similarly, production along the shelves north of Iceland and along the Norwegian coast was

TABLE 1 | Annual average PP calculated by the VPP-model, for the period 2003–2013, for the global domain (domain no. 0) and for the six subdomains in the northern North Atlantic (domain 1–6).

Domain	Area	VPP	VPP	VPP(spring)	$\frac{\text{VPP(spring)}}{\text{VPP}}$
No.	10^{12} m^2	Pg C yr^{-1}	g C m^2 d^{-1}	Pg C yr^{-1}	%
0 (global)	361.9	49.1 ± 1.1	0.37 ± 0.01	–	–
1 (Sub-polar gyre)	0.747	0.15 ± 0.02	0.53 ± 0.06	0.031 ± 0.004	21
2 (Nordic Seas)	0.930	0.16 ± 0.02	0.47 ± 0.05	0.042 ± 0.007	26
3 (Southern shelves)	0.167	0.044 ± 0.003	0.72 ± 0.05	0.010 ± 0.001	22
4 (Shelf north of Iceland)	0.082	0.016 ± 0.002	0.55 ± 0.06	0.004 ± 0.001	27
5 (Shelf along East Greenland)	0.186	0.013 ± 0.003	0.19 ± 0.04	0.002 ± 0.001	12
6 (Shelf along Norway)	0.262	0.074 ± 0.008	0.77 ± 0.08	0.025 ± 0.003	34

Values of the areas in each domain, the total VPP, the corresponding VPP per area, the VPP(spring), i.e., PP from 1st of January to 1st of June, and the ratio between PP(spring) and the annual PP (values shown with standard deviations).

higher than in the Nordic Seas ($p < 0.004$). Thus, shelf PP is greater than in the ambient open sea in the region, except for the shelf along East Greenland.

Contribution of Spring PP to Annual PP

Dramatic peaks in chlorophyll concentration are commonly observed in surface waters during spring in temperate regions (e.g., Henson et al., 2009) and these "blooms" are often assumed to constitute an important signal in the annual PP cycle. As the timing of these blooms differs inter-annually, we examine the contribution of PP over the first 5 months of the year to total annual PP. If the spring bloom makes a disproportionally large contribution to annual PP, we would expect to find a disproportionally large PP during these months. Thus, we estimate "spring" PP by estimating total PP from 1 January – 1 June and by comparing PP during this five-month period to the annual PP, i.e., VPP(spring)/VPP (**Table 1**).

Primary production during the first 5 months of the year contributes with between 12 and 34% of the annual PP in the six domains. The largest contribution of this spring to total PP is seen along the Norwegian shelf, despite the fact that a significant fraction of this shelf area is located at high latitudes (**Table 1**). It is noteworthy that PP during the first 5 months of the year contributes a smaller fraction of the annual PP in the sub-polar gyre south of the GSR (21%) than it does in the Nordic Seas (26%, $p < 0.02$).

Differences in PP could arise from different light conditions between the northern and southern parts of the study area. The accumulated insolation (at the top of the atmosphere) from 1 January–1 June at 70°N [corresponding to an average flux of ∼168 W m^{-2} during the 5 month period, calculated from a global insolation climatology (Hartmann, 1994)] is about 22% less than insolation at 60°N (∼217 W m^{-2}). The fractions of insolation occurring during the 5 month period compared to the annual insolation are 36 and 38% at the two latitudes, respectively. Thus, despite open sea areas north of the GSR receiving relatively less insolation during the spring period, they have a higher percentage of total annual PP occurring during the spring than in the open sea area south of the GSR. The average spring PP per unit area of 0.29 g C m^{-2} in the Nordic Seas is also slightly (not significantly) larger than in the sub-polar gyre (0.27 g C m^{-2} d^{-1}). Together, these results suggest that open sea spring PP south of the GSR is more limited by factors other than light, e.g., mixed layer depth, nutrients or grazing, than is the case north of the GSR.

A similar pattern is noted with respect to shelf sea areas as PP during the first 5 months of the year over the open shelf south of the GSR contributes less (22%) to the annual PP than the open shelf north of the GSR (27%, $p < 0.02$) (**Table 1**). The shelf along east Greenland shows the lowest spring contribution (12%) to annual PP. This can partly be explained by the extensive sea ice cover until early summer along the northern part of the shelf. Relatively high spring production along the ice-free Norwegian shelf contributes with about a third of the annual production (34%). Thus, this domain experiences a significantly more productive spring period than is seen along East Greenland at the western boundary of the basin.

Inter-Annual Variability

Inter-annual variability of PP in the sub-polar area is clearly seen by comparing peak values of PP during the 2003–2013 period, e.g., variations between 2.3–3.1 g C m^{-2} d^{-1} at the southern open shelf or 0.5–1.1 g C m^{-2} d^{-1} along East Greenland (**Figure 3**). Time series from the different subdomains also show that the timing of the initial peak in PP varies significantly from year to year, and that some years are characterized by a relatively strong spring bloom PP signal which is not present in other years. For example, production in 2005 over the northern open shelf shows peak values above 2.8 g C m^{-2} d^{-1} whereas PP in 2007 remains below 1.6 g C m^{-2} d^{-1}. There is also a large inter-annual variation in the structure of the seasonal PP. Some years are characterized by a single peak of PP during spring or summer and a modest production the rest of the growth season, e.g., the sub-polar gyre in 2007, while other years are characterized by an initial bloom followed by a bloom later in the season, e.g., the southern open shelf in 2009 or the Norwegian shelf in 2011. Comparison of PP above the Norwegian shelf and along East Greenland shows how sea ice delays production but also that PP is significantly lower along east Greenland than elsewhere in the sub-polar area.

Seasonal PP

The largest monthly averaged PP between 2003–2013 takes place above the southern open shelf in July and about a month

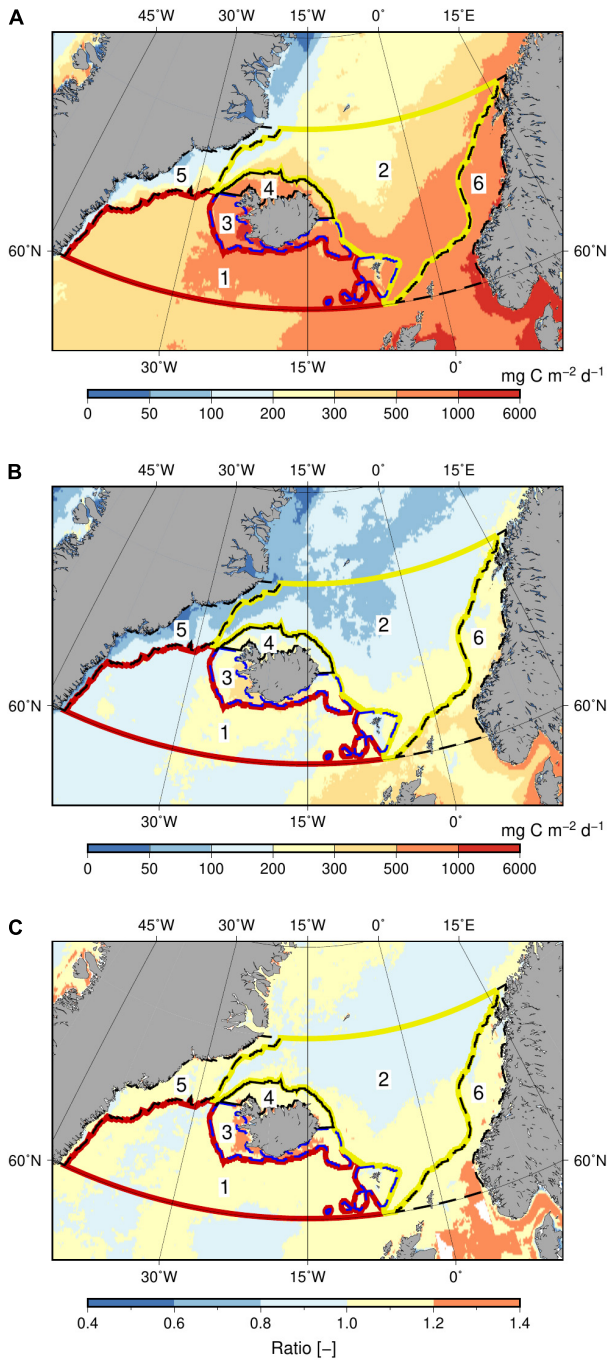


FIGURE 2 | (A) Annually averaged PP in the period 2003–2013 calculated by the VPP-model and **(B)** the associated standard deviation. **(C)** The ratio of PP calculated by the VPP- and the VGPM-model, i.e., VPP/VGPM. The six subdomains are shown.

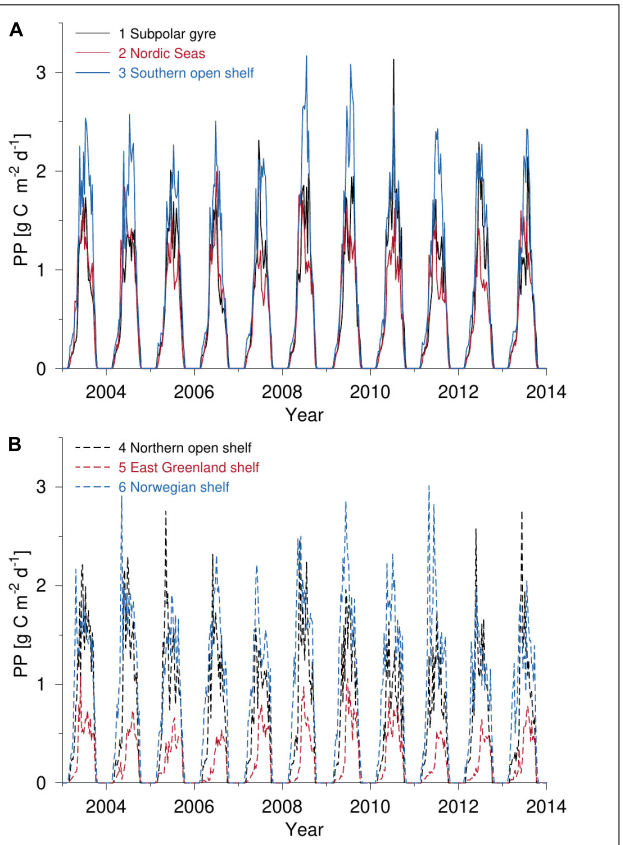


FIGURE 3 | PP calculated by the VPP-model during the 2003–2013 period for **(A)** subdomains 1–3 and **(B)** 4–6.

later than maximum insolation occurs (**Figure 4**). Production above the Norwegian shelf shows similarly high values but also a longer growth season extending from March to September and more closely following the seasonal change in insolation. This may explain the slightly (not significant) higher annual PP above the Norwegian shelf than for the southern open shelf (0.77 and 0.72 g C m^{-2} d^{-1} for the Norwegian and southern open shelves, respectively: **Table 1**). The East Greenland shelf shows an asymmetric seasonal PP distribution pattern with a maximum in July and relatively low area-averaged production. The Nordic Seas, the northern open shelf and the sub-polar gyre all exhibit maximum PP during June, i.e., coincident with maximum insolation. The largest increase in PP is seen in the Nordic Seas and the northern open shelf during April and May, whereas a longer and steady increase characterizes the sub-polar gyre between April and June.

The seasonal evolution of PP estimated by the VGPM model (**Figure 4**) shows qualitatively similar results as the VPP-model (not shown). The largest difference is between the peak July value above the Southern open shelf where the VPP estimates 2.18 g C m^{-2} d^{-1} as opposed to 1.84 g C m^{-2} d^{-1} in the VGPM-model, corresponding to a difference of 16%. Otherwise, the models yield similar results and show only minor differences in the seasonal dynamics, i.e., similar shape and timing of peak PP values. In addition, the absolute values of the monthly averages for the 11-year period are in good accordance. In general, the VPP model PP estimate is 5–15% higher than the VGPM model in the period from April-September.

Seasonal PAR and Chlorophyll

Seasonal PAR in the six areas is mainly driven by the latitudinal distribution between 60–70°N where, for example, the sub-polar gyre receives ∼10% more light than the Nordic Seas from May to July due to its being located at lower latitudes (**Figure 5A**). However, there are some significant differences among the shelf areas. Surface water above the east Greenland shelf is largely covered by sea ice in early spring. Monthly averaged ice cover is about 70% until May, decreasing to 53% in June and the sea ice minimum is first achieved in August (ice cover < 5%). This results in very low area-averaged PAR being received by the East Greenland shelf water in spring and until June and explains the low area-averaged PP in this area (**Figure 4B**). Another difference, which cannot be explained by latitude, is seen between the slightly lower PAR received in the sub-polar gyre than above the Norwegian shelf during spring and summer. Although most of the Norwegian shelf is located at higher latitudes than the sub-polar gyre, the tendency of less cloudiness during spring and summer above the Norwegian shelf results in a more illuminated environment.

The seasonal distribution of chlorophyll in the sub-polar gyre and in the Nordic Seas (**Figure 5C**) resembles the seasonal PP-distribution (**Figure 4**), with a tendency for slightly higher chlorophyll concentrations during spring in the Nordic Seas, which is also reflected in the spring PP-distributions here. Chlorophyll concentrations above the southern open shelf achieve a relatively large maximum in July and this explains the resultant large PP in this area. Low area-averaged chlorophyll values above the east Greenland shelf, due to the large extent of sea ice cover, are also in accordance with the low seasonal PP here. However, the chlorophyll distributions over the Norwegian shelf and in the northern open sea shelf are significantly different from their seasonal PP-distributions, where monthly averaged chlorophyll shows a relatively large spring peak in the two areas (**Figure 5C**) while the PP distribution only shows a gradual increase during spring and early summer (**Figure 4B**). This implies that other factors than chlorophyll concentration are important for explaining the estimated PP in these two areas.

Photosynthetic Parameters and Sea Surface Temperature

In addition to light and chlorophyll concentration, PP depends on the photosynthetic parameters P^B_{max} and α^B (i.e., dependent upon D_{NO3} in the VPP-model). Both the VPP and VGPM models apply the SST-dependent parameterization of P^B_{max} developed by Behrenfeld and Falkowski (1997), and the relatively large SST increase during summer in the six areas (**Figure 5B**) thus implies a corresponding increase in P^B_{max} (**Figure 5D**). The large SST increase above the Norwegian shelf from 5.9°C in March to 13.0°C in August results in a corresponding increase of P^B_{max} from 3.0 to 4.9 μg C (μg chl h) $^{-1}$, i.e., an increase of more than 60%. This implies a correspondingly higher estimate of PP during summer in both models. The onset of the seasonal thermocline is seen to have a similar significant impact where P^B_{max} increases accordingly in all six areas.

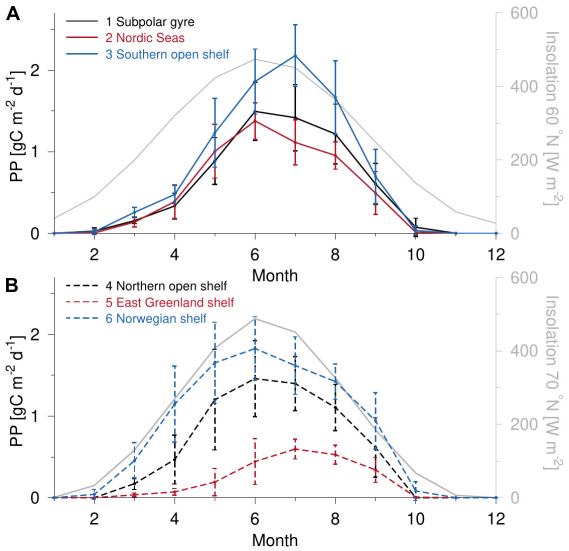


FIGURE 4 | Monthly averaged PP during the 2003–2013 period for **(A)** subdomain 1–3 and **(B)** 4–6 (average values with shown standard deviation). Monthly averaged insolation at the top of the atmosphere is shown for **(A)** 60°N and **(B)** 70°N (gray, right axis).

The SST-dependent parameterization of P^B_{max} was assessed by comparing directly with measurements from the study area (**Figure 6** and **Supplementary Material**). The applied parameterization of P^B_{max} increased from 1.3 to 5 μg C (μg chl h)$^{-1}$ in the SST range between 0 and 13°C whereas measurements showed a more narrow range of 1.2–3.6 μg C (μg chl h)$^{-1}$ and there was no significant increase with temperature (**Figure 6**, dashed line and bullets, respectively). The average value of the measured P^B_{max}-values was 2.4 ± 0.7 μg C (μg chl h)$^{-1}$ (n = 21).

Spatial Correlation of PP

The annual production shows the largest PP above shelf areas, except for the east Greenland shelf. Interaction between shelf and open sea areas was therefore investigated by analyzing the correlation of PP during the growth season from the six domains during the 11-year period (**Table 2**, n = 294–327 for each of the six areas). In general, PP between all the areas is closely correlated because of the PP relationship to seasonal insolation. However, the largest correlation is seen between the sub-polar gyre and the open southern shelf, and between the Nordic Seas and the Norwegian shelf (Pearson's r of 0.91 and 0.88, respectively). This indicates that PP in the sub-polar area is more related to latitude or water masses than to bathymetry. This is also in accordance with conditions at the northern open shelf where the largest, although somehow lower (r = 0.82), correlation is with the Nordic Seas. The east Greenland shelf shows only a relatively weak correlation to the other domains, and the highest correlation is with the open southern shelf and the sub-polar gyre (r = 0.79 and 0.77, respectively) indicating that the correlation is mainly driven by ice-free conditions during spring and early summer in the southern part of this domain.

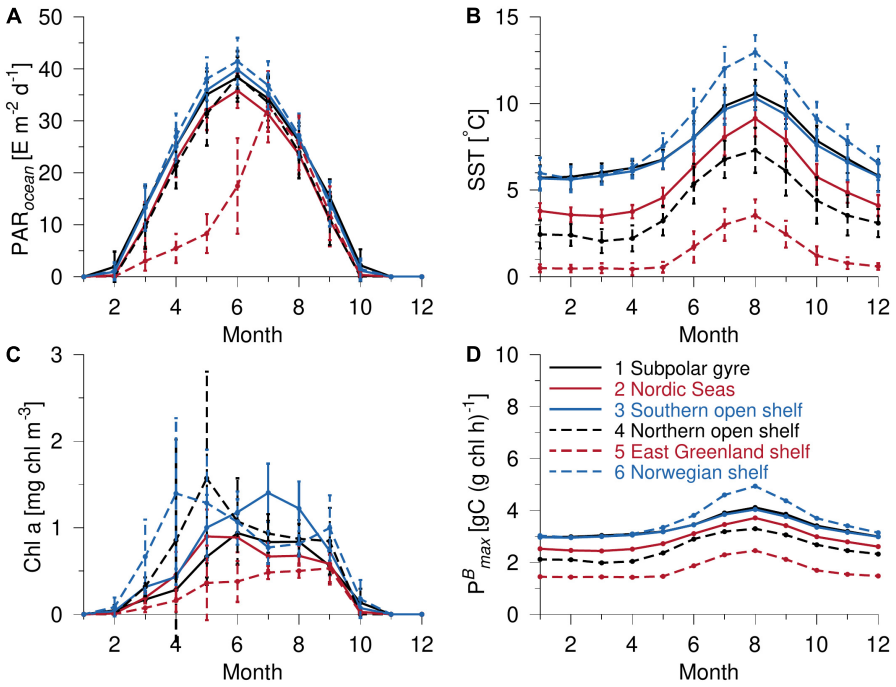


FIGURE 5 | Monthly averaged values (with standard deviation) for the six subdomains in the 2003–2013 period for **(A)** PAR, **(B)** SST, **(C)** chlorophyll a, and **(D)** P^{B}_{max}.

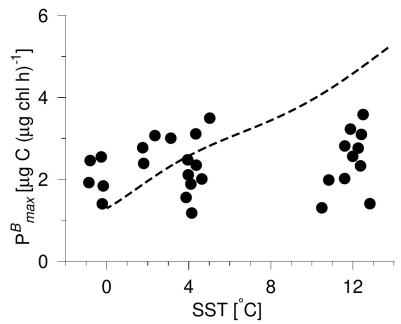


FIGURE 6 | Calculated P^{B}_{max} from incubation experiments versus SST (bullets, water samples are from the surface (5 m) and locations are shown in **Figure 1**), and the applied parameterization of P^{B}_{max} in the VPP and VGPM-models (dashed line).

Light Limitation and PP

The relative influence of light limitation in the six domains was analyzed (**Figure 7**) from the accumulated (acc) monthly (i = 1–12) area-averaged values of PAR_{acc} (µE m^{-2}) and PP_{acc} (g C m^{-2}), respectively, e.g., calculation of PP_{acc} becomes:

$$PP_{acc}(i) = \sum_{m=1}^{i} PP(m)\,\Delta t(m) \quad (2)$$

where PP(m) and Δt(m) are the monthly averaged PP (g C m^{-2} d^{-1}) and the time (number of days) in each month, respectively. The accumulated PP and PAR for each month are normalized with the accumulated annual PP (PP_{ann}, i = 12) and PAR, respectively, i.e., $PP_{acc}(i)/PP_{ann}$ and $PAR_{acc}(i)/PAR_{ann}$. The relationship between these two ratios shows the relative response of accumulated PP to the accumulated PAR. For example, if the accumulated PP is 50% when the area has received 50% of the annual PAR, then phytoplankton is equally effective in using light for PP before and after the time when half of the annual PAR has reached the water surface. Analyzing accumulated PP in relation to the accumulated PAR also considers asymmetries between areas due to sea ice cover or seasonal variability in cloudiness, e.g., the accumulated PP in ice-covered regions can be related to the received accumulated PAR in the water rather than insolation above the (ice-covered) surface.

The relative largest impact from light on PP is seen above the east Greenland shelf where ∼50% of the annual PP is produced when the area has received ∼50% of the annual PAR (**Figure 7**). Thus, while the area receives a relatively small amount

TABLE 2 | Correlation matrix (Pearson's r) between PP in the six subdomains and for the period 2003–2013 (*n* = 294–327, all are significant).

Domain no.	2	3	4	5	6
1	0.82	0.91*	0.67	0.77	0.71
2		0.86	0.82*	0.66	0.88*
3			0.78	0.79*	0.75
4				0.56	0.64
5					0.55

The largest correlation for each subdomain is indicated with an asterisk.

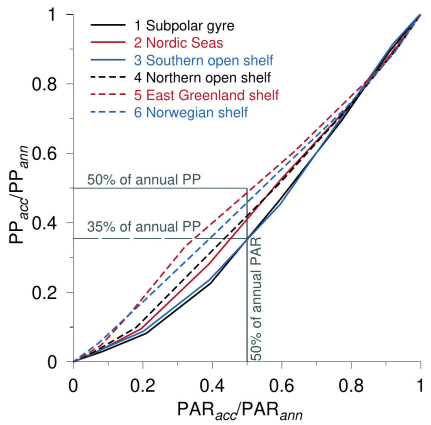


FIGURE 7 | The ratio of monthly accumulated PP (PP$_{acc}$) and the annual PP (PP$_{ann}$) vs. the corresponding ratio of PAR, i.e., PAR$_{acc}$/PAR$_{ann}$ for the six subdomains. Gray lines indicate the 50% level of the annual PP and PAR and the 35% PP-level is shown with a dashed gray line.

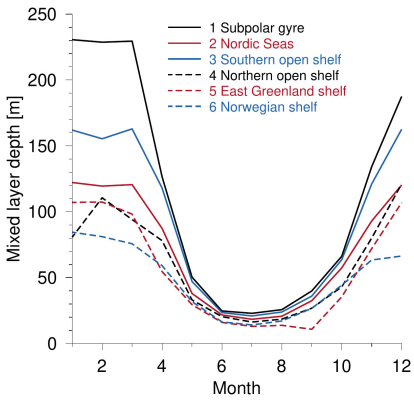


FIGURE 8 | Mixed layer depth in the six domains.

of insolation during the season due to sea ice cover and the high latitudes, phytoplankton efficiently utilize light when it becomes available. Production above the Norwegian shelf is seen to be almost as efficient in terms of light usage. In general, photosynthesis in areas north of the GSR is significantly more effective in using light early in the season than areas south of the GSR, i.e., the sub-polar gyre and the Southern open shelf have only produced ∼35% of the annual production when the areas have received ∼50% of the annual PAR. Thus, phytoplankton in these domains have a relatively less efficient use of light during spring than later in the year.

Seasonal MLD

The deepest mixed layers in the study area are located south of the GSR where MLD in the sub-polar gyre and the southern open shelf area reaches 230 and 160 m during winter, respectively, whereas MLDs were less than 125 m for the other domains (**Figure 8**). Thus, the sub-polar gyre and the southern open shelf have relatively deep mixed layers in the start of spring, and it remains deeper in these domains with respect to the other areas during the rest of the year. MLD from June to August is less than 25 m in the entire study area and, from September, MLD increases in all areas.

DISCUSSION

The results presented here demonstrate differences in the seasonal distribution of PP in the sub-polar gyre and surrounding waters. PP peaks in all regions during summer. When data for the 11-year study period are averaged, the PP occurring during the first 5 months of the year does not make a disproportionally large contribution to annual PP in any of the regions. This suggests that spring blooms do not consistently constitute a significant signal in the annual PP occurring in this region. In the sub-polar gyre and southern open ocean (domains 1 and 3), phytoplankton appear to use available light less efficiently during the spring period than in the more northerly domains.

PP in the Northern North Atlantic

Both total PP per unit area and its seasonal distribution patterns are shown to differ in the different sub-polar water masses studied here. Results from the VPP-model are compared with estimates from the VGPM-model which has been applied in previous model-intercomparison studies (e.g., Carr et al., 2006). Estimates from the two PP-models show a similar pattern with elevated annual PP along the GSR and the Norwegian shelf and low values above the East Greenland shelf. The models employed differ mainly in the treatment of light in the upper ocean and, for the VPP-model, a dependence on nutricline depth. However, nutricline depth levels in this region are generally shallow during the growth season, i.e., less than 20 m (except for a narrow band along the Norwegian coast from July–September where $D_{NO3} < 30$ m). Thus, the nutricline-dependence of photosynthetic parameters in the VPP-model does not contribute significantly to the spatial variability.

The total annual PP in the northern North Atlantic between 60 – 70°N is estimated to 0.46 Pg C yr^{-1}. Although this value is only about 1% of total global annual production (∼49 Pg C yr^{-1}), the area-averaged sub-polar PP of 0.53 g C m^{-2} d^{-1} is ∼42% larger than the global averaged value (0.37 g C m^{-2} d^{-1}). In addition to supplying ecosystems with energy in the form of organic carbon, PP also impacts the ocean carbon uptake. Several studies from individual years and smaller geographical areas have indicated that a peak in PP associated with a spring bloom appears as a dominant signal in the PP pattern (e.g., Zhai et al., 2012). In this study, however, where data (**Figure 3**) are averaged over the 11-year study period, it is shown that the PP occurring in the first 5 months of the year does not make a disproportionally large contribution to annual PP. Thus, spring blooms do not appear to be contributing with a dominant signal in the annual PP patterns in any of the six domains. The parameterized temperature dependence of P^B_{max} would tend to increase PP when SST increases (**Figure 5D**), thereby causing an increase of PP during the warmest period. We argue, however,

that the seasonal PP pattern found here is not a model artifact caused by the temperature dependence of P^B_{max}, as chlorophyll distributions also tend to peak during summer. In addition, we note that a similar seasonal pattern was reported based on PP estimates made from empirical data collected in the coastal waters around Denmark (Lyngsgaard et al., 2017).

Comparison With Measurements

Nevertheless, we compared the P^B_{max} values generated and applied in the models with measured P^B_{max}-values from the area. No significant dependence of P^B_{max} on SST was found for the *in situ* measurements, suggesting that the applied parameterization of P^B_{max} may overestimate PP during the warmest period (**Figure 6**). The parameterized P^B_{max} of 5 μg C (μg chl h) $^{-1}$ at an SST of 13°C is about a factor of two larger than the average value of measured P^B_{max}-values from the area. This implies that the absolute magnitude of PP estimated during summer may be higher than the actual, but it would not change the general shape of the seasonal distribution PP curve generated. Applying a smaller value during the warmest period would tend to increase the relative contribution of estimated PP during spring and, therefore, the estimated ∼25% of the annual PP occurring in the five-month period from 1 January to 1 June may be a low estimate. The spatial and temporal distributions of photosynthetic parameters, i.e., P^B_{max}, are therefore critical aspects to consider when the seasonal PP are evaluated from various PP-models covering the sub-polar region.

Comparison of PP estimated from the VPP-model and values obtained from measurements generally show good accordance in the six domains. Astthorsson et al. (2007) found that the annual PP above the southern open shelf (∼200–300 g C m^{-2} yr^{-1}) was significantly higher than at the shelf north of Iceland (100–200 g C m^{-2} yr^{-1}). This agrees well with the model estimates of the spatial gradients and the annual PP (263 ± 18 and 201 ± 18 g C m^{-2} yr^{-1} for the two areas, respectively: **Table 1**). Relatively high PP estimates (201 g C m^{-2} yr^{-1}, Debes et al., 2008) have also been reported over the shelf around the Faroe Islands. These estimates from the southern and northern open shelf areas are in general accordance with the VPP-estimates. Sanders et al. (2005) estimated the annual new production, i.e., that based on exogenous nutrient input (Dugdale and Goering, 1967), in the Irminger basin located between Greenland and Iceland (in the sub-polar domain) as 36 g C m^{-2} yr^{-1} based on nutrient measurements and satellite data. Similarly, Henson et al. (2006) estimated new production to 60 g C m^{-2} yr^{-1} based on satellite derived silicate distributions. New production is only a fraction of PP and is, thus, a lower bound of PP, and these estimates of new production are also significantly lower than our estimates of PP (100–200 g C m^{-2} yr^{-1}) in the Irminger Sea.

Harrison et al. (2013) estimated PP in the Norwegian Sea, located between the Norwegian shelf and the Greenland Sea, to be 80–120 g C m^{-2} yr^{-1}. This is in general agreement with our estimates of between 100–200 g C m^{-2} yr^{-1} for the area (**Figure 2A**). Zhai et al. (2012) analyzed the annual PP at six locations around Iceland by using satellite data and a vertically resolved model for calculating PP, and comparison with *in situ* measurements indicated that their estimated PP from remotely sensed data were 50% too high. Their estimates of annual PP on the shelves north and south of Iceland showed a similar tendency to a higher production south of Iceland and their values were ∼25% larger for these locations than the corresponding estimates from the VPP-model (**Table 1**). Similarly, their locations in the Icelandic basin and Nordic Seas were in general agreement and ∼25% larger than the VPP-model.

Thus, the simple approach behind the VPP- and VGPM-models, where surface fields of chlorophyll a are the major factor for estimating PP, may represent the general distribution of PP but also lead to significant model-bias when compared to *in situ* measurements [see for example discussion in: Carr et al. (2006); Henson et al. (2006); Richardson et al. (2016)]. Local effects, not included in the models, may be important for PP. For example, the VPP-model considers the depth of the nutricline based on nitrate distributions, which has been shown to determine the fraction of PP occurring below the surface layer in large areas of the ocean (Richardson and Bendtsen, 2019). However, other nutrients are known to be important in the sub-polar area, e.g., silicate (Hátún et al., 2017) and iron (Nielsdóttir et al., 2009), and such limitations are not included in the PP-models used here.

Limitations due to local effects and the simple parameterizations of photosynthetic parameters will impact the absolute values of PP and also the seasonal variation in PP. However, the PP-models used here are mainly driven by the distribution of chlorophyll, and because the mixed layer depth (**Figure 8**) and nutricline depth are relatively shallow during the growth season in the sub-polar area, a significant fraction of total PP is estimated to take place in the upper 10 m. This is within the depth range where chlorophyll can be observed by satellites. Thus, we argue that the differences between the relative distributions found for the six domains are real, and that the different PP-levels between areas north and south of the GSR as well as between shelves and open sea areas reflect the spatial and temporal response of PP to the varying light and nutrient conditions in the sub-polar region.

Production Above Shelf Areas

On average, the shelf region in our study area contributes with a similar amount of PP per unit area as to the annual areal PP in the ambient open sea areas. However, the annual PP above the shelves spans a large interval with the least productive area being found above the east Greenland shelf (0.19 g C m^{-2} d^{-1}) and the most productive above the Norwegian shelf (0.77 g C m^{-2} d^{-1}). Thus, with the exception of the east Greenland shelf, the shelves are characterized by having the greatest area-averaged PP in the study area (**Table 1**). PP above these shelf areas is also characterized by relatively high PP and chlorophyll levels during spring (above the open northern shelf and the Norwegian shelf) and summer (the southern open shelf) where PP can reach values more than 50% higher than those occurring in the ambient open sea (**Figure 3**). Shelf areas are also characterized by a relatively large inter-annual variability where seasonal amplitudes can vary by more than 50% (e.g., large difference above the Norwegian shelf during spring between 2004 and 2005).

Correlation analysis of the 11-year time series of PP between the six areas shows that the greatest correlation is between

neighboring areas. Thus, production above the shelf areas is more closely related to the neighboring open sea areas than other shelf areas in the northern North Atlantic. This indicates that water masses are more important for the seasonal distribution of PP than processes related to differences between shelf-open sea dynamics, e.g., mixing processes. However, shelf areas are characterized by significantly larger PP than the ambient open sea area, e.g., the annual area-averaged PP above the southern open shelf (0.72 g C m^{-2} d^{-1}) is 36% larger than in the sub-polar gyre.

Sub-Polar North-South Gradients in PP

When sub-polar areas have received 50% of the annual insolation in June, the east Greenland and Norwegian shelves and the open sea and shelf area north of GSR have produced 40–50% of their annual PP. The phytoplankton in these domains use light efficiently for photosynthesis during spring and early summer, whereas the sub-polar gyre and the southern open shelf only have produced about 35% of the annual PP in June (**Figure 7**). This implies that ∼65% of the annual PP takes place in the remaining part of the growth season where the area only receives 50% of the annual light. Thus, light harvesting by phytoplankton in the southern areas appears to be more efficient late in the summer season than during the spring. Although shelf production above the southern shelf is significantly greater than in the sub-polar gyre (**Table 1**), the similar low efficiency in light harvesting and the close correlation of PP between these areas indicate common limiting factors during spring and early summer.

The seasonal PP was analyzed at six locations around Iceland by Zhai et al. (2012) and they explained the later onset of PP south of Iceland as being due to a deeper mixed layer in spring and early summer. According to Sverdrup's critical depth hypothesis (Sverdrup, 1953), a net growth of phytoplankton biomass can first occur when the vertically integrated (light-limited) PP exceeds the respiratory losses in the mixed layer. Thus, a decreased MLD tends to increase PP because more biomass is in a more illuminated environment. We, therefore, analyzed the potential impact of MLD on PP in our study area by calculating the seasonal evolution of MLD in the six domains.

The deepest mixed layers in the study area are located south of the GSR where MLD in the sub-polar gyre and the southern shelf reaches 230 and 160 m during winter, respectively. MLDs were less than 140 m for the other domains (**Figure 8**). The sub-polar gyre and the southern open shelf have relatively deep mixed layers at the start of spring, and they remain deeper than MLDs in the other domains during the rest of the year. The relatively inefficient use of light in the sub-polar gyre and the open southern shelf during spring, manifested as a weak slope of the corresponding normalized PP-curves vs. light until June in **Figure 7**, occurs therefore at a time when these domains are characterized by a relatively deep mixed layer. The relatively deep MLD south of the GSR in spring may, therefore, explain the apparent reduced efficiency of light in PP here than in the other domains examined.

Analysis of bloom frequency and start days of blooms in the northern North Atlantic shows that blooms are more frequent in areas north of Iceland and that they, in general, start earlier in the season (Friedland et al., 2016), e.g., spring blooms are frequently seen from late April-May on the shelf north of Iceland whereas the less frequent blooms on the shelf south of Iceland typically start in May-June. This pattern is consistent with the spring peak seen in the seasonal chlorophyll distribution at the northern open shelf area and to a lesser extent in the Nordic Sea domain (**Figure 5C**).

Primary production over the shelf north of Iceland has been shown to correlate with salinity, i.e., PP tends to increase when saline Atlantic water is present (Astthorsson et al., 2007). Variability in water masses and winter convection and the extent of the sub-polar gyre south of Iceland have similarly been shown to explain productivity, biomass and nutrient distributions in the eastern sub-polar gyre (Hátún et al., 2016). Thus, PP in the sub-polar area is impacted by regional scale variability of water mass distributions and their influence on temperature, stratification and nutrients. In addition to the presence of macronutrients, the relatively low concentration of iron in the sub-polar gyre (Nielsdóttir et al., 2009) has been suggested to explain reduced photosynthetic efficiency during the growth season (Ryan-Keogh et al., 2013). The VPP-model only considers nitrate as a limiting nutrient, and nitrate only has a minor influence on the PP-estimates in the study area, so the influence from silicate (Hátún et al., 2017), iron or other limiting substances is not taken into account. In summary, several factors, in addition to MLD, may impact the seasonal PP and explain the seasonal difference in PP between areas on either side of the GSR.

Climate Change and Sub-Polar PP

The sub-polar North Atlantic plays a key role in the climate system where warm and saline subtropical water in the North Atlantic Current is transported into the area and continues toward the Nordic Seas or recirculates and mixes with upper water masses in the sub-polar gyre. This regional circulation constitutes the northern part of the Atlantic Meridional Overturning Circulation (AMOC) and, although transports in the sub-polar gyre and in the North Atlantic Current are not directly coupled (Lozier et al., 2010), they both have a major impact on transport of heat, salt and nutrients. Variability in circulation regimes of the sub-polar gyre therefore directly impacts nutrient concentrations and, thereby, productivity and ecosystem processes in the region (e.g., Hátún et al., 2016, 2017). Thus, large scale changes in circulation patterns in the North Atlantic are expected to impact PP in the sub-polar region. Circulation changes may also affect the relatively strong sink of atmospheric CO_2 in the sub-polar area (Takahashi et al., 2009). Biological production causes a significant drawdown of surface pCO_2 during the growth season and thereby enhances ocean carbon uptake in the area (Takahashi et al., 2002). Thus, feedback between PP and ocean carbon uptake may, in turn, affect global greenhouse gas concentrations.

The combined effect from these physical and biogeochemical changes on PP in the sub-polar area has been simulated in global circulation models. Kwiatkowski et al. (2020) analyzed a multi-model ensemble of Earth System Model (ESM) simulations under CMIP6 and found that PP on a global scale decreased between

0.6 ± 2.5% and 3 ± 9% by year 2100 in two climate change scenarios (a low-emission SSP1-2.6, and a high-emission scenario SSP5-8.5). Changes in PP were characterized by large regional variability and the response of PP in the sub-polar area was found to differ across the GSR. In SSP5-8.5, a relatively large warming of more than 5°C was found for the Arctic by year 2100, and a significant decrease in winter mixed layer depth of more than 60 m was seen in the sub-polar gyre south of the GSR. Areas north of the GSR showed both a decrease and an increase in MLD, partly due to changes in sea ice cover. The largest change in PP was seen in the sub-polar gyre south of the GSR where PP decreased by up to 20–40 g C m^{-2} yr^{-1} (0.05–0.1 g C m^{-2} d^{-1}), corresponding to a reduction of 10–20% of the PP estimated by the VPP-model for the area (**Table 1**). PP increased north of the GSR, partly due to a decrease in sea ice extent.

A decrease in sub-polar productivity in the ESM-simulations is not in accordance with the less efficient light usage of photosynthesis found here for the area south of the GSR (**Figure 7**). A relatively deep MLD in early spring could explain the relatively low PP during spring and early summer south of the GSR whereas areas north of the GSR were up to 15% more efficient in using light early in the season. Thus, a significant decrease in MLD in this region would likely change the seasonal distribution of PP. A change in PP would require a change in nutrient delivery to surface waters in the region. However, a shallower MLD would increase both the length of time in the productive period when phytoplankton in surface waters are nutrient depleted and also the length of time that nutrients will be regenerated in the surface waters. Thus, we would expect that a shallower MLD would lead to an increase in total PP and not the significant decrease predicted by the multi-model ESM study. This discrepancy between ESM-results and the regional VPP-analysis presented in this study may be explained by other factors included in the ESM-models, i.e., changes in nutrients or grazing. However, the importance of these processes for the PP in the sub-polar area is not well understood and requires further studies.

CONCLUSION

Primary production (PP) between 60 – 70°N in the northern North Atlantic (between Greenland and Norway) was analyzed in two PP-models driven by satellite data and nutrient climatology. The two models (VGPM and VPP) showed consistent results when describing annual PP as well as the seasonal distribution of PP. Analysis by the VPP-model resulted in an annual total PP in the area of 0.46 Pg C yr^{-1}, corresponding to about 1% of the global PP. The averaged areal PP of 0.53 g C yr^{-1} was 43% higher than the global average.

Primary production was averaged in six domains, including parts of the (1) Sub-polar gyre and (2) Nordic Seas, (3) the Southern open shelf south of Iceland and including shelf and shallow areas around the Faroes, (4) Northern open shelf area north of Iceland, (5) Eastern shelf along Greenland, and (6) the Western shelf along Norway. Large regional variability in PP was seen between the six domains where the shelf along east Greenland had the lowest annual PP (0.19 g C m^{-2} d^{-1}) while the greatest was seen along the Norwegian shelf (0.77 g C m^{-2} d^{-1}). The open shelf areas north and south of the Greenland-Scotland Ridge (GSR) were found to be more productive than the ambient open sea areas.

The average PP during spring, defined from 1 January – 1 June was found to contribute ∼25% of the annual PP and the greatest contribution of spring production to total was seen above the Norwegian shelf (34%). In general, variability of PP above the open shelves on either side of the GSR was most highly correlated with PP in the adjacent open seas. This indicates that the dominating influence on the timing of seasonal PP is from water masses, rather than processes related to bathymetry.

Primary production estimates are highly sensitive to the parameterization of the photosynthetic parameter P^B_{max}. The parameterization used implies an increase of P^B_{max} during summer due to a higher sea surface temperature (SST). However, comparison with *in situ* measurements of P^B_{max} from the area showed no such dependence on SST. This suggests that PP during the warm period may be overestimated by the parameterization of P^B_{max} applied in the two models. Thus, the PP during summer months may be overestimated here. The general seasonal distribution patterns reported here would, however, remain robust as they are highly dependent on chlorophyll and light distributions.

Areas north of the GSR use light significantly more efficiently for photosynthesis during spring and early summer than in the sub-polar gyre and southern open shelf areas. Thus, light harvesting by phytoplankton in the southern areas first becomes efficient relatively late in the summer season (**Figure 7**). This difference could potentially be explained by nutrient-limitation (e.g., iron and silicate). However, comparison with mixed layer depth (MLD) suggests that deep MLD south of the GSR early in the season is a likely explanation for the less efficient PP compared with the light availability in these areas.

Reduced PP early in the season due to a relatively deep mixed layer implies that PP can potentially increase if MLD decreases significantly. A multi-model ensemble of Earth System Model (ESM) simulations resulted in a significant decrease of MLD and a corresponding decrease of PP by ∼10–20% south of the GSR by year 2100 in a warm climate change scenario (SSP5-8.5). A decrease of MLD would imply a significant increase in PP during spring and early summer according to the analysis by the VPP-model. Thus, this discrepancy between regional estimates from a data-driven PP-model and ESM-simulations requires further analysis and indicates a significant uncertainty on the response of PP in the northern North Atlantic to global warming.

DATA AVAILABILITY STATEMENT

Satellite datasets from the Ocean Productivity site were applied for calculation of PP (https://www.science.oregonstate.edu/ocean.productivity) and nitrate data were analyzed from the World Ocean Atlas (Garcia et al., 2010) (https://www.ncei.noaa.gov/products/world-ocean-atlas).

AUTHOR CONTRIBUTIONS

Both authors listed have made a substantial, direct, and intellectual contribution to the work, and approved it for publication.

FUNDING

This study was supported by a grant from the Carlsberg Foundation (H.M. Queen Margrethe's and Vigdís Finnbogadóttir's Interdisciplinary Research Centre on Ocean, Climate, and Society, CF-20-0071) and from the EU Horizon 2020 Program (ECOTIP) (Grant #869383).

SUPPLEMENTARY MATERIAL

The Supplementary Material for this article can be found online at: https://www.frontiersin.org/articles/10.3389/fmars.2021.785685/full#supplementary-material

REFERENCES

Arnholt, A. T., and Evans, B. (2021). *BSDA: Basic Statistics and Data Analysis. R package version 1.2.1*.

Astthorsson, O. S., Gislason, A., and Jonsson, S. (2007). Climate variability and the Icelandic marine ecosystem. *Deep Sea Res. II* 54, 2456–2477. doi: 10.1016/j.dsr2.2007.07.030

Behrenfeld, M. J., and Falkowski, P. G. (1997). Photosynthetic rates derived from satellite-based chlorophyll concentration. *Limnol. Oceanogr.* 42, 1–20. doi: 10.4319/lo.1997.42.1.0001

Carr, M.-E., Friedrichs, M. A. M., Schmeltz, M., Aita, M. N., Antoine, D., Arrigo, K. R., et al. (2006). A comparison of global estimates of marine primary production from ocean color. *Deep Sea Res. II* 53, 741–770. doi: 10.1016/j.dsr2.2006.01.028

de Boyer Montégut, C., Madec, G., Fischer, A. S., Lazar, A., and Iudicone, D. (2004). Mixed layer depth over the global ocean: an examination of profile data and a profile-based climatology. *J. Geophys. Res.* 109:C12003. doi: 10.1029/2004JC002378

Debes, H., Gaard, E., and Hansen, B. (2008). Primary production on the Faroe shelf: temporal variability and environmental influences. *J. Mar. Syst.* 74, 686–697. doi: 10.1016/j.jmarsys.2008.07.004

Dugdale, R. C., and Goering, J. J. (1967). Uptake of new and regenerated forms of nitrogen in primary productivity. *Limnol. Oceanogr.* 12, 196–206. doi: 10.4319/lo.1967.12.2.0196

Friedland, K. D., Record, N. R., Asch, R. G., Kristiansen, T., Saba, V. S., Drinkwater, K. F., et al. (2016). Seasonal phytoplankton blooms in the North Atlantic linked to the overwintering strategies of copepods. *Elementa* 4:99. doi: 10.12952/journal.elementa.000099

Garcia, H. E., Locarnini, R. A., Boyer, T. P., Antonov, J. I., Zweng, M. M., Baranova, O. K., et al. (2010). "World Ocean Atlas 2009, Volume 4: nutrients (phosphate, nitrate, silicate)," in *NOAA Atlas NESDIS 71*, ed. S. Levitus (Washington, DC: U.S. Government Printing Office).

Harrison, W. G., Børsheim, K. Y., Li, W. K. W., Maillet, G. L., Pepin, P., Sakshaug, E., et al. (2013). Phytoplankton production and growth regulation in the Subarctic North Atlantic: a comparative study of the Labrador Sea-Labrador/Newfoundland shelves and Barents/Norwegian/Greenland seas and shelves. *Prog. Oceanogr.* 114, 26–45. doi: 10.1016/j.pocean.2013.05.003

Hartmann, D. L. (1994). *Global Physical Climatology*. New York, NY: Academic Press.

Hátún, H., Azetsu-Scott, K., Somavilla, R., Rey, F., Johnson, C., Mathis, M., et al. (2017). The subpolar gyre regulates silicate concentrations in the North Atlantic. *Sci. Rep.* 7:14576. doi: 10.1038/s41598-017-14837-4

Hátún, H., Lohmann, K., Matei, D., Jungclaus, J. H., Pacariz, S., Bersch, M., et al. (2016). An inflated subpolar gyre blows life toward the northeastern Atlantic. *Prog. Oceanogr.* 147, 49–66. doi: 10.1016/j.pocean.2016.07.009

Heezen, B. D., Tharp, M., and Ewing, M. (1959). *The Floors of the Ocean: 1. The North Atlantic, Text to accompany the physiographic diagram of the North Atlantic*. New York, NY: Lamont Geological Observatory.

Henson, S. A., Dunne, J. P., and Sarmiento, J. L. (2009). Decadal variability in North Atlantic phytoplankton blooms. *J. Geophys. Res.* 114:C04013. doi: 10.1029/2008JC005139

Henson, S. A., Sanders, R., Holeton, C., and Allen, J. T. (2006). Timing of nutrient depletion, diatom dominance and a lower-boundary estimate of export production for Irminger Basin, North Atlantic. *Mar. Ecol. Progr. Ser.* 313, 73–84. doi: 10.3354/meps313073

Hilligsøe, K. M., Richardson, K., Bendtsen, J., Sørensen, L. L., Nielsen, T. G., and Lyngsgaard, M. M. (2011). Linking phytoplankton community size composition with temperature, plankton food web structure and sea-air CO2 flux. *Deep Sea Res. I* 58, 826–838. doi: 10.1016/j.dsr.2011.06.004

Holte, J., Talley, L. D., Gilson, J., and Roemmich, D. (2017). An Argo mixed layer climatology and database. *Geophys. Res. Lett.* 44, 5618–5626. doi: 10.1002/2017GL073426

Kwiatkowski, L., Torres, O., Bopp, L., Aumont, O., Chamberlain, M., Christian, J. R., et al. (2020). Twenty-first century ocean warming, acidification, deoxygenation, and upper-ocean nutrient and primary production decline from CMIP6 model projections. *Biogeosciences* 17, 3439–3470. doi: 10.5194/bg-17-3439-2020

Laufkötter, C., Vogt, M., Gruber, N., Aita-Noguchi, M., Aumont, O., Bopp, L., et al. (2015). Drivers and uncertainties of future global marine primary production in marine ecosystem models. *Biogeosciences* 12, 6955–6984. doi: 10.5194/bg-12-6955-2015

Lozier, M., Roussenov, V., Reed, M., and Williams, R. G. (2010). Opposing decadal changes for the North Atlantic meridional overturning circulation. *Nat. Geosci.* 3, 728–734. doi: 10.1038/ngeo947

Lyngsgaard, M. M., Markager, S., Richardson, K., Møller, E. F., and Jakobsen, H. H. (2017). How well does chlorophyll explain the seasonal variation in phytoplankton activity? *Estuar. Coasts* 40, 1263–1275. doi: 10.1007/s12237-017-0215-4

Nielsdóttir, M. C., Moore, C. M., Sanders, R., Hinz, D. J., and Achterberg, E. P. (2009). Iron limitation of the postbloom phytoplankton communities in the Iceland Basin. *Glob. Biogeochem. Cycles* 23:GB3001. doi: 10.1029/2008gb003410

Paris, P. J., Walsh, J. P., and Corbett, D. R. (2016). Where the continent ends. *Geophys. Res. Lett.* 43, 208–212. doi: 10.1002/2016GL071130

Press, W. H., Teukolsky, S. A., Vetterling, W. T., and Flannery, B. P. (1992). *Numerical Recipes in FORTRAN: The Art of Scientific Computing*. Cambridge, MA: Press Syndicate of the University of Cambridge.

R Core Team (2021). *R: A Language and Environment for Statistical Computing*. Vienna: R Foundation for Statistical Computing.

Richardson, K., and Bendtsen, J. (2019). Vertical distribution of phytoplankton and primary production in relation to nutricline depth in the open ocean. *Mar. Ecol. Prog. Ser.* 620, 33–46. doi: 10.3354/meps12960

Richardson, K., Bendtsen, J., Kragh, T., and Mousing, E. A. (2016). Constraining the distribution of photosynthetic parameters in the global ocean. *Front. Mar. Sci.* 3:269. doi: 10.3389/fmars.2016.00269

Ryan-Keogh, T. J., Macey, A. I., Nielsdóttir, M. C., Lucas, M. I., Steigenberger, S. S., Stinchcombe, M. C., et al. (2013). Spatial and temporal development of phytoplankton iron stress in relation to bloom dynamics in the high-latitude North Atlantic Ocean. *Limnol. Oceanogr.* 58, 533–545. doi: 10.4319/LO.2013.58.2.0533

Sanders, R., Brown, L., Henson, S., and Lucas, M. (2005). New production in the Irminger Basin during 2002. *J. Mar. Sys.* 55, 291–310. doi: 10.1016/j.jmarsys.2004.09.002

Skogen, M. D., Budgell, W. P., and Rey, F. (2007). Interannual variability in Nordic seas primary production. *ICES J. Mar. Sci.* 64, 889–898. doi: 10.1093/icesjms/fsm063

Steemann Nielsen, E. (1952). The use of radio-active carbon C14 for measuring organic production in the sea. *ICES J. Mar. Sci.* 18, 117–140. doi: 10.1016/0146-6313(58)90015-7

Sverdrup, H. U. (1953). On conditions for the vernal blooming of phytoplankton. *J. Conseil Conseil Int. Pour l'Exploration Mer* 18, 287–295. doi: 10.1093/icesjms/18.3.287

Takahashi, T., Sutherland, S. C., Sweeney, C., Poisson, A., Metzl, N., Tilbrook, B., et al. (2002). Global sea-air CO2 flux based on climatological surface ocean pCO2, and seasonal biological and temperature effects. *Deep Sea Res.* 49, 1601–1622. doi: 10.1016/S0967-0645(02)00003-6

Takahashi, T., Sutherland, S. C., Wanninkhof, R., Sweeney, C., Feely, R. A., Chipman, D. W., et al. (2009). Climatological mean and decadal change in surface ocean pCO2, and net sea-air CO2 flux over the global oceans. *Deep Sea Res.* 56, 554–577. doi: 10.1016/j.dsr2.2008.12.009

Webb, W. L., Newton, M., and Starr, D. (1974). Carbon dioxide exchange of Alnus rubra. A mathematical model. *Oecologia* 17, 281–291. doi: 10.1007/BF00345747

Zhai, L., Gudmundsson, K., Miller, P. I., Peng, W., Guðfinnsson, H., Debes, H. H., et al. (2012). Phytoplankton phenology and production around Iceland and Faroes. *Cont. Shelf Res.* 37, 15–25. doi: 10.1016/j.csr.2012.01.013

Conflict of Interest: The authors declare that the research was conducted in the absence of any commercial or financial relationships that could be construed as a potential conflict of interest.

Publisher's Note: All claims expressed in this article are solely those of the authors and do not necessarily represent those of their affiliated organizations, or those of the publisher, the editors and the reviewers. Any product that may be evaluated in this article, or claim that may be made by its manufacturer, is not guaranteed or endorsed by the publisher.

Copyright © 2021 Richardson and Bendtsen. This is an open-access article distributed under the terms of the Creative Commons Attribution License (CC BY). The use, distribution or reproduction in other forums is permitted, provided the original author(s) and the copyright owner(s) are credited and that the original publication in this journal is cited, in accordance with accepted academic practice. No use, distribution or reproduction is permitted which does not comply with these terms.

frontiers in Marine Science

ORIGINAL RESEARCH
published: 23 December 2021
doi: 10.3389/fmars.2021.778725

Spatial Distribution of Different Age Groups of Herring in Norwegian Sea, May 1996–2020

Sólvá Káradóttir Eliasen[1], Eydna Í. Homrum[1], Jan Arge Jacobsen[1], Inga Kristiansen[1], Guðmundur J. Óskarsson[2], Are Salthaug[3] and Erling Kåre Stenevik[3]*

[1] Faroe Marine Research Institute (FAMRI), Tórshavn, Faroe Islands, [2] Marine and Freshwater Research Institute, Hafnarfjörður, Iceland, [3] Institute of Marine Research (IMR), Bergen, Norway

The commercially important Norwegian spring spawning herring is characterized by its extensive annual migrations and, on a decadal timescale, large shifts in migration patterns. These changes are not well understood, but have previously been linked to temperature, food availability, and size and age composition of the stock. Acoustic and trawl data from the International Ecosystem Surveys in the Nordic Seas, carried out annually in May since 1996, were used to analyze the spatial distribution of herring in the period 1996–2020. The dataset was disaggregated into age classes, and information about where the different age classes feed in May was derived. The analysis of herring feeding patterns in May confirms that the youngest age classes are generally found close to the Norwegian shelf, whereas the older age classes display larger variations in where they are distributed. During the period 1996–1998, the oldest age classes were found in the central and western Norwegian Sea. During the period 1999–2004, the whole stock migrated north after spawning, leaving the regions in the southern Norwegian Sea void of herring. Since 2005 the oldest herring has again congregated in the south-western Norwegian Sea, in the frontal zone between the cooler East Icelandic water and the warmer Atlantic water. There was a significant positive relationship both between stock size and distribution area and between stock size and density. Moreover, it is likely that the strong year classes 1991/1992 and 1998/1999, which were relatively old when the respective changes in migration patterns occurred, were important contributors to the changes observed in 1999 and 2005, respectively.

Keywords: Norwegian spring spawning herring, abundance, year class abundance, spatial distribution, climatic shifts, density dependent spatial dynamics

OPEN ACCESS

Edited by:
Peter Grønkjær, Aarhus University, Denmark

Reviewed by:
Tommaso Russo, University of Rome Tor Vergata, Italy
Susanne Eva Tanner, University of Lisbon, Portugal
Torstein Pedersen, UiT The Arctic University of Norway, Norway

****Correspondence:***
Sólvá Káradóttir Eliasen
solvae@hav.fo

Specialty section:
This article was submitted to Marine Ecosystem Ecology, a section of the journal Frontiers in Marine Science

Received: *17 September 2021*
Accepted: *29 November 2021*
Published: *23 December 2021*

Citation:
Eliasen SK, Homrum EÍ, Jacobsen JA, Kristiansen I, Óskarsson GJ, Salthaug A and Stenevik EK (2021) Spatial Distribution of Different Age Groups of Herring in Norwegian Sea, May 1996–2020. Front. Mar. Sci. 8:778725. doi: 10.3389/fmars.2021.778725

INTRODUCTION

The Norwegian spring spawning herring (hereafter herring) stock varies greatly, both in size and distribution area. After the collapse of the stock in the late 1960s, the stock was confined along the Norwegian coast where it also fed throughout the year. The stock started to grow again in the late 1980s after the strong 1983 year class recruited, and in the mid 1990s the herring reoccupied large parts of the Norwegian Sea following good recruitment in the early 1990s. In 2008–2009 the stock reached its maximum size since the 1950s, after which it has declined again (Dragesund, 1980; Dragesund et al., 1997; ICES, 2021b).

Since the reappearance of the stock in the Norwegian Sea (**Figure 1**), spawning has occurred along the Norwegian coast from around 62°30′N to 68°20′N (Holst and Slotte, 1998; Salthaug et al., 2020). After spawning, the mature part of the stock starts its feeding migration. The feeding season is from April to September, with the main feeding period being May–July (Langøy et al., 2012; Bachiller et al., 2018, 2016). As prior to the stock collapse in the 1960s, the main feeding is now in the Norwegian Sea and adjacent waters (Marti, 1956; Misund et al., 1997; Nøttestad et al., 1999; ICES, 2021b). However, since the reappearance, some variation has been observed in the distribution pattern during summer, with a more northerly distribution during the period 1999–2004 as compared to the period prior and after this (Utne et al., 2012; Gudmundsdottir et al., 2014).

The Norwegian Sea, where the herring feed in the uppermost ∼3–400 m (Misund et al., 1997; Huse et al., 2012; Melle et al., 2020), is characterized by relatively warm water masses in the central and eastern part. The western area is dominated by relatively cold East Icelandic water and water of Arctic origin, thereby creating the sharp Jan Mayen Front along the Jan Mayen Ridge (**Figure 1**). In the south, the sharp Iceland-Faroe Front delineates the Norwegian Sea toward south. On the southern side of the Iceland-Faroe Front, Atlantic water flows eastward toward Norway. The Atlantic water enters the Norwegian Sea in the southeast and flows northward along the Norwegian coast, thus causing this region to be the warmest part of the Norwegian Sea (Read and Pollard, 1992; Blindheim and Østerhus, 2005). The herring has a general diel vertical migration pattern, ascending to the sea surface during the night and residing around 250–400 m during the daytime. However, herring is also occasionally observed in the surface during the daytime and in the deeper layers during the night time (Misund et al., 1997; Huse et al., 2012; Melle et al., 2020).

Numerous studies have shown that the main prey of herring is calanoid copepods, in particular *Calanus finmarchicus* (Rudakova, 1956; Dalpadado et al., 2000; Varpe et al., 2005; Prokopchuk and Sentyabov, 2006; Prokopchuk, 2009; Broms et al., 2012; Langøy et al., 2012; Bachiller et al., 2016; Melle et al., 2020). However, the larger and more nutritious copepod species, *Calanus hyperboreus*, is also considered to be a key component of the herring diet, especially in the south-western areas (Rudakova, 1956; Dalpadado et al., 2000; Gislason and Astthorsson, 2002). Other prey such as amphipods, krill (e.g., *Meganyctiphanes norvegica* and *Thysanoessa inermis*) and pearlside (*Maurolicus muelleri*) are also ingested by the herring when copepods are not available (Rudakova, 1956; Dalpadado et al., 2000; Gislason and Astthorsson, 2002; Prokopchuk and Sentyabov, 2006; Olsen et al., 2007; Melle et al., 2020).

Calanus finmarchicus is the most abundant zooplankton species in the Norwegian Sea (Wiborg, 1955; Dommasnes et al., 2004; Broms et al., 2009). *Calanus hyperboreus* is generally found in waters of more arctic origin, west of the Jan Mayen Front and also in the Jan Mayen frontal zone (Rudakova, 1956; Varpe et al., 2005; Gislason and Silva, 2012; Kristiansen et al., 2019; Melle et al., 2020), where it is an important food item of the herring (Holst et al., 2004). Krill is found on both sides of the Jan Mayen Front, pearlside more along the Norwegian coast, whereas amphipods are found more abundantly west of the Jan Mayen Front (Dalpadado et al., 2000).

Herring is a selective feeder (Pavshtiks, 1956; Rudakova, 1956; Dalpadado et al., 2000; Langøy et al., 2012) and it prefers the largest individuals of copepods which are more energetically beneficial for the herring to ingest compared to small items (Dalpadado et al., 2000). Feeding also has been found to be more intensive near the Jan Mayen Front, where *C. hyperboreus* is found in high concentrations (Rudakova, 1956; Olsen et al., 2007; Kristiansen et al., 2019).

There are several mechanisms thought to influence the herring feeding migration. Interspecies competition between herring, mackerel and blue whiting could affect the food availability and thus the migration (Prokopchuk and Sentyabov, 2006; Utne and Huse, 2012). Experience and learning may help guide the herring toward richer feeding areas (Fernö et al., 1998; Misund et al., 1998; Corten, 2002), and accordingly, predictive orientation mechanisms might improve with age, with the oldest herring being most successful in finding good prey (Kvamme et al., 2003). Also, larger fish have an advantage in the feeding migration as they are able to travel faster and longer distances (Nøttestad et al., 1999). Other environmental cues, such as food availability, predator abundance, sea temperature, currents, differences in day length at boreal latitudes and phytoplankton bloom development, which links to zooplankton abundance, have also been suggested to influence the herring migration (Misund et al., 1997; Fernö et al., 1998; Nøttestad et al., 1999; Broms et al., 2012; Langård et al., 2015; Melle et al., 2020).

Changes in migration pattern have been observed to co-occur with drastic changes in stock size (Dragesund et al., 1997), and have been hypothesized to be caused by changes in stock size as well as by environmental factors (McQuinn, 1997; Corten, 2002; Huse et al., 2002). However, conservatism through previous experience is possibly also causing inertia toward changes in feeding migration (Corten, 2002). Modeling experiments confirm that the relative abundance of determined individuals in a school plays an important role in the collective behavior (Huse et al., 2002). Thus, age composition within the stock could also affect the behavioral choices made during the feeding migration and therefore determine where the stock feeds during the summer (Huse et al., 2010).

The joint International Ecosystem Survey in the Norwegian Sea (IESNS), which targets Norwegian spring spawning herring during its feeding migration, has been carried out every year in May since 1996. Biological and acoustic data are gathered and used to provide age disaggregated abundance indices of herring used in the assessment of the stock by the "Working Group on Widely Distributed Stocks" (WGWIDE) (ICES, 2021b). This 25 years long time-series from the survey therefore provides quantitative information about spatial distribution of different age groups.

The objective of the study is to use these data to investigate patterns in the herring feeding distribution in May, density dependent spatial dynamics in the stock and whether the spatial herring distribution in May changes when drastic changes occur in stock size and age distribution within the stock.

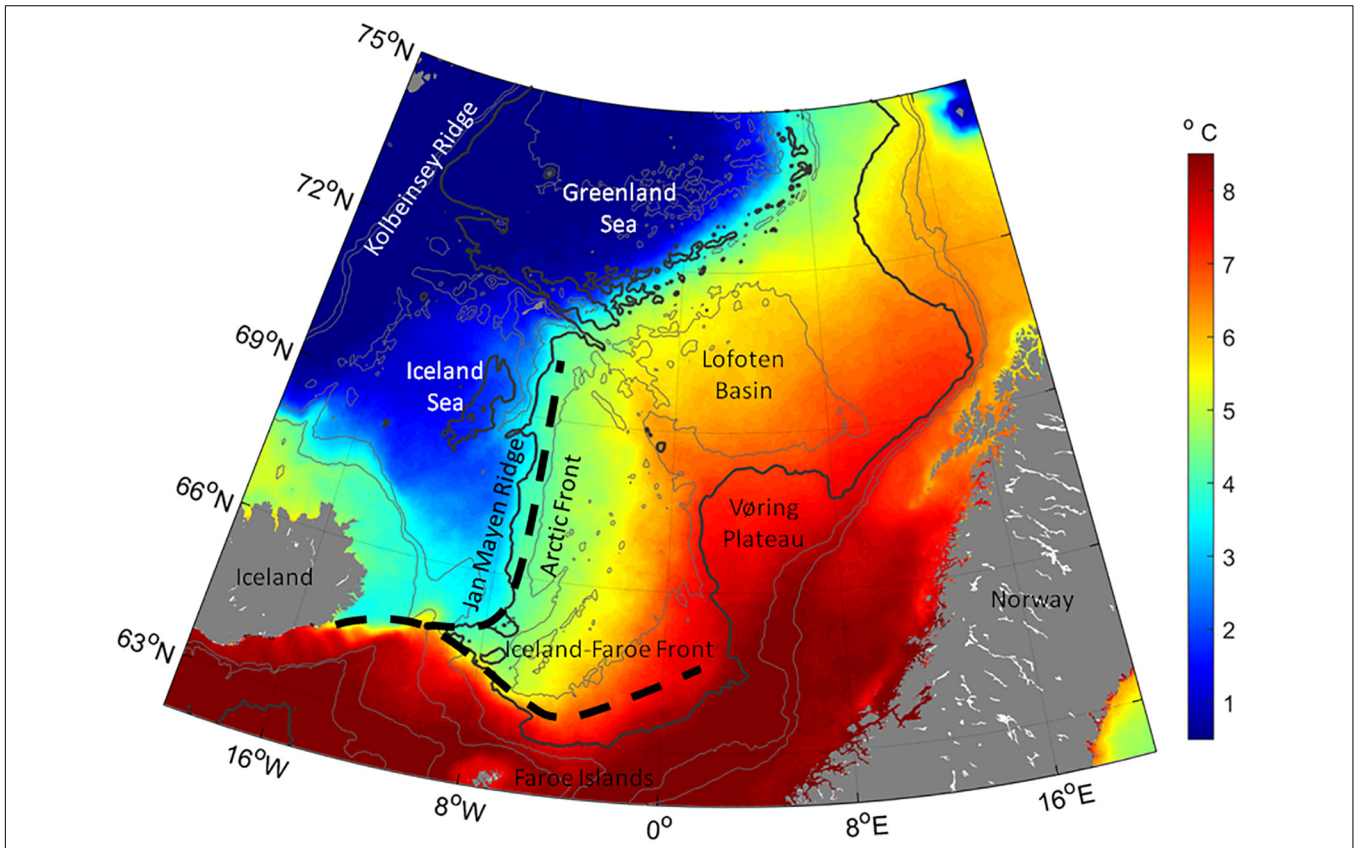


FIGURE 1 | Map of the Norwegian Sea and adjacent waters with the main frontal zones in the area. Map overlaid with average sea surface temperature in May 2003–2020, based on remotely sensed data (from NASA Goddard Space Flight Center, Ocean Ecology Laboratory, Ocean Biology Processing Group). 500, 1,000, 2,000, and 3,000 m depth contours are shown in gray – with the 2,000 m contour in bold.

MATERIALS AND METHODS

Data from the IESNS survey in the period 1996–2020 was used in this work. Generally, the survey starts in the south and progresses northward, after which it continues into the Barents Sea to survey the youngest herring, i.e., immature herring at ages 1–2 years. However, in the current analysis, the survey from the Barents Sea is not included. During this 25 years period, three to five vessels have covered the Norwegian Sea in the IESNS survey. The acoustic and biological data from these surveys are stored in a joint database (PGNAPES), and were retrieved from there by the courtesy of all participating parties.

Unfortunately, the survey data in the database are not complete when it comes to the earliest years, where data from one of the participating vessels is missing each of the years 1997, 1998, 1999, 2001, 2003, 2004, and 2007. Except for 2003, the missing data are always from the south-eastern part of the survey area. This area is always surveyed by two vessels that do alternating transects or in some way cross each other's path. Thus, although some data were missing, its impacts on the results are less than anticipated because of the survey design. The database is complete in 1996, 2000, 2002, 2005–2006, and from 2008 onward.

After quality check of the IESNS data, acoustic data from 92 IESNS cruises, carried out by two to five different vessels each year, were available (**Supplementary Tables 1–3**). The IESNS survey defines the area between 14°W–20°E and 62°N–75°N as the area of consideration and thus the same procedure has been used here.

Fish Data From Trawl Stations

Trawling is carried out opportunistically in IESNS, with varying pelagic trawls, to support the acoustical interpretations with regards to species and size composition of the fish. The trawl stations are spread out intermittently over the whole survey area and at each station, total length (L), whole body weight (W) and age sampling is recorded. Usually 100–300 herring (or as many as the catches allow) are length measured and a subsample of these (30–100) are aged using otoliths or scales. The sample sizes vary among participating countries.

After quality check, data were sorted according to year and geographical rectangle (2° longitudes × 1° latitude). For each rectangle, an age-length-key (ALK) was calculated, based on fish from a slightly larger rectangle (4° longitudes × 2° latitude) that had the same center as the original rectangle, and the ALK from the larger rectangle was then used to assign ages to fish in the original rectangle that were not aged.

A yearly regression was made between age and weight in order to assign weights to fish without recorded weights and in order

to compute average weights in each age class after the ALK was applied. Assuming that the length-weight relationship is given as:

$$W = \alpha \cdot L^{\beta} \quad (1)$$

$$\log(W) = \log(\alpha) + \beta \cdot \log(L) \quad (2)$$

the Matlab routine "polyfit" was used to compute annual α and β.

Subsequently, based on the distribution of fish in each rectangle after the application of the ALK, in rectangles with more than 100 fish with ages, abundance ratios of each year class (i) of herring (ra_i) was computed, as well as the average individual length and weight for each year class (i):

$$ra_i\left(rectangle,\ year\right) = \frac{N_i\left(rectangle,\ year\right)}{N\left(rectangle,\ year\right)} \quad (3)$$

where N is the total number of fish and N_i is the number of fish of year class i.

The abundance ratios were then gridded onto a regular grid (2° longitudes × 1° latitude) using objective mapping (Böhme and Send, 2005), with a 2° longitude and 1° latitude smoothing factor, resulting in spatial fields of ratios of each age, each year. Investigation of error estimates were used to determine how far away from the actual observations the gridded data can extend. Where error estimates were too high, NaNs were filled onto the grid. The error limit was each year subjectively set, based on the internal consistency of the data, which varies from year to year. This way, the maximum spatial range each year was obtained.

In the same manner, mean individual lengths and weights were computed for year and rectangle and gridded onto a regular grid.

Acoustic Data

The acoustic data available in the database are mean *Nautical Area Scattering Coefficient* (NASC) values over 1 nautical mile with varying depth channels (10–50 m) along the survey tracks. The sampling depth was normally 0–500 m. The analyses of the data were constrained to year and geographical rectangles (2° longitudes × 1° latitude) and were as follows:

- Acoustic data were summed vertically for each acoustic log, resulting in the so-called Sa2 value (with the unit Sa2 nm^{-2}).
- Mean Sa2 nm^{-2} was computed for each rectangle.
- The Sa2 nm^{-2} were gridded (see section "Fish Data From Trawl Stations") to estimate acoustic strengths nm^{-2} in rectangles that were left out of the surveyed area.
- Average target strengths and cross sections (Eqs 4, 5) in each rectangle were computed based on the average lengths and weights in each rectangle.
- Total abundance in each rectangle was computed (Eq. 6).
- Based on the relative age distribution and average weights of each age in each rectangle, the abundances and subsequently biomasses of each year class were computed.

The equations describing the above procedure are found in Foote (1987) and are as follows.

The average target strength in each rectangle is calculated based on the weighted average length:

$$TS\left(rectangle, year\right) = 20 \cdot \log\left[< L\left(rectangle,\ year\right) >\right] - 71.9\,dB \quad (4)$$

The cross-section in each rectangle is given as:

$$CS\left(rectangle, year\right) = 4\pi \cdot 10^{0.1 \cdot TS} \quad (5)$$

The total abundance, N, in each rectangle is given as:

$$N\left(rectangle,\ year\right) = \frac{Sa2\ \left(rectangle, year\right)}{CS\left(rectangle, year\right)} \cdot A \quad (6)$$

where A is the area (km^2) of each rectangle.

The average abundances and biomasses, derived from the acoustic values per geographical rectangle, were gridded in the same manner as the abundance ratios, see section "Fish Data From Trawl Stations." These fields were multiplied with the ratio fields in order to compute age and year specific spatial distribution of fish and biomasses.

Area Calculations and Center of Gravity Calculations

The area occupied by the herring stock was computed by adding the areas of rectangles with a biomass higher than 2 tons km^{-2}. This limit was derived by investigating how large part of the biomass is included from year to year with various limits. With the 2 tons km^{-2} limit, more than 86% of the total biomass is always included.

Center of gravity (CG) of each year class was computed from the gridded fields as:

$$Lon_{CG}, Lat_{CG} = \frac{\sum_{ij} Lon_{ij} \times N_{ij}}{\sum_{ij} N_{ij}}, \frac{\sum_{ij} Lat_{ij} \times N_{ij}}{\sum_{ij} N_{ij}} \quad (7)$$

where i,j, indicates grid points. In order to avoid signals from areas with very low abundances, rectangles where the abundance was less than 5% of the maximum abundance were set to 0 before calculating the CG.

Quality Check of the Biological and Acoustic Dataset

Conversion of the acoustic signals to abundance and biomass in general show the same features as the numbers provided by WGWIDE (ICES, 2021b), in particular the last decade of the period (**Supplementary Figures 1A–C**). The deviation from the WGWIDE results is largest for the earliest years, where data from some of the participating vessels were missing in the dataset. The internal consistency between the age groups is relatively high (**Supplementary Figure 1D**).

RESULTS

General Distribution Pattern

The total distribution of adult herring in May for the period 1996–2020 is shown in **Figure 2**. Generally the herring was

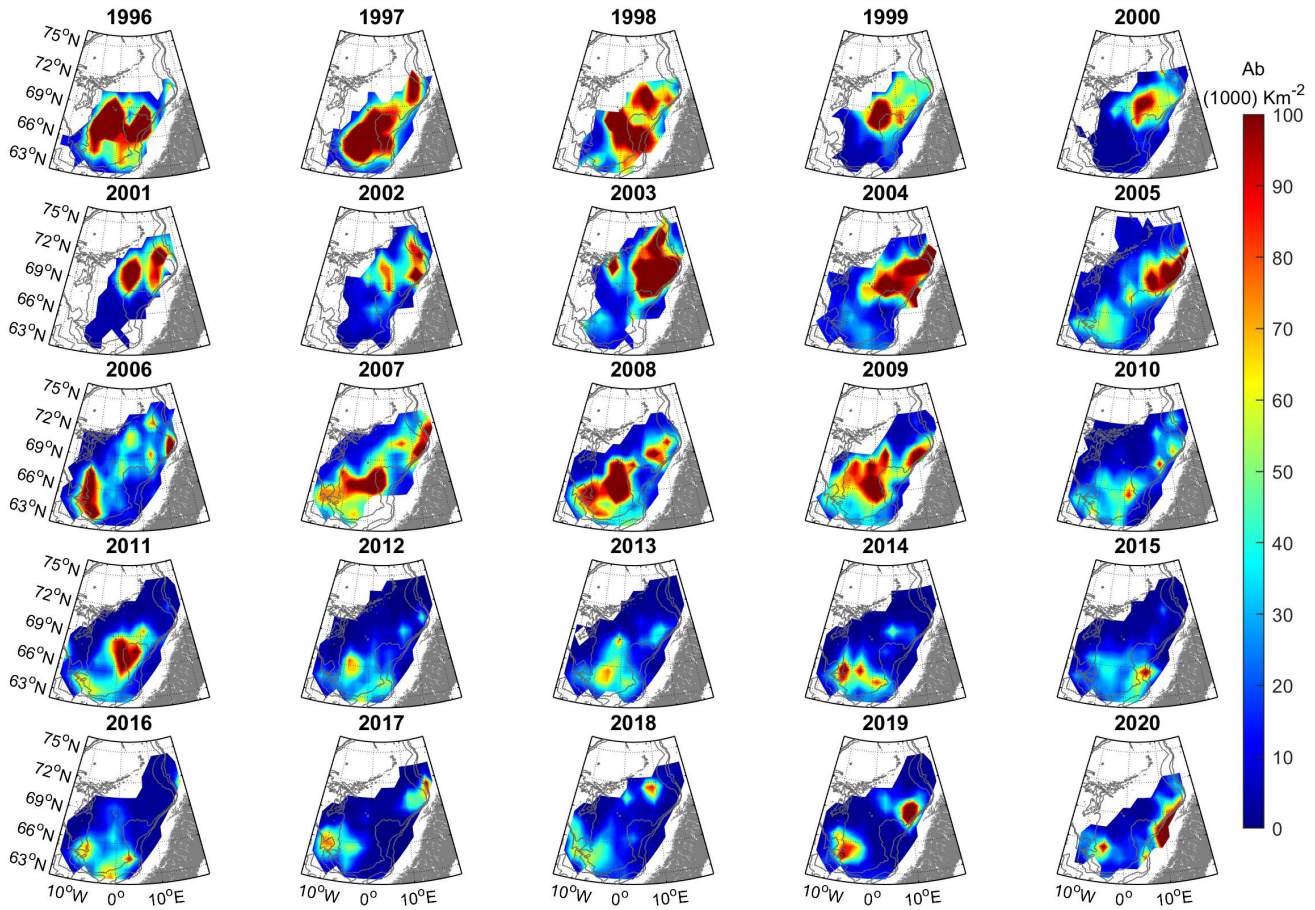


FIGURE 2 | Herring stock distribution in May by year in the period 1996–2020 (Abundance, 10^3 km^{-2}). The colored areas bordering the white non-colored areas denote the boundaries and extent of the survey coverage each year. The darkest blue regions indicate surveyed areas void of herring. 500, 1,000, and 2,000 m depth contours are shown in gray.

distributed along a southwest – northeast axis in May. The most significant deviation from this general pattern was in the 6-year period 1999–2004, where the entire stock only resided in the northernmost part of the Norwegian Sea. Most years the distribution was continuous, from the northeast to the southwest, but, e.g., in 2017–2019 there was a bimodal distribution, with high abundances both in the northeast and southwest, but with almost no herring in the center of the Norwegian Sea (**Figure 2**). The CG of the total stock (**Figure 3**) shows how the stock has switched from a southerly (1996–1998), to a northerly (1999–2004) and again to a southerly (2005–2020) distribution.

Density Dependent Spatial Dynamics

There is a significant positive relationship (Pearson's correlation coefficient $p < 0.01$) between the size of the adult stock (biomass of ages 3+) and size of the distribution area in May. When the stock was large, the distribution area was large and vice versa (**Figure 4A**). Moreover, there is also a significant positive relationship (Pearson's correlation coefficient $p < 0.01$) between the stock size and the stock density (biomass/area) (**Figure 4B**), implying that there are also more tons of herring per km^2 when the stock is large than when it is small, i.e., there is density dependence within the stock.

Disaggregation of the Stock Into Year Classes and Age Groups

Separating the adult herring stock into year classes shows that the youngest year classes (<5 years old) were found more or less just off the Norwegian shelf, on the eastern slopes of the Norwegian Basin and Lofoten Basin (**Supplementary Figure 2**). However, abundant year classes tend to spread out further west into the central Norwegian Sea as compared to smaller year classes. The older age groups were found further west and southwest, irrespective of year class strength.

The youngest fish (3–4 year olds) quite consistently were gathered along the eastern shelf slope of the Norwegian Shelf, mostly in the Lofoten Basin (**Figure 5**, left column). The 5–7 year olds had a more variable distribution, and these year classes were distributed mainly in the central Norwegian Sea (**Figure 5**, middle column). The older herring (age 8+) were mainly distributed in the southwest area of the Norwegian Sea (**Figure 5**, right column).

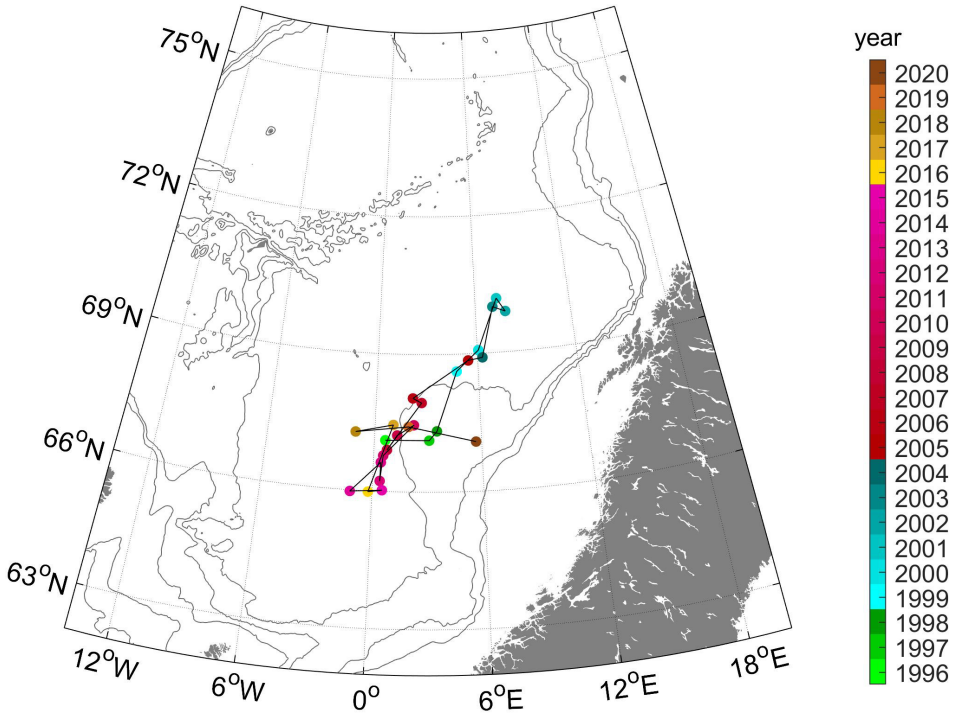


FIGURE 3 | Center of gravity of herring in May in the period 1996–2020. The colors of the markers denote year (as indicated in the scale bar to the right). The 500, 1,000, and 2,000 m depth contours are shown in gray.

In the period 1996–1998, the oldest (age 8+) fish were found in the western part of the Norwegian Sea – between the Vøring Plateau and the Jan Mayen ridge. In the period 1999–2004, both the 8+ and the 5–7 year olds were distributed relatively far north in the Norwegian Sea, but from 2005 and onward the old fish migrated south and west into the southern part of the Norwegian Sea again after spawning, south and west of the Vøring Plateau, and also far west and south in the areas north of the Faroes and east of Iceland (**Figure 5**).

Center of Gravity Analysis

The CG of the youngest herring was located mostly in the northeast, on the Norwegian Shelf slope (**Figure 6**). Herring from 6 years and older were gradually found more southerly and westerly with increasing age and the oldest herring was found farthest away from the Norwegian Shelf. The northern displacement in 1999–2004 was also evident from colored dots in **Figure 6**. Since 2005 the oldest herring congregated in a narrow area where the Jan Mayen Front and the Iceland-Faroe Front meet.

The CG by year class (**Figure 7**) show the typical changes from a location in the north-eastern Norwegian Sea when they were young and the gradual south-western displacement with age. There were, however, some notable exceptions to this pattern, as seen in the early period for the year classes 1989 to 1993. These year classes, when age 6 and older, fed further north in contrast to later year classes, again as a consequence of the northern shift in the summer feeding distribution during the years 1999–2004.

Figure 8 shows the CG's latitude of each year class in May as a function of time. The northern displacement can be seen as a northward shift in the latitude of the CG from 1999 to 2003, and a rather abrupt southward change from 2002 to 2003 of 7–9 year old herring, but surprisingly not age 10 and 11+ herring. However, these followed in 2004. The CG of adult herring has remained in the south since 2004, but with regards to latitude, the younger herring seem to have varied more in recent times, with a slight southward displacement during the period 2011–2016. From 2017, the youngest herring again has been located far north in the Norwegian Sea (**Figure 8**). **Figure 8** also shows that the stock occupies more space when it's large (around 2,008) than when it's small (e.g., around 2,000). The bimodal distribution in 2017–2019 causes the CG's latitude of each year class to be spread out over a wide range of latitudes. However, investigation of the data confirms that the total area, which the stock occupied in this period, was always less than 700×10^3 km^2 (see also **Figures 2**, **4**).

DISCUSSION

Distribution Pattern

Our results confirm density dependent spatial dynamics within the herring stock. The herring stock both occupies a larger area and the stock's density is higher, i.e., higher biomass per km^2, when the stock is large. This might in turn affect the feeding conditions and growth of individual fish when the stock is large. However, the relationship between density and distribution

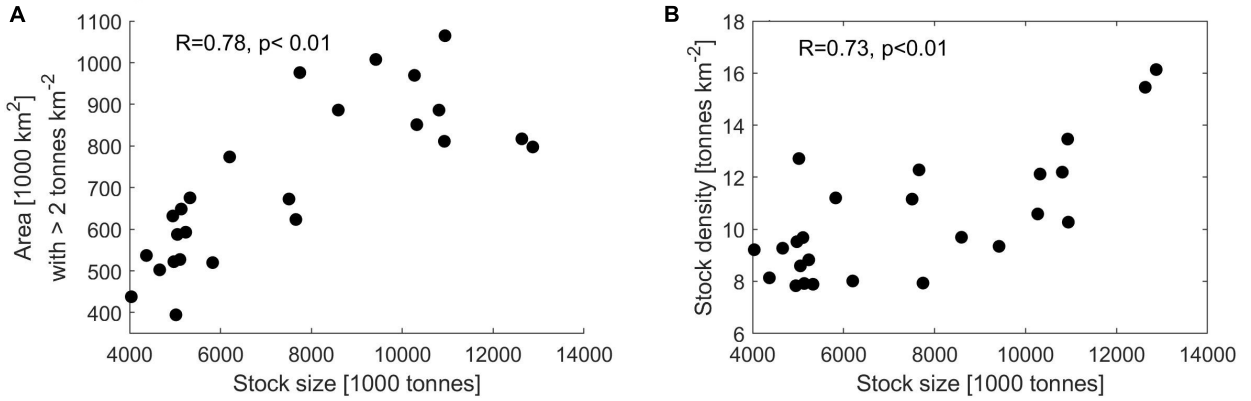


FIGURE 4 | Herring stock size and distribution area **(A)** and herring density (tons km^{-2}) versus stock size **(B)**. The Pearson's linear correlation coefficient has been computed for the data in both panels. In both cases the *p-value* < 0.01.

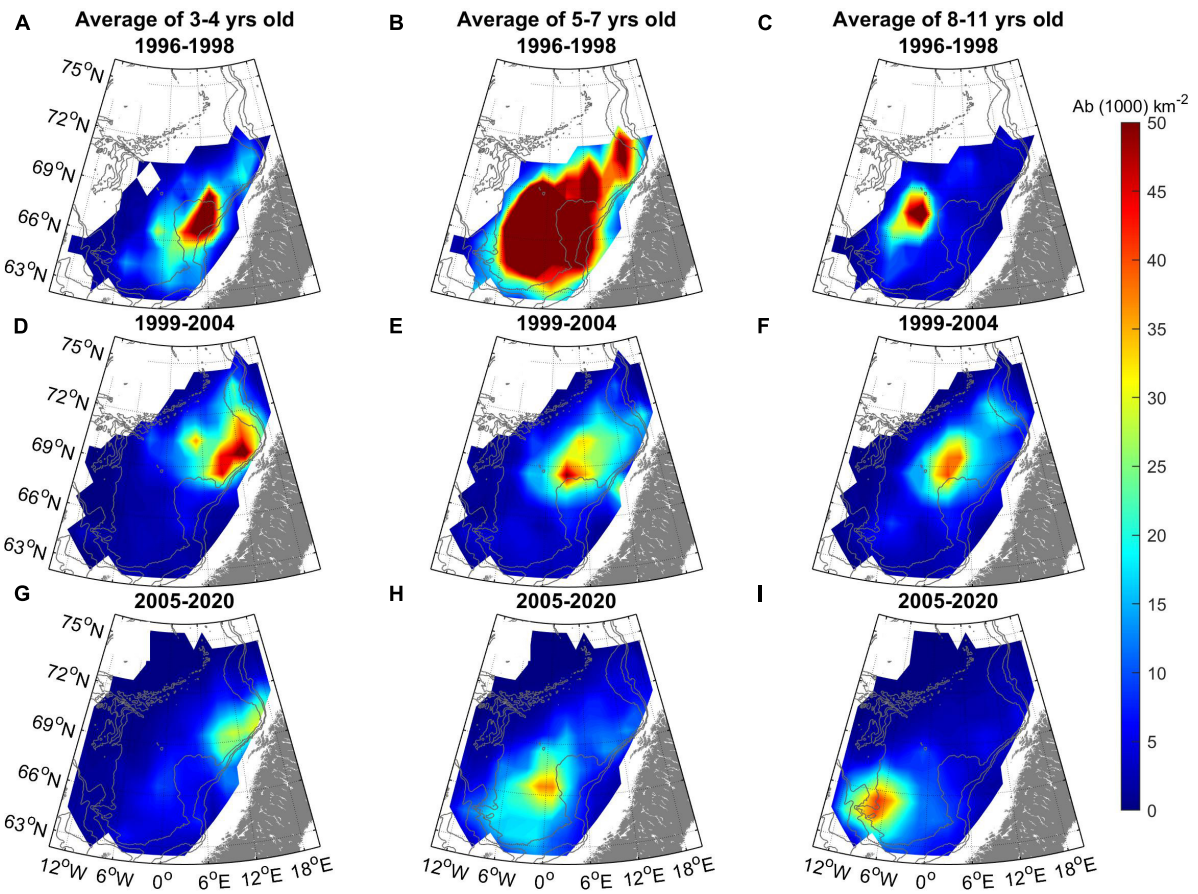


FIGURE 5 | Herring distribution (Abundance, 10^3 km^{-2}) grouped by three age groups [3–4 year olds left column **(A,D,G)**, 5–7 year olds middle column **(B,E,H)**, and 8+ year olds right column **(C,F,I)**] and three periods (1996–1998 upper row, 1999–2004 middle row, and 2005–2020 bottom row). The 500, 1,000, and 2,000 m depth contours are shown in gray.

area only considers biomass per square kilometer, and does not take the vertical dimension into account. It is possible that the stock occupies more space in the water column when the stock is large than when it is small and thereby increase their feeding opportunities. This analysis does not infer anything about biomass per volume.

Suitable "habitat area" for herring has previously been estimated based on temperature conditions in the Norwegian Sea

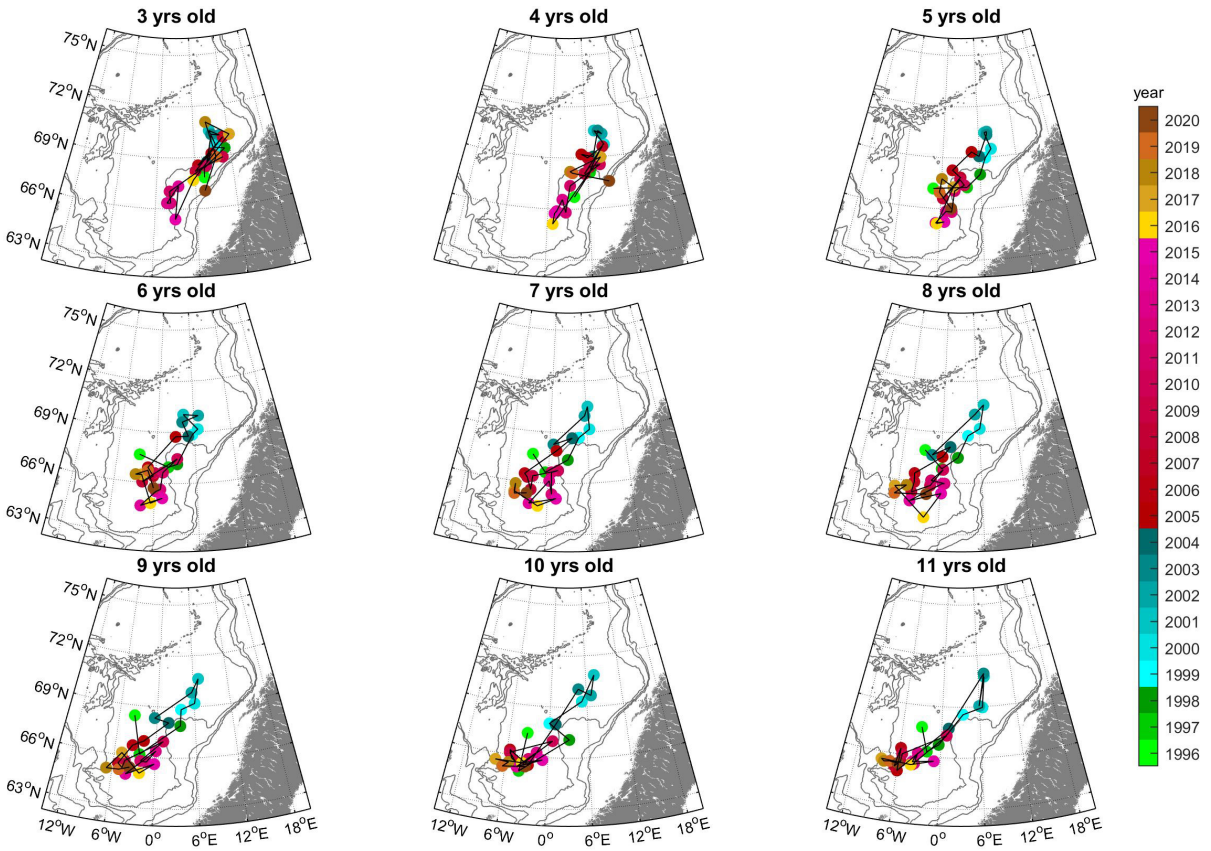


FIGURE 6 | Center of gravity of herring for age groups 3–10 and 11+ in May during 1996–2020. The colors of the markers denote year (as indicated in the scale bar to the right). The 500, 1,000, and 2,000 m depth contours are shown in gray.

(ICES, 2020, 2014). According to that, the herring most years does not seem to fully occupy its potential habitat since there is not a close relationship between calculated potential habitat size and stock size. If the size of the distribution area depends on the size of the stock, one would expect the size of the potential habitat to be a limiting factor only when the stock is large.

A change in distribution during the feeding period in May occurred during the period 1999–2004 when all age groups were distributed in the northern Norwegian Sea. Therefore, three periods were chosen to analyze the age disaggregated distribution: 1996–1998, 1999–2004, and 2005–2020, where the mid period 1999–2004 represents the northern displacement period of the stock.

The CG analysis of each age and each year class confirm that the youngest age classes are the ones that are seen in the eastern part of the Norwegian Sea in May. Furthermore, as the herring grows older, it migrates farther west during the feeding seasons. Surveys conducted close to the spawning period (e.g., Slotte et al., 2018; Salthaug et al., 2020) show that young fish spawn more northerly and later than older fish (Slotte, 1999; Slotte et al., 2000), and thus, the observed difference in positions of the younger and older age classes in May can be due to three different non-exclusive factors: (1) the difference in spawning location at the start of the feeding migration, (2) the fact that older age classes start their feeding migration earlier, due to their earlier spawning, and (3) that old fish have larger body size and are thus able to migrate a longer distance for a given amount of energy used compared to younger and smaller fish (Nøttestad et al., 1999). Regarding the last point there might be a trade-off between food abundance and migration distance. Considering that a small individual needs less food than a large individual, a young fish's need to migrate far from the spawning and wintering areas might not be as great as for a large and old fish.

With regards to where the herring migrate after spawning, the older age groups displayed a larger variation in where they fed in May compared to the younger age groups. The northward shift of the whole stock in 1999 was dominated by the relatively large 1991 and 1992 year classes, which at the time were 7 and 8 years old and accounted for more than 65% of the spawning stock abundance. The stock was at this time 5.853 million tons (ICES, 2021b), which is well above the reference point MSY $B_{trigger}$ (3.184 million tons). The MSY $B_{trigger}$ reference point is a safeguard against an undesirable or unexpected low spawning stock biomass when the fishing pressure is not higher than the so-called "Maximum Sustainable Yield" (MSY) level (ICES, 2021a). In 1998, both the 1991–1992 year classes and other year classes as well, were found in large parts of the Norwegian Sea – including the southern area. However, in 1999 the stock did not migrate

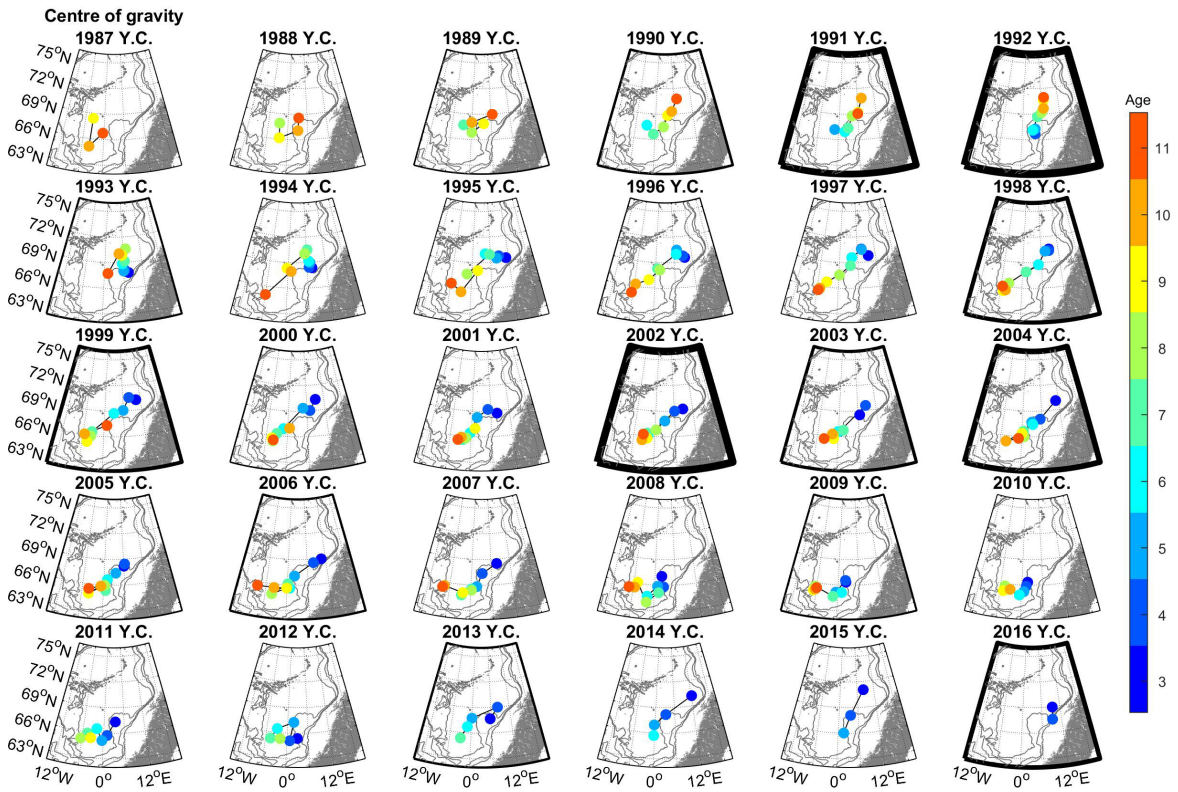


FIGURE 7 | Center of gravity of herring for year classes 1986–2016, in the years where they were 3–10 years old, on separate maps. The colors of the markers denote age (as indicated in the scale bar to the right). Note that the "11 years" dot represents the center of gravity of the year class as 11 years and older. The thickness of the map-frames indicates the strength of each year-class at age 5 (ICES, 2021b). The 500, 1,000, and 2,000 m depth contours are shown in gray.

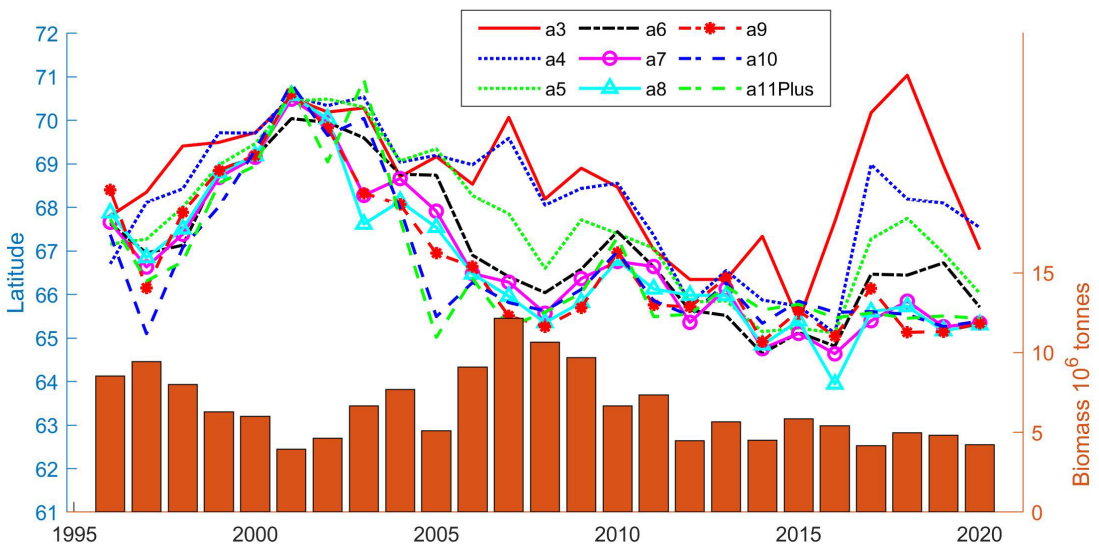


FIGURE 8 | Latitude of center of gravity for age 3–11+, 1996–2020 (lines). Each age group has a different color. Orange bars, with reference to the right axis, show total stock size (including ages 1 and 2) as estimated by the IESNS survey (ICES, 2021b).

into the southern part of the Norwegian Sea to feed in May, but instead only occupied the northern part of the Norwegian Sea. Since year classes 1993 and older had been feeding in the southern part of the Norwegian Sea the previous years, the herring "knew" this migration route and this area. Moreover, this change in migration pattern was not associated with any

drastic change in stock size. It is therefore likely something in the oceanic environment in 1998–1999, that either was attractive in the north or repulsive in the south, which caused the whole herring stock to be absent in the southern part of the Norwegian Sea in May 1999. We do not consider it likely that the herring had first tested the "usual" southern feeding areas before they "decided" to migrate northward to feed. Presumably they "made" this behavioral decision on the way out from the spawning areas, based on some environmental or biological cues.

The northerly displacement in 1999 continued until 2005. At this time the stock was numerically dominated by the 1998 and 1999 year classes and the large 2002 year class was just entering the stock. In May 2005, the 2002 year class only stayed in the north-eastern part of the Norwegian Sea and it was mainly the 1998–1999 year classes that migrated into the south-western part of the Norwegian Sea to feed. This change in migration pattern for these year classes (1998–1999) was not an entirely "new pattern," even though these year classes had not previously been in the southern Norwegian Sea in May. Closer inspection of the distribution areas shows that the 1993 and 1994 year classes already in 2003 migrated south to the area east of Iceland.

Since 2005, the distribution pattern in May has been more or less the same, with only small inter annual variations which can also be seen in the CG for each year class for the herring age-disaggregated distribution. However, since 2017 the youngest year classes have been found more and more north. This new trend in distribution pattern was initiated by the relatively strong 2013 year class, but became more pronounced by the following year classes.

The herring stock is characterized by a large variability in recruitment (Toresen and Østvedt, 2000; ICES, 2021b). The recruitment can vary at least two orders of magnitude and it has been suggested that large year classes are able to change the behavior of the whole stock (Huse et al., 2010, 2002). However, the main changes seen in the last two decades have not been initiated by the youngest age groups of large year classes, but rather by older age groups.

Potential External Drivers

As mentioned in the introduction, changes in migration pattern have been hypothesized – and to some extent linked to – either abrupt changes in stock size or environmental factors. Based on our analyses, the observed changes in feeding migration pattern in 1999 and 2005, respectively, cannot be linked to abrupt changes in stock size. Thus an investigation of environmental factors, that possibly could have influenced the shift, is needed.

The waters north of Iceland became very cold (∼0°C) in 1995 (Astthorsson and Gislason, 2003) and this to some degree continued until 1998 (Malmberg and Valdimarsson, 2003) and relatively high volumes of fresh water were also observed in the East Icelandic Current at the same time (Jónsson, 2007; González-Pola et al., 2020; ICES, 2020). The herring distribution in 1998 did not extend as far west as in the period 2005–2020, which could be due to low temperatures west of and in the Jan Mayen Front during this period. Misund et al. (1997) documented that herring migrated to the Jan Mayen Front, but instead of crossing the front, the herring remained on the eastern side of the front. It is possible that low temperatures west of the Jan Mayen Front in May 1995–1998 acted as a barrier to the herring, prohibiting it to enter the frontal zone area as usual and consequently resulting in a withdrawal from the westernmost areas already in 1998. The mean winter weights of herring prior to this withdrawal were also below average which also can have affected the migration pattern or – vice versa, the low weights were perhaps due to suboptimal feeding conditions (Homrum et al., 2021).

Nonetheless, this withdrawal from the westernmost areas was followed by the northerly shift in 1999, when herring, which in 1996–1998 had occupied the southernmost areas in the Norwegian Sea, also abandoned these. The period in the mid 1990s and the first decade of this millennium was characterized by a weakening Subpolar Gyre, and thus a change in water mass composition and increased salinities and temperatures west of the British Isles (Hátún et al., 2005; Holliday et al., 2020). Whereas a strong Subpolar Gyre implies a stronger influence of nutrient rich subpolar water masses from the Labrador Sea, a weaker Gyre implies larger amounts of southern, nutrient poor water in this region (Hátún et al., 2016). Hátún et al. (2017) linked the weakening of the Subpolar Gyre to decreasing silicate concentration in the water masses entering the Nordic Seas, i.e., downstream from the region west of the British Isles and suggest that decreasing nutrients will cause a decrease in phytoplankton and thus, in turn, a decrease in zooplankton. The water masses that reached the Norwegian Sea were possibly also affected by these changes, both with regards to climate and prey for herring. Moreover, the mean winter weights of herring also continued to be low until around 2002, when they started to increase again (Homrum et al., 2021). It is therefore possible that it was bad feeding conditions that caused the herring to dismiss the southern part of the Norwegian Sea as feeding area in the period 1999–2005.

A decrease in zooplankton biomass indices from the IESNS survey occurred around 2003 (Kristiansen et al., 2016, 2019; ICES, 2020) which was also accompanied by a shift in species composition. The *C. hyperboreus* disappeared from the south-western Norwegian Sea and the abundances of the large overwintered *C. finmarchicus* individuals decreased. Further to this, Kristiansen et al. (2019), showed that the inflow of East Icelandic Water, which originates from the Iceland Sea and flows north and east of Iceland into the Norwegian Sea, where is submerges the Iceland-Faroe Front, decreased at this time, and has been fluctuating at a lower level until around 2017. It is possible that these changes in hydrography and zooplankton phenology and composition, in 2003–2005 caused the herring to again migrate to the previous feeding spot east of Iceland, since this is the source of the *C. hyperboreus* inflow into the Norwegian Sea and chances of finding large copepods are highest there at times when concentrations are low. It is also noteworthy that the CG since 2005 for the oldest fish in the stock, which are the most experienced (Misund et al., 1998; Corten, 2002; Huse et al., 2010), has been in a rather confined area around 65.5°N, 5°W, which is also where the Jan Mayen Front and the Iceland Faroe Front meet. Since the oldest herring has congregated there every May since 2005, it is likely that this area, which has been shown to be

rich in the large and nutritious *C. hyperboreus* and large stages of *C. finmarchicus* (e.g., Kristiansen et al., 2021), has been a feeding hotspot for the herring in recent years. This is further supported by the fact that herring has continued to feed in this area during the summer/autumn season and has had relatively high mean weights since 2005 (Homrum et al., 2021).

A discussion on external drivers during the study period requires mentioning the largest freshening event in the eastern subpolar North Atlantic in 120 years, which occurred 2012–2016 (González-Pola et al., 2020; Holliday et al., 2020). Although it's not likely that changes in salinity would affect the herring directly, changes in salinities are often associated with changes in water mass composition (Hátún et al., 2009; Kristiansen et al., 2019) and thus it could affect the zooplankton composition and thereby the herring feeding conditions. However, the most drastic change in the herring stock distribution during this period was the northerly shift observed in the youngest year classes from 2016 to 2018 (2013–2016 year classes). The 2013 year class was relatively strong (∼16% of the total stock abundance in 2016), but it was in particular the following two small year classes that drove the shift. Even though this is not a major change in distribution and young year classes were found northerly in the period 2005–2008 as well, this minor change in distribution could have been driven by the debut of a new relatively strong year class and by environmental factors.

In order to statistically verify or dismiss possible effects of environmental factors, a multidimensional study of all variables thought to affect the herring is needed. This could, e.g., be a multidimensional modeling or machine learning approach, where significant patterns and relationships are identified. However, the scope of this manuscript only allows a general discussion of external factors, since the aim of the analysis was to investigate whether the observed changes in spatio-temporal distribution of the herring during the feeding phase were caused by changes in age distribution within the stock.

CONCLUSION

The changes in the spatial distribution of Norwegian spring spawning herring in its main feeding period (May) were analyzed with regards to age distribution in the stock. The analysis implies a positive density dependent spatial dynamic in the stock.

The youngest herring were found in the eastern part of the Norwegian Sea closest to the Norwegian shelf and the proportion of older age classes gradually increased in the western areas. In the period 1999–2004, the whole stock abandoned the southern and western part of the Norwegian Sea and only occupied the northernmost parts for 4–6 years. These changes in distribution pattern were not driven by episodic changes, e.g., after a strong year class had just entered the stock. On the contrary, it was older fish (6–8 years old), that were dominating the stock during these changes. Thus, it is likely that external factors drove these changes. During the northern displacement, temperature and salinities increased and zooplankton abundances decreased in the Atlantic water masses upstream from the Norwegian Sea, which could be a reason for why the herring abandoned the southern part of the Norwegian Sea 1999–2004.

The little variation in the center of gravity and high weights for the oldest year classes after 2005 indicates that the frontal zone where the Jan Mayen Front and the Iceland-Faroe Front intersect is a feeding hotspot for herring.

We hope that this work will form a basis for further investigation of links between the herring stock and environmental factors through a multidimensional modeling or machine learning approach.

DATA AVAILABILITY STATEMENT

The data analyzed in this study is subject to the following licenses/restrictions: The data used in the manuscript are stored in a joint database (PGNAPES), and can only be accessed by the consent of all parties. Requests to access these datasets should be directed to GÓ, gjos@hafogvatn.is; AS, aril.slotte@hi.no; and JJ, janarge@hav.fo.

ETHICS STATEMENT

Ethical review and approval was not required for the animal study because no ethics approval was required as per institutional and national guidelines for this study and no animal experiments were performed.

AUTHOR CONTRIBUTIONS

SE composed the story told, did the data analyses, and led the writing process. EH, JJ, GÓ, AS, and ES gave input to the analysis process and to the discussion part of the manuscript. IK gave input to the discussion part of the manuscript. All authors have read, commented, and agreed to the manuscript before submission.

FUNDING

This study was carried out as part of the project "Sustainable multi-species harvest from the Norwegian Sea and adjacent ecosystems" funded by the Research Council of Norway (project number 299554).

ACKNOWLEDGMENTS

All researchers and crew on the IESNS cruises 1996–2020 are thanked for their valuable work in collecting and processing data used in this analysis.

SUPPLEMENTARY MATERIAL

The Supplementary Material for this article can be found online at: https://www.frontiersin.org/articles/10.3389/fmars.2021.778725/full#supplementary-material

REFERENCES

Astthorsson, O. S., and Gislason, A. (2003). Seasonal variations in abundance, development and vertical distribution of Calanus finmarchicus, C. hyperboreus and C. glacialis in the East Icelandic Current. *J. Plankton Res.* 25, 843–854. doi: 10.1093/plankt/25.7.843

Bachiller, E., Skaret, G., Nøttestad, L., and Slotte, A. (2016). Feeding ecology of Northeast Atlantic Mackerel, Norwegian spring-spawning herring and blue whiting in the Norwegian Sea. *PLoS One* 11:e0149238. doi: 10.1371/journal.pone.0149238

Bachiller, E., Utne, K. R., Jansen, T., and Huse, G. (2018). Bioenergetics modeling of the annual consumption of zooplankton by pelagic fish feeding in the Northeast Atlantic. *PLoS One* 13:e0190345. doi: 10.1371/journal.pone.0190345

Blindheim, J., and Østerhus, S. (2005). The Nordic Seas, Main Oceanographic Features. *Geophys. Monogr. Ser.* 158, 11–37. doi: 10.1029/158GM03

Böhme, L., and Send, U. (2005). Objective analyses of hydrographic data for referencing profiling float salinities in highly variable environments. *Deep Sea Res. Part II Top. Stud. Oceanogr.* 52, 651–664. doi: 10.1016/j.dsr2.2004.12.014

Broms, C., Melle, W., and Horne, J. K. (2012). Navigation mechanisms of herring during feeding migration: the role of ecological gradients on an oceanic scale. *Mar. Biol. Res.* 8, 461–474. doi: 10.1080/17451000.2011.640689

Broms, C., Melle, W., and Kaartvedt, S. (2009). Oceanic distribution and life cycle of Calanus species in the Norwegian Sea and adjacent waters. *Deep. Res. Part II Top. Stud. Oceanogr.* 56, 1910–1921. doi: 10.1016/j.dsr2.2008.11.005

Corten, A. (2002). The role of "conservatism" in herring migrations. *Rev. Fish Biol. Fish.* 11, 339–361. doi: 10.1023/A:1021347630813

Dalpadado, P., Ellertsen, B., Melle, W., and Dommasnes, A. (2000). Food and feeding conditions of Norwegian spring-spawning herring (*Clupea harengus*) through its feeding migrations. *ICES J. Mar. Sci.* 57, 843–857. doi: 10.1006/jmsc.2000.0573

Dommasnes, A., Melle, W., Dalpadado, P., and Ellertsen, B. (2004). Herring as a major consumer in the Norwegian Sea. *ICES J. Mar. Sci.* 61, 739–751. doi: 10.1016/j.icesjms.2004.04.001

Dragesund, O. (1980). Biology and population dynamics of the Norwegian spring-spawning herring. *Rapp. Réun. Cons. Int. Explor. Mer.* 177, 43–71.

Dragesund, O., Johannessen, A., and Ulltang, Ø (1997). Varlation in migration and abundance of norwegian spring spawning herring (*Clupea harengus* l.). *Sarsia* 82, 97–105. doi: 10.1080/00364827.1997.10413643

Fernö, A., Pitcher, T. J., Melle, W., Nøttestad, L., Mackinson, S., Hollingworth, C., et al. (1998). The challenge of the herring in the Norwegian sea: making optimal collective spatial decisions. *Sarsia* 83, 149–167. doi: 10.1080/00364827.1998.10413679

Foote, K. G. (1987). Fish target strengths for use in echo integrator surveys. *J. Acoust. Soc. Am.* 82, 981–987.

Gislason, A., and Astthorsson, O. S. (2002). The food of Norwegian spring-spawning herring in the western Norwegian Sea in relation to the annual cycle of zooplankton. *Sarsia* 87, 236–247. doi: 10.1080/00364820260294860

Gislason, A., and Silva, T., (2012). Abundance, composition, and development of zooplankton in the Subarctic Iceland Sea in 2006, 2007, and 2008. *ICES J. Mar. Sci.* 69, 1263–1276. doi: 10.1093/icesjms/fss070

González-Pola, C., Larsen, K. M. H., Fratantoni, P., and Beszczynska-Möller, A. (eds) (2020). *ICES Report on Ocean Climate 2019*. Copenhagen: International Council for the Exploration of the Sea.

Gudmundsdottir, A., Óskarsson, G., Krysov, A., Salthaug, A., Paulsrud Mjørlund, R., Høines, Å., et al. (2014). *Report of the Coastal States Working Group on the Distribution of Norwegian Spring Spawning Herring in the North-East Atlantic and the Barents Sea. Coastal States WG Herring 2014*. Available online at: https://lms.cdn.fo/media/5731/coastal_states_nssh_final_report.pdf?s=Qeeyyg_1gNyRlcPW3dCOMC-VNAw

Hátún, H., Lohmann, K., Matei, D., Jungclaus, J. H., Pacariz, S. V., Bersch, M., et al. (2016). An inflated subpolar gyre blows life towards the northeastern Atlantic. *Prog. Oceanogr.* 147, 49–66. doi: 10.1016/j.pocean.2016.07.009

Hátún, H., Olsen, B., and Pacariz, S. V. (2017). The Dynamics of the North Atlantic Subpolar Gyre Introduces Predictability to the Breeding Success of Kittiwakes. *Front. Mar. Sci.* 4:123. doi: 10.3389/fmars.2017.00123

Hátún, H., Payne, M. R., Beaugrand, G., Reid, P. C., Sandø, A. B., Drange, H., et al. (2009). Large bio-geographical shifts in the north-eastern Atlantic Ocean: from the subpolar gyre, via plankton, to blue whiting and pilot whales. *Prog. Oceanogr.* 80, 149–162. doi: 10.1016/j.pocean.2009.03.001

Hátún, H., Sandø, A. B., Drange, H., Hansen, B., and Valdimarsson, H. (2005). Influence of the Atlantic subpolar gyre on the thermohaline circulation. *Science* 309, 1841–1844. doi: 10.1126/science.1114777

Holliday, N. P., Bersch, M., Berx, B., Chafik, L., Cunningham, S., Florindo-López, C., et al. (2020). Ocean circulation causes the largest freshening event for 120 years in eastern subpolar North Atlantic. *Nat. Commun.* 11:585. doi: 10.1038/s41467-020-14474-y

Homrum, E., Óskarsson, G. J., Ono, K., Hølleland, S., and Slotte, A. (2021). Large-scale changes in the spatiotemporal distribution of Norwegian spring spawning herring (*Clupea harengus*) following warming and freshening of the Norwegian Sea: effects on body growth, somatic condition and gonad development. *Front. Mar. Sci.*

Holst, J. C., Røttingen, I., and Melle, W. (2004). "The Herring," in *The Norwegian Sea Ecosystem*, ed. H. R. Skjoldal (Trondheim: Tapir Academic Press), 203–226.

Holst, J. C., and Slotte, A. (1998). Effects of juvenile nursery on geographic spawning distribution in Norwegian spring-spawning herring (*Clupea harengus* L.). *ICES J. Mar. Sci.* 55, 987–996. doi: 10.1006/jmsc.1998.0371

Huse, G., Fernö, A., and Holst, J. C. (2010). Establishment of new wintering areas in herring co-occurs with peaks in the "first time/repeat spawner" ratio. *Mar. Ecol. Prog. Ser.* 409, 189–198. doi: 10.3354/meps08620

Huse, G., Railsback, S., and Fernö, A. (2002). Modelling changes in migration pattern of herring: collective behaviour and numerical domination. *J. Fish Biol.* 60, 571–582. doi: 10.1006/jfbi.2002.1874

Huse, G., Utne, K. R., and Fernö, A. (2012). Vertical distribution of herring and blue whiting in the Norwegian Sea. *Mar. Biol. Res.* 8, 488–501. doi: 10.1080/17451000.2011.639779

ICES (2014). *2nd Interim Report of the Working Group on Integrated Assessments of the Norwegian Sea (WGINOR)*. Torshavn: ICES.

ICES (2020). *Working Group on the Integrated Assessments of the Norwegian Sea (WGINOR; Outputs From the 2019 Meeting), ICES Scientific Reports. 2:29*. Copenhagen: ICES. doi: 10.17895/ices.pub.5996

ICES (2021b). *Working Group on Widely Distributed Stocks (WGWIDE), Ices Scientific Reports. 3:95*. Copenhagen: ICES. doi: 10.17895/ices.pub.8298

ICES (2021a). *ICES Fisheries Management Reference Points for Category 1 and 2 Stocks; Technical Guidelines. In Report of the ICES Advisory Committee, 2021*. Copenhagen: ICES. doi: 10.17895/ices.advice.7891

Jónsson, S. (2007). Volume flux and fresh water transport associated with the East Icelandic Current. *Prog. Oceanogr.* 73, 231–241. doi: 10.1016/j.pocean.2006.11.003

Kristiansen, I., Gaard, E., Hátún, H., Jónasdóttir, S. H., and Ferreira, A. S. A. (2016). Persistent shift of Calanus spp. in the southwestern Norwegian Sea since 2003, linked to ocean climate. *ICES J. Mar. Sci.* 73:fsv222. doi: 10.1093/icesjms/fsv222

Kristiansen, I., Hátún, H., Jacobsen, J. A., Eliasen, S. K., Petursdottir, H., and Gaard, E. (2021). Spatial variability of the feeding conditions for the Norwegian spring spawning herring in May. *Front. Mar. Sci.*

Kristiansen, I., Hátún, H., Petursdóttir, H., Gislason, A., Broms, C., Melle, W., et al. (2019). Decreased influx of Calanus spp. into the south-western Norwegian Sea since 2003. *Deep. Res. Part I Oceanogr. Res. Pap.* 149:103048. doi: 10.1016/j.dsr.2019.05.008

Kvamme, C., Nøttestad, L., Fernö, A., Misund, O. A., Dommasnes, A., Axelsen, B. E., et al. (2003). Migration patterns in Norwegian spring-spawning herring: why young fish swim away from the wintering area in late summer. *Mar. Ecol. Prog. Ser.* 247, 197–210. doi: 10.3354/meps247197

Langård, L., Skaret, G., Jensen, K. H., Johannessen, A., Slotte, A., Nøttestad, L., et al. (2015). Tracking individual herring within a semi-enclosed coastal marine ecosystem: 3-dimensional dynamics from pre- to post-spawning. *Mar. Ecol. Prog. Ser.* 518, 267–279. doi: 10.3354/meps11065

Langøy, H., Nøttestad, L., Skaret, G., Broms, C., and Fernö, A. (2012). Overlap in distribution and diets of Atlantic mackerel (*Scomber scombrus*), Norwegian spring-spawning herring (*Clupea harengus*) and blue whiting (*Micromesistius poutassou*) in the Norwegian Sea during late summer. *Mar. Biol. Res.* 8, 442–460. doi: 10.1080/17451000.2011.642803

Malmberg, S.-A., and Valdimarsson, H. (2003). Hydrographic conditions in Icelandic waters, 1990-1999. *ICES Mar. Sci. Symp.* 219, 50–60.

Marti, Y. Y. (1956). "The fundamental stages of the life cycle of Atlantic-Scandinavian herring," in *Herring of the North European Basin and Adjacent Seas*, ed L. W. Scattergood (Washington: United States Fish and Wildlife Service), 5–68.

McQuinn, I. H. (1997). Metapopulations and the Atlantic herring. *Rev. Fish Biol. Fish* 7, 297–329. doi: 10.1023/A

Melle, W., Klevjer, T., Strand, E., Wiebe, P. H., Slotte, A., and Huse, G. (2020). Fine-scale observations of physical and biological environment along a herring feeding migration route. *Deep. Res. Part II Top. Stud. Oceanogr.* 180:104845. doi: 10.1016/j.dsr2.2020.104845

Misund, O. A., Melle, W., and Fernö, A. (1997). Migration behaviour of norwegian spring spawning herring when entering the cold front in the norwegian sea. *Sarsia* 82, 107–112. doi: 10.1080/00364827.1997.10413644

Misund, O. A., Vilhjálmsson, H., Jákupsstovu, S. H. í, Røttingen, I., Belikov, S., Astthorsson, O. S., et al. (1998). Distribution, migration and abundance of norwegian spring spawning herring in relation to the temperature and zooplankton biomass in the Norwegian Sea as recorded by coordinated surveys in spring and summer 1996. *Sarsia* 83, 117–127. doi: 10.1080/00364827.1998.10413677

Nøttestad, L., Giske, J., Holst, J. C., and Huse, G. (1999). A length-based hypothesis for feeding migrations in pelagic fish. *Can. J. Fish. Aquat. Sci.* 56, 26–34. doi: 10.1139/f99-222

Olsen, E. M., Melle, W., Kaartvedt, S., Holst, J. C., and Mork, K. A. (2007). Spatially structured interactions between a migratory pelagic predator, the Norwegian spring-spawning herring *Clupea harengus* L., and its zooplankton prey. *J. Fish Biol.* 70, 799–815. doi: 10.1111/j.1095-8649.2007.01342.x

Pavshtiks, E. A. (1956). Seasonal Changes in Plankton and Feeding Migrations of Herring. *Herring North Eur. Basin Adjac. Seas* 1, 104–139.

Prokopchuk, I. (2009). Feeding of the Norwegian spring spawning herring *Clupea harengus* (Linne) at the different stages of its life cycle. *Deep. Res. Part II Top. Stud. Oceanogr.* 56, 2044–2053. doi: 10.1016/j.dsr2.2008.11.015

Prokopchuk, I., and Sentyabov, E. (2006). Diets of herring, mackerel, and blue whiting in the Norwegian Sea in relation to Calanus finmarchicus distribution and temperature conditions. *ICES J. Mar. Sci.* 63, 117–127. doi: 10.1016/j.icesjms.2005.08.005

Read, J. F., and Pollard, R. T. (1992). Water Masses in the Region of the Iceland-Fćroes Front. *J. Phys. Oceanogr.* 22:1365–1378. doi: 10.1175/1520-04851992022<1365

Rudakova, V. A. (1956). "Data on the food of the Atlantic herring," in *Herring of the North European Basin and Adjacent Seas*, ed L. W. Scattergood (Washington: United States Fish and Wildlife Service), 140–155.

Salthaug, A., Stenevik, E. K., Vatnehol, S., Anthonypillai, V., Ona, E., and Slotte, A. (2020). *Survey Report: Distribution and Abundance of Norwegian Spring Spawning Herring During The Spawning Season in 2020*. Bergen: Institute of Marine Research.

Slotte, A. (1999). Effects of fish length and condition on spawning migration in Norwegian spring spawning herring (*Clupea harengus* L.). *Sarsia* 84, 111–127. doi: 10.1080/00364827.1999.10420439

Slotte, A., Johannessen, A., and Kjesbu, O. S. (2000). Effects of fish size on spawning time in Norwegian spring-spawning herring. *J. Fish Biol.* 56, 295–310. doi: 10.1006/jfbi.1999.1161

Slotte, A., Salthaug, A., Højnes, Å, Stenevik, E. K. K., Vatnehol, S., Ona, E., et al. (2018). *Survey Report: Distribution and Abundance of Norwegian Spring Spawning Herring During the Spawning Season in 2018*. Bergen: Institute of Marine Research.

Toresen, R., and Østvedt, O. J. (2000). Variation in abundance of Norwegian spring-spawning herring (*Clupea harengus*, Clupeidae) throughout the 20th century and the influence of climatic fluctuations. *Fish Fish.* 1, 231–256. doi: 10.1111/j.1467-2979.2000.00022.x

Utne, K. R., and Huse, G. (2012). Estimating the horizontal and temporal overlap of pelagic fish distribution in the Norwegian Sea using individual-based modelling. *Mar. Biol. Res.* 8, 548–567. doi: 10.1080/17451000.2011.639781

Utne, K. R., Huse, G., Ottersen, G., Holst, J. C., Zabavnikov, V., Jacobsen, J. A., et al. (2012). Horizontal distribution and overlap of planktivorous fish stocks in the Norwegian Sea during summers 1995 -2006. *Mar. Biol. Res.* 8, 420–441. doi: 10.1080/17451000.2011.640937

Varpe, Ø, Fiksen, Ø, and Slotte, A. (2005). Meta-ecosystems and biological energy transport from ocean to coast: the ecological importance of herring migration. *Oecologia* 146, 443–451. doi: 10.1007/s00442-005-0219-9

Wiborg, K. F. (1955). Zooplankton in relation to hydrography in the Norwegian Sea. *Fisk. Skr. Ser. Havundersøkelser* 11, 1–66.

Conflict of Interest: The authors declare that the research was conducted in the absence of any commercial or financial relationships that could be construed as a potential conflict of interest.

Publisher's Note: All claims expressed in this article are solely those of the authors and do not necessarily represent those of their affiliated organizations, or those of the publisher, the editors and the reviewers. Any product that may be evaluated in this article, or claim that may be made by its manufacturer, is not guaranteed or endorsed by the publisher.

Copyright © 2021 Eliasen, Homrum, Jacobsen, Kristiansen, Óskarsson, Salthaug and Stenevik. This is an open-access article distributed under the terms of the Creative Commons Attribution License (CC BY). The use, distribution or reproduction in other forums is permitted, provided the original author(s) and the copyright owner(s) are credited and that the original publication in this journal is cited, in accordance with accepted academic practice. No use, distribution or reproduction is permitted which does not comply with these terms.

frontiers in Marine Science

ORIGINAL RESEARCH
published: 25 January 2022
doi: 10.3389/fmars.2021.778335

Impact of Decadal Trends in the Surface Climate of the North Atlantic Subpolar Gyre on the Marine Environment of the Barents Sea

Vimal Koul[1,2]*, *Sebastian Brune*[2], *Johanna Baehr*[2] *and Corinna Schrum*[1,2]

[1] Helmholtz Zentrum Hereon, Institute of Coastal Systems, Geesthacht, Germany, [2] Institute of Oceanography, Center for Earth System Research and Sustainability, Universität Hamburg, Hamburg, Germany

The Barents Sea is a key region in the Earth System and is home to highly productive marine resources. An integrated approach for strategic sustainable management of marine resources in such shelf-sea marine ecosystems requires, among many other aspects, a robust understanding of the impact of climate on local oceanic conditions. Here, using a combined observational and modelling approach, we show that decadal climatic trends associated with the North Atlantic Subpolar Gyre (SPG), within the period 1960–2019, have an impact on oceanic conditions in the Barents Sea. We relate hydrographic conditions in the Barents Sea to the decadal variability of the SPG through its impact on the Atlantic Inflow via the Faroe-Shetland Channel and the Barents Sea Opening. When the SPG warms, an increase in the throughput of subtropical waters across the Greenland-Scotland Ridge is followed by an increase in the volume of Atlantic Water entering the Barents Sea. These changes are reflected in pronounced decadal trends in the sea-ice concentration and primary production in the Barents Sea, which follow the SPG after an advective delay of 4–5 years. This impact of the SPG on sea-ice and primary production provides a dynamical explanation of the recently reported 7-year lagged statistical relationship between SPG and cod (*Gadus morhua*) biomass in the Barents Sea. Overall, these results highlight a potential for decadal ecosystem predictions in the Barents Sea.

Keywords: Barents Sea, Subpolar Gyre, Atlantic Inflow, marine ecosystems, decadal variability

OPEN ACCESS

Edited by:
Oeystein Skagseth, Norwegian Institute of Marine Research (IMR), Norway

Reviewed by:
Manuel Bensi, Istituto Nazionale di Oceanografia e di Geofisica Sperimentale, Italy
Anne Britt Sando, Norwegian Institute of Marine Research (IMR), Norway

***Correspondence:**
Vimal Koul
vimal.koul@hereon.de

Specialty section:
This article was submitted to Physical Oceanography, a section of the journal Frontiers in Marine Science

Received: *16 September 2021*
Accepted: *20 December 2021*
Published: *25 January 2022*

Citation:
Koul V, Brune S, Baehr J and Schrum C (2022) Impact of Decadal Trends in the Surface Climate of the North Atlantic Subpolar Gyre on the Marine Environment of the Barents Sea. Front. Mar. Sci. 8:778335. doi: 10.3389/fmars.2021.778335

1. INTRODUCTION

The Subpolar Gyre (SPG) of the North Atlantic is a cyclonically circulating oceanic gyre that exhibits pronounced decadal-to-multidecadal variability in its properties (Delworth et al., 1993; Marshall et al., 2001; Böning et al., 2006; Born and Mignot, 2012). Over the last sixty years, periods of strong decadal trends in surface temperature of the SPG (-60:10 °E, 50:62 °N) have been observed—cooling in the 1960s, the warming in the 1990s and the recent cooling in the 2000s (Dickson et al., 1988; Bersch et al., 2007; Reverdin, 2010; Robson et al., 2016; Piecuch et al., 2017; Holliday et al., 2020). The SPG has also been widely implicated as the source of large-scale changes in the subpolar marine environment (Hátún et al., 2009, 2016), and is thought to influence the properties of the Atlantic Inflow to the Nordic Seas (Hátún et al., 2005; Koul et al., 2020; Asbjørnsen et al., 2021). Recently, the SPG was also shown to impart decadal predictability to the cod (*Gadus morhua*) stock

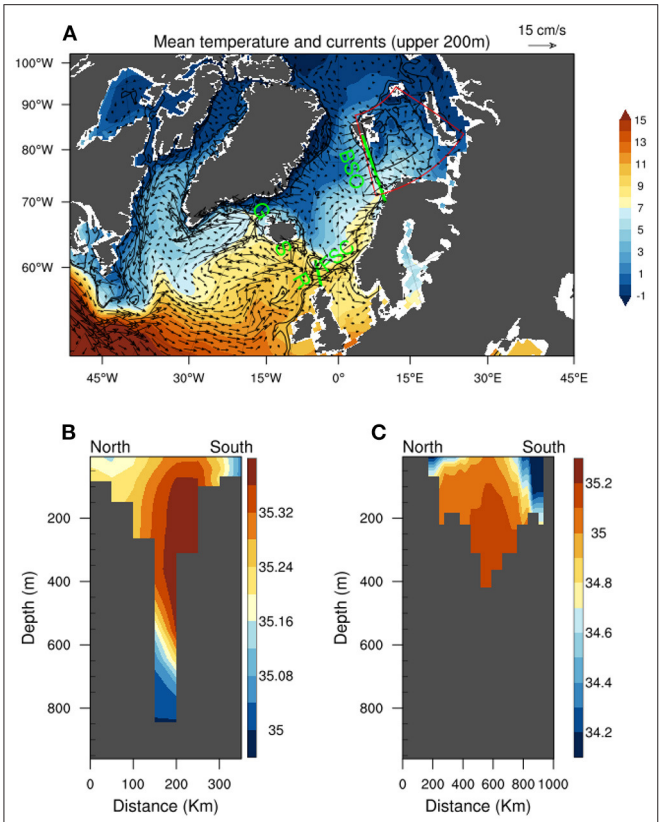


FIGURE 1 | (A) Mean (1960:2019 average) temperature and currents (upper 200 m) in the subpolar North Atlantic from the assimilation experiment. The black lines show 200 m and 500 m isobaths. Mean salinity at the hydrographic section at **(B)** Faroe Shetland Channel (FSC) and **(C)** Barents Sea Opening (BSO). The sections are shown as green lines in **(A)**. The Barents Sea regions analyzed in this study are defined as the black box (for wind stress curl) and red box (for Atlantic Water volume) in **(A)**.

in the Barents Sea (Årthun et al., 2018; Koul et al., 2021). However, the underlying dynamical mechanisms linking the decadal trends in the SPG to the Barents Sea, via the Faroe-Shetland Channel (FSC) and the Barents Sea Opening (BSO) (**Figure 1**), and their impact on local marine environment remained incompletely understood.

The Barents Sea is a highly productive shelf sea and is open to the influence of the Atlantic Ocean through the southwest. It acts as a transition zone for the warm and saline Atlantic Water headed toward the Arctic Ocean and plays an important role in the transformation of Atlantic water masses (Smedsrud et al., 2013). Over the past decades, the climate of the Barents Sea has undergone a dramatic change. The sea-ice area in the Barents Sea has declined by more than 50% in the last 30 years (Årthun et al., 2012), and the area occupied by the warm and saline Atlantic Water has nearly doubled (Dalpadado et al., 2012; Oziel et al., 2017). Observations also reveal large shifts in fish communities resulting from the "Atlantification" [increase in Atlantic Water transport into the Barents Sea and subsequent decline in sea-ice extent, see Årthun et al. (2012)] of the Barents Sea (Fossheim et al., 2015). While the greenhouse gas warming is an important factor in driving these observed long term changes in the Barents Sea, an important role of the variability originating in the subpolar North Atlantic in driving decadal to multi-decadal changes in the Barents Sea has also been well recognised (Levitus et al., 2009; Yashayaev and Seidov, 2015; Årthun et al., 2019).

An important source of climate and ecosystem variability in the Barents Sea is the inflowing Atlantic Water at its southwestern entrance, i.e., at the BSO (Ottersen and Stenseth, 2001; Smedsrud et al., 2010). An increase in the volume flux of the Atlantic Water is positively correlated with the temperature of the Barents Sea (Oziel et al., 2017). At interannual to decadal timescales (1–10 years), the variability in the volume flux of Atlantic Water at the BSO is, in-turn, largely driven by atmospheric variability associated with the North Atlantic Oscillation (NAO, Ingvaldsen et al., 2003; Sandø et al., 2010). For example, periods of a positive NAO are associated with enhanced southwesterly winds which increase the volume flux of Atlantic Water and plankton into the Barents Sea (Drinkwater et al., 2003). However, the relationship between large scale atmospheric winds associated with the NAO and the volume flux of Atlantic Water into the Barents Sea is non-stationary (Smedsrud et al., 2013), and there are periods when the role of local wind forcing dominates (Orvik and Skagseth, 2003; Lien et al., 2017; Muilwijk et al., 2018).

Apart from the variability in the volume flux of the Atlantic Water at the BSO, a change in Barents Sea temperature can occur due to a change in temperature of inflowing Atlantic Water. In this case as well, the NAO can influence the temperature of the inflowing water through its impact on the width of the Norwegian Atlantic Current and thereby controlling how much heat this current exchanges with the atmosphere (Ådlandsvik and Loeng, 1991). Another source of changes in the temperature of inflowing Atlantic Water is the thermohaline anomalies originating in the subpolar North Atlantic which are known to propagate downstream toward the Nordic Seas (Holliday et al., 2008; Yashayaev and Seidov, 2015). On multidecadal timescales (>50 years), the climate of the Barents Sea varies with the Atlantic Multidecadal Variability (AMV, Levitus et al., 2009; Yashayaev and Seidov, 2015), a manifestation of the rise and fall of North Atlantic surface temperatures. Embedded in such variability is decadal to multidecadal variability (also called inter-decadal timescales) associated with the SPG, the impact of which is the focus of the present study.

At decadal to multi-decadal time scales (10–20 years), the origin and propagation of heat and freshwater anomalies into the Nordic Seas and further downstream toward the Arctic has been investigated in observations and model simulations (Glessmer et al., 2014; Årthun and Eldevik, 2016; Langehaug et al., 2019). A consistent view emerging from these studies is that the variability in large scale oceanic circulation in the subpolar North Atlantic is the source of oceanic anomalies propagating into the Nordic Seas and further downstream. However, in light of the reported advective lags, it is not known whether and to what extent the observed hydrographic and biogeochemical anomalies in the Barents Sea follow the decadal trends in the surface climate of the SPG.

In this article, we investigate SPG-driven dynamical links between the variability in the Atlantic Inflow at the FSC and at the BSO extending back to 1960, and the subsequent impact of such variability on the volume of Atlantic Water and the sea-ice in the Barents Sea. We assess three dominant decadal trends in the surface temperature of the SPG whose impact on the Barents Sea is likely to be pronounced. Our results illustrate that the SPG signal can be traced in sub-surface properties at the BSO, and we hypothesise that by modulating the throughput of the Atlantic Water, the SPG causes variability in Atlantic Water volume in the Barents Sea. Our results also illuminate the dynamical basis for the recently reported statistical relationship between the SPG and cod biomass in the Barents Sea (Årthun et al., 2018; Koul et al., 2021). Changes in Atlantic Water volume have an impact on cod biomass through changes in sea-ice extent and primary production in the Barents Sea.

2. MATERIALS AND METHODS

The available oceanic observations in the subpolar North Atlantic cover important hydrographic sections but do not provide a continuous spatiotemporal record of surface and sub-surface temperature, salinity, and velocity fields extending back to 1960s. In this respect, we carry a data assimilation experiment with an Earth System Model that combines available atmospheric and oceanic observations and model output to provide a continuous spatiotemporal record over the past 60 years. The climatological temperature, salinity and velocity fields from this data assimilation experiment over the regions of interest are shown in **Figure 1** and **Supplementary Figure 1**.

Time series of surface temperature over the SPG (area averaged over -60:-10 °E, 50:62 °N) and BSO (area averaged over 10:25 °E, 70:78 °N) from this assimilation experiment compare very well with observations (Koul et al., 2021) and are analyzed in the present work. Additionally, satellite observations of sea-ice concentration (Meier et al., 2021, data retrieved from https://nsidc.org/data/g02202/versions/4/) and chlorophyll-derived net primary production (Behrenfeld and Falkowski, 1997, data retrieved from http://orca.science.oregonstate.edu/1080.by.2160.monthly.hdf.vgpm.m.chl.m.sst.php) are also analyzed to complement the results from the assimilation experiment. The time series of the TSB of Northeast Arctic Cod is obtained from the ICES Arctic Fisheries Working Group's report (http://doi.org/10.17895/ices.pub.6050).

We also analyze the time series of the annual mean volume transport through the FSC and the BSO (see **Figure 1** for the location of these sections). We define "total volume transport" as the volume transport (Sv, 1 Sv $= 10^6$ m^3 s^{-1}) of all eastward (u>0) flowing waters in the entire water column. The 1960–2019 mean total volume transport is about 5.9 Sv at the FSC and 3.65 Sv at the BSO which is larger than the observational estimates of 4 Sv at the FSC (Berx et al., 2013) and 1.8 Sv at the BSO (Skagseth et al., 2008) but within the range of estimates from other global ocean models (Ilıcak et al., 2016). We distinguish the total volume transport from the "Atlantic Inflow," which is defined as the volume transport of all eastward (u>0) flowing waters in the entire water column with T>8.5 °C, S>35.25 at the FSC, and T>5.5 °C, S>35.0 at the BSO. The Atlantic Inflow is essentially the warm and saline part of the total volume transport. Within the Barents Sea, the spatial extent of the volume of the warm and saline water is also analyzed. We define "Atlantic Water" as water with T>3 °C and S>34.8 (Oziel et al., 2016).

2.1. Model

The Max Planck Institute Earth System Model (MPI-ESM) is a global Earth system model, and is used in its low resolution (LR) setup in the present study (hereafter MPI-ESM-LR). The ocean general circulation component of MPI-ESM-LR, the Max Planck Institute Ocean Model, MPIOM (Jungclaus et al., 2013), is a free surface model with primitive equation solved on an Arakawa C-grid, and with hydrostatic and Boussinesq approximations. It has a total of 40 z-levels in the vertical and the surface layer thickness is 12 meters. Formulations by Pacanowski and Philander (1981) are followed for vertical mixing and diffusion, and tracer transport is parameterized following Gent et al. (1995). Statically unstable flow over sills and shelves is represented by a slope-convection scheme (Marsland et al., 2003).

The MPIOM setup used in the study has a rotated grid configuration (GR15) for which the singularity at the North Pole is replaced over Greenland. This has the advantage that horizontal resolution is enhanced north of 50°N, reaching 15 KM near Greenland. Otherwise, the nominal horizontal resolution of MPIOM in LR setup is 1.5 degrees. Embedded in MPIOM is also the ocean biogeochemistry component, the Hamburg Ocean Carbon Cycle model, HAMOCC (Ilyina et al., 2013). Among other processes, HAMOCC incorporates phosphate and oxygen cycles, and defines marine food web based on nutrients, phytoplankton, zooplankton, and detritus (NPZD) based approach.

The atmospheric general circulation component of MPI-ESM-LR is the European Center-Hamburg model, ECHAM, (Stevens et al., 2013). In MPI-ESM1.2-LR, the ECHAM is run at a horizontal resolution of T63 and with 47 vertical levels, the model top being at 0.0 1hPa. The land surface-atmosphere interactions are simulated by the land vegetation module, JSBACH (Reick et al., 2013) which is embedded in ECHAM. A land hydrology module which contains a river-routing scheme is used for interactive simulation of river runoff (Hagemann and Gates, 2003), MPIOM receives the fresh water fluxes due to river runoff as part of the precipitation field from ECHAM.

2.2. Model Experiment

We analyze a data assimilation experiment (1960–2019) carried out with MPI-ESM-LR using an oceanic ensemble Kalman filter (EnKF) and atmospheric nudging. The oceanic EnKF in MPI-ESM-LR (Brune et al., 2015; Brune and Baehr, 2020) assimilates monthly profiles of temperature and salinity from EN4 (Good et al., 2013). Simultaneously, atmospheric vorticity, divergence, temperature, and surface pressure are nudged to ERA40/ERAInterim re-analyses (Dee et al., 2011). It should be noted that neither sea surface temperature from satellite observations nor atmospheric temperature below 900 hPa are assimilated in order to allow for a model-consistent assimilation

across the atmosphere-ocean boundary. The assimilation experiment uses observed solar irradiation, volcanic eruptions, and atmospheric greenhouse gas concentrations (SSP2-4.5 concentrations from 2015 onward) as boundary conditions, taken from CMIP6 (Eyring et al., 2016).

2.3. Trend Analysis and Statistical Significance

We compute linear trends over three periods of 10-years each except for sea-ice concentration and primary production wherein only 9 years from the last decade are considered after taking into account the advective delays from the SPG to the Barents Sea (detailed explanation is provided in the results and discussion sections). The statistical significance of the trend is calculated using a bootstrap approach wherein robust properties of a statistic (in this case the linear trend) are computed through random sampling and replacement to generate a distribution of the statistic. The confidence interval is taken as the 90% range (5^{th} to 95^{th} percentile) of this distribution. Our null hypothesis is that of a zero trend, and we fail to reject the null hypothesis if zero lies within the confidence intervals. Other non-parametric estimates of the linear trend and their statistical significance such as the Theil-Sen estimate of linear trend and the Mann-Kendall test were also evaluated (figures not shown). Except for the statistical significance of the 9-year trends for sea-ice and primary production (in our analysis, at-least 10-years are required for the Mann-Kendall test), our results are robust to these different estimates of decadal trends.

2.4. Correlations and Statistical Significance

All the correlations presented in this article are calculated from detrended time series (linear trend over 1960–2019 is removed). The non-detrended time series are presented in the main text. The statistical significance of correlation is assessed using a two tailed *t*-test. To account for the autocorrelation in the time series, the degrees of freedom is calculated by taking into account the lag-1 autocorrelation of the time series (Bretherton et al., 1999).

3. RESULTS

Decadal trends can be identified in surface temperature (T) and salinity (S) of the SPG over the past sixty years (**Figure 2**). Three decades clearly stand out when the trends were strong: (a) the cooling from 1966 to 1975, coinciding with the "great salinity anomaly" (Dickson et al., 1988), (b) the warming and salinification from 1996 to 2005, coinciding with a marked shift in the NAO phase in the winter of 1995/96 (Bersch et al., 2007), and (c) the cooling from 2006 to 2015, when the largest freshening event in more than a century was observed (Holliday et al., 2020). The basin-wide extent of the spatial patterns of these decadal trends and the concurrence of the periods of cooling and freshening as well as those of warming and salinification suggest that variability in large scale ocean circulation is involved (Piecuch et al., 2017; Koul et al., 2020). In the subsequent analysis, we investigate whether decadal trends corresponding to these three periods also emerge, after some years, in the regional environment of the Barents Sea.

A likely impact of the SPG on local oceanic conditions in the Barents Sea is implicitly hinted by the high correlation between the total stock biomass (TSB) of Northeast Arctic cod and SPG properties (**Figure 2** and **Table 1**). The TSB is the total biomass of mature and immature fish and it reflects the integrated impact of climate on fish population. The TSB time series suggests that the cod has undergone periods of decline and recovery, mainly at decadal to multi-decadal timescales (**Figure 2**). There is a statistically significant and high correlation between the TSB and SPG T/S (see **Table 1**), as was found in earlier investigations (Årthun et al., 2018; Koul et al., 2021). The correlation of TSB with surface salinity ($r = 0.82$) is similarly high as that with surface temperature ($r = 0.77$), which hints at a role of inflowing Atlantic Water into the Barents Sea. Read together with their advective lags, these high positive correlations point toward a possible impact of the SPG variability on cod biomass. As we show below, the SPG-driven changes in the Atlantic Inflow into the Barents Sea plays an important role.

The Atlantic Inflow mainly enters the Barents Sea through the BSO (see **Figure 1** for the location of this region). Before arriving at the BSO, the Atlantic Inflow crosses the Greenland-Scotland Ridge (Hátún et al., 2005) and passes through the FSC (Hansen et al., 2008). As illustrated in **Figure 1**, the core of Atlantic Inflow is seen as subsurface salinity maxima in the water column. Thus, the correlations of the SPG T and S are lower with respective surface T and S at the BSO than with sub-surface T and S (**Figure 3** and **Table 1**). Note that the correlations are calculated from linearly detrended time series. The decadal to multi-decadal variability, particularly the freshening of the BSO from 1970 to 1979 (corresponding to the freshening of the SPG in the late 1960s) clearly emerges in sub-surface salinity time series and to some extent in the corresponding decrease of the sub-surface temperature only. The lack of correlation of the surface T and S at the BSO with the SPG T and S together with pronounced interannual variability at the surface suggests a dominating impact of overlying atmospheric variability.

Another way to assess the impact of SPG on oceanic properties downstream of the Greenland-Scotland Ridge is through the variability in volume transport. The mean total volume transport (see Methods for the definition) is high at the FSC and relatively low at the BSO—the 1960–2019 mean volume transport is about 5.9 Sv at the FSC and 3.65 Sv at the BSO. Downstream of the FSC, the Atlantic Water mixes with ambient water masses and dilutes its properties. This is apparent in the maximum total volume transport which occurs at T = 9-10 °C and S = 35.3-35.4 at the FSC and at T = 6-7 °C and S = 35.0-35.1 at the BSO (**Figure 4**). The decadal to multi-decadal variability seen in the SPG is present in the Atlantic Inflow. The Atlantic Inflow (see Methods for the definition) through the FSC decreased during the cooling and freshening of the SPG in 1960s, the inflow increased during the warming and salinification of the SPG in mid 1990s, and the recent cooling of the SPG has coincided with ongoing reduction of the Atlantic Water (**Figure 4**).

The low frequency character of the Atlantic Inflow at the FSC is also largely seen in the Atlantic Inflow at the BSO ($r = 0.67$,

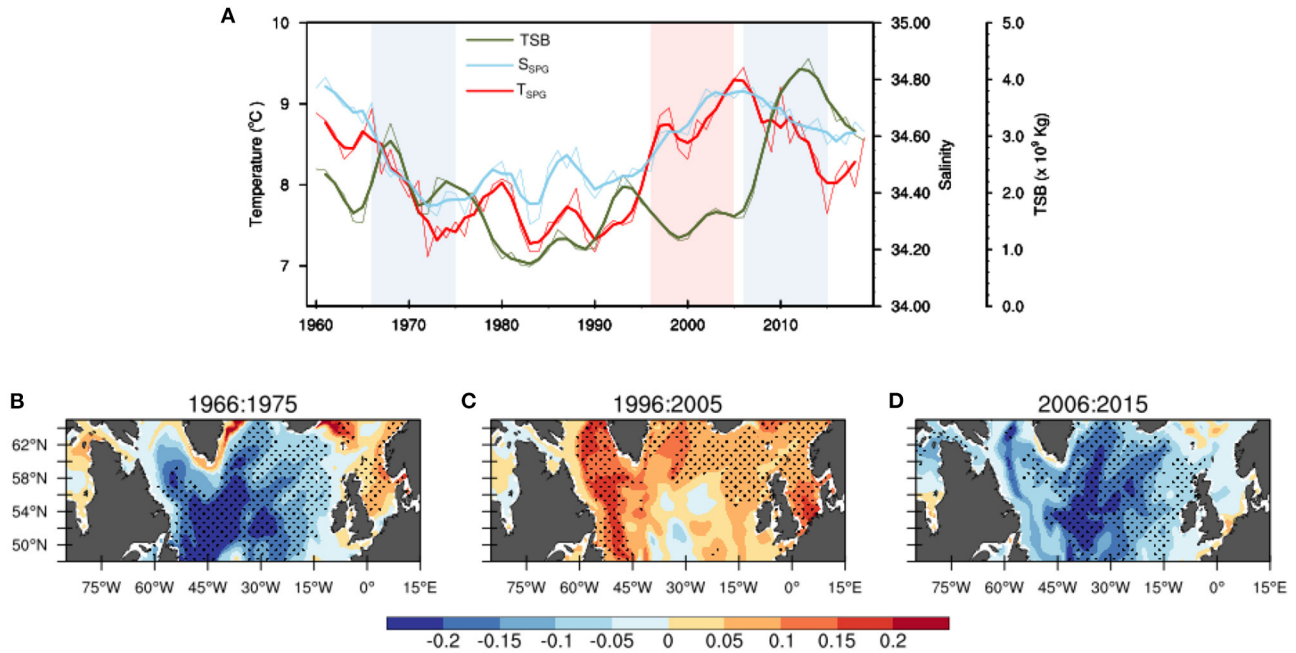


FIGURE 2 | (A). Time series of modelled surface temperature and surface salinity of the North Atlantic Subpolar Gyre (-60:-10 °E, 50:62 °N) from the assimilation experiment, and total stock biomass of cod in the Barents Sea for the period 1960–2019. For each of the time series shown, light lines are annual means and bold lines are three-year running mean values. The time series are not linearly detrended. The blue and red shaded time periods highlight the three dominant decadal trends. Trends in the surface temperature of the North Atlantic Subpolar Gyre ($^oC\ yr^{-1}$) for **(B)** 1966–1975 cooling, **(C)** 1996–2005 warming, and **(D)** 2006–2015 cooling. The stippling marks statistically significant trends at 90% confidence level.

TABLE 1 | Pearson's correlation coefficients (r) among various variables and the lag at which r is maximum (@Lag (years)).

	TSB	*BSO T_{6m}*	*BSO T_{200m}*	*BSO S_{6m}*	*BSO S_{200m}*	*FSC Atl. Inflow*	*BSO Atl. Inflow*	*BS Aw Vol.*	*BS Sice. Ar.*
SPG T_{6m}	**0.77** @7	0.27 @4	0.38 @4	0.31 @4	**0.79** @4	**0.64** @3	**0.59** @4	x	x
SPG S_{6m}	**0.82** @7	0.22 @5	0.41 @4	0.22 @5	**0.76** @4	**0.57** @3	**0.56** @4	x	x
FSC Atl. Inflow	x	x	x	x	x	x	**0.67** @1	x	x
BSO Atl. Inflow	x	x	x	x	x	x	x	**0.80** @1	**-0.51** @1
BS Aw. Vol.	x	x	x	x	x	x	x	x	**-0.62** @0

The bold values are correlations that are significant at 95% confidence level.

lag = 1 year), and both have a statistically significant correlation with SPG T and S (**Table 1**). The variability in the Atlantic Inflow at the BSO is not closely linked with the wind stress curl over the Barents Sea (**Figure 4**). For the time period considered (1960–2019), the correlation between the wind stress curl and the Atlantic Inflow is low and statistically insignificant ($r = 0.25$, lag = 0 year). As is clear from the time series, the wind stress curl exhibits a strong interannual variability. However, wind stress curl drives the total volume transport at the BSO (r = -0.71, **Supplementary Figure 2**). Thus it appears that the warm and saline part of the total volume transport, i.e., the Atlantic Inflow, is related to the variability in the SPG. The respective correlations (**Table 1**) also suggest that the SPG signal is much clearer in the depth-integrated Atlantic Inflow than in temperatures at a single depth.

The volume of Atlantic Water within the Barents Sea (red box in **Figure 1**) shows a general increasing trend from the late 1970s (**Figure 5**). This is inline with the gradual Atlantification of the Barents Sea in the recent decades. The variability of Atlantic Water within the Barents Sea is directly related to the Atlantic Inflow at the BSO (r = 0.8, lag = 1 year, **Figure 5**). In the 1970s, a nearly 30% reduction in the volume of Atlantic Water in the Barents Sea occurred following the sharp decline in the Atlantic Inflow at the BSO during the same period (**Figure 5**). Similarly, Atlantic Water volume increased by about 20% from early 2000s following an increase in Atlantic Inflow. Interestingly, for the period 2010–2019 (corresponding to the most recent cooling/freshening of the SPG after accounting for the advective delays), while there was a decline in the Atlantic Inflow at the BSO (from a high of 1.5 Sv in 2010 to a low of 1.0 Sv in 2019), there was no significant change in the Atlantic Water volume during that period. Similarly, the variability in sea-ice area in the Barents Sea has closely followed the variability in both the Atlantic Inflow at the BSO and the volume of Atlantic Water in the Barents Sea

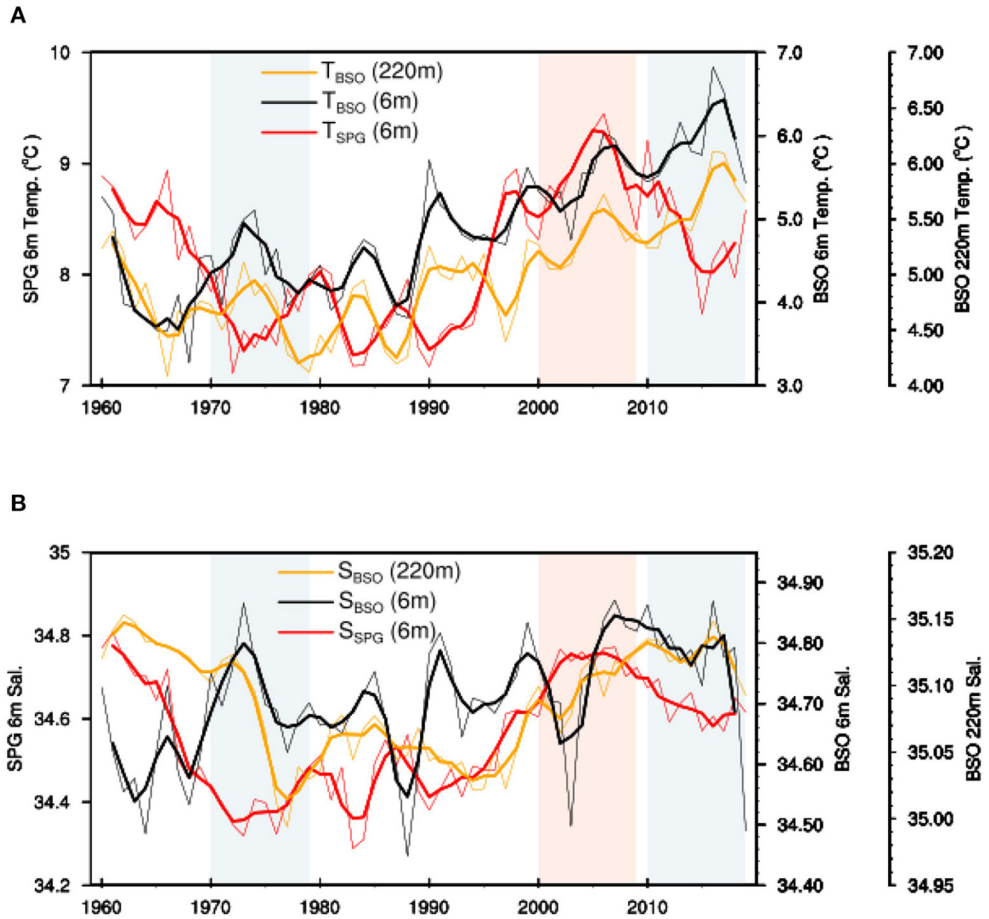


FIGURE 3 | Time series of modelled surface and sub-surface **(A)** temperature and **(B)** salinity in the North Atlantic Subpolar Gyre (-60:10 °E, 50:62 °N) and an the Barents Sea Opening (10:25 °E, 70:78 °N) for the period 1960–2019. For each of the time series shown, light lines are annual means and bold lines are three-year running mean values. The shaded time periods highlight the time periods four years after the respective decadal trends in the SPG.

(**Table 1**). Sea-ice in the Barents Sea grew in the 1970s, declined in the early 2000s and has not undergone a large decline from 2005 to 2019 in the assimilation experiment.

Differences in the spatial extent of the Atlantic Water within the Barents Sea present a more clearer picture of its regional inhomogeneities in Atlantic Water volume (**Figure 6**). Corresponding to the cooling/freshening in the 1970s, a reduction in the volume of Atlantic Water occurred in the southwestern region of the Barents Sea. Similarly, in the late 1990s and early 2000s when more Atlantic Water entered the Barents Sea, an increase in the Atlantic Water volume occurred as far as 35°E. Even for the last decade of our interest (2010–2019), a decline in the Atlantic Water volume has occurred which was not evident from the area integrated time series (**Figure 5**). Clearly, most of this decline is limited to the southwestern region of the Barents Sea from where the Atlantic Water enters the Barents Sea (i.e., along the mean current pathways). The location of the 1°C isotherm at 100 m, applied here as a proxy for the northern limit of the Atlantic Water, also presents a consistent picture, except for the last decade when the isotherm shifted further northward from 2010 to 2019.

Now, we turn to the key aspect of the impact of the SPG, i.e., the changes in the sea-ice extent and primary production in the Barents Sea. An increase in sea-ice area limits the available area for the primary production in the Barents Sea (Dalpadado et al., 2014), which can reduce the feeding grounds of fish communities (Drinkwater et al., 2010). Thus, an impact of SPG on sea-ice area and primary production in the Barents Sea may provide the physical explanation behind the high correlations between SPG and cod biomass (**Figure 2** and **Table 1**). After adjusting for advective delays inferred from preceding analysis, trends in sea-ice area fraction and primary production can be identified along the climatological sea-ice boundary (**Figure 7**). In the first two decades of interest (1971 to 1980 and 2001 to 2010), the trends are strongest in the northern Barents Sea along the sea-ice edge. The first cooling period results in the growth of sea-ice in the Barents Sea and a corresponding decline in the net primary production. Similarly, the 1990s warming of the SPG leads to a decline in the sea-ice area from 2001–2010 and a

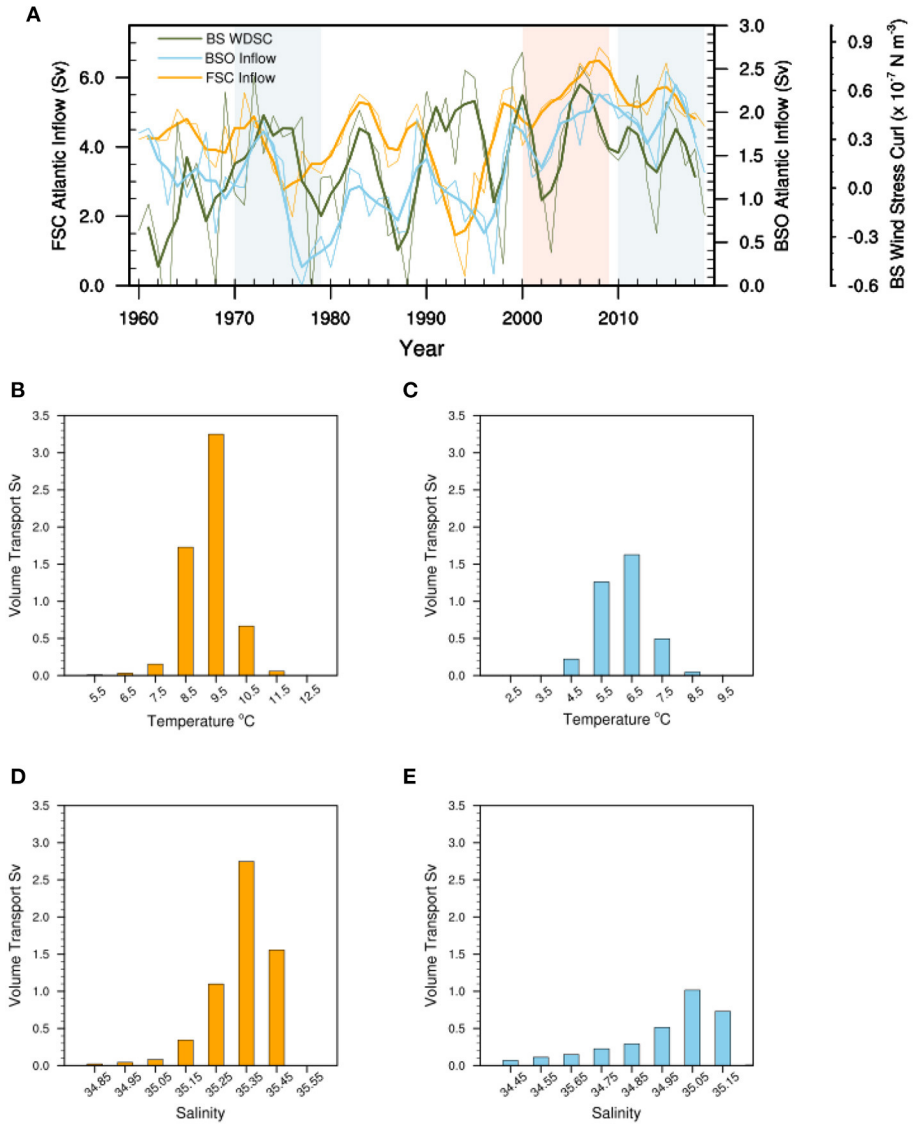


FIGURE 4 | (A) Time series of modelled Atlantic Inflow (Sv, 1 Sv = 10^6 m^3 s^{-1}) across the Faroe Scotland Channel (FSC, orange) and Barents Sea Opening (BSO, blue), and time series of wind stress curl (WDSC, green) over the Barents Sea (black box in **Figure 1A**). For each of the time series shown, light lines are annual means and bold lines are three-year running mean values. The shaded time periods highlight the time periods four years after the respective decadal trends in the SPG. Atlantic Inflow is defined as the volume transport of water with eastward zonal velocity and with T > 8.5 °C and S > 35.25 at the FSC, and T > 5.5 °C and S > 35.0 at the BSO. Histograms of volume transport (Sv) in various temperature (T) and Salinity (S) classes across the **(B,D)**, FSC and **(C,E)**, BSO, respectively. The location of the FSC and the BSO section for computing volume transports is shown in **Figure 1A**.

corresponding increase in primary production. For the period 2011 to 2019, corresponding to the 2006–2015 cooling of the SPG, the increase in the sea-ice area and the resulting decrease in primary production has occurred mainly outside and further north of the Barents Sea. Within the Barents Sea, however, a positive trend in the primary production emerges. This aspect is taken up further in the discussion section.

As we have not assimilated satellite observations into the model, it is instructive to see whether similar trends have emerged in satellite observations of sea-ice concentration and primary production (**Figure 8**). For the decade 2001 to 2010, the decadal trends in observed sea-ice concentration show a similar statistically significant decline as seen in the assimilation experiment. The sea-ice edge moved northwards in this decade owing to the increased heat transport into the Barents Sea. For the decade 2011 to 2020, although a statistically significant trend has not emerged in the Barents Sea, the absence of a declining trend in sea-ice is consistent with the antecedent cooling of the SPG. In the case of observed net primary production, the pronounced increase along the sea-ice edge in the decade when sea-ice retreated northwards, as was seen in the assimilation, is absent. However, in the last decade, 2011–2020, the decline

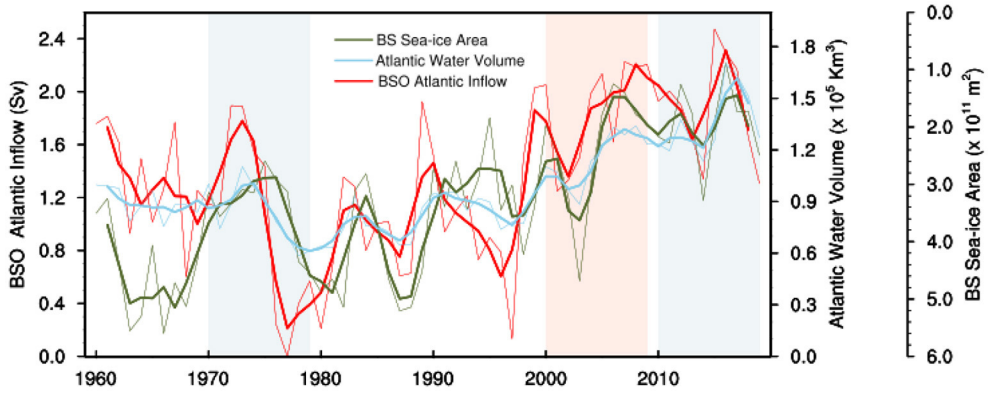


FIGURE 5 | Time series of modelled Atlantic Inflow (Sv) across the Barents Sea Opening (BSO, red), volume of Atlantic Water (Km^3) in the Barents Sea (blue) and total sea-ice area (m^2) in the Barents Sea (green). Following (Oziel et al., 2016), Atlantic Water is defined as water with T > 3.5 °C and S > 34.8 within the Barents Sea. For each of the time series shown, light lines are annual means and bold lines are three-year running mean values. The shaded time periods highlight the time periods four years after the respective decadal trends in the SPG.

within the Barents Sea is inline with reduced Atlantic Water volume (**Figure 6I**) but a statistically significant trend is yet to emerge.

In summary, our results reveal decadal changes in the marine environment of the Barents Sea that are related to the upstream changes in the subpolar North Atlantic. The SPG signal present in the Atlantic Inflow, both at the FSC and the BSO, is closely linked with the volume of Atlantic Water in the Barents Sea, which then has an impact on the sea-ice area and primary production, and consequently, on the cod biomass.

4. DISCUSSION AND CONCLUSIONS

In this article, through a data assimilation experiment, we present evidence to support the hypothesis that oceanic anomalies associated with the SPG have an impact on oceanic conditions in the Barents Sea. Recently, the Northeast Arctic cod biomass was shown to be predicable at multi-year lead times wherein a statistical temperature-cod relationship was leveraged (Årthun et al., 2018; Koul et al., 2021). Here, we present the mechanistic links underlying the statistical temperature-cod relationship, and we reveal SPG-driven co-variability in the Atlantic Inflow at the FSC and the BSO. Our results suggest that SPG-driven changes in the Atlantic Inflow are the primary drivers of decadal trends in the sea-ice area and primary production in the Barents Sea.

Our results, although derived in an Eulerian framework, corroborate the earlier reported 3–5 year advective delay in the propagation of oceanic anomalies from the eastern subpolar North Atlantic into the Barents Sea (Gao et al., 2005; Holliday et al., 2008; Langehaug et al., 2019). Our data assimilation based analysis also shows that the core of the warm and saline Atlantic Water lies at 150–300 m depth in the water column, both in the FSC and at the BSO, consistent with observations (Furevik, 2001; Yashayaev and Seidov, 2015). We find that the SPG signal is more pronounced in subsurface salinity downstream of the Greenland-Scotland Ridge (**Figure 3**). Temperature, due to air-sea interactions, has a short memory of the antecedent forcing history.

The dynamical basis of multiyear changes in volume transport of Atlantic Water into the Barents Sea, following periods of strong decadal trends in the SPG temperature and salinity, is the weakening and strengthening of the SPG circulation. The warming and cooling of the SPG is dynamically related to its weakening and strengthening, respectively (Bersch et al., 2007; Häkkinen et al., 2011; Koul et al., 2019, 2020). The strength of the SPG circulation controls the throughput of subtropical waters crossing the Greenland-Scotland Ridge. It is this SPG-driven waxing and waning of high salinity (and high temperature) waters that is mirrored in the Atlantic Inflow at decadal to multi-decadal timescales. At seasonal and interannual timescales, the SPG signal is contaminated by overlying atmospheric variability.

The interannual to decadal variability in the total volume transport is driven by the wind stress curl over the northern Barents Sea, however, the same is not the case for the Atlantic Inflow (**Supplementary Figure 2** and **Figure 4**). The low frequency variability as seen in Atlantic Inflow at BSO does not match that in the wind stress curl. This suggests that while the total volume transport is wind driven and is an important driver of the variability in sea-ice and primary production in the Barents Sea (Sandø et al., 2021), the warm and saline part of the total volume transport (i.e., the Atlantic Inflow) is instead driven by the variability in SPG-associated changes in temperature and salinity. Nevertheless, the large scale wind field over the subpolar North Atlantic plays an important role in the variability of the SPG circulation (Koul et al., 2020; Holliday et al., 2020).

It is possible that SPG-associated variability in temperature and salinity between the FSC and BSO might lead to local geostrophic circulation anomalies which can in turn influence Atlantic Inflow across the BSO. We do find consistent trends in temperature, salinity and zonal geostrophic currents in the first two decades of our analysis (**Supplementary Figure 3**),

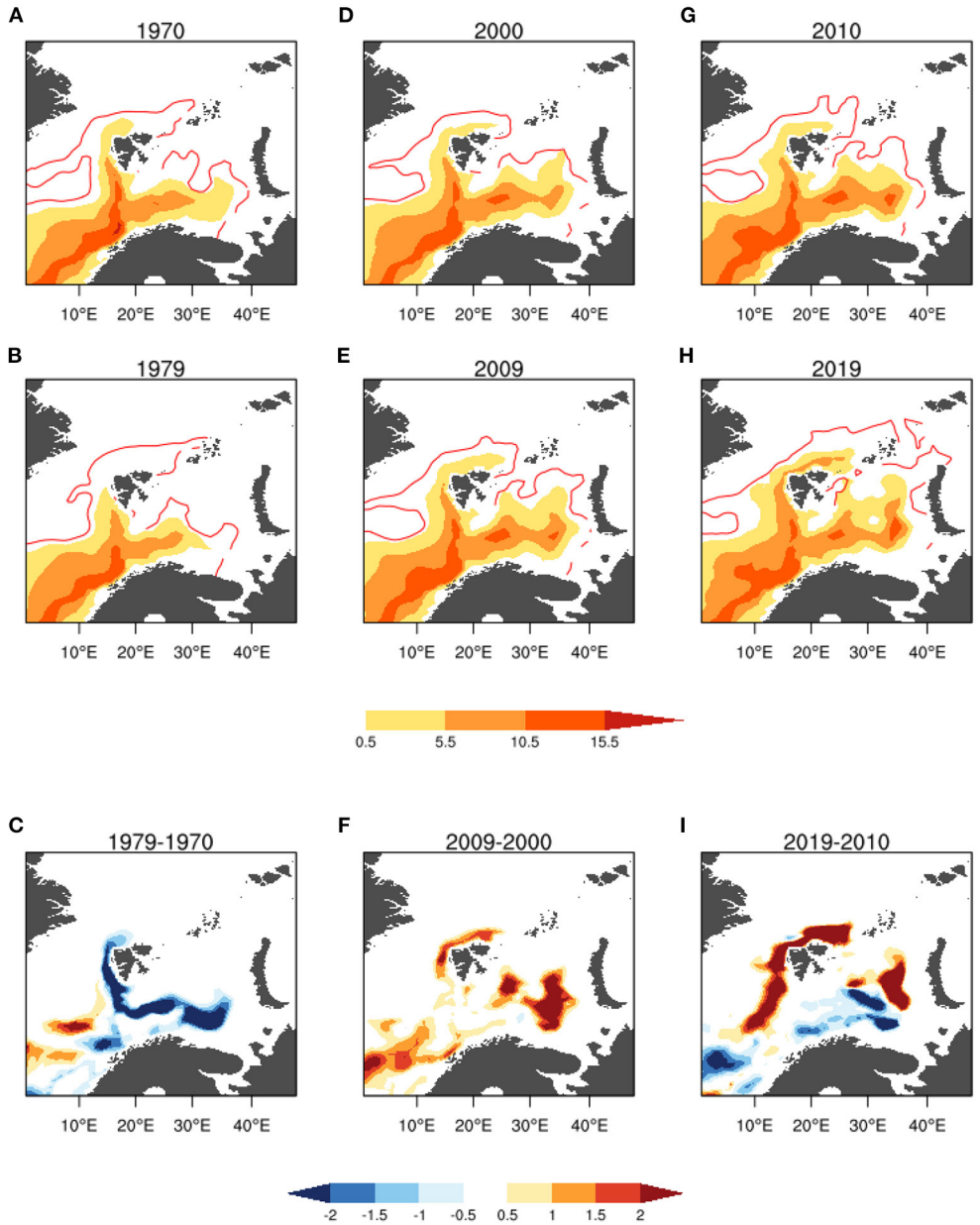


FIGURE 6 | Mean volume of Atlantic Water (x10^2 Km^3) at each grid point from the assimilation experiment over three years centered on **(A)** 1970, **(B)** 1979, their difference **(C)** 1979–1970, **(D)** 2000, **(E)** 2009 and their difference **(F)** 2009–2000. Since the model experiment ends at 2019, the Atlantic Water volume is shown for individual years **(G)** 2010, **(H)** 2019 and their difference **(I)** 2019–2010. The red contour line is the 1°C isotherm at 182 meters model level.

however, except salinity, the trends over the last decade show an inconsistent increase in both temperature and geostrophic currents. This can be due to the fact that in the last decade, the waters at the BSO have freshened and their temperatures have increased (**Figure 3**). This would cause a local steric sea level change resulting in anomalous eastward geostrophic flow. Noting that the trends are spatially incoherent, we leave it to future studies to quantify the impact of such geostrophic current anomalies on Barents Sea temperature and salinity.

Within the Barents Sea, observation show near doubling of the area occupied by the Atlantic Water over the last three to four decades (Oziel et al., 2016). In this article, we show that embedded in the long term trend are decadal changes in the area occupied by the Atlantic Water. In the first two decades analyzed in this study (i.e., 1970–1979 and 2000–2009), the extent of the area occupied by the Atlantic Water follows decadal trends in the SPG temperature, i.e., a decline in the former and an increase in the latter

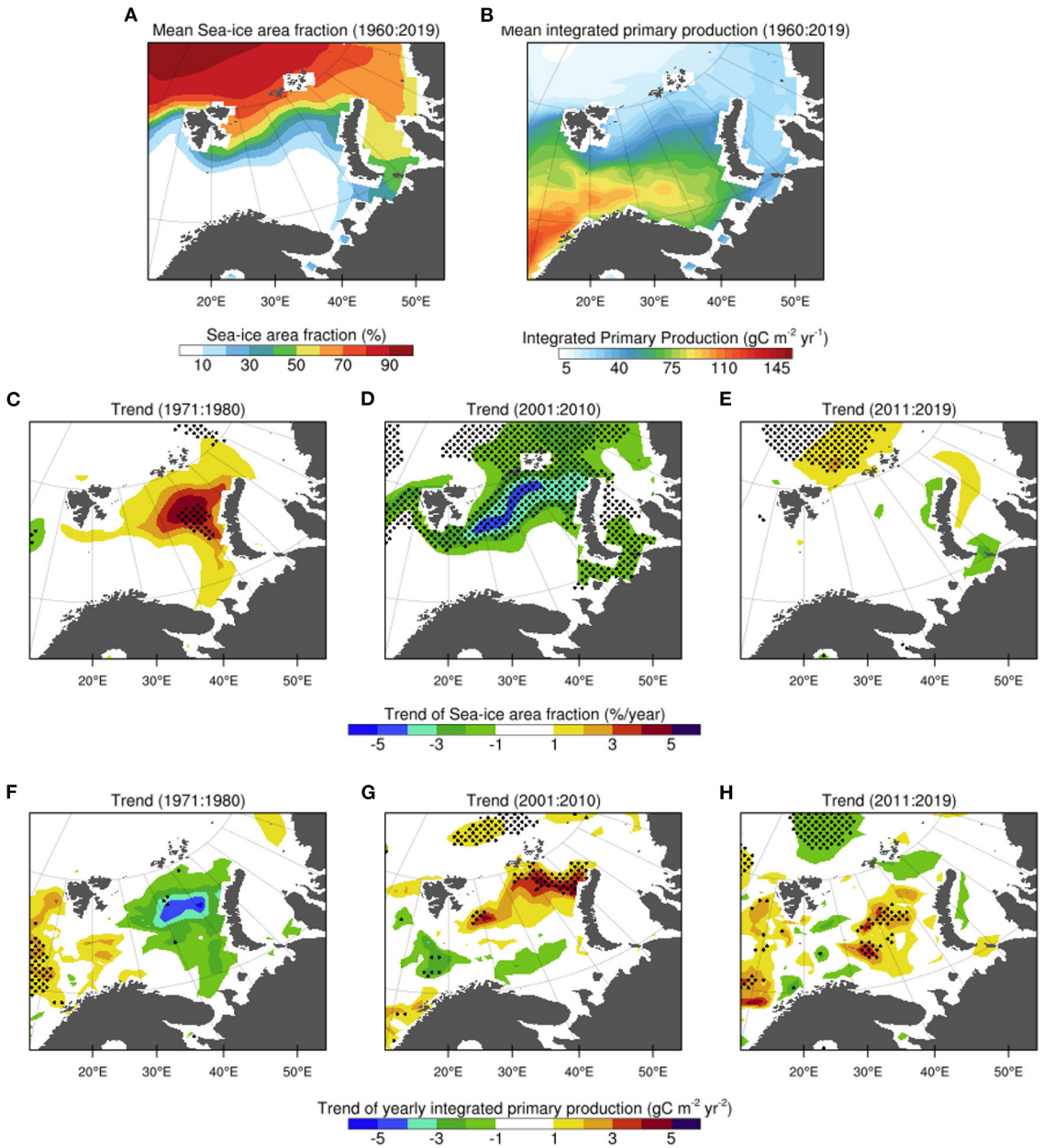


FIGURE 7 | (A) Climatology of the annual mean sea-ice concentration (percent of grid cell occupied by sea-ice) and **(B)** integrated net primary production ($gCm^{-2}yr^{-1}$) for the period 1960–2019 from the assimilation experiment. Trends in annual mean sea-ice concentration (second row) and integrated net primary production (third row) for the three periods **(C,F)** 1971–1980, **(D,G)** 2001–2010, and **(E,H)** 2011–2019. The stippling marks statistically significant trends at 90% confidence level.

decade. While this holds for the last period considered as well (2010–2019), the change is not uniform throughout the Barents Sea. The decline is mainly seen in the southwestern region from where the Atlantic Water enters the Barents Sea. Also, this decline is mainly due to a decrease in salinity than due to a decrease in temperature (**Figure 3** and **Supplementary Figure 3**). The analysis of the differences in Atlantic Water volume for the last decade is based on individual years (2019 and 2011) and thus might be contaminated by interannual variability. A clear signal might have emerged after 2019.

Sea-ice in the Barents Sea exerts a dominant control on the spatial distribution of primary production. Observations over a short record of less than 20 years suggest a bi-modal pattern in the spatial distribution of primary production which closely tracks the position of sea-ice edge during years with large changes

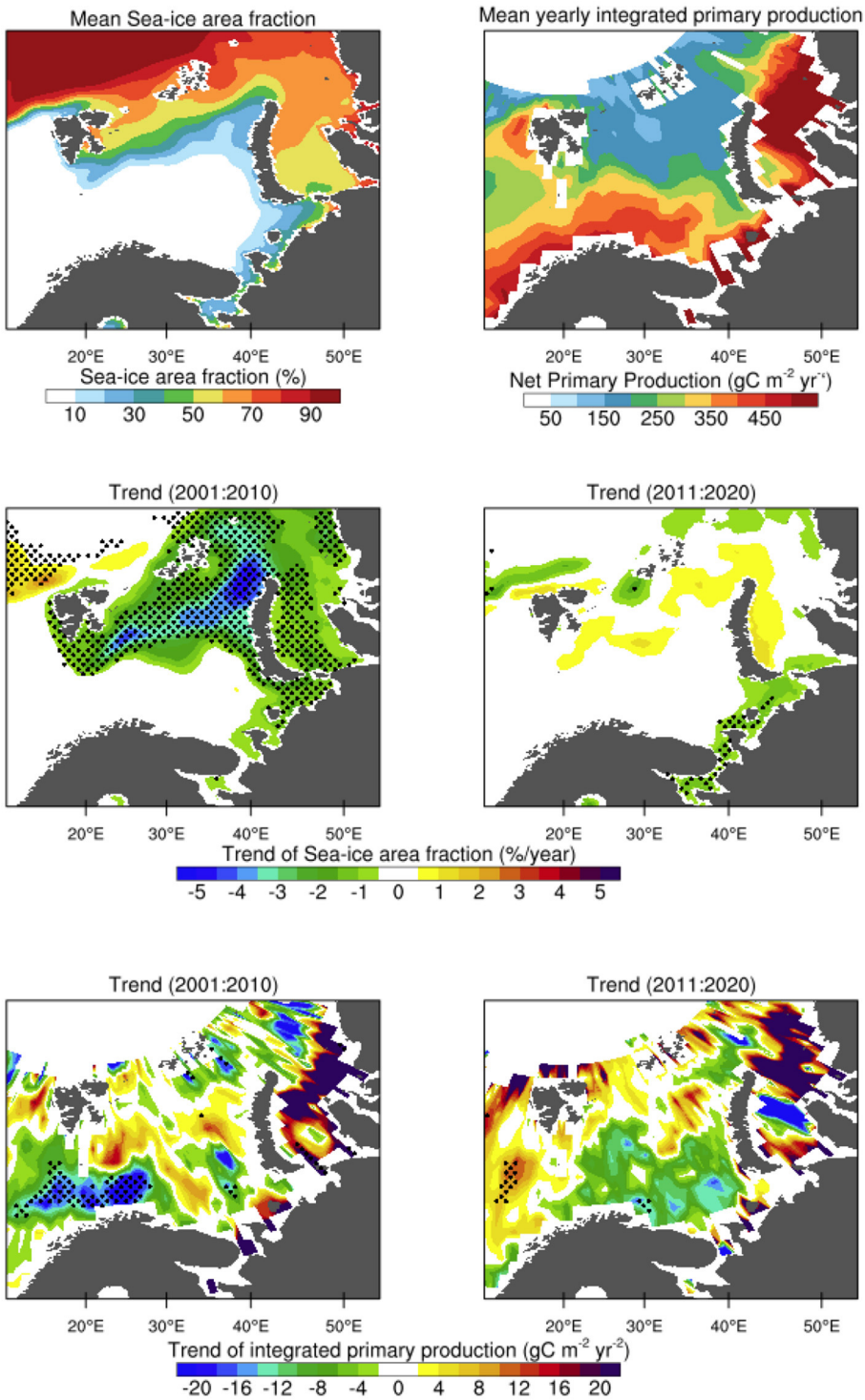


FIGURE 8 | Climatology of the annual mean sea-ice concentration and integrated net primary production ($gCm^{-2}yr^{-1}$) for the period 1997–2020 from satellite observations. Trends in annual mean sea-ice concentration (second row) and integrated net primary production (third row) for the two periods 2001–2010 and 2011–2020. The stippling marks statistically significant trends at 90% confidence level.

in sea-ice extent (Oziel et al., 2017). In our analysis, although we also find that the variability in the primary production closely tracks the sea-ice edge, the spatial pattern of the response of primary production to decadal changes in sea-ice extent is different. We find significant trends in primary production in response to trends in sea-ice area fraction both within and

outside the Barents Sea. For the period 2011–2019, significant increase in sea-ice and decrease in primary production has occurred north of Spitzbergen. This suggests that as the region of interaction between Atlantic Water and sea-ice shifts northward due to long term warming, the influence of the SPG would also extend northward.

Given the advective delays from the subpolar North Atlantic to the Barents Sea, the full impact of recent cooling of the SPG is expected after 2019, which is the last year of our experiment, and which could also explain the absence of significant trends in the northern Barents Sea in the last 9 years of our analysis. This latter conjecture is supported by the trends in the observed sea-ice and primary production for which the year 2020 is included. There is no significant declining trend in sea-ice concentration toward the north and the reduction in primary production is seen within the Barents Sea for the period 2011–2020. The absence of a decline in the sea-ice in the last decade of our analysis is consistent with the predicted slowdown of the sea-ice loss in the Barents Sea sector (Yeager et al., 2015) and satellite observations showing a slight recovery from the 2012 minimum.

The decadal trends in sea-ice and primary production, associated with the SPG, can influence cod biomass in various ways. For example, a large ice-free region allows habitat expansion which favours growth through increased food availability (Ottersen et al., 2010). A northward retreat of sea-ice edge also allows increased northward penetration of nutrients and zooplankton carried by the Atlantic Inflow, both of which can have an impact on the growth of Capelin, the main prey of cod in the Barents Sea. Thus, the high correlation between the SPG temperature, salinity and cod biomass is a manifestation of impact of the SPG on marine environment of the Barents Sea which has implications for predictability of marine ecosystems in this shelf-sea.

DATA AVAILABILITY STATEMENT

The raw data supporting the conclusions of this article will be made available by the authors, without undue reservation.

AUTHOR CONTRIBUTIONS

VK and CS conceived the work and discussed the research plan. VK analyzed the data, model experiments, prepared the figures, and wrote the manuscript. SB carried out model experiments. SB, JB, and CS discussed results, their interpretation, and helped with the improvement of the manuscript.

FUNDING

This study is a contribution to the Excellence Cluster CliCCS - Climate, Climatic Change, and Society at the University of Hamburg, funded by the DFG through Germany's Excellence Strategy EXC 2037 Project 390683824, (JB and CS). This study is also a contribution to the PoF IV Program Changing Earth Sustaining our Future, Topic 4 Coastal Transition Zones under Natural and Human Pressure of the Helmholtz Association. JB and CS were supported by Copernicus Climate Change Service, funded by the EU, under contract C3S-330.

ACKNOWLEDGMENTS

The authors thank the German Computing Center (DKRZ) for providing their computing resources.

SUPPLEMENTARY MATERIAL

The Supplementary Material for this article can be found online at: https://www.frontiersin.org/articles/10.3389/fmars.2021.778335/full#supplementary-material

REFERENCES

Ådlandsvik, B., and Loeng, H. (1991). A study of the climatic system in the barents sea. *Polar Res.* 10, 45–50. doi: 10.3402/polar.v10i1.6726

Årthun, M., Bogstad, B., Daewel, U., Keenlyside, N. S., Sandø, A. B., Schrum, C., et al. (2018). Climate based multi-year predictions of the barents sea cod stock. *PLoS One* 13:e0206319. doi: 10.1371/journal.pone.0206319

Årthun, M., and Eldevik, T. (2016). On anomalous ocean heat transport toward the arctic and associated climate predictability. *J. Clim.* 29, 689–704. doi: 10.1175/JCLI-D-15-0448.1

Årthun, M., Eldevik, T., Smedsrud, L., Skagseth, Ø., and Ingvaldsen, R. (2012). Quantifying the influence of atlantic heat on barents sea ice variability and retreat. *J. Clim.* 25, 4736–4743. doi: 10.1175/JCLI-D-11-00466.1

Årthun, M., Eldevik, T., and Smedsrud, L. H. (2019). The role of atlantic heat transport in future arctic winter sea ice loss. *J. Clim.* 32:3327–3341. doi: 10.1175/JCLI-D-18-0750.1

Asbjørnsen, H., Johnson, H. L., and Årthun, M. (2021). Variable nordic seas inflow linked to shifts in north atlantic circulation. *J. Clim.* 1–50. doi: 10.1175/JCLI-D-20-0917.1

Behrenfeld, M. J., and Falkowski, P. G. (1997). Photosynthetic rates derived from satellite-based chlorophyll concentration. *Limnol. Oceanography* 42, 1–20. doi: 10.4319/lo.1997.42.1.0001

Bersch, M., Yashayaev, I., and Koltermann, K. P. (2007). Recent changes of the thermohaline circulation in the subpolar north atlantic. *Ocean Dyn.* 57, 223–235. doi: 10.1007/s10236-007-0104-7

Berx, B., Hansen, B., Østerhus, S., Larsen, K., Sherwin, T., and Jochumsen, K. (2013). Combining in situ measurements and altimetry to estimate volume, heat and salt transport variability through the faroe–shetland channel. *Ocean Sci.* 9, 39–654. doi: 10.5194/os-9-639-2013

Böning, C. W., Scheinert, M., Dengg, J., Biastoch, A., and Funk, A. (2006). Decadal variability of subpolar gyre transport and its reverberation in the north atlantic overturning. *Geophys. Res. Lett.* 33. doi: 10.1029/2006GL026906

Born, A., and Mignot, J. (2012). Dynamics of decadal variability in the atlantic subpolar gyre: a stochastically forced oscillator. *Clim. Dyn.* 39, 461–474. doi: 10.1007/s00382-011-1180-4

Bretherton, C. S., Widmann, M., Dymnikov, V. P., Wallace, J. M., and Bladé, I. (1999). The effective number of spatial degrees of freedom of a time-varying field. *J. Clim.* 12, 1990–2009. doi: 10.1175/1520-0442(1999)012<1990:TENOSD>2.0.CO;2

Brune, S., and Baehr, J. (2020). Preserving the coupled atmosphere-ocean feedback in initializations of decadal climate predictions. *WIREs Clim. Change* 11:e637. doi: 10.1002/wcc.637

Brune, S., Nerger, L., and Baehr, J. (2015). Assimilation of oceanic observations in a global coupled earth system model with the seik filter. *Ocean Model.* 96, 254–264. doi: 10.1016/j.ocemod.2015.09.011

Dalpadado, P., Arrigo, K. R., Hjøllo, S. S., Rey, F., Ingvaldsen, R. B., Sperfeld, E., et al. (2014). Productivity in the barents sea-response to recent climate variability. *PLoS One* 9:e95273. doi: 10.1371/journal.pone.0095273

Dalpadado, P., Ingvaldsen, R. B., Stige, L. C., Bogstad, B., Knutsen, T., Ottersen, G., et al. (2012). Climate effects on barents sea ecosystem dynamics. *ICES J. Marine Sci.* 69, 1303–1316. doi: 10.1093/icesjms/fss063

Dee, D. P., Uppala, S., Simmons, A., Berrisford, P., Poli, P., Kobayashi, S., et al. (2011). The era-interim reanalysis: Configuration and performance of the data assimilation system. *Quart. J. Roy. Meteorol. Soc.* 137, 553–597. doi: 10.1002/qj.828

Delworth, T., Manabe, S., and Stouffer, R. J. (1993). Interdecadal variations of the thermohaline circulation in a coupled ocean-atmosphere model. *J. Clim.* 6, 1993–2011. doi: 10.1175/1520-0442(1993)006<1993:IVOTTC>2.0.CO;2

Dickson, R. R., Meincke, J., Malmberg, S.-A., and Lee, A. J. (1988). The great salinity anomaly in the northern north atlantic 1968–1982. *Progr. Oceanography* 20, 103–151. doi: 10.1016/0079-6611(88)90049-3

Drinkwater, K. F., Beaugrand, G., Kaeriyama, M., Kim, S., Ottersen, G., Perry, R. I., et al. (2010). On the processes linking climate to ecosystem changes. *J. Marine Syst.* 79, 374–388. doi: 10.1016/j.jmarsys.2008.12.014

Drinkwater, K. F., Belgrano, A., Borja, A., Conversi, A., Edwards, M., Greene, C. H., et al. (2003). The response of marine ecosystems to climate variability associated with the north atlantic oscillation. *Geophys. Monograph Amer. Geophys. Union* 134, 211–234. doi: 10.1029/134GM10

Eyring, V., Bony, S., Meehl, G. A., Senior, C. A., Stevens, B., Stouffer, R. J., et al. (2016). Overview of the coupled model intercomparison project phase 6 (cmip6) experimental design and organization. *Geosci. Model Develop.* 9, 1937–1958. doi: 10.5194/gmd-9-1937-2016

Fossheim, M., Primicerio, R., Johannesen, E., Ingvaldsen, R. B., Aschan, M. M., and Dolgov, A. V. (2015). Recent warming leads to a rapid borealization of fish communities in the arctic. *Nat. Clim. Change* 5, 673–677. doi: 10.1038/nclimate2647

Furevik, T. (2001). Annual and interannual variability of atlantic water temperatures in the norwegian and barents seas: 1980–1996. *Deep Sea Res. Part I Oceanograph. Res. Papers* 48, 383–404. doi: 10.1016/S0967-0637(00)00050-9

Gao, Y., Drange, H., Bentsen, M., and Johannessen, O. M. (2005). Tracer-derived transit time of the waters in the eastern nordic seas. *Tellus B Chem. Phys. Meteorol.* 57, 332–340. doi: 10.3402/tellusb.v57i4.16553

Gent, P. R., Willebrand, J., McDougall, T. J., and McWilliams, J. C. (1995). Parameterizing eddy-induced tracer transports in ocean circulation models. *J. Phys. Oceanography* 25, 463–474. doi: 10.1175/1520-0485(1995)025<0463:PEITTI>2.0.CO;2

Glessmer, M. S., Eldevik, T., Våge, K., Nilsen, J. E. Ø., and Behrens, E. (2014). Atlantic origin of observed and modelled freshwater anomalies in the nordic seas. *Nat. Geosci.* 7, 801–805. doi: 10.1038/ngeo2259

Good, S. A., Martin, M. J., and Rayner, N. A. (2013). En4: Quality controlled ocean temperature and salinity profiles and monthly objective analyses with uncertainty estimates. *J. Geophys. Res. Oceans* 118, 6704–6716. doi: 10.1002/2013JC009067

Hagemann, S., and Gates, L. D. (2003). Improving a subgrid runoff parameterization scheme for climate models by the use of high resolution data derived from satellite observations. *Clim. Dyn.* 21, 349–359. doi: 10.1007/s00382-003-0349-x

Häkkinen, S., Rhines, P. B., and Worthen, D. L. (2011). Warm and saline events embedded in the meridional circulation of the northern north atlantic. *J. Geophys. Res. Oceans* 116. doi: 10.1029/2010JC006275

Hansen, B., Østerhus, S., Turrell, W. R., Jónsson, S., Valdimarsson, H., Hátún, H., et al. (2008). "The inflow of atlantic water, heat, and salt to the nordic seas across the greenland–scotland ridge," in *Arctic–Subarctic Ocean Fluxes* (Dordrecht: Springer), 15–43.

Hátún, H., Lohmann, K., Matei, D., Jungclaus, J. H., Pacariz, S., Bersch, M., et al. (2016). An inflated subpolar gyre blows life toward the northeastern atlantic. *Progr. Oceanography* 147, 49–66. doi: 10.1016/j.pocean.2016.07.009

Hátún, H., Payne, M., Beaugrand, G., Reid, P., Sandø, A., Drange, H., et al. (2009). Large bio-geographical shifts in the north-eastern atlantic ocean: From the subpolar gyre, via plankton, to blue whiting and pilot whales. *Progr. Oceanography* 80, 149–162. doi: 10.1016/j.pocean.2009.03.001

Hátún, H., Sandø, A. B., Drange, H., Hansen, B., and Valdimarsson, H. (2005). Influence of the atlantic subpolar gyre on the thermohaline circulation. *Science* 309, 1841–1844. doi: 10.1126/science.1114777

Holliday, N. P., Bersch, M., Berx, B., Chafik, L., Cunningham, S., Florindo-López, C., et al. (2020). Ocean circulation causes the largest freshening event for 120 years in eastern subpolar north atlantic. *Nat. Commun.* 11, 1–15. doi: 10.1038/s41467-020-14474-y

Holliday, N. P., Hughes, S., Bacon, S., Beszczynska-Möller, A., Hansen, B., Lavin, A., et al. (2008). Reversal of the 1960s to 1990s freshening trend in the northeast north atlantic and nordic seas. *Geophys. Res. Lett.* 35. doi: 10.1029/2007GL032675

Ilıcak, M., Drange, H., Wang, Q., Gerdes, R., Aksenov, Y., Bailey, D., et al. (2016). An assessment of the arctic ocean in a suite of interannual core-ii simulations. part iii: hydrography and fluxes. *Ocean Model.* 100:, 141–161. doi: 10.1016/j.ocemod.2016.02.004

Ilyina, T., Six, K. D., Segschneider, J., Maier-Reimer, E., Li, H., and Núñez-Riboni, I. (2013). Global ocean biogeochemistry model hamocc: Model architecture and performance as component of the mpi-earth system model in different cmip5 experimental realizations. *J. Adv. Model. Earth Syst.* 5, 287–315. doi: 10.1002/jame.20017

Ingvaldsen, R., Loeng, H., Ottersen, G., and Ådlandsvik, B. (2003). "Climate variability in the barents sea during the 20th century with focus on the 1990s," in *ICES Marine Science Symposia*, Vol. 219, 160–168.

Jungclaus, J., Fischer, N., Haak, H., Lohmann, K., Marotzke, J., Matei, D., et al. (2013). Characteristics of the ocean simulations in the max planck institute ocean model (mpiom) the ocean component of the mpi-earth system model. *J. Adv. Model. Earth Syst.* 5, 422–446. doi: 10.1002/jame.20023

Koul, V., Schrum, C., Düsterhus, A., and Baehr, J. (2019). Atlantic inflow to the north sea modulated by the subpolar gyre in a historical simulation with mpi-esm. *J. Geophys. Res. Oceans* 124, 1807–1826. doi: 10.1029/2018JC014738

Koul, V., Sguotti, C., Årthun, M., Brune, S., Düsterhus, A., Bogstad, B., et al. (2021). Skilful prediction of cod stocks in the north and barents sea a decade in advance. *Commun. Earth Environ.* 2, 140. doi: 10.1038/s43247-021-00207-6

Koul, V., Tesdal, J.-E., Bersch, M., Hátún, H., Brune, S., Borchert, L., et al. (2020). Unraveling the choice of the north atlantic subpolar gyre index. *Sci. Rep.* 10, 1–12. doi: 10.1038/s41598-020-57790-5

Langehaug, H. R., Sandø, A. B., Årthun, M., and Ilıcak, M. (2019). Variability along the atlantic water pathway in the forced norwegian earth system model. *Clim. Dyn.* 52, 1211–1230. doi: 10.1007/s00382-018-4184-5

Levitus, S., Matishov, G., Seidov, D., and Smolyar, I. (2009). Barents sea multidecadal variability. *Geophys. Res. Lett.* 36. doi: 10.1029/2009GL039847

Lien, V. S., Schlichtholz, P., Skagseth, Ø., and Vikebø, F. B. (2017). Wind-driven atlantic water flow as a direct mode for reduced barents sea ice cover. *J. Clim.* 30, 803–812. doi: 10.1175/JCLI-D-16-0025.1

Marshall, J., Johnson, H., and Goodman, J. (2001). A study of the interaction of the north atlantic oscillation with ocean circulation. *J. Clim.* 14, 1399–1421. doi: 10.1175/1520-0442(2001)014<1399:ASOTIO>2.0.CO;2

Marsland, S. J., Haak, H., Jungclaus, J. H., Latif, M., and Röske, F. (2003). The max-planck-institute global ocean/sea ice model with orthogonal curvilinear coordinates. *Ocean Model.* 5, 91–127. doi: 10.1016/S1463-5003(02)00015-X

Meier, W. N., F. Fetterer, A. K. Windnagel, and J. S. Stewart. (2021). *NOAA/NSIDC Climate Data Record of Passive Microwave Sea Ice Concentration, Version 4.* Boulder, CO: National Snow and Ice Data Center (NSIDC). doi: 10.7265/efmz-2t65

Muilwijk, M., Smedsrud, L. H., Ilicak, M., and Drange, H. (2018). Atlantic water heat transport variability in the 20th century arctic ocean from a global ocean model and observations. *J. Geophys. Res. Oceans* 123, 8159–8179. doi: 10.1029/2018JC014327

Orvik, K. A., and Skagseth, Ø. (2003). The impact of the wind stress curl in the north atlantic on the atlantic inflow to the norwegian sea toward the arctic. *Geophys. Res. Lett.* 30. doi: 10.1029/2003GL017932

Ottersen, G., Kim, S., Huse, G., Polovina, J. J., and Stenseth, N. C. (2010). Major pathways by which climate may force marine fish populations. *J. Marine Syst.* 79, 343–360. doi: 10.1016/j.jmarsys.2008.12.013

Ottersen, G., and Stenseth, N. C. (2001). Atlantic climate governs oceanographic and ecological variability in the barents sea. *Limnol. Oceanography* 46, 1774–1780. doi: 10.4319/lo.2001.46.7.1774

Oziel, L., Neukermans, G., Ardyna, M., Lancelot, C., Tison, J.-L., Wassmann, P., et al. (2017). Role for atlantic inflows and sea ice loss on shifting phytoplankton blooms in the b arents s ea. *J. Geophys. Res. Oceans* 122, 5121–5139. doi: 10.1002/2016JC012582

Oziel, L., Sirven, J., and Gascard, J.-C. (2016). The barents sea frontal zones and water masses variability (1980–2011). *Ocean Sci.* 12, 169–184. doi: 10.5194/os-12-169-2016

Pacanowski, R., and Philander, S. (1981). Parameterization of vertical mixing in numerical models of tropical oceans. *J. Phys. Oceanography* 11, 1443–1451. doi: 10.1175/1520-0485(1981)011<1443:POVMIN>2.0.CO;2

Piecuch, C. G., Ponte, R. M., Little, C. M., Buckley, M. W., and Fukumori, I. (2017). Mechanisms underlying recent decadal changes in subpolar north atlantic ocean heat content. *J. Geophys. Res. Oceans* 122, 7181–7197. doi: 10.1002/2017JC012845

Reick, C., Raddatz, T., Brovkin, V., and Gayler, V. (2013). Representation of natural and anthropogenic land cover change in mpi-esm. *J. Adv. Model. Earth Syst.* 5, 459–482. doi: 10.1002/jame.20022

Reverdin, G. (2010). North atlantic subpolar gyre surface variability (1895–2009). *J. Clim.* 23, 4571–4584. doi: 10.1175/2010JCLI3493.1

Robson, J., Ortega, P., and Sutton, R. (2016). A reversal of climatic trends in the north atlantic since 2005. *Nat. Geosci.* 9, 513–517. doi: 10.1038/ngeo2727

Sandø, A. B., Mousing, E. A., Budgell, W., Hjøllo, S. S., Skogen, M. D., and Ådlandsvik, B. (2021). Barents sea plankton production and controlling factors in a fluctuating climate. *ICES J. Marine Sci.* 78, 1999–2016. doi: 10.1093/icesjms/fsab067

Sandø, A. B., Nilsen, J. Ø., Gao, Y., and Lohmann, K. (2010). Importance of heat transport and local air-sea heat fluxes for barents sea climate variability. *J. Geophys. Res. Oceans* 115. doi: 10.1029/2009JC005884

Skagseth, Ø., Furevik, T., Ingvaldsen, R., Loeng, H., Mork, K. A., Orvik, K. A., et al. (2008). "Volume and heat transports to the arctic ocean via the norwegian and barents seas," in *Arctic–Subarctic Ocean Fluxes* (Springer), 45–64.

Smedsrud, L. H., Esau, I., Ingvaldsen, R. B., Eldevik, T., Haugan, P. M., Li, C., et al. (2013). The role of the barents sea in the arctic climate system. *Rev. Geophys.* 51, 415–449. doi: 10.1002/rog.20017

Smedsrud, L. H., Ingvaldsen, R., Nilsen, J., and Skagseth, Ø. (2010). Heat in the barents sea: Transport, storage, and surface fluxes. *Ocean Sci.* 6, 219–234. doi: 10.5194/os-6-219-2010

Stevens, B., Giorgetta, M., Esch, M., Mauritsen, T., Crueger, T., Rast, S., et al. (2013). Atmospheric component of the mpi-m earth system model: Echam6. *J. Adv. Model. Earth Syst.* 5, 146–172. doi: 10.1002/jame.20015

Yashayaev, I., and Seidov, D. (2015). The role of the atlantic water in multidecadal ocean variability in the nordic and barents seas. *Progr. Oceanography* 132, 68–127. doi: 10.1016/j.pocean.2014.11.009

Yeager, S. G., Karspeck, A. R., and Danabasoglu, G. (2015). Predicted slowdown in the rate of atlantic sea ice loss. *Geophys. Res. Lett.* 42, 10–704. doi: 10.1002/2015GL065364

Conflict of Interest: The authors declare that the research was conducted in the absence of any commercial or financial relationships that could be construed as a potential conflict of interest.

Publisher's Note: All claims expressed in this article are solely those of the authors and do not necessarily represent those of their affiliated organizations, or those of the publisher, the editors and the reviewers. Any product that may be evaluated in this article, or claim that may be made by its manufacturer, is not guaranteed or endorsed by the publisher.

Copyright © 2022 Koul, Brune, Baehr and Schrum. This is an open-access article distributed under the terms of the Creative Commons Attribution License (CC BY). The use, distribution or reproduction in other forums is permitted, provided the original author(s) and the copyright owner(s) are credited and that the original publication in this journal is cited, in accordance with accepted academic practice. No use, distribution or reproduction is permitted which does not comply with these terms.

frontiers in Marine Science

ORIGINAL RESEARCH
published: 28 January 2022
doi: 10.3389/fmars.2021.777427

Exploring the Potential of Forecasting Fish Distributions in the North East Atlantic With a Dynamic Earth System Model, Exemplified by the Suitable Spawning Habitat of Blue Whiting

Anna K. Miesner[1,2], Sebastian Brune[2], Patrick Pieper[2], Vimal Koul[1,2], Johanna Baehr[2] and Corinna Schrum[1,2]*

[1] Institute of Coastal Systems - Analysis and Modeling, Helmholtz-Zentrum Hereon, Geesthacht, Germany, [2] Institute of Oceanography, Universität Hamburg, Hamburg, Germany

OPEN ACCESS

Edited by:
Hjálmar Hátún, Faroe Marine Research Institute (FAMRI), Faroe Islands

Reviewed by:
Tommaso Russo, University of Rome Tor Vergata, Italy
Gang Hou, Guangdong Ocean University, China
Brian R. MacKenzie, Technical University of Denmark, Denmark

***Correspondence:**
Anna K. Miesner
anna.miesner@hereon.de

Specialty section:
This article was submitted to Marine Fisheries, Aquaculture and Living Resources, a section of the journal Frontiers in Marine Science

Received: *15 September 2021*
Accepted: *22 December 2021*
Published: *28 January 2022*

Citation:
Miesner AK, Brune S, Pieper P, Koul V, Baehr J and Schrum C (2022) Exploring the Potential of Forecasting Fish Distributions in the North East Atlantic With a Dynamic Earth System Model, Exemplified by the Suitable Spawning Habitat of Blue Whiting. Front. Mar. Sci. 8:777427. doi: 10.3389/fmars.2021.777427

Local oceanographic variability strongly influences the spawning distribution of blue whiting (*Micromesistius poutassou*). Here, we explore the potential of using a dynamic Earth System Model (ESM) to forecast the suitable spawning habitat of blue whiting to assist management. Retrospective forecasts of temperature and salinity with the Max Planck Institute ESM (MPI-ESM) show significant skill within blue whiting's spawning region and spawning depth (250–600 m) during the peak months of spawning. While persistence forecasts perform well at shorter lead times (≤2 years), retrospective forecasts with MPI-ESM are clearly more skilful than persistence in predicting salinity at longer lead times. Our results indicate that retrospective forecasts of the suitable spawning habitat of blue whiting based on predicted salinity outperform those based on calibrated species distribution models. In particular, we find high predictive skill for the suitable spawning habitat based on salinity predictions around one year ahead in the area of Rockall-Hatton Plateau. Our approach shows that retrospective forecasts with MPI-ESM show a better ability to differentiate between the presence and absence of suitable habitat over Rockall Plateau compared to persistence. Our study highlights that physical-biological forecasts based on ESMs could be crucial for developing distributional forecasts of marine organisms in the North East Atlantic.

Keywords: species distribution model, habitat preference, spawning, North Atlantic, climate variability, ecological forecast, prediction, MPI-ESM

INTRODUCTION

Current advances of dynamic Earth System Models (ESMs) have permitted skilful predictions of the marine climate (i.e., temperature and salinity) on seasonal to decadal timescales and thereby sparked the development of marine biological forecasts (Payne et al., 2017; Tommasi et al., 2017a; Koul et al., 2021). When a link between the marine climate and marine organisms is identified,

forecasts of the marine climate can be converted into biological forecasts and thereby enable "dynamic ocean management" (Hobday et al., 2016). Until now, the majority of operational examples are distributional forecasts of marine organisms, mostly fish, which are provided at near-real-time to seasonal timescales (Hobday et al., 2011; Eveson et al., 2015; Kaplan et al., 2016; Siedlecki et al., 2016; Lehodey et al., 2018; Malick et al., 2020). This is far below the predictive potential of the ocean where skilful predictions are possible several years and even a decade in advance, as shown in particular for the North Atlantic (Matei et al., 2012; Shaffrey et al., 2017; Tommasi et al., 2017b; Yeager and Robson, 2017). Accordingly, the North Atlantic is promising for exploring the predictive potential of coupled physical–biological forecasts beyond seasonal time scales. An economically important North East Atlantic fish species with an established link between the marine climate and its spawning distribution is blue whiting (*Micromesistius poutassou*; Hátún et al., 2009b; Miesner and Payne, 2018). Therefore, this species serves as an ideal case study to explore the potential of forecasting distributional changes at inter-annual to multi-annual time scales.

Blue whiting is a migratory fish species that is distributed meso-pelagically from the Strait of Gibraltar to off-shore Greenland (Post et al., 2019) and the Barents Sea (Heino et al., 2008; ICES, 2019). Most fishing takes place during spring in an area west of the British Isles where blue whiting aggregate to spawn (NEAFC, 2013). While spawning commonly takes place in the deep waters along the European Continental Shelf, in some years changes in the marine climate trigger a westward expansion of the spawning distribution onto Rockall Plateau and Hatton Bank (**Figure 1C**; Hátún et al., 2009b; Miesner and Payne, 2018). This area of Rockall-Hatton Plateau (RHP) straddles both international and national waters (with disputed economic boundaries; Yiallourides, 2018; Johnson et al., 2019) and forecasting changes in the spawning distribution at inter-annual to multi-annual time scales could therefore be beneficial for a range of stakeholders and nations.

Forecasting spatial changes of the spawning distribution could also be useful for the monitoring and management of blue whiting. Every spring the International Blue Whiting Spawning Stock (IBWSS) survey samples the core spawning region of blue whiting (ICES, 2015). However, sampling is particularly challenging on RHP due to great distance to the ports and frequent bad weather conditions (ICES, 2010). Therefore, forecasting blue whiting in its spawning region with a special focus on RHP (e.g., whether spawning is going to take place on RHP) could be valuable for the IBWSS planning group (pers. communication with Jan Arge Jacobsen, member of the ICES Working Group of International Pelagic Surveys, Faroe Marine Research Institute). Accordingly, a forecast at interannual to multiannual timescales could be used as an objective decision-making tool to adjust the IBWSS survey coverage on RHP.

Forecasting the spatial distribution of marine organisms is related to the theory of the ecological niche or suitable habitat of a species (Payne et al., 2017). Previous work established the mechanistic link between the marine climate (i.e., salinity) and the spawning distribution of blue whiting based on species distribution modelling (Miesner and Payne, 2018). Species distribution models (SDMs) are also termed ecological niche models or habitat models, and represent a common method to define the suitable (i.e., potential) habitat of a species by means of correlative models that link species distribution data with environmental observations (Elith and Leathwick, 2009; Wiens et al., 2009). The suitable habitat of a species is commonly used as a proxy for its spatial distribution and applied in marine ecological forecasts such as for the spatial management of southern bluefin tuna in Australian waters (Hobday and Hartmann, 2006; Eveson et al., 2015), or Pacific sardine in Californian waters (Kaplan et al., 2016; Siedlecki et al., 2016).

Based on the previously developed SDM (Miesner and Payne, 2018) and persistence of salinity, first attempts to operationalise a forecast of the suitable spawning habitat of blue have been undertaken (ICES, 2018; Payne and Lehodey, 2019) and are currently provided two months prior to the IBWSS survey (Payne, 2021). However, due to the highly variable nature of the marine environment, the management of living marine resources, such as fish, challenges the stationary assumption in persistence forecasts (Tommasi et al., 2017a). The oceanographic conditions in the spawning region of blue whiting are characterised by a mixture of warm and saline subtropical Eastern North Atlantic Water coming from the south and cool and fresh subpolar Western North Atlantic Waters from the north (Holliday et al., 2000; Hátún et al., 2009a). The relative mixture of these water masses is related to changes in the North Atlantic Subpolar Gyre (SPG) and creates a distinct marine climatic regime to which blue whiting respond through changes in their spatial distribution (Hátún et al., 2009b; Miesner and Payne, 2018). Generally, a strong SPG leads to fresher and cooler conditions in the spawning region, causing blue whiting to cluster along the continental shelf (Hátún et al., 2009b). A weak SPG promotes more saline and warm subtropical water masses which leads to a westward expansion of the spawning distribution onto Rockall Plateau and Hatton Bank (**Figure 1**; Hátún et al., 2009b; Miesner and Payne, 2018). A modelling study based on blue whiting larvae found that spawning is confined to a certain range of salinity and proposed that this link could form the basis of forecasting changes in the spawning distribution of blue whiting (Miesner and Payne, 2018). The dynamics of the SPG have been shown to be well represented in the dynamic coupled Max Planck Institute Earth System Model (MPI-ESM; Koul et al., 2019). Accordingly, we explore the potential for developing a forecast of the suitable spawning habitat of blue whiting based on annual to multi-annual time scales with MPI-ESM, which could be valuable for both augmenting monitoring surveys, and enhancing long-term management of the species.

In the first part of the study, we assess whether the marine climate, i.e., temperature and salinity, is predictable within the region and depth at which blue whiting spawn during the months of spawning. We judge the quality of the MPI-ESM hindcast by comparing it to two reference data sets: the EN4 objective analysis (Good et al., 2013) and the MPI-ESM ensemble Kalman filter assimilation (Polkova et al., 2019; Brune and Baehr, 2020). In the second part of the study, we analyse two ways to extract information on the suitable spawning habitat from SDMs and

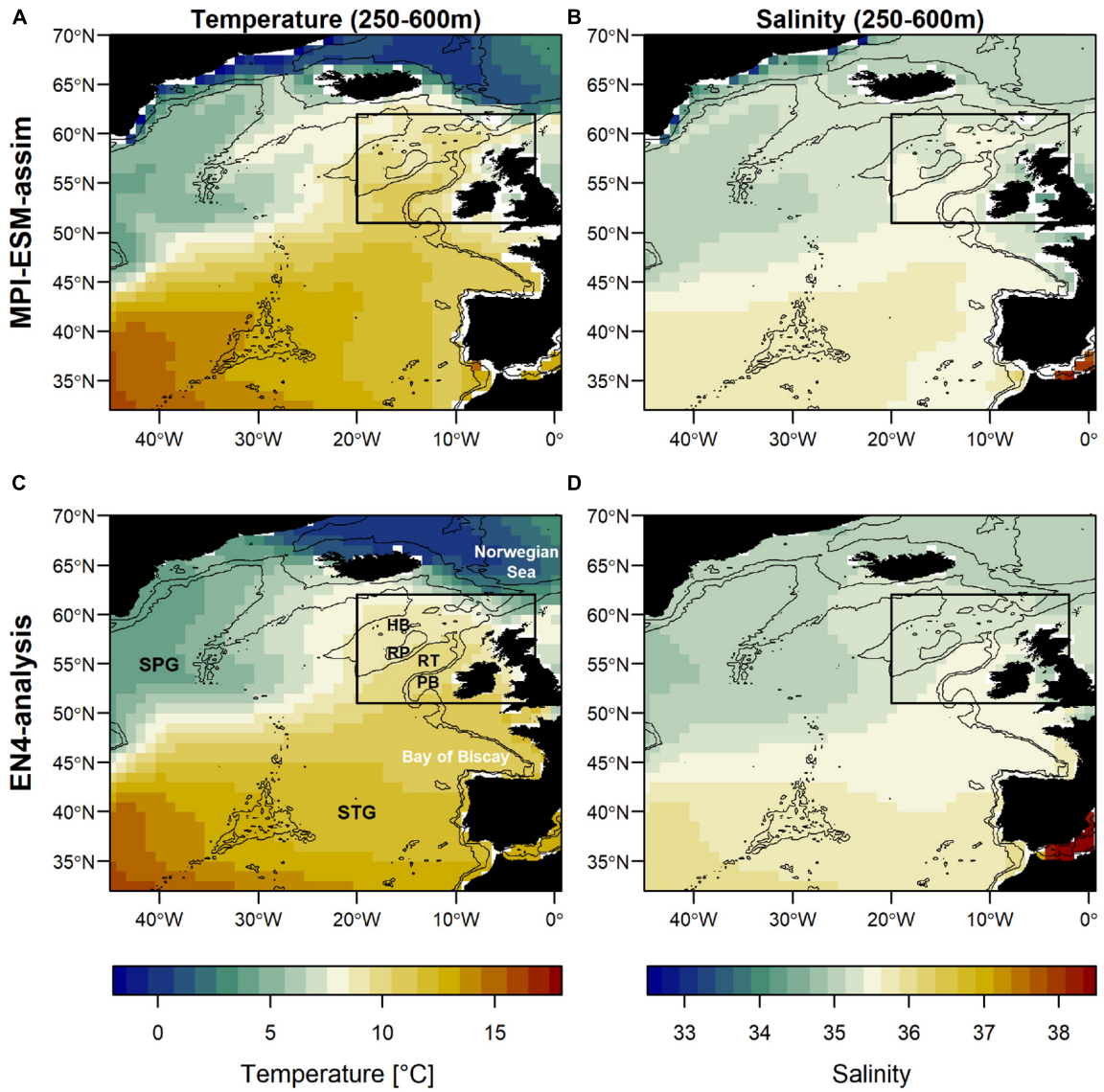


FIGURE 1 | Mean oceanographic conditions in February, March and April (FMA; climatology of 1965–2016) within the spawning depth of blue whiting (250–600m) in terms of temperature (left; **A,C**) and salinity (right; **B,D**) for *MPI-ESM-assim* (top; **A,B**) and *EN4-analysis* (bottom; **C,D**). The black rectangle delineates the study area: the spawning region of blue whiting. Labels in panel **(C)** show the geographic features Hatton Bank (HB), Rockall Plateau (RP), Rockall Trough (RT), Porcupine Bank (PB), and the two dominant gyre systems North Atlantic subpolar gyre (SPG) and the subtropical gyre (STG). Bathymetry is indicated by 600 and 2000 m isobaths.

explore the potential of forecasting the suitable spawning habitat of blue whiting up to five years ahead.

MATERIALS AND METHODS

Modelling and Analysis Strategy

We analyse the skill of 5-year predictions of the marine climate and subsequently of the suitable spawning habitat of blue whiting. These are based on decadal retrospective forecasts, in the following called hindcasts, of the dynamical state of the ocean with MPI-ESM (Polkova et al., 2019; Brune and Baehr, 2020). In the first part of the study, we analyse whether we can make skilful predictions of the marine climate with the MPI-ESM hindcast at spatial and temporal scales relevant for spawning blue whiting. We assess the quality of the hindcast by comparison to two reference products: the EN4 objective analysis (Good et al., 2013) and the MPI-ESM ensemble Kalman filter assimilation (Polkova et al., 2019; Brune and Baehr, 2020), hereafter referred to as *EN4-analysis* and *MPI-ESM-assim*, respectively (**Figure 2**.1).

The spatially complete *EN4-analysis* provides *one* way of filling the gaps between sparsely observed oceanic profiles using iterative optimal interpolation (Good et al., 2013). Another approach is used by *MPI-ESM-assim,* where EN4 profiles are incorporated into the ocean model component of a dynamic ESM. We are aware that, strictly speaking, *MPI-ESM-assim* and

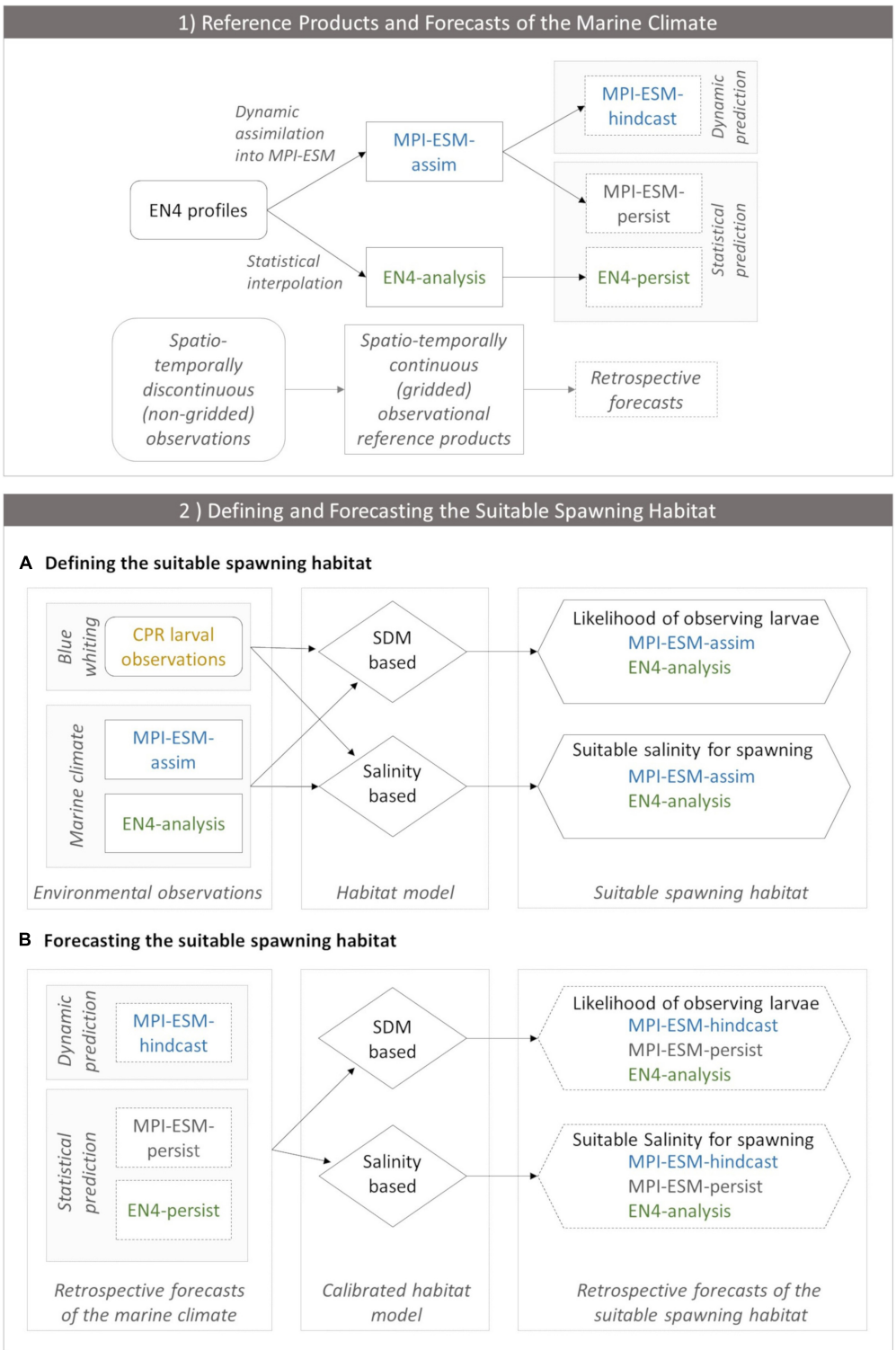


FIGURE 2 | (1) Observational reference products of the marine climate (*EN4-analysis* and *MPI-ESM-assim;* solid boxes) and the corresponding retrospective forecasts (dashed lines) employed in the study and (2) the workflow of defining **(A)** and forecasting **(B)** the suitable spawning habitat of blue whiting. In panel (1) EN4 profiles (rounded box) contain spatio-temporally discontinuous (non-gridded) observations of the marine climate. In order to create spatio-temporally continuous (gridded) observational reference products, either EN4 profiles are assimilated into MPI-ESM resulting in *MPI-ESM-assim* or EN4 profiles are statistically interpolated forming the *EN4-analysis.* Thereby, both *MPI-ESM-assim* and *EN4-analysis* contain the same non-gridded oceanographic observations (EN4 profiles) but their methods to close observational gaps differ. These observational reference products form the basis for retrospective forecasts of the marine climate. *MPI-ESM-assim*

(Continued)

FIGURE 2 | forms the basis for the dynamic prediction system *MPI-ESM-hindcast*. Moreover, *MPI-ESM-assim* and *EN4-analysis* are employed to form the statistical persistence forecasts *MPI-ESM-persist* and *EN4-persist*, respectively. (2) Workflow of defining **(A)** and forecasting **(B)** the suitable spawning habitat of blue whiting, indicating how input data (rectangles) feeds into each habitat model (rhombus) which transform this information into approximations of the suitable spawning habitat (hexagon). **(A)** Environmental observations include CPR larval observations of blue whiting (yellow) and information from the marine climate from either *MPI-ESM-assim* (blue) or *EN4-analysis* (green). These environmental observations calibrate each habitat model. The SDM translates this information into the likelihood of observing larvae for *MPI-ESM-assim* and *EN4-analysis,* respectively, which is a probabilistic proxy for the suitable spawning habitat. The salinity based habitat model transforms the environmental observations into the suitable salinity for spawning for *MPI-ESM-assim* and *EN4-analysis,* respectively, which forms a deterministic proxy for the suitable spawning habitat. **(B)** Forecasts of the suitable spawning habitat are based on retrospective forecasts of the marine climate (dashed rectangles) which includes one dynamic prediction system (*MPI-ESM-hindcast;* blue) and two statistical predictions (*MPI-ESM-persist* or *EN4-persist*; grey and green, respectively). Each retrospective forecast of the marine climate feeds into a calibrated habitat model (either the SDM or salinity based), which transforms this information into retrospective forecasts of the suitable spawning habitat (either in terms of the likelihood of observing larvae for the SDM based habitat model, or the suitable salinity for spawning).

MPI-ESM-hindcast may not be totally independent. Nevertheless, assimilations with MPI-ESM can be used to overcome the problem that oceanic observations insufficiently sample the oceanic state, and to create a consistent reference state (Brune et al., 2015; Brune and Baehr, 2020). Both our reference products rely on EN4 profiles. We therefore expect that the considerable increase in the number of profiles after 2001 with the Argo program decreases the uncertainty in our reference products after 2001. Finally, the predictive skill of the hindcast is assessed retrospectively by comparison to reference forecasts based on *EN4-analysis* and *MPI-ESM-assim* persistence.

In the second part of the study, we analyse whether we can make skilful predictions of the suitable spawning habitat of blue whiting (a workflow of this approach is presented in **Figure 2**.2). We explore two ways to extract information on the suitable spawning habitat from SDMs. While we create novel SDMs based on either *MPI-ESM-assim* or *EN4-analysis* in the first approach, the second method employs the salinity defined as suitable for spawning by Miesner and Payne (2018) to delineate the suitable spawning habitat. The approach that is superior in representing the observed spawning distribution of blue whiting is subsequently employed for the creation of coupled physical-biological forecasts. Here, the suitable spawning habitat of blue whiting is forecasted retrospectively based on the MPI-ESM hindcast and two persistence forecast and their predictive skill is judged against fishery and survey observation.

Study Region and Time Period of Interest

The study region covers the core spawning area of blue whiting west of the British Isles which is sampled annually by the ICES IBWSS survey (ICES, 2015): 20°W to 2°W and 51°N to 62°N (black rectangle in **Figure 1**) and will henceforth be referred to as spawning region. We define RHP by the local bathymetry, following the 1,000 m depth isobath around Rockall Plateau, George Bligh Bank and Hatton Bank finishing west at the border of the IBWSS sampling region. To encompass the depth range where eggs, non-feeding larvae and spawning adults have been observed (Coombs et al., 1981; Hillgruber and Kloppmann, 1999; Ådlandsvik et al., 2001), we define the spawning depth of blue whiting between 250 and 600 m. The main spawning activity of blue whiting takes place during late March and early April which corresponds to the timing of the IBWSS survey (Bailey, 1982; ICES, 2015). Since blue whiting larvae are observed in the surface waters mainly between March and May with a peak in April (Pointin and Payne, 2014; Miesner and Payne, 2018) and need around 3 weeks for the ascent to the surface (Ådlandsvik et al., 2001), it is likely that spawning ranges from February to April.

Accordingly, the average temperate and salinity between February and April (FMA) at 250 to 600 m depth within the spawning region of blue whiting resembles the oceanographic conditions, i.e., the marine climate, experienced by the spawning adults and the larvae.

Observations and Retrospective Forecasts of Temperature and Salinity

Observations of Temperature and Salinity

Monthly observations of ocean temperature and salinity are available from the Met Office Hadley Centre's EN4 data set (Good et al., 2013). Besides quality controlled *in situ* profiles, hereafter termed EN4 profiles, a spatially comprehensive objective analysis is available which uses an iterative optimal interpolation to fill all observational gaps. We use the EN4 objective analysis version 4.2.1 with corrections based on Gouretski and Reseghetti (2010), which is available from 1900 to the present and contains 42 vertical levels and a regular 1° horizontal resolution (Good et al., 2013) and will be referred to as *EN4-analysis*. We select the period 1958–2016 and average yearly FMA-mean values of temperature and salinity vertically over 252–596 m to characterise the marine climate in the spawning region and depth of blue whiting.

Assimilation and Dynamical Hindcasts of Temperature and Salinity

Another way of creating a spatially complete data set that serves as a good estimate of the true state of the ocean, is to incorporate (i.e., assimilate) oceanic observations into a coupled ocean-atmosphere model. We use an experiment from the Max Planck Institute ESM at low resolution (MPI-ESM; Giorgetta et al., 2013). Its ocean component (Jungclaus et al., 2013) contains 40 levels and has an effective resolution of around 0.6°–0.9° (67–100 km) within the spawning region. Monthly observations of oceanic temperature and salinity from EN4 profiles (Good et al., 2013) are assimilated into MPI-ESM using a full-value 16-member ensemble Kalman filter (EnKF) approach (Polkova et al., 2019; Brune and Baehr, 2020). Additionally, the dynamical state of the atmospheric component is nudged toward ERA40/ERAInterim reanalyses from ECMWF (Uppala et al., 2005; Dee et al., 2011), and external forcings of the Phase 5

Coupled Model Intercomparison Project (CMIP5) were applied (Taylor et al., 2012). We run MPI-ESM with these settings from 1958 to 2016 and simulate an assimilation which will henceforth be referred to as *MPI-ESM-assim*. Thereby, *MPI-ESM-assim* dynamically represents observed temperature and salinity in a model-consistent way (Brune and Baehr, 2020).

Based on *MPI-ESM-assim*, a 16-member hindcast ensemble is created (Brune and Baehr, 2020), which will be referred to as *MPI-ESM-hindcast*. *MPI-ESM-hindcast* is initialised every year from the 1st of November 1960 to 2016. In this study, each initialisation is running for 5 years. The time counting from the initialisation date of the hindcast is termed lead time. Accordingly, if the initialisation date is November 1960 and the hindcast is for March (or FMA) 1961, the (mean) lead time is 4 months and within lead year 1, while a hindcast for March (or FMA) 1962 has a lead time of (around) 1 year and 4 months, or within lead year 2.

We regrid both *MPI-ESM-assim* and *MPI-ESM-hindcast* to a $1° \times 1°$ regular grid and create the average of the 16 ensemble members (i.e., the ensemble mean) which we analyse throughout the study. For *MPI-ESM-assim* and *MPI-ESM-hindcast* we average annual FMA-mean values of temperature and salinity vertically between 240 and 600 m to derive the environmental conditions within the spawning depth of blue whiting.

Persistence Forecast

Persistence forecasts are a common reference in seasonal to decadal forecasting used to judge the skill of a hindcast: hindcasts which outperform persistence exemplify the benefit of using a dynamic ESM (Wilks, 2011; Jolliffe and Stephenson, 2012). Persistence forecasts presume that future conditions are equal to past conditions, e.g., a persistence forecast of FMA in 1965 with a lead time of two years, uses observations of FMA in 1963 as a forecast by assuming stationarity for the duration of the forecast (i.e., 2 years). We create persistence forecasts for *EN4-analysis* and *MPI-ESM-assim* for five lead years, termed *EN4-persist* and *MPI-ESM-persist*, respectively.

Predictability of Temperature and Salinity Within the Spawning Region of Blue Whiting

Here, we compare retrospective forecasts (i.e., *MPI-ESM-hindcast*, *MPI-ESM-persist* and *EN4-persist*) to *MPI-ESM-assim* and *EN4-analysis*, by means of the anomaly correlation coefficient (ACC) and the root-mean squared error (RMSE) which are common measures of forecast accuracy (Wilks, 2011; Jolliffe and Stephenson, 2012). We calculate anomalies based on the mean temperature and salinity of the common time period (1965–2016; e.g., FMA 1965 minus mean FMA from 1965 to 2016). In order to remove the influence of long-term trends on the prediction we linearly detrend the time series before calculating the skill. To account for the uncertainty in predictive skill, we perform a bootstrap with 500 iterations of ACC and RMSE for the common time period (the years 1965–2016 are shuffled 500 times with replacement and the ACC/RMSE calculated for each lead year). Significance of the ACC is defined from the 95% confidence interval of the bootstrap. Throughout the study, we show the median ACC and RMSE.

To analyse prediction skill over lead time the detrended anomalies are averaged over the study region and ACC and RMSE calculated. For this, the mean bias between forecast and observation is calculated and subtracted from the forecast for each year before RMSE and ACC are calculated from the respective time series. The confidence interval calculated from the bootstrap is defined as the interquartile range between the lower quartile (25th percentile) and the upper quartile (75th percentile) of the bootstrapped data. For the spatial representation of predictive skill, ACC and RMSE are calculated for each grid point where water depth exceeds 600 m. Water depth is based on NOAAs ETOPO1 product (Amante and Eakins, 2009).

Forecasting the Suitable Spawning Habitat of Blue Whiting Retrospectively

Retrospective Forecasts Based on SDMs

We create novel SDMs with observations of blue whiting larvae from the Continuous Plankton Recorder (CPR) survey (Reid et al., 2003) obtained from the Marine Biological Association in Plymouth. The probability of observing blue whiting larvae is modelled as a function of a fixed geographical model component, including latitude and the day-of-the-year, bathymetry, the solar elevation angle and varying environmental variables (**Table 3**) using Generalised Additive Models (Wood, 2006) analogous to Miesner and Payne (2018). Thus, the SDM accounts for the meridional migration of adults (Bailey, 1982) and the diel vertical migration of larvae (Hillgruber and Kloppmann, 2000) which can affect the capture efficiency of the CPR (Pointin and Payne, 2014). The environmental variables consist of temperature and salinity, since these are predictable with ESMs.

We create two sets of SDMs: one calibrated with environmental data from *EN4-analysis* and another one calibrated with *MPI-ESM-assim*, in order to account for the difference in these products in handling the spatially incomplete EN4 profiles. We calculate the salinity and temperature at the spawning depth of blue whiting during the time of spawning (S_{SPAWN} and T_{SPAWN}), i.e., one month prior to a CPR observation (Miesner and Payne, 2018), by averaging vertically over 252–596 m for EN4 and 240–600 m for MPI-ESM, since the depth layers slightly vary between the two. At locations where water depth is shallower than 252 m for *EN4-analysis* or shallower than 240 m for MPI-ESM, we select variables closest to the seafloor. In order for the SDMs to be comparable, we couple the same CPR observations to *EN4-analysis* and *MPI-ESM-assim*, containing 48 years from 1958 to 2005 including 68,229 observations with 938 presences of blue whiting larvae. The resulting spatial distribution of larval-presence probability can be understood as a proxy for the suitable spawning habitat of blue whiting (Miesner and Payne, 2018).

Validation of the SDM and model selection is in line with Miesner and Payne (2018). As a primary metric for model selection, we choose the Akaike Information Criteria (AIC); Anderson, 2008; Burnham et al., 2011). The explained deviance is equivalent to the coefficient of determination (R^2) and considered an overall indicator of model quality.

We derive the capability of the models to distinguish between the presence and absence of larvae from a contingency table (**Table 1**). We convert the predicted probability of blue whiting larval-occurrence from the SDM into presences and absences by selecting the threshold so that the total number of presences in the prediction data set is equal to the number of presences in the observed dataset, in accordance with Freeman and Moisen (2008). Moreover, we calculate mean values of the true skill statistic (TSS), positive predictive value (PPV), and negative predictive value (NPV) based on four-fold cross validation with 75% of the data used for training and the remaining for validation, with every 4th year included in one fold (**Table 2**; see also Liu et al., 2011; Jolliffe and Stephenson, 2012). Additionally, we consider the area under the receiver operating characteristic curve (AUC), which relates the relative proportions of correctly and incorrectly classified predictions (HR and FAR, respectively) over a range of threshold levels (Brown and Davis, 2006; Liu et al., 2011).

We base the choice of the best performing SDM on two steps. First we create a subset for each of the two SDM sets (one calibrated with *EN4-analysis* and the other with *MPI-ESM-assim*) with all models having AIC differences smaller than 15 (**Table 3**), since models with an AIC difference larger than 15 are considered to be very dissimilar (Anderson, 2008). From these subsets, we select the SDM with the highest predictive performance in terms of TSS, PPV, NPV, and AUC as the "best" performing model and analyse it further.

We create retrospective forecasts of the suitable spawning habitat by coupling the best performing SDMs (**Table 3**) to retrospective forecast of the marine climate for up to five lead years. Specifically, we employ the best performing SDM calibrated with *MPI-ESM-assim* for retrospective forecasts based on *MPI-ESM-hindcast* and *MPI-ESM-persist*. While we use the best performing SDM fitted to *EN4-analysis* for retrospective forecasts based on *EN4-persist*. Within the SDM, we select the 15th of each month as the day-of-year owing to the monthly resolution of environmental data and fix the solar elevation angle to 0°, representative of sunrise or sunset, in line with Miesner and Payne (2018). SDMs are calibrated with full-value temperature and salinity data (i.e., not anomalies) from *MPI-ESM-assim* and *EN4-analysis*, respectively, and transform this information into blue whiting larval presence probability. Therefore, forecasts based on SDMs are directly comparable and there is no need for bias correction.

TABLE 1 | Contingency table used to evaluate the predictive accuracy of binary events.

		Observation	
		Presence	**Absence**
Prediction	Presence	TP (hits)	FP (false alarms)
	Absence	FA (misses)	TA (correct negatives)

The numbers of observations and predictions in each category are represented by TP, FP, FA, and TA.
TP (true positives): correctly predicted presences, hits; FP (false positives): erroneously predicted presences, false alarms; FA (false absences): erroneously predicted absences, misses; TA (true absences): correctly predicted absences.

TABLE 2 | Verification Scores.

Name Quality Measure (Abbreviation)	Definition	Range
Positive Predictive Value (PPV)	TP/(TP + FP)	[0, 1]
Negative Predictive Value (NPV)	TA/(TA + FA)	[0, 1]
Hit Rate (HR)	TP/(TP + FA)	[0, 1]
False Alarm Rate (FAR)	FP/(FP + TA)	[0, 1]
True Skill Statistic (TSS)	HR - FAR	[-1, 1]

*The perfect result of the score is underlined. TP, FP, FN, and TN are entries in the contingency table (**Table 1**).*

Retrospective Forecasts Based on Salinity

As an alternative approach to creating new SDMs, solely the suitable salinity for spawning is used as a proxy for the suitable spawning habitat. A previous study based on SDMs, observations from the CPR and an earlier version of the EN4 objective analysis (EN4.1.1) showed a dome-shaped relationship between salinity (S_{SPAWN}) and the probability of observing blue whiting larvae with a non-zero likelihood of observing larvae at salinities between 35.28 and 35.53 (Miesner and Payne, 2018: SDM 3, **Table 4** and **Figure 9**). This suitable salinity for spawning corresponded well to independent observations from both fishery and scientific surveys (Miesner and Payne, 2018) and is in line with the re-calibrated SDM based on *EN4-analysis* that is applied in this study (SDM_S_{EN4}).

The suitable salinity for spawning in MPI-ESM is bias-corrected to offset the mean deviations between *MPI-ESM-assim* and *EN4-analysis* within the spawning region and during the time period for which validation data is available (0.06 for 1977–2012). Retrospective forecasts of the suitable salinity for spawning are based on full-value retrospective forecasts of salinity with *MPI-ESM-hindcast*, *MPI-ESM-persist* and *EN4-persist*. The respective isohaline where the salinity is defined suitable is used as a proxy for defining those grid cells in our simulation, which are deemed to cover the suitable spawning habitat.

Observations of Adult Blue Whiting

The first data set comprises of acoustic surveys of blue whiting spawning aggregations from 1981 to 2013, spanning 25 years due to incomplete time series. Before 2004 the observations were solely based on Norwegian surveys of the spawning stock, while data from 2004 onward originate from the from the IBWSS survey that is carried out annually for 2 weeks from late March to early April (ICES, 2016). The survey records acoustic data continuously along its cruise tracks and provides estimates of blue whiting biomass. While most years had a resolution of 0.5° latitude × 1° longitude, the data resolution is coarser for the period 2002–2006 with 1° latitude × 2° longitude.

The second set of independent observations consists of monthly fishery catch statistics of blue whiting from 1977 to 2012 from the NEAFC (2013) targeting spawning adults with a resolution of 0.5° latitude × 1° longitude. The fishery data is averaged over March and April, in congruence with the IBWSS survey data.

For both, the survey and the fishery data, the grid cells within the spawning region where blue whiting were observed

TABLE 3 | Model fitting results for species distribution models (SDM) calibrated with different environmental reference data (Env. Data).

Env. Data	Model	Formulation, f()	DevExpl	AIC	ΔAIC	TSS	PPV	NPV	AUC
MPI-ESM-assim	SDM_SSS_{MPI}	GEO + SSS	0.470	5337	101	0.358	0.367	0.991	0.964
	SDM_SST_{MPI}	GEO + SST	0.470	5325	89	0.359	0.367	0.991	0.966
	SDM_S_{MPI}	GEO + S_{SPAWN}	0.471	5319	83	0.360	0.368	0.991	0.965
	SDM_T_{MPI}	GEO + T_{SPAWN}	0.466	5362	126	0.351	0.360	0.991	0.965
	$SDM_SST+SSS_{MPI}$	GEO + SSS + SST	0.478	5259	23	0.370	0.378	0.992	0.966
	SDM_S+T_{MPI}	GEO + S_{SPAWN} + T_{SPAWN}	0.478	5257	21	0.366	0.375	0.992	0.966
	SDM_SSTSSS_{MPI}	GEO + SSS x SST	0.479	5255	19	0.372	0.381	0.991	0.965
	SDM_ST_{MPI}	GEO + S_{SPAWN} x T_{SPAWN}	0.482	5236	0	0.368	0.377	0.991	0.966
EN4-analysis	SDM_SSS_{EN4}	GEO + SSS	0.461	5408	148	0.349	0.358	0.991	0.964
	SDM_SST_{EN4}	GEO + SST	0.468	5343	83	0.356	0.365	0.991	0.965
	SDM_S_{EN4}	GEO + S_{SPAWN}	0.476	5268	8	0.367	0.376	0.992	0.966
	SDM_T_{EN4}	GEO + T_{SPAWN}	0.469	5341	81	0.353	0.362	0.992	0.964
	$SDM_SST+SSS_{EN4}$	GEO + SSS + SST	0.472	5309	49	0.361	0.370	0.991	0.965
	SDM_S+T_{EN4}	GEO + S_{SPAWN} + T_{SPAWN}	0.478	5260	0	0.351	0.360	0.991	0.964
	SDM_SSTSSS_{EN4}	GEO + SSS x SST	0.474	5289	29	0.365	0.374	0.991	0.966
	SDM_ST_{EN4}	GEO + S_{SPAWN} x T_{SPAWN}	0.476	5271	11	0.342	0.350	0.991	0.964

The geographical baseline model (GEO) includes latitude x day-of-the-year + solar elevation angle + log-transformed depth; in accordance with Miesner and Payne (2018). Environmental variables include, sea surface salinity (SSS), sea surface temperature (SST), and salinity and temperature at the spawning depth of blue whiting during the time of spawning (S_{SPAWN} and T_{SPAWN}, respectively).
With DevExpl, explained deviance; AIC, Akaike Information Criteria; ΔAIC, difference in AIC relative to the smallest AIC value within the model set. For predictive skill measures the mean value based on 4-fold cross validation is given: TSS, true skill statistic; PPV, positive predictive value; NPV, negative predictive value, area under the relative operating characteristic curve (AUC). Models with ΔAIC < 15 are highlighted with a grey shaded background.

or caught are treated as presence. All remaining cells are treated as absences, since absences of fish are hardly reported in catch statistics (e.g., for the months March and April only 0.1% of the available fisheries data within the spawning region were absences) and are also low in the survey (0.9% within the spawning region). Therefore, including the absence data would render the observations unfit for model- and forecast evaluation.

Predictive Skill of the Suitable Spawning Habitat Forecast

Observations of adult blue whiting in March and April are compared to retrospective forecasts of blue whiting's suitable spawning habitat averaged over March and April and for each lead year (0–5) using binary verification metrics based on the contingency table (**Table 1**). Accordingly, the output of the biological forecasts are brought to the same spatial grid as the observations (0.5° latitude × 1° longitude). Predicted presence-probabilities from the SDM are converted into presence and absence by selecting the threshold where predicted prevalence from the SDM is equal to observed prevalence (Freeman and Moisen, 2008). For the salinity based forecast, each grid cell within the range of the suitable salinity for spawning is defined as presence (of suitable habitat) and the remaining as absence.

We quantify predictability via TSS, the difference between Hit Rate and False Alarm Rate (**Table 2**). A TSS of 1 indicates that the forecast's accuracy is perfect, and a TSS of zero is associated with a purely random forecast (**Table 2**). In each grid point, all entries of the contingency table must be sufficiently filled for our analysis to be robust and viable. To ensure statistical reliability, we prescribe this condition for each 500-fold bootstrap iteration. In practice, the counts of true presences (TP) and false absences (FA) are the critical indicators. Thus, we neglect grid-cells when the sum of both critical indicators is equal to zero in at least one bootstrap iteration.

First, we evaluate both definitions of the suitable spawning habitat against fishery and survey data. Afterward, we select retrospective forecasts of the suitable spawning habitat at lead year 0 with best observational agreement in terms of TSS for more detailed analysis.

We analyse the predictive skill at RHP by pooling the bootstrapped forecast verification metrics (i.e., TSS) for each lead year over this region (averaging 40 and 46 grid cells for the survey and the fishery data, respectively). Uncertainty is expressed in terms of the interquartile range between the lower quartile (25th percentile) and the upper quartile (75th percentile)

TABLE 4 | Agreement of the suitable spawning habitat with independent observations of adult blue whiting observed in the IBWSS survey and caught in fishery (NEAFC) during March and April within the spawning region.

Observation	Habitat	Env. Data	PPV	NPV	HR	FAR	TSS
Survey (IBWSS)	SDM	EN4-analysis	0.49	0.63	0.54	0.45	0.08
		MPI-ESM-assim	0.49	0.52	0.38	0.39	0.00
	Suitable Salinity	EN4-analysis	0.31	0.83	0.75	0.63	0.12
		MPI-ESM-assim	0.49	0.70	0.77	0.59	0.18
Fishery (NEAFC)	SDM	EN4-analysis	0.38	0.74	0.49	0.41	0.08
		MPI-ESM-assim	0.33	0.68	0.33	0.34	-0.01
	Suitable Salinity	EN4-analysis	0.24	0.87	0.77	0.62	0.10
		MPI-ESM-assim	0.33	0.77	0.72	0.59	0.10

*The suitable spawning habitat comprises of the best performing species distribution models (SDM, SDM_S_{EN4} and SDM_ST_{MPI}) and based on the suitable salinity for spawning calibrated with different environmental reference data (Env. Data, MPI-ESM-assim and EN4-analysis); i.e., resembling a retrospective forecast for lead year 0. Mean values within the spawning region were calculated from the 500-fold bootstrap, with variables noted in **Table 3**.*

of the bootstrapped data. We define significance of the TSS by the 95% confidence interval of the bootstrap.

In order to analyse inter-annual variations in skill, we calculate the annually TSS averaged over RHP for retrospective forecasts made approximately one year ahead. Due to the different initialisation dates we compare *MPI-ESM-hindcast* with a lead time of around 16 months (lead year 2) to persistence forecasts at 12 months lead (lead year 1 for *EN4-persist* and *MPI-ESM-persist*).

The Suitable Spawning Habitat as an Indicator for Spawning on Rockall-Hatton Plateau

Finally, we evaluate whether retrospective forecast of the suitable spawning habitat can be applied to anticipate whether spawning takes place on RHP. For each year, the spatial coverage of blue whiting observations on RHP is calculated as the percentage of grid cells within RHP containing presences of blue whiting from fishery/survey observations in March and April. Likewise, the percentage of grid cells within RHP containing suitable habitat in RHP is calculated for each year in March and April, based on retrospective forecasts with *MPI-ESM-hindcast* for lead year 2 (16 months ahead) and persistence forecasts for lead year one (12 months ahead) with *EN4-persist* and *MPI-ESM-persist*.

RESULTS

Representations of the Marine Climate in EN4-Analysis and MPI-ESM-Assim

The large-scale features of temperature and salinity from February to April (FMA) are similar in *MPI-ESM-assim* and *EN4-analysis* within the spawning depth of blue whiting (250–600 m; **Figure 1**). However, on smaller scales (e.g., RP, RT), *MPI-ESM-assim* and *EN4-analysis* differ. Within the spawning region and spawning depth of blue whiting, anomalies of temperature agree well in *EN4-analysis* and *MPI-ESM-assim* (overall correlation in FMA of 0.85, bias 0.66°C; **Figure 3A**), while differences are more pronounced in terms of salinity (correlation 0.51; bias 0.08; **Figure 3B**). *EN4-analysis* and *MPI-ESM-assim* show similar temporal deviations from climatology and multi-decadal variability in both temperature and salinity. Both observational products show more saline and warmer water up to the 1970s and rather low anomalies around 1975 and from 1986 to around 1995, followed by an increase up to around 2010 and a stark decrease in subsequent years, again in line with observations from the eastern Ellet Line around Rockall Plateau (Holliday et al., 2015, 2020). During some periods, e.g., around 1965 and 1995 there is a tendency of *MPI-ESM-assim* to show a higher amplitude of deviations in terms of salinity than *EN4-analysis* (**Figure 3B**). Deviations from climatology are less pronounced for *MPI-ESM-hindcast*, as shown for lead year 2, in particular for salinity during the past 20 years of the study period (**Figure 3B**).

Predictive Skill of the Marine Climate

Within the spawning region of blue whiting, *MPI-ESM-hindcast* shows greater predictive skill for salinity compared to temperature and is more skilful than *MPI-ESM-persist*, when compared to *MPI-ESM-assim* (**Figure 4**). The salinity within the spawning region and spawning depth can skilfully be predicted for more than 4 years ahead (**Figures 4B,D**). In terms of the ACC, the hindcast of salinity outperforms persistence for all analysed lead years (**Figure 4B**), while the predictive skill of temperature is similar to persistence and degrades further after lead year 3 (**Figure 4A**). Moreover, salinity is more predictable than temperature, with a median ACC above 0.6 for all lead years analysed (**Figures 4A,B**).In terms of the RMSE *MPI-ESM-hindcast* is more skilful than *MPI-ESM-persist* in predicting both temperature and salinity, with most pronounced differences for temperature (**Figures 4C,D**), indicating that the hindcast is superior in representing the amplitude of observed variations in salinity, and in particular temperature. The RMSE of the persistence forecasts increases with increasing lead times, while

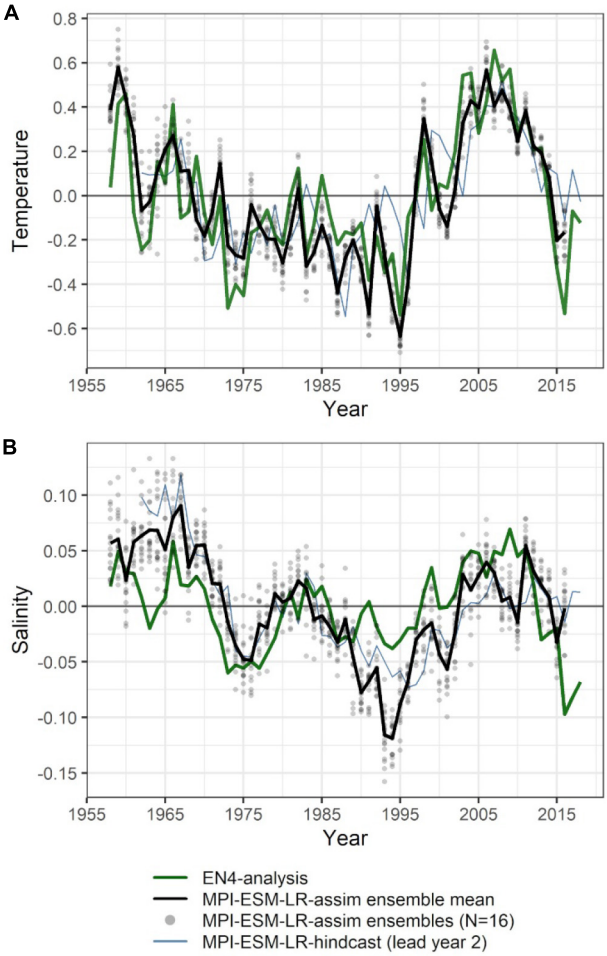


FIGURE 3 | Mean FMA temperature **(A)** and salinity **(B)** anomalies averaged over the spawning depth of blue whiting (250–600 m) within the spawning region (black rectangle in **Figure 1**). Data from *EN4-analysis* is indicated by the green line. The ensemble mean of the assimilation run of MPI-ESM (*MPI-ESM-assim*) is indicated by the black line and its individual ensembles are shown as grey dots, where overlapping ensembles create darker shades. *MPI-ESM-hindcast* of lead year 2 is added as blue line.

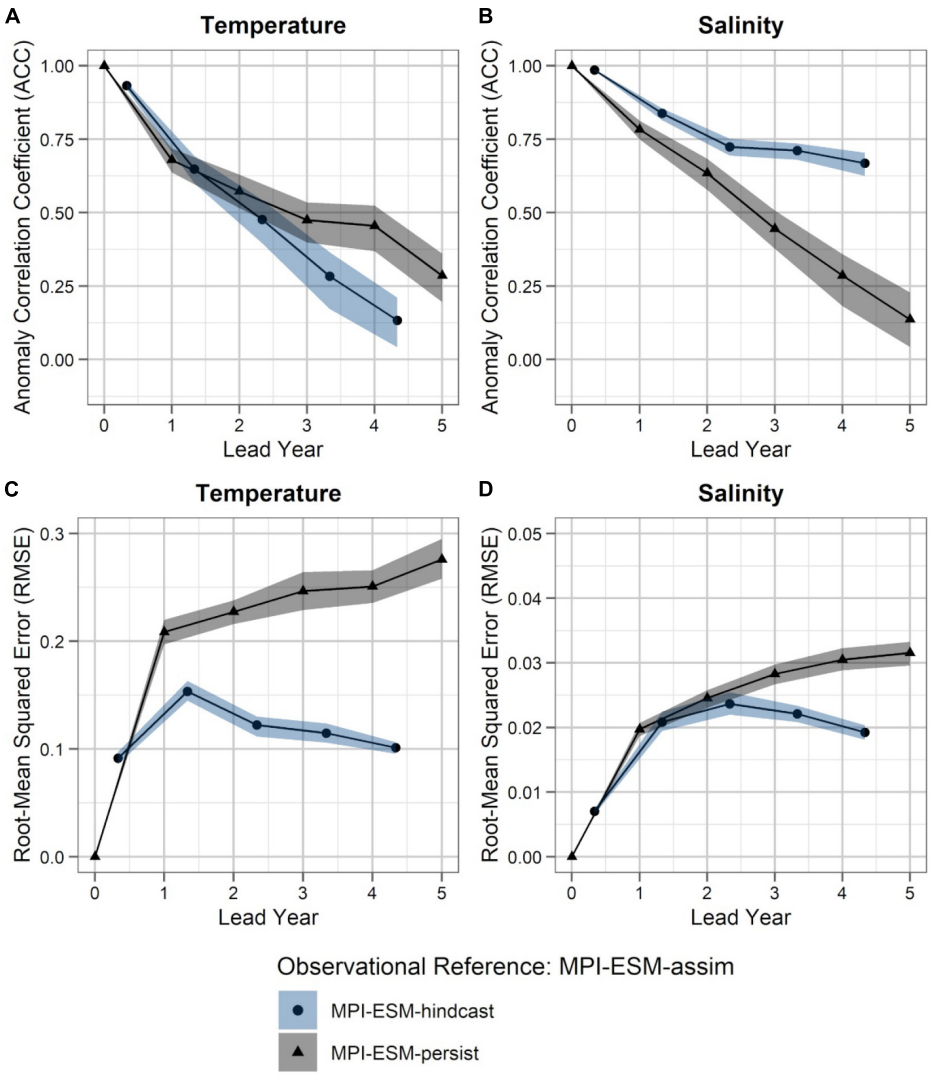


FIGURE 4 | Predictability of temperature (left; **A,C**) and salinity anomalies (right; **B,D**) averaged over 250–600 m in FMA within the spawning region (black rectangle in **Figure 1**), measured in terms of the anomaly correlation coefficient (ACC; top row) and root-mean squared error (RMSE; bottom row) of *MPI-ESM-hindcast* (bullet; blue area) and *MPI-ESM-persist* (triangle; grey), judged against *MPI-ESM-assim*. The connected bullets/triangles indicate the median and the blue/grey shaded areas indicate spread based on the lower and the upper quartile of a 500-fold bootstrap. Two correlations (or RMSEs) are markedly different when their respective shaded areas show no overlap.

the RMSE is rather constant for the hindcast from lead year 2 onward, indicating a greater accuracy of the hindcast with increasing lead times compared to persistence. Comparing *MPI-ESM-hindcast* to *EN4-analysis* shows a similar pattern for temperature; however, *MPI-ESM-hindcast* shows for salinity has a higher uncertainty and outperforms *EN4-persist* only after lead year 3 (**Figure 5**). Overall, the predictive skill of *MPI-ESM-persist* (**Figure 4**) and *EN4-persist* (**Figure 5**) is nearly identical and both show slightly higher ACC for salinity than for temperature.

Accordingly, considering both oceanographic reference products, a clear advantage of using *MPI-ESM-hindcast* in contrast to persistence is found after lead year three for salinity (**Figures 4B,D**, **5B,D**). This indicates that salinity can skilfully be predicted with *MPI-ESM-hindcast* at multi-annual lead times within blue whiting's spawning region and spawning depth during the peak months of spawning. For temperature, the hindcast is only superior in predicting the amplitude, but not the phase of observed variations, as indicated by significantly different values of RMSE but similar values of ACC when comparing persistence to *MPI-EM-hindcast* (**Figures 4A,C**, **5A,C**).

There are two large regions of high predictive skill of *MPI-ESM-hindcast* during FMA: one in the SPG region south west of Iceland and within the STG west off the European mainland, which are separated by a region of low predictive skill entering the spawning region from the south-west (**Figures 6**, **7**), similar to findings by Koenigk and Mikolajewicz (2009), Matei et al. (2012) Brune et al. (2018) and Frölicher et al. (2020).

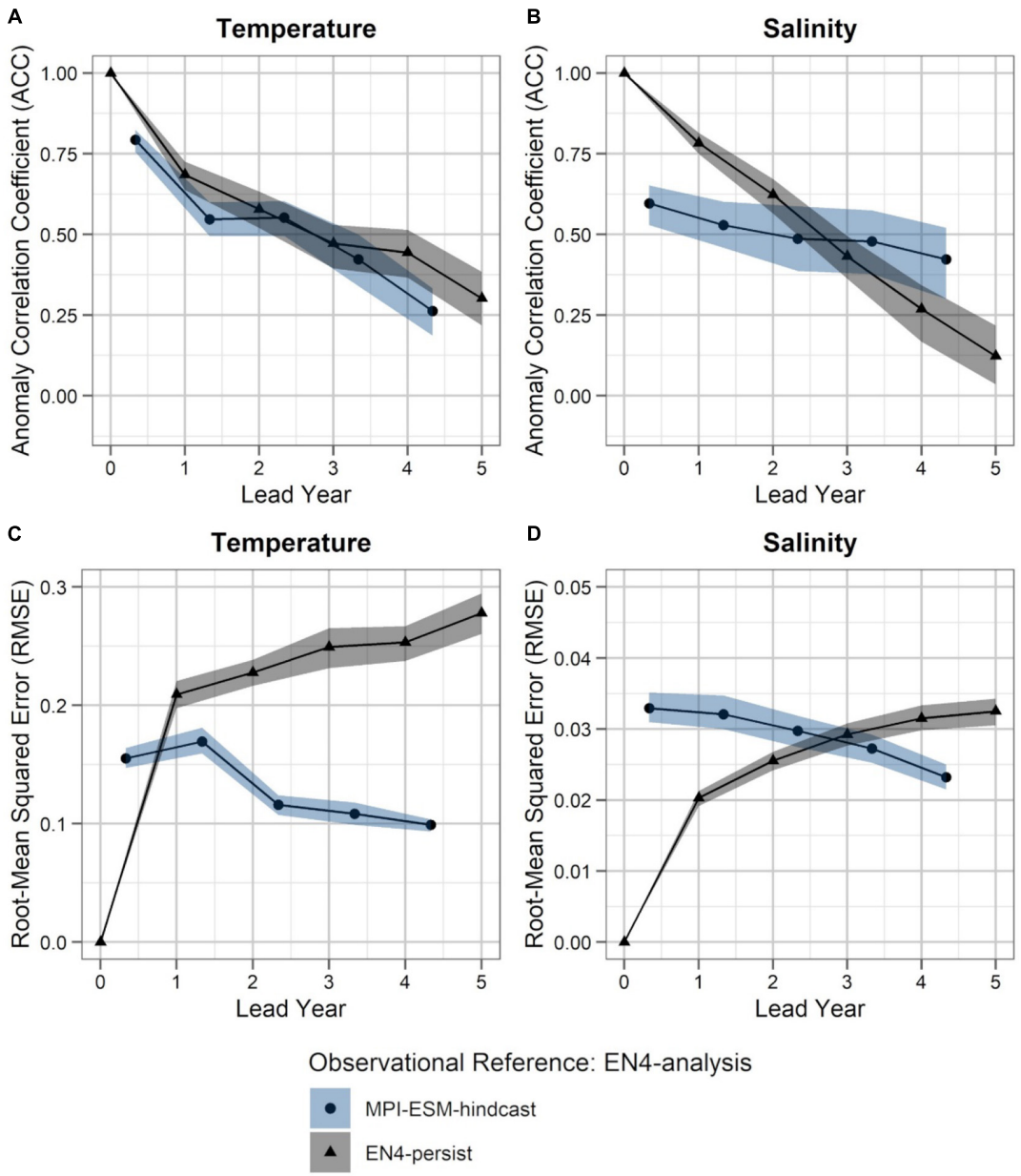


FIGURE 5 | Predictability of temperature (left; **A,C**) and salinity anomalies (right; **B,D**) averaged over 250–600 m in FMA within the spawning region (black rectangle in **Figure 1**), measured in terms of the anomaly correlation coefficient (ACC; top row) and root-mean squared error (RMSE; bottom row) of *MPI-ESM-hindcast* (bullet; blue area) and *EN4-persist* (triangle; grey), judged against *EN4-analysis*. The connected bullets/triangles indicate the median and the blue/grey shaded areas indicate spread based on the lower and the upper quartile of a 500-fold bootstrap. Two correlations (or RMSEs) are markedly different when their respective shaded areas show no overlap.

Zooming into the spawning region of blue whiting, the predictive skill is highest around Rockall Plateau and within Rockall Trough from Porcupine Bank toward the northeast, while predictive skill within the spawning region is lowest in the south-west around 45°N–50°N (**Figures 6**, 7). In terms of the ACC, *MPI-ESM-hindcast* of salinity is superior to temperature. However, for lead year 3 a strong decay in predictive skill is seen with regions toward the south–west of the spawning region, where correlations between *MPI-ESM-hindcast* and *MPI-ESM-assim* become insignificant for our analysis (**Figure 6**). Similarly, predictive skill in terms of RMSE is lowest toward the south-west (**Figure 7**).

Overall, the better hydrodynamic representation of *MPI-ESM-assim* compared to *EN4-analysis* together with the high predictive skill of salinity, specifically over longer lead times and in the area around RHP, with *MPI-ESM-hindcast*, encourage

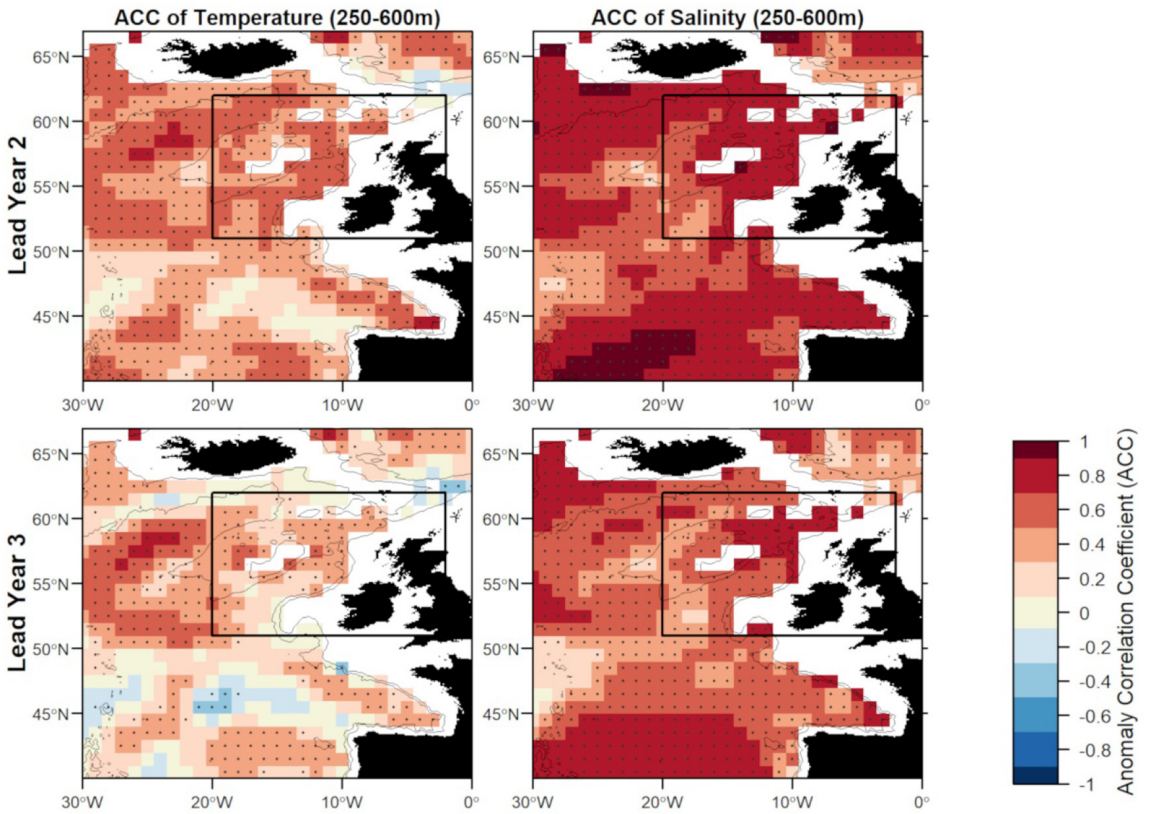


FIGURE 6 | Anomaly correlation coefficient (ACC) of temperature **(left)** and salinity **(right)** in FMA at lead year 2 (≈16 months) **(top)** and lead year 3 (≈28 months) **(bottom)** comparing *MPI-ESM-hindcast* to *MPI-ESM-assim*. Dots show significant correlations at the 95% confidence level, calculated from 500 bootstrap samples. The black rectangle delineates the study area: the spawning region of blue whiting; and black lines indicate the 600 and 2,000 m isobath.

the design of coupled-physical biological forecasts based on MPI-ESM.

The Suitable Spawning Habitat of Blue Whiting defined via SDMs and Salinity

We explore two ways of defining the suitable spawning habitat of blue whiting. In the first approach, SDMs are calibrated using various combinations of temperature and salinity from either *MPI-ESM-assim* or *EN4-analysis* (**Table 3**). For each oceanographic reference product the SDM with the highest predictive performance are SDM_ST_{MPI} and SDM_S_{EN4} (**Table 3**). These two SDMs are analysed further.

Specifically, for SDMs calibrated with environmental data from *MPI-ESM-assim*, including salinity and temperature at the spawning depth of blue whiting clearly yields the best performing model in terms of model parsimony with larval CPR data, showing the lowest AIC values and highest explained deviance (SDM_ST_{MPI}, **Table 3**). However, the cross-validated predictive skill of SDM_ST_{MPI} is similar to SDM_S_{EN4}, which is the best performing SDM calibrated with *EN4-analysis* which solely includes salinity as environmental variable (**Table 3**). Therefore, considering the predictive skill it seems irrelevant whether we use *MPI-ESM-assim* or *EN4-analysis* to calibrate the SDMs. For all SDMs the NPV is much larger than the PPV (**Table 3**), indicating that the SDMs are better in describing the absence of suitable habitat than its presence.

In order to compare output from the SDMs to the suitable salinity for spawning, we convert the likelihood of observing larvae into a binary variable, namely the presence and absence of suitable habitat. The threshold for this conversion is a probability of approximately 0.3 (i.e., for *EN4-analysis* (*MPI-ESM-assim*): 0.28 (0.31) in the survey data, and 0.29 (0.34) in the fishery data). Probabilities that exceed (subceed) this threshold translate to presences (absences) of suitable habitat.

For both SDMs, the region defined as suitable for spawning (probability $\gtrapprox$ 0.3) is centred within the spawning region spanning from the European Continental Shelf onto Rockall Plateau. For SDM_ST_{MPI}, however, the suitable spawning habitat extends further west beyond RHP which is not supported by observations (**Figures 8A,B**). Generally, both SDMs show a more contracted distribution toward the continental shelf in 1991 and a slightly more expanded westward distribution in 2005, however, both fail to reveal the full extent of the observed distributional changes.

The second approach uses the suitable salinity for spawning as a proxy for the suitable spawning habitat and there are large differences between the two approaches in the way the

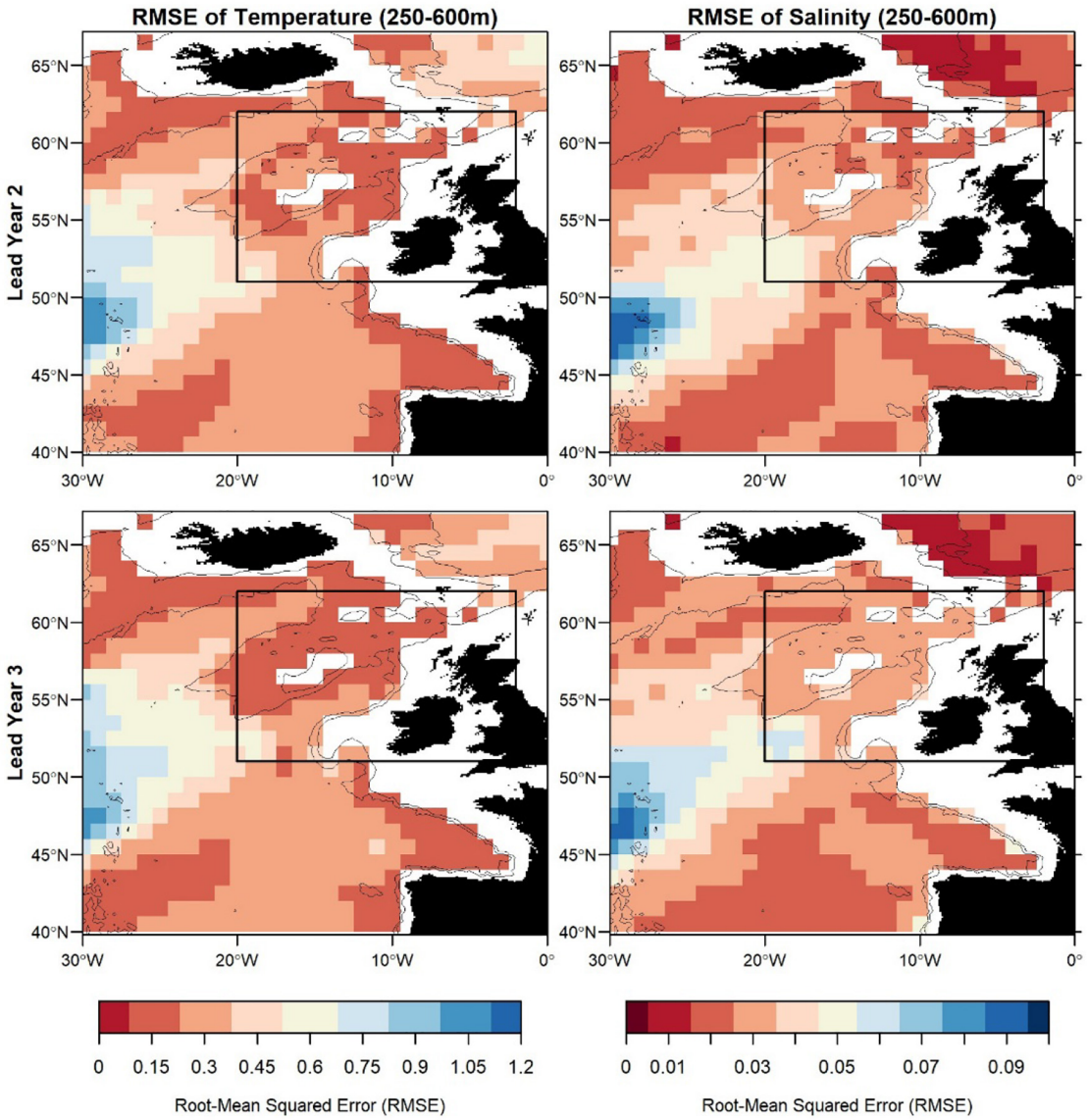


FIGURE 7 | Root-mean squared error (RMSE) of temperature **(left)** and salinity **(right)** in FMA at lead year 2 (≈16 months) **(top)** and lead year 3 (≈28 months) **(bottom)** comparing *MPI-ESM-hindcast* to *MPI-ESM-assim*. The black rectangle delineates the study area: the spawning region of blue whiting.

suitable habitat is spatially expressed (**Figure 8**). The suitable salinity for spawning has a considerably larger spatial extent than the suitable habitat based on SDMs and thereby is a better general definition of the potentially suitable habitat that rather overestimates suitable habitat in areas beyond the spawning region of blue whiting. Therefore, the agreement between the suitable salinity for spawning and independent observations is best within the spawning region.

Furthermore, different spatial representations of the marine climate from the two oceanographic reference products affect the spatial distribution of the suitable spawning habitat (**Figure 8**). The suitable spawning habitat of blue whiting is more affected by the vicinity of bathymetric features, in particular Rockall Plateau, when based on *MPI-ESM-assim* in comparison to *EN4-analysis*. The difference between *MPI-ESM-assim* and *EN4-analysis* becomes most apparent, however, when comparing the suitable salinity for spawning for two years with contrasting marine climatic regimes. In 1991 the marine climate in the spawning region of blue whiting is characterised by rather cold and fresh conditions (**Figure 3**) and most blue whiting are observed along the continental shelf from northern Scotland toward Porcupine Bank and south of Rockall Plateau within Rockall Trough (**Figures 8A,C**). To the contrary in 2005, conditions become more warm and saline in the spawning region (**Figure 3**) and in response, blue whiting show an expanded spawning distribution that stretches from the continental shelf over RHP with a larger north-westward extent (**Figures 8B,D**).

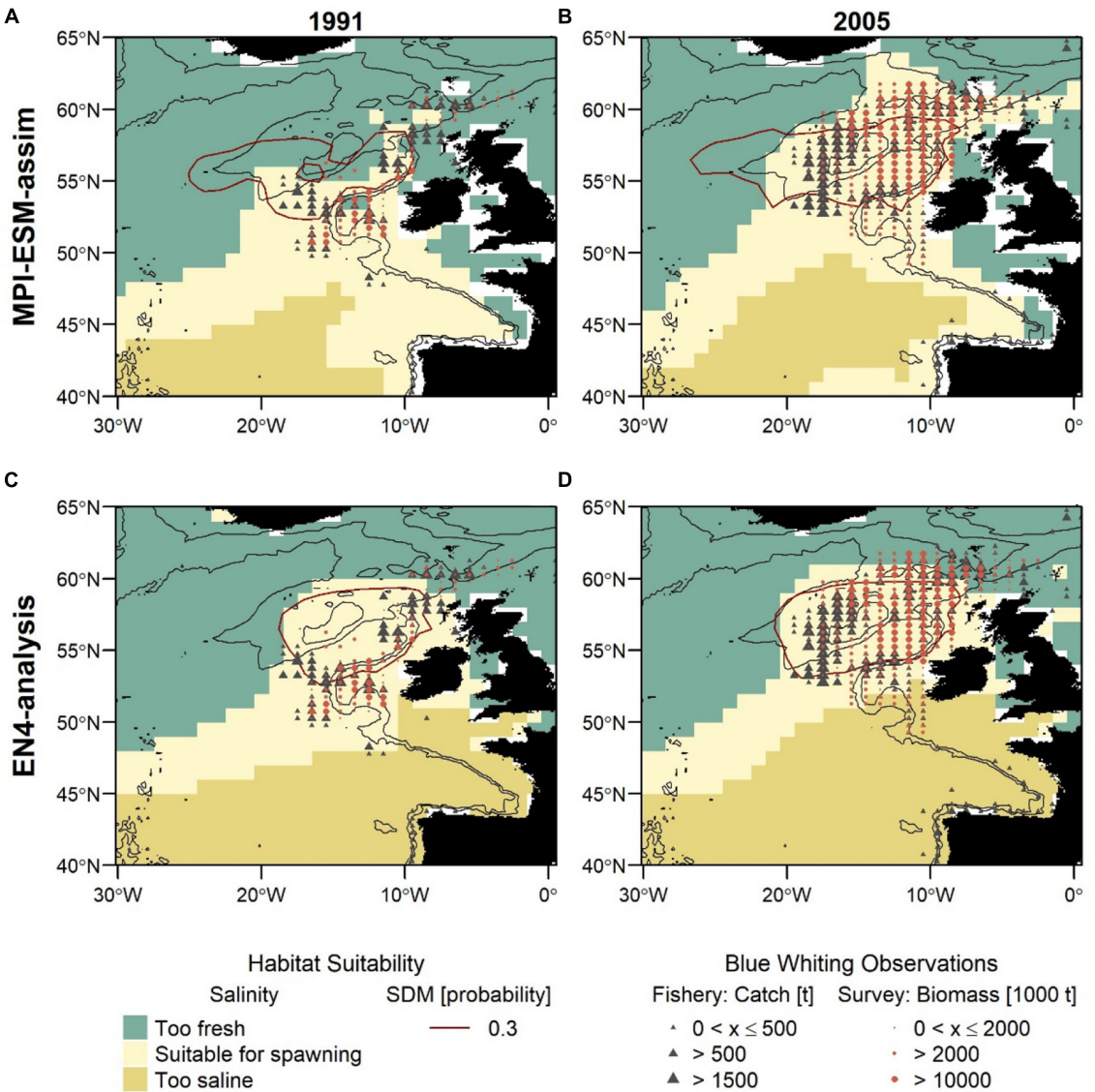


FIGURE 8 | Blue whiting habitat suitability in 1991 (left; **A,C**) and 2005 (right; **B,D**) for *MPI-ESM-assim* (top; **A,B**) and *EN4-analysis* (bottom; **C,D**) compared to observations of adult blue whiting from scientific surveys (IBWSS; red bullet) and fishery catch data (NEAFC; grey triangle) during March and April. Habitat suitability is shown for both the suitable salinity for spawning (background fill) and the probability of observing blue whiting larvae from SDMs (red contour lines; **A,B**: SDM_ST_{MPI}; **C,D**: SDM_S_{EN4}), where 0.3 resembles the threshold for converting the larval-presence probability into presence and absence of suitable habitat. Bathymetry is indicated by 600 and 2,000 m isobaths.

While these spatial changes imprint on in the suitable salinity for spawning in *MPI-ESM-assim*, *EN4-analysis* fails to resolve changes between 1991 and 2005. In particular in the area around RHP, *EN4-analysis* shows hardly any difference between the two years (**Figures 8C,D**), while *MPI-ESM-assim* reproduces the absence of suitable habitat on Rockall Plateau in 1991 (**Figure 8A**) and the presence of suitable habitat over most of RHP in 2005 (**Figure 8B**). Accordingly, the dynamic properties of *MPI-ESM-assim* and its ability to account for bathymetric constraints might be better suited to reflect the suitable spawning habitat of blue whiting during FMA, in particular in the area of RHP.

Another difference between the two reference products, that is visible for both years is that in *MPI-ESM-assim* the suitable salinity for spawning extends southward along the continental shelf passing the Spanish and Portuguese coast (**Figures 8A,B**). This extension is supported by fishery observations (**Figures 8A,B**).

Within the spawning region, habitat definitions based on the suitable salinity for spawning generally have a higher agreement with independent fishery and survey observations as judged by higher mean values of NPV, HR, and TSS compared to habitat definitions based on SDMs (**Table 4**). The SDM-based definition is only better in terms of PPV for SDM_S_{EN4} and the FAR. Both

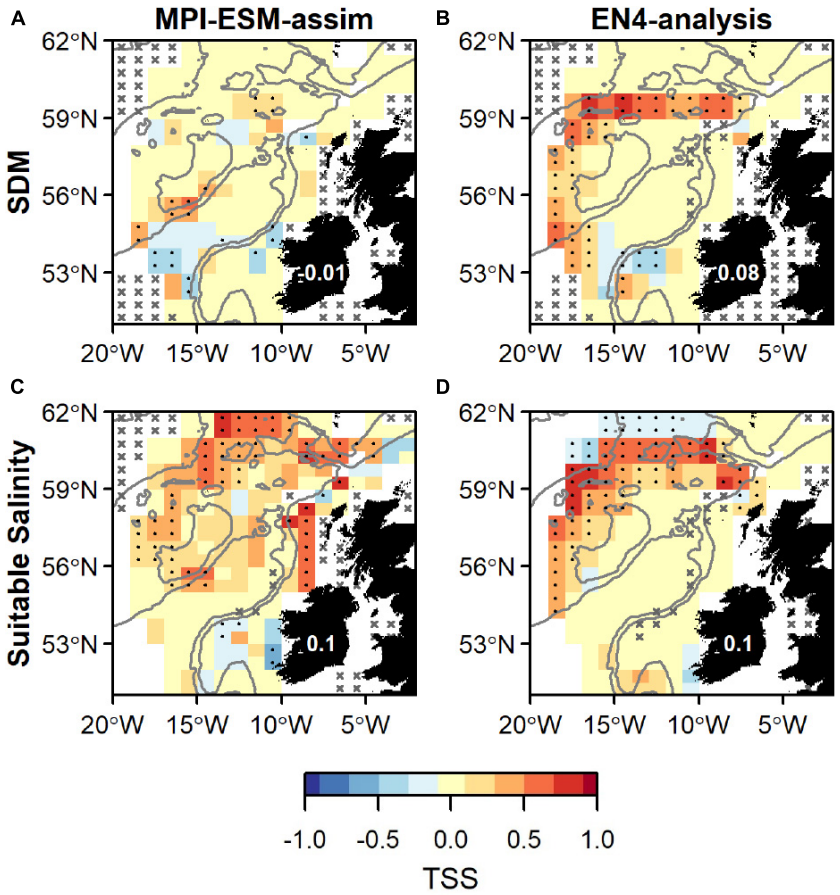


FIGURE 9 | Agreement between the suitable spawning habitat and observations of adult blue whiting from the IBWSS survey in terms of the True Skill Statistics (TSS) during March and April. The suitable spawning habitat is defined through Species Distribution Models (SDM) (top row; **A,B**) or the suitable salinity for spawning (bottom row; **C,D**) and based on *MPI-ESM-assim* (left; **A,C**) and *EN4-analysis* (right; **B,D**). In a and b the best performing SDMs (**Table 3**) were chosen: SDM_ST_{MPI} **(A)** and SDM_S_{EN4} **(B)**. Dots show significant correlations at the 95% confidence level and crosses indicate regions where the predictive skill cannot be evaluated confidently due to sparse observational data, both based on a 500-fold bootstrap. Good predictive quality (TSS > 0) is indicated by red colours (where HR > FAR) and the mean TSS within the plotted region (excluding regions with crosses) is noted on Ireland. The grey lines indicate the 600 m and 2,000 m isobath.

habitat definitions are more useful in describing an absence of suitable habitat within the spawning region (higher NPV) than presence of suitable habitat (lower PPV).

Overall, spatially averaged values of TSS within the spawning region are low (<0.2), however all habitat definitions show greatest agreement with observations from the IBWSS survey in the region around Rockall Plateau and north–east of it (**Figure 9**). SDM_ST_{MPI} shows least agreement with observations (overall TSS = 0) and even displays significantly negative values of TSS in particular around Porcupine Bank (**Figure 9A**), followed by SDM_S_{EN4} with an overall TSS of 0.08 (**Figure 9B**). The suitable spawning habitat in terms of salinity in *MPI-ESM-assim* shows best agreement with observations from the scientific survey in terms of TSS, with positive values mainly in the north-eastern part of the study region and on RHP (**Figure 9C**). In contrast to *MPI-ESM-assim,* differences between the two habitat definitions are smaller for *EN4-analysis* (**Figure 9** and **Table 4**).

Accordingly, the definition of the suitable spawning habitat based on salinity shows better agreement with independent observations than applying the full SDMs. Therefore, we create retrospective forecast of the suitable salinity for spawning and analyse its predictive skill in further detail.

Predictive Skill of the Retrospectively Forecasted Suitable Spawning Habitat Based on Salinity

Generally, retrospective forecasts of the suitable salinity for spawning based on *MPI-ESM-hindcast* approximately one year ahead have a higher predictive skill than persistence based forecasts (**Figure 10**). However, overall values of TSS are low with 0.13 when compared to both survey and fishery data and differences to persistence-based forecast are small and in the range of 0.02–0.03 (**Figures 10A–C**).The predictive skill of all retrospective forecasts is highest on RHP especially west of Rockall Plateau and in the northern part of the spawning region, while low or no predictive skill is found within deeper parts of Rockall Trough and Porcupine Bank (**Figures 10A–C**).

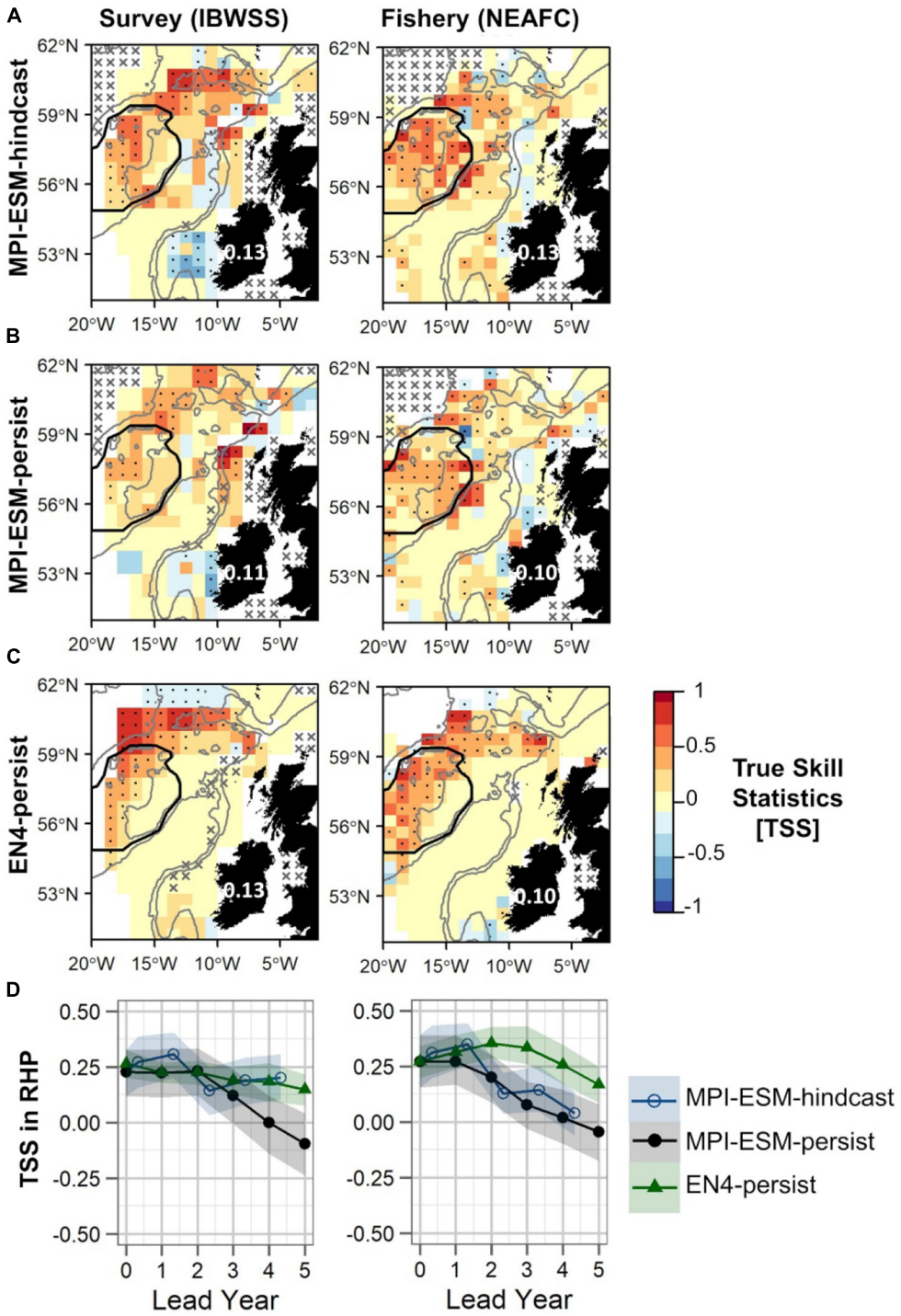


FIGURE 10 | Predictive quality of retrospectively forecasted suitable spawning habitat based on the suitable salinity for spawning with *MPI-ESM-hindcast* **(A)**, *MPI-ESM-persist* **(B)**, and *EN4-persist* **(C)** in terms of the True Skill Statistics (TSS) for March and April judged against observations of adult blue whiting from surveys (IBWSS) (left) and fishery (NEAFC) (right) approximately one year ahead **(A–C)**; and spatially averaged over Rockall-Hatton Plateau (RHP; region delineated in black in the maps above) for each lead year **(D)**. The last panel **(D)** shows *MPI-ESM-hindcast* (blue circle), *MPI-ESM-persist* (black bullet) and *EN4-persist* (green triangle) with the shaded areas indicating the spread based on the lower and the upper quartile of a 500-fold bootstrap. Retrospective forecasts are distinctly different when their respective shaded areas do not overlap. Due to the different initialisation dates, panels **(A–C)** show the hindcast with a lead time of around 16 months and the persistent forecasts with a 12 months lead. In panels **(A–C)** dots show significant correlations at the 95% confidence level and crosses indicate regions where the predictive skill cannot be evaluated confidently, both based on a 500-fold bootstrap. Good predictive quality (TSS > 0) is indicated by red colours (where HR > FAR) and the mean TSS within the plotted region (excluding regions with crosses) is noted over Ireland. The grey lines indicate the 600 and 2,000 m isobaths.

Results are similar when compared to both survey and fishery observations. However, significantly positive TSS values on Rockall Plateau and Porcupine Bank are only found for *MPI-ESM-hindcast* and *MPI-ESM-persist* when compared to fishery data (**Figures 10A,B**). The high predictability of retrospective forecasts on and north-east of RHP, are in line with the high predictability of the marine climate, specifically salinity, found for this region (**Figures 6**, **7**).

Within RHP, retrospective forecasts of the suitable salinity for spawning perform similarly for shorter lead times (<2 years) with *MPI-ESM-hindcast* being slightly but not significantly more skilful than persistence based forecasts (**Figure 10D**). The forecast horizon at which *MPI-ESM-hindcast* is more skilful than persistence differs for the two oceanographic data sets and for the two observational data sets of blue whiting. *MPI-ESM-hindcast* has more skill than *MPI-ESM-persist* after lead year 3 when assessed by the survey data, however, when compared to the fishery data both show similar skill. *EN4-persist* shows a similar or higher predictive skill than *MPI-ESM-hindcast* after lead year 2, as judged by survey and fishery observations, respectively.

Retrospective forecasts of the suitable spawning habitat approximately 1 year in advance show prominent inter-annual variations in predictive skill on RHP, which can roughly be divided into three periods (**Figure 11A**): From 1985 to 1995, *MPI-ESM-hindcast* shows the highest skill with values of TSS as high as 0.89 as judged against fishery data while *EN4-persist* mainly shows no skill. Around the 2000s this reverses when *EN4-persist* has greater values of TSS than *MPI-ESM-hindcast*. However, during this time the differences in retrospective forecast skill is high depending on the observational data set chosen and retrospective forecasts based on *MPI-ESM-persist* and *MPI-ESM-hindcast* and generally have higher TSS values and hence are more skilful when judged against fishery data in comparison to survey data, indicating a rather large uncertainty in observing blue whiting on RHP. From 2006 onward, forecast skill converges to a range of TSS around 0 to 0.5.

These marked changes in the predictive skill over RHP (**Figure 11A**) coincide with changes in the importance of RHP as a spawning ground (**Figure 11B**) which in turn are affected by oceanographic variability on the spawning region (Hátún et al., 2009b; Miesner and Payne, 2018). Around 1990 when the marine climate in the spawning region is characterised rather cold and fresh conditions, most spawning takes place along the continental shelf and less on RHP (Hátún et al., 2009a,b; Miesner and Payne, 2018) as shown for 1991 (**Figures 8A,C**). The importance of RHP as a spawning ground stays low until 1998 with less (or equal) than 30% of blue whiting being observed or caught on RHP (**Figure 11B**). Likewise, *MPI-ESM-persist* and particularly *MPI-ESM-hindcast* show only small fractions of RHP with suitable spawning habitat around 1990 (**Figure 11B**),

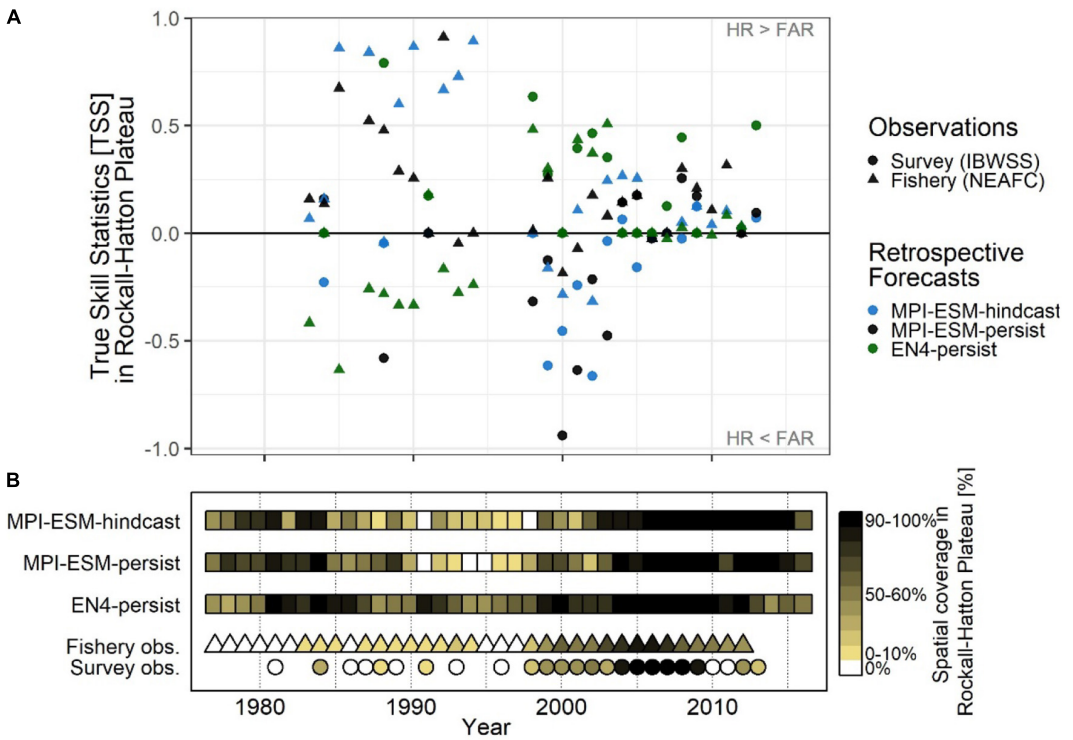


FIGURE 11 | Average inter-annual forecast skill on Rockall-Hatton Plateau (RHP; see **Figures 10A–C**) in terms of the True Skill Statistics (TSS) **(A)**; and the spatial coverage of suitable spawning habitat in RHP (% of grid cells) **(B)** based on retrospective forecasts of the suitable salinity for spawning approximately one year ahead with *MPI-ESM-hindcast*, *MPI-ESM-persist* and *EN4-persist* judged against observations of adult blue whiting from surveys (IBWSS; bullet) and fishery (NEAFC; triangle) during March and April. In case observations of blue whiting were absent on RHP [**(B)**: white triangles/bullets = 0%] the TSS is not calculated. Note that observational absences can also indicate that there was no fishing in RHP and shows the absence of IBWSS survey coverage on RHP in the particular year.

resulting in unprecedentedly high forecast skill with values of TSS of 0.85 (**Figure 11A**). In contrast, *EN4-persist* constantly shows suitable habitat in more than 30% of RHP. This inability of *EN4-analysis* to show the absence of suitable spawning habitat over RHP leads to the low predictive skill of *EN4-persist* until around 1998 (**Figure 11**).

After 1998 both temperature and salinity increase in the spawning region (**Figure 3**) which is associated with a north- and westward expansion so the spawning distribution (Hátún et al., 2009a,b; Miesner and Payne, 2018) and blue whiting are observed over a larger area of RHP (**Figure 11B**). In line with observations from the Ellet Line (Holliday et al., 2015), *EN4-analysis* shows an increase in temperature and salinity above the climatological average from around 2000–2009 (**Figure 3**). *MPI-ESM-assim*, however shows negative anomalies, particularly in salinity around 2000 (**Figure 3**). Accordingly, *MPI-ESM-hindcast* and *MPI-ESM-persist* both underestimate the suitability of the spawning habitat (**Figure 11B**) resulting in the absence of skill over RHP around 2000 (**Figure 11A**). In congruence with the period of high temperature and salinity around 2005, which is found in both *EN4-analysis* and *MPI-ESM-assim* (**Figure 3**), also the spatial coverage of blue whiting over RHP peaks and blue whiting are observed over most (if not all) of RHP (**Figure 11B**). Since all retrospective forecasts also show suitable spawning habitat on RHP (**Figure 11B**), forecasts skill converges with mainly positive TSS values, in particular for persistence based forecasts (**Figure 11A**).

In summary, a clear advantage of creating forecasts of the suitable spawning habitat of blue whiting with MPI-ESM compared to *EN4-analysis*, is the ability of MPI-ESM to differentiate between the presence and absence of suitable spawning habitat over RHP. In particular, *MPI-ESM-hindcast* skilfully forecasts distributional changes over RHP around a year in advance.

DISCUSSION

We find a higher predictability of salinity compared to temperature within the spatio-temporal domain relevant for spawning blue whiting. Few studies explicitly compare the predictability of salinity and temperature, as presented in this study. One exception is a perfect model experiment that indicated that sea surface salinity is potentially more predictable at inter-annual timescales than sea surface temperature for most oceanic regions of the mid to high latitudes, including the Northeast Atlantic (Koenigk and Mikolajewicz, 2009). In another study, sea surface salinity within the SPG region showed a higher potential predictability compared to both sea surface temperature and upper 300 m heat content with ACC of salinity as high as 0.8 for lead year 2–5 (Mignot et al., 2016), similar to the skill of *MPI-ESM-hindcast* versus *MPI-ESM-assim* in our study (**Figure 4B**). While the mean RMSE for lead year 2–5 of around 0.5 for temperature and 0.05 for salinity (Mignot et al., 2016) is slightly higher than our results indicate (**Figures 4C,D**, **5C,D**).

The marine climate in the spawning region of blue whiting is influenced by the low-frequency dynamics of the SPG that contributes to recurrent periods of relatively high or relatively low salinity spanning over 5–10 years (Holliday et al., 2000; Koul et al., 2019). The salinity signal from the SPG is passively advected with the general ocean circulation toward the North East Atlantic (Mauritzen et al., 2006) and thereby into the spawning region of blue whiting. As such, salinity acts as an indicator for circulation changes in the subpolar North Atlantic (Mauritzen et al., 2006) and the low-frequency dynamics of the SPG that acts on (multi-) decadal timescales (Koul et al., 2019) likely contributes to the high predictability of salinity in spawning region of blue whiting. Specifically, the upper ocean at RHP and the north-eastern Rockall Trough in the vicinity of the continental slope generally show lower oceanographic variability (Holliday et al., 2015) with recurrent and prolonged periods of anomalously high/low salinity (Holliday et al., 2000; Koul et al., 2019). Therefore, predictions of the marine climate and the suitable habitat with *MPI-ESM-hindcast* show particularly high levels of predictive skill around RHP and in the north-eastern spawning region.

To the contrary, variations in the strength of the SPG affect the position and flow trajectory of the North Atlantic Current and thereby introduce oceanographic variability in the area of Rockall Trough (Holliday et al., 2000; Hátún et al., 2009a; Koul et al., 2019). Rockall Trough is one of the main pathways of the North Atlantic Current, in particular, when the SPG is strong, while the current branches off west of Rockall Plateau, when the SPG is weak (Hátún et al., 2005; Holliday et al., 2020). This oceanographic variability affects the predictability of the marine climate in the Eastern North Atlantic resulting in particularly low predictive skill at the entrance of Rockall Trough in the south-western area of the spawning region.

One key result from this study is that differences in the spatial representation of the marine climate affect the spatial expression of the suitable spawning habitat. Differences in the spatial representation of the marine climate arise from the different methods that are used in *EN4-analysis* and *MPI-ESM-assim* to distribute information of observed oceanic temperature and salinity profiles over the study region in time and space. As a dynamic ocean model, *MPI-ESM-assim* inherently accounts for dynamics and bathymetric features by distributing oceanic properties such as temperature and salinity dynamically consistent around ridges and seamounts such as Rockall Plateau and through channels like Rockall Trough (**Figures 1A,B**). In contrast, in *EN4-analysis* observational gaps are filled by means of statistics and not physics. The objective interpolation used in *EN4-analysis* statistically interpolates between observed profiles and is therefore less capable of representing hydrodynamics, resulting in rather smooth contours of temperature and salinity, disconnected from bathymetry.

The more differentiated representation of the marine climate around bathymetric features in *MPI-ESM-assim*, results in a superior ability of *MPI-ESM-persist* and *MPI-ESM-hindcast* to predict the absence of suitable habitat on RHP. Skilfully forecasting distributional changes of the suitable spawning habitat on RHP could be particular value to the scientific monitoring and management of the stock. Distributional changes are most pronounced on RHP (Hátún et al., 2009b; Miesner

and Payne, 2018). Moreover, sampling on RHP is challenging. In particular, the great distance to ports and recurrent periods of bad weather have resulted in insufficient survey coverage on RHP in some years (e.g., 2010) which can lead to an underestimation of the stock's biomass (ICES, 2010). Therefore, the high inter-annual predictive skill of the marine climate and the suitable spawning habitat around RHP with MPI-ESM with marks a success.

A major challenge that is common to all ecological forecasts that aim at forecasting the spatial distribution of living organisms, is the way habitat is related to the distribution of a species (Payne et al., 2017). Here, the suitable spawning habitat of blue whiting delineates environmental conditions that are suitable for spawning (i.e., in terms of salinity). However, just because a region is suitable for spawning does not necessarily mean that the location is occupied by the fish and spawning takes place. Due to non-resolved processes such as migration dynamics, density dependent effects on distribution or other biotic interactions such competition and predation, not the entire suitable habitat is necessarily occupied by the species (Guisan and Zimmermann, 2000; Colwell and Rangel, 2009; Elith and Leathwick, 2009). Therefore, the actual distribution might be smaller than their potentially suitable habitat, which is clearly seen for the suitable salinity for spawning (**Figure 8**).While the SDMs delineate the core spawning region west of the British Isles, which is recognised to be the main spawning region of blue whiting (Bailey, 1982; ICES, 2019), they underestimate the spatial (i.e., latitudinal) extent of the spawning distribution. Possible reasons are that the SDMs are constrained by geographic and spatio-temporal parameters and the choice of the threshold for converting probabilities into presences of suitable habitat.

Since habitat models are superior in predicting absences compared to presences, as seen for both approaches applied in this study (**Tables 3**, **4**), the skill of forecasting species distributions is asymmetric (Payne et al., 2021). Consequently, retrospective forecasts of the suitable spawning habitat (e.g., on RHP) with *MPI-ESM-hindcast*, have higher skill in predicting the absence of suitable habitat (i.e., no spawning on RHP) than their presence.

Nevertheless, instantaneous observations of freely moving animals, like fish, only provide a snapshot of their distribution. We cannot be certain whether the observed adult blue whiting were actively spawning or migrating. Additionally, observations might not cover the entire spawning distribution, e.g., fishermen focus on the most profitable regions with highest fish aggregations while smaller aggregations might be left untouched. Therefore, observations of fish carry uncertainties that affect the assessment biological forecast skill. In particular, our analysis of inter-annual biological forecasts reveals at times massive differences in skill when judged by either fishery or survey data. This highlights the need to consider multiple biological observational data sets for validating coupled physical-biological forecasts.

We define the suitable spawning habitat of blue whiting based on SDMs in a generalised additive modelling framework (Miesner and Payne, 2018). There is, however, a multitude of other modelling options. We cannot rule out that another statistical SDM approach, for example, based on machine learning such as random forest (Breiman, 2001) which is designed for generating predictions (Elith and Leathwick, 2009) might have resulted in a better performance of SDM-based predictions. Additionally applying an ensemble of different modelling techniques would enable accounting for uncertainty in defining the suitable habitat (Araújo and New, 2007).

Salinity seems to be a good proxy for the spawning distribution of blue whiting within its spawning region because it shows good agreement with independent observations (Miesner and Payne, 2018). Salinity can have a direct effect on fish, in particular on early life stages, by affecting their osmoregulation (Varsamos et al., 2005) or egg (Sundby and Kristiansen, 2015) and larval buoyancy as shown for blue whiting (Ådlandsvik et al., 2001). Compared to temperature, however, salinity has a less direct effect on most marine organisms (Rijnsdorp et al., 2009). Therefore, salinity is most likely a proxy for other processes that affect the spawning distribution of blue whiting more directly. Most notably, temperature and salinity are often correlated and form central water mass characteristics. Since each water mass possesses characteristic hydrographic and biogeochemical properties, it functions as distinct habitat for marine organisms. Saline waters of subtropical origin provide a higher abundance of warm-water zooplankton species which are smaller (Hátún et al., 2009a) and thus more favourable prey items of blue whiting larvae (Bailey, 1982) than larger zooplankton species that occupy fresher subpolar waters (Hátún et al., 2009a). Consequently, the suitable salinity for spawning might resemble subtropical water masses with good feeding conditions for blue whiting larvae. The feature of salinity to act as a passive tracer, unmodulated by atmospheric processes, might contribute to the more prominent role of salinity, as opposed to temperature, for defining the suitable spawning habitat of blue whiting.

Due to the imminent importance of salinity as water mass characteristic, it might also be promising to consider salinity for characterising the species–environment relationship of other marine organisms and for creating coupled physical-biological forecasts. The importance of salinity for anticipating distributional changes has also been shown for a range of pelagic species along the US Northeast Shelf (McHenry et al., 2019). The study emphasised that bottom salinity was generally more important in explaining range shifts than temperature, and that projections based solely on temperature masked the species' climate vulnerability (McHenry et al., 2019). This highlights the prominence of salinity as independent variable in statistical models that predict spatial changes of marine organisms. In agreement, we also find that salinity prediction skill bears a great potential for creating novel coupled physical–biological forecasts.

In regions where local predictability of the marine climate is low, a potential for creating coupled physical–biological forecasts might lie in lagged correlations from regions of high predictability, such as the SPG region. Changes in the SPG affect the relative share of water masses in the Eastern North Atlantic and result in large bio-geographical shifts of blue whiting and a variety of other marine organisms ranging from phyto- and zooplankton, to whales and seabirds (Drinkwater et al., 2003; Hátún et al., 2009a). Additionally, SPG-driven changes of

temperature and salinity travel downstream into the North Sea (Núñez-Riboni and Akimova, 2017; Koul et al., 2019) and Barents Sea, and thereby affect the abundance and productivity of some local fish species and introduce predictability via adjective delays (Akimova et al., 2016; Koul et al., 2021). Since retrospective forecasts of the marine climate with *MPI-ESM-hindcast* in the SPG region show significant skill (Brune et al., 2018; Brune and Baehr, 2020), and Post et al. (2021) found a lagged response between the marine climate south-west of Iceland and the abundance of blue whiting and other boreal fish species in Greenlandic waters, we envision a great potential for developing coupled physical–biological forecasts of fish abundance and distribution based on MPI-ESM in the North Atlantic and its adjacent seas (Koul et al., 2021).

CONCLUSION

Using blue whiting as a case study, we show that *MPI-ESM-hindcast* skilfully predicts the marine climate, specifically salinity, in the North East Atlantic several years ahead, which translates to predictability of distributional shifts in the species' suitable spawning habitat a year in advance. We find that the suitable salinity for spawning proves to be a better proxy for the suitable spawning habitat than applying a SDM. While the definition of the suitable habitat is species specific and requires careful consideration, many aspects from this study can be generalised and are also applicable to other species. Hence, ESMs bear great potentials for forecasting fish distributions in the North East Atlantic.

One of the main advantages in delineating and forecasting the suitable habitat with MPI-ESM is the ESM's representation of hydrographic processes, which is superior to the statistical product *EN4-analysis* for the conducted analysis. The dynamic consistency and ability of an ESM to consider hydrodynamics can therefore offer advantages over a solely statistical oceanographic data product, specifically for coupled physical–biological forecasts in regions with distinct bathymetry, e.g., over seamounts, plateaus or shelfs, which typically depict preferred habitat features for many marine species, as seen for blue whiting. Since skilful biological forecasts at inter-annual time scales, as presented in this study, are beyond the prediction horizon of the first generation of biological forecast products (Payne et al., 2017), they present an innovation of marine biological forecasts.

Another insight from this study is the higher predictive skill of deep-water salinity compared to temperature and its impending importance as water mass and habitat characteristic in the North East Atlantic. For many commercially important fish species in the North Atlantic a wealth of observational records exist and environmental drivers for distributional changes are known (Trenkel et al., 2014; and references therein). This could offer the possibility to delineate the species' suitable habitat by combining existing observations of the species in combination with skilful observational oceanographic data sets. Moreover, including salinity in coupled physical–biological forecasts could offer a valuable contribution toward predicting distributional shifts of marine living organisms and for creating novel marine ecological forecasts.

DATA AVAILABILITY STATEMENT

Monthly observations of ocean temperature and salinity are available from the Met Office Hadley Centre's EN4 data set. In this study version EN4.2.1 was used with corrections based on Gouretski and Reseghetti (2010), which can be downloaded at https://www.metoffice.gov.uk/hadobs/en4/download-en4-2-1.html. Temperature and salinity fields for MPI-ESM can be downloaded at https://cera-www.dkrz.de/WDCC/ui/cerasearch/entry?acronym=DKRZ_LTA_1075_ds00008. Bathymetry data from the ETOPO1 Global Relief Model is publicly available at https://www.ngdc.noaa.gov/mgg/global/.

AUTHOR CONTRIBUTIONS

AM conceived the work, performed the analysis and wrote the manuscript. SB created the MPI-ESM hindcast and assimilation experiments. AM, SB, VK, and PP discussed the results. CS and JB provided guidance on the overall direction of the work. All authors reviewed the manuscript.

FUNDING

This research is funded through the Earth and Environment Research Programme of the Helmholtz Association Germany and is a contribution to the Subtopic "Coastal System Sustainability against the Backdrop of Natural and Anthropogenic Drivers" of Topic 4 "Coastal Transition Zones under Natural and Human Pressure" of the PoF IV research program Earth and Environment "Changing Earth-Sustaining our Future." Moreover, the study is funded by the Deutsche Forschungsgemeinschaft (DFG, German Research Foundation) under Germany's Excellence Strategy—EXC 2037 "CLICCS—Climate, Climatic Change, and Society"—Project Number: 390683824, contributing to the Center for Earth System Research and Sustainability (CEN) of Universität Hamburg. JB and S.B were supported by Copernicus Climate Change Service, funded by the EU, under contract C3S-330. Analysis of the CPR samples from 1979 to 2005 was funded by the United Kingdom Department of Environment, Fisheries and Rural Affairs (Defra, project MF1101). The funders had no role in study design, data collection and analysis, decision to publish, or preparation of the manuscript.

ACKNOWLEDGMENTS

We wish to thank André Düsterhus for his constructive and helpful comments. Moreover, we wish to thank the German Climate Computing Centre (DKRZ) where the model simulations were performed.

REFERENCES

Ådlandsvik, B., Coombs, S., Sundby, S., and Temple, G. (2001). Buoyancy and vertical distribution of eggs and larvae of blue whiting (*Micromesistius poutassou*): observations and modelling. *Fish. Res.* 50, 59–72. doi: 10.1016/S0165-7836(00)00242-3

Akimova, A., Núñez-Riboni, I., Kempf, A., and Taylor, M. H. (2016). Spatially-resolved influence of temperature and salinity on stock and recruitment variability of commercially important fishes in the north sea. *PLoS One* 11:e0161917. doi: 10.1371/journal.pone.0161917

Amante, C., and Eakins, B. W. (2009). *ETOPO1 1 Arc-Minute Global Relief Model: Procedures, Data Sources and Analysis. NOAA Technical Memorandum NESDIS NGDC*. Washington, DC: NOAA, 24. doi: 10.7289/V5C8276M

Anderson, D. R. (2008). *Model Based Inference in the Life Sciences: A Primer on Evidence*. New York, NY: Springer New York, doi: 10.1007/978-0-387-74075-1

Araújo, M. B., and New, M. (2007). Ensemble forecasting of species distributions. *Trends Ecol. Evol.* 22, 42–47. doi: 10.1016/j.tree.2006.09.010

Bailey, R. S. (1982). The population biology of blue whiting in the North Atlantic. *Adv. Mar. Biol.* 19, 257–355. doi: 10.1016/S0065-2881(08)60089-9

Breiman, L. (2001). Random forests. *Mach. Learn.* 45, 5–32. doi: 10.1023/A:1010933404324

Brown, C. D., and Davis, H. T. (2006). Receiver operating characteristics curves and related decision measures: a tutorial. *Chemom. Intell. Lab. Syst.* 80, 24–38. doi: 10.1016/j.chemolab.2005.05.004

Brune, S., and Baehr, J. (2020). Preserving the coupled atmosphere–ocean feedback in initializations of decadal climate predictions. *WIREs Clim. Chang.* 11:e637. doi: 10.1002/wcc.637

Brune, S., Düsterhus, A., Pohlmann, H., Müller, W. A., and Baehr, J. (2018). Time dependency of the prediction skill for the North Atlantic subpolar gyre in initialized decadal hindcasts. *Clim. Dyn.* 51, 1947–1970. doi: 10.1007/s00382-017-3991-4

Brune, S., Nerger, L., and Baehr, J. (2015). Assimilation of oceanic observations in a global coupled Earth system model with the SEIK filter. *Ocean Model.* 96, 254–264. doi: 10.1016/j.ocemod.2015.09.011

Burnham, K. P., Anderson, D. R., and Huyvaert, K. P. (2011). AIC model selection and multimodel inference in behavioral ecology: some background, observations, and comparisons. *Behav. Ecol. Sociobiol.* 65, 23–35. doi: 10.1007/s00265-010-1029-6

Colwell, R. K., and Rangel, T. F. (2009). Hutchinson's duality: the once and future niche. *Proc. Natl. Acad. Sci. U.S.A.* 106(Suppl. 2), 19651–19658. doi: 10.1073/pnas.0901650106

Coombs, S. H., Pipe, R. K., and Mitchell, C. E. (1981). The vertical distribution of eggs and larvae of blue whiting (*Micromesistius poutassou*) and Mackerel (*Scomber scombrus*) in the Eastern North Atlantic and North Sea. *Rapp. Proc. Verb. Cons. Int. Explor. Mer* 178, 188–195.

Dee, D. P., Uppala, S. M., Simmons, A. J., Berrisford, P., Poli, P., Kobayashi, S., et al. (2011). The ERA-Interim reanalysis: configuration and performance of the data assimilation system. *Q. J. R. Meteorol. Soc.* 137, 553–597. doi: 10.1002/qj.828

Drinkwater, K. F., Belgrano, A., Borja, A., Conversi, A., Edwards, M., Greene, C. H., et al. (2003). "The response of marine ecosystems to climate variability associated with the North Atlantic Oscillation," in *The North Atlantic Oscillation: Climatic Significance and Environmental Impact*, eds J. W. Hurrell, Y. Kushnir, G. Ottersen, and M. Visbeck (Washington, DC: American Geophysical Union), 211–234. doi: 10.1029/134GM10

Elith, J., and Leathwick, J. R. (2009). Species distribution models: ecological explanation and prediction across space and time. *Annu. Rev. Ecol. Evol. Syst.* 40, 415–436. doi: 10.1146/annurev.ecolsys.l

Eveson, J. P., Hobday, A. J., Hartog, J. R., Spillman, C. M., and Rough, K. M. (2015). Seasonal forecasting of tuna habitat in the Great Australian Bight. *Fish. Res.* 170, 39–49. doi: 10.1016/j.fishres.2015.05.008

Freeman, E. A., and Moisen, G. G. (2008). A comparison of the performance of threshold criteria for binary classification in terms of predicted prevalence and kappa. *Ecol. Modell.* 217, 48–58. doi: 10.1016/j.ecolmodel.2008.05.015

Frölicher, T. L., Ramseyer, L., Raible, C. C., Rodgers, K. B., and Dunne, J. (2020). Potential predictability of marine ecosystem drivers. *Biogeosciences* 17, 2061–2083. doi: 10.5194/bg-17-2061-2020

Giorgetta, M. A., Jungclaus, J., Reick, C. H., Legutke, S., Bader, J., Böttinger, M., et al. (2013). Climate and carbon cycle changes from 1850 to 2100 in MPI-ESM simulations for the coupled model intercomparison project phase 5. *J. Adv. Model. Earth Syst.* 5, 572–597. doi: 10.1002/jame.20038

Good, S. A., Martin, M. J., and Rayner, N. A. (2013). EN4: quality controlled ocean temperature and salinity profiles and monthly objective analyses with uncertainty estimates. *J. Geophys. Res. Ocean.* 118, 6704–6716. doi: 10.1002/2013JC009067

Gouretski, V., and Reseghetti, F. (2010). On depth and temperature biases in bathythermograph data: development of a new correction scheme based on analysis of a global ocean database. *Deep Res. Part I* 57, 812–833. doi: 10.1016/j.dsr.2010.03.011

Guisan, A., and Zimmermann, N. E. (2000). Predictive habitat distribution models in ecology. *Ecol. Modell.* 135, 147–186. doi: 10.1016/S0304-3800(00)00354-9

Hátún, H., Payne, M. R., Beaugrand, G., Reid, P. C., Sandø, A. B., Drange, H., et al. (2009a). Large bio-geographical shifts in the north-eastern Atlantic Ocean: from the subpolar gyre, via plankton, to blue whiting and pilot whales. *Prog. Oceanogr.* 80, 149–162. doi: 10.1016/j.pocean.2009.03.001

Hátún, H., Payne, M. R., and Jacobsen, J. A. (2009b). The North Atlantic subpolar gyre regulates the spawning distribution of blue whiting (*Micromesistius poutassou*). *Can. J. Fish. Aquat. Sci.* 66, 759–770. doi: 10.1139/F09-037

Hátún, H., Sandø, A. B., Drange, H., Hansen, B., and Valdimarsson, H. (2005). Influence of the Atlantic Subpolar Gyre on the thermohaline circulation. *Scienc* 309, 1841–1844. doi: 10.1126/science.1114777

Heino, M., Engelhard, G. H., and Godø, O. R. (2008). Migrations and hydrography determine the abundance fluctuations of blue whiting (*Micromesistius poutassou*) in the Barents Sea. *Fish. Oceanogr.* 17, 153–163. doi: 10.1111/j.1365-2419.2008.00472.x

Hillgruber, N., and Kloppmann, M. (1999). Distribution and feeding of blue whiting *Micromesistius poutassou* larvae in relation to different water masses in the Porcupine Bank area, west of Ireland. *Mar. Ecol. Prog. Ser.* 187, 213–225. doi: 10.3354/meps187213

Hillgruber, N., and Kloppmann, M. (2000). Vertical distribution and feeding of larval blue whiting in turbulent waters above Porcupine Bank. *J. Fish Biol.* 57, 1290–1311. doi: 10.1111/j.1095-8649.2000.tb00488.x

Hobday, A. J., and Hartmann, K. (2006). Near real-time spatial management based on habitat predictions for a longline bycatch species. *Fish. Manag. Ecol.* 13, 365–380. doi: 10.1111/j.1365-2400.2006.00515.x

Hobday, A. J., Hartog, J. R., Spillman, C. M., and Alves, O. (2011). Seasonal forecasting of tuna habitat for dynamic spatial management. *Can. J. Fish. Aquat. Sci.* 68, 898–911. doi: 10.1139/f2011-031

Hobday, A. J., Spillman, C. M., Paige Eveson, J., and Hartog, J. R. (2016). Seasonal forecasting for decision support in marine fisheries and aquaculture. *Fish. Oceanogr.* 25, 45–56. doi: 10.1111/fog.12083

Holliday, N. P., Bersch, M., Berx, B., Chafik, L., Cunningham, S., Florindo-López, C., et al. (2020). Ocean circulation causes the largest freshening event for 120 years in eastern subpolar North Atlantic. *Nat. Commun.* 11:585. doi: 10.1038/s41467-020-14474-y

Holliday, N. P., Cunningham, S. A., Johnson, C., Gary, S. F., Griffiths, C., Read, J. F., et al. (2015). Multidecadal variability of potential temperature, salinity, and transport in the eastern subpolar North Atlantic. *J. Geophys. Res. Ocean.* 120, 5945–5967. doi: 10.1002/2015JC010762

Holliday, N. P., Pollard, R. T., Read, J. F., and Leach, H. (2000). Water mass properties and fluxes in the Rockall Trough, 1975-1998. *Deep Res. Part I Oceanogr. Res. Pap.* 47, 1303–1332. doi: 10.1016/S0967-0637(99)00109-0

ICES (2010). *Advice October 2010. Widely Distributed and Migratory Stocks Blue Whiting in Subareas I – IX, XII, and XIV*. Available online at: https://www.ices.dk/sites/pub/PublicationReports/Advice/2010/2010/whb-comb.pdf (accessed September 9, 2021).

ICES (2015). *Manual for International Pelagic Surveys (IPS). Series of ICES Survey Protocols SISP 9. Version 1.00. Working Group of International Pelagic Surveys*. Copenhagen: ICES. doi: 10.17895/ices.pub/7582

ICES (2016). *Stock Annex for Blue Whiting (Subareas I-IX, XI I and XIV). Working Group for Widely Distributed Stocks*. 1–36. Available online at: https://www.ices.dk/sites/pub/PublicationReports/StockAnnexes/2016/whb-comb_SA.pdf (accessed September 9, 2021).

ICES (2018). *Interim Report of the Working Group on Seasonal to Decadal Prediction of Marine Ecosystems (WGS2D)*. Copenhagen: ICES, 42.

ICES (2019). *Stock Annex: Blue Whiting (Micromesistius poutassou) in Subareas 1-9, 12, and 14 (Northeast Atlantic and Adjacent Waters)*. Available online at:

https://www.ices.dk/sites/pub/PublicationReports/StockAnnexes/2019/whb.27.1-91214_SA.pdf (accessed September 9, 2021).

Johnson, D. E., Barrio Froján, C., Neat, F., Van Oevelen, D., Stirling, D., Gubbins, M. J., et al. (2019). Rockall and Hatton: resolving a super wicked marine governance problem in the high seas of the Northeast Atlantic Ocean. *Front. Mar. Sci.* 6:69. doi: 10.3389/fmars.2019.00069

Jolliffe, I. T., and Stephenson, D. B. (2012). *Forecast Verification: A Practitioner's Guide in Atmospheric Science*, 2nd Edn, eds I. T. Jolliffe and D. B. Stephenson (Chichester: Wiley-Blackwell).

Jungclaus, J. H., Fischer, N., Haak, H., Lohmann, K., Marotzke, J., Matei, D., et al. (2013). Characteristics of the ocean simulations in the Max Planck Institute Ocean Model (MPIOM) the ocean component of the MPI-Earth system model. *J. Adv. Model. Earth Syst.* 5, 422–446. doi: 10.1002/jame.20023

Kaplan, I. C., Williams, G. D., Bond, N. A., Hermann, A. J., and Siedlecki, S. A. (2016). Cloudy with a chance of sardines: forecasting sardine distributions using regional climate models. *Fish. Oceanogr.* 25, 15–27. doi: 10.1111/fog.12131

Koenigk, T., and Mikolajewicz, U. (2009). Seasonal to interannual climate predictability in mid and high northern latitudes in a global coupled model. *Clim. Dyn.* 32, 783–798. doi: 10.1007/s00382-008-0419-1

Koul, V., Schrum, C., Düsterhus, A., and Baehr, J. (2019). Atlantic Inflow to the North Sea modulated by the Subpolar Gyre in a Historical simulation With MPI-ESM. *J. Geophys. Res. Ocean.* 124, 1807–1826. doi: 10.1029/2018JC014738

Koul, V., Sguotti, C., Årthun, M., Brune, S., Düsterhus, A., Bogstad, B., et al. (2021). Skilful prediction of cod stocks in the North and Barents Sea a decade in advance. *Commun. Earth Environ.* 2:140. doi: 10.1038/s43247-021-00207-6

Lehodey, P., Senina, I., Wibawa, T. A., Titaud, O., Calmettes, B., Conchon, A., et al. (2018). Operational modelling of bigeye tuna (*Thunnus obesus*) spatial dynamics in the Indonesian region. *Mar. Pollut. Bull.* 131, 19–32. doi: 10.1016/j.marpolbul.2017.08.020

Liu, C., White, M., and Newell, G. (2011). Measuring and comparing the accuracy of species distribution models with presence-absence data. *Ecography (Cop.)* 34, 232–243. doi: 10.1111/j.1600-0587.2010.06354.x

Malick, M. J., Siedlecki, S. A., Norton, E. L., Kaplan, I. C., Haltuch, M. A., Hunsicker, M. E., et al. (2020). Environmentally driven seasonal forecasts of Pacific Hake distribution. *Front. Mar. Sci.* 7:578490. doi: 10.3389/fmars.2020.578490

Matei, D., Pohlmann, H., Jungclaus, J. H., Müller, W., Haak, H., and Marotzke, J. (2012). Two Tales of initializing decadal climate prediction experiments with the ECHAM5/MPI-OM Model. *J. Clim.* 25, 8502–8523. doi: 10.1175/JCLI-D-11-00633.1

Mauritzen, C., Hjøllo, S. S., and Sandø, A. B. (2006). Passive tracers and active dynamics: a model study of hydrography and circulation in the northern North Atlantic. *J. Geophys. Res.* 111:C08014. doi: 10.1029/2005JC003252

McHenry, J., Welch, H., Lester, S. E., and Saba, V. (2019). Projecting marine species range shifts from only temperature can mask climate vulnerability. *Glob. Chang. Biol.* 25, 4208–4221. doi: 10.1111/gcb.14828

Miesner, A. K., and Payne, M. R. (2018). Oceanographic variability shapes the spawning distribution of blue whiting (*Micromesistius poutassou*). *Fish. Oceanogr.* 27, 623–638. doi: 10.1111/fog.12382

Mignot, J., García-Serrano, J., Swingedouw, D., Germe, A., Nguyen, S., Ortega, P., et al. (2016). Decadal prediction skill in the ocean with surface nudging in the IPSL-CM5A-LR climate model. *Clim. Dyn.* 47, 1225–1246. doi: 10.1007/s00382-015-2898-1

NEAFC (2013). Report from the NEAFC Working Group on Collating Information on the Distribution of All Life Stages of Blue Whiting in the North-East Atlantic and the Distribution of Catches from the Stock, London, 26 – 28 November 2013. London: NEAFC.

Núñez-Riboni, I., and Akimova, A. (2017). Quantifying the impact of the major driving mechanisms of inter-annual variability of salinity in the North Sea. *Prog. Oceanogr.* 154, 25–37. doi: 10.1016/j.pocean.2017.04.004

Payne, M. R. (2021). *Blue Whiting Spawning Habitat Forecast. ICES WGS2D Forecast Sheet 01-20210118*. 1–6. Available online at: https://fishforecasts.dtu.dk/forecasts/blue-whiting-spawning-habitat (accessed October 21, 2021).

Payne, M. R., and Lehodey, P. (2019). "Review of the use of ocean data in European fishery management and monitoring applications," in *Copernicus Marine Service Ocean State Report. Issue 3. Journal of Operational Oceanography. 12*:*Sup1*, eds K. von Schuckmann and P.-Y. Le Traon (London: Taylor & Francis), 48–52. doi: 10.1080/1755876X.2019.1633075

Payne, M. R., Hobday, A. J., MacKenzie, B. R., Tommasi, D., Dempsey, D. P., Fässler, S. M. M., et al. (2017). Lessons from the first generation of marine ecological forecast products. *Front. Mar. Sci.* 4:289. doi: 10.3389/fmars.2017.00289

Payne, M. R., Miesner, A. K., Keenlyside, N., Yang, S., and Yeager, S. G. (2021). Skilful decadal-scale distribution shifts prediction of fish habitat. *bioRxiv* [Preprint] 1–23. doi: 10.1101/2021.07.07.451446

Pointin, F., and Payne, M. R. (2014). A Resolution to the blue whiting (*Micromesistius poutassou*) population paradox? *PLoS One* 9:e106237. doi: 10.1371/journal.pone.0106237

Polkova, I., Brune, S., Kadow, C., Romanova, V., Gollan, G., Baehr, J., et al. (2019). Initialization and ensemble generation for decadal climate predictions: a comparison of different methods. *J. Adv. Model. Earth Syst.* 11, 149–172. doi: 10.1029/2018MS001439

Post, S., Fock, H. O., and Jansen, T. (2019). Blue whiting distribution and migration in Greenland waters. *Fish. Res.* 212, 123–135. doi: 10.1016/j.fishres.2018.12.007

Post, S., Werner, K. M., Núñez-Riboni, I., Chafik, L., Hátún, H., and Jansen, T. (2021). Subpolar gyre and temperature drive boreal fish abundance in Greenland waters. *Fish Fish.* 22, 161–174. doi: 10.1111/faf.12512

Reid, P. C., Colebrook, J. M., Matthews, J. B. L., Aiken, J., and Team, C. P. R. (2003). The continuous plankton recorder: concepts and history, from Plankton Indicators to undulating recorders. *Prog. Oceanogr.* 58, 117–173. doi: 10.1016/j.pocean.2003.08.002

Rijnsdorp, A. D., Peck, M. A., Engelhard, G. H., Möllmann, C., and Pinnegar, J. K. (2009). Resolving the effect of climate change on fish populations. *ICES J. Mar. Sci.* 66, 1570–1583. doi: 10.1093/icesjms/fsp056

Shaffrey, L. C., Hodson, D., Robson, J., Stevens, D. P., Hawkins, E., Polo, I., et al. (2017). Decadal predictions with the HiGEM high resolution global coupled climate model: description and basic evaluation. *Clim. Dyn.* 48, 297–311. doi: 10.1007/s00382-016-3075-x

Siedlecki, S. A., Kaplan, I. C., Hermann, A. J., Nguyen, T. T., Bond, N. A., Newton, J. A., et al. (2016). Experiments with seasonal forecasts of ocean conditions for the Northern region of the California current upwelling system. *Sci. Rep.* 6:27203. doi: 10.1038/srep27203

Sundby, S., and Kristiansen, T. (2015). The principles of buoyancy in marine fish eggs and their vertical distributions across the world oceans. *PLoS One* 10:e0138821. doi: 10.1371/journal.pone.0138821

Taylor, K. E., Stouffer, R. J., and Meehl, G. A. (2012). An overview of CMIP5 and the experiment design. *Bull. Am. Meteorol. Soc.* 93, 485–498. doi: 10.1175/BAMS-D-11-00094.1

Tommasi, D., Stock, C. A., Hobday, A. J., Methot, R. R., Kaplan, I. C., Eveson, J. P., et al. (2017a). Managing living marine resources in a dynamic environment: the role of seasonal to decadal climate forecasts. *Prog. Oceanogr.* 152, 15–49. doi: 10.1016/j.pocean.2016.12.011

Tommasi, D., Stock, C. A., Pegion, K., Vecchi, G. A., Methot, R. D., Alexander, M. A., et al. (2017b). Improved management of small pelagic fisheries through seasonal climate prediction. *Ecol. Appl.* 27, 378–388. doi: 10.1002/eap.1458

Trenkel, V. M., Huse, G., MacKenzie, B. R., Alvarez, P., Arrizabalaga, H., Castonguay, M., et al. (2014). Comparative ecology of widely distributed pelagic fish species in the North Atlantic: implications for modelling climate and fisheries impacts. *Prog. Oceanogr.* 129, 219–243. doi: 10.1016/j.pocean.2014.04.030

Uppala, S. M., Kållberg, P. W., Simmons, A. J., Andrae, U., Bechtold, V. D. C., Fiorino, M., et al. (2005). The ERA-40 re-analysis. *Q. J. R. Meteorol. Soc.* 131, 2961–3012. doi: 10.1256/qj.04.176

Varsamos, S., Nebel, C., and Charmantier, G. (2005). Ontogeny of osmoregulation in postembryonic fish: a review. *Comp. Biochem. Physiol. Part A Mol. Integr. Physiol.* 141, 401–429. doi: 10.1016/j.cbpb.2005.01.013

Wiens, J. A., Stralberg, D., Jongsomjit, D., Howell, C. A., and Snyder, M. A. (2009). Niches, models, and climate change: assessing the assumptions and uncertainties. *Proc. Natl. Acad. Sci. U.S.A.* 106, 19729–19736. doi: 10.1073/pnas.0901639106

Wilks, D. S. (2011). *Statistical Methods in the Atmospheric Sciences:* International Geophysics Series, 3rd Edn, Vol. 100. Amsterdam: Elsevier Inc. doi: 10.1016/B978-0-12-385022-5.00001-4

Wood, S. N. (2006). *Generalized Additive Models: An Introduction with R*. London: Chapman Hall, 391.

Yeager, S. G., and Robson, J. I. (2017). Recent progress in understanding and predicting Atlantic Decadal climate variability. *Curr. Clim. Chang. Rep.* 3, 112–127. doi: 10.1007/s40641-017-0064-z

Yiallourides, C. (2018). It takes four to tango: quadrilateral boundary negotiations in the North-East Atlantic. *Mar. Policy* 87, 78–83. doi: 10.1016/j.marpol.2017.10.007

Conflict of Interest: The authors declare that the research was conducted in the absence of any commercial or financial relationships that could be construed as a potential conflict of interest.

The handling Editor declared a past co-authorship with one of the authors VK.

Publisher's Note: All claims expressed in this article are solely those of the authors and do not necessarily represent those of their affiliated organizations, or those of the publisher, the editors and the reviewers. Any product that may be evaluated in this article, or claim that may be made by its manufacturer, is not guaranteed or endorsed by the publisher.

Copyright © 2022 Miesner, Brune, Pieper, Koul, Baehr and Schrum. This is an open-access article distributed under the terms of the Creative Commons Attribution License (CC BY). The use, distribution or reproduction in other forums is permitted, provided the original author(s) and the copyright owner(s) are credited and that the original publication in this journal is cited, in accordance with accepted academic practice. No use, distribution or reproduction is permitted which does not comply with these terms.

frontiers in Marine Science

ORIGINAL RESEARCH
published: 09 February 2022
doi: 10.3389/fmars.2021.781675

Planktic Foraminiferal Assemblages in Surface Sediments From the Subpolar North Atlantic Ocean

Nibedita Sahoo[1,2], Syed Mohammad Saalim[1]*, Alexander Matul[3], Rahul Mohan[1], Anna Tikhonova[3] and Nina Kozina[3]*

[1] ESSO-National Centre for Polar and Ocean Research, Ministry of Earth Sciences, Vasco-da-Gama, India, [2] School of Earth, Ocean and Atmospheric Sciences (SEOAS), Goa University, Taleigao, India, [3] Shirshov Institute of Oceanology, Russian Academy of Sciences, Moscow, Russia

The subpolar North Atlantic (SPNA) Ocean has complex hydrography, and moderates the global climate through the Atlantic Meridional Overturning Circulation (AMOC). The surface water mass dynamics in SPNA and the upper limb of AMOC, govern the plankton distribution. Specifically, the habitat of modern planktic foraminifera is strongly affected by the SPNA hydrography. In the present study, 25 surface sediment samples from the Labrador Sea to the Iceland-Faroe-Shetland Channel (IFSC) were examined for planktic foraminifera distribution along a latitudinal transect at 59.50°N. The planktic foraminifera distribution followed the transition in water mass structure in the study area from the Sub-Arctic water in the west to the warm North Atlantic water in the east. Temperature and salinity are two dominant ecological factors controlling planktic foraminifera assemblages in the region. This hydrographic contrast was also reflected in the ratio of *Neogloboquadrina pachyderma*/*Neogloboquadrina incompta* along the transect. Based on the cluster analysis, the planktic foraminifera assemblages could be assigned to three groups. A cold/polar group in the Labrador Sea, a mixed (both cold and warm) group in the Irminger Sea and IFSC, and a warmer temperate group in the eastern part of the transect were represented by different planktic foraminifera assemblages. Additionally, a decrease in *Globorotalia inflata* in the eastern transect and an increase in *Turborotalita quinqueloba* in the Iceland basin and Irminger Sea was observed in our study when compared with the published dataset. From this, we suggest a shift in planktic assemblages in the SPNA. The present study on the distribution of modern planktic foraminifera can help paleoceanographic reconstructions in the SPNA ocean.

Keywords: planktic foraminifera, subpolar North Atlantic, cluster analysis, subpolar gyre, water mass

OPEN ACCESS

Edited by:
Teresa Sofia Giesta da Silva, Marine and Freshwater Research Institute, Iceland

Reviewed by:
Lucilla Capotondi, Institute of Marine Science, National Research Council (CNR), Italy
Iria Sala, University of Strathclyde, United Kingdom
Matthew Walker, University of Leeds, United Kingdom

****Correspondence:***
Nibedita Sahoo
nibedita.geo92@gmail.com
Syed Mohammad Saalim
sa_saalim2006@hotmail.com

Specialty section:
This article was submitted to Marine Ecosystem Ecology, a section of the journal Frontiers in Marine Science

Received: *23 September 2021*
Accepted: *17 December 2021*
Published: *09 February 2022*

Citation:
Sahoo N, Saalim SM, Matul A, Mohan R, Tikhonova A and Kozina N (2022) Planktic Foraminiferal Assemblages in Surface Sediments From the Subpolar North Atlantic Ocean. Front. Mar. Sci. 8:781675. doi: 10.3389/fmars.2021.781675

INTRODUCTION

Planktic foraminifera are unicellular protists widely distributed in the modern oceans. They thrive in the upper ocean water column and are constrained by various environmental parameters, especially water mass characteristics (temperature, salinity, nutrients, etc.) and food availability (Parker, 1960; Bé and Tolderlund, 1971; CLIMAP Project Members, 1976; Ortiz and Mix, 1992;

Schiebel and Hemleben, 2005, 2017; Rebotim et al., 2017). The calcium carbonate shells of planktic foraminifera are one of the major biogenic components of marine sediments. Planktic foraminifera species and assemblages are excellent indicators of ambient environmental factors and have been widely used to infer paleoenvironments (Kucera, 2007; Schiebel et al., 2017). The depth stratification and ecological preferences of planktic foraminifera play a vital role in reconstructing paleoceanographic changes. However, the paleoenvironmental reconstructions rely on a better understanding of the modern foraminiferal ecology and factors governing their abundance in different water masses. The distribution and ecology of planktic foraminifera have been studied in the plankton tows, sediment traps, and surface sediments from the world oceans (Berger, 1969; Thunell and Reynolds, 1984; Schiebel and Hemleben, 2000; Schiebel et al., 2001; Jonkers et al., 2010; Meilland et al., 2020). The studies referred are either confined to different basins or show regional heterogeneity. A complete ecological and spatial distribution of planktic foraminifera is understudied in the subpolar North Atlantic (SPNA) ocean, an area influenced by the large-scale changes in the surface hydrography on both short and large timescale (such as seasonal, annual, interannual, and decadal).

The SPNA exhibits significant west to east oceanographic gradients from the subarctic to temperate regions (McCartney and Talley, 1982; Read, 2000; Brambilla and Talley, 2008). In particular, the SPNA hydrography is characterized by the presence and interaction of different warm and cold surface water currents (Read, 2000; García-Ibáñez et al., 2015). The strength and extent of the Subpolar Gyre (SPG) influence the hydrography in the SPNA (Hátún et al., 2005; Staines-Urías et al., 2013). The hydrographic diversity strongly affects the distribution of modern planktic foraminifera in the SPNA, resulting in the occurrence of several cold-, warm- and mixed-water planktic foraminifera associations (Bé and Tolderlund, 1971; Ottens, 1991; Schiebel et al., 2001).

The enhanced warming of the high latitude regions in recent decades has led to major oceanographic shifts and resulted in the changing ecology of various planktic faunas (Fossheim et al., 2015; Oziel et al., 2017; Neukermans et al., 2018; Jonkers et al., 2019). Especially, planktic foraminiferal assemblages in high latitude oceans have shown a change in diversity, with an influx of temperate species (Stangeew, 2001; Schiebel et al., 2017; Jonkers et al., 2019; Meilland et al., 2020). As opposed to the single dominant species found in polar regions (Bé and Tolderlund, 1971), several plankton tow experiments reported a rise in warmer-water foraminiferal species in polar regions (Stangeew, 2001; Jonkers et al., 2019; Meilland et al., 2020). The distribution of modern planktic foraminifera reported from the SPNA ocean is mainly confined to either the western (Stangeew, 2001; Jonkers et al., 2010) or the eastern SPNA ocean (Schiebel and Hemleben, 2000). These studies are based mainly upon plankton tows and infer the planktic foraminifera populations with respect to seasonality. Several studies discuss the variations in planktic foraminifera assemblage structure in a latitudinal as well as a longitudinal transect, pertaining to a change in water mass structure in Nordic seas as well as in the Subarctic Pacific (Stangeew, 2001; Kuroyanagi and Kawahata, 2004; Chapman, 2010; Pados and Spielhagen, 2014; Meilland et al., 2020); but not in the SPNA ocean. Thus, the main objective of the present study is to assess the spatial distribution of planktic foraminiferal assemblages and their ecological preferences in the SPNA ocean. Moreover, this becomes interesting as SPNA has complex hydrography, showing an east-west gradient in its physiographic properties, which significantly modulates the planktic foraminiferal distribution. This study, covering the entire SPNA from west to east, would improve our understanding of planktic foraminifera distribution related to various environmental parameters of different water masses and significant shifts in high-latitude regions.

OCEANOGRAPHIC CONTEXT

The SPNA Ocean has a very complex hydrographic system owing to the interaction of different types of surface currents, such as the warm North Atlantic Current (NAC) and its derivatives-East Reykjanes Ridge Current (ERRC), Irminger Current (IC), and cold fresh East Greenland Current (EGC), West Greenland Current (WGC), and Labrador Current (LC) affecting the diverse regional environments (Pollard et al., 1996; Read, 2000; Brambilla and Talley, 2008; Daniault et al., 2016). The NAC, an extension of the Gulf stream, brings warm and saline water to the region through various branches (Daniault et al., 2016; **Figure 1A**). EGC brings cold and less saline water to the SPNA ocean along the eastern coast of Greenland. These currents and the associated water masses are controlled by the dynamics of cyclonic Subpolar Gyre (SPG). A strengthened and expanded SPG brings more subpolar water from the western SPNA to the eastern SPNA through the eastern limb of SPG. A weakened and contracted gyre brings subtropical warm water to the east SPNA through the eastern limb of SPG (Staines-Urías et al., 2013). The upper water mass at the east SPNA gets colder and denser as it travels downstream toward the Labrador Sea through mixing with the surrounding subpolar water mass and air-sea interaction (Read, 2000).

In general, alternating warm and cold water currents create a prominent hydrological contrast along the studied transect at 59.50°N (**Figures 1B–D**). The annual average temperature and salinity of the surface water (averaged for a water depth of 0–100 m) vary from 10.33°C and 35.28 PSU on the eastern side, through 8.12°C and 35.00 PSU on the central part near Reykjanes Ridge, to 4.60°C and 34.57 PSU in the Labrador Sea (Locarnini et al., 2018; Zweng et al., 2018). The primary productivity in the region (chlorophyll-*a* concentration) ranges from 5.80 [ln (mg/L)] to 8.00 [ln (mg/L)] (**Figure 1D**).

The hydrographic dynamics in the SPNA are associated with different-scale eddies and hydrological fronts, bringing more nutrient-rich water to the region. The warm subtropical water from the NAC and cold subpolar water are separated by the subpolar front, creating a highly productive region (Taylor and Ferrari, 2011a). The eddies associated with Iceland Basin and Irminger Sea bring more nutrient-rich water to the surface

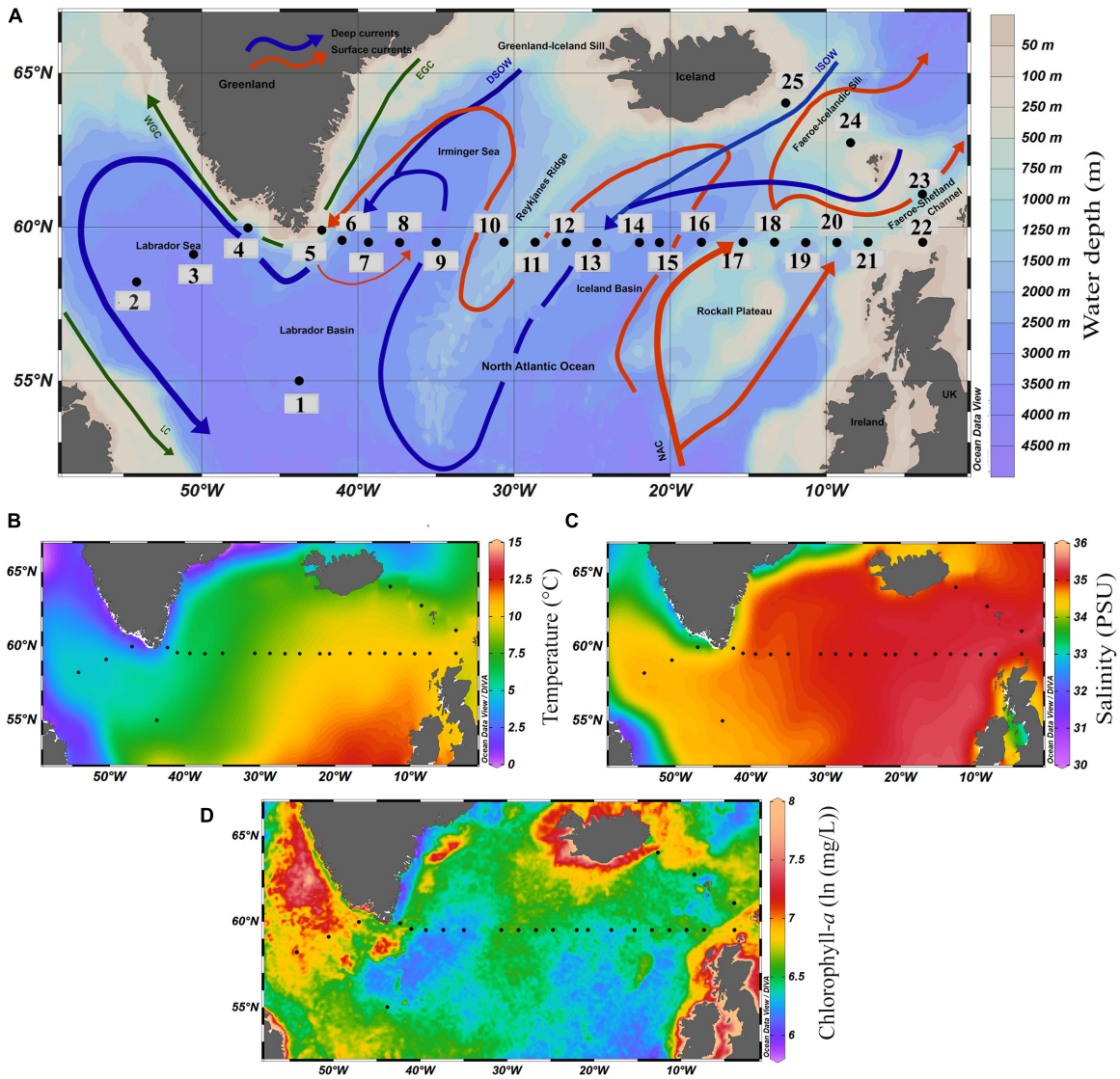


FIGURE 1 | (A) Map showing locations of surface sediment samples and major ocean currents in subpolar North Atlantic Ocean (Schlitzer, 2015). Total 25 samples along 59.50°N latitude were retrieved during Akademik Ioffe 51 cruise; the black dots represent the locations of the surface sediment samples and the numbers denote the name of the stations. Warm and cold surface currents are in red and green, respectively, and cold deep currents are shown in blue color. NAC, North Atlantic Current; EGC, East Greenland Current; WGC, West Greenland Current; ISOW, Iceland-Scotland Overflow water; DSOW, Denmark Strait Overflow Water; LC, Labrador Current; Map showing surficial distribution of, **(B)** Annual average Sea Surface Temperature (SST,°C). **(C)** Annual average Sea Surface Salinity (SSS, PSU), and **(D)** Annual average Chlorophyll-*a* [ln (mg/L)] of the modern ocean.

(Mahadevan et al., 2012). This makes the SPNA a highly productive region (Taylor and Ferrari, 2011a; Mahadevan et al., 2012). Also, the extent and strength of the SPG circulation directly impact productivity changes in SPNA (Hátún et al., 2009). The increased freshening of the SPNA and decreased Atlantic Meridional Overturning Circulation (AMOC) strength have a negative effect on primary productivity (Osman et al., 2019). The productivity of plankton communities in SPNA exhibits clear seasonal character peaking from spring to autumn after the shutdown of winter convection and the formation of stable surface stratification (Taylor and Ferrari, 2011b). Primary productivity, along with the other physical parameters, controls the distribution of planktic foraminifera assemblages (Bé and Tolderlund, 1971; Schiebel and Hemleben, 2017). The abundance of foraminifera species is also linked with chlorophyll-*a* (Chl-*a*) concentration (Schiebel et al., 2001; Kuroyanagi and Kawahata, 2004; Retailleau et al., 2011).

MATERIALS AND METHODS

Sediment Samples

A total of 25 surface sediment samples were collected using Van Veen grab sampler on board the R/V Akademik Ioffe 51st cruise

during the summer (June–July) of 2016. The top sediment (0–1 cm) section was carefully scooped from the collected samples for this study. The samples were collected along a latitudinal transect from the Labrador Sea in the west, to Iceland-Faroe-Shetland Ridge (IFSR) in the east of the SPNA ocean, with a depth varying between 158 m at station 22 and 3,477 m at station 3 (**Figure 1A**). Of these 25 stations, 21 were from the west-east transect along latitude ∼59.50°N; one sample was from 55.00°N in the Labrador Basin, and three were from a southeast-northwest transect in IFSR (**Figure 1A**; for more information, see **Supplementary Table 1**).

Foraminiferal Counts and Calcium Carbonate Content

Around ∼5 g sediment was freeze-dried per sample and soaked in de-ionized water for 6 h, followed by wet sieving through 63 and 500 μm sieves. The >63 μm residue was then dry sieved over >100 μm mesh. The size fraction of >100 μm was chosen for faunal study to avoid any underestimation of small-sized species, e.g., *Turborotalita quinqueloba*, *Globigerinita uvula* following previous studies (Bauch, 1994; Kandiano and Bauch, 2002; Husum and Hald, 2012). The sieved fraction of >100 μm was split using a micro-splitter until a minimum of 300 planktic foraminifera specimens were picked from each sample (CLIMAP Project Members, 1976). The planktic foraminifera species were counted and identified to species level using a stereo-zoom microscope (Nikon SMZ1500 with the magnification of 112X) following the taxonomic nomenclature by Kennett and Srinivasan (1983) and Hemleben et al. (1989). The planktic foraminifera specimens were well preserved in all the samples, and no significant fragmentation of the planktic foraminifera was found. The total planktic foraminifera abundances (TPF) per one gram of dry sediment (ind. × g^{-1}), the individual species abundances per one gram of dry sediment (ind. × g^{-1}), and their relative abundances (%) were calculated.

For the estimation of the $CaCO_3$ content, we measured the Total Inorganic Carbon (TIC, weight%) of all the samples using a Coulometer (UIC, Inc. CM5017). We followed the method of Espitalié et al. (1977) to estimate the $CaCO_3$%,

$$CaCO_3 = (TC - TOC) \times 8.33\,(\%) \quad (1)$$

$$TC - TOC = TIC \quad (2)$$

$$CaCO_3 = TIC \times 8.33\,(\%) \quad (3)$$

In Eqs. 1, 2, TC is Total Carbon and TOC is Total Organic Carbon.

Environmental Parameters

The annual average temperature and salinity data were obtained from the World Ocean Atlas 2018 (WOA18)[1] from the National Oceanic and Atmospheric Administration (NOAA) (Locarnini et al., 2018; Zweng et al., 2018). Both temperature and salinity data were averaged over 0–100 m of water depth. The depth range (0–100 m) was preferred due to the occurrence of the maximum abundance of planktic foraminifera in the upper 100 m water column in the northeast Atlantic (Schiebel and Hemleben, 2000). Annual average Chl-*a* (mg m^{-3}) data was taken from the Moderate Resolution Imaging Spectroradiometer (MODIS) (NASA Goddard Space Flight Center, 2018) Chl-*a* concentration Level 3 data[2] from the year 2001 to 2018 (**Figure 1D**). These data were used to analyze the relationship between planktic foraminifera distribution and main environmental variables along the transect.

Statistical Analyses

Statistical analyses were carried out to facilitate the understanding between various environmental parameters and the relative species abundance. A strict criterion was followed wherein species showing relative abundances greater than 2% in at least three stations were considered for statistical analyses.

Principal Component Analysis

Principal Component Analysis (PCA) was performed on the environmental parameters, such as temperature, salinity, water depth of sampling point, Chl-*a* with total planktic foraminifera abundances, and species percentages using the software STATISTICA v. 10 (StatSoft). This method of statistical correlation has been used to understand the major environmental factors responsible for variation in the distribution of the planktic foraminifera assemblages (Mallo et al., 2017). The marked correlations are significant at a $p < 0.05$.

Cluster Analysis

A hierarchical cluster analysis was performed on the planktic foraminifera assemblages to delineate different groups of stations using the Bray Curtis similarity index. Each group was represented by its characteristic foraminiferal assemblage. This analysis has been used previously to identify the relationship between the group of stations and different water masses based on their specific planktic foraminifera assemblages (Parker and Berger, 1971; Thunell, 1978; Ottens, 1991). We also performed the similarity percentages (SIMPER) analysis (Clarke, 1993) to determine the individual species contribution to each cluster group.

RESULTS

Total Planktic Foraminifera and Calcium Carbonate

The TPF varied between 1,212 and 183,557 ind. g^{-1}. The highest abundance occurred at station 10 (water depth of 1,531 m) near the Reykjanes Ridge, while the lowest abundance was at station 23 (water depth of 158 m), in Faroe-Shetland Channel (FSC). Interestingly, few stations (2, 3, 4, and 13) located at deeper depths in the Labrador Sea, east of Greenland and Reykjanes Ridge exhibited low TPF, along with the samples at shallow regions (5, 24, and 25), which are generally marked by the lowest

[1]https://www.ncei.noaa.gov/access/world-ocean-atlas-2018/

[2]http://oceancolor.gsfc.nasa.gov/cgi/l3

TPF (**Figures 2A,B**). Subsequently, the $CaCO_3$ content in the surface sediments varied from 9% at station 4 (water depth of 2,389 m), near the southwest coast of Greenland, to 74% at station 17 (water depth of 1,514 m), at the western side of the Rockall Plateau. Furthermore, the TPF and $CaCO_3$ content varied concomitantly (**Figure 2A**).

We found significant variations in the distribution of planktic foraminifera species along the transect. A total of nine species occurred in our samples: *Globigerinita glutinata*, *Neogloboquadrina pachyderma*, *Neogloboquadrina incompta*, *Turborotalita quinqueloba*, *Globigerina bulloides*, *Globigerinita uvula*, *Globorotalia inflata*, *Globorotalia scitula*, and *Orbulina* sp. (**Figure 3**). The list of planktic foraminifera species and their ecological information can be found in **Supplementary Table 2**. Among all, the former six species were the most abundant. Together, they contribute at least 80% to the planktic foraminifera community.

The former five species were consistently present along the transect except at a few stations; whereas, *G. inflata* was present only in the eastern part of the transect (absent toward the west of Reykjanes Ridge). However, in the western part of the transect, in the Labrador Sea and Irminger Sea, the sampled stations were dominated by *N. pachyderma*. Moreover, it is the only species found in the two sampling sites of the Labrador Sea, constituting 100% of the assemblage (**Figure 4A**).

Variations in Relative Abundances of Planktic Foraminifera Species

The relative abundance of planktic foraminifera species varied considerably from west to east along the transect (**Figure 4**). *Neogloboquadrina pachyderma* was the most abundant species in the western part of the transect consisting of 100% of the assemblage in sediment fraction of >100 μm in the Labrador Sea (**Figure 4A**). This species was more abundant in the Labrador and Irminger Seas, and its concentration decreased toward the eastern part of the transect. The species was absent from stations 15, 20, 21, and 22 on the eastern side of the Iceland Basin. The average relative abundance of *N. incompta* was 22% in the transect with the highest value of 43% (station 20) near the Scottish shelf and nil in the Labrador Sea (stations 2 and 3) (**Supplementary Table 3** and **Figure 4B**). Higher relative abundance was seen in the IFSC (average 41%) followed by the Iceland basin-Rockall Plateau (average 27%) and the lowest in the Irminger Sea (average 12%) and the Labrador Sea (average 2%). *Globorotalia inflata* was concentrated only in the eastern transect with the highest relative abundance of 5% at stations 25 and 14 in the Iceland-Faroe Ridge and the Iceland Basin (**Figure 4C**). The average relative abundance of *G. inflata* was 2% in the eastern part of the transect. Likewise, the average *G. glutinata* percentage along the transect was 19%, with the highest abundance of 45% (station 14) in the Iceland Basin, although absent in the Labrador Sea (**Supplementary Table 3** and **Figure 4D**). *Globigerina bulloides* percentage was low in this area, with an average value of 4%. *Globigerina bulloides* showed the maximum abundance of 20% at station 10 in the Reykjanes Ridge area. While, the abundance of *G. bulloides* was nil at stations 2, 3, 22, and 23 in the Labrador Sea and near the Scottish shelf (**Figure 4E**). The relative abundance of *T. quinqueloba* increased (>25%) in specific sites in the Irminger Sea, Iceland Basin, and off Scotland, with relatively lower percentages in other stations ranging between 0 and 21% (**Figure 4F**). *Globigerinita uvula* was present in the samples with very low relative abundance, highest as 5% near the Scottish shelf (station 21). The occurrence of *G. uvula* was patchy in the transect. *Globorotalia scitula* and *Orbulina* sp. were very rare. *G. scitula* was found only in the eastern Iceland basin (stations 14, 15, and 16) with <1% and near the east coast of Greenland (station 4) with 4%. *Orbulina* sp. was found only at two stations in the eastern Iceland basin and Iceland-Faroe Ridge (stations 14 and 23).

Ratio *Neogloboquadrina pachyderma*/*Neogloboquadrina incompta* Along E–W Transect

The distribution of the species *N. pachyderma* and *N. incompta* is significantly influenced by the temperature and salinity of the region. Also, a change in the relative abundance of *N. pachyderma* and *N. incompta* is linked to specific summer (Sea Surface Temperature) SST values of the water mass (Žarić et al., 2005). Hence, to document the variation in water mass properties (temperature and salinity) from west to east along the sampled transect, the ratio of *N. pachyderma* and *N. incompta* was used. Along the transect, the relative abundance of *N. pachyderma* was observed to increase significantly from the eastern to the western part. However, *N. incompta* exhibited an opposite trend with the *N. pachyderma* abundance from east to west (**Figure 5A**). To better interpret the variation of these two species with respect to water mass (temperature and salinity) along the transect, we analyzed the ratio of the two species (**Figure 5**). The ratio of *N. pachyderma*/*N. incompta* decreased toward the eastern side of the transect. Also, a higher ratio of >2 was observed toward the western part of the transect, where lower temperature and salinity values were attained (**Figure 5B**).

Principal Component Analysis

To assess the ecological preferences of the planktic foraminifera and their relation to the environmental parameters in the SPNA ocean, PCA was performed. The first two PCA factors explain 86.98% of the total variance. The first factor explains 60.71%, and the second factor explains 26.27% (**Figure 6**). Factor 1 has positive loadings on temperature and salinity computed for the first 100 m (average) of the water column, whereas factor 2 has a positive loading with superficial Chl-*a*. In the PCA analysis, both temperature and salinity vary in the same trend. However, both the parameters have an individual influence on the abundance and distribution of planktic foraminiferal species in the studied area. From the correlation table (**Table 1**), *G. glutinata*, *N. incompta*, and *G. inflata* exhibit positive values regarding temperature (0–100 m) with r values 0.75, 0.81, and 0.48, respectively, and salinity (0–100 m) with r values 0.67, 0.86, and 0.41, respectively. *Neogloboquadrina pachyderma* shows a negative correlation with temperature ($r = -0.76$) and salinity ($r = -0.73$). *Neogloboquadrina incompta* shows a negative

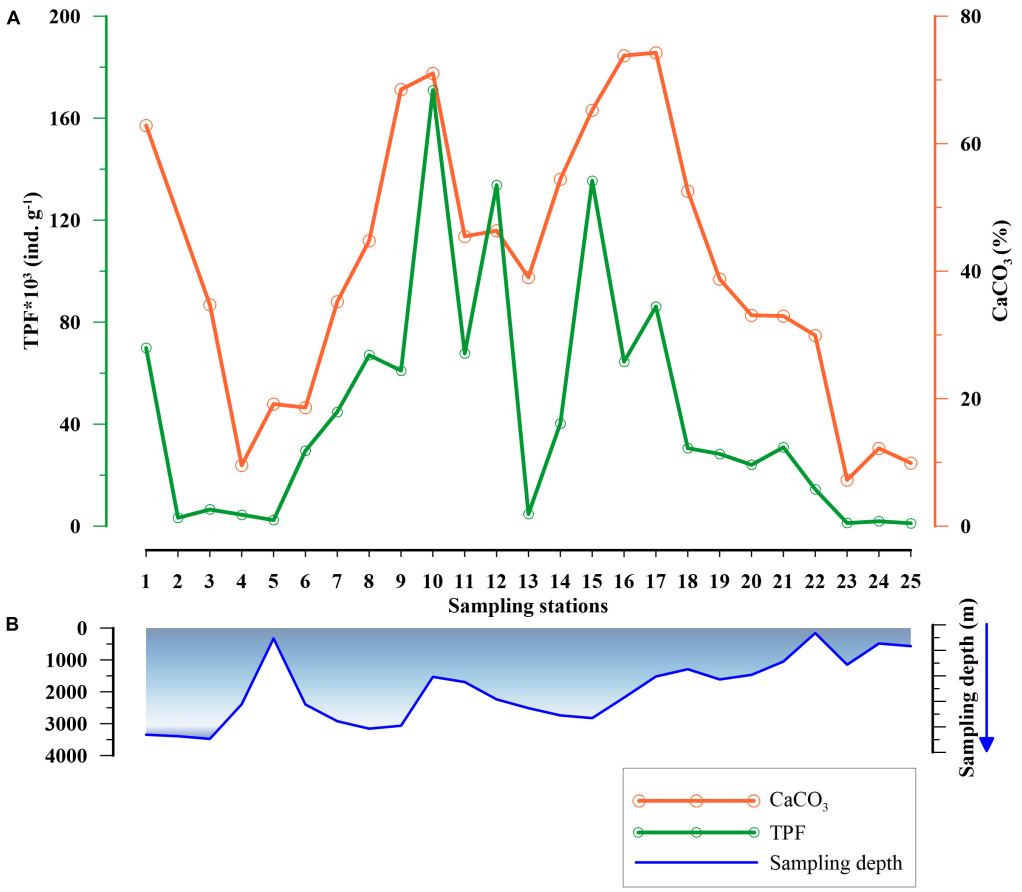


FIGURE 2 | (A) Variation in Total Planktic Foraminiferal (TPF) abundance in numbers per gram sediment (ind. g^{-1}) (in green) and calcium carbonate ($CaCO_3$)% (in orange) at different stations, and **(B)** the blue curve depicts the sampling depth (m) of the stations in the subpolar North Atlantic Ocean.

correlation with water depth. Other species have no significant correlation with any of the environmental parameters.

Cluster Analysis

A hierarchical cluster analysis was performed on the planktic foraminifera dataset to delineate different groups of stations having specific assemblages using the Bray Curtis similarity index (**Figure 7**). Based on the similarity index, stations along the transect can be divided into three distinct cluster groups I, II, and III. The species percentage discussed in this section refers to the individual species contribution (%) to different clusters, further analyzed from SIMPER analysis.

Cluster Group I

Cluster group I includes three stations, 2, 3, and 4, from the central and northeastern Labrador Sea (**Figure 7**). The planktic foraminifera assemblages associated with this group are dominated by *N. pachyderma*. Other planktic foraminifera species *N. incompta*, *G. bulloides*, *T. quinqueloba*, and *G. scitula*, though present in station 4, do not contribute to the similarity percentage of this cluster group. Only *N. pachyderma* contributes 100% to Cluster I. The average similarity between these samples was 76.63% in the Bray Curtis similarity analysis.

Cluster Group II

Cluster group II includes 13 stations from two separate areas within the transect: (1) western half of transect from Reykjanes Ridge to Irminger Sea and central SPG (stations 1, 5, 6, 7, 8, 9, 10, and 12), (2) eastern/northeastern end of transect including the stations from northernmost Rockall Plateau and Iceland-Faroe-Shetland sill (stations 18, 19, 23, 24, and 25) (**Figure 7**). Compared to monospecific planktic foraminifera associations of Cluster group I, assemblages from Cluster group II are mixed, consisting of almost all the species found in the study area. The most abundant species are *N. pachyderma* (30%), *N. incompta* (21%), *G. glutinata* (18%), *T. quinqueloba* (16%), and *G. bulloides* (9%). The average similarity of the Cluster group II was 78.81% in the samples.

Cluster Group III

Cluster III groups nine stations (11, 13, 14, 15, 16, 17, 20, 21, and 22) on the eastern side of the transect from the Reykjanes Ridge to Rockall Plateau and off Scotland (**Figure 7**). However, few stations from the eastern part of the transect (stations 12, 18, and 19) are included in Cluster group II. The planktic foraminiferal assemblages in this region consist mainly of *G. glutinata* (30%), *N. incompta* (27%), *T. quinqueloba* (22%), *G. bulloides* (7%), and

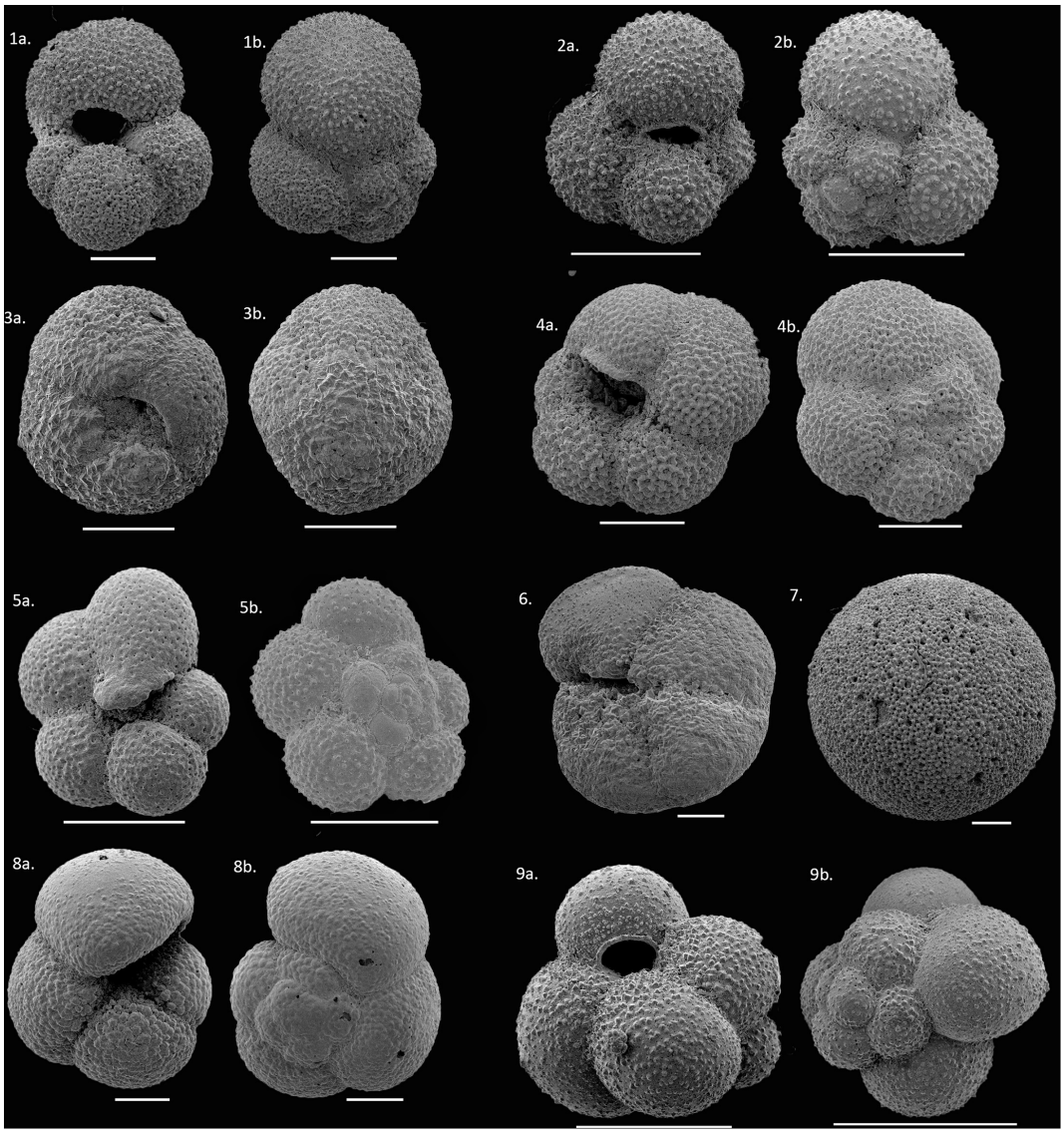


FIGURE 3 | Scanning Electron Micrograph (SEM) images of planktic foraminifera species observed in the present study. **(1a,b)** *Globigerina bulloides* (*G. bulloides*), **(2a,b)** *Globigerinita glutinata* (*G. glutinata*), **(3a,b)** *Neogloboquadrina pachyderma* (*N. pachyderma*), **(4a,b)** *Neogloboquadrina incompta* (*N. incompta*), **(5a,b)** *Turborotalita quinqueloba* (*T. quinqueloba*), **(6)** *Globorotalia scitula* (*G. scitula*), **(7)** *Orbulina* sp. **(8a,b)** *Globorotalia inflata* (*G. inflata*), **(9a,b)** *Globigerinita uvula* (*G. uvula*); Scale bars 100 μm.

G. uvula (6%). The average similarity between the samples in this group is 80.71%.

DISCUSSION

Distribution and Abundance of Planktic Foraminifera in the Subpolar North Atlantic

Planktic foraminifera distribution is majorly governed by the contrasting water mass characteristics in the SPNA ocean. Total planktic foraminifera co-varied with the calcium carbonate content in the surface sediments along the sampled transect from the Labrador Sea to Faroe-Shetland Ridge (**Figure 2A**). A positive correlation $r = 0.72$ between the two suggests planktic foraminifera as the main contributor to the biogenic carbonate in the SPNA. A similar observation representing planktic foraminifera as a key component of bottom ocean carbonate was also reported by Honjo and Manganini (1993); Ziveri et al. (1995), and Retailleau et al. (2012). The distribution of planktic foraminifera is primarily based on sea-surface temperature and salinity of the region (Thunell, 1978). However, particularly in the North Atlantic Ocean, SST plays a dominant role (Stangeew, 2001). Along the transect in this study, the lowest planktic foraminifera abundances in the Labrador Sea can be attributed

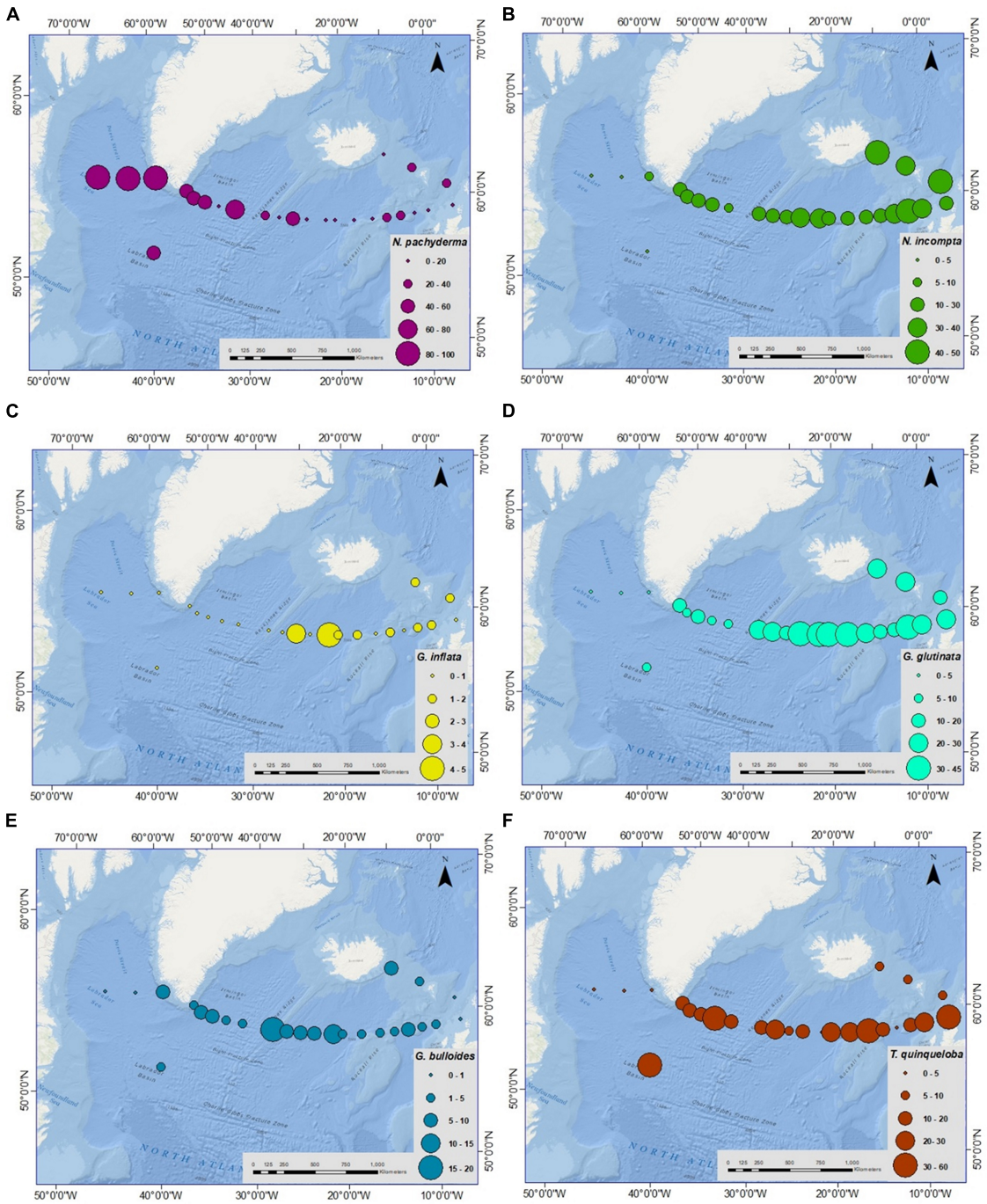


FIGURE 4 | Spatial variation in relative abundance (%) of planktic foraminiferal species **(A)** *Neogloboquadrina pachyderma* (*N. pachyderma*), **(B)** *Neogloboquadrina incompta* (*N. incompta*), **(C)** *Globorotalia inflata* (*G. inflata*), **(D)** *Globigerinita glutinata* (*G. glutinata*), **(E)** *Globigerina bulloides* (*G. bulloides*), **(F)** *Turborotalita quinqueloba* (*T. quinqueloba*) from Labrador Sea to Faroe-Shetland channel. Please note the percentage range for each species is different.

to persistent low annual average (0–100 m) temperature of 3–4°C and salinity of 34.86 PSU. Such low temperature causes a low saturation state for $CaCO_3$ and accounts for a low pH in the Labrador Sea (Azetsu-Scott et al., 2010). These characteristic physical parameters (low temperature, salinity, and pH) of the Labrador Sea are due to the influx of cold and fresh polar water by EGC, fresh Arctic water coming through the Canadian Arctic Archipelago (Melling et al., 2008) and the modified Atlantic water (relatively cooler than North Atlantic Water) coming through IC (Pollard et al., 2004). Furthermore, some parts of the Labrador Sea are influenced by relatively much lower pH water mass coming through the Canadian Arctic Archipelago

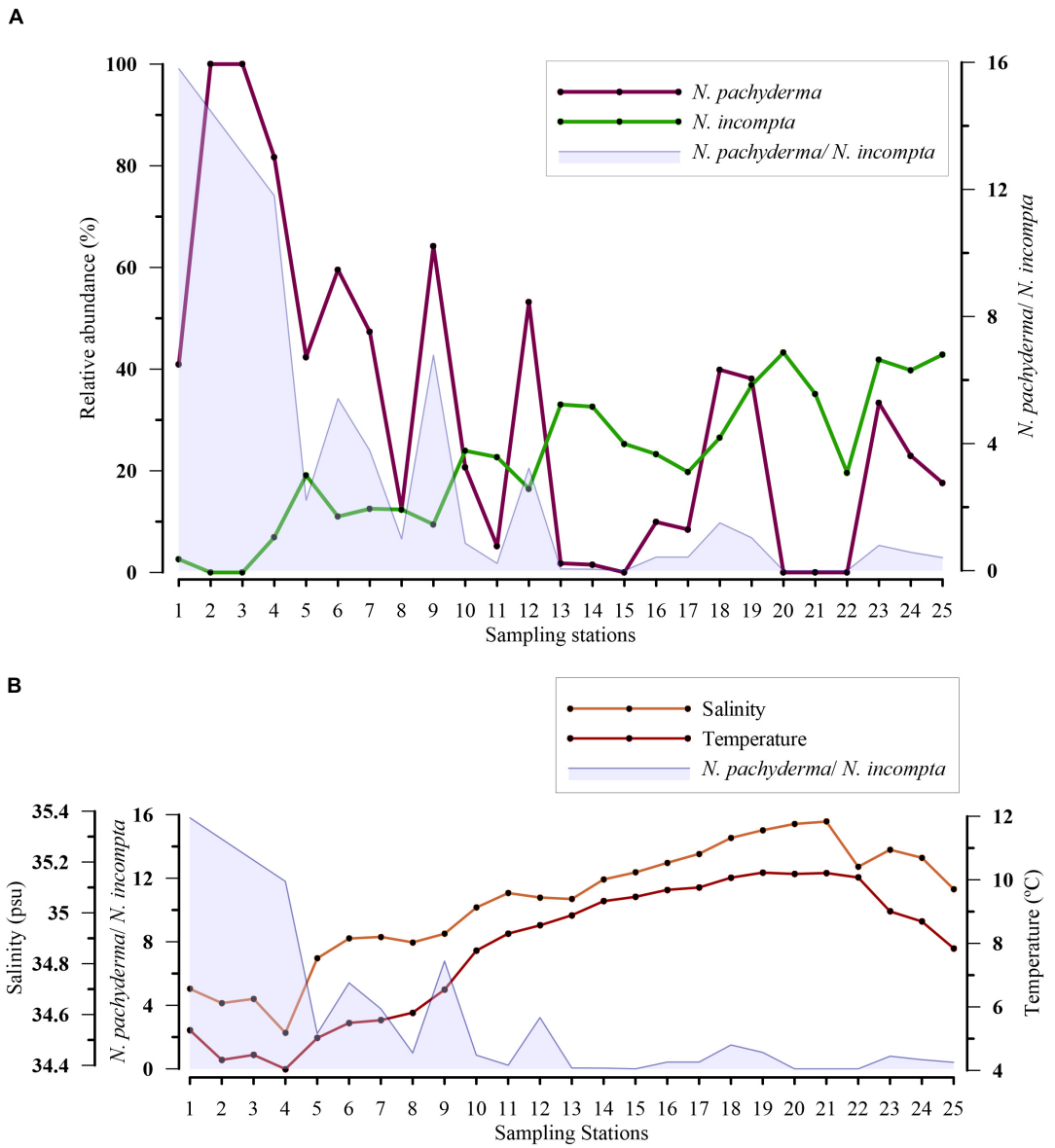


FIGURE 5 | (A) Variation in relative abundance (%) of *Neogloboquadrina pachyderma* (*N. pachyderma*) and *Neogloboquadrina incompta* (*N. incompta*) along the transect and variation in the ratio of *N. pachyderma*/*N. incompta* against the sampled stations is shown in blue; **(B)** Plot showing a relation between the ratio of *N. pachyderma* and *N. incompta* abundance with sea surface temperature and salinity.

(Azetsu-Scott et al., 2010). The low pH acts as an additional factor causing low planktic foraminifera abundances as it is detrimental to the calcitic foraminifera shells and limits planktic foraminiferal abundance. The decreasing rate of deep water formation, linked to the current climate change scenario (Rahmstorf et al., 2015; Thornalley et al., 2018), increases the residence time of the cold deep water at the formation site. This also might cause the dissolution of the highly susceptible foraminiferal shells resulting in low planktic foraminifera abundance. Another area with low planktic foraminifera abundances is the shallow water region of Faroe-Shetland Ridge. Planktic foraminifera is more abundant in the open ocean than in neritic zones with shallow water depths (Schmuker, 2000; Retailleau et al., 2009). The water mass near Faroe-Shetland is entrained by a tongue of cold and fresh nutrient-poor Arctic water brought by East Iceland Current (EIC), which can additionally cause a decline in the productivity in the region.

Planktic foraminifera was most abundant in the middle of the transect covering the eastern Iceland Basin to the central Irminger Sea, which is influenced by the modified nutrient-rich Atlantic water. The presence of Subpolar Front (SPF) in this area near Reykjanes Ridge aids in enhanced planktic foraminiferal abundances in the SPNA as frontal regions are characterized by the uplifting of nutrient-rich waters, which

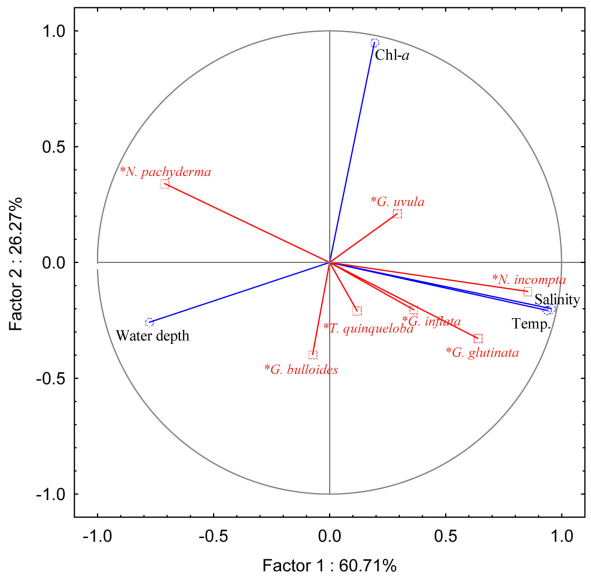


FIGURE 6 | Principal component analysis (PCA) plot of the relative abundance of the different species (*N. pachyderma*: *Neogloboquadrina pachyderma*; *N. incompta*: *Neogloboquadrina incompta; G. inflata*: *Globorotalia inflata; G. glutinata*: *Globigerinita glutinata*; *G. bulloides*: *Globigerina bulloides*; *T. quinqueloba*: *Turborotalita quinqueloba*; *G. uvula*: *Globigerinita uvula*) with different environmental parameters [average temperature (Temp., °C) and salinity (PSU) of the first 100 m of the water column, Chlorophyll-*a* concentration (Chl-*a*, mg m^{-3}) and water depth (m)].

allows a greater abundance of phytoplankton and leads to higher primary productivity (Lutjeharms et al., 1985; Kimura et al., 2000). Further, eddy activity in the Irminger Sea and Iceland Basin is responsible for strong mixing at the surface, enriching the surface water with nutrients (Knutsen et al., 2005) which increases primary productivity and hence, the planktic foraminifera abundances in the region.

The planktic foraminiferal number is comparable with the sediment trap and plankton tow datasets previously reported in the SPNA ocean (Schiebel and Hemleben, 2000; Schiebel, 2002). The planktic foraminiferal shells vary from 1.20×10^3 to 1.80×10^5 g^{-1} (present study) with varying sampling depth. Samples from the open ocean at a depth of 2,000 m exhibit comparable numbers with Lundgreen (1996), which represents 1.60×10^5 planktic foraminifera tests $year^{-1}$ [extrapolated tests day^{-1} in September from 47°50'N, >100 μm (Table 3 in Schiebel, 2002)]. However, a decrease in flux with depth is associated due to the biologically mediated dissolution of planktic foraminifera through the water column while settling (Schiebel and Hemleben, 2000). Further, the relative abundances found in the multi net samples from the BIOTRANS area and at 57°N, 20–22°W of Schiebel and Hemleben (2000) is comparable to the planktic foraminifera species composition in our study. Hence, the species assemblage in the surface sediment in this area represents the upper water mass assemblages. Pados and Spielhagen (2014) also reported a similar observation from Fram Strait. Moreover, the mean lateral transportation for the smaller species *T. quinqueloba* and *N. pachyderma* is 50–100 and 25–50 km in the Fram Strait, respectively (Gyldenfeldt et al., 2000). From this, we can suggest no significant effect of lateral transportation on planktic foraminifera assemblages in the SPNA ocean.

Species Ecological Preferences

The polar to subpolar species *N. pachyderma* was found to be a single dominant species in the Labrador Sea in the present study. A significant increasing trend was observed in the relative abundance of *N. pachyderma* toward the western part of the transect in the study area (**Figure 4A**). Our data show a strong negative correlation of *N. pachyderma* relative abundance with both temperature ($r = -0.76$) and salinity ($r = -0.73$), marking its dominance in the cold fresh Polar water of Labrador and Irminger Seas (**Table 1**). Previous studies (Kohfeld et al., 1996; Greco et al., 2019) exhibited a number of environmental factors controlling the abundance and distribution of *N. pachyderma*. This species is observed abundantly in low temperature and low saline regions (Bé and Tolderlund, 1971), which is also evident in our study. Moreover, abundances of *N. pachyderma* of ≥95 and <50% correspond to a summer temperature of <4 and ≥9°C, respectively (Bé and Tolderlund, 1971). The occurrence of *N. pachyderma* has been reported to vary as a function of salinity, presence/absence of sea ice, and deep chlorophyll maximum (Stangeew, 2001; Jonkers et al., 2010; Greco et al., 2019). Usually, *N. pachyderma* abundances show a two-way pulse in its flux in North Atlantic; one in summer at maximum stratification and another in spring (Tolderlund and Bé, 1971; Jonkers et al., 2010). Some studies reported that food availability (Chl-*a* concentration, as a proxy of phytoplankton biomass) also affects the distribution of *N. pachyderma* like other planktic foraminifera (Fairbanks and Wiebe, 1980; Kohfeld et al., 1996; Schiebel and Hemleben, 2005). However, our results for SPNA suggest a statistically validated relationship of *N. pachyderma* abundances with water temperature and salinity but weak dependence on Chl-*a* concentrations ($r = 0.17$ in **Table 1**). Although, it should be noted that the weak correlation of *N. pachyderma* with Chl-*a* may be a result of considering only the most superficial layer in this statistical analysis.

In the present study, *T. quinqueloba* shows a patchy distribution. It is observed maximum in the Irminger Sea and the eastern Iceland Basin in our study. Its occurrence has no significant statistical correlation with temperature and salinity along the sampled transect. Although *T. quinqueloba* has been previously reported to vary with primary productivity (Volkmann, 2000), its abundance did not correlate with Chl-*a* concentration in the present study. Meilland et al. (2020) have also documented the same in the Barents Sea opening. This could be due to the specific habitat and food preference of the species, which cannot be represented by Chl-*a* data alone. *T. quinqueloba* has been described to be associated with water mass fronts (Hemleben et al., 1989; Husum and Hald, 2012) and are most abundant at regions of mixing of different water masses and enrichment in the nutrients (Johannessen et al., 1994; Husum and Hald, 2012).

Along the sampled transect, *N. incompta* follows the opposite trend compared to *N. pachyderma* exhibiting decreasing

TABLE 1 | Correlation factors for the relative abundance of planktic foraminifera (*Neogloboquadrina pachyderma*, *Neogloboquadrina incompta*, *Globigerina bulloides*, *Turborotalita quinqueloba*, *Globorotalia inflata*, *Globigerinita glutinata*, and *Globigerinita uvula*) with different environmental parameters [average temperature (Temp., °C) and salinity (PSU) of the first 100 m of the water column, Chlorophyll-*a* (Chl-*a*, mg m^{-3}) and water depth (m)].

	Neogloboquadrina pachyderma	*Neogloboquadrina incompta*	*Globigerina bulloides*	*Turborotalita quinqueloba*	*Globorotalia inflata*	*Globigerinita glutinata*	*Globorotalia uvula*
Water depth	0.44	−0.62	0.08	−0.07	−0.07	−0.30	−0.37
Salinity	−0.73	0.86	−0.04	0.14	0.41	0.67	0.17
Temp.	−0.76	0.81	0.00	0.14	0.48	0.75	0.23
Chl-*a*	0.18	0.05	−0.43	−0.19	−0.05	−0.14	0.22

Numbers in red show significant correlations ($p < 0.05$).

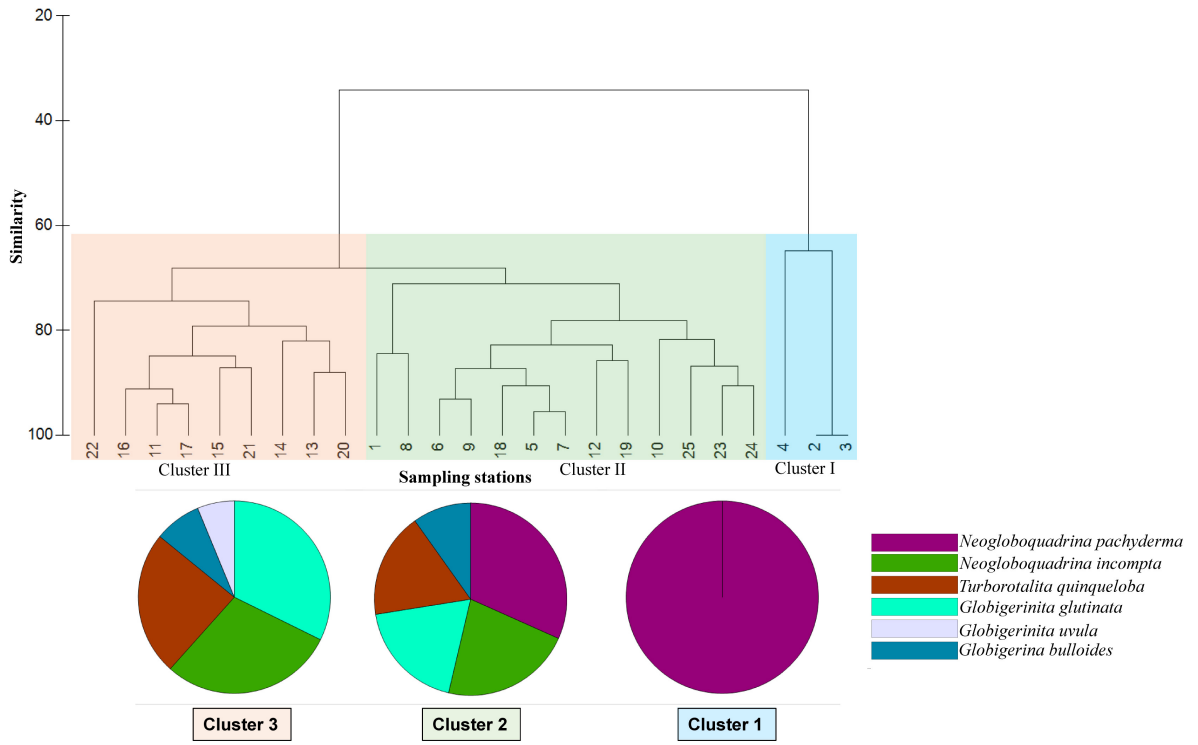


FIGURE 7 | Hierarchical cluster analysis of stations based on foraminiferal assemblages (Bray Curtis similarity). The pie charts show the contribution of different species to different clusters (by SIMPER analysis).

abundance in the subpolar waters of the Irminger and the Labrador Seas. Its abundance has strong positive correlation with temperature (r = 0.81) and salinity (r = 0.86; **Table 1**). Also, the negative correlation of *N. incompta* percentages with water depth (bathymetry) (r = −0.61) supports its higher abundance in shallow waters of the Iceland-Faroe-Shetland Channel. This observation is coherent with other studies wherein *N. incompta* was abundant in <100 m water depth in eastern North Atlantic (Schiebel et al., 2001; Husum and Hald, 2012). It prefers shallow stratified warm water (>8°C) (Ortiz et al., 1995; Schiebel et al., 2001). *Neogloboquadrina incompta* is also related to high nutrient and Chl-*a* concentration (Ortiz et al., 1995; Kuroyanagi and Kawahata, 2004; Kretschmer et al., 2018). However, in the present study, no significant correlation of *N. incompta* abundances with Chl-*a* concentration (r = 0.05) was found. This might be due to the changing food habits of the species with respect to the availability of food in this region. Also, we have taken the superficial Chl-*a* data for the analysis, which could cause a no-correlation with species abundance as *N. incompta* thrives in 50–150 m depth of the water column.

In the present study, *G. glutinata* was most abundant in the central part of the Iceland Basin and decreased toward the western and eastern sides of the sampled transect. *Globigerinita glutinata* is a cosmopolitan species with no specific environmental limits (Schiebel et al., 2017). This species has been shown to dominate planktic foraminifera assemblages in the high latitude areas only recently (Schiebel et al., 2017; Spooner et al., 2020). In the subpolar ocean, the species abundance can increase in summer with shallow thermocline depth depending upon food availability (Stangeew, 2001). Some authors have suggested, it increases with the onset of spring bloom (Ottens, 1992), and few link it with a change in the possible food habitat

(Meilland et al., 2020; Spooner et al., 2020). We found that the species occurrence has a positive correlation with temperature (r = 0.75) and salinity (r = 0.67) along the transect showing the species' affinity toward warmer and more saline water mass, but no correlation with Chl-*a*. *Globigerinita glutinata* was also reported to have a strong relationship with seasonality and food availability, especially associated with diatoms (Schiebel and Hemleben, 2000). Our data in this region shows the distribution of *G. glutinata* is related to the temperature and salinity variation rather than Chl-*a* concentration.

In the present study, temperate to subpolar species *G. bulloides* relative abundance shows a weak negative correlation (r = −0.42) with Chl-*a* concentration and also does not depend on temperature and salinity (**Figure 6**). Here, *G. bulloides* is maximum over Reykjanes Ridge and central Iceland Basin. Generally, this species is most abundant in highly productive subpolar and tropical regions and is specifically marked as an upwelling indicator species in the tropics (Bé and Tolderlund, 1971; Schiebel et al., 2001; Salgueiro et al., 2010). However, a negative correlation possibly can be due to a change in the nature of food habitat in the area. Meilland et al. (2020) suggested Chl-*a* may not always represent a good indicator for foraminiferal distribution, showing no link between Chl-*a* and the productivity indicator species *T. quinqueloba* and *G. uvula* in the Barents Sea. Thus, *G. bulloides* can also be summed as a ubiquitous subpolar species and does not follow any specific trend in the SPNA ocean.

Globigerinita uvula is a temperate to polar species, constituting 0.50–2% of the assemblages (Schiebel and Hemleben, 2017), which is consistent with our data. Recently, increased abundances of this species in surface water assemblages from subpolar to polar regions (Stangeew, 2001; Retailleau et al., 2011; Meilland et al., 2020) have been noticed, but it was not reflected in the surface sediment assemblages (Meilland et al., 2020) as also seen in our data. As the plankton tow study provides information, particularly during the sampling period, *G. uvula* abundance in the water column at that particular period can increase depending on the favorable conditions and can be different from surface sediment assemblage. The small-sized-less resistant species may have low preservation potential while settling in sediment, causing an enhancement of the same in the water column and not in sediment. Moreover, the lower settling velocity of this species gives rise to a higher concentration of its tests in the water column. *Globigerinita uvula* mainly concentrated in <100 μm fraction (Schiebel et al., 2017), might also be a reason for the low abundance of the same in >100 μm in our study. There is no correlation of *G. uvula* percentages in our data with temperature or salinity. The occurrence of *G. uvula* presumably co-varies with primary productivity (Volkmann, 2000; Schiebel and Hemleben, 2017) and generally have a seasonal production in spring and early summer (Schiebel et al., 1995). However, it exhibits an insignificant correlation with Chl-*a* concentrations along the transect. In a recent finding, Meilland et al. (2020) have also shown no significant correlation between Chl-*a* content and *G. uvula* occurrence as they showed a more dependency on food composition rather than concentration.

Globorotalia inflata has a low abundance and is present only on the eastern side of the transect. Generally, its occurrence ranges from subpolar to subtropical waters (Schiebel et al., 2017). In the subpolar ocean, its intrusion represents the influence of warmer water coming through the North Atlantic Current (NAC). It thrives at the base of the seasonal thermocline (100–200 m) (Ganssen and Kroon, 2000; Cléroux et al., 2007). *G. inflata* abundance depends on the surface, and subsurface nutrient enrichment (Schiebel et al., 2017), i.e., eddies and frontal mixing supports its distribution. However, we found only weak positive correlation of *G. inflata* abundances with temperature (r = 0.47) and salinity (r = 0.41) but no relation to Chl-*a* concentrations (r = −0.05).

Abundances of the subtropical species *G. scitula* and *Orbulina* sp. are rare and very low in SPNA. However, *G. scitula* and *Orbulina* sp. have been described as subtropical species and are associated with NAC (Ottens, 1991). Hence, their presence can indicate the entrainment of warm NAC water in the study area. Moreover, the absence of correlation of planktic foraminifera with Chl-*a* in the study area is probably due to the fact that the chlorophyll data represent only the superficial layer and not the 0–100 m.

Faunal Assemblages

Along the sampled transect in the SPNA Ocean, the stations are grouped into three distinct faunal groups based on hierarchical cluster analysis.

Labrador Sea - Polar Group (Cluster Group I)

The Labrador Sea has the coldest water mass along the transect. It is influenced by the cold surface currents EGC, WGC, LC, and relatively warmer surface current IC. Also, it receives fresh Arctic water through the Canadian Arctic Archipelago. Cluster group I, associated with the Labrador Sea, comprises a single species *N. pachyderma* (100%) (**Figure 7**). *Neogloboquadrina pachyderma* is dominant in subpolar and polar conditions (Bé and Tolderlund, 1971; Volkmann, 2000). A decrease in species diversity and richness often occurs in regions of high environmental stress (Keller and Abramovich, 2009) which is the case in the Labrador Sea. The elevated abundance of *N. pachyderma* in the region can also be explained by the good preservation of these thick-shelled species as that is more resistant to dissolution than *T. quinqueloba* and *G. uvula* (Berger, 1973; Boltovskoy and Wright, 2013).

Study on modern-day planktic foraminifera assemblages in the Labrador Sea is rare. A previous study by Stehman (1972) documented two species, *N. pachyderma* and *G. bulloides*, in >200 μm mesh size from the Labrador Sea. Besides, the dominance of single species in this study can be due to an underestimation of the foraminiferal species with smaller size fractions. The size range considered in the present study is >100 μm with relative abundances of *N. pachyderma* 100%. Conversely, Stangeew (2001) had reported high abundances of small-sized (>63 μm fraction) *T. quinqueloba* (46.80%), *G. uvula* (3.50%), along with *G. glutinata* (20.80%), *N. pachyderma* (19.60%), *N. incompta* (2.60%), *G. bulloides* (6.40%),*G. scitula* (<1%), and *G. inflata* (<1%) in the convection region of the Labrador Sea in 0–200 m water column. We compared our surface sediment data of station 3 with the plankton tow results of Stangeew (2001). To ascertain whether the

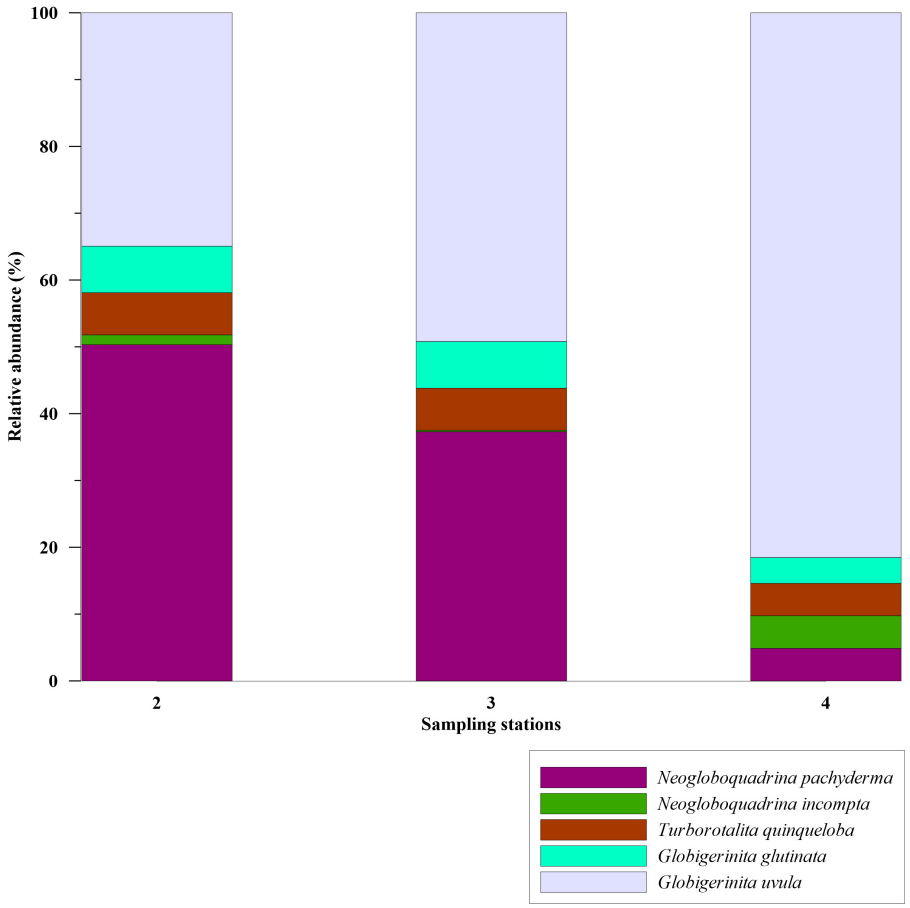


FIGURE 8 | Relative abundance (%) of planktic foraminiferal species in 63–100 μm size fraction from the stations of Labrador Sea, shown in bar plots.

species abundances are size-dependent, we examined the 63–100 μm size fraction in the samples of the Labrador Sea. In this fraction, compared to >100 μm fraction, the smaller-sized species *G. uvula* were more dominant with 37–80% abundance (**Figure 8**). The dominance of *N. pachyderma* in >100 μm fraction and of *G. uvula* in 63–100 μm fraction infers that size plays a significant role in the analysis of planktic foraminifera assemblages, which was also observed in previous studies (Carstens et al., 1997; Husum and Hald, 2012).

In polar regions, Bé and Tolderlund (1971) reported *N. pachyderma* to be the most abundant in >200 μm fraction. Whereas, Carstens et al. (1997) and Volkmann (2000) found the species abundance to be reduced to 60% in the fraction of >63 μm and 70% in the fraction of >125 μm, respectively. Also, test sizes of *T. quinqueloba* in Nordic Seas have been found to differ in the past under varying climatic conditions with shell sizes becoming larger under the Atlantic water influence (Bauch, 1994). As both the size fractions in the Labrador Sea samples from our study are dominant in the cold and fresh water species *N. pachyderma* and *G. uvula*, we suggest a stronger influence of fresh melt water and EGC influenced water than the warmer IC water in the Labrador Sea. This can be evident as the recent fresh water/melt water flux increased in the eastern Labrador Sea (Yang et al., 2016; Zhang et al., 2021).

Irminger Sea and Iceland-Faroe-Shetland Subpolar Group (Cluster Group II)

This group includes two areas: (1) the western side of the transect within central and northern subpolar gyre (east of Greenland, Irminger Sea, and Reykjanes Ridge), (2) the eastern side of transect in the Iceland-Faroe-Shetland Channel (IFSC), and on the northernmost Rockall Plateau between the two pathways of NAC. Cluster group II is comprised of mixed assemblages of temperate to subpolar species *N. incompta*, *G. glutinata*, and *T. quinqueloba*, and cold-water species *N. pachyderma*. On the western part of the transect, the cold fresh water of EGC comes in contact with relatively warm and more saline water of IC (Dickson et al., 2007). Thus, a mixed assemblage is expected in the region. The dominance of *N. pachyderma* explains this, followed by a significant abundance of *T. quinqueloba* and *N. incompta*. While, in the eastern side of the transect, assemblages consist primarily of *N. incompta* together with *T. quinqueloba* and *N. pachyderma*, mainly in the IFSC region. In the IFSC, the Arctic water (lobe of cold water north of Iceland coming in the southern Norwegian Sea) interacts with the warm Atlantic water coming

with NAC. Modified North Atlantic Water (MNAW), a cooler water mass than Eastern North Atlantic Water (ENAW), is found in the upper water masses at IFSC and in some parts of the Rockall Plateau (Read, 2000). A mixed assemblage of both cold and warm species represents a mixing of cold and warm water. Planktic foraminifera assemblages of Group II reflect the greater influence of the polar water in the western SPNA.

Central North Atlantic (Iceland Basin, Northwestern Rockall Plateau, Off Scotland) Temperate Group (Cluster Group III)

The region toward the east of the transect, Iceland basin, Rockall Plateau, receives warm water from NAC (Pollard et al., 2004). This group is associated with predominantly temperate and subpolar species assemblages in the central North Atlantic, which exhibit the warmer-water affinity. The most abundant species of this group are *G. glutinata*, *N. incompta*, and *T. quinqueloba*, while *G. bulloides* and *G. uvula* are less abundant. In the central Iceland basin, more of *N. incompta* and *G. glutinata* represents a warmer water influence. Also, the presence of *G. inflata* and *Orbulina* sp. in this group shows the influence of warm subtropical water (Ottens, 1992). *Globigerinita uvula*'s contribution to the assemblage (6%) shows the presence of fresher melt water at the surface in summer.

Turborotalita quinqueloba percentages are higher at the sites near the NAC pathways in Iceland Basin, near Scotland, and the Reykjanes Ridge. NAC, in this region, acts as a frontal zone, separating the cold fresh subpolar water mass and warm saline subtropical water mass (Read, 2000; Daniault et al., 2016). *Turborotalita quinqueloba* is a front indicator species; hence, its higher abundance at the eastern Iceland basin and Reykjanes Ridge reflects the proximity of the frontal zone in the studied transect.

Neogloboquadrina pachyderma Versus *Neogloboquadrina incompta* Ratio as an Indicator for Change in Water Mass Property

Neogloboquadrina pachyderma is a subpolar to polar species with an increase in abundance poleward (Bé and Tolderlund, 1971). While *N. incompta*, reported earlier as a dextral variety of *N. pachyderma*, is preferably found in relatively warmer and more saline waters. In the present study, *N. incompta* represented its association with temperate/subtropical characteristics of NAC in the region, as the PCA plot demonstrated (**Figure 6**). The abundance of both species depends on physicochemical factors, such as the temperature and salinity of the water mass, presence/absence of sea ice, stratification, and food availability (Jonkers et al., 2010; Greco et al., 2019; Meilland et al., 2020). The highest abundances of *N. pachyderma* match with an optimum temperature range of −0.50 to 17°C, whereas maximum percentages of *N. incompta* occur at 8.50–21.40°C (Žarić et al., 2005, based on sediment traps study; Hilbrecht, 1996, based on surface sediments study). The critical temperature for the shift from the dominance of *N. pachyderma* to *N. incompta* is at ≥9°C (Žarić et al., 2005). In our study, the highest abundances of *N. pachyderma* are concentrated in the Irminger and Labrador Seas at an average temperature of 5.54°C and average salinity of 34.96 PSU. Contrary to this, *N. incompta* is most abundant in the eastern side of the North Atlantic, with maximum abundances at an average temperature of 6.82°C and salinity of 35.05 PSU. The turnover in prevailing abundances of *N. pachyderma*/*N. incompta* takes place near Reykjanes Ridge (**Figure 5**). We suggest a change in water mass properties from the change in assemblages at the western side of Reykjanes Ridge, previously documented by authors from earlier studies (McCartney and Talley, 1982; Read, 2000). This can be illustrated by the ratio between the abundances of *N. pachyderma* and *N. incompta* along transect plotted against the temperature and salinity (average of upper 100 m water column) (**Figure 5B**). The ratio of *N. pachyderma* and *N. incompta* was found to be >1 in the western side with the highest values at the temperature of <4.60°C and salinity of <34.80–35 PSU in the present study. Our results on differences in the abundances of *N. pachyderma* and *N. incompta* on the transect across SPNA are in agreement with previous data on this species ratio as an indicator of the changes in water mass distribution in Nordic Seas and SPNA (Eynaud, 2011). Updating data on the *N. pachyderma*/*N. incompta* ratio improves the use of this tool for paleoceanographic studies, as demonstrated by Eynaud et al. (2009). This is evident with the hydrographic change across the Reykjanes Ridge in the upper water masses.

A Shift in Planktic Foraminiferal Assemblages in the North Atlantic

The recent trends in warming and its associated processes have led to the change in ecology and distribution of planktic foraminifera in the North Atlantic (Jonkers et al., 2019; Meilland et al., 2020). Schiebel et al. (2017) and Meilland et al. (2020) have reported a marked change in planktic foraminifera assemblages and their diversity, with an influx of temperate species increasing their dominance in the region.

We have compared our planktic foraminifera assemblage data with previously published data presenting samples collected in the North Atlantic from Matul et al. (2018), which also includes Pflaumann et al. (2003) dataset, to see if there is any change in planktic foraminiferal assemblages. Their dataset consists of the surface sediment assemblages from the SPNA ocean. We analyzed the average species composition for each region, i.e., I. Irminger Sea II. Iceland Basin and III. Rockall Plateau and IFSC in both datasets. The assemblages observed in the dataset mentioned above and our samples are generally similar in species composition except for the absence of *Globorotalia hirsuta* and *Globorotalia truncatulinoids* in the present data.

We compared the planktic foraminifera relative abundance data for each region in both datasets (**Figure 9**) to illustrate a possible effect of the oceanographic shift on the planktic foraminifera assemblages. The most significant faunal change within the groups was found in the Irminger Sea and Iceland basin. Irminger Sea assemblage is comprised of *N. pachyderma*, *N. incompta*, *G. glutinata*, *G. bulloides*, and *T. quinqueloba*

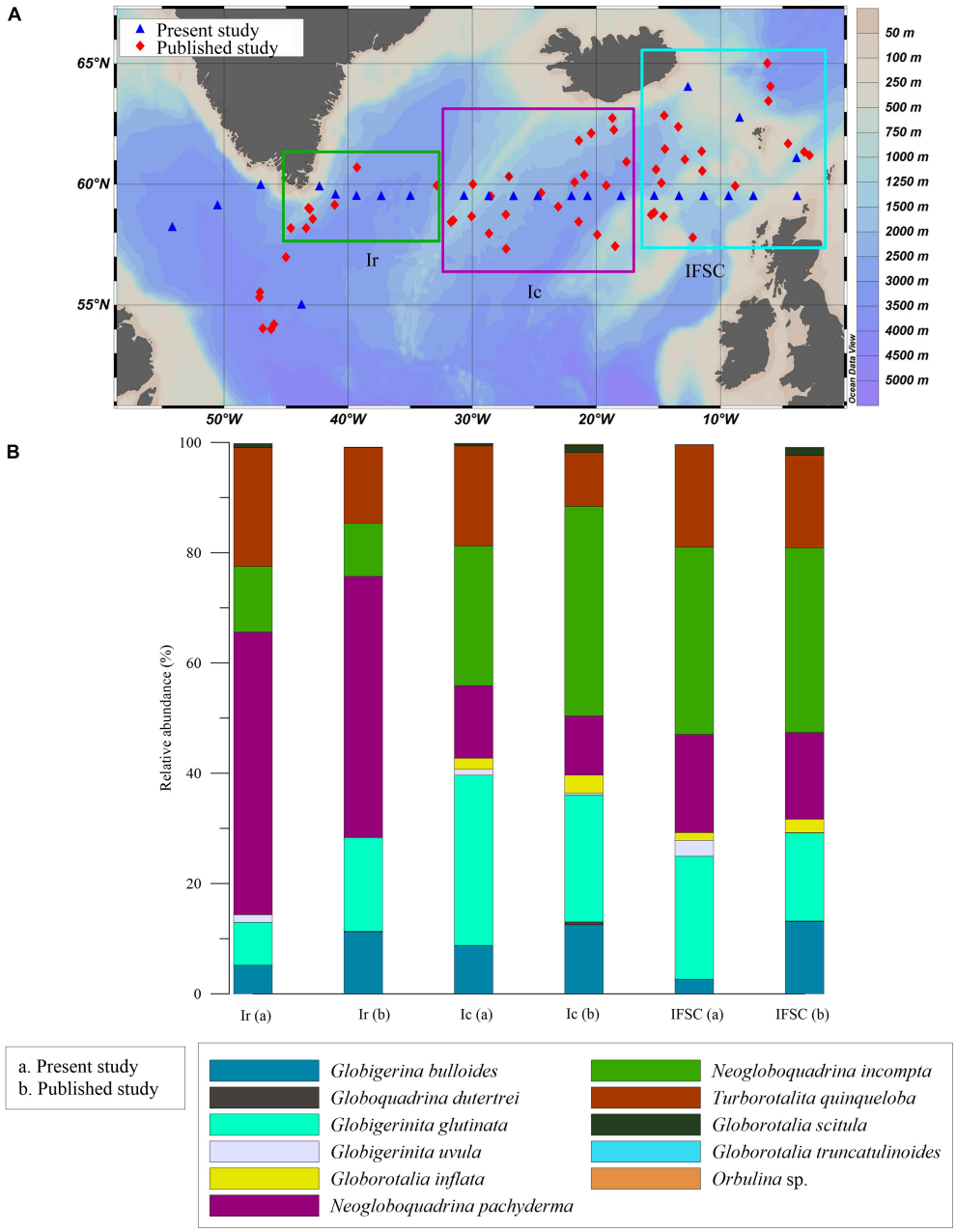


FIGURE 9 | (A) Map showing locations of the samples from Matul et al. (2018) (red diamond) and from our study (blue triangle). **(B)** Comparison of the relative abundance (%) of planktic species from this study (a) with Matul et al. (2018) (b), shown in the bar chart; Ir, Irminger Sea; Ic, Iceland Basin; IFSC, Rockall Plateau and Iceland-Faroe-Shetland Channel.

in our study. Whereas, Iceland basin and Rockall Plateau-IFSC assemblage consist of all the species of the Irminger Sea assemblage along with *G. inflata* in the present study. Compared to Matul et al.'s (2018) data, *T. quinqueloba* percentage has increased, and percentages of *G. bulloides* and *G. glutinata* has decreased in our study area in the Irminger Sea. Likewise, in the Iceland basin, *T. quinqueloba* percentage has increased, and *G. glutinata* and *G. bulloides* percentage have decreased in this study in comparison to Matul et al.'s (2018) data. The present study also observed an increased relative abundance of *G. glutinata* and decreased *G. bulloides* in Rockall Plateau-IFSC region. Thus, an increase in subpolar species *T. quinqueloba* in the Irminger Sea and Iceland Basin from our data could indicate an increase in surface productivity and a relative increase in the cold subpolar water influx in the region. Also, a decrease in *G. inflata* percentage in both the Iceland basin and Rockall-IFSC could indicate a decrease in the influx of warm NAC water to the region (Staines-Urías et al., 2013).

The abundance of *G. inflata* at the eastern side of the transect has been used as a potential indicator of the NAC water influx (Staines-Urías et al., 2013). A lower NAC influx is linked with a strengthened and expanded SPG (more eastward) and vice-versa (Hátún et al., 2005; Staines-Urías et al., 2013). Hence, a decreased influx of *G. inflata* at the eastern side of the transect, i.e., near Faroes, can be due to strengthened and expanded SPG. Moreover, an ongoing increase in the Greenland Ice sheet melt affects the Irminger Sea and the Labrador Sea the most, increasing fresh water influx (Bamber et al., 2012; Yang et al., 2016). The Labrador Sea assemblage in our study also shows an increase in cold water species *N. pachyderma* (>100 μm), *G. uvula*, and *T. quinqueloba* (>63 μm), indicating a possible drop in temperature and salinity of the upper water column with an increased influence of SPG activity and an increase in freshwater flux. Thus, a slight shift in planktic foraminiferal assemblage in the SPNA ocean was observed in the present dataset. A further study on the present planktic foraminiferal distribution in the water column (plankton tow) in the SPNA ocean will be an important addition to this study.

CONCLUSION

The present study documents the planktic foraminiferal distribution and species composition in the SPNA Ocean.

(1) In the SPNA Ocean, the recent planktic foraminifera in surface sediments shows a close correlation with the surface-subsurface water mass structure.
(2) Based on cluster analysis, three planktonic foraminifera groups could be identified across the transect in the SPNA Ocean. The polar group is marked by the dominance of *N. pachyderma* in the Labrador Sea. The mixed group is represented by both warm and cold assemblage (*N. pachyderma*, *N. incompta*, *G. glutinata*, and *T. quinqueloba*) from the different locations on the western and eastern sides of the transect. Lastly, a warm temperate group included stations from Reykjanes Ridge to Iceland Basin and Rockall Plateau with warm-water assemblage composed of *G. glutinata*, *N. incompta*, *T. quinqueloba*, *G. bulloides*, and *G. uvula*.
(3) The ratio *N. pachyderma* and *N. incompta* can be used as a proxy to identify the difference between cold Irminger water and relatively warmer Atlantic water in the studied transect.
(4) The distribution of *N. pachyderma* in the Labrador Sea indicates the presence of cold and fresh water mass. In the Labrador Sea, *N. pachyderma* was dominant in >100 μm fraction while *G. uvula* dominated in 63–100 μm fraction. It can be concluded that size is an important factor in studying the planktic foraminiferal abundances and distribution of species.
(5) A comparison of our planktic foraminifera data with the previous dataset reveals a slight shift in planktic foraminiferal assemblage in the SPNA ocean.

DATA AVAILABILITY STATEMENT

The original contributions presented in the study are included in the **Supplementary Material**, further inquiries can be directed to the corresponding author/s.

AUTHOR CONTRIBUTIONS

NS carried out the analysis and wrote the original draft of the manuscript along with the conceptualization. SS contributed toward data curation, visualized, conceptualized, wrote, and revised the manuscript. AM provided samples, additional data, and helped to wrote the manuscript. RM supervised the work and reviewed the original draft of the manuscript. AT and NK collected the samples. All authors contributed to the article and approved the submitted version.

FUNDING

This work was supported by the ESSO-National Centre for Polar and Ocean Research, Ministry of Earth Sciences, India. AM, AT, and NK acknowledge the Russian Science Foundation, Project No. 21-17-00235, with additional funding from the Ministry of Science and Higher Education of the Russian Federation, SIO theme no. 0128-2021-0006 (sediment sampling during cruise).

ACKNOWLEDGMENTS

The authors would like to thank the Director, ESSO-NCPOR, Ministry of Earth Sciences (MoES), for supporting the research at NCPOR (Contribution no. J-72/2021-22). NS was grateful to ESSO and NCPOR, for providing research fellowship. The authors thank the crew and participants of the 51st cruise of the RV *Akademik Ioffe* in 2016 for help in retrieving the sediment samples. Sahina Ghazi and Akshaya are acknowledged for SEM analysis of samples. The authors also extend their sincere gratitude to Polar Micropaleontology and the Past Climate group, NCPOR, for their contribution to this study.

SUPPLEMENTARY MATERIAL

The Supplementary Material for this article can be found online at: https://www.frontiersin.org/articles/10.3389/fmars.2021.781675/full#supplementary-material

REFERENCES

Azetsu-Scott, K., Clarke, A., Falkner, K., Hamilton, J., Jones, E. P., Lee, C., et al. (2010). Calcium carbonate saturation states in the waters of the Canadian Arctic Archipelago and the Labrador Sea. *J. Geophys. Res. Oceans* 115:C11021. doi: 10.1029/2009JC005917

Bamber, J., Van Den Broeke, M., Ettema, J., Lenaerts, J., Rignot, E., and Bauch, H. A. (2012). Recent large increases in freshwater fluxes from Greenland into the North Atlantic. *Geophys. Res. Lett.* 39:L19501.

Bauch, H. A. (1994). Significance of variability in *Turborotalita quinqueloba* (Natland) test size and abundance for paleoceanographic interpretations in the Norwegian-Greenland Sea. *Mar. Geol.* 121, 129–141. doi: 10.1016/0025-3227(94)90162-7

Bé, A. W. H., and Tolderlund, D. S. (1971). "Distribution and ecology of living planktonic Foraminifera in surface waters of the Atlantic and Indian oceans," in *Micropalaeontology of the Oceans*, eds B. M. Funnel and W. R. Riedel (London: Cambridge University Press), 105–149.

Berger, W. H. (1969). Ecologic patterns of living planktonic foraminifera. *Deep Sea Res. Oceanograph. Abs.* 16, 1–24. doi: 10.1038/s41598-020-77179-8

Berger, W. H. (1973). Deep-sea carbonates. *J. Foraminiferal Res.* 3, 187–195. doi: 10.2113/gsjfr.3.4.187

Boltovskoy, E., and Wright, R. C. (2013). *Recent Foraminifera*. Berlin: Springer Science & Business Media.

Brambilla, E., and Talley, L. D. (2008). Subpolar mode water in the northeastern Atlantic: 1. *J. Geophys. Res. Ocean.* 113, 1–18. doi: 10.1029/2006JC004062

Carstens, J., Hebbeln, D., and Wefer, G. (1997). Distribution of planktic foraminifera at the ice margin in the Arctic (Fram Strait). *Mar. Micropaleontol.* 29, 257–269. doi: 10.1016/S0377-8398(96)00014-X

Chapman, M. R. (2010). Seasonal production patterns of planktonic foraminifera in the NE Atlantic Ocean: implications for paleotemperature and hydrographic reconstructions. *Paleoceanography* 25:A1101. doi: 10.1016/j.marmicro.2005.02.008

Clarke, K. R. (1993). Non-parametric multivariate analyses of changes in community structure. *Aust. J. Ecol.* 18, 117–143. doi: 10.1111/j.1442-9993.1993.tb00438.x

Cléroux, C., Cortijo, E., Duplessy, J. C., and Zahn, R. (2007). Deep-dwelling foraminifera as thermocline temperature recorders. *Geochem. Geophy. Geosy.* 8:4 doi: 10.1029/2006GC001474

Daniault, N., Mercier, H., Lherminier, P., Sarafanov, A., Falina, A., Zunino, P., et al. (2016). The northern North Atlantic Ocean mean circulation in the early 21st century. *Prog. Oceanogr.* 146, 142–158. doi: 10.1016/j.pocean.2016.06.007

Dickson, R., Rudels, B., Dye, S., Karcher, M., Meincke, J., and Yashayaev, I. (2007). Current estimates of freshwater flux through Arctic and subarctic seas. *Prog. Oceanogr.* 73, 210–230. doi: 10.1016/j.pocean.2006.12.003

Espitalié, J., Laporte, J. L., Madec, M., Marquis, F., Leplat, P., Paulet, J., et al. (1977). Rapid method for source rocks characterization and for determination of petroleum potential and degree of evolution. *Revue De L InstitutFrancais Du Petrole* 32, 23–42.

Eynaud, F. (2011). Planktonic foraminifera in the Arctic: potentials and issues regarding modern and quaternary populations. *IOP Conf. Ser. Earth Environ. Sci. IOP Publishing.* 14:012005. doi: 10.1088/1755-1315/14/1/012005

Eynaud, F., De Abreu, L., Voelker, A., Schönfeld, J., Salgueiro, E., Turon, J. L., et al. (2009). Position of the Polar Front along the western Iberian margin during key cold episodes of the last 45 ka. *Geochem. Geophy. Geosy.* 10:Q07U05.

Fairbanks, R. G., and Wiebe, P. H. (1980). Foraminifera and chlorophyll maximum: vertical distribution, seasonal succession, and paleoceanographic significance. *Science* 209, 1524–1526.

Fossheim, M., Primicerio, R., Johannesen, E., Ingvaldsen, R. B., Aschan, M. M., and Dolgov, A. V. (2015). Recent warming leads to a rapid borealization of fish communities in the Arctic. *Nat. Clim. Change.* 5, 673–677. doi: 10.1038/nclimate2647

Ganssen, G. M., and Kroon, D. (2000). The isotopic signature of planktonic foraminifera from NE Atlantic surface sediments: implications for the reconstruction of past oceanic conditions. *J. Geol. Soc. London.* 157, 693–699. doi: 10.1144/jgs.157.3.693

García-Ibáñez, M. I., Pardo, P. C., Carracedo, L. I., Mercier, H., Lherminier, P., Rios, A. F., et al. (2015). Structure, transports and transformations of the water masses in the Atlantic Subpolar Gyre. *Prog. Oceanogr.* 135, 18–36. doi: 10.1016/j.pocean.2015.03.009

Greco, M., Jonkers, L., Kretschmer, K., Bijma, J., and Kucera, M. (2019). Depth habitat of the planktonic foraminifera Neogloboquadrina pachyderma in the northern high latitudes explained by sea-ice and chlorophyll concentrations. *Biogeosciences* 16, 3425–3437. doi: 10.5194/bg-16-3425-2019

Gyldenfeldt, A. B. V., Carstens, J., and Meincke, J. (2000). Estimation of the catchment area of a sediment trap by means of current meters and foraminiferal tests. *Deep Sea Res. Part II Top. Stud. Oceanogr.* 47, 1701–1717. doi: 10.1016/s0967-0645(00)00004-7

Hátún, H., Payne, M. R., Beaugrand, G., Reid, P. C., Sandø, A. B., Drange, H., et al. (2009). Large bio-geographical shifts in the north-eastern Atlantic Ocean: from the subpolar gyre, via plankton, to blue whiting and pilot whales. *Prog. Oceanogr.* 80, 149–162. doi: 10.1016/j.pocean.2009.03.001

Hátún, H., Sandø, A. B., Drange, H., Hansen, B., and Valdimarsson, H. (2005). Influence of the Atlantic subpolar gyre on the thermohaline circulation. *Science* 309, 1841–1844. doi: 10.1126/science.1114777

Hemleben, Ch, Spindler, M., and Anderson, R. (1989). *Modern Planktonic Foraminifera*. New York: Springer.

Hilbrecht, H. (1996). "Extant planktonic foraminifera and the physical environment in the Atlantic and Indian Oceans," in *Mitteilungen Aus Dem Geologischen Institut Der Eidgen*, (Zürich: Technischen Hochschule Und Der Universität), 93.

Honjo, S., and Manganini, S. J. (1993). Annual biogenic particle fluxes to the interior of the North Atlantic Ocean; studied at 34 N 21 W and 48 N 21 W. *Deep Sea Res. Part II Top. Stud. Oceanogr.* 40, 587–607. doi: 10.1016/0967-0645(93)90034-K

Husum, K., and Hald, M. (2012). Arctic planktic foraminiferal assemblages: implications for subsurface temperature reconstructions. *Mar. Micropaleontol.* 96, 38–47. doi: 10.1016/j.marmicro.2012.07.001

Johannessen, T., Jansen, E., Flatøy, A., and Ravelo, A. C. (1994). "The relationship between surface water masses, oceanographic fronts and paleoclimatic proxies in surface sediments of the Greenland, Iceland, Norwegian Seas," in *Proceedings of the Carbon cycling in the glacial ocean: constraints on the ocean's role in global change*, (Berlin: Springer), 61–85. doi: 10.1007/978-3-642-78737-9_4

Jonkers, L., Brummer, G. J. A., Peeters, F. J. C., Van Aken, H. M., and De Jong, M. F. (2010). Seasonal stratification, shell flux, and oxygen isotope dynamics of leftcoiling *N. pachyderma* and *T. quinqueloba* in the western subpolar North Atlantic. *Paleoceanography* 25, 1–13. doi: 10.1029/2009PA001849

Jonkers, L., Hillebrand, H., and Kucera, M. (2019). Global change drives modern plankton communities away from the pre-industrial state. *Nature* 570, 372–375. doi: 10.1038/s41586-019-1230-3

Kandiano, E. S., and Bauch, H. A. (2002). Implications of planktic foraminiferal size fractions for the glacial-interglacial paleoceanography of the polar North Atlantic. *J. Foraminiferal Res.* 32, 245–251. doi: 10.2113/32.3.245

Keller, G., and Abramovich, S. (2009). Lilliput effect in late Maastrichtian planktic foraminifera: response to environmental stress. *Palaeogeogr. Palaeoclimatol. Palaeoecol.* 284, 47–62. doi: 10.1016/j.palaeo.2009.08.029

Kennett, J. P., and Srinivasan, M. S. (1983). *Neogene Planktonic Foraminifera*. Pennsylvania: Hutchinson Ross Publ. Go, 265.

Kimura, S., Nakata, H., and Okazaki, Y. (2000). Biological production in meso-scale eddies caused by frontal disturbances of the Kuroshio Extension. *ICES J. Mar. Sci.* 57, 133–142. doi: 10.1006/jmsc.1999.0564

Knutsen, Ø, Svendsen, H., Øterhus, S., Rossby, T., and Hansen, B. (2005). Direct measurements of the mean flow and eddy kinetic energy structure of the upper ocean circulation in the NE Atlantic. *Geophys. Res. Lett* 321:14 doi: 10.1029/2005GL023615

Kohfeld, K. E., Fairbanks, R. G., Smith, S. L., and Walsh, I. D. (1996). *Neogloboquadrina pachyderma* (sinistral coiling) as paleoceanographic tracers in polar oceans: evidence from Northeast Water Polynya plankton tows, sediment traps, and surface sediments. *Paleoceanography* 11, 679–699. doi: 10.1029/96PA02617

Kretschmer, K., Jonkers, L., Kucera, M., and Schulz, M. (2018). Modeling seasonal and vertical habitats of planktonic foraminifera on a global scale. *Biogeosciences* 15, 4405–4429. doi: 10.5194/bg-15-4405-2018

Kucera, M. (2007). "Chapter six planktonic foraminifera as tracers of past oceanic environments," in *Methods in late Cenozoic paleoceanography, Development in Marine Geology*, eds C. Hillaire-Marcel, and A. de Vernal. (New York, NY: Elsevier), 213–262. doi: 10.1016/s1572-5480(07)01011-1

Kuroyanagi, A., and Kawahata, H. (2004). Vertical distribution of living planktonic foraminifera in the seas around Japan. *Mar. Micropaleontol.* 53, 173–196. doi: 10.1016/j.marmicro.2004.06.001

Locarnini, R. A., Mishonov, A. V., Baranova, O. K., Boyer, T. P., Zweng, M. M., Garcia, H. E., et al. (2018). World Ocean Atlas 2018. *Mishonov. Technical.* 81:52. doi: 10.1364/OE.443151

Lundgreen, U. (1996). Aminosa"uren im Nordatlantik: partikelzusammensetzung und Remineralisierung. *Berichte aus dem Institut für Meereskunde an der Christian-Albrechts-Universität Kiel* 283, 1–128. doi: 10.1007/s11306-018-1416-y

Lutjeharms, J. R. E., Walters, N. M., and Allanson, B. R. (1985). "Oceanic frontal systems and biological enhancement," in *Antarctic Nutrient Cycles and Food Webs*, eds W. R. Siegfried, P. R. Condy, and R. M. Laws (Berlin: Springer), 11–21. doi: 10.1007/978-3-642-82275-9_3

Mahadevan, A., D'asaro, E., Lee, C., and Perry, M. J. (2012). Eddy-driven stratification initiates North Atlantic spring phytoplankton blooms. *Science* 337, 54–58. doi: 10.1126/science.1218740

Mallo, M., Ziveri, P., Graham Mortyn, P., Schiebel, R., and Grelaud, M. (2017). Low planktic foraminiferal diversity and abundance observed in a spring 2013 west-east Mediterranean Sea plankton tow transect. *Biogeosciences* 14, 2245–2266. doi: 10.5194/bg-14-2245-2017

Matul, A., Barash, M. S., Khusid, T. A., Behera, P., and Tiwari, M. (2018). Paleoenvironment Variability during Termination I at the Reykjanes Ridge, North Atlantic. *Geoscience* 8:375. doi: 10.3390/geosciences8100375

McCartney, M. S., and Talley, L. D. (1982). The subpolar mode water of the North Atlantic Ocean. *J. Phys. Oceanogr.* 12, 1169–1188. doi: 10.1175/1520-0485(1982)012<1169:tsmwot>2.0.co;2

Meilland, J., Howa, H., Hulot, V., Demangel, I., Salaün, J., and Garlan, T. (2020). Population dynamics of modern planktonic foraminifera in the western Barents Sea. *Biogeosciences* 17, 1437–1450. doi: 10.5194/bg-17-1437-2020

Melling, M., Agnew, T. A., Falkner, K. K., Greenberg, D. A., Lee, C. M., Munchow, A., et al. (2008). "Fresh-water fluxes via Pacific and Arctic outflows across Canadian Polar Shelf," in *Arctic-Subarctic Ocean Fluxes, Defining the Role of the Northern Seas in Climate*, eds R. R. Dickson, J. Meinke, and P. Rhines (Dordrecht: Springer), 193–247.

NASA Goddard Space Flight Center (2018). *Moderate-resolution Imaging Spectroradiometer (MODIS) Aqua Chlorophyll Data, 2018: Reprocessing. NASA OB.DAAC.* Available online at: https://doi.org/10.5067/AQUA/MODIS/L3B/CHL/2018 [accessed Feb 20, 2019]

Neukermans, G., Oziel, L., and Babin, M. (2018). Increased intrusion of warming Atlantic water leads to rapid expansion of temperate phytoplankton in the Arctic. *Glob. Chang. Biol.* 24, 2545–2553. doi: 10.1111/gcb.14075

Ortiz, J. D., and Mix, A. C. (1992). "The spatial distribution and seasonal succession of planktic foraminifera in the California Current off Oregon," in *Upwelling systems: Evolution since the Early Miocene. Geological Society*, Vol. 64, eds C. P. Summerhayes, W. L. Prell, and K. C. Emeis (London: Special Publications), 197–213.

Ortiz, J. D., Mix, A. C., and Collier, R. W. (1995). Environmental control of living symbiotic and asymbiotic foraminifera of the California Current. *Paleoceanography* 10, 987–1009. doi: 10.1029/95pa02088

Osman, M. B., Das, S. B., Trusel, L. D., Evans, M. J., Fischer, H., Grieman, M. M., et al. (2019). Industrial-era decline in subarctic Atlantic productivity. *Nature* 569, 551–555. doi: 10.1038/s41586-019-1181-8

Ottens, J. J. (1991). Planktic foraminifera as North Atlantic water mass indicators. *Oceanol. Acta* 14, 123–140. doi: 10.1371/journal.pone.0239373

Ottens, J. J. (1992). April and August Northeast Atlantic surface water masses reflected in planktic foraminifera. *Netherlands J. Sea Res.* 28, 261–283. doi: 10.1016/0077-7579(92)90031-9

Oziel, L., Neukermans, G., Ardyna, M., Lancelot, C., Tison, J. L., Wassmann, P., et al. (2017). Role for Atlantic inflows and sea ice loss on shifting phytoplankton blooms in the Barents Sea. *J. Geophys. Res. Oceans* 122, 5121–5139. doi: 10.1002/2016JC012582

Pados, T., and Spielhagen, R. F. (2014). Species distribution and depth habitat of recent planktic foraminifera in Fram Strait, Arctic Ocean. *Polar Res.* 33:483 doi: 10.3402/polar.v33.22483

Parker, F. L. (1960). Living planktonic foraminifera from the Equatorial and Southeast Pacific. Science reports of the Tohoku University. 2nd series, Geology. *Special* 4, 71–82.

Parker, F. L., and Berger, W. H. (1971). Faunal and solution patterns of planktonic foraminifera in surface sediments of the South Pacific. *Deep Sea Res. Oceanograph. ABS.* 18, 73–107. doi: 10.1016/0011-7471(71)90017-9

Pflaumann, U., Sarnthein, M., Chapman, M., d'Abreu, L., Funnell, B., Huels, M., et al. (2003). Glacial North Atlantic: Sea-surface conditions reconstructed by GLAMAP 2000. *Paleoceanography* 18:1065

Pollard, R. T., Griffiths, M. J., Cunningham, S. A., Read, J. F., Pérez, F. F., and Ríos, A. F. (1996). Vivaldi 1991 - A study of the formation, circulation and ventilation of Eastern North Atlantic Central Water. *Prog. Oceanogr.* 37, 167–172. doi: 10.1016/S0079-6611(96)00008-0

Pollard, R. T., Read, J. F., Holliday, N. P., and Leach, H. (2004). Water masses and circulation pathways through the Iceland basin during Vivaldi 1996. *J. Geophys. Res. C. Ocean* 109, 1–10. doi: 10.1029/2003JC002067

CLIMAP Project Members. (1976). The surface of the ice-age earth. *Science* 191, 1131–1137. doi: 10.1126/science.191.4232.1131

Rahmstorf, S., Box, J. E., Feulner, G., Mann, M. E., Robinson, A., Rutherford, et al. (2015). Exceptional twentieth-century slowdown in Atlantic Ocean overturning circulation. *Nat. Clim. Change.* 5, 475–480. doi: 10.1038/nclimate2554

Read, J. F. (2000). CONVEX-91: water masses and circulation of the Northeast Atlantic subpolar gyre. *Prog. Oceanogr.* 48, 461–510. doi: 10.1016/S0079-6611(01)00011-8

Rebotim, A., Voelker, A. H. L., Jonkers, L., Waniek, J. J., Meggers, H., Schiebel, R., et al. (2017). Factors controlling the depth habitat of planktonic foraminifera in the subtropical eastern North Atlantic. *Biogeosciences* 14, 827–859. doi: 10.5194/bg-14-827-2017

Retailleau, S., Eynaud, F., Mary, Y., Abdallah, V., Schiebel, R., and Howa, H. (2012). Canyon heads and river plumes: how might they influence neritic planktonic foraminifera communities in the SE Bay of Biscay? *J. Foraminiferal Res.* 42, 257–269. doi: 10.2113/gsjfr.42.3.257

Retailleau, S., Howa, H., Schiebel, R., Lombard, F., Eynaud, F., Schmidt, S., et al. (2009). Planktic foraminiferal production along an offshore–onshore transect in the south-eastern Bay of Biscay. *Cont. Shelf Res.* 29, 1123–1135. doi: 10.1016/j.csr.2008.12.021

Retailleau, S., Schiebel, R., and Howa, H. (2011). Population dynamics of living planktic foraminifers in the hemipelagic southeastern Bay of Biscay. *Mar. Micropaleontol.* 80, 89–100. doi: 10.1016/j.marmicro.2011.06.003

Salgueiro, E., Voelker, A. H., de Abreu, L., Abrantes, F., Meggers, H., and Wefer, G. (2010). Temperature and productivity changes off the western Iberian margin during the last 150 ky. *Quat. Sci. Rev.* 29, 680–695.

Schiebel, R. (2002). Planktic foraminiferal sedimentation and the marine calcite budget. *Global Biogeochem Cy.* 16, 3–21.

Schiebel, R., and Hemleben, C. (2000). Interannual variability of planktic foraminiferal populations and test flux in the eastern North Atlantic Ocean (JGOFS). *Deep Sea Res. Part II Top. Stud. Oceanogr.* 47, 1809–1852. doi: 10.1016/S0967-0645(00)00008-4

Schiebel, R., and Hemleben, C. (2005). Modern planktic foraminifera. *Paläontologische Zeitschrift* 79, 135–148. doi: 10.1007/BF03021758

Schiebel, R., and Hemleben, C. (2017). *Planktic Foraminifers in the Modern Ocean*. Berlin: Springer, 1–358.

Schiebel, R., Hiller, B., and Hemleben, C. (1995). Impacts of storms on recent planktic foraminiferal test production and CaCO3 flux in the North Atlantic at 47° N, 20° W (JGOFS). *Mar. Micropaleontol.* 26, 115–129.

Schiebel, R., Spielhagen, R. F., Garnier, J., Hagemann, J., Howa, H., Jentzen, A., et al. (2017). Modern planktic foraminifers in the high-latitude ocean. *Mar. Micropaleontol.* 136, 1–13. doi: 10.1016/j.marmicro.2017.08.004

Schiebel, R., Waniek, J., Bork, M., and Hemleben, C. (2001). Planktic foraminiferal production stimulated by chlorophyll redistribution and entrainment of nutrients. *Deep Sea Res. Part I Oceanogr. Res. Pap.* 48, 721–740. doi: 10.1016/S0967-0637(00)00065-0

Schlitzer, R. (2015). Data Analysis and Visualization with Ocean Data View. *CMOS Bull. SCMO* 43, 9–13.

Schmuker, B. (2000). The influence of shelf vicinity on the distribution of planktic foraminifera south of Puerto Rico. *Mar. Geol.* 166, 125–143. doi: 10.1016/S0025-3227(00)00014-1

Spooner, P. T., Thornalley, D. J., Oppo, D. W., Fox, A. D., Radionovskaya, S., Rose, N. L., et al. (2020). Exceptional 20th century ocean circulation in the Northeast Atlantic. *Geophys. Res. Lett.* 47:e2020GL087577. doi: 10.1029/2020GL087577

Staines-Urías, F., Kuijpers, A., and Korte, C. (2013). Evolution of subpolar North Atlantic surface circulation since the early Holocene inferred from planktic foraminifera faunal and stable isotope records. *Quat. Sci. Rev.* 76, 66–81. doi: 10.1016/j.quascirev.2013.06.016

Stangeew, E. (2001). *Distribution and Isotopic Composition of Living Planktonic Foraminifera N. pachyderma (sinistral) and T. quinqueloba in the High Latitude North Atlantic*. Ph.D. thesis, Kiel: Christian-Albrechts Universität.

Stehman, C. F. (1972). Planktonic foraminifera in Baffin Bay. *Davis Strait and the Labrador Sea. Atl. Geol.* 8, 13–19.

Taylor, J. R., and Ferrari, R. (2011b). Shutdown of turbulent convection as a new criterion for the onset of spring phytoplankton blooms. *Limnol. Oceanogr.* 56, 2293–2307. doi: 10.4319/lo.2011.56.6.2293

Taylor, J. R., and Ferrari, R. (2011a). Ocean fronts trigger high latitude phytoplankton blooms. *Geophys. Res. Lett* 38:2011 doi: 10.1029/2011GL049312

Thornalley, D. J., Oppo, D. W., Ortega, P., Robson, J. I., Brierley, C. M., Davis, R., et al. (2018). Anomalously weak Labrador Sea convection and Atlantic overturning during the past 150 years. *Nature* 556, 227–230. doi: 10.1038/s41586-018-0007-4

Thunell, R. C. (1978). Distribution of recent planktonic foraminifera in surface sediments of the Mediterranean Sea. *Mar. Micropaleontol.* 3, 147–173. doi: 10.1016/0377-8398(78)90003-8

Thunell, R. C., and Reynolds, L. A. (1984). Sedimentation of planktonic foraminifera; seasonal changes in species flux in the Panama Basin. *Micropaleontology* 30, 243–262.

Tolderlund, D. S., and Bé, A. W. (1971). Seasonal distribution of planktonic foraminifera in the western North Atlantic. *Micropaleontology* 17, 297–329. doi: 10.1126/science.209.4464.1524

Volkmann, R. (2000). Planktic foraminifers in the outer Laptev Sea and the Fram Strait—Modern distribution and ecology. *J. Foraminiferal Res.* 30, 157–176. doi: 10.2113/0300157

Yang, Q., Dixon, T. H., Myers, P. G., Bonin, J., Chambers, D., Van Den Broeke, M. R., et al. (2016). Recent increases in Arctic freshwater flux affects Labrador Sea convection and Atlantic overturning circulation. *Nat. Commun.* 7, 1–8. doi: 10.1038/ncomms10525

Žarić, S., Donner, B., Fischer, G., Mulitza, S., and Wefer, G. (2005). Sensitivity of planktic foraminifera to sea surface temperature and export production as derived from sediment trap data. *Mar. Micropaleontol.* 55, 75–105. doi: 10.1016/j.marmicro.2005.01.002

Zhang, J., Weijer, W., Steele, M., Cheng, W., Verma, T., and Veneziani, M. (2021). Labrador Sea freshening linked to Beaufort Gyre freshwater release. *Nat. Commun.* 12, 1–8. doi: 10.1038/s41467-021-21470-3

Ziveri, P., Thunell, R. C., and Rio, D. (1995). Export production of coccolithophores in an upwelling region: results from San Pedro Basin, Southern California Borderlands. *Mar. Micropaleontol.* 24, 335–358. doi: 10.1016/0377-8398(94)00017-h

Zweng, M. M., Reagan, J. R., Seidov, D., Boyer, T. P., Locarnini, R. A., Garcia, H. E., et al. (2018). World Ocean Atlas 2018, Volume 2: Salinity. *Mishonov Technical.* 82:50.

Conflict of Interest: The authors declare that the research was conducted in the absence of any commercial or financial relationships that could be construed as a potential conflict of interest.

Publisher's Note: All claims expressed in this article are solely those of the authors and do not necessarily represent those of their affiliated organizations, or those of the publisher, the editors and the reviewers. Any product that may be evaluated in this article, or claim that may be made by its manufacturer, is not guaranteed or endorsed by the publisher.

Copyright © 2022 Sahoo, Saalim, Matul, Mohan, Tikhonova and Kozina. This is an open-access article distributed under the terms of the Creative Commons Attribution License (CC BY). The use, distribution or reproduction in other forums is permitted, provided the original author(s) and the copyright owner(s) are credited and that the original publication in this journal is cited, in accordance with accepted academic practice. No use, distribution or reproduction is permitted which does not comply with these terms.

frontiers in Marine Science

ORIGINAL RESEARCH
published: 14 February 2022
doi: 10.3389/fmars.2022.822978

Declining Pre-bloom *Calanus finmarchicus* Egg Production Adjacent to Two Major Overwintering Regions in the Northeastern Atlantic

Sólvá Jacobsen, Eilif Gaard and Hjálmar Hátún*

Faroe Marine Research Institute, Tórshavn, Faroe Islands

Calanus finmarchicus is a key secondary producer in the North Atlantic. Shortly prior to the spring bloom the animals ascend from diapause at depth to surface waters, where the females spawn partly, based on winter lipid reserves. *C. finmarchicus* eggs are an important prey of first feeding fish larvae inhabiting North Atlantic shelves during early spring and are thus essential for larval survival. Comprehensive late April surveys have been carried out on and around the Faroe shelf, which is located between the Northeast Atlantic and the Nordic Seas, for more than two decades. One aim is to investigate the critical match-mismatch between the spring bloom development, zooplankton reproduction and occurrence of first feeding fish larvae. In this study, we examine spatial and temporal changes in pre-bloom reproductive activity of *C. finmarchicus* on and around the shelf using a unique dataset of more than 8,000 examined females sampled during the period 1997–2020. Enhanced productivity was observed on the north-western side of the shelf, where the main flow of oceanic water to the inner permanently well mixed shelf takes place. We attribute this increased productivity to enhanced food (phytoplankton) availability in the seasonally stratified outer shelf, slightly upstream of the main egg production area. Both individual egg production rates and the fraction of spawning females declined throughout the Faroe shelf during the examined period. This decline could not be explained by the employed environmental parameters. The declining pre-bloom egg production may have consequences for first feeding fish larvae.

Keywords: ***Calanus finmarchicus*, egg (production), temperature, chlorophyll, pre-bloom, Faroe shelf**

OPEN ACCESS

Edited by:
Martin Edwards,
Plymouth Marine Laboratory,
United Kingdom

Reviewed by:
Edward Buskey,
University of Texas at Austin,
United States
Akash R. Sastri,
Institute of Ocean Sciences, Canada

****Correspondence:***
Sólvá Jacobsen
solvaj@hav.fo

Specialty section:
This article was submitted to Marine Ecosystem Ecology, a section of the journal Frontiers in Marine Science

Received: *26 November 2021*
Accepted: *11 January 2022*
Published: *14 February 2022*

Citation:
Jacobsen S, Gaard E and Hátún H (2022) Declining Pre-bloom Calanus finmarchicus Egg Production Adjacent to Two Major Overwintering Regions in the Northeastern Atlantic. Front. Mar. Sci. 9:822978. doi: 10.3389/fmars.2022.822978

INTRODUCTION

Calanus finmarchicus is a key secondary producer and the most studied copepod species in the North Atlantic, ranging geographically from the Gulf of Maine to the North Sea (Melle et al., 2014). Although *C. finmarchicus* is an oceanic copepod species, it dominates the zooplankton biomass in Faroese waters (Gaard, 1999). The species is an essential food source for a number of pelagic fish stocks, and an important prey for larvae and juveniles of benthic fish species including Faroe Plateau cod (*Gadus morhua*) larvae and juveniles. In particular, *C. finmarchicus* eggs are the dominant prey of first feeding cod larvae, which are spawned on the Faroe shelf during February-April (Gaard and Steingrund, 2001; Jacobsen et al., 2020), and they are an important prey in neighboring shelves as well (Heath and Lough, 2007). Hence, a temporal match between the abundance of larvae and

C. finmarchicus eggs may be of critical importance for subsequent cod recruitment (Hjort, 1914; Cushing, 1990). One of the key life history traits for *C. finmarchicus* is dormancy, a strategy acquired in order to persist through seasonally adverse conditions (i.e., winter). As such, in late summer in the Northeast Atlantic pre-adult *C. finmarchicus* copepodites descend to deep waters within the Norwegian Sea gyre and the Atlantic subpolar gyre to overwinter in a resting state known as diapause (e.g., Heath et al., 2000).

The Faroe Islands are situated on the Iceland-Scotland ridge, which divides the mentioned gyres, and thus two major overwintering regions of *C. finmarchicus* (**Figure 1A**). Off the Faroe Shelf, the water in the upper layers (0–500 m) is dominated by relatively warm and saline Modified North Atlantic Water (MNAW) (Hansen and Østerhus, 2000), a mixture of subtropical waters and cold and low-saline, but zooplankton rich, waters from the subpolar gyre (Hátún et al., 2005, 2009). Since the MNAW-carrying currents are coming from the south-west, the temperature and salinity on the outer Faroe shelf is generally higher on the western side and lower on the eastern side. MNAW subsequently cross the Iceland-Faroe Ridge in a clock-wise path around the Faroe shelf, while they are cooled and freshened by an admixture of colder, less saline as well as zooplankton rich water from the Norwegian Sea and the East Icelandic Current (EIC) (**Figure 1A**; Larsen et al., 2012; Kristiansen et al., 2016). Under the MNAW layer, cold and less saline overflow water flows equator-wards from the depths of the Norwegian Sea. During winter and early spring, this overflow carries large quantities of zooplankton through the Faroe Shetland Channel and further through the Faroe Bank Channel into the North Atlantic Ocean (Heath et al., 2000). This overflow is often regarded as a main source of *C. finmarchicus* for the Faroe shelf (Gaard and Hansen, 2000; Jónasdóttir et al., 2008). The MNAW currents, enriched by *C. finmarchicus* in the north-eastern Iceland Basin, might, however, be a more direct source of this copepod for the Faroe shelf (**Figure 1A**). Consequently, *C. finmarchicus* that are advected onto the Faroe shelf may originate both from sources in the Nordic Seas (blue in **Figure 1A**) and sources in the Northeast Atlantic (brown in **Figure 1A**), where the water mass characteristics are very different. *C. finmarchicus* diapause duration has been shown to be significantly shorter in the Northwestern Atlantic (i.e., west of the Faroes) than in the Nordic Seas (north of the Faroes) (Melle et al., 2014).

The Faroe Shelf may be divided into exclusive domains based on oceanography (Larsen et al., 2008, 2009), and on phytoplankton (biomass and species composition) variability (Gaard, 1996; Eliasen et al., 2017). One main division is formed by the tidal front at the approximately 100–150 m bottom depth contour, which separates the permanently well mixed inner shelf from the surrounding seasonally stratified outer shelf (**Figures 1B**, **2A**; Hansen et al., 2005; Larsen et al., 2008, 2009). The inner Faroe shelf is characterized by strong tidal currents with a clockwise residual circulation around the islands (Larsen et al., 2008). Effective winter cooling in the shallow waters and excess precipitation over land result in lower temperature and salinity during spring on the inner shelf than in the outer shelf waters (Larsen et al., 2009). This difference in hydrographic conditions between the inner and outer shelf also affects the distribution, composition and productivity of zooplankton (Gaard, 1999; Jacobsen et al., 2018). On average, the Eastern Banks (see **Figure 1B**) bloom first, i.e., in April and the bloom on the inner shelf typically occurs in May. In June, the outer shelf contains the highest near-surface chlorophyll concentrations. In addition to this, there is an area to the west of the shelf, the Western Region (WR) (Hátún et al., 2013; **Figure 1B**), where the shelf is wide, the tidal currents are weak and where early spring chlorophyll means and variances are particularly high resulting from several events of temporary stratification, before the permanent summer stratification sets in, typically in late May/early June (Eliasen et al., 2017). The main influx of oceanic and outer shelf water to the inner shelf likely takes place through the WR, *via* three channelized flows, whereof the influx immediately west of the Islands likely is the strongest (Hátún et al., 2013; Rasmussen et al., 2014; **Figures 1B**, **2A**). The initiation of the spring bloom on the inner shelf usually occurs in May, but the timing as well as the magnitude is highly variable between years (Debes et al., 2008a; Eliasen et al., 2019). There is generally an inverse relationship between late winter/early spring temperature and the initiation and magnitude of the spring bloom (Hansen et al., 2005).

Once in the upper layers, *C. finmarchicus* molt into adults and reproduction begins. Long-term monitoring of zooplankton on the Faroe shelf has shown that the abundance and biomass of *C. finmarchicus* fluctuates markedly between years (Gaard and Hansen, 2000; Gaard, 2003; Jacobsen et al., 2018). A part of this variation is due to changes in the copepod's advection and productivity (Gaard, 2000), while the highly variable mid-summer abundances are likely induced by interannual variability in grazing pressure by 0-group fish (Jacobsen et al., 2019). The egg production rates (EPR) of *C. finmarchicus* have previously been linked to the phytoplankton spring bloom, as shown on both sides of the North Atlantic (Stenevik et al., 2007; Head et al., 2013a,b; Melle et al., 2014) as well as locally on the Faroe Shelf (Gaard, 2000; Debes et al., 2008b). Interannual variability in the timing of the spring bloom on the Faroe shelf influences reproduction, and consequently the number of generations completed (Gaard, 2000; Debes and Eliasen, 2006; Debes et al., 2008b). Local seasonal studies of *C. finmarchicus* EPR show that the production increases shortly after ascent in April, i.e., during the pre-bloom, then declines, before increasing again after the initiation of the spring bloom (Gaard, 2000; Debes et al., 2008b). Laboratory experiments have revealed that temperature also is a factor that may influence EPR positively, shortening the spawning intervals (Hirche et al., 1997). However, females tend to be larger in cold waters, and large females typically produce more eggs than small females (Head et al., 2013a; Melle et al., 2014). Furthermore, the initial reproduction phase, which most often occurs during the pre-bloom, is significant. Average EPR in the Northeast Atlantic during the pre-bloom correspond to approximately 10 eggs female^{-1} day^{-1} (Niehoff et al., 1999, 2011; Gislason, 2005; Stenevik et al., 2007; Jónasdóttir et al., 2008; Debes et al., 2008b; Kristiansen et al., 2021). This phase, which is likely supported by internal lipid reserves (Irigoien et al., 2008; Madsen et al., 2008), is the focus of the present paper.

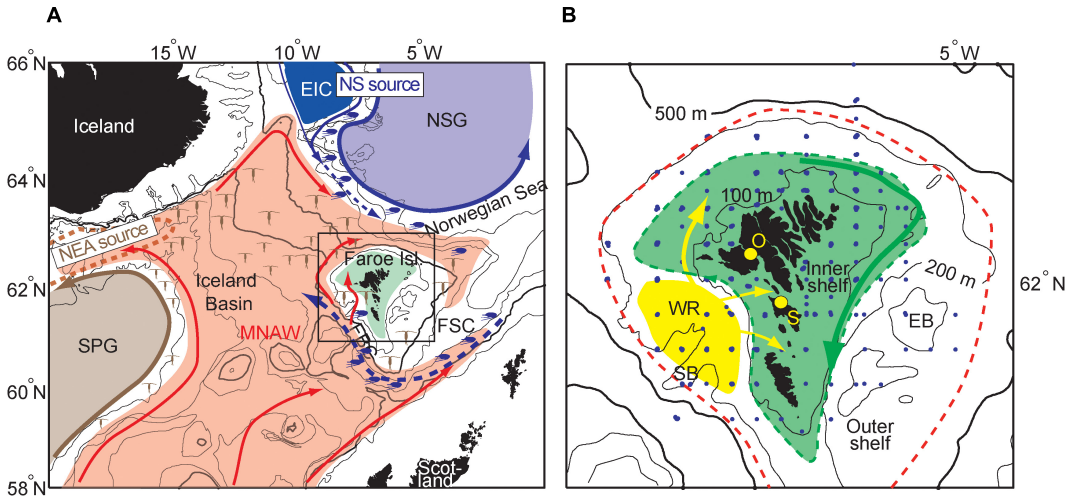


FIGURE 1 | Map of the study area with bottom depth contours. **(A)** The main warm (red arrows) and cold (blue arrows) currents influencing and carrying *C. finmarchicus* to the Faroe shelf (green) are displayed. *C. finmarchicus* originating from the Northeast Atlantic (NEA source) are colored brown, while *C. finmarchicus* from the Norwegian Sea (NS source) are illustrated in blue. **(B)** Distribution of *C. finmarchicus* egg production stations (blue dots) on and around the Faroe shelf 1997–2020. The green dashed line represents the approximate position of the Faroe shelf front (Larsen et al., 2009) separating the permanently mixed inner shelf (green) from the seasonally stratified outer shelf. "O" and "S" denote fixed coastal stations on the shelf. SPG, Subpolar Gyre; MNAW, Modified North Atlantic Water; EIC, East Icelandic Current; NSG, Norwegian Sea Gyre; FSC, Faroe Shetland Channel; WR, Western Region; SB, Skeivi Banki; EB, Eastern Banks.

There are, as previously mentioned, regional differences in the entry into and emergence from diapause (e.g., Planque et al., 1997; Kristiansen et al., 2016). How these are controlled remains largely unknown. One suggestion is that control may be *via* internal biological processes linked to the accumulation and utilization of lipids prior and during diapause, which are modulated by environmental conditions, e.g., temperature (Johnson et al., 2008; Head et al., 2013b; Jónasdóttir et al., 2019). Rising temperatures have caused a clear northward shift in *C. finmarchicus* distribution in recent decades (Reygondeau and Beaugrand, 2011). However, oceanic warming will not be uniform in the North Atlantic. Some regions will warm less than others (Drijfhout et al., 2012), while deep water warming will lag that at the surface (Li et al., 2013). In the Faroe area, observed phenology changes in *C. finmarchicus* around 2003–2007 resulted in earlier emergence of the individuals (Kristiansen et al., 2016; Jacobsen et al., 2018). The observed changes in this region are most likely attributed to either (1) a change in water mass distribution in the area altering the abundance and timing of the copepod and/or (2) a recent warming of the North Atlantic waters inducing earlier emergence. However, potential changes in the pre-bloom EPR have so far remained unknown.

The main objective of this paper is to explore the pre-bloom *C. finmarchicus* egg production on and around the Faroe shelf from 1997 to 2020, and to establish how the pre-bloom egg production responds to changes in environmental conditions. Firstly, we identify egg reproduction "hotspots" based on egg production spatial analyses. Next, we describe temporal variability in the egg production, and compare these to environmental conditions. This study provides the hitherto most comprehensive set of estimates of pre-bloom *C. finmarchicus* EPR in Faroese waters and perhaps all North Atlantic.

MATERIALS AND METHODS

Samples for *C. finmarchicus* egg production measurements were collected with R/V Magnus Heinason in and around the Faroe shelf in late April during the years 1997–2020 (except for 2002 and 2010) (**Table 1** and **Figure 1B**). Temperature and chlorophyll *a* (hereafter termed just chlorophyll) samples were also collected enabling examination of relationships between *C. finmarchicus* production and its habitat.

C. finmarchicus females, used for egg production measurements were collected with a WP-2 net with a mesh size of 200 μm and a 2 L non-filtering cod-end. The net was hauled from 50 m depth to the surface with a speed of 0.3–0.5 m s^{-1}. Immediately after sampling, healthy females were sorted into 0.5 L plastic containers filled with 60 μm filtered seawater (one female per container) and incubated at *in situ* temperature (flowing ambient water) and dim light for 24 h. Each container was equipped with a "false-bottom" consisting of 300 μm mesh size net, to minimize egg cannibalism. Replicates of between 5 and 20 females were incubated at each station. Following the incubation period, the content of the chamber was filtered through a 30 μm sieve and the eggs counted under a stereomicroscope. In a subset of years, the prosome length of a portion of females was measured to the nearest 0.1 mm with an ocular micrometer (**Table 1**).

The CTD (Conductivity, Temperature, Depth) data used in this study is the same material as was utilized in Jacobsen et al. (2018), but updated to include 2017–2020. Temperature and fluorescence (designed to measure chlorophyll) were measured with a Seabird Electronics SBE911 plus CTD, equipped with a rosette sampler. Samples for chlorophyll measurements were taken at 5, 20, and 40 m depth at a subset of

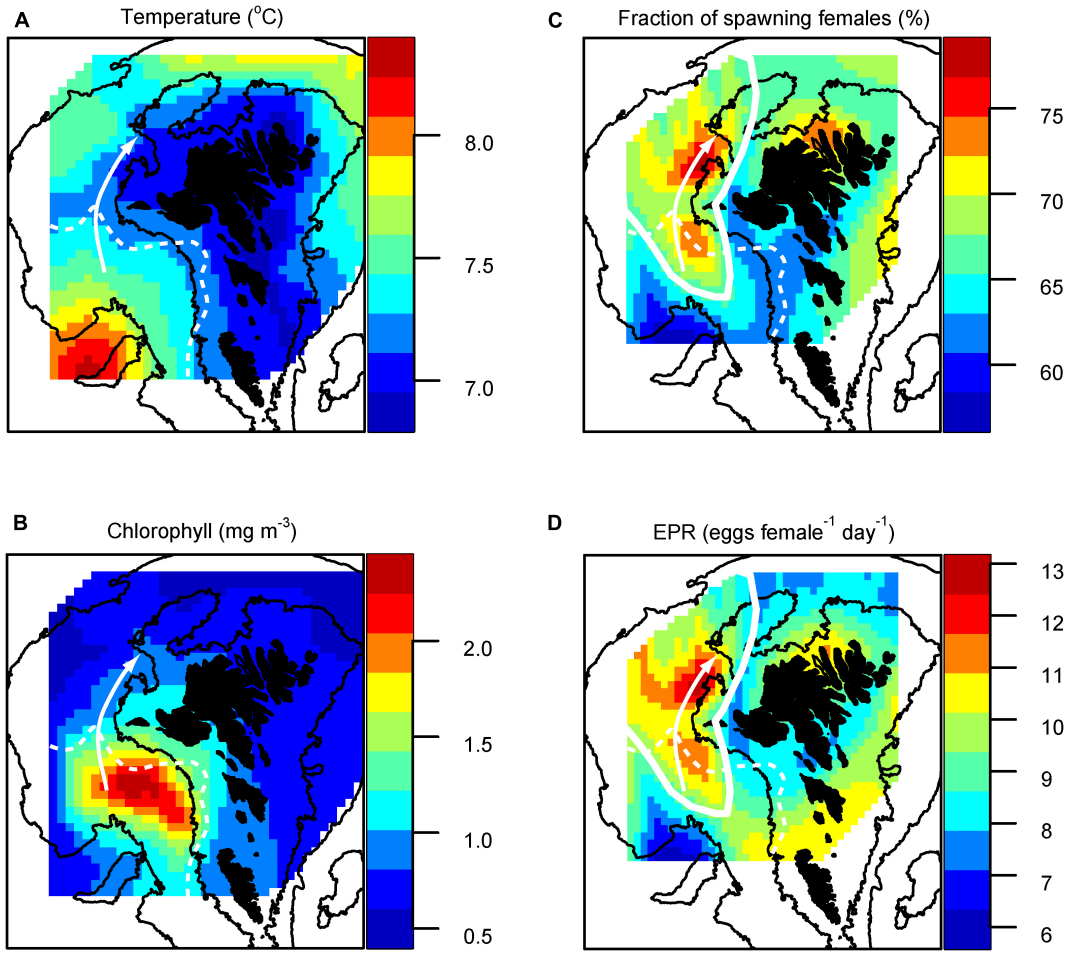


FIGURE 2 | Mean (1997–2020) distribution in **(A)** temperature, **(B)** chlorophyll, **(C)** *C. finmarchicus* spawning fraction and **(D)** individual egg production rates (eggs female^{-1} day^{-1}) in the uppermost 50 m on the Faroe Shelf in late April. The dashed curves illustrate the typical position of the tidal front between the WR and the inner shelf, and the white arrows represent the inflow region. The white full line in **(C,D)** shows the domain of the north-western area, averaged to produce the time series in **Figure 4**. Yearly distribution maps are provided in **Supplementary Material**.

stations each year. These were analyzed spectrophotometrically according to Parsons et al. (1984). Fluorescence values from the CTD were converted to chlorophyll using linear regression analysis between fluorescence and chlorophyll from the extracted samples as described in Salter et al. (2020). No CTD data exist for 2017 and no fluorescence data exist for 2020. For each station calibrated/converted temperature and chlorophyll values were averaged over 6–50 m depth (as the uppermost 5 m are often affected by large signal-to-noise ratio), so as to be comparable to the EPR.

In addition, temperature was measured at coastal station O using Aanderaa, Sensordata followed by Starmon temperature recorders (**Figure 1B**). At station S samples were collected for chlorophyll measurements, which were analyzed spectrophotometrically (Parsons et al., 1984). The coastal stations are landbased monitoring sites, where temperature has been logged continuously and samples for chlorophyll have been collected weekly since the 1997 (Debes et al., 2008a; Eliasen et al., 2017). Data from stations O and S are expected to represent the entire inner shelf, since the location of the stations is where the water column is always well mixed from surface to bottom (Larsen et al., 2008). The coastal measurements are presented together with the cruise CTD data, and the coastal measurements are used when comparing environmental variables with EPR data.

EPR observations are spatio-temporally scattered. Therefore, prior to spatial analysis, stations were grouped onto a 0.125° latitude × 0.25° longitude grid. Regions with < 10 observations were then excluded before mapping temporal averages using the package "mba" in R (R Core Team, 2018). Because of the spatio-temporal scattering of observations, relationships between EPR and environmental variables were based on pre-bloom period annual means. Since the EPR data is not normally distributed, we used non-parametric tests to evaluate temporal trends and to compare means. A p-value < 0.05 was considered statistically significant.

TABLE 1 | Sampling dates and collection summary of data used in this study.

Year	Date	Stations occupied	No. of females incubated	No. of females length measured
1997	April 25–29	32	233	-
1998	April 17–25	69	621	
1999	April 23–27	52	502	-
2000	April 28–May 2	32	182	-
2001	April 20–24	44	456	-
2002	-	-	-	-
2003	April 25–29	44	589	-
2004	April 20–27	55	818	46
2005	April 15–25	72	1,267	645
2006	April 20–25	41	633	-
2007	April 27–May 1	27	377	-
2008	April 25–29	9	113	48
2009	April 24–28	21	290	23
2010	-	-	-	-
2011	April 29–May 2	14	177	-
2012	April 27–May 1	19	276	-
2013	April 25–29	13	172	-
2014	April 27–29	15	205	57
2015	April 24–28	9	88	-
2016	April 28–May 1	20	281	-
2017	April 28–May 2	19	225	-
2018	April 27–30	9	107	-
2019	April 25–29	22	277	148
2020	April 24–27	20	282	3
Total		**658**	**8,171**	**970**

RESULTS

The upper layer (6–50 m) late April average (1997–2020) temperature map in **Figure 2A** shows a colder inner Faroe shelf surrounded by warmer outer shelf/offshelf waters, which is caused by more effective winter cooling of the shallower water column. Intrusion of relatively warm oceanic waters onto the WR overlays the colder and denser shelf waters, and thus establishes stratification, evident as a warm tongue. The typical position of the sharp tidal front between the stratified WR and the well mixed inner shelf (evident in synoptic temperature maps, not shown) is illustrated in **Figure 2A**.

Chlorophyll concentrations were, on average, highest over the WR (**Figure 1B**) during late April, and phytoplankton from this regions appears to emanate across the tidal front and onto the inner shelf (**Figure 2B**). The main spring bloom initiates after April, and the chlorophyll concentrations are therefore generally low.

On average, the highest fraction of spawning females and the highest mean EPR during the pre-bloom in late April were observed in the inflow region from the WR and into the inner shelf, immediately west of the Islands (**Figures 2C,D**). The values are elevated immediately south of the tidal front, while the highest values are observed within the well mixed inner shelf. This stands in contrast to the lowest values in the oceanic waters over the so-called Skeivi Banki (see **Figure 1B**).

Out of the 8,171 females that were incubated, 5,299 laid eggs. Individual daily EPR ranged from 0 to 139 eggs female^{-1} day^{-1}. 85% of the females laid less than 20 eggs, and only 0.1% or 11 females laid more than 100 eggs. Of these 11 females, the only one that was length measured was 3.1 mm, i.e., larger than average.

Upper layer (6–50 m) late April mean temperature increased steadily around the turn of the century from roughly 6.5 to 7.5°C (**Figure 3A**). Since 2003 the temperature has varied between approximately 7 and 8°C with no apparent trend. Variability in the average CTD temperature values sampled on the inner shelf (domain defined by the 100 m depth contour) corresponded well with measurements from coastal station O (**Figure 3A**).

In most years the phytoplankton concentrations were low in late April. The variability between years was, however, pronounced and no long-term trend is discernible (**Figure 3B**). The start of the spring bloom (defined as the day of year when the chlorophyll concentration $\geq$ 1 mg m^{-3}) had generally not occurred during the time of sampling, except in year 2000, 2008–2010, and 2018. Similar to the temperature, spatially averaged chlorophyll values sampled on the inner shelf with the CTD corresponded well with values sampled at coastal station S

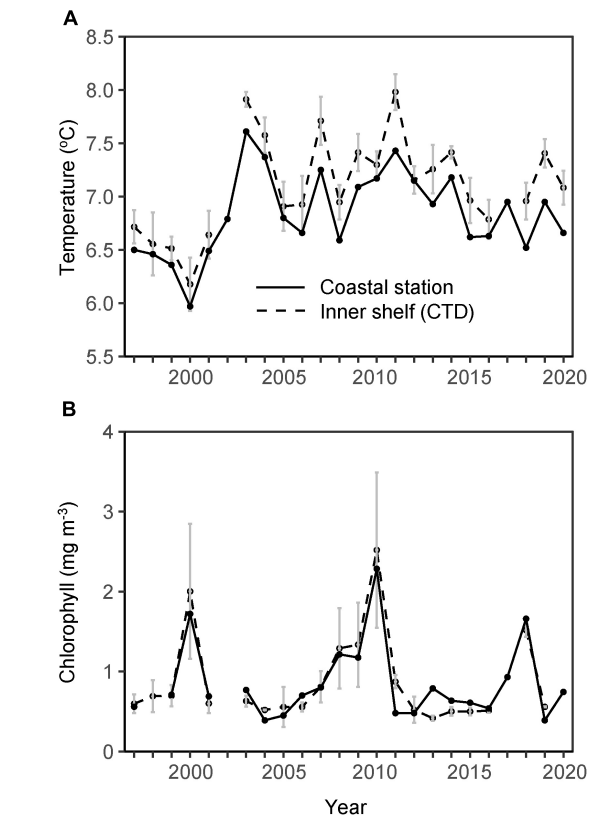


FIGURE 3 | (A) Temperature and **(B)** chlorophyll from CTD casts, averaged vertically over 6–50 m and laterally over the inner shelf (dashed black lines, domain defined by the 100 m depth contour) and from coastal stations O and S, respectively (solid black lines) in late April 1997–2020 (Jacobsen et al., 2018, updated). Vertical lines show spatial standard deviation for the CTD casts.

(**Figure 3B**). This means both that the station S chlorophyll data are representative for the large parts of the shelf during late April, and that bloom dynamics in the WR likely have a large impact on the observed variability.

The overall pre-bloom period mean fraction of spawning females (SF) ranged from ∼40 to 95%. The SF was highly variable between years, with peaks around the turn of the century and in 2018 (**Figure 4A**). An inspection of the linear regression slope between the SF and year showed a statistically significant decreasing trend on the inner shelf ($r_s = -0.47$, $p = 0.03$) (**Figure 4A**). The decline corresponded to approximately 2% each year.

Pre-bloom mean EPR varied from 2 to 20 eggs female^{-1} day^{-1}, with peaks in 2000, 2003, 2007, and 2018 (**Figure 4B**). A visual examination of the mean EPR indicated higher rates during the period 1997–2007 compared with 2008–2020, which was confirmed by a Wilkoxon rank sum test ($p = 0.04$) (**Figure 5**). The mean value for the period 1997–2007 was 12.8 eggs female^{-1} day^{-1}, while it was 7.1 eggs female^{-1} day^{-1} in 2008–2020. This difference in EPR was also apparent if females not producing eggs were excluded before testing (Wilkoxon rank sum test, $p = 0.04$).

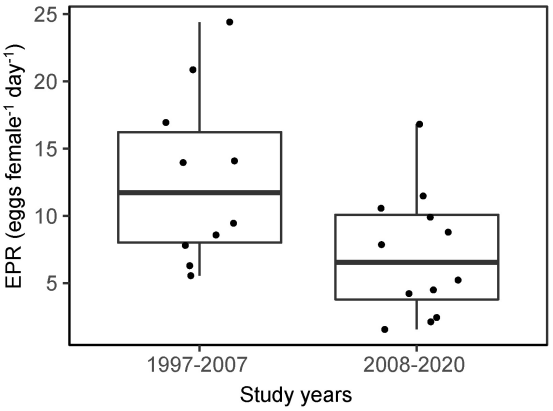


FIGURE 5 | Jitter and box plot of individual egg production rates (eggs female^{-1} day^{-1}) on the Faroe shelf in late April during the time periods 1997–2007 and 2008–2020. The line in the middle of the boxes represents the median, and the lower and upper ends of the box are the 25 and 75% quartiles, respectively. The lower and upper whiskers are constructed according to R's default box plot code (R Core Team, 2018). The points represent observations.

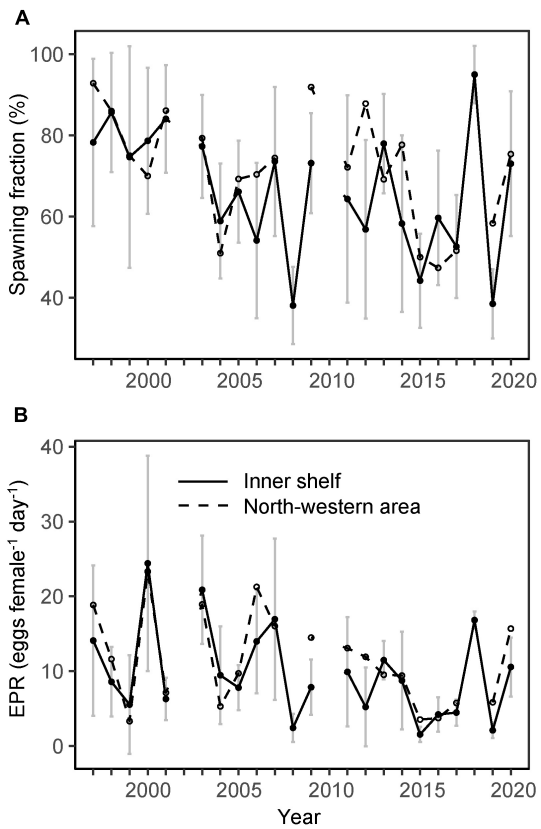


FIGURE 4 | Mean *C. finmarchicus* **(A)** fraction of spawning females and **(B)** individual egg production rates (eggs female^{-1} day^{-1}) on the inner Faroe shelf (solid black line, domain defined by the 100 m depth contour) and in the north-western area (dashed black line, area outlined in **Figures 2C,D**) in late April 1997–2020. Vertical lines show spatial standard deviation for the inner shelf.

Although, EPR values in general were higher in the north-western area (domain outlined in **Figures 2C,D**), there was no statistical difference between pre-bloom mean values for the inner shelf and the north-western area ($p > 0.1$). Thus, since there is more data for the inner shelf, we use inner shelf EPR for the remainder of the paper.

The decrease in SF and EPR was apparent over most of the shelf, but particularly on the inner shelf (**Figure 6**).

Exploratory data analysis did not suggest that EPR was significantly positively correlated to sea temperature (at coastal station O) even when excluding years when chlorophyll concentrations exceed 1 mg m^{-3} ($r_s = 0.34$, $p > 0.1$, **Figure 7A**). Nevertheless, no low values (< 5 eggs female^{-1} day^{-1}) were observed at temperatures above 7°C, indicating that temperature may still have an effect.

The positive relationship between EPR and chlorophyll levels (at coastal station S) approached significance ($r_s = 0.39$, $p = 0.08$, **Figure 7B**), and low EPR values were not observed at chlorophyll levels above 1.5 mg m^{-3} (i.e., in 2000 and 2018).

Pre-bloom mean female prosome length was 2.7 mm. There was a significant negative correlation between seawater temperature (6–50 m) and female size ($r = -0.35$, $p < 0.01$, **Figure 8A**). However, there was a significant positive correlation between size of the females and EPR ($r_s = 0.13$, $p < 0.01$, **Figure 8B**). Since females were only length measured in a subset of study years, it could not be determined whether the mean size of the females had changed during the examined period (i.e., from 1997 to 2020).

DISCUSSION

In this article, we have investigated temporal and spatial variations in pre-bloom *C. finmarchicus* egg production on and

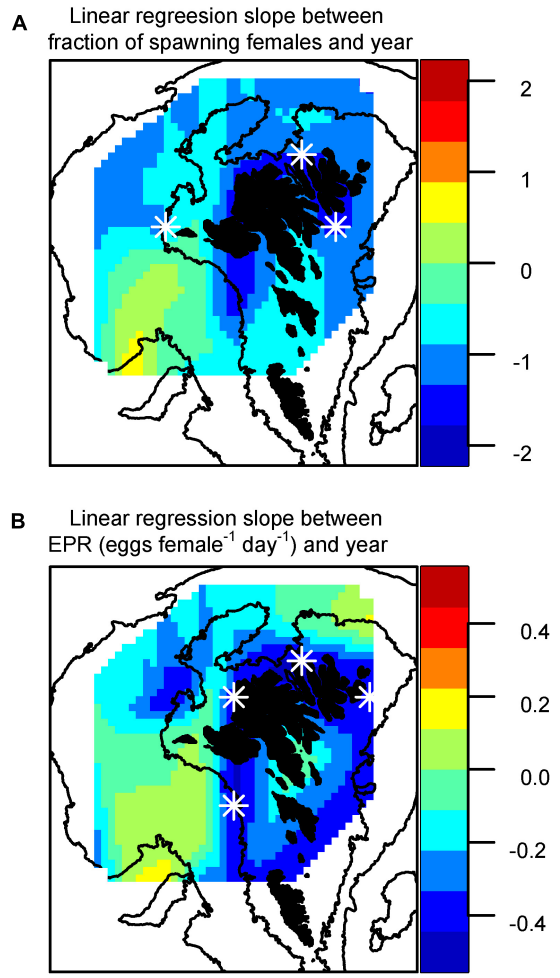


FIGURE 6 | Distribution of slopes of the linear regression for the change in **(A)** fraction of spawning females and **(B)** individual egg production rates (eggs female^{-1} day^{-1}) as a function of year. Stars (*) indicate locations where $p < 0.1$.

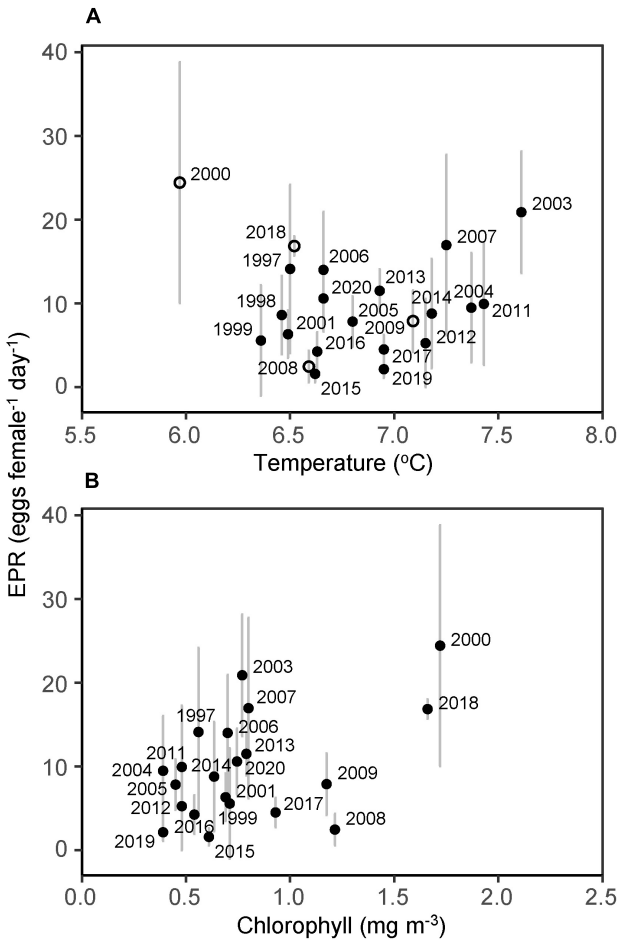


FIGURE 7 | Individual egg production rates (eggs females^{-1} day^{-1}) on the inner shelf in late April vs. **(A)** temperature at station O (open circles indicate bloom years) and **(B)** chlorophyll at station S 1997–2020. Vertical lines indicate standard deviation.

around the Faroe shelf during the years 1997–2020 in relation to relevant available environmental variables. Comparisons with other field measurements indicate similar pre-bloom EPR to those reported in the literature from adjacent areas (Niehoff et al., 1999, 2011; Gislason, 2005; Stenevik et al., 2007; Jónasdóttir et al., 2008; Kristiansen et al., 2021). Enhanced SF and individual EPR were localized in the main inflow region north-west of the islands. However, both the SF and individual EPR decreased during the examined period. To our knowledge, this study is the first to report long-term changes in pre-bloom *C. finmarchicus* egg production in the whole North Atlantic.

The most pronounced influx of outer shelf water to the inner shelf takes place *via* the WR (Hátún et al., 2013; Rasmussen et al., 2014). Jacobsen et al. (2018) showed that the abundance of *C. finmarchicus* eggs, nauplii and copepodites in late April is highest in oceanic waters, especially over the Skeivi Banki region (**Figure 1B**), and much lower in the north-eastern area of the shelf. This stands in contrast to the SF and EPR discussed here, indicating that most of the overwintered *C. finmarchicus* that populate the shelf during the pre-bloom are presumably advected through the WR. Once on the shelf, the tidal currents distribute the individuals in an anti-cyclonic circulation pattern around the islands (Larsen et al., 2008). The relatively high abundance of phytoplankton (food) in the WR probably enhances the copepods' reproduction leading to the relatively high EPR observed in the north-western area (**Figures 2B–D**). This assumption is supported by Madsen et al. (2008) who found that females residing in the south-western area of the shelf contained more food in their guts compared with their counterparts in the north-eastern area of the shelf (Madsen et al., 2008). Madsen et al. (2008) also found markedly higher wax ester content in females outside the tidal front than on the inner shelf, suggesting that females that recently have entered the inner shelf in this region, may partly fuel their egg production by their lipid store. Using numbers from Stenevik et al. (2007), the energy need of *C. finmarchicus* to produce an average of

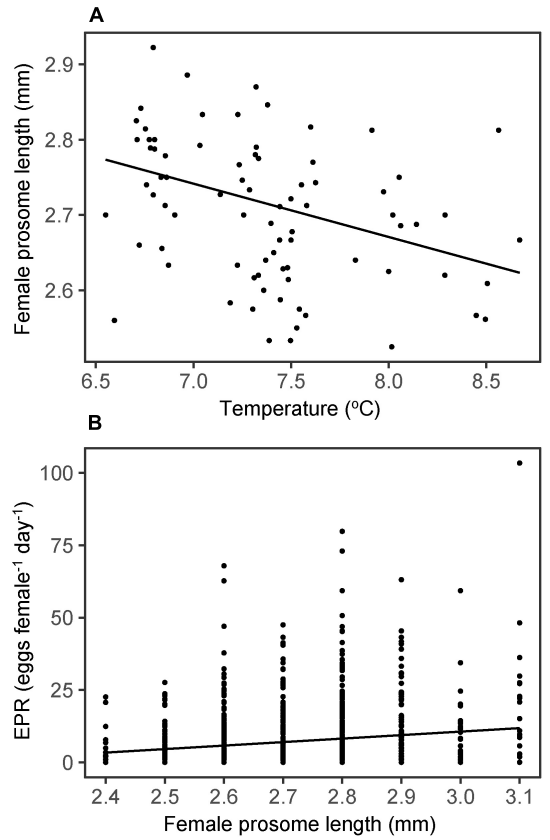


FIGURE 8 | (A) Mean female size (prosome length) vs. temperature (6–50 m) at a given station [*PL* = 3.17-0.06 (T)] and **(B)** individual egg production rates (eggs female^{-1} day^{-1}) vs. female size [EPR = -25.61 + 12.07 (PL)].

10 eggs female^{-1} day^{-1} is 6.9 μg C day^{-1}. Assuming a pre-bloom carbon to chlorophyll ratio of 49 (Meyer-Harms et al., 1999) and a *C. finmarchicus* filtering rate of 0.133 l day^{-1} (Meyer-Harms et al., 1999), this translates to a required chlorophyll concentration of 1.4 mg m^{-3}. Late April mean chlorophyll values in the WR exceed this threshold (**Figure 2B**). Thus, it is feasible to assume that the increased EPR observed in the north-western area are a direct effect of increased food consumption. However, the production is clearly also partly fueled by lipid stores as the energy demand to support the observed mean EPR is in most cases higher than the concurrent chlorophyll concentrations. It is noteworthy that the productive north-western area is close to densely populated seabird cliffs [e.g., the only gannet (*Morus bassanus*) colony in the Faroes], and it is just upstream of the main spawning region of cod (Gaard and Steingrund, 2001; Ottosen et al., 2018).

Despite the partial spatial overlap between EPR and chlorophyll, over the temporal scale of the present study, the relationship between EPR and food availability only approached statistical significance (**Figure 7B**), and we found no significant temporal relationship between EPR and temperature (**Figure 7A**). Overall, it may be difficult to discern the effects of these factors independently in the field, where the effects of one factor may be overridden by the other. Chlorophyll concentrations on the Faroe shelf tend to decrease with increasing temperatures (Hansen et al., 2005), and this could have contributed to the apparent lack of relationship between ambient temperature and EPR and chlorophyll and EPR, respectively. Furthermore, the effect of temperature on EPR might be outweighed by the fact that female prosome length, and thus also the EPR, decrease with increasing temperature (**Figure 8**).

Both the SF and EPR decreased during the 24 years study period (**Figures 4–6**), but the decline could not be explained by the employed environmental parameters. Several potential reasons for the decline, meriting further research, are suggested below:

(i) In addition to mere food abundance, food quality (phytoplankton species composition and particle size) may affect the EPR. Diatoms, which require silicate for growth, have been shown to be positively selected by *C. finmarchicus* (Meyer-Harms et al., 1999). A decline in pre-bloom silicate concentrations has been observed throughout the subpolar North Atlantic during the last three decades (Hátún et al., 2017), which likely has a negative effect on diatom growth. This could have affected the pre-bloom EPR in e.g., 2008 and 2009, when chlorophyll concentrations were relatively high (>1 mg m^{-3}), but the EPR were low (**Figure 7B**).

(ii) Several authors have shown a positive relationship between female size and EPR (e.g., Jónasdóttir et al., 2005; Head et al., 2013a; Melle et al., 2014). In **Figure 8B** we also show, that the egg production potential of *C. finmarchicus* on and around the Faroe shelf is influenced by the size of the female. The *C. finmarchicus* population on the shelf is likely a mixture of animals derived from the Iceland Basin (Hátún et al., 2016) and Norwegian Sea (Gaard and Hansen, 2000; Jónasdóttir et al., 2008; **Figure 1A**). Females in the Norwegian Sea are significantly larger than females from the Iceland Basin (Jónasdóttir et al., 2008; Kristiansen et al., 2021), which could lead to increased EPR by females derived from the Norwegian Sea (Kristiansen et al., 2021). Thus, the variability in EPR may reflect variability in the distribution of different *C. finmarchicus* populations (or water masses) surrounding the Faroe shelf.

(iii) Jacobsen et al. (2018) concluded that there had been a change in *C. finmarchicus* phenology in the outer Faroe shelf in 2007 resulting in earlier emergence of the population as the copeodite stage composition in late April changed from dominance of overwintered late stage (CIV-CVI) copepodites to dominance of early stage (CI-CIII) copepodites. This is the same year as the shift in EPR occurred (**Figures 4B**, **5**). A similar change took place in 2003 north of the Faroe Islands in the south-western Norwegian Sea (Kristiansen et al., 2016). Earlier emergence would inevitably lead to an earlier peak in pre-bloom egg production. Thus, although we observe a reduction in EPR in late April, the production might only have been displaced to an earlier point in the season, i.e., a phenological shift.

(iv) Alternatively, the reduced EPR may be a direct consequence of global warming. Although, the temperature on the Faroe shelf showed no apparent temporal trend (**Figure 3A**), temperatures in deep waters (i.e., overwintering locations) surrounding the Faroes have increased by approximately 0.1°C (Hansen et al., 2016). Increased temperatures may lead to lower body sizes and lower internal lipid stores, affecting the EPR negatively. Unfortunately, female size was not measured on a regular basis during the present time-series study and we could not determine if there have been temporal changes in mean female length. We recommend measuring a subset of females and preserving individuals for lipid content in all future experiments.

C. finmarchicus is, as mentioned, a principal food source for several species of fish, including fish larvae that inhabit the Faroe shelf during spring and summer. In particular, studies have shown that *C. finmarchicus* eggs are the pre-dominant food of first feeding Faroe Plateau cod larvae during spring, i.e., in late April and early May (Gaard and Steingrund, 2001; Jacobsen et al., 2020). Thus, with regards to first feeding fish larvae spawned on the Faroe shelf in spring, a reduction or possible mismatch in prey, i.e., *C. finmarchicus* egg abundance and fish larval abundance could have an impact on recruitment to the cod stock. Since the Faroe shelf is situated near two major overwintering regions of *C. finmarchicus*—the Atlantic subpolar gyre and the Norwegian Sea gyre (Heath et al., 2000)—our findings might also be relevant for neighboring shelf ecosystems. Further studies on this important topic on the Faroe shelf should respect spatial oceanographic structures on the shelf, and emphasize on the productive inflow in the north-western area.

CONCLUDING REMARKS

We here demonstrate that the Faroe shelf is not homogenous regarding pre-bloom *Calanus finmarchicus* egg production. On average, the highest EPR were on the north-western side of the shelf, close to the area where the phytoplankton spring bloom is initiated and to the main cod spawning grounds. This is also where the influx of oceanic waters to the inner shelf is largest. Underlying marked inter-annual variability there was a significant reduction in the fraction of spawning females and EPR on the inner shelf during the last two decades. As evident from the current study, resolving the pre-bloom *C. finmarchicus* egg production is not a trivial task. Neither could variability in phytoplankton biomass nor temperature fully explain the observed variability in EPR. Other factors, such as (*i*) declining silicate concentrations in the North Atlantic, (*ii*) variability in water mass distribution surrounding the Faroes, (*iii*) a phenology change that happened in 2007 and (*iv*) increased overwintering temperatures, could all have affected the EPR. Our findings might reflect conditions over large parts of the Northeastern Atlantic and the Nordic Seas.

DATA AVAILABILITY STATEMENT

Publicly available datasets were analyzed in this study. The CTD data used in the study can be found here: http://envofar.fo/data/index.php?dir=Hydrography%2FCRUISES&sort=N&order=A and the environmental data from station S is located at: http://envofar.fo/data/index.php?dir=Timeseries&sort=N&order=A. The original contributions presented in the study are included in the article/**Supplementary Material**, further inquiries can be directed to the corresponding author/s.

AUTHOR CONTRIBUTIONS

SJ conceived the study, did the data analyses, and led the writing process in correspondence with HH and EG. EG produced the egg production data. All authors have read, commented, and agreed to the manuscript before submission.

SUPPLEMENTARY MATERIAL

The Supplementary Material for this article can be found online at: https://www.frontiersin.org/articles/10.3389/fmars.2022.822978/full#supplementary-material

REFERENCES

Cushing, D. H. (1990). Plankton production and year-class strength in fish populations: an update of the Match/Mismatch hypothesis. *Adv. Mar. Biol.* 26, 249–293.

Debes, H. H., and Eliasen, K. (2006). Seasonal abundance, reproduction and development of four key copepod species on the Faroe shelf. *Mar. Biol. Res.* 2, 249–259. doi: 10.1080/17451000600798787

Debes, H. H., Gaard, E., and Hansen, B. (2008a). Primary production on the Faroe shelf: temporal variability and environmental influences. *J. Mar. Syst.* 74, 686–697. doi: 10.1016/j.jmarsys.2008.07.004

Debes, H. H., Eliasen, K., and Gaard, E. (2008b). Seasonal variability in copepod ingestion and egg production on the Faroe shelf. *Hydrobiologia* 600, 247–265. doi: 10.1007/s10750-007-9238-3

Drijfhout, S., van Oldenborgh, G. J., and Cimatoribus, A. (2012). Is a decline of AMOC causing the warming hole above the North Atlantic in observed and modeled warming patterns? *J. Clim.* 25, 8373–8379. doi: 10.1175/JCLI-D-12-00490.1

Eliasen, S. K., Hátún, H., Larsen, K. M. H., Hansen, B., and Rasmussen, T. A. S. (2017). Phenologically distinct phytoplankton regions on the Faroe Shelf - identified by satellite data, in-situ observations and model. *J. Mar. Syst.* 169, 99–110. doi: 10.1016/j.jmarsys.2017.01.015

Eliasen, S. K., Hátún, H., Larsen, K. M. H., Vang, H. B. M., and Rasmussen, T. A. S. (2019). The Faroe shelf spring bloom onset explained by a 'Critical Volume Hypothesis.'. *J. Mar. Syst.* 194, 91–101. doi: 10.1016/j.jmarsys.2019.02.005

Gaard, E. (1996). Phytoplankton community structure on the Faroe Shelf. *Fróðskaparrit* 44, 95–106.

Gaard, E. (1999). The zooplankton community structure in relation to its biological and physical environment on the Faroe shelf, 1989-1997. *J. Plankton Res.* 21, 1133–1152. doi: 10.1093/plankt/21.6.1133

Gaard, E. (2000). Seasonal abundance and development of *Calanus finmarchicus* in relation to phytoplankton and hydrography on the Faroe Shelf. *ICES J. Mar. Sci.* 57, 1605–1611. doi: 10.1006/jmsc.2000.0963

Gaard, E. (2003). Plankton variability on the Faroe Shelf during the 1990s. *ICES Mar. Sci. Symp*. 219, 182–189.

Gaard, E., and Hansen, B. (2000). Variations in the advection of *Calanus finmarchicus* onto the Faroe Shelf. *ICES J. Mar. Sci.* 57, 1612–1618. doi: 10.1006/jmsc.2000.0962

Gaard, E., and Steingrund, P. (2001). Reproduction of faroe plateau cod: spawning grounds, egg advection and larval feeding. *Fróðskaparrit* 48, 87–103. doi: 10.1002/9781119460701.ch3

Gislason, A. (2005). Seasonal and spatial variability in egg production and biomass of *Calanus finmarchicus* around Iceland. *Mar. Ecol. Prog. Ser.* 286, 177–192. doi: 10.3354/meps286177

Hansen, B., Eliasen, S. K., Gaard, E., and Larsen, K. M. H. (2005). Climatic effects on plankton and productivity on the Faroe Shelf. *ICES J. Mar. Sci.* 62, 1224–1232. doi: 10.1016/j.icesjms.2005.04.014

Hansen, B., Larsen, K. M. H., Hátún, H., and Østerhus, S. (2016). A stable faroe bank channel overflow 1995-2015. *Ocean Sci.* 12, 1205–1220. doi: 10.5194/os-12-1205-2016

Hansen, B., and Østerhus, S. (2000). North Atlantic–Nordic Seas exchanges. *Prog. Oceanogr.* 45, 109–208. doi: 10.1016/S0079-6611(99)00052-X

Hátún, H., Azetsu-Scott, K., Somavilla, R., Rey, F., Johnson, C., Mathis, M., et al. (2017). The subpolar gyre regulates silicate concentrations in the North Atlantic. *Sci. Rep.* 7:14576. doi: 10.1038/s41598-017-14837-4

Hátún, H., Larsen, K. M. H., and Debes, H. (2013). *The Western Region*. Technical Report Nr.: 13- 07. Faroe Islands: Havstovan.

Hátún, H., Lohmann, K., Matei, D., Jungclaus, J. H., Pacariz, S. V., Bersch, M., et al. (2016). An inflated subpolar gyre blows life toward the northeastern Atlantic. *Prog. Oceanography* 147, 49–66. doi: 10.1016/j.pocean.2016.07.009

Hátún, H., Payne, M. R., Beaugrand, G., Reid, P. C., Sandø, A. B., Drange, H., et al. (2009). Large bio-geographical shifts in the north-eastern Atlantic Ocean: from the subpolar gyre, *via* plankton, to blue whiting and pilot whales. *Prog. Oceanogr.* 80, 149–162. doi: 10.1016/j.pocean.2009.03.001

Hátún, H., Sande, A. B., Drange, H., Hansen, B., and Valdimarsson, H. (2005). Ocean science: influence of the atlantic subpolar gyre on the thermohaline circulation. *Science* 309, 1841–1844. doi: 10.1126/science.1114777

Head, E. J. H., Harris, L. R., Ringuette, M., and Campbell, R. W. (2013a). Characteristics of egg production of the planktonic copepod, *Calanus finmarchicus*, in the Labrador Sea: 1997-2010. *J. Plankton Res.* 35, 281–298. doi: 10.1093/plankt/fbs097

Head, E. J. H., Melle, W., Pepin, P., Bagøien, E., and Broms, C. (2013b). On the ecology of *Calanus finmarchicus* in the Subarctic North Atlantic: a comparison of population dynamics and environmental conditions in areas of the Labrador Sea-Labrador/Newfoundland Shelf and Norwegian Sea Atlantic and Coastal Waters. *Prog. Oceanogr.* 114, 46–63. doi: 10.1016/j.pocean.2013.05.004

Heath, M. R., Fraser, J. G., Gislason, A., Hay, S. J., Jónasdóttir, S. H., and Richardson, K. (2000). Winter distribution of *Calanus finmarchicus* in the Northeast Atlantic. *ICES J. Mar. Sci.* 57, 1628–1635. doi: 10.1006/jmsc.2000.0978

Heath, M. R., and Lough, R. G. (2007). A synthesis of large-scale patterns in the planktonic prey of larval and juvenile cod (*Gadus morhua*). *Fish. Oceanogr.* 16, 169–185. doi: 10.1111/j.1365-2419.2006.00423.x

Hirche, H. J., Meyer, U., and Niehoff, B. (1997). Egg production of *Calanus finmarchicus*: effect of temperature, food and season. *Mar. Biol.* 127, 609–620. doi: 10.1007/s002270050051

Hjort, J. (1914). "Fluctuations in the great fisheries of northern Europe viewed in the light of biological research," in *Proceedings of the Rapports et ProcésVerbaux des Réunions du Conseil Permanent International pour l'Exploration de la Mer*, Copenhagen.

Irigoien, X., Fernandes, J. A., Grosjean, P., Denis, K., Albaina, A., and Santos, M. (2008). Spring zooplankton distribution in the Bay of Biscay from 1998 to 2006 in relation with anchovy recruitment. *J. Plankton Res.* 31, 1–17. doi: 10.1093/plankt/fbn096

Jacobsen, S., Gaard, E., Hátún, H., Steingrund, P., Larsen, K. M. H., Reinert, J., et al. (2019). Environmentally driven ecological fluctuations on the faroe shelf revealed by fish juvenile surveys. *Front. Mar. Sci.* 6:559. doi: 10.3389/fmars.2019.00559

Jacobsen, S., Gaard, E., Larsen, K. M. H., Eliasen, S. K., and Hátún, H. (2018). Temporal and spatial variability of zooplankton on the Faroe shelf in spring 1997–2016. *J. Mar. Syst.* 177, 28–38. doi: 10.1016/j.jmarsys.2017.08.004

Jacobsen, S., Nielsen, K. K., Kristiansen, R., Grønkjær, P., Gaard, E., and Steingrund, P. (2020). Diet and prey preferences of larval and pelagic juvenile Faroe Plateau cod (*Gadus morhua*). *Mar. Biol.* 167:122. doi: 10.1007/s00227-020-03727-5

Johnson, C. L., Leising, A. W., Runge, J. A., Head, E. J. H., Pepin, P., Plourde, S., et al. (2008). Characteristics of *Calanus finmarchicus* dormancy patterns in the Northwest Atlantic. *ICES J. Mar. Sci.* 65, 339–350. doi: 10.1093/icesjms/fsm171

Jónasdóttir, S. H., Richardson, K., Heath, M. R., Ingvarsdóttir, A., and Christoffersen, A. (2008). Spring production of *Calanus finmarchicus* at the Iceland-Scotland Ridge. *Deep Sea Res. I Oceanogr. Res. Pap.* 55, 471–489. doi: 10.1016/j.dsr.2007.12.009

Jónasdóttir, S. H., Trung, N. H., Hansen, F., and Gärtner, S. (2005). Egg production and hatching success in the calanoid copepods *Calanus helgolandicus* and *Calanus finmarchicus* in the North Sea from March to September 2001. *J. Plankton Res.* 27, 1239–1259. doi: 10.1093/plankt/fbi091

Jónasdóttir, S. H., Wilson, R. J., Gislason, A., and Heath, M. R. (2019). Lipid content in overwintering *Calanus finmarchicus* across the Subpolar Eastern North Atlantic Ocean. *Limnol. Oceanogr.* 64, 2029–2043. doi: 10.1002/lno.11167

Kristiansen, I., Gaard, E., Hátún, H., Jónasdóttir, S. H., and Ferreira, S. A. (2016). Persistent shift of *Calanus* spp. in the southwestern Norwegian Sea since 2003, linked to ocean climate. *ICES J. Mar. Sci.* 73, 1319–1329. doi: 10.1093/icesjms/fsv222

Kristiansen, I., Jónasdóttir, S. H., Gaard, E., Eliasen, S. K., and Hátún, H. (2021). Seasonal variations in population dynamics of *Calanus finmarchicus* in relation to environmental conditions in the southwestern Norwegian Sea. *Deep Sea Res. I Oceanogr. Res. Pap.* [Epub ahead of print] doi: 10.1016/j.dsr.2021.103508

Larsen, K. M. H., Hansen, B., and Svendsen, H. (2008). Faroe shelf water. *Continent. Shelf Res.* 28, 1754–1768. doi: 10.1016/j.csr.2008.04.006

Larsen, K. M. H., Hansen, B., and Svendsen, H. (2009). The Faroe Shelf front: properties and exchange. *J. Mar. Syst.* 78, 9–17. doi: 10.1016/j.jmarsys.2009.02.003

Larsen, K. M. H., Hátún, H., Hansen, B., and Kristiansen, R. (2012). Atlantic water in the Faroe area: sources and variability. *ICES J. Mar. Sci.* 69, 802–808. doi: 10.1093/icesjms/fss028

Li, C., von Storch, J. S., and Marotzke, J. (2013). Deep-ocean heat uptake and equilibrium climate response. *Clim. Dyn.* 40, 1071–1086. doi: 10.1007/s00382-012-1350-z

Madsen, M. L., Gaard, E., and Hansen, B. W. (2008). Wax-ester mobilization by female *Calanus finmarchicus* (Gunnerus) during spring ascendance and advection to the Faroe Shelf. *ICES J. Mar. Sci.* 65, 1112–1121. doi: 10.1093/icesjms/fsn097

Melle, W., Runge, J., Head, E., Plourde, S., Castellani, C., Licandro, P., et al. (2014). The North Atlantic Ocean as habitat for *Calanus finmarchicus*: environmental factors and life history traits. *Prog. Oceanogr.* 129, 244–284. doi: 10.1016/j.pocean.2014.04.026

Meyer-Harms, B., Irigoien, X., Head, R., and Harris, R. (1999). Selective feeding on natural phytoplankton by *Calanus finmarchicus* before, during, and after the 1997 spring bloom in the Norwegian Sea. *Limnol. Oceanogr.* 44, 154–165. doi: 10.4319/lo.1999.44.1.0154

Niehoff, B., Hirche, H.-J., and Bamstedt, U. (2011). The reproduction of *Calanus finmarchicus* in the Norwegian Sea in spring. *Sarsia* 85, 15–22. doi: 10.1080/00364827.2000.10414552

Niehoff, B., Klenke, U., Hirche, H. J., Irigoien, X., Head, R., and Harris, R. (1999). A high frequency time series at Weathership M, Norwegian Sea, during the 1997 spring bloom: the reproductive biology of *Calanus finmarchicus*. *Mar. Ecol. Prog. Ser.* 176, 81–92. doi: 10.3354/meps176081

Ottosen, K. M., Steingrund, P., Magnussen, E., and Payne, M. R. (2018). Distribution and timing of spawning Faroe Plateau cod in relation to warming spring temperatures. *Fish. Res.* 198, 14–23.

Parsons, T. R., Maita, Y., and Lalli, C. M. (1984). *A Manual of Chemical & Biological Methods for Seawater Analysis*. Oxford: Pergamon Press, 115.

Planque, B., Hays, G. C., Ibanez, F., and Gamble, J. C. (1997). Large scale spatial variations in the seasonal abundance of *Calanus finmarchicus*. *Deep Sea Res. I Oceanogr. Res. Pap.* 44, 315–326. doi: 10.1016/S0967-0637(96)00100-8

R Core Team (2018). *R: A Language and Environment for Statistical Computing*. Vienna: R Foundation for Statistical Computing.

Rasmussen, T. A. S., Olsen, S. M., Hansen, B., Hátún, H., and Larsen, K. M. H. (2014). The Faroe shelf circulation and its potential impact on the primary production. *Continent. Shelf Res.* 88, 171–184. doi: 10.1016/j.csr.2014.07.014

Reygondeau, G., and Beaugrand, G. (2011). Future climate-driven shifts in distribution of *Calanus finmarchicus*. *Glob. Change Biol.* 17, 756–766. doi: 10.1111/j.1365-2486.2010.02310.x

Salter, I., Eliasen, S. K., and Jacobsen, S. (2020). *Variability in the Relationship Between in Situ Fluorescence and Chlorophyll-A Concentration in Faroese Waters (2012-2019): Recommendations for Database Management*. Technical Report Nr.: 20-02. Faroe Islands: Havstovan.

Stenevik, E. K., Melle, W., Gaard, E., Gislason, A., Broms, C. T., Prokopchuk, I., et al. (2007). Egg production of *Calanus finmarchicus*-A basin-scale study. *Deep Sea Res. II Top. Stud. Oceanogr.* 54, 2672–2685. doi: 10.1016/j.dsr2.2007.08.027

Conflict of Interest: The authors declare that the research was conducted in the absence of any commercial or financial relationships that could be construed as a potential conflict of interest.

Publisher's Note: All claims expressed in this article are solely those of the authors and do not necessarily represent those of their affiliated organizations, or those of the publisher, the editors and the reviewers. Any product that may be evaluated in this article, or claim that may be made by its manufacturer, is not guaranteed or endorsed by the publisher.

Copyright © 2022 Jacobsen, Gaard and Hátún. This is an open-access article distributed under the terms of the Creative Commons Attribution License (CC BY). The use, distribution or reproduction in other forums is permitted, provided the original author(s) and the copyright owner(s) are credited and that the original publication in this journal is cited, in accordance with accepted academic practice. No use, distribution or reproduction is permitted which does not comply with these terms.

frontiers in Marine Science

ORIGINAL RESEARCH
published: 04 March 2022
doi: 10.3389/fmars.2022.813977

Comparison Between Trophic Positions in the Barents Sea Estimated From Stable Isotope Data and a Mass Balance Model

*Torstein Pedersen**

Department of Arctic and Marine Biology, Faculty of Biosciences, Fisheries and Economy, UiT The Arctic University of Norway, Tromsø, Norway

The trophic position concept is central in system ecology, and in this study, trophic position (TP) estimates from stable-isotopes and an Ecopath mass-balance food web model for the Barents Sea were compared. Two alternative models for estimating TP from stable isotopes, with fixed or scaled trophic fractionation were applied. The mass-balance model was parametrized and balanced for year 2000, was comprised of 108 functional groups (Gs), and was based on biomass and diet data largely based on predator stomach data. Literature search for the Barents Sea Large Marine Ecosystem revealed 93 sources with stable isotope data (δ^{15}N values) for 83 FGs, and 25 of the publications had trophic position estimated from nitrogen stable isotopes. Trophic positions estimated from the mass-balance model ranged to 5.1 TP and were highly correlated with group mean δ^{15}N values, and also highly correlated with the original literature estimates of trophic positions from stable isotopes. On average, TP from the mass-balance model was 0.1 TP higher than the original literature TP estimates (TP_{SIR}) from stable isotopes. A trophic enrichment factor (TEF) was estimated assuming fixed fractionation and minimizing differences between trophic positions from Ecopath and TP predicted from δ^{15}N values assuming a baseline value for δ^{15}N calculated for pelagic particulate organic matter at a baseline TP of 1.0. The estimated TEF of 3.0‰ was lower than the most commonly used TEF of 3.4 and 3.8‰ in the literature. The pelagic whales and pelagic invertebrates functional groups tended to have higher trophic positions from Ecopath than from stable isotopes while benthic invertebrate functional groups tended to show an opposite pattern. Trophic positions calculated using the scaled trophic fractionation approach resulted in lower TP than from Ecopath for intermediate TPs and also a larger TP range in the BS. It is concluded that TPs estimated from δ^{15}N values using a linear model compared better to the Ecopath model than the TPs from scaled fractionation approach.

Keywords: ecosystem structure, trophic enrichment factor, Arctic ecosystem, ecosystem comparison, polar bear, food web

OPEN ACCESS

Edited by:
Peter Grønkjær, Aarhus University, Denmark

Reviewed by:
Sharon Z. Herzka, Center for Scientific Research and Higher Education in Ensenada (CICESE), Mexico
Agnes M. L. Karlson, Stockholm University, Sweden

***Correspondence:**
Torstein Pedersen
Torstein.Pedersen@uit.no

Specialty section:
This article was submitted to Marine Ecosystem Ecology, a section of the journal Frontiers in Marine Science

Received: *12 November 2021*
Accepted: *28 January 2022*
Published: *04 March 2022*

Citation:
Pedersen T (2022) Comparison Between Trophic Positions in the Barents Sea Estimated From Stable Isotope Data and a Mass Balance Model. Front. Mar. Sci. 9:813977. doi: 10.3389/fmars.2022.813977

INTRODUCTION

Following the introduction of integer trophic levels by Lindeman (1942) and fractional trophic levels by Odum and Heald (1975), the use of trophic levels has developed and it has become a conceptual pillar in ecosystem analysis. Fractional trophic levels have also been termed trophic positions (TP) in the literature (Odum and Heald, 1975; Vander Zanden and Rasmussen, 2001; Hussey et al., 2014a). TP is included in the theoretical basis and calculation of many ecosystem metrics and indicators such as trophic efficiency, transfer efficiency and omnivory index (Shannon et al., 2014). Furthermore, TP is an important predictor of trophic enrichment of pollutants in food webs (Hop et al., 2002; Jæger et al., 2009). TP estimates have been used in analysis of ecosystem structure, effects of harvesting, trophic control mechanisms, and how trophic cascades propagate within an ecosystem (Pauly et al., 1998; Frank et al., 2007). Trophic position estimates may be useful for evaluation of fisheries exploitation and management strategies, and it is important to evaluate methods used to estimate trophic positions and factors affecting uncertainty in these estimates.

Trophic position has been estimated from methods based on body size (Basedow et al., 2010), stomach content (Odum and Heald, 1975), stable isotopes (Hobson and Welch, 1992; Hobson et al., 2002), combination of stable-isotope and body size (Jennings et al., 2008), binary diet matrices (Blanchet et al., 2019) and mass-balance food web models (Polovina, 1985; Christensen, 1995). There are relatively few studies comparing results from different methods, but a common approach to evaluate the parametrization of mass-balance models has been to compare the TPs from the mass-balance models with independent TP estimates from stable isotopes (Kline et al., 1998; Nilsen et al., 2008; Navarro et al., 2011; Du et al., 2020). McCormack et al. (2019) reviewed comparisons of TP estimates from stable isotope (SI) and mass-balance models and suggested that comparison of food web model attributes with measures of stable isotopes composition of taxa, has a potential for improving ecosystem model parameterization.

The use of stable isotopes for estimating TP is based on the assumption of an enrichment (increase) in the heavier ^{15}N isotope relative to the lighter ^{14}N isotope between consumer and food source (Post, 2002). The ratio of stable isotopes of nitrogen ($\delta^{15}N$) may be enriched by about 2 to 4‰ per trophic level and this increase has been termed trophic fractionation, diet–tissue discrimination factor or trophic enrichment factor (TEF) (Post, 2002; Hussey et al., 2014a; Linnebjerg et al., 2016).

Two alternative methods for estimating TP from SIR, fixed fractionation and scaled fractionation, have been applied (Post, 2002; Hussey et al., 2014a). In the fixed fractionation approach, TP can be estimated from stable isotope values ($\delta^{15}N$) from a $\delta^{15}N$ baseline value ($\delta^{15}N_{base}$) of a group at baseline TP (TP_{base}) (**Table 1**). The baseline organism is typically a primary producer, a copepod, or an invertebrate suspension feeder, and a constant trophic enrichment factor (TEF) describes the increase in $\delta^{15}N$ per trophic level (Post, 2002) (Eq. 1). This is termed the linear model in this study.

$$TP_{lin} = TP_{base} + (\delta^{15}N - \delta^{15}N_{base})/TEF \quad (1)$$

The choice of baseline organism and baseline trophic position vary between studies (Casey and Post, 2011). In the Barents Sea, several baseline groups and organisms have been selected; pelagic particulate organic matter (pPOM) at TP = 1 and copepods and bivalves at TP = 2 (Hop et al., 2002; Hallanger et al., 2011a; Fuhrmann et al., 2017). Consistent strong spatial gradients in $\delta^{15}N$ values of lower trophic level organisms and $\delta^{15}N$ baseline values have been observed within the West-Greenland and in the North Sea ecosystems (Jennings et al., 2008; Hansen et al., 2012; MacKenzie et al., 2014). Such spatial gradients in $\delta^{15}N$ baseline values (isoscapes) have been used when inferring trophodynamics from stable isotopes (Jennings et al., 2008; MacKenzie et al., 2014), but isoscapes have so far not been established for the Barents Sea. The Barents Sea Large Marine Ecosystem comprise both open water habitat and numerous fjords and these habitats differ with regard to environmental conditions which may influence stable isotope patterns of organisms (**Figure 1**; Fuhrmann et al., 2017; McGovern et al., 2020).

In Arctic marine ecosystems, a TEF in the range 3.4–3.8‰ has been commonly applied to most ecological groups (Hobson et al., 2002; Søreide et al., 2006), but a lower TEF (e.g., 2.4‰) has been applied to some areas and to birds in some studies (Hobson and Clark, 1992; Hop et al., 2002; Hoondert et al., 2021). Experimental studies indicate that TEF may depend on taxonomic class (Caut et al., 2009) and on diet quality, and thus vary between trophic groups such as herbivores, carnivores, and detritivores (McCutchan et al, 2003; Vanderklift and Ponsard, 2003; Martínez del Rio et al., 2009; McMahon et al., 2015). For the BS, it is uncertain if a common TEF for all FGs would be applicable given that there are many taxonomic and functional groups.

The fixed fractionation model (Eq. 1) has been questioned and an alternative scaled fractionation suggested (Hussey et al., 2014a). In the scaled fractionation approach (Hussey et al., 2014a), alternative TP values are calculated assuming that TEF decreases with increasing diet $\delta^{15}N$ values resulting in lower $\delta^{15}N$ value increments per TP at high $\delta^{15}N$ values. Application of the scaled model results in a larger range of TP than assuming a constant TEF (Hussey et al., 2014a). The scaled model has been applied to a cephalopod species in the Barents Sea (Golikov et al., 2019), but it is uncertain how it will perform for other FGs.

Mass-balance models, such as Ecopath, estimate trophic positions of functional groups based on input data on biomass, production per biomass, consumption per biomass, assimilation efficiency, diet, and fisheries catches (Christensen et al., 2005). Ecopath models usually represent an annual average of mass flows in an ecosystem (Christensen et al., 2005). When comparing TPs from mass-balance models and SI, there is a need to match season, space, and ontogeny for the data input for two methods (McCormack et al., 2019). Ontogenetic changes in $\delta^{15}N$

TABLE 1 | Overview of definition of acronyms in alphabetical order.

Acronym	Definition
BS	Barents Sea
DC	Weight proportion (carbon) of prey in diet
$\delta^{15}N_{base}$ value	Baseline $\delta^{15}N$ value for group at TP_{base}
$\delta^{15}N_{lim}$ value	The highest $\delta^{15}N$ value with positive trophic enrichment factor used in the scaled model, see Hussey et al. (2014a)
$\delta^{15}N_{TP}$ value	Observed $\delta^{15}N$ value for an organism for which a trophic position (TP_{sca}) will be calculated using a scaled model (Eq. 4)
FG	Functional group (see list of FGs in **Table 2**)
iPOM	Ice algal particulate organic matter
pPOM	Pelagic particulate organic matter
POM	Particulate organic matter
RMSD	Root mean squared deviation (Eq. 3) is a measure of deviation between observed and model predicted values
r	Pearson correlation coefficient
r_s	Spearman correlation coefficient
sPOM	Surface sediment particulate organic matter
TEF	Trophic enrichment factor (‰) per trophic position
TP_{base}	Baseline TP for lower TP group
TP	Trophic position
TP_{ec}	Trophic positions for various functional groups estimated from the Ecopath mass balance model for the Barents Sea (Pedersen et al., 2021) (Eq. 2)
TP_{lin}	Trophic position calculated from a linear model with fixed fractionation (constant trophic enrichment factor) according to Eq. (1).
TP_{sca}	Trophic position calculated from a scaled trophic fractionation model assuming a decrease in trophic enrichment factor with increasing trophic position according to Eq. (4).
TP_{SIR}	Trophic positions calculated from fixed fractionation models and published in the literature sources

values of organisms may coincide with seasonal food-pulses and $\delta^{15}N$ values have been found to change with stage or body size in a number of taxa (Jennings et al., 2008; Ramsvatn and Pedersen, 2012; Jennings and Van Der Molen, 2015). When structuring mass-balance models (e.g., Ecopath models) it is common to use size and age structured multi-stanza groups to represent ontogenetic changes in diet composition, TP, growth and mortality rates (Ahrens et al., 2012).

Several mass-balance models with varying functional group resolution has been parametrized for the Barents Sea and Norwegian Sea (Blanchard et al., 2002; Dommasnes et al., 2002; Skaret and Pitcher, 2016; Bentley et al., 2017; Berdnikov et al., 2019; Pedersen et al., 2021), but so far no TP-comparisons between model and stable-isotope data have been performed for the area. For other ecosystems, comparisons between TP estimated from SI and mass-balance models generally show positive correlations between TPs estimated by the two methods (Kline et al., 1998; Milessi et al., 2010; Navarro et al., 2011; McCormack et al., 2019; Hoover et al., 2021). For Ullsfjord, a fjord area at 70°N within the Barents Sea Large Marine Ecosystem (LME), TPs from a mass-balance model and SI have been compared and correlated well (Nilsen et al., 2008). Previous estimates of trophic positions of organisms in the Barents Sea from stable isotopes have been based on various baseline organisms and values for $\delta^{15}N$ baseline and trophic enrichment factors. In this study, TPs from a recently developed mass-balance model (Ecopath) for the Barents Sea with high trophic resolution (Pedersen et al., 2021), will be compared with published data on stable isotopes and TP.

The specific aims of this study were to investigate:

(i) If $\delta^{15}N$ values for functional groups differ between open water and fjords and change with latitude within the Barents Sea.
(ii) If TPs from the Ecopath model and published TPs from SI correspond.
(iii) If TPs estimated from stable isotope using a fixed fractionation model or a scaled fractionation model show better correspondence to TPs from Ecopath.
(iv) The range of trophic positions in the Barents Sea ecosystem.

MATERIALS AND METHODS

Study Area

The study area included the Barents Sea Large Marine Ecosystem (BS) and only data sampled from within this area were included (**Figure 1**). The Barents Sea Large Marine Ecosystem is a shelf-ecosystem (area 2,010,000 km) with an average depth of 230 m and is characterized by inflow of warm nutrient-rich Atlantic water from the southwest (Loeng, 1991; Loeng and Drinkwater, 2007; Skjoldal and Mundy, 2013). In the north and northeast BS, cold Arctic water dominates and BS is partially ice-covered with a seasonal change in ice coverage. Phytoplankton is the dominant primary producer but ice algae are also important in ice-covered waters (Sakshaug et al., 1994). Primary production is highest in the warmer Atlantic ice-free part of the BS. Copepods and krill are major grazers on phytoplankton, and there is a rich and diverse fauna of benthic invertebrates (Jørgensen et al., 2017).

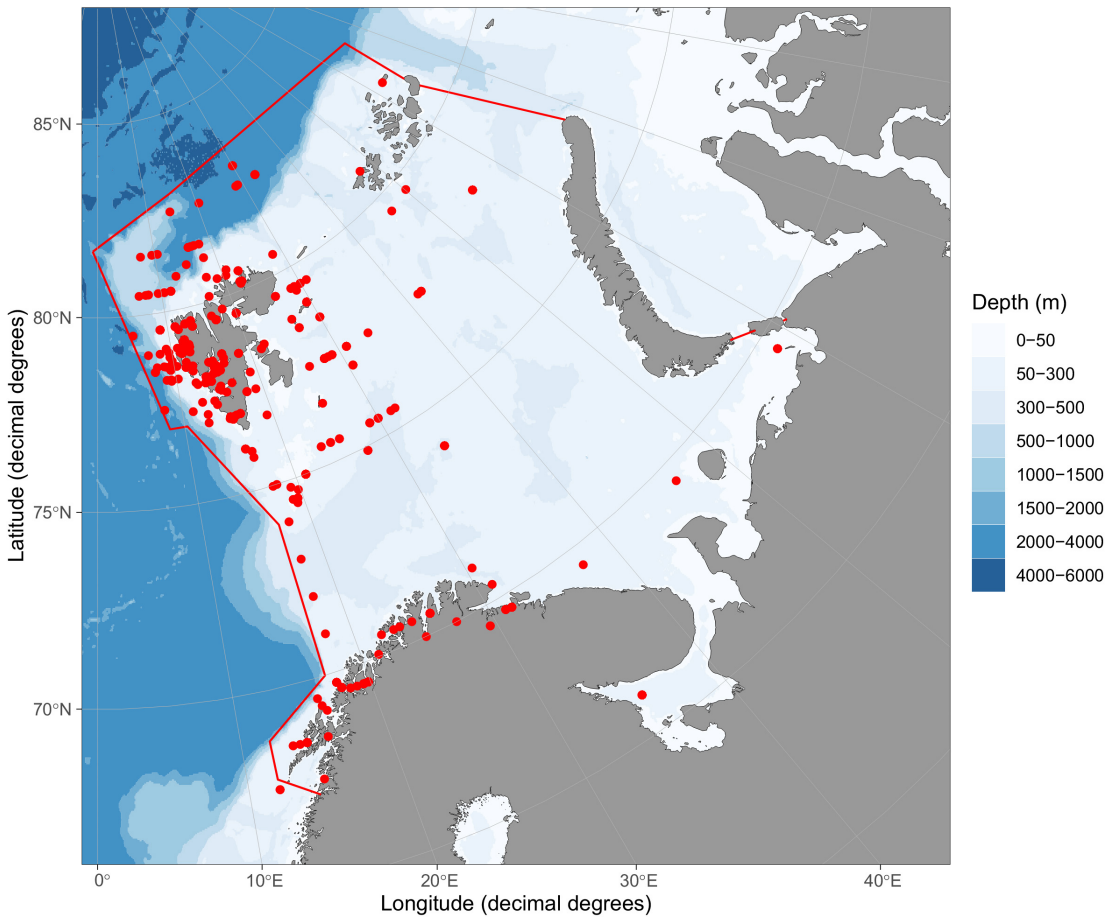


FIGURE 1 | Map of Barents Sea large marine ecosystem. Borders of the ecosystem are shown by red lines based on https://www.pame.is/projects/ecosystem-approach/arctic-large-marine-ecosystems-lme-s. Positions for sampling of data entries are shown by red dots. Map was created using R-package ggOceanMaps (Vihtakari, 2021).

Both pelagic and demersal fishes, sea birds, seals, and whales are abundant, and polar bears is present in the northern part of the BS (Sakshaug et al., 1994). There are several distinct carbon flow pathways from lower to higher trophic FGs; the copepod pathway, the krill pathway, the microbial food web pathway, and the benthic invertebrate pathway (Pedersen et al., 2021). The large stocks of planktivorous fishes, e.g., capelin, polar cod, and small herring are major prey sources for whales, seals, birds, and large demersal and benthic fish FGs (Bogstad et al., 2015; Pedersen et al., 2021).

A few studies have reported average SI values, from locations both within and outside BS, and these values were included if there were no statistical significant differences between values within and outside BS. Data from fjord areas within the BS were included.

Mass-Balance Model for the Barents Sea

A trophically highly resolved mass-balance model for the Barents Sea for year 2000 has been developed (Pedersen et al., 2021) and was used to provide model based estimates of TPs. The model comprises 108 functional groups (FGs) (**Table 2**). Nineteen FGs were multi-stanza FGs, i.e., groups were divided into adult/large and juvenile/small groups with separate input values, diet compositions, and TPs (**Table 2**). When parametrizing Ecopath mass-balance models, the major input to the mass-balance model are biomass (g C m^{-2}), production/biomass ($year^{-1}$) and consumption/biomass ratios ($year^{-1}$), ecotrophic efficiency, proportion of unassimilated food, catches, and diet compositions (Christensen et al., 2005). Ecotrophic efficiency is the proportion of the production of a group that is consumed within the model. Data on biomass were taken from stock assessments for exploited fish and mammal FGs and from literature for other FGs (Pedersen et al., 2021). The Ecopath model is balanced to assure that the production of each FG is sufficient to match the demands from predation, fishery, and other losses. During the balancing process, the initial values of the diet matrix may be modified.

Ecopath calculates trophic position (TP_{ec}) of the FGs and the $TPec_{,j}$ of each predator group ***j*** using the equation:

$$TPec_{,j} = 1 + \sum_{i=1}^{n} DC_{ij} TPec_{,i} \quad (2)$$

TABLE 2 | Overview of functional groups for which output values from Ecopath were aggregated into major categories.

Aggregated category	Ecopath groups within the category
Polar bears	**(1) Polar bears**
Whales	**(2) Minke whale, (3) Fin whale, (4) Blue whale,** (5) Bowhead, (6) Humpback whale, (7) White whale, (8) Narwhale, (9) Dolphins, **(10) Harbor porpoise, (11) Killer whales,** (12) Sperm whale
Seals	**(13) Harp seal, (14) Harbor seal,** (15) Grey seal, **(16) Ringed seal, (17) Bearded seal, (18) Walrus**
Birds	**(19) Northern fulmar, (20) Black legged kittiwake, (21) Other gulls and surface feeders, (22) Little auk, (23) Brunnich guillemot,** (24) Common guillemot and razorbill, (25) Atlantic puffin, **(26) Benthic feeding piscivorous birds, (27) Benthic invertebrate feeding birds**
Benthic and demersal fishes	**(28) Greenland shark, (29) Northeast Arctic cod (3+), (30) Northeast Arctic cod (0–2), (31) Coastal cod (2+), (32) Coastal cod (0–1), (33) Saithe (3+), (34) Saithe (0–2), (35) Haddock (3+), (36) Haddock (0–2), (37) Other small gadoids, (38) Large Greenland halibut, (39) Small Greenland halibut, (40) Other piscivorous fish, (41) Wolffishes, (42) Stichaeidae, (43) Other small benthivorous fishes, (44) Other large benthic invertebrate feeding fish, (45) Thorny skate, (46) Long rough dab, (47) Other benthivore flatfish, (59) Large redfish, (60) Small redfish**
Pelagic fishes	**(48) Large herring, (49) Small herring, (50) Capelin (3+), (51) Capelin (0–2), (52) Polar cod (2+), (53) Polar cod (0–1), (54) Blue whiting,** (55) Sand eel, **(56) Other pelagic planktivorous fish, (57) Lumpfish,** (58) Mackerel, **(61) Atlantic salmon**
Pelagic invertebrates	**(62) Cephalopods, (63) Scyphomedusae, (64) Chaetognaths, (65) *Thysanoessa*, (66) Large krill, (67) Ctenophora, (68) Pelagic amphipods, (69) Symphagic amphipods, (70) Pteropods, (71) Medium sized copepods, (72) Large calanoids,** (73) Small copepods, **(74) Other large zooplankton,** (75) Appendicularians, (76) Ciliates, (77) Heterotrophic dinoflagellates, (78) Heterotrophic nanoflagellates
Benthic predatory invertebrates	**(79) Northern shrimp (*Pandalus borealis*), (80) Crangonid and other shrimps, (81) Other large crustaceans, (82) Crinoids, (83) Predatory asteroids, (84) Predatory gastropods, (85) Predatory polychaetes, (86) Other predatory benthic invertebrates, (101) Snow crab,** (102) Large red king crab, **(103) Medium red king crab,** (104) Small red king crab
Benthic detritivorous invertebrates	**(87) Detritivorous polychaetes, (88) Small benthic crustaceans, (89) Small benthic molluscs, (90) Large bivalves, (91) Detritivorous echinoderms, (92) Large epibenthic suspension feeders, (93) Other benthic invertebrates, (94) Meiofauna, (96)** Benthic foraminifera
Primary producers	**(97) Diatoms*, (98) Autotroph flagellates*, (99) Ice algae**, (100) Macroalgae**

**Included in pPOM. **Included in iPOM.Functional group numbers are shown in brackets.Groups with $\delta^{15}N$ values are shown in bold.*

Where DC_{ij} is the proportion of prey, ***i*** in the diet of predator ***j,*** and $TPec_{,i}$ is the trophic position of FG ***i***. In Ecopath it is assumed that all the detritus groups have trophic position 1 (Christensen et al., 2005).

Stable Isotope Data, Sources and Overview

Literature was searched for sources containing $\delta^{15}N$ values for organisms and/or trophic position (TP_{SIR}) estimated from $\delta^{15}N$ values for the Barents Sea LME area (**Figure 1**), resulting in a total of 93 sources with data (**Supplementary Table 1**). The SI-data included values from living groups and on $\delta^{15}N$ values from organic matter in surface sediment samples. TP and $\delta^{15}N$ values were registered for the lowest taxonomic level reported in the publication and were allocated to FGs that matched the Ecopath functional groups (**Table 2**).

For each data entry with SI values, the variables registered included: the year or time period and month of sampling, geographical sampling area, location, whether data were sampled in a fjord (binary habitat variable; fjord = 1, open water = 0). Position or geographic range of sampling (latitude and longitude of sampling were registered). The sampling location was registered by entering either the exact latitude and longitude when reported, or the midpoint of the geographical area of sampling represented by the lowest and highest integer latitude and longitude including the sampling area. The species name or higher taxonomic level, or if the sample comprised particulate organic matter (POM) of three categories; pPOM (pelagic particulate organic matter), sPOM (POM from surface sediment), iPOM (ice algal particulate organic matter) was registered. If data on size or stage were available, it was recorded. The entries were allocated to FGs based on the feeding category (i.e., herbivore, detritivorous or predatory), and the number of replicates the $\delta^{15}N$ value were based on and the $\delta^{15}N$ value were noted (**Supplementary Table 2**).

To obtain model independent values for TEF that could help to explain deviations from model predicted TPs, literature was searched to obtain estimated values on TEF from experiments and field studies with known diet source for organisms in FGs that are distributed within the BS. It was required that at least the genus of the species is distributed within the BS.

Data Analysis, Trophic Position-Stable Isotope Relationships and Statistical Analysis

Data that were only available in plots were digitized using a digitizer (WebPlotDigitizer[1]). Data entries represented by average values for $\delta^{15}N$ and TP_{SIR} were calculated for given taxa when there were several values for the same taxa, sampling position, and time. Separate data entries were recorded for

[1]https://automeris.io/WebPlotDigitizer/

different sampling positions or sampling times. Values for separate size or stage groups within a taxa, and for various sampling times (seasons), locations, and sampling years were kept in their original format. Data entries were allocated to functional groups (FGs) matching the Ecopath groups based on information from literature (i.e., Kędra et al., 2010; Planque et al., 2014; Sokołowski et al., 2014; Jumars et al., 2015; Renaud et al., 2015; Pedersen et al., 2021). Ontogenetic effects are partly included in the Ecopath model by the specification of groups for small and large individuals (multi-stanza FGs) for a number of species; Northeast arctic cod, coastal cod, saithe, haddock, Greenland halibut, redfish, capelin, polar cod and red king crab (**Table 2**). Data entries were allocated to the multi-stanza FGs based on information about age and body size given in the source. $\delta^{15}N$ or TP_{SIR} values reported for broad categories (e.g., "copepods") that were too broad to match the FGs (e.g., three copepod FGs in the Ecopath model, **Table 2**) were not included in the further analysis. All taxa names were checked to be in accordance with the accepted names in World Register of Marine Species[2] (accessed 20 June 2021) and presently unaccepted names in the original sources were corrected (**Supplementary Table 2**).

Further analysis of the isotope data were made in several major steps corresponding to the aims (I–IV) given in the introduction. Since the Ecopath mass-balance model give TPs for an average state of the BS ecosystem, the stable isotope data were treated to represent average conditions.

(I) The total data set was unbalanced with regard to geographic position and season of sampling (**Figure 1** and **Supplementary Table 3**). There were few samples from open water in the southern part of the Barents Sea and most samples were taken during the summer months (**Figure 1** and **Supplementary Table 3**). A large proportion (61%) of the total number of $\delta^{15}N$ values were from samples taken in fjord habitats. It was considered inappropriate to apply statistical methods that were dependent on balanced designs. For FGs with sufficient number ($n > 5$) of $\delta^{15}N$ values, $\delta^{15}N$ values were plotted versus latitude and month-values with different plotting symbols for open water and fjord habitats to assess if there were obvious spatial or seasonal trends. Whether $\delta^{15}N$ values were correlated with latitude was examined using the Spearman rank correlation coefficient (r_s) applying the cor.test in package stats in R. *P*-values for multiple tests were adjusted according to Benjamini and Hochberg (1995) using p.adjust in package stats in R. Values deviating more than 3 SD from the mean of the FG were identified as outliers.

The FG mean $\delta^{15}N$ values and the difference between the mean-values for fjord and open water habitat for each FG were calculated. Whether the frequency distributions of $\delta^{15}N$ values for each habitat (open water or fjord) deviated from normal distributions was examined using Shapiro-Wilks test (shapiro.test in package stats in R), and for distributions not deviating from normality, two-group *t*-tests with separate variances were applied to test if the mean were equal in fjords and open-water habitats. For groups where $\delta^{15}N$ values from at least one habitat deviated from normality, a two-sample non-parametric Mann–Whitney test was applied to test if central tendency differed for δ15N values between habitats.

(II) Average $\delta^{15}N$ and TP values were calculated for each FG with values on $\delta^{15}N$ and/or trophic position value from stable isotopes given in literature sources (TP_{SIR}), For FGs with only one $\delta^{15}N$ and TP_{SIR} value, this value was used to represent the FG. A total of 83 and 65 FGs had $\delta^{15}N$ and TP_{SIR} values, respectively. In addition to the living functional groups, values of $\delta^{15}N$ measured from sediment sampled particulate organic matter (sPOM) were entered as representative for the FG "detritus from other sources" which is a functional group in Ecopath and a major food source for benthic detritivorous invertebrates and bacteria.

Values of TP_{ec} and TP_{SIR} were compared in bi-scatter plots and the Pearson correlation coefficient was estimated. TP_{ec} and TP_{SIR} values for each FG were compared and whether there was a significant difference between TP_{ec} and TP_{SIR} was examined using a Wilcoxon two-sample paired sample test (Zar, 1999). The significance level was set to 5% in all statistical tests.

The root mean squared deviation (RSMD) (Piñeiro et al., 2008), represent the mean deviation of model predicted TP values (yp_i) with respect to the observed ones here taken as TP_{ec} ($yo_i = TP_{ec}$).

$$RMSD = \sqrt{\frac{1}{n-1}\sum_{i=1}^{n}\left(ypi - yoi\right)^2} \tag{3}$$

where n is the number of pairs of observed and predicted values. RMSD has unit trophic position and lower RMSD values indicate better fit of model predictions to observations than do higher RMSD values.

(III) Since there is a range of possible TEF values, a linear best-fit model was estimated to represent the average relationship between TP and $\delta^{15}N$ values. The model was fitted to two alternative sets of data; (i) from open water and fjord habitat, and (ii) from only open water data. This was chosen because open water represent the majority of the area in the BS and because most of the Ecopath background data is from open water. The model estimated TEF by minimizing the sum of squared differences between values for TP_{ec} and TP predicted from $\delta^{15}N$ values (TP_{lin}) using Eq. (1). The baseline TP was set to 1.0 and the $\delta^{15}N$ baseline value was set to the average $\delta^{15}N$ value for pPOM representing phytoplankton which is the dominating primary producer in BS (Sakshaug et al., 1994). The model was fitted to the data (TP_{ec} and the average $\delta^{15}N$ values for each FG) applying the nls function with least-squares estimation in package stats in R. The values for TP_{base} and $\delta^{15}N_{base}$ were kept fixed during the estimation.

Pelagic particulate organic matter-samples may contain heterotrophic organisms such as bacteria and protozoa in addition to phytoplankton (Stowasser et al., 2012), and the effects of choosing an alternative TP_{base} of 1.2 in the linear best-fit model for data from both open water and fjord habitats were tested.

A scaled model for calculating TP was based on the description by Hussey et al. (2014a,b) (Eq. 4). The scaled model requires that a primary consumer (base) is selected with its $\delta^{15}N$ value ($\delta^{15}N_{base}$

[2]https://www.marinespecies.org/

value) and its trophic position (TP_{base}). The TP (TP_{sca}) of an organism with known $\delta^{15}N$ value ($\delta^{15}N_{TP}$) can then be calculated

$$TP_{sca} = \left(\frac{log\left(\delta^{15}N_{lim} - \delta^{15}N_{base}\right) - \log\left(\delta^{15}N_{lim} - \delta^{15}N_{TP}\right)}{k}\right) + TP_{base} \quad (4)$$

where

$$k = -\log\left(\frac{\beta 0 - \delta^{15}N_{lim}}{-\delta^{15}N_{lim}}\right) \quad (5)$$

and

$$\delta^{15}N_{lim} = -\frac{\beta 0}{\beta 1} \quad (6)$$

The approach adapted to Arctic ecosystems by Linnebjerg et al. (2016) and Golikov et al. (2019) was followed and $\delta^{15}N_{base}$ was set to the $\delta^{15}N$ value of 7.20‰ for *Calanus glacialis* in the Barents Sea and assuming TP_{base} to be 2.0. β0 and β1 are coefficients used to calculate $\delta^{15}N_{lim}$ which is the highest $\delta^{15}N$ value with positive TEF. The values of β0 (5.92) and β1 (−0.27) were estimated in a meta-analysis by Hussey et al. (2014a). In this study, TP_{sca} values were calculated for individual $\delta^{15}N$ values at the data entry level before average TP_{sca} values were calculated for each FG.

The residual TPs (TP_{ec}–TP_{lin}) from the linear best-fit model and the deviations (TP_{ec}–TP_{sca}) for the scaled model (Eqs 2 and 3) for the 83 FGs were calculated and inspected visually in plots. RMSD (Eq. 3) was calculated taking TP_{ec} as observed and TP_{lin} or TP_{sca} as predicted values. The 83 FGs were aggregated into 10 categories (**Table 2**) based on previous assignment of functional groups into aggregated categories in the Ecopath model (Pedersen et al., 2021) and TP residuals for FGs were plotted in box plots. Whether residuals differed significantly between FGs of these aggregated categories was examined using a Kruskal–Wallis test (Zar, 1999). Polar bears were not included in this test since the test needs more than one value in each category.

(IV) Maximum TP of FGs for the various methods were recorded to indicate range of TP for the BS ecosystem.

RESULTS

Overview

A total of 83 functional groups of organisms had a total of 1,832 $\delta^{15}N$ values. The number of $\delta^{15}N$ values per FG varied from 1 to 126 (**Table 2** and **Supplementary Table 4**). Many of the $\delta^{15}N$ values had not been used to calculate TP_{SIR} values in the original sources and 759 TP_{SIR} values from 65 functional groups were published in the original sources. In addition, the material included a total of 87 $\delta^{15}N$ values from samples of sediment organic matter (sPOM) (**Supplementary Table 3**).

Latitude and Habitat Effects

For $\delta^{15}N$ values from both habitats and including pPOM, iPOM and sPOM, $\delta^{15}N$ values and latitude were significantly correlated for few (12%) FGs (**Supplementary Table 5**), with negative correlations for large bivalves ($r_s = -0.32$, $n = 113$; $p = 0.009$), large suspension feeders ($r_s = -0.66$, $n = 23$; $p = 0.009$) and polar cod (age 2+) ($r_s = -0.70$, $n = 15$; $p = 0.04$). For data from only open water, no FGs had significant correlations between $\delta^{15}N$ values and latitude (**Supplementary Table 5**).

A large majority, with 22 of 26 of the living FGs with sufficient number of $\delta^{15}N$ values to compare (n for both habitats > 5), had higher mean $\delta^{15}N$ values in open water than in fjord habitat (**Supplementary Table 5**). The proportion of the FGs with higher $\delta^{15}N$ values in open water than in fjords was 85% and the median $\delta^{15}N$ values of the FGs were higher for open water than for fjord habitat (Wilcoxon two-sample paired-samples test; $p = 0.001$). Tests for equality between $\delta^{15}N$ values in fjord or open water habitat within separate FGs in normally distributed groups (mean) or for groups deviating from normal distributions (central tendency) showed significantly lower $\delta^{15}N$ values in fjord habitat for sPOM (**Supplementary Table 5**). Average sPOM and pPOM $\delta^{15}N$ values were 1.1 and 1.5‰ lower in fjords than for open water, respectively (**Supplementary Table 5**). Both sPOM and pPOM had largest variability in some Svalbard fjords at 77–80°N (**Supplementary Figure 1**). Detrivorous echinoderms and small benthic mollusks also showed significant habitat differences with $\delta^{15}N$ values that were 1.3 to 2.0‰ lower in fjords than in open water (**Supplementary Table 5**).

Benthic predatory invertebrate FGs, other small benthivorous fishes, and Stichaeidae had $\delta^{15}N$ values that were 0.3 to 2.0‰ lower in fjords than in open water, but the differences were not significant for single FGs (**Supplementary Table 5**). For pelagic invertebrates and fish groups, the $\delta^{15}N$ values did not differ significantly between the open water and fjord habitat (**Supplementary Table 5**).

$\delta^{15}N$ values from the methane seep areas in the western part of the BS were included in the material (Åström et al., 2019; **Supplementary Table 1**) and, among the taxa sampled, the chemosymbiotic polychaetes *Siboglinidae* had low deviating $\delta^{15}N$ values in the range of – 3.7 to 4.5‰ (Åström et al., 2019). Some deviating low $\delta^{15}N$ values for pPOM and some benthic invertebrates from a spring bloom situation were observed in the data set (Silberberger et al., 2018; **Supplementary Table 1**) from the Vesterålen area (68^{o}N) (Silberberger et al., 2018; **Supplementary Figure 1**). The values above were included in the analysis.

Comparison of Trophic Position From Ecopath and From Isotopes

On average, TP_{ec} was slightly higher than the original TP_{SIR} reported in the literature sources with an average pairwise difference of 0.10 TL (**Supplementary Table 4**), but the difference was not significant (Wilcoxon two-sample paired test, $n = 65$; $p = 0.07$). TP_{ec} were strongly positively correlated with the original TP_{SIR} values in the papers ($r = 0.89$; $p < 0.0001$, $n = 65$) (**Figure 2**). RMSD was 0.4 TP (**Table 3**).

On the FG level and for data pooled from both habitats, TP_{ec} was strongly positively correlated with FG mean $\delta^{15}N$ values ($r = 0.90$, $n = 83$) (**Figure 3A** and **Supplementary Figure 2**). The average $\delta^{15}N$ values for the three primary producer FGs were

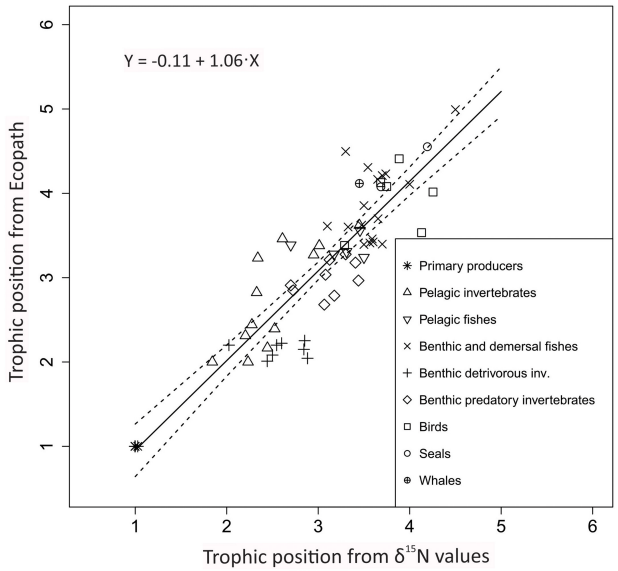


FIGURE 2 | Comparison of trophic positions estimated through Ecopath (*y*-axis) and average trophic positions for each functional group (*x*-axis) from stable isotopes (TP_{SIR}) based on TP values reported in the literature sources. Symbols are shown for aggregated categories. Continuous line shows linear regression line and stippled lines show 95% confidence intervals.

similar: phytoplankton (pPOM) (4.4‰, SD = 2.0, n = 78), ice algae (iPOM) (4.2‰, SD = 1.4, n = 24) and macroalgae (4.6‰, SD = 1.2, n = 63) (**Supplementary Table 4**). The average $\delta^{15}N$ value of sPOM (av. 5.0‰, SD = 1.7, n = 87) was also similar to the values for the primary producers.

The $\delta^{15}N$ value of 4.4‰ for pPOM was chosen as $\delta^{15}N$ baseline at TP of 1.0 for the linear best-fit model since phytoplankton is the major primary producer FG in the ecosystem (Sakshaug et al., 1994). The fit of the linear model for both open water and fjord data ($TP_{lin} = 1 + (\delta^{15}N - 4.4)/TEF$), resulted in a TEF of 3.0‰ (95% CI 2.9, 3.1). RMSD was 0.4 TP (**Table 3**). The TEF from the linear best-fit model was within the range of 2.7 to 3.8‰ published for the BS ecosystem (**Supplementary Table 6**) (**Figure 4**). The linear best-fit model was intermediate compared to published linear TP-SI models for BS that were based on various values for TP_{base} (1, 2, or 3), $\delta^{15}N_{base}$ values, and TEF values (**Figure 4**).

For the linear model for both open water and fjord data, the median of the residuals for TP of FGs (Polar bears was not included) differed significantly between aggregated categories (Kruskal–Wallis, $\chi^2 = 21.8$, df = 8; $p = 0.005$) (**Figure 5**). Whales and the pelagic invertebrate FGs had predominantly positive residuals ($TP_{lin} < TP_{ec}$) while the benthic detritivorous- and predatory invertebrate FGs had predominantly negative residuals ($TP_{lin} > TP_{ec}$) (**Figure 5**). Seals, birds, benthic, demersal, and pelagic fish FGs had residuals centered approximately around zero (**Figure 5**).

At the FG-level, the five FGs with the highest positive residuals were: small Greenland halibut (1.1 TP), Ctenophora (0.9 TP), Atlantic salmon (0.9 TP), pelagic amphipods (0.8 TP), and blue whales (0.7 TP). The groups with the five most negative residuals were: other gulls and surface feeders (−1.0 TP), capelin (3+) (−0.8 TP), predatory asteroids (−0.7 TP), predatory gastropods (−0.6 TP), and detrivorous echinoderms (−0.6 TP).

The alternative linear model for all habitats with pPOM as N_{base} assuming a TP_{base} of 1.2 resulted in a TEF of 3.2‰ (95% CI 3.1, 3.4) and a RMSD of 0.4 TP (**Table 3**). To test if inclusion

TABLE 3 | Overview of major results from comparison of trophic positions from Ecopath and calculation of trophic positions using fixed fractionation (linear model) and scaled fractionation.

Model	Data	TP_{base}, $\delta^{15}N_{base}$	Measure and/or variables	Value (*n*)
Linear	Both habitats, published TP_{SIR}	Various	*r* for TP_{ec} vs. TP_{SIR}	0.89 (65)
			RMSD	0.4 TP
	Both habitats	1.0, 4.4‰	*r* for TP_{ec} vs. $\delta^{15}N$ values	0.90 (83)
			TEF	3.0‰
			RMSD	0.4 TP
			Maximum TP_{lin}	5.4
		1.2, 4.4‰	*r* for TP_{ec} vs. $\delta^{15}N$ values	0.90 (83)
			TEF	3.2‰
			RMSD	0.4 TP
			Maximum TP_{lin}	5.3
	Only open water	1.0, 4.9‰	*r* for TP_{ec} vs. $\delta^{15}N$ values	0.82 (68)
			TEF	2.9‰
			RMSD	0.5 TP
			Maximum TP_{lin}	5.4*
Scaled	Both habitats	2.0	RMSD	0.6 TP
			Maximum TP_{sca}	6.0
	Only open water	2.0	RMSD	0.6 TP
			Maximum TP_{sca}	6.0*

**All polar bears were assumed to belong to open water habitat.TP, trophic position; r, Pearson correlation coefficient; n, number of functional groups.*

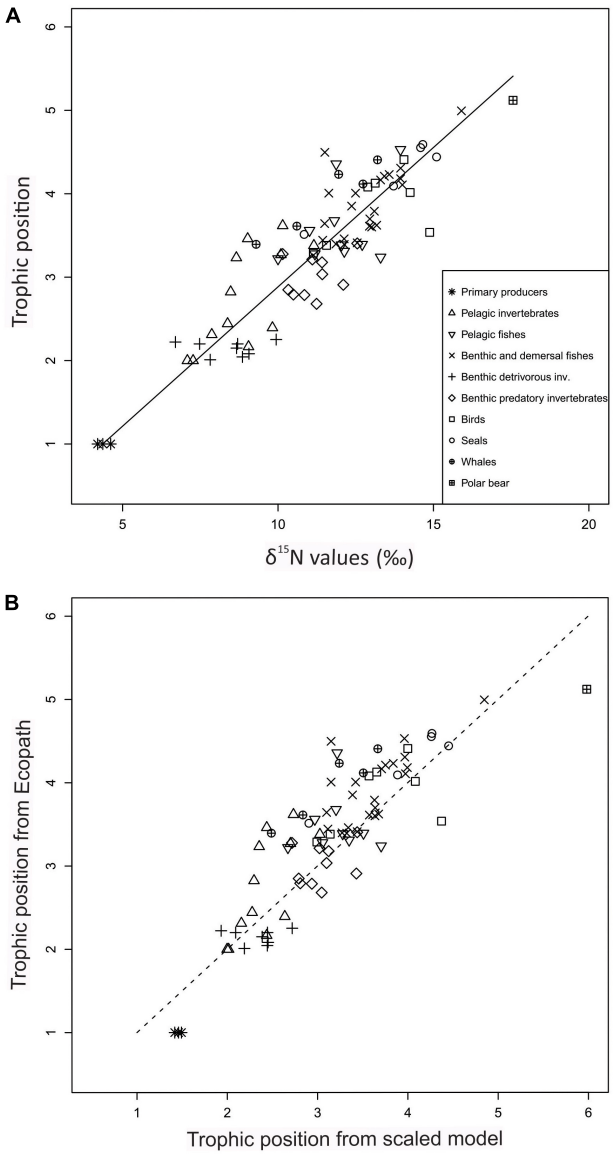


FIGURE 3 | Relationship between trophic positions estimated from Ecopath (*y*-axis) and from alternative models (linear and scaled) from δ^{15}N values for 83 functional groups (*x*-axis) for the Barents Sea for both open water and fjord habitats. Symbols show FGs in major categories. **(A)** Trophic position estimated from Ecopath (*y*-axis) and line shows trophic positions predicted by linear best-fit model from δ^{15}N values (*x*-axis) [$TP_{lin} = 1 + (\delta^{15}N + 4.4)/3.0$]. **(B)** Trophic position from Ecopath (TP_{ec}, *y*-axis) and trophic position estimated by scaled model (TP_{sca}) from δ^{15}N values (Eq. 3, *x*-axis) for functional groups. Stippled line show (1:1) line. In the scaled model, baseline TP (TP_{base}) was 2.0 and baseline δ^{15}N value ($\delta^{15}N_{base}$) was set to 7.2‰.

of the SI data from fjords had a major influence on the results, an analysis with only open water data were undertaken. The data from open water comprised 708 δ^{15}N values from 68 living functional groups and in addition, there was 52 δ^{15}N values from sediment samples. The average δ^{15}N value for pPOM of 4.9‰ (SD = 1.7), based on 39 values for open water, was higher than the value for the total material (4.4‰). At the FG level, δ^{15}N values were strongly correlated to TP from Ecopath (r = 0.82, n = 68). The value for pPOM was used as baseline (N_{base} = 4.9‰) and the fit of the linear model for the open water material ($TP_{lin} = 1 + (\delta^{15}N - 4.9)/TEF$) resulted in a TEF of 2.9‰ (95% CI 2.7, 3.0) which was very similar to the TEF estimated for the total material from both habitats. The fit of the linear model to the average FG values and the test for differences in residuals between categories (Kruskal–Wallis, χ^2 = 24.8, df = 8; p = 0.002) and the residual patterns for open water data was also very similar to the fit for the data from both habitats (**Supplementary Figure 3**). RMSD was 0.5 TP (**Table 3**). This imply that the major patterns in between FG variability of TP were similar for the two data sets (both habitats vs. open water only).

Trophic Positions From Scaled Model and Range of Trophic Position

Trophic positions for FGs calculated by the scaled model with a reference TP of 2.0 for the total material from both habitats showed a curved relationship between TP_{sca} and δ^{15}N values (**Figure 6**). TP_{sca} were lower than the TP_{ec} for most FGs with the largest differences for TP_{sca} between ca. 2.5 to 4.5 (**Figure 3B**). RMSD was 0.6 TP (**Table 3**). The results when applying the scaled model on open water δ^{15}N values were very similar to the results from the scaled model for all habitats (**Supplementary Figure 4**) and RMSD was 0.6 TP (**Table 3**).

Trophic positions from Ecopath ranged from 1.0 for primary producers to 5.1 for polar bears. The maximum TP_{lin} estimated by the linear best-fit model for the total material was 5.4 for polar bears. The TP_{sca} for polar bears from the scaled model TP was 6.0 (SD = 1.6, n = 43) which is 0.9 higher than the TP_{ec} for polar bears (**Figure 3B** and **Table 3**). Among the original published TP_{SIR} values, Greenland shark had the maximum FG average with a TP of 4.5 but there was no TP estimate for polar bears.

Trophic Enrichment Factors From Published Experiments and Field Studies With Known Diet

Median TEF was 3.5‰ (n = 7) and 2.7‰ (n = 12) for detritivorous invertebrates and for vertebrates, respectively (**Supplementary Table 7**). The TEF values of detritivorous invertebrate FGs were significantly higher than for vertebrates (whales, seals, polar bear and fish FGs) (**Figure 7**) (Mann–Whitney, U = 13; p = 0.02). Polar bears had a relatively low TEF of 2.0‰.

DISCUSSION

Variability in Trophic Positions and δ^{15}N Values Related to Latitude and Habitat

The limited range in δ^{15}N values for both sPOM and pPOM in BS open water habitat along the latitudinal gradient, suggest that there were small changes with latitude for δ^{15}N values at the base of the food web. In a meta-analysis based on δ^{15}N values for a number of species from the Svalbard area, Hoondert et al. (2021) found no latitudinal effect. Phytoplankton is the main primary

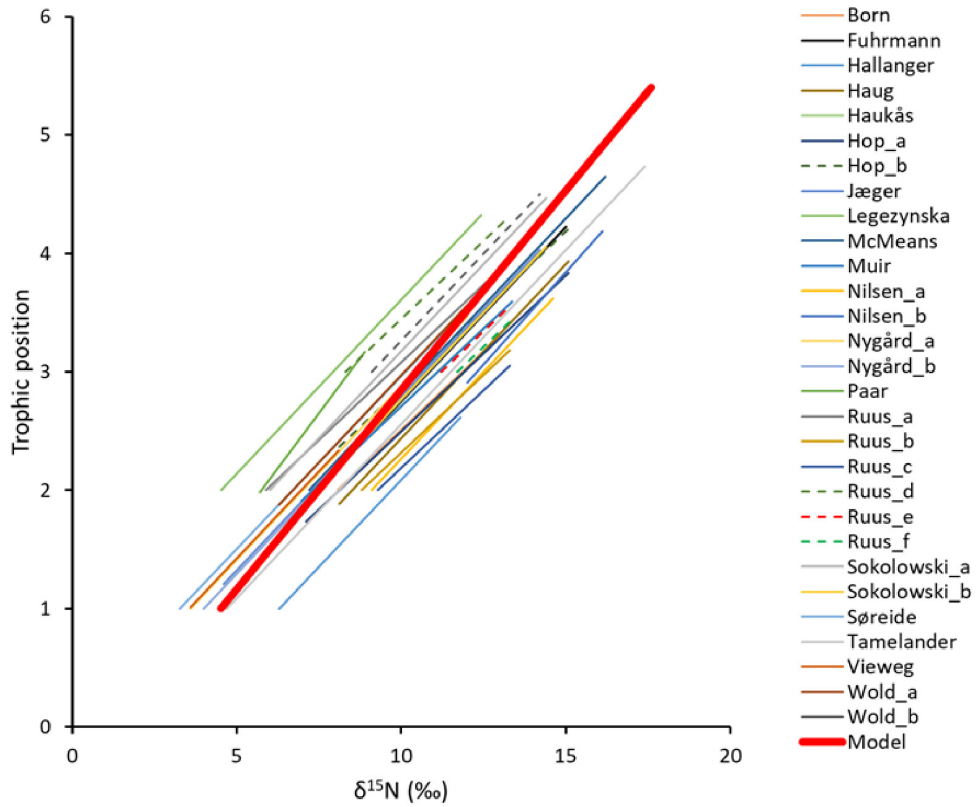


FIGURE 4 | Comparison of 29 published linear relationships between trophic positions (TP) and $\delta^{15}N$ values from literature from the Barents Sea Large Marine Ecosystem. Red bold line show the linear best-fit model for the TP- $\delta^{15}N$ value relationship estimated in this study for all habitats. The linear best-fit relationship had a $\delta^{15}N_{base}$ value of 4.4‰ for TP_{base} = 1 and a TEF of 3.0‰. Values for the published SI-TP relationships are given in **Supplementary Table 6**. Sources for short-names in the figure legend; Born (Born et al., 2003), Fuhrmann (Fuhrmann et al., 2017), Hallanger (Hallanger et al., 2011b), Haug (Haug et al., 2017), Haukås (Haukås et al., 2007), Hop a and b (Hop et al., 2002), Jæger (Jæger et al., 2009), Legeżyńska (Legeżyńska et al., 2012), McMeans (McMeans et al., 2013), Muir (Muir et al., 2003), Nilsen a and b (Nilsen et al., 2008), Nygård a and b (Nygård et al., 2012), Paar (Paar et al., 2019), Ruus a–f (Ruus et al., 2015), Sokołowski a and b (Sokołowski et al., 2014), Tamelander (Tamelander et al., 2006), Vieweg (Vieweg et al., 2012), Wold a and b (Wold et al., 2011).

producer in the BS (Sakshaug et al., 1994), and nitrate is the major source of nitrogen for phytoplankton during the spring/summer bloom in the BS (Tamelander et al., 2009). In support of limited range in baseline $\delta^{15}N$ value at both low and high latitudes within the BS, seawater nitrate $\delta^{15}N$ had stable values of c. 5.1‰ for both Atlantic and Arctic water in the BS (Tuerena et al., 2020). Tuerena et al. (2020) found no clear trend in $\delta^{15}N$ values for nitrate or for particulate nitrogen with increasing latitude in the BS. This apparent stability in BS in lower TP $\delta^{15}N$ values is in contrast to persistent latitudinal gradients in $\delta^{15}N$ values in the North Sea and at West-Greenland (Jennings et al., 2008; Hansen et al., 2012; MacKenzie et al., 2014).

That only a few FGs showed a change in $\delta^{15}N$ values with latitude in the BS may be a result of a relatively stable baseline $\delta^{15}N$ value. The decrease in $\delta^{15}N$ values with increasing latitude observed in some FGs [large bivalves, large epibenthic suspension feeders, and polar cod (2+)] reflect effects on $\delta^{15}N$ values that hypothetically may be caused by changes in temperature or diet composition and quality with latitude. The decreasing trend in $\delta^{15}N$ values with latitude in the BS for the three FGs is opposite to the increase in $\delta^{15}N$ values with increasing latitude found in open water at West-Greenland for *Calanus finmarchicus* and the krill species *Thysanoessa raschii* (Hansen et al., 2012). The latitudinal trend at West-Greenland was explained as a result of high $\delta^{15}N$ values in high Arctic blooms due to partial depletion of the nitrate pool and higher renewal by deep nitrate resulting in lower $\delta^{15}N$ values further south (Hansen et al., 2012). Carroll et al. (2014) observed that $\delta^{15}N$ values of the large bivalve *Ciliatocardium ciliatum* was lower in Artic than in Atlantic waters in the BS and this is consistent with the trend in the total material in this study. The authors suggested that this difference may be due to higher rates of primary production, recycling in the pelagic and heterotrophy in Atlantic than in Arctic waters (Carroll et al., 2014). When large bivalves are used as baseline organisms for estimation of TP from $\delta^{15}N$, spatial trends in their $\delta^{15}N$ values will affect TP estimates for higher TPs.

For polar cod, the decrease in $\delta^{15}N$ values with latitude may be caused by a change in diet composition with increasing latitude. Polar cod inhabiting drift ice in the northernmost area of the BS feed, to a large degree, on symphagic fauna (Lønne and Gulliksen, 1989) while the diet of polar cod in open water may be more varied including copepods, pelagic amphipods, krill and

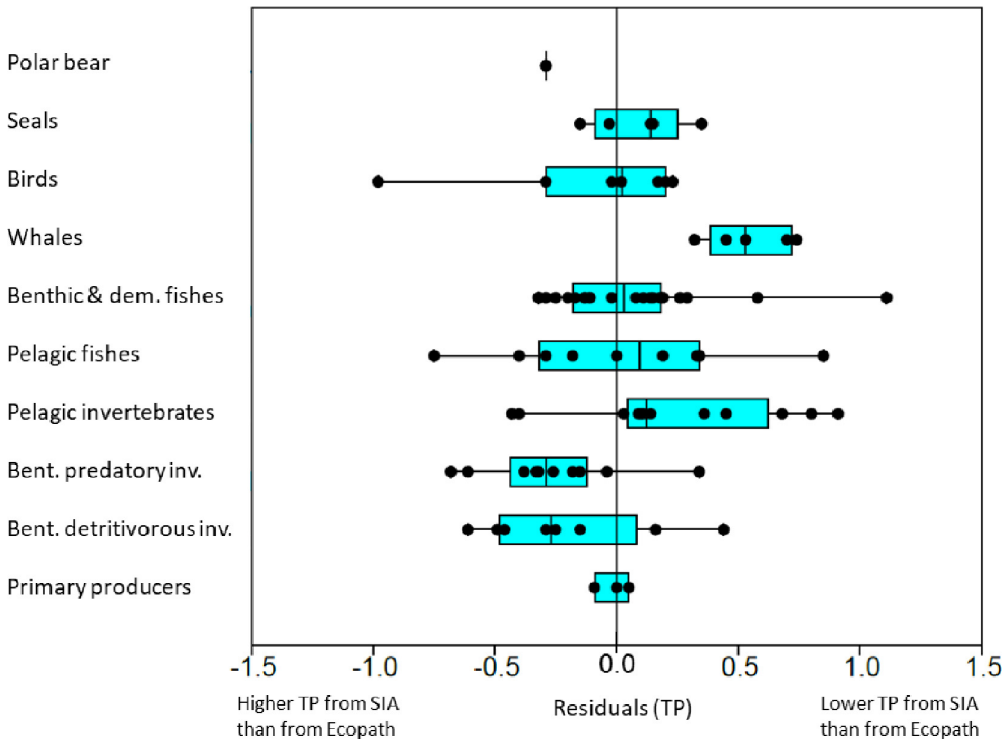


FIGURE 5 | Box-plot of residuals for trophic position values from Ecopath for functional groups predicted by the linear best-fit model for trophic position from $\delta^{15}N$ values. The functional groups were grouped into major categories. The linear best-fit relationship had a $\delta^{15}N_{base}$ value of 4.4‰ for TP_{base} = 1 and a TEF of 3.0‰ estimated for all habitats (open water and fjord). Positive residuals shows when TP from Ecopath is larger than predicted from $\delta^{15}N$ values. Black points show residuals for individual FGs within each major category. Vertical line in boxes show median and boxes show 25–75% quartiles and whiskers show minimal and maximal values.

fish (Aune et al., 2021). Symphagic fauna in the drift ice may have lower TP than diet sources in open water which may cause the observed trend. In support of this, the symphagic amphipod *Apherusa glacialis* which is a dominating prey source for polar cod in ice covered habitats had very low mean $\delta^{15}N$ values in the study (5.4‰) compared to iPOM (4.8‰) (Kohlbach et al., 2016), and consumption of these amphipods may have contributed to the low $\delta^{15}N$ values of polar cod at high latitudes.

The difference between open water and some fjords at Svalbard which had lower $\delta^{15}N$ values for sPOM than in open water have also earlier been observed by Knies et al. (2007). There is freshwater supply of particulate terrestrial organic nitrogen with low $\delta^{15}N$ values in some high Arctic fjords at Svalbard (Koziorowska et al., 2016; McGovern et al., 2020). Low $\delta^{15}N$ values in particles in freshwater runoff to inner fjord areas at Svalbard may contribute to low $\delta^{15}N$ values for lower TP benthic invertebrate FGs in fjord areas at Svalbard (McGovern et al., 2020). The very low $\delta^{15}N$ values both in sediments (sPOM), pelagic POM (pPOM) and benthic invertebrates from some fjord areas at Svalbard, suggest a bottom-up effect propagating from phytoplankton and detritus to benthic invertebrate detritivores and benthic invertebrate predators. The lack of a clear fjord-effect for major zooplankton FGs (e.g., medium sized copepods and *Thysanoessa*) may be caused by advection of these FGs into fjord areas from open water areas. The effect of the lower $\delta^{15}N$ value for pPOM used as baseline value (4.4‰ for both habitats compared to 4.9‰ for open water habitat) for the linear model results was low since the estimates of TEF (2.9 vs. 3.0‰) for the two data sets were similar (**Table 3**). This suggest that the overall effect of the terrestrial input of light nitrogen to the fjords on the results for FGs at higher trophic positions is low.

In this study, the fjord areas, especially in the Svalbard area, generally had a high density of samples and data entries per unit area compared to the large open water area (**Figure 1**). Despite the variability in pPOM, the isotopic baselines for the total material comprising both open water and fjord (4.4‰) and the open water habitat (4.9‰) were similar (**Table 3**). Thus, the fjord-open water habitat effect did not largely affect the linear best-fit estimates of TEF, RMSD and maximum TP. This suggests that this habitat-difference does not markedly affect the results from the comparison of TPs from SI and Ecopath.

That open water had higher $\delta^{15}N$ values than some fjords for sPOM and benthic invertebrates in the Barents Sea is in contrast to the pattern observed along the coast of Greenland, where higher $\delta^{15}N$ values were observed in pelagic groups in fjords than offshore (Hansen et al., 2012). The inshore-open water gradient in lower trophic level $\delta^{15}N$ values in the Barents Sea are also in contrast to the large gradient in the North Sea with high $\delta^{15}N$ values in the southern shallow part with large freshwater input than the lower $\delta^{15}N$ values in the deeper northern North

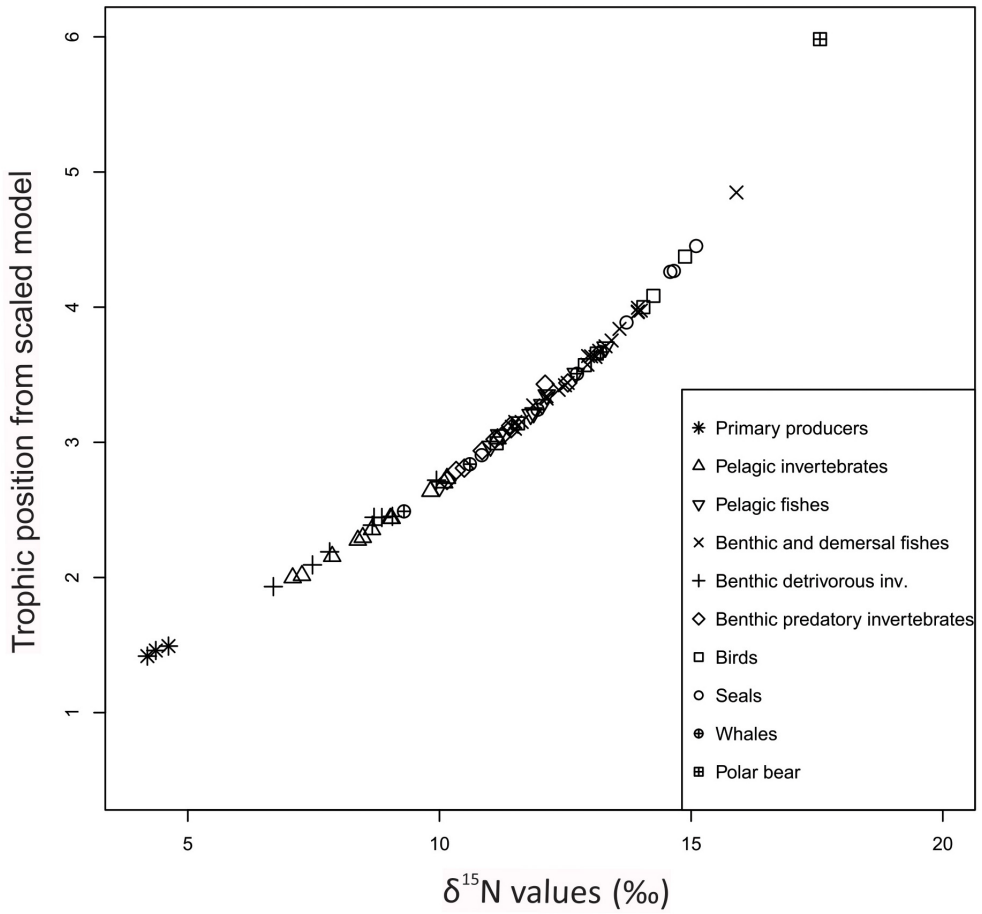


FIGURE 6 | Relationship between trophic position from scaled model (TP_{sca}) and $\delta^{15}N$ values for various functional groups (FGs).

Sea (Jennings et al., 2008; MacKenzie et al., 2014). The habitat gradient in $\delta^{15}N$ values from the Barents Sea resembles the pattern in the Beaufort Sea with low $\delta^{15}N$ values in terrestrial organic material from river input (Bell et al., 2016).

The deviating low $\delta^{15}N$ values for some FGs from areas with methane seeps in the western part of the BS have been well described by Åström et al. (2019). The few deviating low $\delta^{15}N$ values for pPOM and some benthic invertebrates from the southern part of the BS LME (Silberberger et al., 2018), probably indicate local effects that did not markedly affect the overall results because of the low number of entries identified as outliers (Silberberger et al., 2018).

Comparison of Trophic Positions Estimated From Ecopath and Linear Trophic Position-SI Relationship

The TP_{ec} values from Ecopath and the original TP_{SIR} from stable isotopes were similar for most FGs in the BS ecosystem. TP_{SIR} was calculated using linear TP-SI relationships were based on a various baseline organisms, baseline $\delta^{15}N$ value and TEF values, and were calculated for different purposes. The strong correlation between TP_{ec} and TP_{lin} estimated using the linear best-fit model, also indicates a good correspondence between the two methods.

The deviations from the linear best –fit linear TP- SI relationship estimated in this study may be caused by factors affecting both the TPs from Ecopath and from $\delta^{15}N$ values. That most pelagic invertebrate FGs had higher TP_{ec} than TP_{lin} (positive residuals), may indicate that these FGs had low TEF values. Microzooplankton FGs are included in the Ecopath model with the FGs heterotrophic nanoflagellates, ciliates, and heterotrophic dinoflagellates, but no SI values were available for these FGs. Experiments indicate that protists may be isotopically "invisible" using bulk stable isotopes due to their very low bulk $\delta^{15}N$ value enrichment (Gutiérrez-Rodríguez et al., 2014; Landry and Décima, 2017; Park et al., 2021). The microzooplankton FGs are active and have a large production in the BS, and ciliates and dinoflagellates are important prey groups for a number of pelagic invertebrate FGs (Rat'kova and Wassmann, 2002; De Laender et al., 2010; Pedersen et al., 2021). In the Ecopath model used in this study for the BS, microzooplankton amounted to 7–32% of the diet of the copepods FGs, krill (*Thysanoessa*) and pelagic amphipods (Pedersen et al., 2021). Thus, a low TEF of the microzooplankton FGs may contribute to low $\delta^{15}N$ values

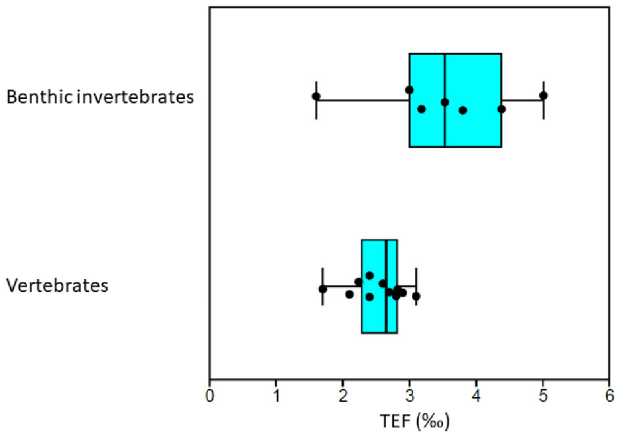


FIGURE 7 | Comparison of trophic enrichment factors (TEF) from published experiments and field studies with known diet for benthic invertebrates and vertebrates (mammals, fish, and birds) that are present in the Barents Sea at least at the genus level. Each black point represent an estimated TEF value. Vertical line in boxes show median and boxes show 25–75% quartiles and whiskers show minimal and maximal values. **Supplementary Table 7** gives details on literature sources.

for their predator FGs and hence low TP_{lin} values and positive residuals. There are few experimental data on TEF for pelagic invertebrates. That the predominantly herbivorous pelagic FGs (copepod groups and krill groups) had small residuals indicate higher TEF values than for the pelagic planktonic predators such as pelagic amphipods, cephalopods, Ctenophora, and Scyphozoa which had high residuals, and this may fit with the diet-quality hypothesis.

The positive residuals from the linear TP-SI relationship for whales may suggest that this group also had relatively low TEF compared to other groups, and the low values for TEF from literature sources for whales may give support to this explanation. The whale FGs with SI data in this study included baleen and toothed whales and long distance seasonal migrants (blue whales, fin whales, minke whales) and all-year resident whales in the Barents Sea (e.g., harbor porpoise and killer whales). Individual feeding specialization was found for killer whales and polar bears (Blévin et al., 2019; Jourdain et al., 2020). Some killer whales specialize in feeding on coastal seals and show high $\delta^{15}N$ values while the majority of the individuals feed on herring (Jourdain et al., 2020), and have relatively low $\delta^{15}N$ values and low standard deviation of $\delta^{15}N$ value (SD = 0.05) (**Supplementary Table 4**).

Benthic detritivorous and benthic predatory invertebrate FGs were the other aggregated categories deviating most from the linear average TP- SI model with higher TP_{lin} than TP_{ec}. It is possible that the diet composition of benthic detritivorous FGs in Ecopath generally contain too little heterotrophic FGs (e.g., bacteria and other microorganisms) and this may contribute to relative low TP_{ec} of these FGs compared to TP from stable isotopes. In Ecopath, all detritus are assigned to TP = 1.0 by convention, while the $\delta^{15}N$ values of detritus from organisms at higher TPs are likely to correspond to the TP of the organisms producing detritus. This may contribute to a reduce TPs from Ecopath compared to TPs from SI.

The higher TP_{lin} than TP_{ec} of benthic invertebrate FGs could also indicate relatively high values for TEF for these FGs in the BS. This interpretation is supported by the relatively high TEF values from experiments with detritivorous invertebrates. Vanderklift and Ponsard (2003) found that mollusks and crustaceans had lower TEF and related this to the mode of nitrogen excretion. Crustaceans and mollusks excrete ammonia (i.e., are ammonotelic) and had lower TEF than taxonomic groups that were ureotelic or uricotelic. However, in this study, the two other important taxa dominating among benthic detritivorous FGs, polychaetes and echinoderms, also excrete ammonia to a large degree (Davoult et al., 1991; Thiel et al., 2017). Thus, it is more likely that the low TEF values of the benthic detritivorous FGs in this study are related to diet composition than to nitrogen excretion mode.

Fractionation is dependent on diet quality and Adams and Sterner (2000) found that TEF of a zooplankton species (*Daphnia magna*) increased with increasing carbon:nitrogen ratio in the food. In the marine fish *Fundulus heteroclitus*, TEF was largest for diets with low $\delta^{15}N$ values, i.e., a larger difference between consumer and diet $\delta^{15}N$ values (Elsdon et al., 2010). In this study, it seems most likely that the negative residuals for most benthic invertebrate FGs are due to high TEF values for detritivorous FGs feeding on low quality detritus (i.e., high C:N ratio) and that predatory benthic invertebrates get relatively high $\delta^{15}N$ values because their benthic detritivorous invertebrate prey have high $\delta^{15}N$ values.

Seasonal variation in $\delta^{15}N$ values are common in aquatic invertebrates (Woodland et al., 2012), and seasonal variability in baseline $\delta^{15}N$ value may potentially affect the usefulness of TP-SI models. The pelagic primary production in Arctic ecosystems is highly seasonal and food pulses propagate to higher trophic levels with time delay (Falk-Petersen et al., 2007). The spring phytoplankton bloom is based on nitrate as its main nutrient, but after the bloom phytoplankton production is, to a large degree, based on regenerated nutrients (Kristiansen et al., 1994; Tamelander et al., 2009). This may contribute to seasonal variations in $\delta^{15}N$ values and computed trophic position for species and FGs (Hoondert et al., 2021). Some FGs (e.g., copepod FGs) are omnivorous and change diet seasonally from phytoplankton in spring and summer to protozoa and detritus during summer (De Laender et al., 2010; Kohlbach et al., 2021). Generally, high $\delta^{15}N$ values of have been observed in several FGs during winter and spring when feeding at lower trophic levels are reduced (Olive et al., 2003; Hertz et al., 2015). Hertz et al. (2015) found an average increase in $\delta^{15}N$ values of fasting of 0.5‰, and in the BS, Carroll et al. (2014) found higher $\delta^{15}N$ values (ca. 0.5–1.0‰) in the large bivalve *Ciliatocardium ciliatum* during spring than in fall. That the majority of stable isotope samples in the material analyzed in this paper were sampled during spring, summer, and autumn suggest that they were representative of the most productive season.

Other factors, such as ontogeny and gender, may also influence $\delta^{15}N$ values. Ontogenetic effects are partly included in the Ecopath model by the specification of multi-stanza FGs for

a number of fish species with separate groups for small and large fishes. Hoondert et al. (2021) found a clear effect of sex with females having higher $\delta^{15}N$ values than males, but it is unlikely that a gender – biased sampling would have affected this study markedly.

The TEF of 3.0‰ estimated by the linear best-fit model with TP_{base} of 1.0 was lower than the most commonly used TEF of 3.4 and 3.8‰ in the literature, but seems reasonable compared to the TEF values from experiments and field studies with known diet for organisms that occur in BS. The value (3.0‰) is also close to the average TEF of 3.1‰ calculated for four Arctic pelagic food webs including data from Svalbard (Hoondert et al., 2021). The corresponding TEF for benthic food webs was higher (3.4‰) (Hoondert et al., 2021). The TP of the pPOM used as TP_{base} is uncertain because POM contain heterotrophic organisms, but assuming a TP_{base} of 1.2 resulted in a TEF of 3.2‰ which is in the middle of the range of 2.7 to 3.8‰ commonly applied for TEF in the BS. The RMSD values were identical for linear models with TP_{base} of 1.0 and 1.2 but were lower than the RMSD for the scaled model indicating a better correspondence with Ecopath TPs for TPs from the linear model than from the scaled model.

The average pairwise difference of 0.10 TP between TP_{SIR} from stable isotopes and TP_{ec} from the Ecopath model in this study is in the same range as differences for FGs in TP between published mass-balance models for the BS. The average pairwise differences between TPs for FGs estimated by the Ecopath model in this study for minke whales, harp seals, fish and pelagic invertebrate FGs and corresponding TPs from four other mass-balance models for the Barents Sea and the Barents Sea and Norwegian Sea area varied from +0.25 to −0.25 TP (Pedersen et al., 2021).

Trophic Positions From the Scaled Model and Range of Trophic Positions

That TPs from the scaled model differed systematically from TP from Ecopath for intermediate TP in the range of 2.5 to c. 4.5 ($TP_{sca} < TP_{ec}$) and above 5 TP ($TP_{sca} > TP_{ec}$), is caused by the assumed decrease in TEF with increasing TP underlying the scaled method. In Ecopath, TPs of specific FGs at intermediate TPs were affected by diet compositions of their food source FGs at lower TPs. Uncertainty in diet composition vary between FGs and this uncertainty may affect uncertainty of TPs for single groups. The maximum TP of 6.0 for the scaled model for the Barents Sea was higher than the maximum TP from the linear model for both habitats ($TP_{lin} = 5.4$) and TP from Ecopath ($TP_{ec} = 5.1$) and the linear best-fit model, showing that the maximum TP for the BS is sensitive to choice of method.

The values for maximum TP for the BS from the linear model ($TP_{lin} = 5.4$) and Ecopath ($TP_{ec} = 5.1$) are similar to maximum TP values for most other Arctic ecosystems using linear models (Linnebjerg et al., 2016; Hoondert et al., 2021). Hoondert et al. (2021) found a maximum TP of 4.9 for the Svalbard area within the BS using a linear model with TEF of 3.39 and 3.44‰ for the pelagic and benthic part of the food web, respectively. Maximum TP values of 4.8 to 5.3 were reported for three other Arctic ecosystems (Hoondert et al., 2021). Polar bears has the highest TP value among the FGs in ecosystems where polar bears was present (Hoondert et al., 2021). Earlier published Ecopath models for the BS did not include polar bears as FG. In the Barents Sea, some polar bears also prey on terrestrial prey and birds which have lower $\delta^{15}N$ values than seals (Lippold et al., 2019). Blanchet et al. (2019) estimated TP for polar bears to 5.2 in the BS based on a binary diet matrix and this value is close to the value from the Ecopath model (TP = 5.1).

The difference of 0.6 TP between maximum TP from the scaled and the linear method for BS was much less than the corresponding differences for the West-Greenland ecosystem. Here the scaled model resulted in a much larger maximum TP_{sca} value of 8.6 compared to maximum TPs calculated by linear TP-SI models of 5.2 and 5.6 assuming TEFs of 3.4‰ 3.2‰, respectively (Linnebjerg et al., 2016). The fish-based scaling relationship from Hussey et al. (2014a,b) may not capture the TEF patterns for invertebrate and mammal FGs that are important in Arctic ecosystems. This suggests that, for the BS, a linear model may be sufficient to predict TP from $\delta^{15}N$ values for most purposes. Further improvement in TP-prediction for specific FGs or categories and ecosystem range in TP may be achieved by conducting experiments with organisms feeding on known diet to estimate both bulk TEF and compound specific (amino acid, fatty acid) SI-analysis.

Limitations of the Study

The data set used in this study was not balanced with regard to environmental factors such as season (month), latitude, bottom depth, and geographic regions within the BS. All these factors may influence $\delta^{15}N$ values and hence TP estimates. Furthermore, the sampled tissue and treatment (i.e., lipid extraction, acid treatment) of the samples varied, potentially affecting the $\delta^{15}N$ values used in this study (Sotiropoulos et al., 2004; Canseco et al., 2021). It is known that lipid extraction may affect $\delta^{15}N$ values but effects seem to vary between studies. Lipid extraction caused a ca. 1‰ increase in $\delta^{15}N$ values in fish muscle (Elsdon et al., 2010). Cloyed et al. (2020) found no effect of lipid extraction $\delta^{15}N$ values in dolphins and Caut et al. (2009) found that discrimination factors for nitrogen did not differ in samples from many types of organisms with and without lipid extraction. It was not attempted to correct for effects of various treatment and tissues since it was difficult to find relevant conversion factors.

For some FGs, $\delta^{15}N$ values were based on few entries, and lower number of entries could have contributed to high residuals for some FGs with few entries (n) such as capelin (3+) ($n = 1$) and blue whale ($n = 1$). That the $\delta^{15}N$ averages for multi-species FGs were calculated without weighting species-specific $\delta^{15}N$ values by the biomass of species will give more influence to species with many entries but with low biomass than less-studied species with higher biomass but less entries. This approach was chosen since biomasses of some species are uncertain.

CONCLUSION

Few FGs had $\delta^{15}N$ values that were correlated with latitude. Sediment POM, pelagic POM and some benthic detritivorous and benthic predatory invertebrate FGs had lower $\delta^{15}N$ values

in some fjords at Svalbard than in open water. This was likely caused by freshwater supply of POM of terrestrial origin with low $\delta^{15}N$ values. TPs from the mass-balance model (Ecopath) corresponded well with published TPs based on $\delta^{15}N$ values. TPs from Ecopath and linear best-fit model for TP-SI relationship also corresponded well with an estimate of TEF of 3.0‰. The linear model predicted lower TPs from $\delta^{15}N$ values than from Ecopath for pelagic invertebrates and whales and higher TPs for benthic invertebrates, and this was likely a result of lower TEF for pelagic groups and whales than for benthic invertebrates. A scaled model approach resulted in generally lower TPs than from Ecopath for TP in the range from ca. 2.5 to 4.5 The range of TP in the BS ecosystem varied when estimated by Ecopath, linear and scaled models with maximum TPs of 5.1, 5.4 and 6.0, respectively. It is concluded that the TPs from Ecopath and from a linear TP-SI model corresponded better than between TPs from Ecopath and the scaled approach.

DATA AVAILABILITY STATEMENT

The original contributions presented in the study are included in the article **Supplementary Material**, further inquiries can be directed to the corresponding author.

ETHICS STATEMENT

Ethical review and approval was not required for the animal study because the study was done using published information and did not involve new experiments or sampling.

AUTHOR CONTRIBUTIONS

TP has done all work with the manuscript except the checking of scientific species names which was done by Johanna Hovinen.

FUNDING

The Research Council of Norway provided partial support through the project "The Nansen Legacy" (RCN#276730). The Norway-Canada collaborative project "A Transatlantic innovation arena for sustainable development in the Arctic" (CoArc) also provided partial support for this work (Project Number 8048 at Akvaplan-niva and QZ-15/0457 at Norwegian Ministry of Foreign Affairs).

ACKNOWLEDGMENTS

Johanna Hovinen is thanked for checking scientific names of the data entries. Anders Nielsen is thanked for help with language.

SUPPLEMENTARY MATERIAL

The Supplementary Material for this article can be found online at: https://www.frontiersin.org/articles/10.3389/fmars.2022.813977/full#supplementary-material

REFERENCES

Adams, T. S., and Sterner, R. W. (2000). The effect of dietary nitrogen content on trophic level 15N enrichment. *Limnol. Oceanogr.* 45, 601–607.

Ahrens, R. N. M., Walters, C. J., and Christensen, V. (2012). Foraging arena theory. *Fish Fish.* 13, 41–59.

Aune, M., Raskhozheva, E., Andrade, H., Augustine, S., Bambulyak, A., Camus, L., et al. (2021). Distribution and ecology of polar cod (*Boreogadus saida*) in the eastern Barents Sea: a review of historical literature. *Mar. Environ. Res.* 166:105262. doi: 10.1016/j.marenvres.2021.105262

Basedow, S. L., Tande, K. S., and Zhou, M. (2010). Biovolume spectrum theories applied: spatial patterns of trophic levels within a mesozooplankton community at the polar front. *J. Plankton Res.* 32, 1105–1119. doi: 10.1093/plankt/fbp110

Bell, L. E., Bluhm, B. A., and Iken, K. (2016). Influence of terrestrial organic matter in marine food webs of the Beaufort Sea shelf and slope. *Mar. Ecol. Prog. Ser.* 550, 1–24. doi: 10.3354/meps11725

Benjamini, Y., and Hochberg, Y. (1995). Controlling the false discovery rate: a practical and powerful approach to multiple testing. *J. R. Stat. Soc. Ser. B* 57, 289–300. doi: 10.1111/j.2517-6161.1995.tb02031.x

Bentley, J. W., Serpetti, N., and Heymans, J. J. (2017). Investigating the potential impacts of ocean warming on the Norwegian and Barents Seas ecosystem using a time-dynamic food-web model. *Ecol. Model.* 360, 94–107.

Berdnikov, S., Kulygin, V., Sorokina, V., Dashkevich, L., and Sheverdyaev, I. (2019). An integrated mathematical model of the large marine ecosystem of the Barents Sea and the White Sea as a tool for assessing natural risks and efficient use of biological resources. *Dokl Earth Sci.* 487, 963–968.

Blanchard, J., Pinnegar, J., and Mackinson, S. (2002). Exploring marine mammal-fishery interactions using 'Ecopath with Ecosim': modelling the Barents Sea ecosystem. *Sci. Ser. Tech. Rep. CEFAS Lowestoft* 117:52.

Blanchet, M.-A., Primicerio, R., Frainer, A., Kortsch, S., Skern-Mauritzen, M., Dolgov, A. V., et al. (2019). The role of marine mammals in the Barents Sea foodweb. *ICES J. Mar. Sci.* 76, i37–i53.

Blévin, P., Aars, J., Andersen, M., Blanchet, M.-A., Hanssen, L., Herzke, D., et al. (2019). Pelagic vs coastal—key drivers of pollutant levels in barents sea polar bears with contrasted space-use strategies. *Environ. Sci. Technol.* 54, 985–995. doi: 10.1021/acs.est.9b04626

Bogstad, B., Gjøsæter, H., Haug, T., and Lindstrøm, U. (2015). A review of the battle for food in the Barents Sea: cod vs. marine mammals. *Front. Ecol. Evol.* 3, 1–17.

Born, E., Outridge, P., Riget, F., Hobson, K., Dietz, R., Øien, N., et al. (2003). Population substructure of North Atlantic minke whales (*Balaenoptera acutorostrata*) inferred from regional variation of elemental and stable isotopic signatures in tissues. *J. Mar. Syst.* 43, 1–17.

Canseco, J., Niklitschek, E., and Harrod, C. (2021). Variability in δ13C and δ15N trophic discrimination factors for teleost fishes: a meta-analysis of temperature and dietary effects. *Rev. Fish Biol. Fish.* 1–17.

Carroll, M. L., Ambrose, W. G. Jr., Ryan, S. K., and Johnson, B. J. (2014). Bivalve growth rate and isotopic variability across the barents sea polar front. *J. Mar. Syst.* 130, 167–180. doi: 10.1016/j.jmarsys.2013.10.006

Casey, M. M., and Post, D. M. (2011). The problem of isotopic baseline: reconstructing the diet and trophic position of fossil animals. *Earth-Sci. Rev.* 106, 131–148. doi: 10.1016/j.earscirev.2011.02.001

Caut, S., Angulo, E., and Courchamp, F. (2009). Variation in discrimination factors (Delta N-15 and Delta C-13): the effect of diet isotopic values and applications for diet reconstruction. *J. Appl. Ecol.* 46, 443–453.

Christensen, V. (1995). A model of trophic interactions in the North Sea in 1981, the year of the stomach. *Dana* 11, 1–28.

Christensen, V., Walters, C., and Pauly, D. (2005). *Ecopath with Ecosim: a User's guide*. Vancouver, BC: Fisheries Centre of University of British Columbia.

Cloyed, C. S., DaCosta, K. P., Hodanbosi, M. R., and Carmichael, R. H. (2020). The effects of lipid extraction on δ13C and δ15N values and use of lipid-correction models across tissues, taxa and trophic groups. *Methods Ecol. Evol.* 11, 751–762.

Davoult, D., Gounin, F., and Janquin, M.-A. (1991). Ammonium excretion by the ophiurid *Ophiothrix fragilis* as a function of season and tide. *Mar. Biol.* 111, 425–429.

De Laender, F., Oevelen, D. V., Soetaert, K., and Middelburg, J. J. (2010). Carbon transfer in herbivore-and microbial loop-dominated pelagic food webs in the southern Barents Sea during spring and summer. *Mar. Ecol. Prog. Ser.* 398, 93–107.

Dommasnes, A., Christensen, V., Ellertsen, B., Kvamme, C., Melle, W., Nøttestad, L., et al. (2002). An ecopath model for the Norwegian Sea and Barents Sea. 2001: fisheries impacts on North Atlantic ecosystems. *Fish. Cen. Res. Rep.* 9, 213–239.

Du, J., Makatipu, P. C., Tao, L. S., Pauly, D., Cheung, W. W., Peristiwady, T., et al. (2020). Comparing trophic levels estimated from a tropical marine food web using an ecosystem model and stable isotopes. *Estuar. Coast. Shelf Sci.* 233:106518.

Elsdon, T. S., Ayvazian, S., McMahon, K. W., and Thorrold, S. R. (2010). Experimental evaluation of stable isotope fractionation in fish muscle and otoliths. *Mar. Ecol. Prog. Ser.* 408, 195–205. doi: 10.3354/meps08518

Falk-Petersen, S., Pavlov, V., Timofeev, S., and Sargent, J. R. (2007). *Climate Variability and Possible Effects on Arctic Food Chains: the Role of Calanus. Arctic Alpine Ecosystems and People in a Changing Environment*. Berlin: Springer.

Frank, K. T., Petrie, B., and Shackell, N. L. (2007). The ups and downs of trophic control in continental shelf ecosystems. *Trends Ecol. Evol.* 22, 236–237. doi: 10.1016/j.tree.2007.03.002

Fuhrmann, M. M., Pedersen, T., and Nilssen, E. M. (2017). Trophic niche of the invasive red king crab *Paralithodes camtschaticus* in a benthic food web. *Mar. Ecol. Prog. Ser.* 565, 113–129.

Golikov, A. V., Ceia, F. R., Sabirov, R. M., Belyaev, A. N., Blicher, M. E., Arboe, N. H., et al. (2019). Food spectrum and trophic position of an Arctic cephalopod, *Rossia palpebrosa* (Sepiolida), inferred by stomach contents and stable isotope (δ^{13}C and δ^{15}N) analyses. *Mar. Ecol. Prog. Ser.* 632, 131–144.

Gutiérrez-Rodríguez, A., Décima, M., Popp, B. N., and Landry, M. R. (2014). Isotopic invisibility of protozoan trophic steps in marine food webs. *Limnol. Oceanogr.* 59, 1590–1598. doi: 10.4319/lo.2014.59.5.1590

Hallanger, I. G., Ruus, A., Warner, N. A., Herzke, D., Evenset, A., Schøyen, M., et al. (2011a). Differences between Arctic and Atlantic fjord systems on bioaccumulation of persistent organic pollutants in zooplankton from Svalbard. *Sci. Total Environ.* 409, 2783–2795. doi: 10.1016/j.scitotenv.2011.03.015

Hallanger, I. G., Warner, N. A., Ruus, A., Evenset, A., Christensen, G., Herzke, D., et al. (2011b). Seasonality in contaminant accumulation in Arctic marine pelagic food webs using trophic magnification factor as a measure of bioaccumulation. *Environ. Toxicol. Chem.* 30, 1026–1035. doi: 10.1002/etc.488

Hansen, J. H., Hedeholm, R. B., Sünksen, K., Christensen, J. T., and Grønkjær, P. (2012). Spatial variability of carbon (δ 13 C) and nitrogen (δ 15 N) stable isotope ratios in an Arctic marine food web. *Mar. Ecol. Prog. Ser.* 467, 47–59. doi: 10.3354/meps09945

Haug, T., Falk-Petersen, S., Greenacre, M., Hop, H., Lindstrøm, U., Meier, S., et al. (2017). Trophic level and fatty acids in harp seals compared with common minke whales in the Barents Sea. *Mar. Biol. Res.* 13, 1–14.

Haukås, M., Berger, U., Hop, H., Gulliksen, B., and Gabrielsen, G. W. (2007). Bioaccumulation of per-and polyfluorinated alkyl substances (PFAS) in selected species from the Barents Sea food web. *Environ. Pollut.* 148, 360–371. doi: 10.1016/j.envpol.2006.09.021

Hertz, E., Trudel, M., Cox, M. K., and Mazumder, A. (2015). Effects of fasting and nutritional restriction on the isotopic ratios of nitrogen and carbon: a meta-analysis. *Ecol. Evol.* 5, 4829–4839. doi: 10.1002/ece3.1738

Hobson, K. A., and Clark, R. G. (1992). Assessing avian diets using stable isotopes II: factors influencing diet-tissue fractionation. *Condor* 94, 189–197. doi: 10.2307/1368808

Hobson, K. A., Fisk, A., Karnovsky, N., Holst, M., Gagnon, J.-M., and Fortier, M. (2002). A stable isotope (δ13C, δ15N) model for the North Water food web: implications for evaluating trophodynamics and the flow of energy and contaminants. *Deep Sea Res. Part II Top. Stud. Oceanogr.* 49, 5131–5150. doi: 10.1016/s0967-0645(02)00182-0

Hobson, K. A., and Welch, H. E. (1992). Determination of trophic relationships within a high arctic marine food web using delta-C-13 and delta-n-15 analysis. *Mar. Ecol. Prog. Ser.* 84, 9–18. doi: 10.3354/meps084009

Hoondert, R. P., van den Brink, N. W., van den Heuvel-Greve, M. J., Ragas, A. M., and Hendriks, A. J. (2021). Variability in nitrogen-derived trophic levels of Arctic marine biota. *Polar Biol.* 44, 119–131. doi: 10.1007/s00300-020-02782-4

Hoover, C., Giraldo, C., Ehrman, A., Suchy, K. D., MacPhee, S. A., Brewster, J. D., et al. (2021). The Canadian Beaufort Shelf trophic structure: evaluating an ecosystem modelling approach by comparison with observed stable isotopic structure. *Arctic Sci.* doi: /10.1139/as-2020-0035

Hop, H., Borgå, K., Gabrielsen, G. W., Kleivane, L., and Skaare, J. U. (2002). Food web magnification of persistent organic pollutants in poikilotherms and homeotherms from the Barents Sea. *Environ. Sci. Technol.* 36, 2589–2597. doi: 10.1021/es010231l

Hussey, N. E., MacNeil, M. A., McMeans, B. C., Olin, J. A., Dudley, S. F., Cliff, G., et al. (2014a). Rescaling the trophic structure of marine food webs. *Ecol. Lett.* 17, 239–250.

Hussey, N. E., MacNeil, M. A., McMeans, B. C., Olin, J. A., Dudley, S. F., Cliff, G., et al. (2014b). Corrigendum to Hussey et al. (2014). *Ecol. Lett.* 17:768.

Jennings, S., Barnes, C., Sweeting, C. J., and Polunin, N. V. C. (2008). Application of nitrogen stable isotope analysis in size-based marine food web and macroecological research. *Rapid Commun. Mass Spectr.* 22, 1673–1680. doi: 10.1002/rcm.3497

Jennings, S., and Van Der Molen, J. (2015). Trophic levels of marine consumers from nitrogen stable isotope analysis: estimation and uncertainty. *ICES J. Mar. Sci.* 72, 2289–2300. doi: 10.1111/1365-2656.12504

Jourdain, E., Andvik, C., Karoliussen, R., Ruus, A., Vongraven, D., and Borgå, K. (2020). Isotopic niche differs between seal and fish-eating killer whales (*Orcinus orca*) in northern Norway. *Ecol. Evol.* 10, 4115–4127. doi: 10.1002/ece3.6182

Jumars, P. A., Dorgan, K. M., and Lindsay, S. M. (2015). Diet of worms emended: An update of Polyhaete feeding guilds. *Annu. Rev. Mar. Sci.* 7, 497–520. doi: 10.1146/annurev-marine-010814-020007

Jæger, I., Hop, H., and Gabrielsen, G. W. (2009). Biomagnification of mercury in selected species from an Arctic marine food web in Svalbard. *Sci. Total Environ.* 407, 4744–4751. doi: 10.1016/j.scitotenv.2009.04.004

Jørgensen, L. L., Archambault, P., Blicher, M., Denisenko, N., Guðmundsson, G., Iken, K., et al. (2017). *Benthos. State of the Arctic Marine Biodiversity Report*. Akureyri: Conservation of Arctic Flora and Fauna (CAFF).

Kędra, M., Gromisz, S., Jaskuła, R., Legeżyńska, J., Maciejewska, B., Malec, E., et al. (2010). Soft bottom macrofauna of an all taxa biodiversity site: hornsund (77○ N, Svalbard). *Pol. Polar Res.* 31, 309–326. doi: 10.2478/v10183-010-0008-y

Kline, T. C., Pauly, D., and Quinn, T. J. I. I. (1998). *Cross-Validation for Trophic Level Estimates From a Mass-Balance Model of Prince William Sound Using N15/N14 Data. Fishery Stock Assessment Models. Alaska Sea Grant College Program Report No. AK-SG-98-01*. Fairbanks: University of Alaska Fairbanks.

Knies, J., Brookes, S., and Schubert, C. J. (2007). Re-assessing the nitrogen signal in continental margin sediments: new insights from the high northern latitudes. *Earth Planet. Sci. Lett.* 253, 471–484.

Kohlbach, D., Graeve, M., Lange, A., David, C., Peeken, I., and Flores, H. (2016). The importance of ice algae-produced carbon in the central Arctic Ocean ecosystem: food web relationships revealed by lipid and stable isotope analyses. *Limnol. Oceanogr.* 61, 2027–2044.

Kohlbach, D., Schmidt, K., Hop, H., Wold, A., Keck-Habahbeh, A., Belt, S. T., et al. (2021). Winter carnivory and diapause counteract the reliance of Barents Sea zooplankton on ice algae. *Front. Mar. Sci.* 8:266.

Koziorowska, K., Kuliński, K., and Pempkowiak, J. (2016). Sedimentary organic matter in two Spitsbergen fjords: terrestrial and marine contributions based on carbon and nitrogen contents and stable isotopes composition. *Continental Shelf Res.* 113, 38–46.

Kristiansen, S., Farbrot, T., and Wheeler, P. A. (1994). Nitrogen cycling in the barents sea–seasonal dynamics of new and regenerated production in the marginal ice zone. *Limnol. Oceanogr.* 39, 1630–1642.

Landry, M. R., and Décima, M. R. (2017). Protistan microzooplankton and the trophic position of tuna: quantifying the trophic link between micro-and mesozooplankton in marine foodwebs. *ICES J. Mar. Sci.* 74, 1885–1892. doi: 10.1093/icesjms/fsx006

Legeżyńska, J., Kędra, M., and Walkusz, W. (2012). When season does not matter: summer and winter trophic ecology of Arctic amphipods. *Hydrobiologia* 684, 189–214. doi: 10.1007/s10750-011-0982-z

Lindeman, R. L. (1942). The trophic-dynamic aspect of ecology. *Ecology* 23, 399–418.

Linnebjerg, J. F., Hobson, K. A., Fort, J., Nielsen, T. G., Møller, P., Wieland, K., et al. (2016). Deciphering the structure of the West Greenland marine food web using stable isotopes (δ13C, δ15N). *Mar. Biol.* 163:230.

Lippold, A., Bourgeon, S., Aars, J., Andersen, M., Polder, A., Lyche, J. L., et al. (2019). Temporal trends of persistent organic pollutants in Barents Sea polar bears (*Ursus maritimus*) in relation to changes in feeding habits and body condition. *Environ. Sci. Technol.* 53, 984–995. doi: 10.1021/acs.est.8b05416

Loeng, H. (1991). "Features of the physical oceanographic conditions of the Barents Sea," in *Proceedings of the Pro MAre Symposium on Polar Marine Ecology, Trondheim, 12-16 May 1990, Book 10. Polar Research*, Trondheim.

Loeng, H., and Drinkwater, K. (2007). An overview of the ecosystems of the Barents and Norwegian Seas and their response to climate variability. *Deep-Sea Res.Part II Top. Stud. Oceanogr.* 54, 2478–2500.

Lønne, O., and Gulliksen, B. (1989). Size, age and diet of polar cod, *Boreogadus saida* (Lepechin 1773), in ice covered waters. *Polar Biol.* 9, 187–191. doi: 10.1007/bf00297174

MacKenzie, K., Longmore, C., Preece, C., Lucas, C., and Trueman, C. (2014). Testing the long-term stability of marine isoscapes in shelf seas using jellyfish tissues. *Biogeochemistry* 121, 441–454.

Martínez del Rio, C., Wolf, N., Carleton, S. A., and Gannes, L. Z. (2009). Isotopic ecology ten years after a call for more laboratory experiments. *Biol. Rev.* 84, 91–111. doi: 10.1111/j.1469-185X.2008.00064.x

McCormack, S. A., Trebilco, R., Melbourne-Thomas, J., Blanchard, J. L., Fulton, E. A., and Constable, A. (2019). Using stable isotope data to advance marine food web modelling. *Rev. Fish Biol. Fish.* 29, 277–296.

McCutchan, J. H. Jr., Lewis, W. M. Jr., Kendall, C., and McGrath, C. C. (2003). Variation in trophic shift for stable isotope ratios of carbon, nitrogen, and sulfur. *Oikos* 102, 378–390.

McGovern, M., Pavlov, A. K., Deininger, A., Granskog, M., Leu, E. S., Søreide, J., et al. (2020). Terrestrial inputs drive seasonality in organic matter and nutrient biogeochemistry in a high arctic fjord system (Isfjorden. Svalbard). *Front. Mar. Sci.* 7:542563.

McMahon, K. W., Thorrold, S. R., Elsdon, T. S., and McCarthy, M. D. (2015). Trophic discrimination of nitrogen stable isotopes in amino acids varies with diet quality in a marine fish. *Limnol. Oceanogr.* 60, 1076–1087. doi: 10.1002/lno.10081

McMeans, B. C., Arts, M. T., Lydersen, C., Kovacs, K. M., Hop, H., Falk-Petersen, S., et al. (2013). The role of Greenland sharks (*Somniosus microcephalus*) in an Arctic ecosystem: assessed via stable isotopes and fatty acids. *Mar. Biol.* 160, 1223–1238.

Milessi, A. C., Danilo, C., Laura, R. G., Daniel, C., Javier, S., and Rodriguez-Gallego, L. (2010). Trophic mass-balance model of a subtropical coastal lagoon, including a comparison with a stable isotope analysis of the food-web. *Ecol. Model.* 221, 2859–2869.

Muir, D., Savinova, T., Savinov, V., Alexeeva, L., Potelov, V., and Svetochev, V. (2003). Bioaccumulation of PCBs and chlorinated pesticides in seals, fishes and invertebrates from the White Sea, Russia. *Sci. Total Environ.* 306, 111–131. doi: 10.1016/s0048-9697(02)00488-6

Navarro, J., Coll, M., Louzao, M., Palomera, I., Delgado, A., and Forero, M. G. (2011). Comparison of ecosystem modelling and isotopic approach as ecological tools to investigate food webs in the NW Mediterranean Sea. *J. Exp. Mar. Biol. Ecol.* 401, 97–104. doi: 10.1016/j.jembe.2011.02.040

Nilsen, M., Pedersen, T., Nilssen, E. M., and Fredriksen, S. (2008). Trophic studies in a high latitude fjord ecosystem - a comparison of stable isotope analyses (delta ^{13}C and delta ^{15}N) and trophic-level estimates from a mass-balance model. *Can. J. Fish. Aqua. Sci.* 65, 2791–2806. doi: 10.1139/f08-180

Nygård, H., Berge, J., Søreide, J. E., Vihtakari, M., and Falk-Petersen, S. (2012). The amphipod scavenging guild in two Arctic fjords: seasonal variations, abundance and trophic interactions. *Aquat. Biol.* 14, 247–264. doi: 10.3354/ab00394

Odum, W. E., and Heald, E. J. (1975). "The detritus-based food-web of an estuarine mangrove community," in *Estuarine Research*, ed. L. E. Cronin (New York, NY: Acdemic Press).

Olive, P. J., Pinnegar, J. K., Polunin, N. V., Richards, G., and Welch, R. (2003). Isotope trophic-step fractionation: a dynamic equilibrium model. *J. Anim. Ecol.* 72, 608–617. doi: 10.1046/j.1365-2656.2003.00730.x

Park, J. Y., Jung, J.-H., Kwak, J. H., Park, H. G., Kang, C.-K., and Park, H. J. (2021). Trophic enrichment factors of carbon and nitrogen isotopic ratios (Δ13C and Δ15N) in four marine ciliates. *Front. Microbiol.* 12:721157. doi: 10.3389/fmicb.2021.721157

Pauly, D., Christensen, J., Dalsgaard, J., Froese, R., and Torres, F. C. (1998). Fishing down marine food webs. *Science* 279, 860–863.

Pedersen, T., Mikkelsen, N., Lindstrøm, U., Renaud, P. E., Nascimento, M. C., Blanchet, M.-A., et al. (2021). Overexploitation, recovery and warming of the Barents Sea ecosystem during 1950-2013. *Front. Mar. Sci.* 8:732637.

Piñeiro, G., Perelman, S., Guerschman, J. P., and Paruelo, J. M. (2008). How to evaluate models: observed vs. predicted or predicted vs. observed? *Ecol. Model.* 216, 316–322.

Planque, B., Primicerio, R., Michalsen, K., Aschan, M., Certain, G., Dalpadado, P., et al. (2014). Who eats whom in the Barents Sea: a food web topology from plankton to whales: Ecological Archives E095-124. *Ecology* 95, 1430–1430. doi: 10.1890/13-1062.1

Polovina, J. J. (1985). An approach to estimating an ecosystem box model. *Fish. Bull. US* 83, 457–460.

Post, D. M. (2002). Using stable isotopes to estimate trophic position: models, methods, and assumptions. *Ecology* 83, 703–718. doi: 10.1111/j.1095-8649.2012.03251.x

Paar, M., Lebreton, B., Graeve, M., Greenacre, M., Asmus, R., and Asmus, H. (2019). Food sources of macrozoobenthos in an Arctic kelp belt: trophic relationships revealed by stable isotope and fatty acid analyses. *Mar. Ecol. Prog. Ser.* 615, 31–49. doi: 10.3354/meps12923

Ramsvatn, S., and Pedersen, T. (2012). Ontogenetic niche changes in haddock *Melanogrammus aeglefinus* reflected by stable isotope signatures, delta^{13}C and delta^{15}N. *Mar. Ecol. Prog. Ser.* 451, 175–185. doi: 10.3354/meps09604

Rat'kova, T. N., and Wassmann, P. (2002). Seasonal variation and spatial distribution of phyto-and protozooplankton in the central Barents Sea. *J. Mar. Syst.* 38, 47–75. doi: 10.1016/s0924-7963(02)00169-0

Renaud, P. E., Løkken, T. S., Jørgensen, L. L., Berge, J., and Johnson, B. J. (2015). Macroalgal detritus and food-web subsidies along an Arctic fjord depth-gradient. *Front. Mar. Sci.* 2:31. doi: 10.3389/fmars.2015.00031

Ruus, A., Øverjordet, I. B., Braaten, H. F. V., Evenset, A., Christensen, G., Heimstad, E. S., et al. (2015). Methylmercury biomagnification in an Arctic pelagic food web. *Environ. Toxicol. Chem.* 34, 2636–2643. doi: 10.1002/etc.3143

Sakshaug, E., Bjørge, A., Gulliksen, B., Loeng, H., and Mehlum, F. (1994). Structure, biomass distribution, and energetics of the pelagic ecosystem in the Barents Sea: a synopsis. *Polar Biol.* 14, 405–411.

Shannon, L., Coll, M., Bundy, A., Gascuel, D., Heymans, J. J., Kleisner, K., et al. (2014). Trophic level-based indicators to track fishing impacts across marine ecosystems. *Mar. Ecol. Prog. Ser.* 512, 115–140. doi: 10.3354/meps10821

Silberberger, M. J., Renaud, P. E., Kröncke, I., and Reiss, H. (2018). Food-web structure in four locations along the European shelf indicates spatial differences in ecosystem functioning. *Front. Mar. Sci.* 5:119.

Skaret, G., and Pitcher, T. J. (2016). *An Ecopath With Ecosim Model of the Norwegian Sea and Barents Sea Validated Against Time Series of Abundance. Fisken og Havet nr. 7-2016*. Bergen: Institute of Marine Research.

Skjoldal, H., and Mundy, P. (2013). *Large Marine Ecosystems (LMEs) of the Arctic Area. Revision of the Arctic LME Map*. Tromsø: Arctic Council.

Sokołowski, A., Szczepańska, A., Richard, P., Kędra, M., Wołowicz, M., and Węsławski, J. (2014). Trophic structure of the macrobenthic community of Hornsund, Spitsbergen, based on the determination of stable carbon and nitrogen isotopic signatures. *Polar Biol.* 37, 1247–1260. doi: 10.1007/s00300-014-1517-7

Sotiropoulos, M., Tonn, W., and Wassenaar, L. (2004). Effects of lipid extraction on stable carbon and nitrogen isotope analyses of fish tissues: potential consequences for food web studies. *Ecol. Freshw. Fish* 13, 155–160.

Stowasser, G., Atkinson, A., McGill, R., Phillips, R., Collins, M. A., and Pond, D. (2012). Food web dynamics in the Scotia Sea in summer: a stable isotope study. *Deep Sea Res. Part II Top. Stud. Oceanogr.* 59, 208–221. doi: 10.1016/j.dsr2.2011.08.004

Søreide, J. E., Hop, H., Carroll, M. L., Falk-Petersen, S., and Hegseth, E. N. (2006). Seasonal food web structures and sympagic–pelagic coupling in the European

Arctic revealed by stable isotopes and a two-source food web model. *Prog. Oceanogr.* 71, 59–87. doi: 10.1016/j.pocean.2006.06.001

Tamelander, T., Kivimäe, C., Bellerby, R. G., Renaud, P. E., and Kristiansen, S. (2009). Base-line variations in stable isotope values in an Arctic marine ecosystem: effects of carbon and nitrogen uptake by phytoplankton. *Hydrobiologia* 630, 63–73.

Tamelander, T., Renaud, P. E., Hop, H., Carroll, M. L., Ambrose, W. G. Jr., and Hobson, K. A. (2006). Trophic relationships and pelagic–benthic coupling during summer in the Barents Sea Marginal Ice Zone, revealed by stable carbon and nitrogen isotope measurements. *Mar. Ecol. Prog. Ser.* 310, 33–46.

Thiel, D., Hugenschütt, M., Meyer, H., Paululat, A., Quijada-Rodriguez, A. R., Purschke, G., et al. (2017). Ammonia excretion in the marine polychaete *Eurythoe complanata* (Annelida). *J. Exp. Biol.* 220, 425–436.

Tuerena, R. E., Hopkins, J., Ganeshram, R. S., Norman, L., de la Vega, C., Jeffreys, R., et al. (2020). Nitrate assimilation and regeneration in the Barents Sea: insights from nitrogen isotopes. *Biogeosciences* 18, 637–653.

Vander Zanden, M. J., and Rasmussen, J. B. (2001). Variation in delta N-15 and delta C-13 trophic fractionation: Implications for aquatic food web studies. *Limnol. Oceanogr.* 46, 2061–2066.

Vanderklift, M. A., and Ponsard, S. (2003). Sources of variation in consumer-diet δ 15 N enrichment: a meta-analysis. *Oecologia* 136, 169–182. doi: 10.1007/s00442-003-1270-z

Vieweg, I., Hop, H., Brey, T., Huber, S., Ambrose, W. G. Jr., and Gabrielsen, G. W. (2012). Persistent organic pollutants in four bivalve species from Svalbard waters. *Environ. Pollut.* 161, 134–142. doi: 10.1016/j.envpol.2011.10.018

Vihtakari, M. (2021). *ggOceanMaps: Plot Data on Oceanographic Maps Using 'ggplot2'. R Package Version 1.1.* Available online at: https://CRAN.R-project.org/package=ggOceanMaps

Wold, A., Jæger, I., Hop, H., Gabrielsen, G. W., and Falk-Petersen, S. (2011). Arctic seabird food chains explored by fatty acid composition and stable isotopes in Kongsfjorden, Svalbard. *Polar Biol.* 34, 1147–1155. doi: 10.1007/s00300-011-0975-4

Woodland, R. J., Magnan, P., Glémet, H., Rodríguez, M. A., and Cabana, G. (2012). Variability and directionality of temporal changes in δ 13 C and δ 15 N of aquatic invertebrate primary consumers. *Oecologia* 169, 199–209. doi: 10.1007/s00442-011-2178-7

Zar, J. H. (1999). *Biostatistical Analysis*. Upper Saddle River, NJ: Prentice-Hall.

Åström, E. K., Carroll, M. L., Sen, A., Niemann, H., Ambrose, W. G. Jr., Lehmann, M. F., et al. (2019). Chemosynthesis influences food web and community structure in high-Arctic benthos. *Mar. Ecol. Prog. Ser.* 629, 19–42.

Conflict of Interest: The author declares that the research was conducted in the absence of any commercial or financial relationships that could be construed as a potential conflict of interest.

Publisher's Note: All claims expressed in this article are solely those of the authors and do not necessarily represent those of their affiliated organizations, or those of the publisher, the editors and the reviewers. Any product that may be evaluated in this article, or claim that may be made by its manufacturer, is not guaranteed or endorsed by the publisher.

Copyright © 2022 Pedersen. This is an open-access article distributed under the terms of the Creative Commons Attribution License (CC BY). The use, distribution or reproduction in other forums is permitted, provided the original author(s) and the copyright owner(s) are credited and that the original publication in this journal is cited, in accordance with accepted academic practice. No use, distribution or reproduction is permitted which does not comply with these terms.

frontiers in Marine Science

ORIGINAL RESEARCH
published: 04 March 2022
doi: 10.3389/fmars.2022.823066

Horizontal and Vertical Migration of Anglerfish *Lophius piscatorius* in Relation to Hydrography in Faroese Waters

Lise Helen Ofstad[1], Hjálmar Hátún[1], Torstein Pedersen[2], Petur Steingrund[1] and Bjarni Mikkelsen[1]*

[1] Faroe Marine Research Institute, Tórshavn, Faroe Islands, [2] Department of Arctic and Marine Biology, UiT – The Arctic University of Norway, Tromsø, Norway

Adult anglerfish conduct annual migrations between spawning areas and feeding areas; for Faroese waters this migration has so far not been described. Therefore, anglerfish migration and distribution in Faroese waters was investigated by mark-recapture studies, including data storage tags, as well as data from scientific trawl surveys, commercial trawlers and gillnetters. The fish distribution was compared to hydrographical conditions such as sea surface- and bottom temperature. A clear seasonal offshore-onshore migration was observed. Anglerfish occupied shallower waters (<200 m) during summer and deeper waters, especially on the western side of the Faroe shelf, during winter. This seasonal movement was most evident for sexually mature fish longer than 70 cm indicating spawning in deep waters during winter. Further, during winter anglerfish experienced cold water, which indicated that they were distributed close to the main interface of cold water masses surrounding the shelf. The fish were mostly located in warm water (6.5–11°C) and seldom occurred in colder waters than 4°C. Anglerfish appeared generally inactive, only around 5% of the total data storage tag recordings showed more than 5 m vertical movement between two subsequent hourly recordings. This vertical activity varied seasonally by being higher during winter than summer and diurnally by being higher during night time than day time, indicating that sunrise and day length played an important role in vertical movements.

Keywords: anglerfish, data storage tag, hydrography, Faroe Islands, *Lophius piscatorius*, mark-recapture, migration

OPEN ACCESS

Edited by:
Stefano Aliani, Consiglio Nazionale delle Ricerche (CNR), Italy

Reviewed by:
Steven Campana, University of Iceland, Iceland
Jorge Paramo, University of Magdalena, Colombia

****Correspondence:***
Lise Helen Ofstad
liseo@hav.fo

Specialty section:
This article was submitted to Marine Ecosystem Ecology, a section of the journal Frontiers in Marine Science

Received: *26 November 2021*
Accepted: *24 January 2022*
Published: *04 March 2022*

Citation:
Ofstad LH, Hátún H, Pedersen T, Steingrund P and Mikkelsen B (2022) Horizontal and Vertical Migration of Anglerfish Lophius piscatorius in Relation to Hydrography in Faroese Waters. Front. Mar. Sci. 9:823066. doi: 10.3389/fmars.2022.823066

INTRODUCTION

Anglerfish (genus *Lophius*) have an affinity for the relatively warm water masses of the mid-latitudes. The anglerfish species *Lophius piscatorius* in the northeast Atlantic is a boreal fish, which generally is distributed between the Straits of Gibraltar and the western Mediterranean Sea (Caruso, 1983) in the south, Icelandic waters in the west (Solmundsson et al., 2010) and the Barents Sea in the north (Thangstad et al., 2006). They occupy mainly muddy to gravel bottom biotopes, from the sublittoral zone to depths of around 1,000 m (Caruso, 1983; Mouritsen, 2007). Unlike the boreal zones on land, the oceanic edges of the important boreal biogeographical zone domain shift horizontally from year to year, and even more rapidly on a vertical basis.

Migration between different habitats is a common behavior among fish populations (Wootton, 1990). Seasonal migration has been directly observed or hypothesized to exist among various

Lophius species such as *L. litulon* in Japanese waters (Yoneda et al., 2002), *L. americanus* in the northwest Atlantic (Steimle et al., 1999; Richards et al., 2008), *L. budegassa* (Landa et al., 2001) and *L. piscatorius* (Laurenson et al., 2005) in the northeast Atlantic. Such migration could be due to spawning- and/or feeding activities, or as a response to thermal conditions (Wootton, 1990). Countercurrent migrations to spawning grounds are considered important as this allows passive egg and larval drift back onto suitable nursery areas (Harden-Jones, 1968) and has been suggested for *L. piscatorius* (Laurenson et al., 2001). The thermal window with optimal performance for fishes are typically narrowest for spawners, eggs and larvae and wider for juveniles and growing adults (Pörtner and Farrell, 2008), and it is expected that spawning *L. piscatorius* also have a narrow temperature preference.

The marine environment in the northeastern Atlantic is highly influenced by the presence of Modified North Atlantic Waters (MNAW) with temperatures around 8°C (Hansen and Østerhus, 2000; **Figure 1**), which is a mixture of waters with origin from the North Atlantic Current, the Bay of Biscay and from the cold subpolar gyre (SPG). The hydrographic properties of the MNAW are influenced by variations in the dynamics of the SPG, which regulates the relative contribution of cold/low-saline subarctic and warm/salty Atlantic source waters to the mixed MNAW (Hátún et al., 2005). A major weakening of the SPG after the mid-1990s resulted in a warming/salinification of the water masses in the northeastern Atlantic, and a major expansion of the boreal biogeographical zone, exemplified by a sudden northwestward expansion of both blue whiting in Faroese waters (Hátún et al., 2009a,b) and anglerfish in Icelandic waters (Solmundsson et al., 2010).

Faroe Islands are located on the Iceland-Scotland ridge (62°N, 7°W, **Figure 1**), and are embedded in the poleward flow of MNAW both on the northern and southern side of the Faroe Plateau. The environment around Faroe Islands is characterized by strong temperature gradients, and the biogeographical zonation is three dimensional in these waters (Cisewski et al., 2021). Very cold water (<0°C) flows equatorward across the seafloor of the Iceland-Scotland ridge (500–800 m), and there is a very sharp thermocline – *the main interface* – between this overflow and the inflow of MNAW. This interface constitutes a biogeographic boundary between boreal species [e.g., cod (*Gadus morhua*), haddock (*Melanogrammus aeglefinus*)] above/to the south and Arctic and subarctic species below/to the north [e.g., Greenland halibut (*Reinhardtius hippoglossoides*)]. This interface intersects the Faroe Plateau at 400–500 m depths, and outcrops in the surface north of the Faroes, as the Iceland-Faroe Front (**Figure 1**). On the Faroe Plateau, a tidal front at around 120 m depths partly separates the Central Shelf waters from the Outer Shelf (Larsen et al., 2008; Eliasen et al., 2017a) and the surrounding oceanic waters. There are, however, three main conduits on the western side of the shelf which carry oceanic/Outer Shelf waters directly onto the central shelf (Hátún et al., 2013; Eliasen et al., 2017b). The central shelf is suggested to function as a retention area that keeps fish eggs/larvae and other planktonic organisms on the shelf (Gaard and Steingrund, 2001). The shallow water around the Faroe Plateau probably serves as a nursery ground for juvenile anglerfish in Faroese waters (Ofstad et al., 2013).

Anglerfish feeding areas are generally in shallow shelf waters (<200 m), notably areas where they are well camouflaged by the bottom substrate and are visible to attract potential fish prey by using their distinctive fishing rod (Laurenson et al., 2004). Although large adult anglerfish are able to eat large predatory fish, e.g., Greenland halibut, and occasionally even also seabirds (Perry et al., 2013), their main prey in European waters are Norway pout (*Trisopterus esmarki*) and blue whiting (*Micromesistius poutassou*) (Fariña et al., 2008).

Little is known about the spawning areas of anglerfish in the northeast Atlantic and seasonal spawning and feeding migrations (ICES, 2018). It has been speculated that spawning may take place in deep water (>300 m), e.g., west of the British Isles (Tåning, 1943; Hislop et al., 2001). Also, there are indications of anglerfish spawning areas in Norwegian fjords (Bjelland and Asplin, 2007), in Icelandic waters (Solmundsson et al., 2010) and in Faroese waters (Tåning, 1943; Ofstad and Laurenson, 2007; Ofstad et al., 2013). The spawning areas in Faroese waters seem to be located southwest of the Faroe Plateau ("Skeivibanki" area) and in the Faroe Bank area (Ofstad et al., 2013). Observations of spawning males and females, egg ribbons and pelagic anglerfish larvae suggest that the main spawning season is from February to April (Ofstad et al., 2013). Long distance migration of *L. piscatorius* has been reported from mark-recapture experiments, with movements between Shetlandic-, Norwegian-, Icelandic- and Faroese waters (Laurenson et al., 2005; Thangstad et al., 2006). However, the migration rate is generally very low, indicating low mixing between these areas.

Although anglerfish rest on the seabed when feeding, they are also known to swim pelagically, and can even reside near the surface at times. Anglerfish are caught near the surface (pelagic) over deep water (>1,000 m) (Hislop et al., 2001; Solmundsson et al., 2010). Periodical vertical movements have been documented from one tagged *L. americanus*, which was most active during nights (Rountree et al., 2008).

Lophius piscatorius are common in Faroese waters (Mouritsen, 2007) while *L. budegassa* very seldomly have been caught in this area (Thangstad et al., 2006). The anglerfish stock in Faroese waters appears to be productive (Ofstad, 2013) and anglerfish have traditionally been taken as bycatch in the demersal trawl fisheries (e.g., for cod, haddock and saithe). Landings data of anglerfish in Faroese waters exist back to 1903 (Jákupsstovu, 2004). The direct fishery for anglerfish started in the early 1990s (Reinert, 1995). For the last three decades, small trawlers (<700 HP) and gillnetters have landed more than 90% of the anglerfish catches in Faroese waters. The fishery and management in Faroese waters is described in Thangstad et al., 2006 and ICES, 2021.

The aims of this paper were to investigate whether anglerfish undertake seasonal horizontal and vertical migrations and, if demonstrated, investigate possible drivers for such migrations such as reproduction and spawning, feeding and hydrographical conditions. Particularly, it was analyzed whether there were seasonal differences in: (i) horizontal and depth distributions and displacement distances and (ii) vertical activity level of anglerfish.

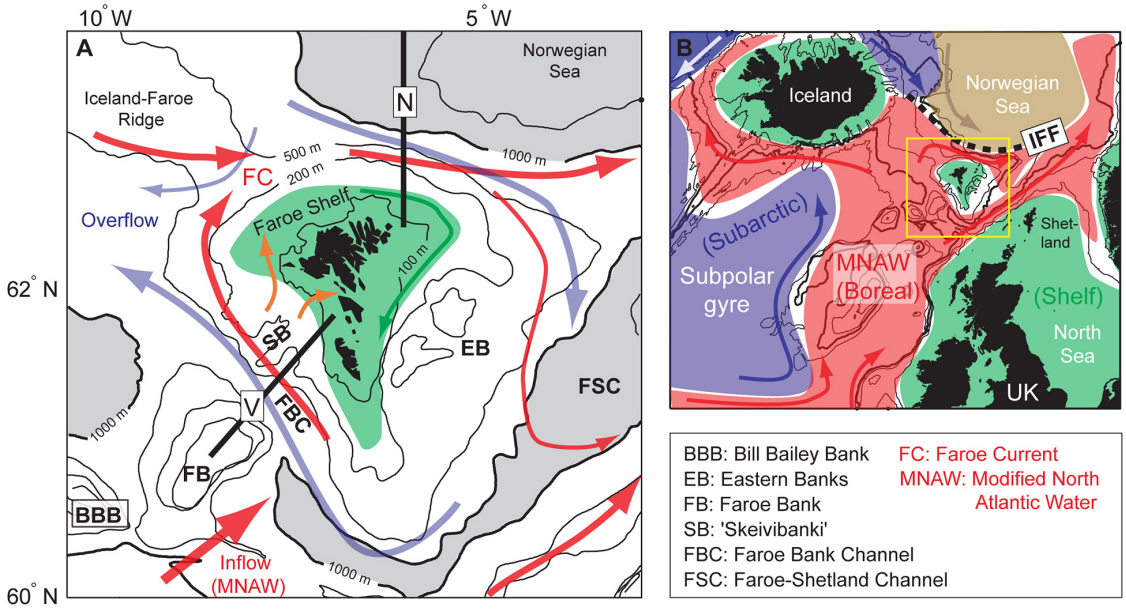


FIGURE 1 | Overview over **(A)** the Faroe shelf study region and **(B)** the broader surroundings, colored by the main biogeographic zones (*subarctic*- blue, *boreal*- red and *shelves*- green). The yellow square in panel **(B)** outlines the domain in panel **(A)**, and the black dashed line represents the Iceland-Faroe Front (IFF). Red arrows indicate relatively warm Atlantic currents and blue arrows show cold currents, which in panel **(A)** are comprised of deep overflows. The green arrow in panel **(A)** represents the clockwise central shelf circulation, while the orange arrows illustrate the main onto-shelf flows. Locations of two standard hydrographic transects (Sections N and V) are shown with black lines. The 100, 200, 500, 1,000 and, 2,000 m depth contours are shown in panel **(A)**, and the deepest regions (>1,000 m) are gray shaded.

Various methods have been used to investigate migration and movement of fish; such as information from commercial fisheries and/or catch rates from surveys (Armannsson et al., 2007), tagging by conventional tags (Solmundsson et al., 2005; Armannsson et al., 2007) and data storage tags (DSTs, Rountree et al., 2008; Armannsson and Jonsson, 2012). Here we present results of horizontal and vertical migration of anglerfish *L. piscatorius* in Faroese waters using all these methods and we relate these migrations to hydrographical conditions.

MATERIALS AND METHODS

Commercial Fishery (Catches and Logbooks)

Landing data of anglerfish in Faroese waters date back to 1903 to 2003 (Jákupsstovu, 2004). Since 2000, catch data in tons by area and gear have been derived from Statistics Faroe Islands[1] and official annual total catches from Faroese Coastal Guard.[2]

To map and compare the spatial distribution of anglerfish in May–October (summer) and in November–April (winter), logbooks from eight single trawlers (<700 HP) and three gillnetters that were targeting anglerfish in the period 2000–2010 were used. The logbooks had information on date, position and catch. To visualize the location of the main fishing areas the logbook information was split into small statistical squares (0.05°N by 0.10°W) and mapping only those squares with more than one haul and where anglerfish constituted more than 50% of the catch in weight.

Research Surveys

In addition to information from the commercial fishery, anglerfish data were also available from the annual trawl groundfish surveys during spring (February–April) and summer (August–September), as well as from dedicated anglerfish surveys during the years 2002–2003. Anglerfish catch in kg/h, lengths and trawl depths from the annual groundfish trawl surveys on the Faroe Plateau in February/March and August and on the Faroe Bank in March/April and September for the period 2000–2020 were used in this study. The Faroese bottom groundfish surveys are described in ICES (2021). The survey data from the plateau and the bank are merged, and presented as a *spring* season (February–April) and a *summer* season (August and September) (**Table 1**). In addition, data from two dedicated anglerfish surveys in February 2002 and 2003, using bottom trawl equipped with a tickler chain, were used. These anglerfish surveys covered the shallow fishing area east of the Faroe Islands at depths from 100 to 200 m, the fishing area southwest of the Faroe Islands ("Skeivibanki," 200–350 m) and on the Faroe Bank at depths from 100 to 900 m.

For visualization of spatial distributions on maps, anglerfish kg/h from each individual annual groundfish trawl survey were first log-transformed [y = *ln*(value + 1)], then gridded using

[1]www.hagstovan.fo
[2]www.vorn.fo

TABLE 1 | Year, date and number (N) of stations where bottom temperatures (Tb) and sea surface temperatures (SST) were registered in the annual spring- and summer groundfish surveys on the Faroe Plateau and on the Faroe Bank.

	Faroe Plateau						Faroe Bank					
	Spring survey			Summer survey			Spring survey			Summer survey		
Year	Date	N Tb	N SST	Date	N Tb	N SST	Date	N Tb	N SST	Date	N Tb	N SST
2000	3/3–27/3			11/8–2/9			31/3–4/4	23	21	15/9–19/9	26	26
2001	2/3–25/3			10/8–1/9			29/3–3/4	29	9	14/9–18/9	26	21
2002	1/3–25/3			10/8–3/9			4/4–8/4	29	27	13/9–17/9	28	24
2003	28/2–25/3			8/8–30/8	197	197	28/3–1/4	17	14	11/9–16/9	27	27
2004	27/2–19/3	68	68	6/8–28/8	200	146				10/9–14/9	29	29
2005	25/2–20/3	77	77	5/8–27/8	153	153				8/9–12/9	29	29
2006	23/2–16/3	100	100	4/8–27/8	200	200	24/3–28/3	24	24	7/9–11/9	29	29
2007	23/2–23/3	61	61	2/8–24/8	113	113	24/3–27/3	24	24	6/9–11/9	27	27
2008	10/3–31/3			1/8–22/8	103	103	1/4–3/4			4/9–8/9	29	29
2009	27/2–21/3			31/7–20/8	160	160	26/3–31/3	23	23	3/9–7/9	27	27
2010	27/2–20/3	100	100	6/8–25/8	199	199	25/3–30/3	29	29	9/9–13/9	29	29
2011	26/2–25/3	100	94	5/8–26/8	200	200	26/3–29/3	25	25	8/9–13/9	24	24
2012	25/2–18/3	100	100	8/9–28/9	200	200	22/3–26/3	29	29	30/9–4/10	29	29
2013	21/2–13/3	100	100	1/8–21/8	200	200	21/3–24/3			6/9–10/9		
2014	21/2–21/3	98	98	1/8–21/8	200	200	22/3–26/3			4/9–8/9		
2015	19/2–21/3	96	96	6/8–26/8			22/3–24/3			10/9–14/9		
2016	18/2–10/3	100	100	5/8–27/8	200	200	17/3–21/3	29	29	8/9–13/9	24	24
2017	24/2–24/3	86	86	3/8–24/8	199	198	26/3–28/3	16	16	7/9–12/9	28	28
2018	23/2–20/3			2/8–23/8	201		22/3–26/3			6/9–10/9		
2019	21/2–18/3			1/8–22/8	199		21/3–26/3			5/9–9/9	29	
2020	22/2–24/3			1/8–19/8			19/3–22/3			9/9–14/9		

Objective Mapping (Bohme and Send, 2005), and finally back-transformed (e^y). The annual fields were averaged prior to plotting. In addition, a cumulative frequency distribution (cdf) was applied to plot the frequency of the depth and bottom temperature measurements vs. anglerfish catch (kg/h) for the Faroe Plateau surveys for the period 2003–2019 (**Table 1**), following the example of Perry and Smith (1994). The null hypothesis of random association between anglerfish catch (kg/h) in the research trawl surveys and the habitat variable (depth or bottom temperature) were examined using a randomization procedure. A total of 2,000 randomizations were performed in each test and a p-value was calculated based on a test-statistic for deviation between the cdf for the habitat and the cdf for the catch-weighted habitat function (Perry and Smith, 1994). The mean depth distribution of anglerfish was calculated by splitting all length data pooled for 2000–2020 from the Faroe Plateau groundfish surveys and anglerfish surveys into 10 cm bins and where the mean depths and associated 95% confidence intervals were calculated in R (R Core Team, 2014).

Hydrography

We used the subpolar gyre index, described in Hátún and Chafik (2018), as a proxy for the general hydrographic (Hátún et al., 2005) and biogeographic (Hátún et al., 2009b) states in the northeastern Atlantic. A low gyre index reflects warm and saline conditions and a high index reflects colder and fresher waters around the Faroes.

During the scientific spring and summer surveys, some trawl hauls were complemented by samplings of bottom temperatures and sea surface temperatures (SSTs) (**Table 1**). The bottom temperatures were recorded by Starmon mini and/or Starmon TD sensors,[3] attached to the trawl doors, while the SST were obtained from temperature recordings from the cooling water intake of the research vessel. Bottom temperature registrations, averaged over each individual trawl haul, were available from some of the annual groundfish surveys (see **Table 1**). These data have been mapped for each respective spring and summer surveys using Objective Mapping (Bohme and Send, 2005), and subsequently averaged, in order to obtain the seasonal climatologies for each individual season.

Temperature data from two vertical standard hydrographic sections (V and N), sampled during February and late August/early September during the years 2013–2019 have been utilized. Section V extends from the Faroe Bank, across the Faroe Bank Channel and onto the Faroe shelf, while the meridional Section N (at 6°W) stretches from the north Faroe shelf and into the central parts of the Norwegian Sea (**Figure 1**). Averaged sections from the two seasons are visualized using the software Ocean Data View (ODV, R. Schlitzer, 2007[4]).

[3]www.star-oddi.com

[4]http://odv.awi.de

Mark-Recapture

Anglerfish migration in Faroese waters was investigated by mark-recapture data, and a mark-recapture project, using gillnetters, was carried out during two periods, 2005–2006 and 2009–2011, using both conventional spaghetti tags (N = 436) and Data Storage Tags (DSTs) (N = 55) (**Table 2**). The conventional tags were t-anchor tags from Floy tag Inc., Seattle, United States (FD-89sl, 3" total length, 1" monofilament, orange color). The DSTs were of the DST milli type produced by Star-Oddi (see text footnote 3), recording depth (pressure) and temperature, and where also a 10 cm yellow plastic tube was attached as an external marker (**Supplementary Figure 1**).

Anglerfish were tagged with conventional tags attached to the tail muscle, on fish of lengths from 53 to 124 cm. A new procedure was used for attaching the DSTs, that were inserted subcutaneously dorsally (**Supplementary Figure 1**; Richards et al., 2011) and not inside the buccal cavity as used in a pilot project (Thangstad et al., 2006). Details on the tagging procedure are provided in Ofstad (2013). The DSTs were programmed to record temperature and depth minimum once every hour. In addition more intensive recordings were applied for selected time intervals (Ofstad, 2013). However, here only data recorded once every hour were used, the first three days of data were excluded and only fish recaptured more than one month after tagging were used in the analysis. Recapture rate of anglerfish tagged from gillnets in Faroese waters was relatively high, 10% for conventional tags and 27% for DSTs (**Table 2**).

In order to investigate potential changes in migration during the year, data was divided in four seasons; (November–February, March–April, May–August, and September–October). Vertical activity was defined as instances when the fish changed depth by more than 5 m from one registration to the next registration 60 min later, and only DST data recordings every full hour (e.g., 12:00, 13:00) were used. A vertical activity index (%) was calculated as total number of vertical activity registrations × 100/total registrations for a given time period (each month or by each hour of the day in each season). The vertical activity index was calculated for the 10 DSTs individually. The vertical activity index (%) by month was used to investigate whether anglerfish had seasonal changes in vertical activity, whereas the vertical activity index (%) by hour (of day in particular seasons) explored seasonal changes in diurnal vertical activities. Hours of high vertical activity were calculated as the hours per month where the vertical activity index was larger than 3% (Ofstad, 2013). The sun angle at the Faroe Islands (62°N, 7°W) was calculated using the solar position algorithm by Reda and Andreas (2004) (**Supplementary Table 1**).

TABLE 2 | Overview of the Faroese mark-recapture project of anglerfish tagged from gillnets north of the Faroe Islands.

Period	Gear	Season	Floy tags		Data storage tags	
			Tagged	Recapture (%)	Tagged	Recapture (%)
2005–2006	Gillnet	Jun–Sep	370	37 (10.0)		
2009–2011	Gillnet	May–Jul	66	10 (15.2)	55	17 (30.9)

RESULTS

Anglerfish Catches and Major Shifts in Marine Climate

The anglerfish catches in Faroese waters reached a maximum of more than 5,000 tons in 2005–2006, thereafter dropping to moderately high values of around 2,200–2,500 tons in 2008–2011, and declined to low pre-1995 values of less than 1,400 tons in 2012–2018 (**Figure 2**). The catches have again increased to moderately high values of around 2,600 tons in 2019–2020.

There appears to be a link between the increase and decrease in anglerfish landings (abundance) in Faroese waters and a weakening and subsequently intensification of the subpolar gyre index (SPG, **Figure 2**). The SPG weakened abruptly in 1996 (note inverse gyre index scale in **Figure 2**), and was in a generally weakened state, with warm and saline conditions in the NE Atlantic (low gyre index), until 2013. During the years 2014–2016, the SPG strengthened back to the strong state of the early 1990s (Hátún and Chafik, 2018), but it has yet again weakened to moderate size/strength in 2019.

The first tagging period (2005–2006) thus coincided with very high anglerfish catches/abundances, while the second tagging initiative occurred during a period with moderate catches/abundances (2009–2011), as emphasized with the gray bars in **Figure 2**.

Main Fishery Areas of Anglerfish

Commercial logbook data showed that the main anglerfish fishing areas for small trawlers (<700 HP) differed during the year with a deeper distribution in November–April (**Figure 3A**) than during May–October (**Figure 3B**). There were two distinct trawl fishing areas in winter; one southwest of the Faroe Islands, where there is an indentation in the Faroe slope called "Skeivibanki," and the

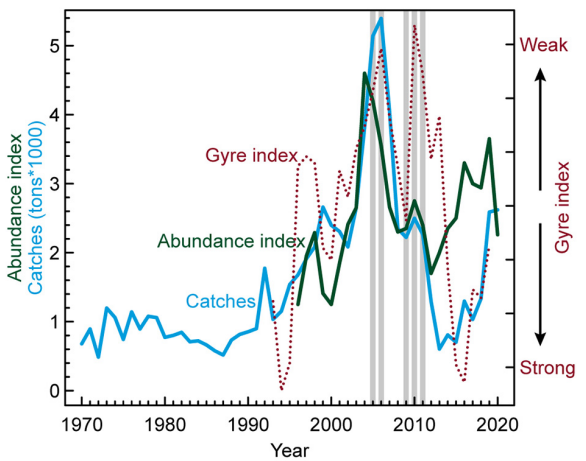


FIGURE 2 | Catches of anglerfish in Faroese waters (1970–2020), abundance index of proportion of anglerfish-hauls in the summer groundfish survey (1996–2020) and the gyre index (1993–2019). The gillnet anglerfish tagging years are indicated with gray vertical bars. The northeastern Atlantic is anomalously warm when the gyre index is weak.

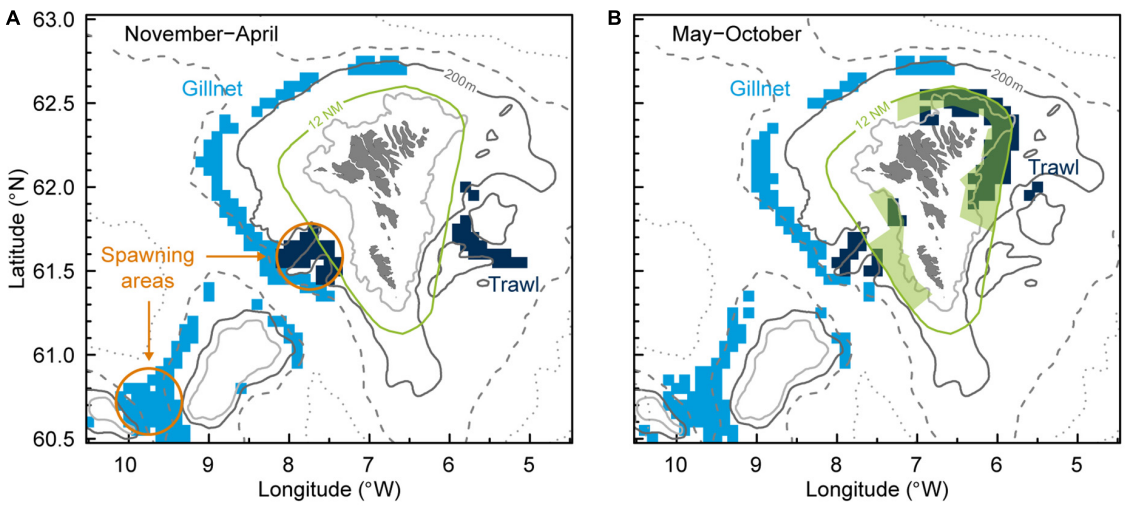


FIGURE 3 | Main anglerfish fishing areas in Faroese waters (anglerfish constituted more than 50% of the catch in weight per settings/hauls) are shown for gillnet and trawl less than 700 HP in panel **(A)** November–April and **(B)** May–October. Depth contours shown for 100, 200, 500, and 1,000 m. Anglerfish spawning areas are indicated as orange circles (Ofstad et al., 2013). Note that there are both annually and seasonally closed areas for trawling, on both the Faroe Plateau and Faroe Bank (ICES, 2021), and that some shallower areas inside 12 NM around the Faroe Islands are only open for small trawlers (<700 HP) during summer (green areas).

other one southeast of the Faroes, in a region referred to as the Eastern Banks (Eliasen et al., 2016). During summer, most of the trawling activity took place along an area on the shallower central shelf, north and east of the Faroe Islands (**Figure 3B**). Note that this shallow area was only open for small trawlers (<700 HP), mainly during May to August (ICES, 2021).

There was no apparent seasonal shift in the gillnet fishery. The gillnetters were fishing in deep waters (>380 m) on the slopes west and north of the Faroe Islands, in addition to the area between the Faroe Bank and Bill Bailey Bank farther west (**Figure 3**). The gillnetters are restricted to fish deeper than 380 m on the shelf area, except for one gillnetter that was allowed to fish shallower in an area north of the Faroe Islands.

Spatial Distribution of Anglerfish From the Groundfish Surveys

Catches from the annual spring- and summer groundfish surveys on the Faroe Plateau and on the Faroe Bank generally overlap and confirm the spatial patterns derived from the commercial fishing activity. The spatial distribution of anglerfish was well described by the surveys (**Figures 4A,B**). The cumulative distribution functions for bottom depth and catch-weighted depths deviated significantly for both the spring survey (p = 0.0005) (**Figure 5A**) and the summer survey (p = 0.0005) (**Figure 5B**), indicating that anglerfish occupy a deeper depth range within the survey area during the spring survey and oppositely, anglerfish occupy a shallower depth range during the summer survey. Note that the catch rates were much higher in August than in March (2.6 vs. 1.2 kg/h, **Supplementary Table 2**).

Spring Survey (February–March)

During the main spawning period in February–April, anglerfish clearly congregated in the "Skeivibanki" area and to the west of the Faroe Bank (**Figure 4A**). There was also a small concentration of fish east of the Faroe Islands (∼6°W), however slightly shallower than what appeared from the trawl fisheries (see **Figure 3A**). The fish abundance in this eastern region was much lower than in the two western areas. Anglerfish also congregated in deeper waters along the northwestern margin of the Faroe slope (**Figure 4A**).

Summer Survey (August–September)

Anglerfish concentrations were more spread out during August–September, compared to spring, and there was a clear movement toward shallower waters (**Figure 4B**). There were still high abundances NW off the Faroe Bank, and just inside the "Skeivibanki" area, in a region previously referred to as the Western Region (Hátún et al., 2013). The highest abundances during late summer were, however, on the eastern side of the Faroe shelf (∼62°N, 6°W), where also large trawling activity took place (**Figure 3B**).

Size-Differentiated Mean Depth Residence

Survey data from the Faroe Plateau showed that the medium sized anglerfish (40–60 cm) generally occupied the shallowest waters (**Figure 6**), while both the smaller fish (<40 cm) and especially the larger fish (>60 cm) occupied deeper waters. This difference was most pronounced during the spring surveys when the small fish moved out to ∼250–300 m depths, and the largest fish moved to depths deeper than 250 m whereas the medium size anglerfish occupied the 150–250 m depth range. During the summer surveys, all fish sizes generally stayed in waters shallower than 250 m (**Figure 6**).

Hydrography

Averaged (years) horizontal surface and bottom temperature fields, based on data from the groundfish surveys (2000–2020,

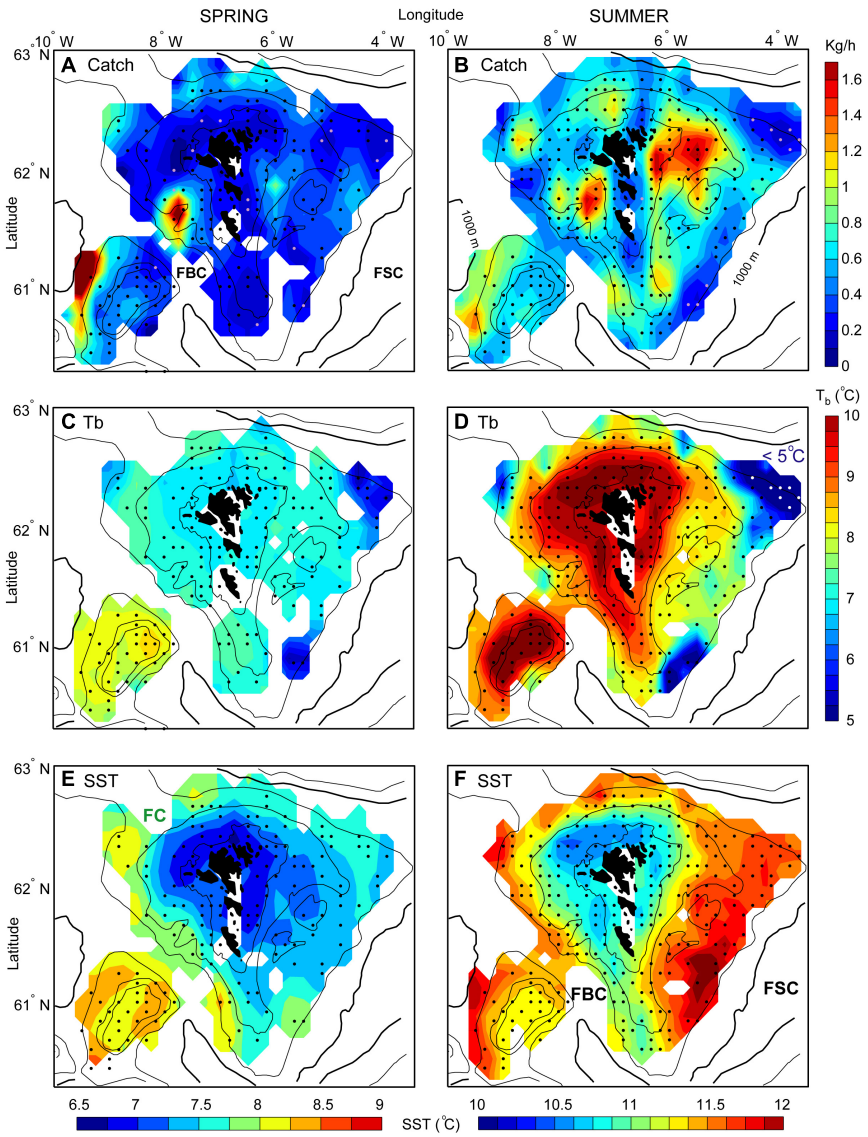


FIGURE 4 | Distribution of anglerfish (catch, kg/h), bottom temperatures (Tb) and Sea Surface Temperature (SST) in Faroese waters from two annual Faroese groundfish surveys in spring **(A,C,E)** and summer **(B,D,F)**. The data are gridded for each seasonal survey, and averaged over the years 2000–2020 (see "Materials and Methods"). The 100, 200, 500, and 1,000 m depth contours are shown. The black dots [and a few light purple dots when 0 anglerfish is caught in panels **(A,B)**] represent standard trawl station positions for each season. Note that the darkest blue coloring in panel **(D)** can have temperatures lower than 5°C (indicated by the white dots). FBC, Faroe Bank Channel; FSC, Faroe-Shetland Channel. Note that the color scales are different for the catch, Tb and SST data.

Table 1), and averaged vertical transects (2013–2020) from the Faroe Bank across the Faroe Plateau and north into the Norwegian Sea, provided an oceanographic context that was vital for the interpretation of both the survey-based anglerfish distributions and the fish tag data (see below).

Spring (February–March)

During spring, the study region was characterized by relatively high temperatures on the western side of the Faroe Plateau, and along the clockwise path of the Faroe Current around the plateau. This was evident both in the bottom temperatures (**Figure 4C**) and in the sea surface temperatures (SSTs) (**Figure 4E**). Lateral temperature gradients between oceanic and shelf waters were therefore much stronger on the western and northern sides, compared to the eastern side. Bottom temperatures in the spawning regions at "Skeivibanki" and along the NW slope were around 7–7.5°C during this period, while the region NW of the Faroe Bank was dominated by water layers warmer than 8°C. Temperatures on the central shelf were below 7°C, both at the bottom and at the surface (**Figures 4C,E**, **7A**), and thus lower than the surrounding water masses. A closer inspection of the temperature registrations from the trawl hauls showed that anglerfish in spring were mainly caught in temperatures from 5 to 8°C (c.f. **Figures 4A,C**

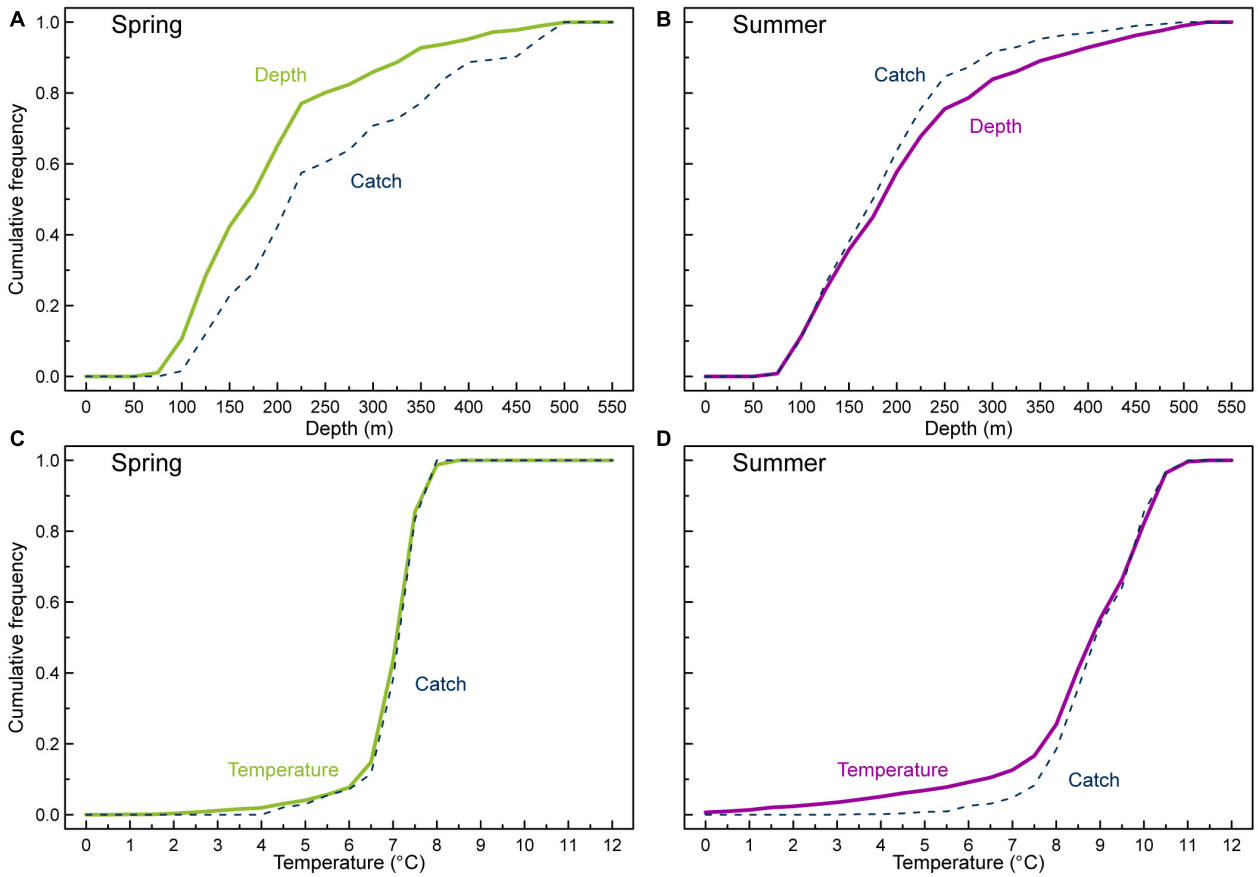


FIGURE 5 | Cumulative frequency distribution of depth and temperature together with anglerfish catch weighted functions from the Faroe Plateau surveys for spring **(A,C)** and summer **(B,D)**.

and **Supplementary Table 2**). The cumulative distribution functions for temperature and catch-weighted temperatures from the spring survey did not deviate significantly (p = 0.42) (**Figure 5C**), indicating that anglerfish were not seeking out a particular range of temperatures within the survey area during this season.

Summer (August–September)

A firmly established tidal front in late summer created a "halo" around the plateau, located between the 100 and 200 m isobaths (**Figures 4D,F**). SST was still lowest within the halo, while the bottom temperatures on the central shelf were higher than in deeper waters. During the August survey, the largest catches of anglerfish were taken within, or at the boundary of, this "halo" (c.f. **Figures 4B,D,F**) at bottom temperatures in the range 8–10.5°C, and SSTs in excess of 10.8°C. A closer trawl-by-trawl inspection revealed significant catches in waters as cold as 5.5°C, suggesting that anglerfish did seek the locations where the main interface intersected the seafloor, also during summer (**Supplementary Table 2**). The cumulative distribution functions for temperature and catch-weighted temperatures from the summer survey deviated significantly (p = 0.002) (**Figure 5D**), indicating that anglerfish were seeking out a warmer temperature range within the survey area.

The Main Interface

Very few anglerfish were caught in temperatures below 5°C (**Figures 5C,D** and **Supplementary Table 2**). This isotherm, which marks the vertical boundary between the Atlantic water above, and subarctic and overflow waters below (i.e., the main interface, Cisewski et al., 2021; Hátún et al., 2021), was, on average, located at ∼500 m depths in the Faroe Bank Channel (**Figure 7**). It intersected the seafloor at ∼450 m at the northern Faroe slope, from where it ascended northwards, and outcropped at the surface as the Iceland-Faroe Front (at ∼350 km in **Figure 7B**). The position of this interface was roughly the same in spring and summer, although strong near-surface thermal stratification in August/September obscured any clear outcropping in the Iceland-Faroe Front.

The bottom temperature maps show two "cold spots" (<5°C) along the border of the Faroe-Shetland Channel, which reveals locations where the main interface intercepts the seafloor (**Figures 4C,D**). At the NE corner of the Faroe Plateau (∼62.5°N, 4.5°W), cold waters from underneath the Faroe Current turned southwards into the Faroe-Shetland Channel and near the

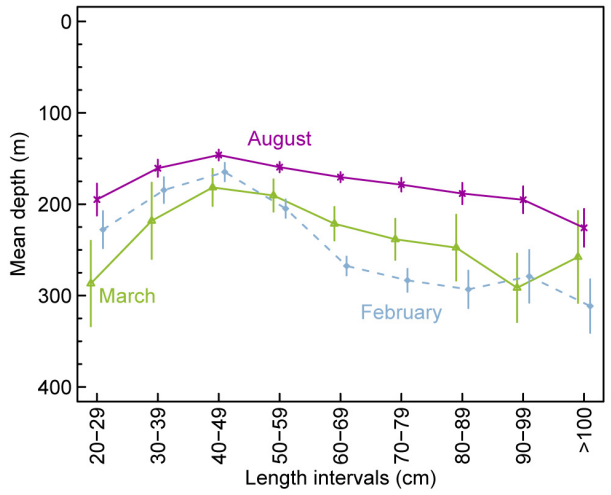


FIGURE 6 | Mean depth distribution of anglerfish versus anglerfish size from the groundfish survey (2000–2020) on the Faroe Plateau in late February/March (lime) and August (purple line), and from the anglerfish survey during February in 2002 and 2003 (stippled light blue line). The bars indicate 95% confidence intervals.

southern tip of the plateau (~61°N, 6°W), cold waters from the Faroe-Shetland Channel pressed up against this deeper part of the plateau (the Eastern Banks) (Berx et al., 2013). Anglerfish completely avoided these cold spots, as is emphasized by the light dots in **Figure 4D**. At the NW side of the plateau (~62.5°N, 8.5°W), there was a third region with relatively cold bottom water, which likely reflected the presence of Iceland-Faroe Ridge overflow water (Beaird et al., 2016).

Migration of Anglerfish Based on Conventional Tagging

The results from 60 recaptured anglerfish tagged with conventional tags showed that the displacement distances between tagging position and recapture position ranged from 2.4 to 636.0 km. Of the anglerfish tagged from gillnets north of the Faroe Islands in summer (May–August), only 27% of the recaptures from the winter period November–February had displacement distances of less than 30 km. Most of these fish moved from the tagging region north of the Faroe Islands and southwest to the "Skeivibanki" region with depths >200 m, bordering the Faroe Bank Channel (**Figure 8A**). In addition, in the period March–April, some of the tagged fish were recaptured on the slope southwest of the tagging site. In contrast, 82% of the fish recaptured during the following summer (May–August) had displacement distances of less than 30 km and almost all were recaptured at depths less than 200 m (**Figure 8B**). This could suggest homing migration behavior since the fish were recaptured relatively close to the tagging site. The homing behavior is further supported by two anglerfish recaptured with DSTs in June and July at around 200 m depth close to the tagging site, after one year in liberty, during which period they had also been in deep water (<300 m) in the winter (**Supplementary Figure 3**). Only two out of 60 recaptured anglerfish had performed long distance migrations, one recaptured in Icelandic waters and one in Norwegian waters.

Depth and Temperature Range of Anglerfish Based on Data-Storage Tags

A total of 10 DST tagged anglerfish, >70 cm long at tagging and with time at liberty of more than three months, were recaptured. All 10 fish showed large shifts in distribution depths (**Figure 9A**), which reflects a clear offshore-onshore seasonal migration. Similar to the survey data, the tagged fish occupied shallow waters (<200 m depth) during the summer (May–September) and deep waters (>300 m) during the winter (November–February) (**Table 3** and **Figure 9A**). Intermittent periods were recognized in September–October and March–April, when the depth distributions showed a transitional phase.

The DSTs ambient temperature readings showed that anglerfish mostly occupied water warmer than 7°C, regardless of the time of the year (**Figure 9B** and **Table 4**). During spring (February–March), the fish occupied waters of around 7°C, which is the typical bottom temperature at the slope of the Faroe Plateau during this season (**Figures 4**, **7**). The deepest registration was 525 m. Although anglerfish rarely moved deeper than 450 m (**Figure 9A**), the DSTs occasionally recorded water temperatures much colder than 7°C, in extreme case below 2°C (**Figure 9B** and **Supplementary Figures 2, 3**). This coincided with vertical undulations of the main interface (**Figure 7**; Cisewski et al., 2021; Hátún et al., 2021), which can lift frigid overflow type waters up toward the areas inhabited by anglerfish, probably the spawning region of anglerfish – both at the west and north Faroe slope. This dynamics was exemplified by hourly shifts in temperature for single fishes by as much as >6°C (from 0.2 to 6.5°C) (**Supplementary Figures 2, 3**). This rapid temperature change (0.7–5.6°C) from one hour to the next was only registered in the deeper water during winter (November–February, **Figure 9B**). Anglerfish never occupied cold water masses below 4°C for longer periods than one day.

During late summer, the fish were distributed in waters of 9–10.5°C (**Table 4**). This result complied with the average depth distribution of anglerfish, spatially (**Figure 4B**) and vertically (**Figure 9A**), and with the average bottom temperatures at these locations and during this season (**Figures 7B**, **9B**).

Individual anglerfish apparently undertook pronounced vertical migrations as shown by the rapid changes in depth from >150 to 0–80 m (**Figure 9A** and **Supplementary Figures 2, 3**). Presumed vertical movement pattern, which was observed during all months of the year, almost always resulted in the occupation of a different bottom depth when settled to the bottom again (**Supplementary Figures 2, 3**).

Vertical Activity of Anglerfish Based on Data-Storage Tags

Incidences of vertical activity for anglerfish in Faroese waters amounted to 5% of all depth registrations, and were more frequent during the late autumn and winter time than during the summer time (**Figure 10A**). There was also a close linkage

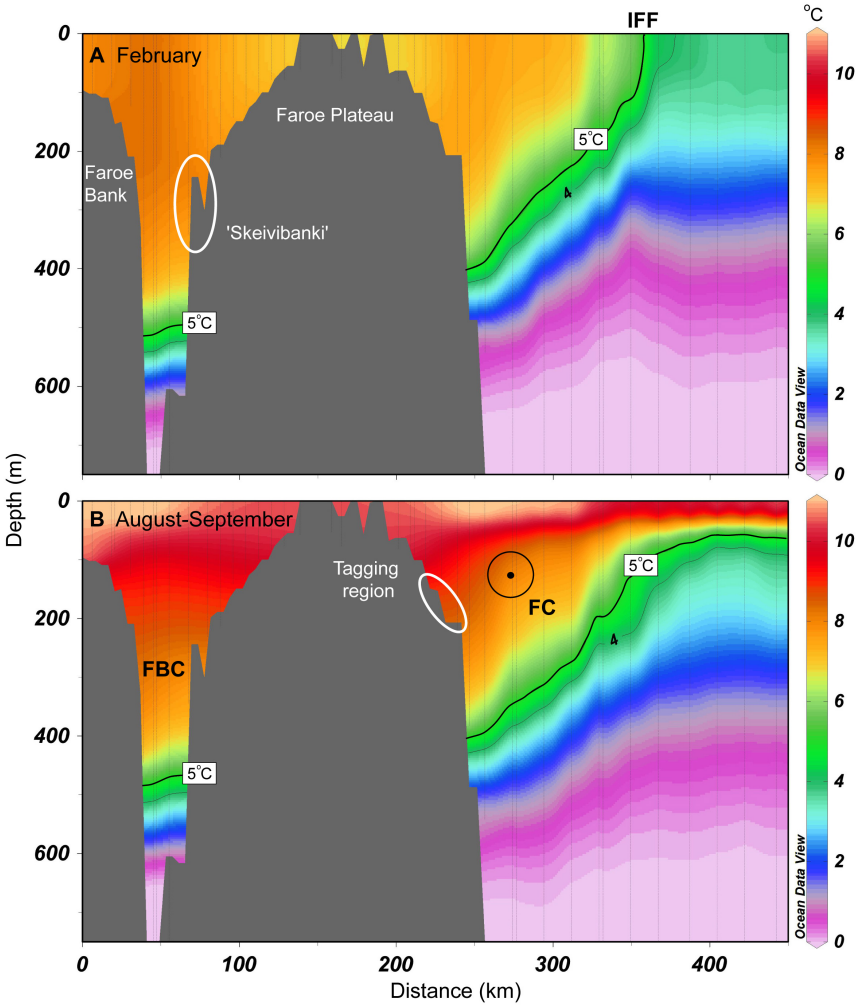


FIGURE 7 | Average temperature sections (2013–2018) from the Faroe Bank, across the Faroe Plateau and following Section N toward north during **(A)** February and **(B)** late August/early September. The 5°C isotherm (and weakly the 4°C) is emphasized with black lines. This illustrates the lower tolerance of anglerfish, and it also coincides with the main interface between the upper MNAW and the underlying cold overflow source waters. Ovals show the spawning region near "Skeivibanki" **(A)** and the tagging region **(B)**. FBC, Faroe Bank Channel; IFF, Iceland-Faroe Front; FC, Faroe Current (directed out of the paper).

between vertical activity and the timing of sunrise and sunset (**Supplementary Table 1**) as the fish were most active during the night and became passive soon after sunrise (**Figure 10B**). The linkage between the activity index and the timing of sunrise and sunset holds for all seasons (November–February, March–April, May–August and September–October), and there were therefore more hours of high vertical activity during the day in winter time than during the day in summer time (**Figure 10B**).

DISCUSSION

Our study region on and around the Faroe Plateau and the Faroe Bank is located close to cold-side boundaries of the boreal biogeographic zone, both horizontally and laterally. The southwestern approach of the Atlantic water currents makes the western side of the Plateau warmer, while the eastern side is colder, and thus closer to the edge of the boreal zone. Immediately under the Atlantic waters, and north of the Iceland-Faroe Front, the environment is much colder and truly (Sub-) Arctic.

The boreal anglerfish in Faroese waters generally occupies Atlantic waters, and is therefore in favorable temperature conditions. Because of the sharp lateral and vertical temperature gradients between the Atlantic and subarctic waters, anglerfish may, however, approach their distribution limit during their seasonal migration to deeper layers. Small changes to the marine climate may therefore influence the dynamics of this fish stock.

The previously reported two-step weakening of the subpolar gyre around 1997 and 2003 (Hátún et al., 2005), and the following "borealization" of the northeastern Atlantic (Hátún et al., 2009b), did apparently result in increased abundances of anglerfish in Faroese waters (**Figure 2**). The fish tag data, used in the present study, were obtained from this warm period.

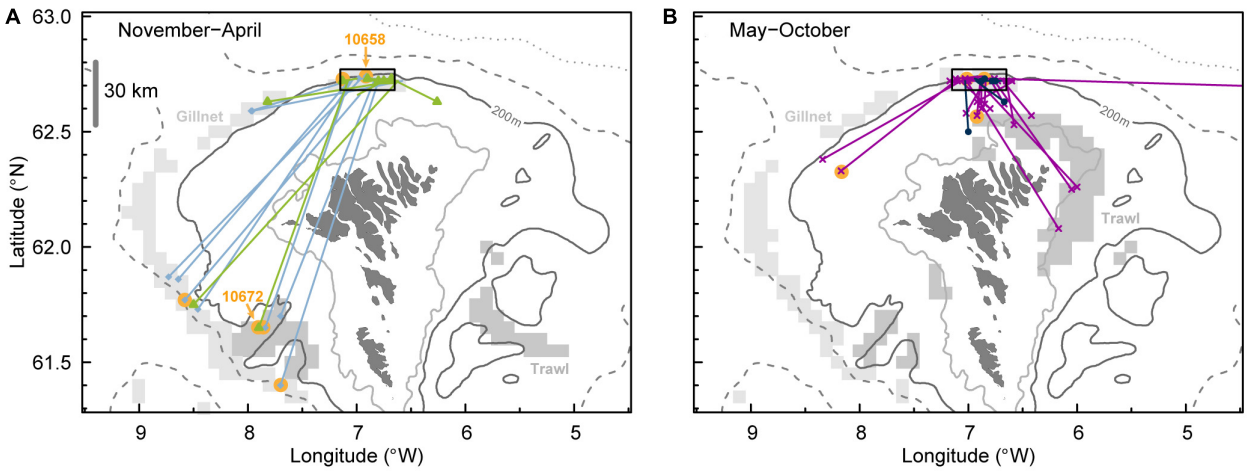


FIGURE 8 | Horizontal movements of anglerfish tagged from gillnet north of the Faroe Islands (black rectangle) mainly in May–August. Recaptures during winter/spring are shown in panel **(A)**, differentiated between November–February (light blue) and March–April (lime). Recaptures during summer/fall are shown in panel **(B)**, differentiated between May–August (purple) and September–October (dark blue). The orange dots represent recapture of anglerfish with data storage tags and results from DST 10672 and DST 10658 are presented in **Supplementary Figures 2, 3**. Depth contours are shown for 100, 200, 500 (dashed), and 1,000 m (dotted). The main fishing areas are presented for small trawlers (gray rectangles) and gillnetters (light gray rectangles) (from **Figure 3**).

TABLE 3 | Depth registrations once per hour as percentages of total registrations per months.

Depth (m)	Month												
	Jan	**Feb**	**Mar**	**Apr**	**May**	**Jun**	**Jul**	**Aug**	**Sep**	**Oct**	**Nov**	**Dec**	**Total**
<50			0.0	0.1	0.2	0.0	0.1	0.1	0.0	0.3	0.1	0.0	0.1
50–100	0.2	0.0	1.7	2.2	1.0	0.4	**13.3**	**14.8**	3.1	2.6	2.5	0.1	3.9
100–150	6.3	**10.5**	**63.5**	**49.4**	**59.9**	**74.5**	**56.9**	**58.6**	**45.1**	**43.3**	**19.1**	**15.9**	**41.3**
150–200	**24.3**	**26.3**	**20.5**	**47.2**	**39.0**	**24.0**	**28.1**	**26.2**	**41.3**	**34.5**	**34.7**	**37.6**	**32.0**
200–250	6.0	6.3	5.3	1.1		1.1	1.6	0.3	5.0	**11.9**	**12.4**	6.0	5.1
250–300	4.8	3.2	0.4					0.0	3.8	6.0	**13.7**	8.2	3.8
300–350	8.0	8.4	2.1						1.6	1.5	4.8	7.1	2.8
350–400	**24.8**	**17.3**	1.2						0.0		8.2	**12.6**	5.2
400–450	**19.1**	**15.9**	2.8								4.4	**12.5**	4.3
450–500	6.5	**11.0**	2.0										1.3
500–550		1.3	0.4										0.1
Total reg.	6,889	4,844	4,366	3,578	6,289	6,800	7,531	8,071	7,867	8,783	8,425	7,577	81,020
Median	352.4	319.3	137.9	148.3	144.7	136.1	122.0	122.4	152.6	153.5	194.1	192.7	
SE	1.35	1.74	1.25	0.46	0.34	0.28	0.35	0.33	0.54	0.53	0.95	1.19	

Data are pooled from 10 recaptured anglerfish with DST. Bold values indicate more than 10% time in given depth interval.

Seasonal Migration and Depth Distribution

A clear seasonal offshore-onshore migration of anglerfish in Faroese waters is revealed by the DSTs data, and this pattern is further supported by the recaptures of conventionally tagged anglerfish, depth distribution of anglerfish caught in surveys and logbook data from commercial trawlers. The overall pattern showed that the fish congregated at "Skeivibanki" on the western side of the Faroe Plateau, and along the northwestern slope of the Faroe Bank during the winter/spring spawning period (**Figures 3A**, **4A**). This pattern, and results in Tåning (1943); Ofstad and Laurenson (2007), and Ofstad et al. (2013), suggests that the two mentioned locations are spawning hotspots for anglerfish. Anglerfish migrate offshore from the Faroe shelf in November to February, which is the spawning season (Ofstad and Laurenson, 2007; Ofstad et al., 2013), and more than 80% of the anglerfish with high gonadosomatic indices or with maturity stage of ripe or running gonads were caught deeper than 200 m mainly in the "Skeivibanki" area and west of Faroe Bank in the period January to April (Ofstad et al., 2013).

The "Skeivibanki" region is located upstream of a main conduit of oceanic water onto the Faroe shelf (**Figure 1**), and this influx will therefore advect the offspring onto the Faroe Plateau. Ofstad et al. (2013) showed that the depth distribution of small

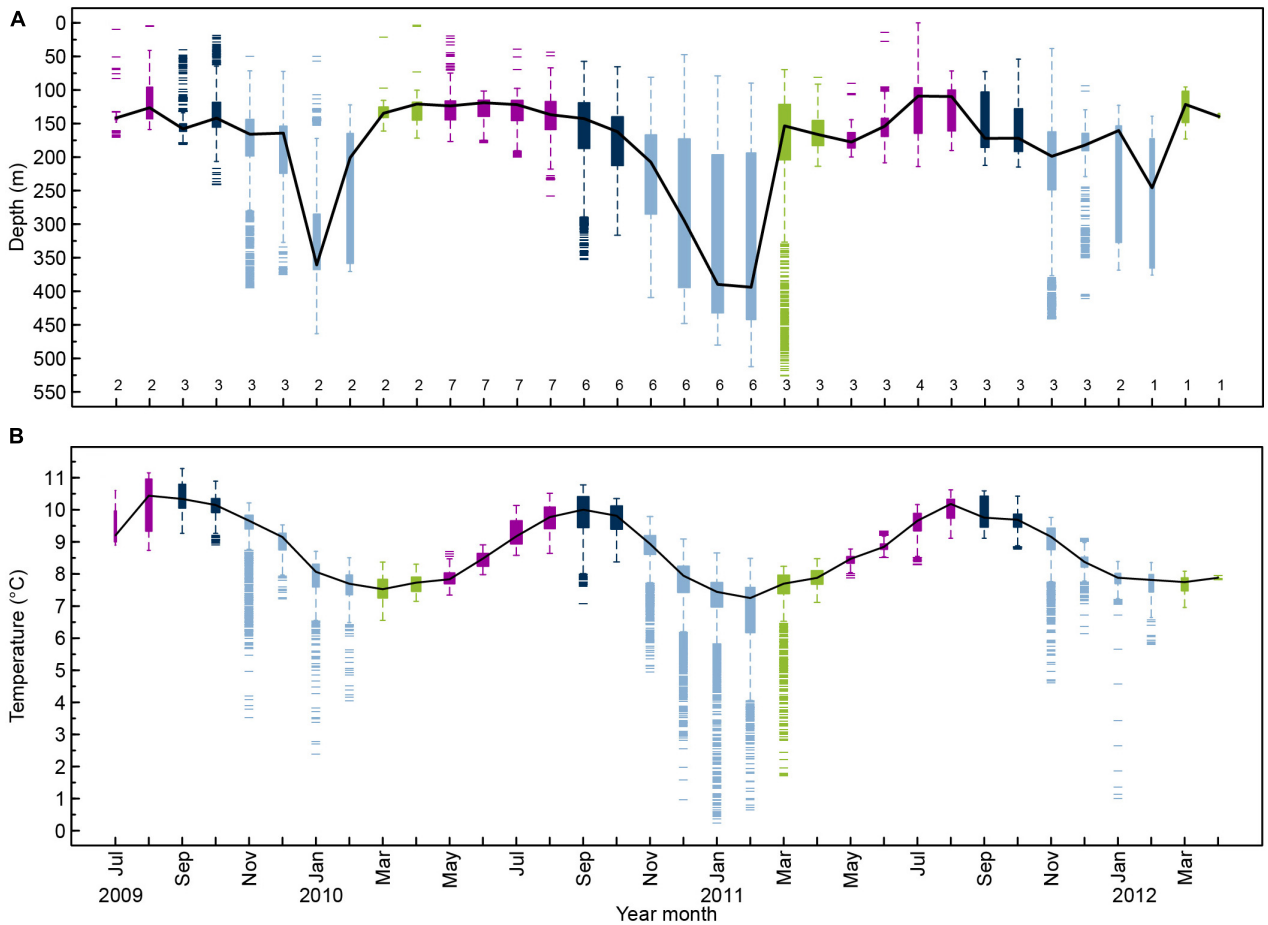


FIGURE 9 | Distributions of **(A)** depth and **(B)** ambient temperature per month for the period July 2009 to April 2012 from pooled DST data of 10 anglerfish larger than 70 cm. The numbers inside the *x*-axis is number of anglerfish. The black line is the median, the box represents the upper and lower quartile, the error bars are upper and lower extremes (excluding outliers) and the short lines are outliers. The outliers are defined as values 1.5 times larger than the inter-quartile range. The width of the box indicates the sample size (a broader box indicates larger sample size). The colors indicate different seasons.

anglerfish (<50 cm) was relatively stationary, and concluded from this evidence that the Faroe Plateau, shallower than around 300 m, is a nursery area.

After spawning in late winter/spring, adult anglerfish migrate shoreward and disperse over the Faroe Plateau, although with congregation in relatively shallow waters east of the islands (**Figure 4B**). The waters northwest of the Faroe Bank, and near "Skeivibanki" are, however, still occupied during summer. The shallower distribution in the summer (**Figure 6**), at depths between 100–200 m, indicates that, in addition to being a nursery area, the Faroe Plateau is probably also a main feeding area. Diet analyses indicated that the stomach fullness index in summer time was higher in shallow water (<200 m) compared to deep waters (>200 m) (Ofstad, 2013). Also, many potential prey species, such as cod (*Gadus morhua*), haddock (*Melanogrammus aeglefinus*), blue whiting (*Micromesistius poutassou*), Norway pout (*Trisopterus esmarkii*) and lemon sole (*Microstomus kitt*), were available in relative high abundance at these depths in summer (Steingrund et al., 2009).

Tagging data demonstrate that anglerfish migrated more than 30 km from the feeding areas to their spawning site during the winter season and arrived "home" again to their feeding area, close to the tagging site, the following summer (see example in **Supplementary Figure 3**). During summer, however, anglerfish were fairly stationary. We therefore hypothesize that anglerfish undertake homing migrations, similar to the behavior of cod in Faroese waters (Joensen et al., 2005). Faroese anglerfish were very rarely recaptured in foreign waters which is in accordance with previous mark-recapture studies showing low mixing between regions (Laurenson et al., 2005; Thangstad et al., 2006). The seasonal movement pattern of anglerfish in Faroese waters thus seems to fit nicely into the concept of the fish migration triangle (Harden-Jones, 1968) with the nursery area located on the Faroe Plateau, and where adult fish migrate off the Faroe Plateau during the winter to deeper spawning areas, especially in the "Skeivibanki" area and back onto the Faroe Plateau for feeding in summer.

TABLE 4 | Temperature registrations once per hour as percentages of total registrations per months.

Temp. (°C)	Month												
	Jan	**Feb**	**Mar**	**Apr**	**May**	**Jun**	**Jul**	**Aug**	**Sep**	**Oct**	**Nov**	**Dec**	**Total**
11–11.5								1.4	1.8				0.3
10.5–11							0.0	8.0	**17.5**	3.2			2.8
10–10.5							2.3	**36.2**	**33.9**	**34.8**	1.6		**11.0**
9.5–10							**40.3**	**26.1**	**23.9**	**39.6**	**24.2**	0.0	**15.5**
9–9.5						4.7	**29.7**	**26.9**	**14.4**	**16.3**	**33.9**	**14.6**	**13.9**
8.5–9	2.3	0.1			**13.2**	**58.6**	**27.6**	1.4	5.5	6.0	**23.2**	**15.1**	**13.9**
8–8.5	**18.9**	**12.3**	**14.0**	**27.8**	**39.6**	**36.6**	0.2		2.3	0.1	8.0	**38.1**	**15.1**
7.5–8	**37.6**	**32.8**	**48.5**	**53.8**	**43.1**	0.1			0.6		3.3	**15.8**	**15.4**
7–7.5	**21.9**	**27.8**	**29.0**	**18.3**	4.0				0.0		2.7	7.5	7.2
6.5–7	7.5	7.6	4.2								1.6	2.6	1.7
6–6.5	4.1	5.4	0.7								0.8	2.4	1.0
5.5–6	2.6	4.1	0.8								0.4	1.6	0.7
5–5.5	1.5	2.8	1.1								0.2	0.7	0.4
4.5–5	0.9	2.7	0.5								0.1	0.5	0.3
4–4.5	0.8	1.9	0.3								0.0	0.4	0.2
3.5–4	0.3	1.0	0.3								0.0	0.3	0.1
3–3.5	0.3	0.6	0.3									0.2	0.1
2.5–3	0.2	0.6	0.1									0.2	0.1
2–2.5	0.2	0.1	0.1										0.0
1.5–2	0.3	0.1	0.1									0.0	0.0
1–1.5	0.3	0.0											0.0
0.5–1	0.2	0.1										0.0	0.0
0–0.5	0.1												0.0
Total reg.	6,889	4,844	4,366	3,578	6,289	6,800	7,531	8,071	7,867	8,783	8,425	7,577	81,020
Median	7.6	7.4	7.6	7.8	8.0	8.6	9.4	9.9	10.1	9.8	9.1	8.2	
SE	0.012	0.016	0.010	0.005	0.004	0.003	0.005	0.006	0.007	0.005	0.008	0.011	

Data are from 10 recaptured anglerfish with DST. Bold values indicate more than 10% time in that interval.

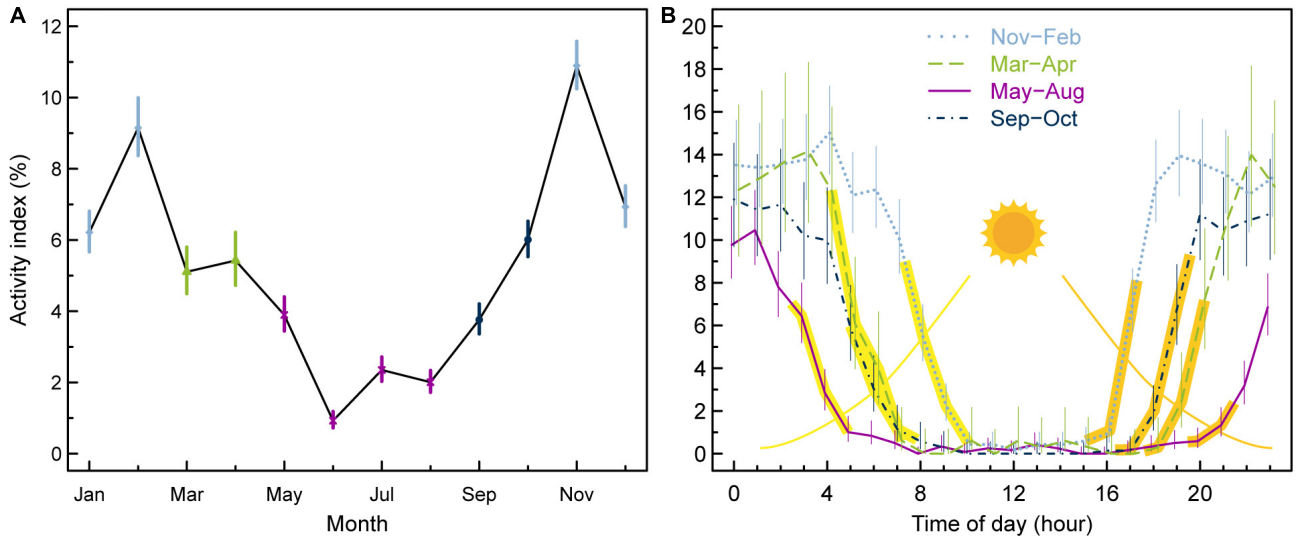


FIGURE 10 | Activity index (%) per month **(A)** and per hour of the day **(B)** for four seasons from pooled DST data of 10 anglerfish larger than 70 cm. The yellow/orange areas indicate the ranges of sunrise/sunset for the different periods (**Supplementary Table 1**). The error bars indicate 95% confidence intervals.

Seasonal migration was also shown for anglerfish in Shetland waters from conventional tagging, where recaptured fish had moved offshore in November to April (Laurenson et al., 2005). This suggested that anglerfish dispersed from inshore grounds in autumn, and Shetland fishermen informed that the areas toward the shelf edge were targeted in the winter period due to high catch rates (Laurenson et al., 2005). Such migration was also shown for *L. americanus* on Georges Bank (Siemann et al., 2018). Similar seasonal shifts in distribution have been observed for other fish species on the Faroe Plateau, including cod (Tåning, 1940; Ottosen et al., 2017), saithe (*Pollachius virens*) (Homrum, 2012) and plaice (*Pleuronectes platessa*) (Tåning, 1943).

Congregation Near the Main Interface

The DSTs show that anglerfish migrate into deeper waters after November, and generally occupy depths of 350–400 m, during winter (**Figure 9A**). This was close to the average position of the main interface between warm Atlantic water and the cold underlying Arctic water (**Figure 7**).

The boreal anglerfish clearly has an affinity for warmer waters, and were seldom caught in waters with temperatures below 4°C, which is the same lower limit as reported for Icelandic waters (Solmundsson et al., 2010) and Norwegian waters (Anonymous, 2012). However, tags on fish that resided stationary at around 400 m depths recorded rapid temperature drops to below 2°C (**Figure 9** and **Supplementary Figures 2, 3**), which demonstrates that anglerfish positioned themselves in, or near, the zone where internal bores carry cold waters upslope. This behavior was, however, only evident during the November–March period. Anglerfish are apparently attracted toward this interface during the spawning period. The reason for this behavior is, however, not known, but there may be several possibilities.

Anglerfish spawn their eggs in long (up to 10 m) gelationous and buoyant ribbons, supposedly in a single batch (Bowman, 1920; Afonso-Dias and Hislop, 1996; Fariña et al., 2008). The bowl-shaped deep just north of "Skeivibanki" creates a retention system, which could provide ideal conditions for fish to congregate and ensure successful fertilization. The main inflow of zooplankton rich oceanic waters takes place in the near-surface layers between "Skeivibanki" and the inner Faroe shelf (Rasmussen et al., 2014; Eliasen et al., 2017a; Jacobsen et al., 2018) and this could be optimal for larval feeding and survival. The fact that spawning anglerfish encounter the interface could be caused by their preference for the mentioned deep, where also internal bores likely carry cold water upslope. In this way, the attraction toward the interface might just be a coincident.

Active search for the specific density layers in the interface could be to the assure neutral buoyancy, which can keep the eggs away from either the bottom or the water surface, where the predation pressure likely is high. It could also be a search for optimal temperatures and/or oxygen conditions for the gelatinous egg ribbons, found in the strong clines associated with the interface. Since the anglerfish are resident in the spawning area for an extended period, they probably also need to feed, therefore the large biomasses congregating along the interface (Cisewski et al., 2021) could be an attraction mechanism. The main interface is located deeper at lower latitudes (Hátún et al., 2021), which coincide with that spawning occurs in deeper waters for anglerfish south of the Faroes (Hislop et al., 2001). This could be a sign that anglerfish generally are attracted to the border of the main interface where oceanographic gradients provide the best long term/overall spawning success.

Vertical Activity

Anglerfish in the pelagic zone have previously been observed and H. C. Müller wrote about observations of anglerfish in the surface already 150 years ago (Joensen, 1965). Tuna-longliners and blue whiting trawl surveys in April over deep waters as well as pelagic 0-group survey on the Faroe Plateau in June/July have all reported pelagic anglerfish catches (Faroe Marine Research Institute, Unpublished data). Despite vertical movements, anglerfish were inactive 95% of the time, so it is evidently a demersal species. There are several hypotheses for the vertical movement behavior of anglerfish, such as individuals undertaking short horizontal shifts (Hislop et al., 2000), spawning/feeding migration using tidal currents (Laurenson et al., 2005), pelagic feeding excursions and prolonged stay either for spawning or feeding (Solmundsson et al., 2010). Perhaps some of the vertical activity in deep water during winter could be spawning "rises" as seen for Atlantic halibut (*Hippoglossus hippoglossus*) (Armsworthy et al., 2014).

We have shown that the vertical activity of anglerfish is closely linked to the sun angle, and therefore light intensity (**Figure 10B**). The fish rest shortly after sunrise, and move vertically soon after sunset. This diurnal vertical variability is also evident for fish residing at depth of several hundred meters, where ambient day-night contrast is very small. We therefore find it unlikely that light intensity directly triggers vertical motion of anglerfish. The sun angle, on the other hand, closely controls Dial Vertical Migration of a large biomass of mesopelagic and pelagic species in Faroese waters (Cisewski et al., 2021), which, in turn, could trigger motion of the predatory anglerfish. The movement of biota toward the seafloor during the day hours likely motivates anglerfish to start feeding, and thus to reside motionless on the seafloor while attracting prey fish with their fishing rod. Higher vertical activity during night was also shown from pop-up satellite tags in Icelandic waters (V. Sigurðsson, Personal Communications) and for a single DST tagged individual of *L. americanus* in the northwest Atlantic (Rountree et al., 2008).

Vertical activity was also higher during winter compared to summer, which partly can be explained by the evident diurnal cycle, with more activity in the dark hours during winter. The seasonal cycle is probably also linked to the pronounced seasonal offshore-onshore migration during the year. Anglerfish are slow swimmers and likely perform selective tidal migrations between spawning and feeding areas (Laurenson et al., 2005), as has also been documented for Atlantic cod (Righton et al., 2007). This means moving up from the seafloor when currents are in the desired direction, and staying at the bottom, when currents are opposing. The apparent attraction toward the main interface during winter could also introduce vertical motion, since this interface undulates on tidal to monthly time scales (Cisewski et al., 2021).

Vertical migration of anglerfish has been documented also in other areas in the northeast Atlantic, both from DSTs

(Thangstad et al., 2006) and from pelagic catches of anglerfish (Hislop et al., 2000; Laurenson et al., 2005; Thangstad et al., 2006; Solmundsson et al., 2010) and from pop-up satellite tags in Icelandic waters (V. Sigurðsson, Personal Communications) and vertical migration was also observed for cod on the Faroe Plateau (Ottosen et al., 2017).

There are various possibilities for the findings in this paper that could be investigated in the future, e.g., further analysis of the DST results of the 10 anglerfish to seek more details in the anglerfish behavior and migratory path. Mark-recapture experiments with both conventional tags and DSTs could be repeated, preferably in other places on the Faroe Plateau and on the Faroe Bank, to investigate for additional spawning areas. A potential northward shift in the distribution of anglerfish in the Northeast Atlantic, in response to climate change and increasing temperatures, could be investigated with the aim to reveal effects on prey fish populations.

Conclusions

The main findings in this study documented that anglerfish in Faroese waters performed seasonal offshore-onshore migrations, staying in shallow waters (<200 m) during the summer and in deep waters (>250 m) during winter. Also, that anglerfish were mostly located in boreal water with a temperature range of 6–11°C and rarely colder than 4°C. Anglerfish appeared mainly inactive, but for 5% of the time they displayed vertical movements, and they were most vertically active during winter on the seasonal scale and during night on a daily scale. This is the first time a clear seasonal offshore-onshore migration is demonstrated in Faroese waters from DSTs. Here is also provided the first documentation of a seasonal and daily pattern in vertical activity of anglerfish, and both aspects provide new valuable insights into the movement and migration pattern of anglerfish in Faroese waters.

DATA AVAILABILITY STATEMENT

The raw data supporting the conclusions of this article will be made available by the authors, without undue reservation.

ETHICS STATEMENT

Ethical review and approval was not required for the animal study because the samples were taken from scientific research trips and from commercial catches, which do not fall under the national or EU legislation regarding animal welfare.

AUTHOR CONTRIBUTIONS

LO, HH, TP, and PS developed the main idea. LO compiled and analyzed the anglerfish data. HH contributed with information on the oceanography. LO and HH wrote the manuscript, with feedback from TP, PS, and BM. All authors approved the submitted version.

FUNDING

This research was funded by the Faroe Marine Research Institute, Faroese Research Council, and Faroese Fisheries Research Fund.

ACKNOWLEDGMENTS

Thanks to the late Rógvi Mouritsen and Kristian Zachariassen for help with the anglerfish tagging, the skipper Kristin Wilhelmsen and the crew onboard gillnetter "Gudrun" for help during the tagging trips and the crew onboard the research vessel "Magnus Heinason" for help during anglerfish surveys and tagging trips, Chevonne Angus for discussions of the DST placement, Eydna í Homrum for comments on earlier drafts and the two reviewers for comments. We also thank all the fishermen that have delivered tagged anglerfish and staff at the Faroe Marine Research Institute for their help.

SUPPLEMENTARY MATERIAL

The Supplementary Material for this article can be found online at: https://www.frontiersin.org/articles/10.3389/fmars.2022.823066/full#supplementary-material

Supplementary Figure 1 | Illustration of how the red Floy t-tag and the data storage tag were attached dorsally on an anglerfish. This fish was recaptured after 12 days at sea. The data storage tag was inserted surgically under the anglerfish skin with a yellow plastic tube as a marker outside and the red Floy-tag was fastened by a tagging gun.

Supplementary Figure 2 | (A) Illustration of results from data-storage tag 10672. Tagged 7. May 2010, 81 cm length. Recaptured north of "Skeivibanki" 15. January 2012 (**Figure 8A**), 97 cm in length. 618 days of liberty. **(B)** Extraction of incidences of internal bores which carry cold water upslope.

Supplementary Figure 3 | (A) Illustration of results from data-storage tag 10658. Anglerfish, 72 cm, tagged 25/7-2009, north of the Faroe Islands and recaptured 17/2-2011 not far from tagging site (**Figure 8A**), 83 cm in length. 571 days at liberty. **(B)** Extraction of incidences of vertical movements in shallow waters and likely incidences of internal bores in deep waters which carry cold water upslope.

REFERENCES

Afonso-Dias, I. P., and Hislop, J. R. G. (1996). The reproduction of anglerfish *Lophius piscatorius* Linnaeus from the north-west coast of Scotland. *J. Fish Biol.* 49, 18–39.

Anonymous (2012). *Havforskningsrapporten 2012*. Norway: Institute of Marine Research.

Armannsson, H., and Jonsson, S. T. (2012). Vertical migrations of saithe (*Pollachius virens*) in Icelandic waters as observed with data storage tags. *ICES J. Mar. Sci.* 69, 1372–1381.

Armannsson, H., Jonsson, S. T., Neilson, J. D., and Marteinsdottir, G. (2007). Distribution and migration of saithe (*Pollachius virens*) around Iceland inferred from mark-recapture studies. *ICES J. Mar. Sci.* 64, 1006–1016.

Armsworthy, S. L., Trzcinski, M. K., and Campana, S. E. (2014). Movements, environmental associations, and presumed spawning locations of Atlantic halibut (Hippoglossus hippoglossus) in the northwest Atlantic determined using archival satellite pop-up tags. *Mar. Biol.* 161, 645–656. doi: 10.1007/s00227-013-2367-5

Beaird, N. L., Rhines, P. B., and Eriksen, C. C. (2016). Observations of seasonal subduction at the Iceland-Faroe Front. *J. Geophys. Res. Ocean* 121, 4026–4040. doi: 10.1002/2015JC011501

Berx, B., Hansen, B., Østerhus, S., Larsen, K. M., Sherwin, T. J., and Jochumsen, K. (2013). Combining *in situ* measurements and altimetry to estimate volume, heat and salt transport variability through the Faroe-Shetland Channel. *Ocean Sci.* 9, 639–654. doi: 10.5194/os-9-639-2013

Bjelland, O., and Asplin, L. (2007). *Are Norwegian Fjords Important Spawning Areas for Anglerfish (Lophius piscatorius)?* Copenhagen: ICES.

Bohme, L., and Send, U. (2005). Objective analyses of hydrographic data for referencing profiling float salinities in highly variable environments. *Deep. Res. II Top. Stud. Oceanogr.* 52, 651–664.

Bowman, A. (1920). The eggs and larvae of the angler *Lophius piscatorius* L. in Scottich waters. *Rep. Fish. Board Scotland* 11, 1–55.

Caruso, J. H. (1983). The systematics and distribution of the lophiid anglerfishes. 2. Revisions of the genera *Lophiomus* and *Lophius*. *Copeia* 1983, 11–30.

Cisewski, B., Hátún, H., Kristiansen, I., Hansen, B., Larsen, K. M. H., Eliasen, S. K., et al. (2021). Vertical migration of pelagic and mesopelagic scatterers from ADCP backscatter data in the Southern Norwegian Sea. *Front. Mar. Sci.* 7:542386. doi: 10.3389/fmars.2020.542386

Eliasen, S. K., Hansen, B., Larsen, K. M. H., and Hátún, H. (2016). The exchange of water between the Faroe Shelf and the surrounding waters and its effect on the primary production. *J. Mar. Syst.* 153, 1–9. doi: 10.1016/j.jmarsys.2015.08.004

Eliasen, S. K., Hátún, H., Larsen, K. M. H., and Jacobsen, S. (2017a). Faroe shelf bloom phenology – The importance of ocean-to-shelf silicate fluxes. *Cont. Shelf Res.* 143, 43–53. doi: 10.1016/j.csr.2017.06.004

Eliasen, S. K., Larsen, K. M. H., Hansen, B., and Rasmussen, T. A. S. (2017b). Phenologically distinct phytoplankton regions on the Faroe Shelf - identified by satellite data, *in-situ* observations and model. *J. Mar. Syst.* 169, 99–110. doi: 10.1016/j.jmarsys.2017.01.015

Fariña, A. C., Azevedo, M., Landa, J., Duarte, R., Sampedro, P., Costas, G., et al. (2008). *Lophius* in the world: a synthesis on the common features and life strategies. *ICES J. Mar. Sci.* 65, 1272–1280.

Gaard, E., and Steingrund, P. (2001). Reproduction of Faroe plateau cod: spawning grounds, egg advection and larval feeding. *Fróðskaparrit* 48, 87–103. doi: 10.1002/9781119460701.ch3

Hansen, B., and Østerhus, S. (2000). North Atlantic-Nordic Seas exchanges. *Prog. Oceanogr.* 45, 119–208.

Harden-Jones, R. F. (1968). *Fish Migration*. London: Edward Arnold.

Hátún, H., and Chafik, L. (2018). On the recent ambiguity of the North Atlantic subpolar gyre index. *J. Geophys. Res. Oceans* 123, 5072–5076.

Hátún, H., Chafik, L., and Larsen, K. M. H. (2021). The Norwegian Sea gyre – a regulator of Iceland-Scotland ridge exchanges. *Front. Mar. Sci.* 8:694614. doi: 10.3389/fmars.2021.694614

Hátún, H., Larsen, K. M. H., and Debes, H. H. (2013). *The Western Region*. Tórshavn: Havstovan.

Hátún, H., Payne, M. R., and Jacobsen, J. A. (2009a). The North Atlantic subpolar gyre regulates the spawning distribution of blue whiting (*Micromesistius poutassou*). *Can. J. Fish. Aquat. Sci.* 66, 759–770. doi: 10.1139/f09-037

Hátún, H., Payne, M. R., Beaugrand, G., Reid, P. C., Sandø, A. B., Drange, H., et al. (2009b). Large bio-geographical shifts in the north-eastern Atlantic Ocean: from the subpolar gyre, *via* plankton, to blue whiting and pilot whales. *Prog. Oceanogr.* 80, 149–162. doi: 10.1016/j.pocean.2009.03.001

Hátún, H., Sandø, A. B., Drange, H., Hansen, B., and Valdimarsson, H. (2005). Influence of the Atlantic subpolar gyre on the thermohaline circulation. *Science* 309, 1841–1843. doi: 10.1126/science.1114777

Hislop, J. R. G., Gallego, A., Heath, M. R., Kennedy, F. M., Reeves, S. A., and Wright, P. J. (2001). A synthesis of the early life history of the anglerfish, *Lophius piscatorius* (Linnaeus, 1758) in northern British waters. *ICES J. Mar. Sci.* 58, 70–86. doi: 10.1006/jmsc.2000.0991

Hislop, J. R. G., Holst, J. C., and Skagen, D. (2000). Near-surface captures of post-juvenile anglerfish in the North-east Atlantic – an unsolved mystery. *J. Fish Biol.* 57, 1083–1087. doi: 10.1006/jfbi.2000.1364

Homrum, E. í. (2012). *The Effects of Climate and Ocean Currents on Faroe Saithe*. Ph.D. thesis. Tórshavn: Fróðskaparsetur Føroya.

ICES (2018). *Report of the Benchmark Workshop on Anglerfish Stocks in the ICES Area (WKANGLER), 12–16 February 2018, Copenhagen, Denmark*. Copenhagen: ICES, 177.

ICES (2021). *Northwestern Working Group (NWWG)*. Copenhagen: ICES, 838. doi: 10.17895/ices.pub.8186

Jacobsen, S., Gaard, E., Larsen, K. M. H., Eliasen, S. K., and Hátún, H. (2018). Temporal and spatial variability of zooplankton on the Faroe shelf in spring 1997–2016. *J. Mar. Syst.* 177, 28–38. doi: 10.1016/j.jmarsys.2017.08.004

Jákupsstovu, S. H. í. (2004). *Fiskiskapur við Føroyar í 100 ár*. Copenhagen: ICES.

Joensen, J. S. (1965). H. C. Müller og 'Færøernes Fiskefauna'. *Fróðskaparrit* 14, 24–58.

Joensen, J. S., Steingrund, P., Henriksen, A., and Mouritsen, R. (2005). Migration of cod (*Gadus morhua*): tagging experiments at the Faroes 1952–1965. *Fróðskaparrit* 53, 100–135.

Landa, J., Duarte, R., Fariña, A. C., Bruno, I., and Castro, J. (2001). *Mark-Recapture Studies of Black Anglerfish (Lophius budegassa) in the North-Eastern Atlantic: Preliminary Results*. Copenhagen: ICES.

Larsen, K. M. H., Hansen, B., and Svendsen, H. (2008). Faroe Shelf Water. *Cont. Shelf Res.* 28, 1754–1768.

Laurenson, C. H., Hudson, I. R., Jones, D. O. B., and Priede, I. G. (2004). Deep water observations of anglerfish (*Lophius piscatorius* L.) in the north-eastern Atlantic Ocean by means of remotely operated vehicle. *J. Fish Biol.* 65, 947–960.

Laurenson, C. H., Johnson, A., and Priede, I. G. (2005). Movements and growth of monkfish *Lophius piscatorius* tagged at the Shetland Islands, Northeastern Atlantic. *Fish. Res.* 71, 185–195. doi: 10.1016/j.fishres.2004.08.020

Laurenson, C. H., Priede, I. G., Bullough, L. W., and Napier, I. R. (2001). *Where are the Mature Anglerfish? The population biology of Lophius piscatorius in Northern European Waters*. Copenhagen: ICES, 15.

Mouritsen, R. (2007). *Fiskar undir Føroyum*. Torshavn: Føroya Skúlabókagrunnur.

Ofstad, L. H. (2013). *Anglerfish Lophius piscatorius L. in Faroese Waters. Life History, Ecological Importance and Stock Status*. Ph.D. thesis. Tromsø: University of Tromsø, 108.

Ofstad, L. H., and Laurenson, C. H. (2007). *Biology of Anglerfish Lophius piscatorius in Faroese Waters*. Copenhagen: ICES, 16.

Ofstad, L. H., Pedersen, T., and Steingrund, P. (2013). Maturation, reproduction and early life history of anglerfish *Lophius piscatorius* in Faroese waters. *Fróskaparrit* 60, 114–133.

Ottosen, K. M., Pedersen, M. W., Eliasen, S. K., Setingrund, P., Magnussen, E., and Rasmussen, T. A. S. (2017). Migration patterns of the Faroe Plateau cod (*Gadus morhua*, L.) revealed by data storage tags. *Fish. Res.* 195, 37–45. doi: 10.1016/j.fishres.2017.06.014

Perry, M. C., Olsen, G. H., Richards, R. A., and Osenton, P. C. (2013). Predation on dovekies by goosefish over deep water in the Northwest Atlantic Ocean. *Northeast. Nat.* 20, 148-154.

Perry, R. I., and Smith, S. J. (1994). Identifying habitat associations of marine fishes using survey data: an application to the Northwest Atlantic. *Can. J. Fish. Aquat. Sci.* 51, 589–602. doi: 10.1139/f94-061

Pörtner, H. O., and Farrell, A. P. (2008). Physiology and climate change. *Science* 322, 690–692. doi: 10.1016/j.virol.2017.08.015

R Core Team (2014). *R: A Language and Environment for Statistical Computing*. Vienna: R Foundation for Statistical Computing.

Rasmussen, T. A. S., Olsen, S. M., Hansen, B., Hátún, H., and Larsen, K. M. H. (2014). The Faroe shelf circulation and its potential impact on the primary production. *Cont. Shelf Res.* 88, 171–184. doi: 10.1016/j.csr.2014.07.014

Reda, I., and Andreas, A. (2004). Solar position algorithm for solar radiation applications. *Sol. Energy* 76, 577–589. doi: 10.1016/j.solener.2003.12.003

Reinert, J. (1995). "Deep water resources in Faroese waters to the south, southwest and west of the Faroes - a preliminary account," in *Deep-Water Fisheries of the North Atlantic Oceanic Slope*', ed. A. G. Hopper (Dordrecht: Kluwer Academic Publisher), 201–225. doi: 10.1007/978-94-015-8414-2_6

Richards, A., Moser, J., Dunnigan, B., and Alade, L. A. (2011). Archival tagging methods for monkfish. *Trans. Am. Fish. Soc.* 140, 582–586. doi: 10.1080/00028487.2011.584802

Richards, R. A., Nitschke, P. C., and Sosebee, K. A. (2008). Population biology of monkfish Lophiusamericanus. *ICES J. Mar. Sci.* 65, 1291–1305. doi: 10.1093/icesjms/fsn108

Righton, D., Quayle, V. A., Hetherington, S., and Burt, G. (2007). Movements and distribution of cod (*Gadus morhua*) in the southern North Sea and English Channel: results from conventional and electronic tagging

experiments. *J. Mar. Biol. Assoc. U. K.* 87, 599–613. doi: 10.1017/s0025315407054641

Rountree, R. A., Gröger, J. P., and Martins, D. (2008). Large vertical movements by a goosefish, *Lophius americanus*, suggests the potential of data storage tags for behavioral studies of benthic fishes. *Mar. Freshw. Behav. Physiol.* 41, 73–78. doi: 10.1080/10236240801934065

Siemann, L. A., Huntsberger, C. J., Leavitt, J. S., and Smolowitz, R. J. (2018). Summering on the bank: seasonal distribution and abundance of monkfish on George Bank. *PLoS One* 13:e0206829. doi: 10.1371/journal.pone.0206829

Solmundsson, J., Jonsson, E., and Bjornsson, H. (2010). Phase transition in recruitment and distribution of monkfish (*Lophius piscatorius*) in Icelandic waters. *Mar. Biol.* 157, 295–305. doi: 10.1007/s00227-009-1317-8

Solmundsson, J., Palsson, J., and Karlsson, H. (2005). Fidelity of mature Icelandic plaice (*Pleuronectes platessa*) to spawning and feeding grounds. *ICES J. Mar. Sci.* 62, 189–200. doi: 10.1016/j.icesjms.2004.11.012

Steimle, F. W., Morse, W. W., and Johnson, D. L. (1999). *Goosefish, Lophius americanus, Life History and Habitat Characteristics*. Washington: NOAA, 31.

Steingrund, P., Clementsen, D., and Mouritsen, R. (2009). Higher food abundance reduces the catchability of cod (*Gadus morhua*) to longlines on the Faroe Plateau. *Fish. Res.* 100, 230–239. doi: 10.1016/j.fishres.2009.08.002

Tåning, Å. V. (1940). Migration of cod marked on the spawning places off the Faroes. *Meddr. Komm. Danmarks Fisk.-og Havunders. Ser. Fiskeri* 10.

Tåning, Å. V. (1943). *Lophius*. In Report on the Danish Oceanographical Expeditions 1908–1910 to the Mediterranean and Adjacent Seas. *Biology* II:30.

Thangstad, T., Bjelland, O., Nederaas, K. H., Jónsson, E., Laurenson, C. H., and Ofstad, L. H. (2006). Anglerfish (*Lophius* spp.) in Nordic Waters. *TemaNord* 2006:570.

Wootton, R. J. (1990). *Ecology of Teleost Fishes*. London: Chapman and Hall.

Yoneda, M., Tokimura, M., Horikawa, H., Yamamoto, K., Matsuyama, M., and Matsuura, S. (2002). Spawning migration of the anglerfish *Lophius litulon* in the East China and Yellow Seas. *Fish. Sci.* 68, 310–313. doi: 10.2331/fishsci.68.sup1_310

Conflict of Interest: The authors declare that the research was conducted in the absence of any commercial or financial relationships that could be construed as a potential conflict of interest.

Publisher's Note: All claims expressed in this article are solely those of the authors and do not necessarily represent those of their affiliated organizations, or those of the publisher, the editors and the reviewers. Any product that may be evaluated in this article, or claim that may be made by its manufacturer, is not guaranteed or endorsed by the publisher.

Copyright © 2022 Ofstad, Hátún, Pedersen, Steingrund and Mikkelsen. This is an open-access article distributed under the terms of the Creative Commons Attribution License (CC BY). The use, distribution or reproduction in other forums is permitted, provided the original author(s) and the copyright owner(s) are credited and that the original publication in this journal is cited, in accordance with accepted academic practice. No use, distribution or reproduction is permitted which does not comply with these terms.

frontiers in Marine Science

ORIGINAL RESEARCH
published: 10 March 2022
doi: 10.3389/fmars.2022.823006

Spatial Variability of the Feeding Conditions for the Norwegian Spring Spawning Herring in May

Inga Kristiansen[1], Hjálmar Hátún[1], Jan Arge Jacobsen[2], Sólvá K. Eliasen[1], Hildur Petursdottir[2] and Eilif Gaard[1]*

[1] Faroe Marine Research Institute, Tórshavn, Faroe Islands, [2] Marine and Freshwater Research Institute, Hafnarfjörður, Iceland

The abundant and ecologically important copepods *Calanus finmarchicus* and *Calanus hyperboreus* within the Norwegian and Iceland Seas are key prey species of Norwegian spring spawning herring. The volume flux of East Icelandic Water, which carries the mentioned zooplankton species into the southern Norwegian Sea, is highly variable. The years 1996–2002 have previously been characterized as high influx years, 2003–2016 as low influx years and since 2017 a reversal to higher influx has been apparent. Hydrographic and zooplankton data, as well as fish data on herring (size and diet content), from the International Ecosystem Surveys in the Nordic Seas in May have been used in this study. Focus is on the south-western Norwegian Sea, where herring has regularly been observed in May since 2005 and where changes in plankton availability and in the hydrographic environment have also been observed. Diet biomass from 2017–2020 (higher influx period) showed higher stomach fullness compared to 2007–2011 (lower influx period). Furthermore, the highest stomach fullness is observed in the westernmost feeding region—referred to as the *Feeding Spot*. The scrutinized diet content showed a notably higher biomass of ingested *C. hyperboreus* in 2020 compared to 2007–2011, indicating a preference for the larger and more nutritious copepod. Zooplankton analysis from May 2020 revealed that the core of the western feeding region, i.e., the area with highest zooplankton biomass, was located within the subarctic waters immediately north/west of the junction between the Iceland-Faroe Front and the Jan Mayen Front. The core area was mainly represented by overwintering stages and the derived adult stages of *C. finmarchicus* and *C. hyperboreus*. Interplay between food availability and accessibility, in terms of temperature, to the *Feeding Spot*, is discussed.

Keywords: East Icelandic Current, *Calanus hyperboreus*, *Calanus finmarchicus*, zooplankton biomass, diet composition, NSSH herring, feeding distribution, temperature

OPEN ACCESS

Edited by:
Martin Edwards, Plymouth Marine Laboratory, United Kingdom

Reviewed by:
Terry Whitledge, Retired, Fairbanks, AK, United States
Daria Martynova, Zoological Institute (RAS), Russia

****Correspondence:***
Inga Kristiansen
ingak@hav.fo

Specialty section:
This article was submitted to Marine Ecosystem Ecology, a section of the journal Frontiers in Marine Science

Received: *26 November 2021*
Accepted: *04 February 2022*
Published: *10 March 2022*

Citation:
Kristiansen I, Hátún H, Jacobsen JA, Eliasen SK, Petursdottir H and Gaard E (2022) Spatial Variability of the Feeding Conditions for the Norwegian Spring Spawning Herring in May. Front. Mar. Sci. 9:823006. doi: 10.3389/fmars.2022.823006

INTRODUCTION

The Norwegian Spring Spawning herring (*Clupea harengus*) is the largest herring stock in the world. Due to the sheer stock size, remarkable dynamic structure and high economic value, this stock continues to be a favorite subject of scientific study with many remaining unanswered questions. The variable feeding migration is one important aspect of the stock dynamics, and this is the focus of the present paper.

The general herring migration route is performed in a clockwise pattern that covers warm northward flowing Atlantic water (AW) in the eastern Norwegian Sea and cold Arctic and subarctic waters flowing in a south-easterly direction in the western Norwegian Sea and northeastern Icelandic Sea (**Figure 1**; Holst et al., 2004). After spawning along the Norwegian coast in February-March (Holst and Slotte, 1998), the herring enters the Norwegian Sea with a progressive westward feeding migration. In the classical view, the main feeding season extends from early May to late July, which herring use to fill its energy reserves for subsequent overwintering and spawning (Bachiller et al., 2016).

As reviewed by Skjoldal et al. (2004), the herring stock underwent three major shifts in their migration pattern from the early 1950s to the early 1990s. During the warm period, from 1950–1964, the feeding region stretched from north and east of Iceland to Jan Mayen. It was the adult herring that were paving the migratory route (Pavshtiks, 1956), feeding in the heated surface layer within the East Icelandic Current in May and June (Østvedt, 1965; Jakobsson and Østvedt, 1996). During the latter half of the 1960s, the water temperature became unusually low north of Iceland and feeding conditions deteriorated within this region (Thórdardóttir, 1977). During the same period, the stock size decreased dramatically and finally collapsed. A new migration pattern emerged in the early 1970s, when the herring remained along the Norwegian coast during the feeding period. When a large year class emerged in 1983, the need for a larger feeding area increased and from 1986 the herring was again feeding over large parts of the Norwegian Sea (Holst et al., 2002).

Since the mid-1990s, different herring feeding patterns, in May, have also emerged. During the years 1996–1998, the herring mainly migrated along the eastern side of the Jan Mayen Front (JMF) (Misund et al., 1998; Holst et al., 2002). In 1999, the herring stock became abruptly confined north of 66°N (Holst et al., 1999, 2004), with nearly no herring east of Iceland (Eliasen et al., 2021). After 2003, and more persistently since 2005 to present, the herring stock did again adopt a southwestern migration toward the southwestern Norwegian Sea. Adult herring are presently densely aggregating against the slope of the Jan Mayen Ridge (Eliasen et al., 2021) (∼65.5°N, 5°W in **Figure 1**), which the authors refer to as the "feeding hotspot"—hereafter simply the Feeding Spot (FS). Homrum et al. (in review) has shown that the best growth conditions of herring, during this early feeding period, are observed in the southwestern Norwegian Sea, which might reflect the abundant food availability in this region.

Copepods of the genus *Calanus*, including the larger copepodite stages of *Calanus finmarchicus* and the larger *Calanus hyperboreus*, of Arctic origin, are considered to be the main prey of herring (Dalpadado et al., 2000; Gislason and Astthorsson, 2002; Melle et al., 2020). *C. finmarchicus* is the dominant zooplankton species, both numerically and in terms of biomass, within the Norwegian Sea and most herring-prey discussions have therefore focused on this species (e.g., Broms et al., 2012; Utne et al., 2012; Melle et al., 2020). However, *C. hyperboreus* dominates the zooplankton biomass in the southeastern part of the Iceland Sea in May (Astthorsson and Gislason, 2003; Strand et al., 2020; Gislason et al., 2021). This larger and more nutritious copepod is increasingly preyed upon further westwards during the migration in May (Dalpadado et al., 2000; Melle et al., 2020), and its abundance might therefore have larger impact on the herring feeding distribution than previously anticipated.

The East Icelandic Current advects *C. hyperboreus* and large stages of *C. finmarchicus*, into the southwestern Norwegian Sea (**Figure 1**; Kristiansen et al., 2019; Skagseth et al., in review). The typical view of the East Icelandic Current as a broad flow from the Icelandic Sea into the Norwegian Sea must, however, be nuanced. Ocean currents in this region closely follow the bathymetry, and the flow of cold and low-saline East Icelandic Water (EIW) is actually channeled by two branches: a shallow branch (∼750 m bottom depths) along the Iceland slope and directly continuing southeastward along the northern flank of the Iceland-Faroe Ridge, and a deeper branch (∼1,100 m bottom depths), which veers clockwise around the northeastward protruding plateau from the Icelandic continental slope (see the 1,000 m isobath in **Figure 1**). The deep branch merges with the southward flow along the Jan Mayen Ridge (Semper et al., 2020; Hátún et al., 2021) in the vicinity of the FS.

Although the deep flows are topographically controlled, stratification in the water column allows the near-surface waters to shift laterally. East of Iceland, the frontal zones are characterized by inter-annual fluctuations in longitudinal position which are related to a variable volume of EIW (Blindheim, 2004; Kristiansen et al., 2016, 2019). Before reverting back to zooplankton and herring, we summarize the most distinct oceanographic changes since the mid-1990s (Malmberg and Valdimarsson, 2003; Macrander et al., 2014; Kristiansen et al., 2019; Holliday et al., 2020; ICES, 2020).

After a drop in the North Atlantic Oscillation (NAO) index during the winter 1995–1996 (Holliday et al., 2008), the subpolar gyre weakened markedly (Häkkinen and Rhines, 2004), resulting in increased temperature and salinities in the AW flowing into the Nordic Seas (Hátún et al., 2005). Around the same time, from 1996–1998, the Arctic waters approaching Iceland from the northwest cooled and became fresher. These years are also known as the Polar Years north of Iceland (Malmberg and Valdimarsson, 2003). These two concurrent events resulted in contrasting oceanographic conditions northeast of Iceland during the late 1990s. In 2003, the circulation of both the subpolar gyre (Hátún et al., 2005) and the Norwegian Sea gyre (Hátún et al., 2021) were particularly weak. The weakened Norwegian Sea gyre reduced the eastward transport of the EIW into the Norwegian Sea (Serra et al., 2010). Simultaneously, the further weakening of the subpolar gyre lead to an even stronger increase in temperature and salinity in the Modified North Atlantic Water (MNAW; Hátún et al., 2005; Larsen et al., 2012) which propagated throughout the Nordic Seas (Malmberg and Valdimarsson, 2003; Holliday et al., 2008; Richter and Maus, 2011). These cascading events coincide with a more westward broadening of the AW currents (Blindheim et al., 2000) as well as reduced abundance of *C. hyperboreus* and the larger copepodite stages of *C. finmarchicus* (Kristiansen et al., 2019). This reversed after 2015 to this present period. This period is characterized by an intensifying subpolar gyre (Hátún and Chafik, 2018) and the largest drop in seawater salinities ever observed in the northeast Atlantic (Holliday et al., 2020), and together with an

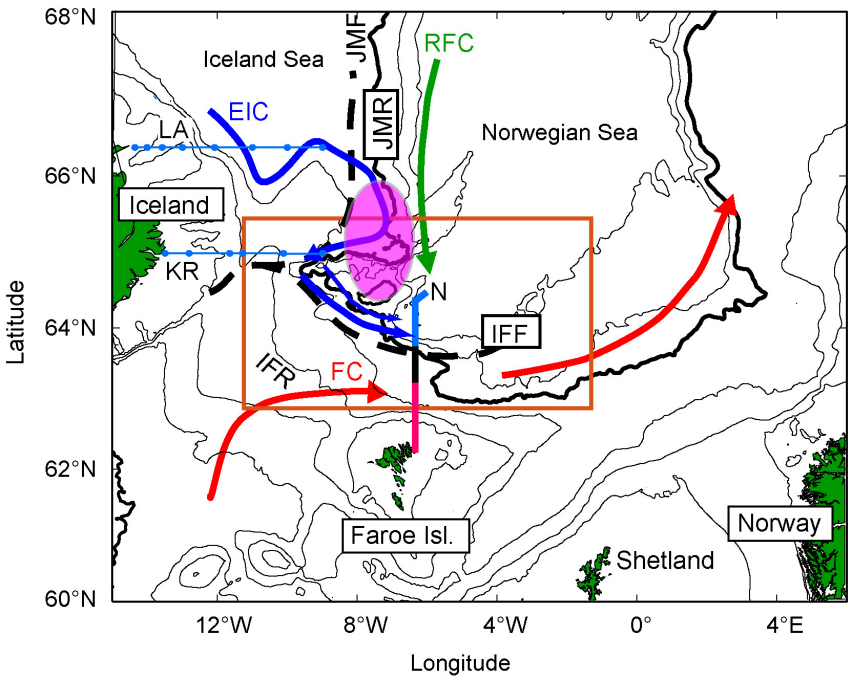


FIGURE 1 | Map of the study region. The orange box defines the main study area. The black stippled lines show the approximate position of the Iceland-Faroe Front (IFF) and Jan Mayen Front (JMF), separating the south-eastward flowing East Icelandic Current (EIC) (blue) and poleward flowing Atlantic Waters (red). The purple circle illustrates the area where the densest aggregation of older herring is observed since around 2003, in May (Eliasen et al., 2021). The Icelandic monitoring sections (KR and LA) are shown in blue, while the Faroese section (N) is divided into an Atlantic (red), frontal (black), and subarctic (blue) regions. FC, Faroe Current; RFC, Recirculated Faroe Current (green); IFR, Iceland Faroe Ridge; JMR, Jan Mayen Ridge; KR, Krossanes; and LA, Langanes East. The 200, 500, 1,000, 2,000 (bold), 2,500, and 3,000 m isobaths are shown in black.

increased influx of EIW (Kristiansen et al., 2019), the Norwegian Sea has freshened. However, due to reduced heat loss from the region, the Norwegian Sea has simultaneously experienced warming (Mork et al., 2019).

ICES (2020) has reported historically low zooplankton concentrations since 2003, although it has been slightly increasing again after 2015. This coincides with an increased abundance and expansion of the herring stock during spring and summer (Utne et al., 2012). However, it remains difficult to evaluate the effect of feeding pressure on zooplankton biomass in May, since the zooplankton sampling and trawling occur at the same time. Understanding herring behavior is complicated as multiple factors may influence stock structure, such as temperature, food availability, recruitment, stock size and inherent learned behavior between generations (Misund et al., 1997; Fernö et al., 1998; Skjoldal et al., 2004). However, Eliasen et al. (2021) find no link between internal stock dynamics such as the entrance of strong year classes and changes in the distribution pattern in May, and thus concluded that the observed major distribution shifts of old herring are primarily induced by the external factors such as temperature and/or food abundance.

The present work is done in parallel with the following four papers: Eliasen et al. (2021); Hátún et al. (2021), Homrum et al. (in review), and Skagseth et al. (in review) in association with a Research Topic in Frontiers in Marine Science. We here provide information on some key aspects of temperature, zooplankton composition and abundance and herring stomach content in the vicinity of the FS. Combined with key findings from the other papers, this will be used to assess the most plausible drivers underlying the variable distribution of herring in May. In our discussion, we pose two hypothesis: *The abundance of adult herring at the FS in May is determined by: Hyp (I) accessibility to the FS (thermal restriction) and/or Hyp (II) food abundance between Norwegian slope and the FS.*

METHODS

Sea Surface Temperature

In order to show the long-term average temperature conditions for zooplankton and herring in May, sea surface temperatures (SST) in May from 2003 to 2020, based on remotely sensed data with 4.64 km resolution (from MODIS, NASA Goddard Space Flight Centre, Ocean Ecology Laboratory, Ocean Biology Processing Group), were downloaded from http://marine.copernicus.eu and averaged. In addition, daily SST (from multisensory merged, level 3 satellite observations, with a 0.02 degrees latitudinal and longitudinal resolution) was also used to estimate the oceanic conditions. The period under investigation is from 30th April to 9th May 2020, which coincides with the International Ecosystem Survey in the Nordic Seas (IESNS). Temperature and salinity at 100 and 200 m depth,

measured with a Conductivity, Temperature, Depth (CTD) during the IESNS survey, are included in the **Supplementary material** (**Supplementary Figure 1**). This period also concurs with available microscopic analysis of zooplankton (see Section Zooplankton Distribution in May 2020) and herring stomach analysis (see Section Herring Diet Composition).

Hydrographic Conditions at Two Eastern Icelandic Sections

Two standard monitoring sections, Krossanes (KR) and Langanes East (LA) (**Figure 1** and **Supplementary Figures 2, 3**), enabled a detailed investigation of the hydrographic conditions, in May, in the vicinity of the FS. A CTD was used to collect the temperature and salinity data from 1991 to 2020. To examine the potential time varying thermal restriction to the FS, a temperature and salinity time series of the two outermost stations at section LA (LA7 and LA8) was created by taking the average over the 80–120 m depth levels. This was done in order to avoid the rapidly changing influence of surface stratification. Data is not available at LA in 1998. A Hovmöller (depth-time) diagram from KR6, which is the station closest to the FS, reveals long-term temperature changes through the water column, just downstream of the FS.

Calanus finmarchicus and *Calanus hyperboreus* at Section N

Section N is located north of the Faroe Islands, from 62°20'N to 64°50'N and at longitude between 6°00'W and 6°05'W (**Figure 1**). The zooplankton time-series at Section N covers 25 years of observations in May, starting in 1993. No data are available for 1996, 1998, and 2006. Zooplankton samples were collected by vertical hauls from 50 m depth to the surface using a WP-2 net, with a mesh size of 200 μm. The towing speed was 0.5 m s^{-1}. On board, the samples were preserved with 4% formaldehyde. In the laboratory, the samples were divided into subsamples with a Motoda cylinder splitter, and an aliquot of around 200–300 animals from each sample was identified and counted. *C. finmarchicus* copepodites were also classified into developmental stages. For this purpose, averages from stations located within the subarctic region (**Figure 1**) are included in this study. Calanus *glacialis*, which is also distributed with the East Icelandic Current, is morphological very similar to *C. finmarchicus*. However, as *C. glacialis* is an arctic shelf species and only comprises less than 1% of the zooplankton biomass within the East Icelandic Current (Astthorsson and Gislason, 2003; Strand et al., 2020), molecular studies were not used to discriminate between these two species.

Zooplankton Distribution in May 2020

Co-occurring with CTD stations during the IESNS survey, zooplankton samples were collected according to the same method as stated in Section *Calanus finmarchicus* and *Calanus hyperboreus* at Section N. Each sample was split in two, where one half was preserved in 4% buffered formalin and identified to lowest taxonomic level possible using a stereomicroscope. The larger zooplankton species including krill and amphipods are not sampled representatively using a WP-2 net and are therefore excluded from this data analysis. The most common zooplankton species that were found in herring stomachs were selected for further investigation (**Supplementary Table 1**). The numbers were converted to biomass (**Table 1**) and were gridded onto a regular grid of 1° longitude by 0.5° latitude using objective mapping (Böhme and Send, 2005).

Zooplankton Biomass Within the Norwegian and Iceland Seas

The zooplankton biomass used in our analysis is collected in May from 1996 to 2020 during the IESNS survey. Samples were collected within the uppermost 200 m with WP-2 nets of 180 or 200 μm mesh size and subsequently split into two, where one half was dried and weighed to measure total biomass. Data are presented as g dry weight per m^2 (ICES, 2020). The survey data were gridded as described in Section Zooplankton Distribution in May 2020. Areas with sparse sampling, where the associated error map exceeded the selected threshold of less than 7 years sampled within a grid cell during the 25-year long sampling period, were excluded from further analysis. The average biomass within the region is divided into the following four periods: 1996–1998, 1999–2002, 2003–2016, and 2017–2020. The selected periods are chosen based on a combination of information including the herring distribution, in May, since the mid-1990s (Eliasen et al., 2021), hydrographic changes described by Skagseth et al. (in review) and *Calanus* spp. abundance within the subarctic region of Section N (Kristiansen et al., 2019).

Herring Diet Composition

Lengths of 100 herring were randomly obtained from a sub-sample taken at each trawl station during the IESNS survey in May. Trawling for herring occurred on regular intervals based on the acoustic readings. Stomach samples of the first 10 fishes were collected and immediately frozen. Analysis of diet composition of stomachs collected in 2007 to 2011 and in 2020 was carried out within 6 months after sampling. Each stomach was cleared of the remaining debris on the outside and was subsequently weighted before and after emptying the stomach content as wet weight. Stomachs were carefully opened with scissors and the consumed prey was identified to lowest taxonomic level possible using a stereomicroscope. A Metoda Splitter was used to create sub-samples when the prey became too numerous to count. The prey content in herring stomachs collected from 2017 to 2019 was only weighted as wet weight, without examining the prey composition, as these had been frozen for more than 18 months. These were used, together with stomachs collected from 2007 to 2011 and 2020, to determine the stomach fullness index (SFI). SFI was calculated as wet weight of the stomach content (g) divided by fish length (cm) cubed and multiplied by 10^3 (Deblois and Rose, 1995). The biomass, as dry weight, of the dominant ingested prey groups was calculated using length-weight relationships from literature (Hay et al., 1991; Hirche, 1997; **Table 1**). Average length of *C. finmarchicus* developmental stages was based on measurements from Section N, within the upper 200 m, in May (Kristiansen et al., 2021).

TABLE 1 | Mean length and regression coefficients (a) and exponents (b) for converting length (mm) to dry weight (mg) of dominant prey species in the environment and in the herring stomach content.

Species	Mean length (L), (mm)								Dry weight (mg)*		References
	Nau	C1	C2	C3	C4	C5	C6f	C6m	a	b	
C. finmarchicus	0.41	-	-	-	-	-	-	-	0.0174	2.27	Hay et al., 1991
C. finmarchicus		0.83 (66)	1.14 (78)	1.53 (78)	2.06 (69)	2.57 (86)	2.81 (98)	2.75 (64)	0.0073	3.46	Hay et al., 1991
C. hyperboreus	-	-	-	-	3.5	5	7.4	-			Hirche, 1997

References used for calculating the length-weight relationships are noted. Average length of Calanus finmarchicus developmental stages was used from Section N in May (Kristiansen et al., 2021). The number of individuals measured is shown in brackets.
**Dry weight (mg) = a * L (mm)^b.*

Statistical Analysis

R Core Team and Matlab were used interchangeable to analyze data while the statistical analysis was only conducted in R. All data were checked for normality before a statistical test was applied. The non-parametric Kruskal-Wallis test was used to confirm whether the phenology shift of *C. finmarchicus* and the abundance of *C. hyperboreus* could be defined according to the most distinct oceanographic changes since the mid-1990s. These are divided into three periods, 1993–2002, 2003–2014, and 2015–2020. For the SFI data, the non-parametric Mann-Whitney *U*-test was used to test whether there was a significant difference between two periods, 2007–2011 versus 2017–2020. A linear regression analysis was used to document changes in temperature before versus after 2003 and the average increase in temperature since 2004.

RESULTS

Variable Influx of Large *Calanus* Into the Southern Norwegian Sea

We follow and update the approach by Kristiansen et al. (2016, 2019), and proxy the variable influx of zooplankton from the Icelandic tongue into the southern Norwegian Sea using data from the thoroughly sampled standard monitoring Section N (Kristiansen et al., 2016, 2019).

Larger individuals of *C. finmarchicus*, including the juveniles, i.e., stages C4 and C5 and the adults (C6), dominated the population (>80%, **Figure 2**) during 1993–2002 (cold and low-saline high influx period), followed by a sudden phenological shift in 2003, which persisted until 2014 (warming and more saline low influx period). During the lower volume influx period, the numbers of juveniles and adults decreased to around 30% while the abundance of the recruits, i.e. stage C1–C3, increased to 70%. The environmental shift back to a fresher, but still warm, high influx after ∼2015 (Mork et al., 2019) resulted in dominance of *C. finmarchicus* juveniles and adults comparable to the previous high influx period. Calculating the ratio between the older (C4–C6) and younger (C1–C3) stages, followed by the Kruskal-Wallis test, confirms significant changes in the population structure during the three periods, 1993–2002, 2003–2014, and 2015–2020 ($p < 0.05$). The abundance of *C. hyperboreus* did also increase during the recent shift, although not to the same high values as observed during the earliest high influx period (**Figure 2A**). Nevertheless, there is a significant difference in the population abundance of *C. hyperboreus* during the three periods mentioned above (Kruskal-Wallis test, $p < 0.05$).

Herring Stomach Fullness and Diet Composition

To investigate whether the variable influx of zooplankton has any impact on the herring feeding dynamics, the estimated

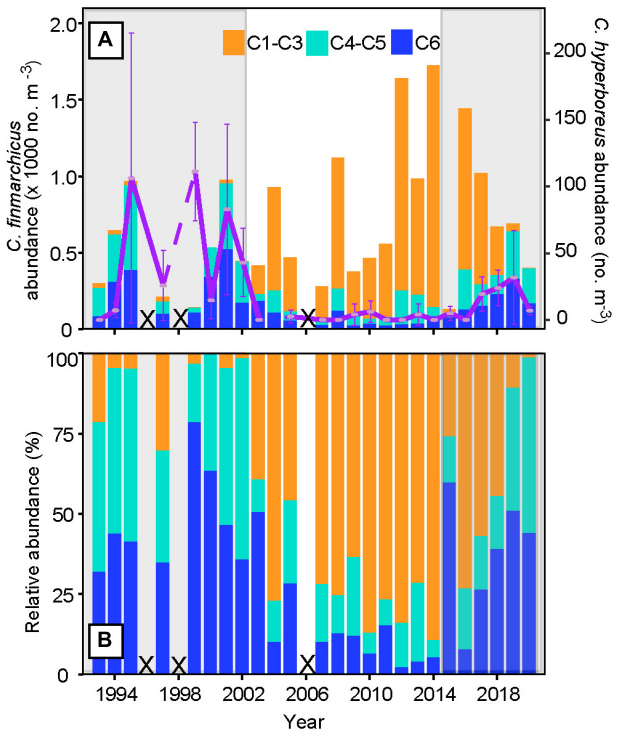


FIGURE 2 | Stage composition of *Calanus finmarchicus* and mean abundance of *Calanus hyperboreus* within the subarctic region at Section N [**(A)**, blue line in **Figure 1**] and [**(B)** relative abundance of *C. finmarchicus*, from 1993 to 2020]. The developmental stages of *C. finmarchicus* are grouped into recruits (C1–C3, orange), juveniles (C4–C5, light blue), and adults (C6, dark blue), while the mean abundance of all *C. hyperboreus* stages is shown in purple, together with the 95% confidence interval. The periods from 1993–2002 and 2015 to 2020 are highlighted in gray to illustrate co-occurring increased influx of arctic water into the southwestern Norwegian Sea (Skagseth et al., in review). Years with missing data are marked with crosses.

SFI is first gridded for each year (May), and subsequently the low influx period (2007–2011) is contrasted against the recent high influx period (2017–2020) using composite analysis (**Figure 3**). The gridded values are based on the values presented in **Supplementary Figure 4**. SFI was very low throughout the Norwegian Sea during the low influx period, with slightly elevated values only in the Icelandic tongue, upstream of the FS (**Figure 3A**). During the higher influx period, SFI significantly increased (Mann Whitney *U*-test, $p < 0.05$). Values were particularly high near Iceland and southwest of the FS (**Figure 3B**). There was also a marked increase along the Faroe Current, in and south of the IFF, and a marked "blob" with high values is evident in the eastern part of the study region (∼65°N, 0°W).

Stomach content was generally higher in the western area compared to the eastern area (**Figure 4**). The years 2008 and 2009 account for the higher values during the low influx period, with the stomach content being dominated by both *Calanus* spp. (see also **Supplementary Figures 5B,C**). However, in 2020, krill resulted in the highest wet weight value, which releases the highest SFI value near Iceland in **Figure 3B** (see also **Supplementary Figures 4I, 5F**). The high values, marking the "blob" in the eastern region, are from 2017 and 2019. The stomachs from these years were only weighed, and thus the diet composition is unknown.

Out of 104 analyzed herring stomachs, we found that the number of *C. finmarchicus* was, by far, the most common ingested species (**Supplementary Table 1**). *C. hyperboreus*, *Metridia* spp., krill and amphipods were also frequently encountered during the diet analysis. As krill and amphipods vary in size and weight, and dry weight data of these species were not available from 2007–2011, these were excluded from the biomass analysis of herring diet. When converted to biomass, using the length-weight relationship in **Table 1**, *C. finmarchicus* and *C. hyperboreus* clearly dominated while the others became unnoticeable. Therefore only the *Calanus* spp. are presented in **Figure 4**. During the low influx years of EIW, majority of the stomach biomass was dominated by *C. finmarchicus*, although highest values in 2007 and 2008 were represented by *C. hyperboreus*. In contrast, during the high volume influx in 2020, *C. hyperboreus* was found at all stations and more than 50% of the ingested content was represented by *C. hyperboreus*.

Zooplankton Distribution and Composition in May 2020

To get a better view of the prey abundance near the FS, zooplankton samples collected during the IESNS cruise (**Figure 5A**), were differentiated to species level. The biomass distribution of *C. finmarchicus* and *C. hyperboreus* in May, are presented in **Figures 5B–D**. Sharply contrasting hydrographic conditions characterized this region, with stations 1 and 2 being located at the edge of pure EIW, stations 4, 5, 9, 10, 13, and 14 are located in AW, stations 3, 6, and 7 are taken in recirculated Norwegian North Atlantic Water (NNAW, yellow-green colors in **Figure 6A**), while the rest are taken in more mixed near-front waters (**Figure 5A**, see Figure caption for stations numbers). The highest concentrations of the overwintered *C. finmarchicus* population (G_0) (stages C4 and C6) is sampled in the southward flow along the Jan Mayen Ridge (station 2, **Figure 5A**). However, high biomass values are also recorded at station 1 and 3 (**Figure 5C**).

The highest abundances of C. *hyperboreus* (stages C3–C6) were sampled at station 1 (**Figure 5**), within the eastward extension of the arctic water from the Iceland Sea and—maybe surprisingly—farther east at station 8 (**Figure 5D**). Relatively high values are also observed between these locations (stations 2, 3, and 5). Increased concentrations of *C. hyperboreus* therefore roughly coincide with the G_0 and adult *C. finmarchicus* population.

Although the younger stages of *C. finmarchicus* (nauplii and stages C1-C3) are not preferred herring food, they are also included in order to illustrate the contrast between subarctic water and AW (**Figure 5B**). High abundances were exclusively limited to stations 4 and 5, which is in the direct inflow of AW from the Iceland Basin. Since these likely represent the first generation (G_1), this illustrates the earlier phenological cycle in these warmer waters. We should also bear in mind that the actual nauplii number are likely to be higher in the environment as the 200 μm WP-2 used undersamples the small-sized nauplii.

Hydrographic Boundaries and Inter-Annual Changes

Horizontal Temperature Distribution (Sea Surface Temperatures Maps)

A climatological SST map over the FS (2003–2020, **Figure 6A**) shows that the Icelandic tongue contains cold surface water (1–2°C) on average in May, and the southeastern tip of this tongue veers clockwise around the underwater plateau which extends eastwards from Iceland. This suggests that topographically controlled deep flows influence the hydrography all the way to the surface, at least during May. The steep escarpment between this plateau and previously mentioned underwater valley blocks direct southward flow, and thus redirects these currents west toward the head of the valley, before these cold waters are allowed to continue toward the Faroe slope. This establishes the JMF between pure EIW and NNAW, which begins at the steep northern slope of this valley and continues north along the Jan Mayen Ridge.

The marked SST contrast at 64.5–65.0°N near Iceland (and at monitoring station KR5, see **Supplementary Figures 2, 3**) shows the sharpest part of the IFF, which separates AW from the subarctic waters from the north. The northernmost limit of AW is observed at 10–11°W, and this retroflection of the AW flow is likely guided by the shallower part of the plateau (see 500 m isobaths in **Figure 6A**). East of the constriction point at the head of the underwater valley, the IFF—now as a slightly more diffuse front between AW and NNAW—continues toward the southeast, roughly following the 2000 m isobath.

Interannual Temperature Variability Near the Feeding Spot

The depth-time plot of temperatures at standard hydrographic station KR6 (**Figure 6B**), shows the environment which the herring has experienced in May, shortly before continuing its westward migration across the JMF and into the FS.

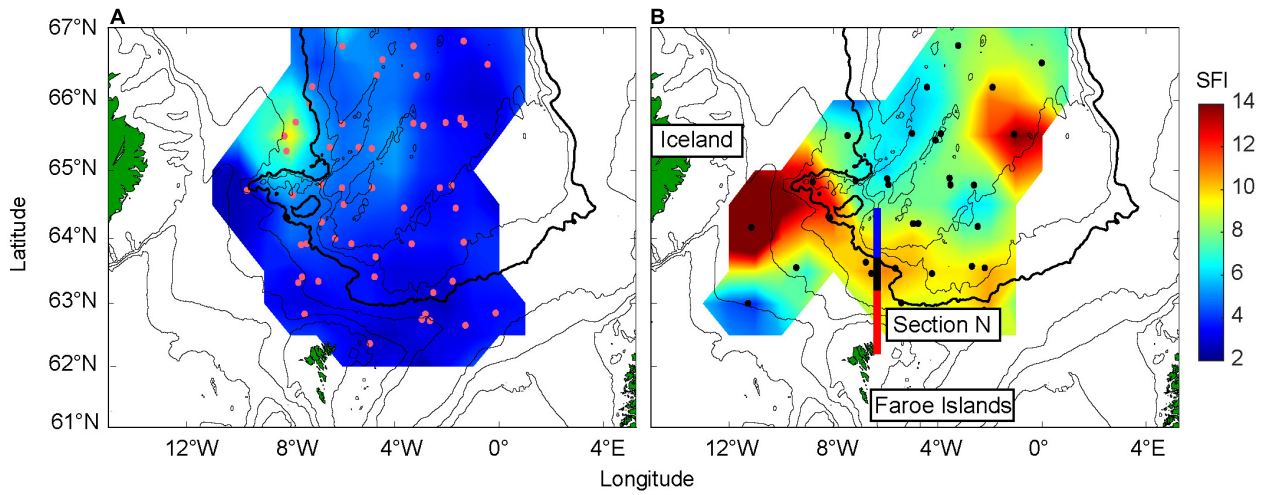


FIGURE 3 | Stomach fullness index (SFI) values averaged over contrasting periods [**(A)**, low influx period] 2007–2011 versus [**(B)**, high influx period] 2017–2020. The data have been gridded for each year, and the fields are subsequently averaged over the mentioned years. The colored regions along Section N are described in **Figure 1**. The purple **(A)** and black **(B)** dots show the positions where stomach samples were collected. The 200, 500, 1,000, 2,000 (bold), 2,500, and 3,000 m depth contours are shown.

Characteristic temperature peaks are observed in 1998, 2003, 2008, and 2017, which are also evident throughout the Nordic Seas (Malmberg and Valdimarsson, 2003; Hátún et al., 2005; Mork et al., 2019). Since around 2005, and more evidently since 2008, the depth of the 2°C isotherm has been increasing, between 30 and 120 m depths before 2003 to 80–280 m depths after 2005.

There is a significant difference in temperature before versus after 2003 (Welch t-test, $p < 0.05$). From the early 1990s to early 2000s, the temperature fluctuated at lower levels, with peaks observed in 1993 and 1996 (**Figure 6C**). In 2003, the temperature increased sharply by about 1.3°C. The following year, the temperature dropped again, although it continued to remain warmer than prior to 2003. The temperature has thereafter steadily increased, with a slight drop in 2019 and 2020. A regression analysis for the period 2004–2020 confirmed a significant positive trend with $p < 0.05$ and an average increase in temperature of 0.06°C per year. The salinity roughly follows the temperature pattern by being fresher during the colder years and more saline during the warmer years. After fluctuating at a higher level for a decade, the salinity dropped in 2014 and again in 2018 to 2020. In these years, the temperature did not decline with the salinity values.

DISCUSSION

Combining our results with key findings from Eliasen et al. (2021); Hátún et al. (2021), Homrum et al. (in review), and Skagseth et al. (in review), we discuss the most plausible drivers underlying the highly variable herring migration in May. Since Eliasen et al. (2021) find that the observed major distribution shifts of old herring are primarily induced by external factors such as temperature and/or food abundance, we limit the discussion to these two parameters.

The Feeding Spot

The FS frames the focus of the present study (**Figure 1**). Argo floats from the Iceland Sea (Hátún et al., 2021) and calculations of the arctic water thickness and its eastward distribution from the Iceland Sea and into the Norwegian Sea (Skagseth et al., in review) consistently demonstrate how closely arctic water is confined along the 2,000 m depth contour along the Jan Mayen Ridge, which at its southern end turns sharply west into a deep sea "valley" (at ∼65°N), and then continues southeastwards. The marine environment north/west of the 2,000 m isobaths (the Icelandic tongue) is therefore very different from the water east/south of this isobaths. A northward "leakage" of AW from the northernmost retroflection point of the warm current (at 10–11°W, **Figures 5**, **6A**) has an impact on the environment on the plateau which extends eastward from Iceland (65–66°N). We propose that the FS actually is a band of undiluted subarctic water veering clockwise between the 1,400 and 2,000 m isobaths, as is evident by bluish colors in the climatological SST map (**Figure 6A**). Our snap-shot view of both SST and *in situ* zooplankton in this region reveals the strong contrasts—high concentrations of overwintering *C. finmarchicus* (G_0) and *C. hyperboreus* and absence of small *C. finmarchicus* (G_1) in the subarctic water, and vice versa for the AW. This underscores the importance of respecting oceanographic boundaries, when carrying out such surveys, and subsequently analyzing the data. We also show that herring stomachs are persistently full within this particular region, and that stomach content almost solely is composed of the mentioned copepods. In addition, Homrum et al. (in review) demonstrate that herring occupying the western feeding area have the highest somatic condition. As the diet comprised increased abundance of *C. hyperboreus* during increased availability, suggests that *C. finmarchicus* may not be the only driver

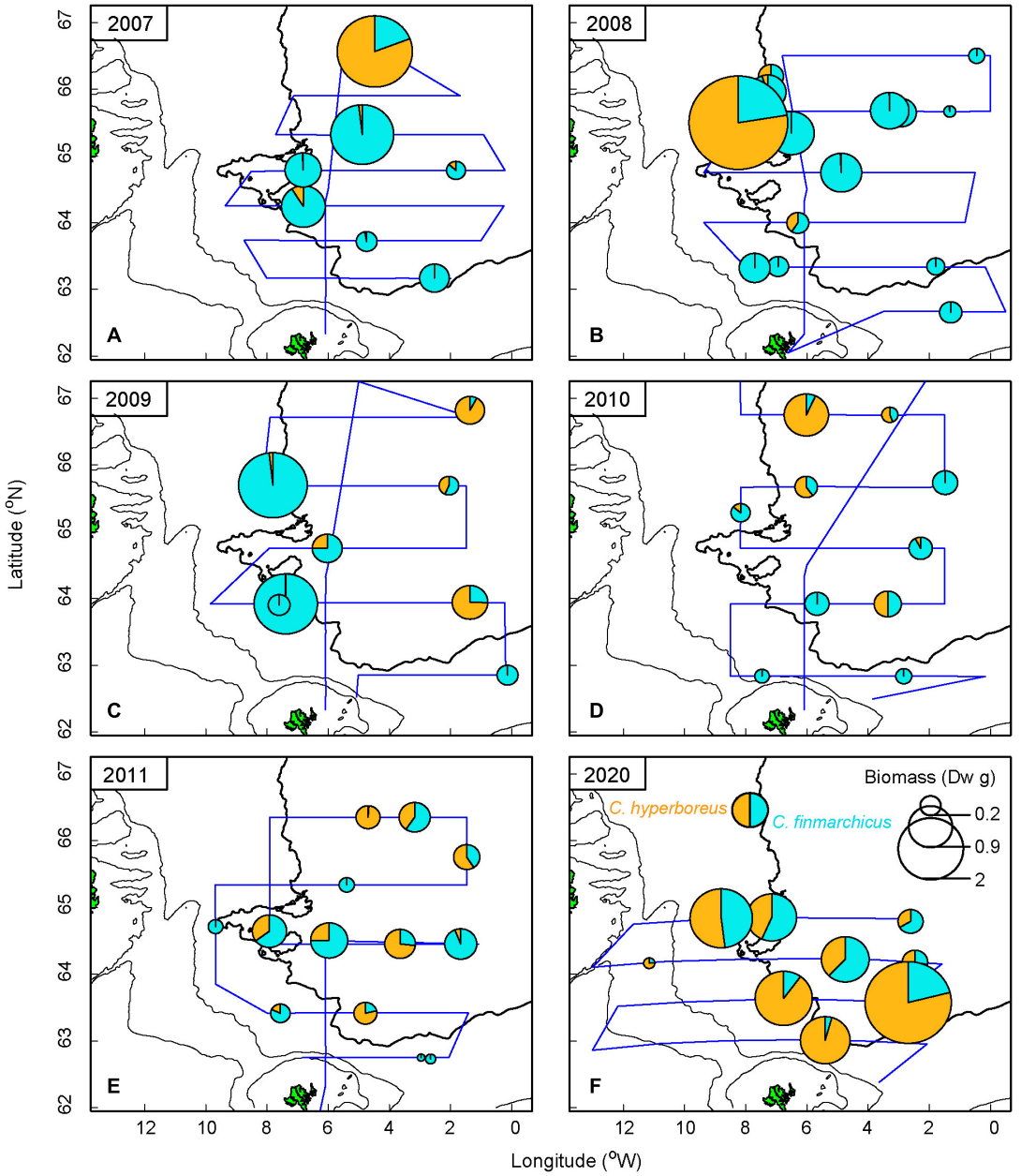


FIGURE 4 | Dry weight (Dw) of diet composition of the most common copepods—*Calanus finmarchicus* and *Calanus hyperboreus*—found in herring stomachs. Observations are from 2007 to 2011 **(A–E)** and 2020 **(F)**. The blue line represents cruise tracks each year. Data analysis on diet composition is not available for the years 2017–2019. The 2,000 m depth contour is shown in bold.

for the east to west migration during the feeding season. A unique aspect of the FS is that it consistently hosts large abundances of *C. hyperboreus*, and the recurrent congregation at this spot therefore strongly suggests that biomass of *C. hyperboreus* becomes increasingly more influential as the herring progresses further westwards during the feeding migration in May. These observations suggest that *the FS is a highly persistent/dependable food source for Norwegian spring spawning herring in May*.

Drivers for the Herring Occupancy of the Feeding Spot

Interannual variability in the influx of cold and zooplankton-rich waters into the Norwegian Sea strongly impacts the zooplankton community structure at the north Faroe slope (Section N, **Figure 2**; Kristiansen et al., 2016, 2019) as well as along the Norwegian slope (Svinøy Section, Skagseth et al., in review). This synchrony confirms a spatially extended biological influence from the western region.

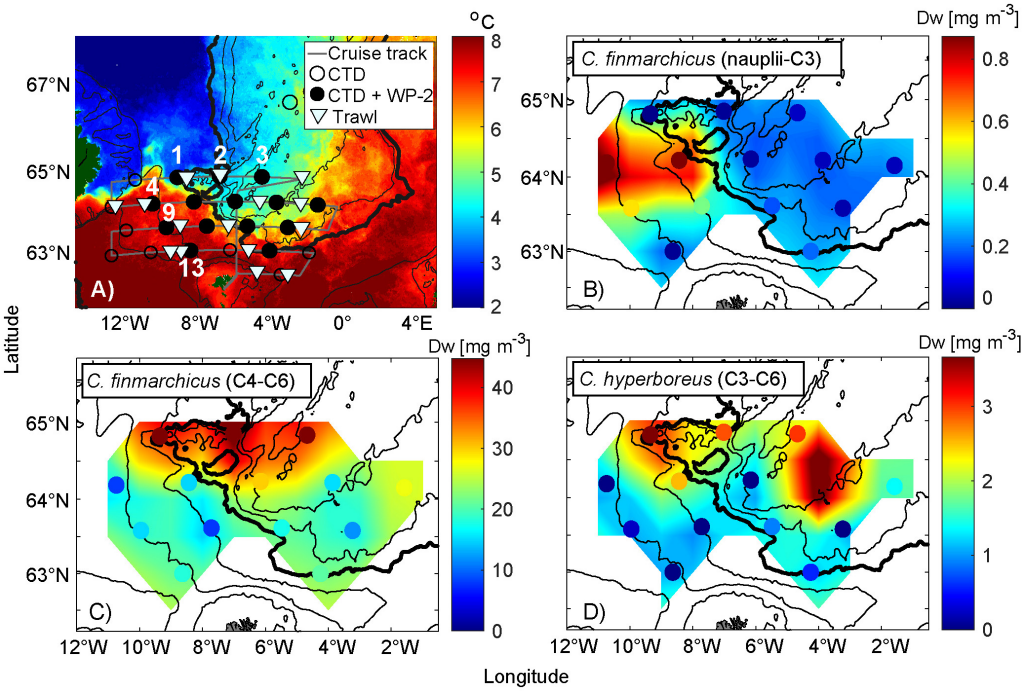


FIGURE 5 | Biomass distribution of *Calanus* spp. in relation to hydrographic conditions in May 2020. **(A)** Average satellite-based sea surface temperature from 30th April to 9th May, **(B)** biomass of *Calanus finmarchicus* developmental stages nauplii-C3 (dry weight, Dw), **(C)** *Calanus finmarchicus* C4–C6, and **(D)** *Calanus hyperboreus*. The colored dots represent the sampling position as well as actual value. Detailed information is displayed in **(A)** including the sampling positions of only CTD measurements (circled dots) and CTD measurements together with counted zooplankton data (black dots) and average trawling positions (triangles). The black dotted stations along the cruise track (gray) are numbered from left to right. The northernmost track line contains stations from 1 to 3. Below are stations 4–8, followed by stations 9–12. The stations along the southernmost track line include 13–14. Stations 1 and 2 in **(A)** are in a region of particular interest. The 200, 500, 1,000, 2,000 (bold), 2,500, and 3,000 m depth contours are shown. Note that the map scale in **(A)** is different from the other three subplots. The scales of *Calanus* spp. concentrations also vary.

We here consider the idealistic perspective that the FS represents the dominant food (zooplankton) source within the Norwegian Sea, and that lower zooplankton abundances in west and/or reduced eastward water transport (influx) results in lower abundances of the overwintered *C. finmarchicus* and *C. hyperboreus* in the central and eastern part of the Norwegian Basin.

After spawning, adult herring migrate toward regions with higher food concentrations (Pavshtiks, 1956; Broms et al., 2012; Melle et al., 2020), and they could therefore be influenced by "enviroregulation," as has been suggested for mackerel (Reid et al., 1997). Thus, decreasing overall zooplankton abundances would, decreasing overall zooplankton abundances would therefore compel herring to migrate closer to this source, i.e., the FS. We therefore consider the zooplankton abundance between the spawning grounds along the Norwegian shelf and the FS as a potential driver for westward migration. It is also well-known that the entrance of herring to the FS is limited by the local sea temperatures (Jakobsson and Østvedt, 1996; Misund et al., 1997). Since the relative importance of variable temperature and zooplankton abundance is not well understood, we will discuss the following hypotheses: *The abundance of adult herring at the FS in May is determined by: Hypothesis I (Hyp I) accessibility to the FS (thermal restriction) and/or Hypothesis II (Hyp II) food abundance between Norwegian slope and the FS.*

These hypotheses are discussed against the backdrop of contrasting herring distribution periods, 1996–1998, 1999–2002, and 2003–2016, inspired by Eliasen et al. (2021), in addition to the increase in subarctic waters masses (Mork et al., 2019; Holliday et al., 2020; Skagseth et al., in review) and the increase in *C. hyperboreus* and the large stages of *C. finmarchicus* in the southwestern Norwegian Sea, 2017–2020, shown herein. To compliment the spatio-temporally limited zooplankton and stomach data, presented in the present study, we also utilize the total zooplankton biomass from the IESNS survey, vertically averaged over the upper 200 m and temporally averaged over the periods mentioned above (**Figure 7**, with the raw data presented in **Supplementary Figure 6**).

The parameters used to assess the overall conditions for each period (see **Table 2**) are: *Herring distribution* (8 + years old) (Eliasen et al., 2021, their **Figure 6**), *Temperature* near the FS (**Figure 6C**, details below), *Influx* of subarctic water masses (EIW and Arctic Intermediate Water) to the southern Norwegian Sea (Kristiansen et al., 2019; Skagseth et al., in review), *Calanus sizes* at Sections N (**Figure 2**) and the Svinøy Section (Skagseth et al., in review), where "large" refers to high abundance of the

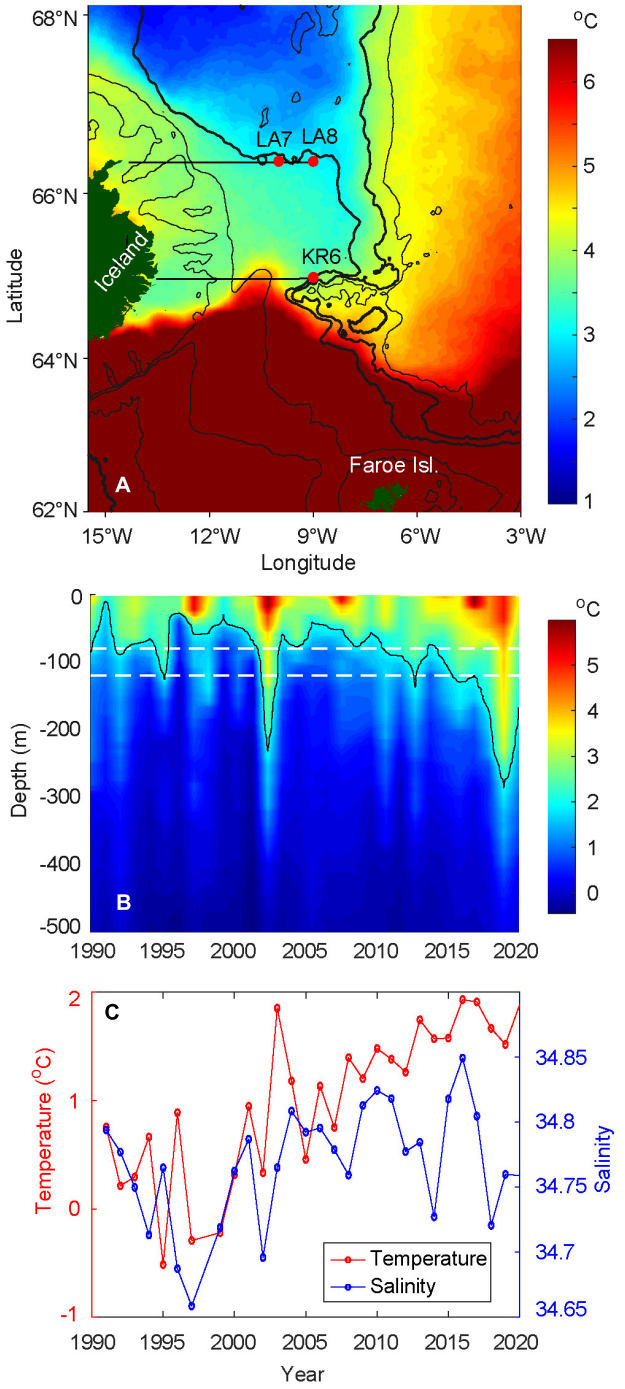


FIGURE 6 | Hydrographic conditions near the feeding spot. **(A)** Average sea surface temperatures, in May, from 2003–2020, **(B)** depth-time plot of temperature, at KR6 from 1991 to 2020, and **(C)** average temperature and salinity conditions in May at LA7 and LA8, from 1991 to 2020, at depth between 80 and 120 m [white dashed lines in **(B)**]. See **Supplementary Figures 2, 3** for detailed hydrographic conditions for the selected Icelandic sections. In **(C)**, data is not available in 1998. The red dots in **(A)** are the positions of the selected Icelandic sections. The 200, 500, 1,400 (bold), 2,000 (bold), and 2,500 m isobaths are shown in black. In **(B)**, the 2°C isothermal limit is displayed in black.

large C. *finmarchicus* stages (C4–C6) and high abundances of *C. hyperboreus*, and "small" refers to high abundance of the smaller C. *finmarchicus* stages (C1–C3), and low abundances of C. *hyperboreus*, *Food west* (Iceland Sea and western Norwegian Sea) and *Food East* (eastern Norwegian Sea). Prior to 2007, the food abundance estimates are purely based on the IESNS survey (**Figure 7**), while intermittently from 2007–2011, and again from 2017–2020, the evaluation of these data is complemented by stomach data (**Figures 3**, **4**).

The waters at KR6 are thermally stratified in May in the upper ∼150 m, with upper temperatures higher than 2°C, which is tolerable for herring. On top of the general warming through the observation period (1991–2020) rides strong interannual variability, likely induced by variable intrusions of AW, as well as air-sea heat exchanges. At the upstream LA stations, there is a thin and likely intermittent thermal stratification, with average near-surface temperatures just over 2°C and thus near the herring tolerance limit. Our "Temperature near the FS" parameter (**Table 2**) is estimated by a depth-average under the spring mixed layer (80–120 m) (ICES, 2016) at stations LA7 and LA8. This sensitive region experienced sub-zero temperatures during the late 1990s, but has warmed by about 2°C since then.

1996–1998

Adult herring congregated in the central and northern Norwegian Sea and were largely absent from the FS (Eliasen et al., 2021). Both temperatures and salinities were at their lowest through the observation period, supporting Hyp I. The influx of subarctic waters into the Norwegian Sea was very high (Kristiansen et al., 2019; Skagseth et al., in review), and the transported *Calanus* sizes were probably relatively large. This metric is, however, uncertain due to lack of data at Section N in 1996 and 1998. Food abundance was high on the western side, and much lower on the eastern side (**Figure 7A**), which supports Hyp II. The conditions for the four periods are summarized in **Table 2**.

1999–2002

Herring occupied the southern Lofoten Basin, and were totally absent from the FS (the literature references are hereafter as in the previous paragraph, if not stated otherwise). The northeastward displacement coincided with a continuous high influx, although declining throughout the period. The sustained high flow of nutrient-rich waters from the west contained increased zooplankton concentrations (**Figure 7B**), which likely boosted the secondary production the following consecutive years during spring. The transported *Calanus* sizes were at their largest during the observation period and the zooplankton biomass was also at its highest throughout the study region, including along the Norwegian slope and in the Lofoten Basin. This supports Hyp II. We suggest that the continued low temperature hindered herring in entering the FS, which supports Hyp I.

2003–2016

Herring started to shift southwards in 2003, and were congregating at the FS from 2005 and afterward. There was a marked temperature increase in 2003, and after a slight decline

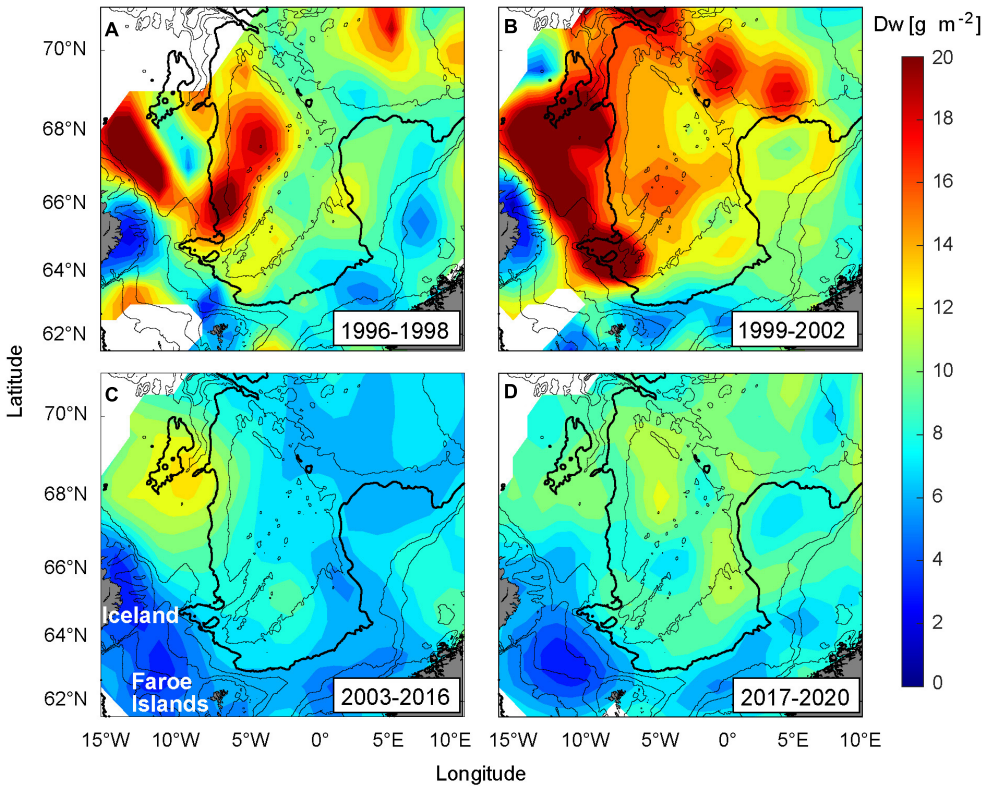


FIGURE 7 | Biomass of zooplankton (dry weight, Dw) distribution in May, averaged over the upper 200 m, and divided into the following four periods. **(A)** 1996–1998, **(B)** 1999–2002, **(C)** 2003–2016, and **(D)** 2017–2020. The 200, 500, 1,000, 2,000 (bold), and 3,000 m depth contours are shown.

TABLE 2 | Overview over relevant parameters for assessing the posed hypotheses during the four contrasting periods.

Parameters	1996–1998	1999–2002	2003–2016	2017–2020
Herring distribution	Not in FS (in central Norw. Sea)	Not in FS (in southern Lofoten B.)	At FS (fully shifted in 2005)	At FS (younger year classes north)
Somatic condition	Very poor	Poor	Good	Good
FS temperature	Very cold	Cold	Relatively warm	Relatively warm
Influx	Very high	Declining	Low	Increasing
Calanus sizes	Relatively large (uncertain, lack of data)	Large	Small	Large
Food west	High	Very high	Low (IESNS) (Medium stomachs, **Figure 3A**)	Very low (IESNS) (Fuller stomachs, **Figure 3B**)
Food east	Low	High	Very low (IESNS) (Empty stomachs, **Figure 3A**)	Low (IESNS) (Fuller stomachs, **Figure 3B**)
Hypothesis I	Supported	Supported	Supported	Not supported
Hypothesis II	Supported	Supported	Supported	Supported

See Discussion for the description of the parameters. The hypothesis state that the abundance of adult herring at the Feeding Spot is determined by (Hypothesis I) accessibility to the FS (thermal restriction) and/or (Hyppthesis II) food abundance between Norwegian slope and the Feeding Spot.

in 2005, the temperatures steadily increased until 2016, which strongly supports Hyp I. The influx was much reduced, and only small *Calanus* sizes were transported eastwards during this period. The food availability had reduced drastically throughout the Norwegian and the Iceland Seas (**Figure 7C**), which was also reflected in the somatch content (**Figure 3A**). Moderate values of both zooplankton biomass and SFI were only observed at, and upstream of, the FS, which thus strongly supports Hyp II.

2017–2020

Adult herring were still congregating at the FS. Despite a salinity decline, the temperatures at the FS remained high (**Figure 6B**), which supports Hyp I. The EIW influx and the *Calanus* sizes increased at both the north Faroe and Norwegian slopes, although not to the pre-2003 levels. The food on the western side was still relatively low, while a moderate increase had taken place on the eastern side (**Figure 7D**). The SFI maps, however, suggest

a marked increase (compared to the 2007–2011 period), and species differentiated stomach data reveal a large consumption of *C. hyperboreus* in the southeastern, as well as in the southwestern, Norwegian Sea (**Figure 4F**). Hyp II is therefore not supported.

Although this tentative evaluation does not provide final proofs, it suggests that the FS is indeed important for the condition of the herring stock, and that low temperatures can restrict herring from utilizing this important region. We also find that generally high abundances of zooplankton in the Norwegian Sea reduces the motivation to seek the FS.

Some Remaining Questions

Absence of herring from the FS in May (1996–2002, **Table 2**) is associated with poor somatic conditions during autumn (Homrum et al., in review), while the somatic conditions improved after 2003, when herring persistently congregated near the FS. While this supports our view of FS being an important and persistent feeding region, it also poses the apparent conundrum: poor conditions coincide with large zooplankton influx, while good conditions follow years with reduced influx. The improving somatic conditions after 2003 are likely due to more persistent feeding activity in Icelandic waters into the autumn months (Homrum et al., in review). This information fuels us with a second question: Is this temporally extended western occupation a prosperous sign of the increased abundance of a second *C. finmarchicus* generation during recent years (Strand et al., 2020), or is this an impoverished sign of reduced feeding conditions during spring and summer?

While temperature and food abundances clearly are important drivers for herring post-spawning migration dynamics, closer scrutiny of the feeding dynamics should include aspects like "learning" as the stock is able to gather in regions with high zooplankton densities due to their memory capabilities (Corten, 2000) as well as social learning (Corten, 2002).

It is, furthermore, tempting to ask if the temporally extended stay in Icelandic waters could influence recruitment at the spawning grounds along the Norwegian shelf. More than a hundred years ago Helland-Hansen and Nansen (1909) postulated that increased influx of subarctic waters toward the Norwegian shelf could have beneficial impact on e.g., herring recruitment. It is therefore noteworthy that recent good year-classes were spawned in 2002 and 2016, when high abundances of *C. hyperboreus* and larger *C. finmarchicus developmental* stages (**Figure 2**) were transported toward Norway, while the intermediate years, with mainly smaller individuals of *C. finmarchicus* and hardly any *C. hyperboreus*, did not provide any really good year classes. A thorough treatment of these questions is, however, beyond the scope of the present work whose focus is on conditions in May.

CONCLUSION

Our assessment, based on results presented herein, and in four other parallel papers, suggest that there is an optimal Feeding Spot (FS) for Norwegian spring spawning herring east of Iceland, in a region where confluence of cold subarctic waters from the Iceland Sea and south along the Jan Mayen Ridge lead to persistent supply of *Calanus hyperboreus* and large overwintered *Calanus finmarchicus*. Herring stomachs are persistently full in this region, and when a large part of the herring stock congregates at this location, the somatic conditions are high. Low temperatures can, however, restrict herring from entering this region, which results in deteriorated somatic conditions. There are also indications that zooplankton abundance in the Norwegian Sea regulates the motivation of herring to swim all the way from the spawning grounds along the Norwegian shelf to the FS. This food-driven "enviroregulation" would predict an eastward shifted herring distribution in May after 2016. However, this was not evident as the older herring remained in the FS, indulging on elevated food concentrations whilst temperature conditions remained suitable.

DATA AVAILABILITY STATEMENT

The original contributions presented in the study are included in the article/**Supplementary Material**, further inquiries can be directed to the corresponding author.

AUTHOR CONTRIBUTIONS

IK and HH composed the story. IK did the data analysis and led the writing process. HH, SE, JJ, and EG provided input to the data, analysis, and discussion. HP provided invaluable Icelandic data. All co-authors have read, commented, and agreed to the manuscript before submission.

FUNDING

This study was funded by the Fisheries Research Fund of the Faroe Islands (project number 19/00645), and comprised a part of a Ph.D. project on the ecology of *C. finmarchicus* in relation to environmental conditions in the southwestern Norwegian Sea.

ACKNOWLEDGMENTS

We are grateful for the help and constructive comments from co-workers, WGINOR members, and reviewers. We also wish to extend our gratitude to getting access to the PGNAPES database and to Solveig Olafsdottir for providing and discussing hydrographic data from the two Icelandic monitoring sections.

SUPPLEMENTARY MATERIAL

The Supplementary Material for this article can be found online at: https://www.frontiersin.org/articles/10.3389/fmars.2022.823006/full#supplementary-material

REFERENCES

Astthorsson, O. S., and Gislason, A. (2003). Seasonal variations in abundance, development and vertical distribution of *Calanus finmarchicus*, *C. hyperboreus* and *C. glacialis* in the East Icelandic Current. *J. Plankton Res.* 25, 843–854. doi: 10.1093/plankt/25.7.843

Bachiller, E., Skaret, G., Nøttestad, L., and Slotte, A. (2016). Feeding ecology of northeast atlantic mackerel, norwegian spring-spawning herring and blue whiting in the norwegian sea. *PLoS One* 2:25. doi: 10.5061/dryad.f5r7f

Blindheim, J. (2004). "Oceanography and climate," in *The Norwegian Sea Ecosystem*, ed. H. R. Skjoldal (Trondheim: Tapir Academic Press), 65–96.

Blindheim, J., Borovkov, V., Hansen, B., Malmberg, S., and Turrell, W. R. (2000). Upper layer cooling and freshening in the Norwegian Sea in relation to atmospheric forcing. *Deep Sea Res. I* 47, 655–680. doi: 10.1016/s0967-0637(99)00070-9

Böhme, L., and Send, U. (2005). Objective analyses of hydrographic data for referencing profiling float salinities in highly variable environments. *Deep Sea Res. II* 52, 651–664. doi: 10.1016/j.dsr2.2004.12.014

Broms, C., Melle, W., and Horne, J. K. (2012). Navigation mechanisms of herring during feeding migration: the role of ecological gradients on an oceanic scale. *Mar. Biol. Res.* 8, 461–474. doi: 10.1080/17451000.2011.640689

Corten, A. (2000). A possible adaptation of herring feeding migrations to a change in timing of the *Calanus finmarchicus* season in the eastern North Sea. *ICES J. Mar. Sci.* 57, 1261–1270. doi: 10.1006/jmsc.2000.0812

Corten, A. (2002). The role of " conservatism " in herring migrations. *Rev. Fish Biol. Fish.* 11, 339–361.

Dalpadado, P., Ellertsen, B., Melle, W., and Dommasnes, A. (2000). Food and feeding conditions of Norwegian spring-spawning herring (*Clupea harengus*) through its feeding migrations. *ICES J. Mar. Sci.* 57, 843–857. doi: 10.1006/jmsc.2000.0573

Deblois, E. M., and Rose, G. A. (1995). Effect of foraging activity on the shoal structure of cod (*Gadus morhua*). *Can. J. Fish. Aquat. Sci.* 52, 2377–2387. doi: 10.1139/f95-830

Eliasen, S. K., Homrum, E. I., Jacobsen, J. A., Kristiansen, I., Óskarsson, G. J., Salthaug, A., et al. (2021). Spatial distribution of different age groups of herring in Norwegian Sea, May 1996-2020. *Front. Mar. Sci.* 8:778725. doi: 10.3389/fmars.2021.778725

Fernö, A., Pitcher, T. J., Melle, W., Nøttestad, L., Mackinson, S., Hollingworth, C., et al. (1998). The challenge of the herring in the Norwegian Sea: making optimal collective spatial decisions. *Sarsia* 83, 149–167. doi: 10.1080/00364827.1998.10413679

Gislason, A., and Astthorsson, O. S. (2002). The food of Norwegian spring-spawning herring in the western Norwegian Sea in relation to the annual cycle of zooplankton. *Sarsia* 87, 236–247. doi: 10.1080/00364820260294860

Gislason, A., Gudmundsson, K., Olafsdottir, S. R., and Petursdottir, H. (2021). Inter-annual and decadal variability of *Calanus finmarchicus* and *C. hyperboreus* in Subarctic waters north of Iceland 1990-2020. *ICES J. Mar. Sci.* 79:246. doi: 10.1093/icesjms/fsab218

Häkkinen, S., and Rhines, P. B. (2004). Decline of subpolar North Atlantic circulation during the 1990s. *Science* 304, 555–559. doi: 10.1126/science.1094917

Hátún, H., and Chafik, L. (2018). On the recent ambiguity of the North Atlantic Subpolar Gyre Index. *J. Geophys. Res.* 123, 1–5. doi: 10.1029/2018JC014101

Hátún, H., Chafik, L., and Larsen, K. M. H. (2021). The Norwegian Sea Gyre – a regulator of iceland-scotland ridge exchanges. *Front. Mar. Sci.* 8:694614. doi: 10.3389/fmars.2021.694614

Hátún, H., Sandø, A. B., Drange, H., Hansen, B., and Valdimarsson, H. (2005). Influence of the Atlantic subpolar gyre on the thermohaline circulation. *Science* 309, 1841–1844. doi: 10.1126/science.1114777

Hay, S., Kiørboe, T., and Matthews, A. (1991). Zooplankton biomass and production in the North Sea during the Autumn Circulation Experiment, October 1987-March 1988. *Cont. Shelf Res.* 11, 1453–1476. doi: 10.1016/0278-4343(91)90021-W

Helland-Hansen, B., and Nansen, F. (1909). *The Norwegian Sea - Its Physical Oceanography Based Upon the Norwegian Researches 19001904*. Kristiania: Det Mallingske Bogtrykkeri.

Hirche, H. J. (1997). Life cycle of the copepod *Calanus hyperboreus* in the Greenland Sea. *Mar. Biol.* 128, 607–618. doi: 10.1007/s002270050127

Holliday, N. P., Bersch, M., Berx, B., Chafik, L., Cunningham, S., Florindo-López, C., et al. (2020). Ocean circulation causes the largest freshening event for 120 years in eastern subpolar North Atlantic. *Nat. Commun.* 11:585. doi: 10.1038/s41467-020-14474-y

Holliday, N. P., Hughes, S. L., Bacon, S., Beszczynska-Möller, A., Hansen, B., Lavín, A., et al. (2008). Reversal of the 1960s to 1990s freshening trend in the northeast North Atlantic and Nordic Seas. *Geophys. Res. Lett.* 35:L03614. doi: 10.1029/2007GL032675

Holst, J. C., Blindheim, J., Couperus, B., Hammer, C., Jákupsstovu, H., Melle, W., et al. (1999). *Report on Surveys of the Distribution, Abundance and Migrations of the Norwegian Spring-Spawning Herring, Other Pelagic Fish and the Environment of the Norwegian Sea and Adjacent Waters in Late Winter, Spring and Summer of 1999*. Available online at: https://www.hav.fo/PDF/Ritgerdir/2001/PGSPFN_report_2001.pdf (accessed April 1, 2021).

Holst, J. C., Dragesund, O., Hamre, J., Misund, O. A., and Østvedt, O. J. (2002). Fifty years of herring migrations in the Norwegian Sea. *ICES Mar. Sci. Symp.* 215, 352–360.

Holst, J. C., Røttingen, I., and Melle, W. (2004). "The Herring," in *The Norwegian Sea Ecosystem*, ed. H. R. Skjoldal (Trondheim: Tapir Academic Press), 203–226.

Holst, J. C., and Slotte, A. (1998). Effects of juvenile nursery on geographic spawning distribution in Norwegian spring-spawning herring (*Clupea harengus* L.). *ICES J. Mar. Sci.* 55, 987–996. doi: 10.1006/jmsc.1998.0371

Homrum, E. I., Óskarsson, G. J., Ono, K., Hølleland, S., and Slotte, A. (in review). Large-scale changes in the spatiotemporal distribution of Norwegian spring spawning herring (*Clupea harengus*) following warming and freshening of the Norwegian Sea: effects on somatic condition and gonad development. *Front. Mar. Sci.*

ICES (2016). *Report of the Working Group of International Pelagic Surveys (WGIPS), 18-22 January, Dublin, Ireland. ICES CM 2016/SSGIEOM:05*. (Dublin: ICES), 433.

ICES (2020). Working group on the integrated assessments of the Norwegian Sea (WGINOR; outputs from 2020 meeting). *ICES Sci. Rep.* 3:114. doi: 10.17895/ices.pub.8021

Jakobsson, J., and Østvedt, O. J. (1996). *A Preliminary Review of Joint Investigations on the Distribution of Herring in the Norwegian and Iceland Seas 1950-1970*. Available online at: https://imr.brage.unit.no/imr-xmlui/bitstream/handle/11250/105621/CM_1996_H_14.pdf?sequence=1&isAllowed=y (accessed April 1, 2021).

Kristiansen, I., Gaard, E., Hátún, H., Jónasdóttir, S., and Ferreira, A. S. A. (2016). Persistent shift of Calanus spp. in the southwestern Norwegian Sea since 2003, linked to ocean climate. *ICES J. Mar. Sci.* 73, 1319–1329. doi: 10.1038/278097a0

Kristiansen, I., Hátún, H., Petursdottir, H., Gislason, A., Broms, C., Melle, W., et al. (2019). Decreased influx of *Calanus* spp. into the south-western Norwegian Sea since 2003. *Deep. Res. Part I Oceanogr. Res. Pap.* 149:103048. doi: 10.1016/j.dsr.2019.05.008

Kristiansen, I., Jónasdóttir, S. H., Gaard, E., Eliasen, S. K., and Hátún, H. (2021). Seasonal variations in population dynamics of *Calanus finmarchicus* in relation to environmental conditions in the southwestern Norwegian Sea. *Deep Sea Res. Part I Oceanogr. Res. Pap.* 171:103508. doi: 10.1016/j.dsr.2021.103508

Larsen, K. M. H., Hátun, H., Hansen, B., and Kristiansen, R. (2012). Atlantic water in the Faroe area: sources and variability. *ICES J. Mar. Sci.* 69, 802–808. doi: 10.1093/icesjms/fst048

Macrander, A., Valdimarsson, H., and Jónsson, S. (2014). Improved transport estimate of the East Icelandic Current 2002–2012. *J. Geophys. Res.* 119, 3407–3424. doi: 10.1002/2013JC009517

Malmberg, S. A., and Valdimarsson, H. (2003). Hydrographic conditions in Icelandic waters, 1990-1999. *ICES J. Mar. Sci.* 219, 50–60.

Melle, W., Klevjer, T., Strand, E., Wiebe, P. H., Slotte, A., and Huse, G. (2020). Fine-scale observations of physical and biological environment along a herring feeding migration route. *Deep Res. Part II* 180:104845. doi: 10.1016/j.dsr2.2020.104845

Misund, O. A., Melle, W., and Fernö, A. (1997). Migration behaviour of norwegian spring spawning herring when entering the cold front in the norwegian sea. *Sarsia* 82, 107–112. doi: 10.1080/00364827.1997.10413644

Misund, O. A., Vilhjálmsson, H., Jákupsstovu, S. H. Í, Røttingen, I., Belikov, S., Asthorsson, O., et al. (1998). Distribution, migration and abundance

of norwegian spring spawning herring in relation to the temperature and zooplankton biomass in the Norwegian Sea as recorded by coordinated surveys in spring and summer 1996. *Sarsia* 83, 117–127. doi: 10.1080/00364827.1998.10413677

Mork, K. A., Skagseth, Ø., and Søiland, H. (2019). Recent warming and freshening of the Norwegian Sea observed by Argo data. *J. Clim.* 32, 3695–3705. doi: 10.1175/JCLI-D-18-0591.1

Østvedt, O. J. (1965). The migration of Norwegian herring to Icelandic waters and the environmental conditions in May-June 1961-1964. *Fisk. Skr. Ser. Havundersøkelser* 13, 29–47.

Pavshtiks, E. A. (1956). Seasonal changes in plankton and feeding migrations of herring. *Herring North Eur. Basin Adjac. Seas* 1, 104–139. doi: 10.1890/08-1817.1

Reid, D. G., Turrell, W. R., Walsh, M., and Corten, A. (1997). Cross-shelf processes north of Scotland in relation to the southerly migration of Western mackerel. *ICES J. Mar. Sci.* 54, 168–178. doi: 10.1006/jmsc.1996.0202

Richter, K., and Maus, S. (2011). Interannual variability in the hydrography of the Norwegian Atlantic Current: frontal versus advective response to atmospheric forcing. *J. Geophys. Res. Oceans* 116:C12031. doi: 10.1029/2011JC007311

Semper, S., Pickart, R. S., Våge, K., Larsen, K. M. H., Hátún, H., and Hansen, B. (2020). The Iceland-Faroe Slope Jet: a conduit for dense water toward the Faroe Bank Channel overflow. *Nat. Commun.* 11:5390. doi: 10.1038/s41467-020-19049-5

Serra, N., Käse, R. H., Köhl, A., Stammer, D., and Quadfasel, D. (2010). On the low-frequency phase relation between the Denmark Strait and the Faroe-Bank Channel overflows. *Tellus A* 62, 530–550. doi: 10.1111/j.1600-0870.2010.00445.x

Skagseth, Ø., Broms, C., Gundersen, K., Hátún, H., Kristiansen, I., Mork, K. A., et al. (in review). Atlantic and Arctic waters in the Norwegian Basin, between year variability and potential ecosystem implication. *Front. Mar. Sci*.

Skjoldal, H. R., Saetre, R., Faernö, A., Misund, O. A., and Røttingen, I. (eds) (2004). *The Norwegian Sea Ecosystem*. Trondheim: Tapir Academic Press.

Strand, E., Bagøien, E., Edwards, M., Broms, C., and Klevjer, T. (2020). Spatial distributions and seasonality of four *Calanus* species in the Northeast Atlantic. *Prog. Oceanogr.* 185:102334. doi: 10.1016/j.pocean.2020.102344

Thórdardóttir, T. (1977). "Primary production in north Icelandic waters in relations to recent climatic changes," in *Polar Oceans*, ed. M. J. Dunbar (Calgary: Arctic Institute-North America), 655–665.

Utne, K. R., Huse, G., Ottersen, G., Christian Holst, J., Zabavnikov, V., Arge Jacobsen, J., et al. (2012). Horizontal distribution and overlap of planktivorous fish stocks in the Norwegian Sea during summers. *Mar. Biol. Res.* 8, 420–441. doi: 10.1080/17451000.2011.640937

Conflict of Interest: The authors declare that the research was conducted in the absence of any commercial or financial relationships that could be construed as a potential conflict of interest.

Publisher's Note: All claims expressed in this article are solely those of the authors and do not necessarily represent those of their affiliated organizations, or those of the publisher, the editors and the reviewers. Any product that may be evaluated in this article, or claim that may be made by its manufacturer, is not guaranteed or endorsed by the publisher.

Copyright © 2022 Kristiansen, Hátún, Jacobsen, Eliasen, Petursdottir and Gaard. This is an open-access article distributed under the terms of the Creative Commons Attribution License (CC BY). The use, distribution or reproduction in other forums is permitted, provided the original author(s) and the copyright owner(s) are credited and that the original publication in this journal is cited, in accordance with accepted academic practice. No use, distribution or reproduction is permitted which does not comply with these terms.

frontiers in Marine Science

ORIGINAL RESEARCH
published: 15 March 2022
doi: 10.3389/fmars.2022.824614

Impacts of a Changing Ecosystem on the Feeding and Feeding Conditions for Atlantic Salmon During the First Months at Sea

Kjell Rong Utne[1], Øystein Skagseth[1], Vidar Wennevik[1], Cecilie Thorsen Broms[1], Webjørn Melle[1] and Eva B. Thorstad[2]*

[1] Institute of Marine Research, Bergen, Norway, [2] Norwegian Institute for Nature Research (NINA), Trondheim, Norway

During the last decades, many wild Atlantic salmon populations have declined dramatically. One hypothesis for an observed reduction in salmon marine growth and survival is reduced abundance of prey. However, the effect of spatial and temporal variation in marine prey abundance on post-smolt feeding conditions is poorly understood. Here we use stomach content data from 2572 salmon post-smolts sampled during 25 years in the Northeast Atlantic Ocean to examine spatial and temporal changes in diet and stomach fullness. Sandeel larvae west of Scotland and Ireland and in the northern North Sea, herring larvae in the eastern part of the Norwegian Sea, and amphipods in the western part of the Norwegian Sea were particularly important prey species. There was a reduction of fish larvae in the post-smolt stomachs over a large geographic area when comparing the period 1995–2004 to 2008–2019. This may be result of a bottom-up driven process, as increasing extent of Arctic Water masses and zooplankton abundance were positively correlated with post-smolt stomach fullness in the Norwegian Sea. Furthermore, the interspecific competition for fish larvae between post-smolts and mackerel may have increased with a larger mackerel stock expanding the feeding migrations northwards since 2007.

Keywords: Norwegian Sea, fish larvae, zooplankton, mackerel, oceanography, diet

OPEN ACCESS

Edited by:
Alberto Basset, University of Salento, Italy

Reviewed by:
Daniel James Madigan, University of Windsor, Canada
John Kocik, Northeast Fisheries Science Center, United States

****Correspondence:***
Kjell Rong Utne
kjell.rong.utne@hi.no

Specialty section:
This article was submitted to Marine Ecosystem Ecology, a section of the journal Frontiers in Marine Science

Received: *29 November 2021*
Accepted: *22 February 2022*
Published: *15 March 2022*

Citation:
Utne KR, Skagseth Ø, Wennevik V, Broms CT, Melle W and Thorstad EB (2022) Impacts of a Changing Ecosystem on the Feeding and Feeding Conditions for Atlantic Salmon During the First Months at Sea. Front. Mar. Sci. 9:824614. doi: 10.3389/fmars.2022.824614

INTRODUCTION

Since the 1960s, many wild Atlantic salmon populations have declined dramatically, both because of human impacts in rivers and coastal areas, and ecosystem effects in the ocean causing increased mortality in the marine phase (Parrish et al., 1998; Otero et al., 2011; Forseth et al., 2017; ICES, 2021a). Individual growth during the marine phase has been reduced in many regions, concurring with lower marine survival (Friedland et al., 2000; Jonsson and Jonsson, 2004; Todd et al., 2008; Jonsson et al., 2016). Several causes for the reduction in growth and survival have been suggested, spanning from increased numbers and spatial shifts of predators, or reduced prey availability due to interspecific competition, to anthropogenic activity such as fish farming (e.g., Parrish et al., 1998; Jonsson et al., 2016; Vollset et al., 2016; Thorstad et al., 2021). The vast ocean areas used by Atlantic salmon as marine feeding grounds, and the lack of annual ocean surveys targeting Atlantic salmon, have limited the possibilities of detailed studies addressing the different hypotheses on why marine growth and survival have declined. There is large regional and temporal variation in marine growth and survival of Atlantic salmon (ICES, 2021a; Vollset et al., 2022), further complicating such studies.

Despite being one of the world's most studied fish species, detailed knowledge of the ocean distribution of Atlantic salmon has been limited. Recent studies based on advances in genetic and electronic tagging methods have shown how Atlantic salmon post-smolts (the life stage when they have entered the marine environment for the first time and until the end of the first winter in the sea) and adults use large areas of the North Atlantic Ocean, and how salmon from different regions vary in their migration patterns and distribution (Strøm et al., 2017; Bradbury et al., 2021; Gilbey et al., 2021; Rikardsen et al., 2021). The increased knowledge on the oceanic distribution of Atlantic salmon has provided new opportunities to analyze and understand the causality underlying the variation in marine growth and survival. The distribution of post-smolts from different European regions in the northeast-Atlantic Ocean was recently mapped (Gilbey et al., 2021). The area west of Ireland and Scotland and further north into the Norwegian Sea is an important migratory pathway for post-smolts in the Northeast Atlantic. These results form an important basis for studies aiming at addressing how regional mechanisms affect post-smolt growth and survival in the Northeast Atlantic.

The first months at sea are thought to be a critical period for the overall marine growth, survival and time spent at sea of Atlantic salmon (McCarthy et al., 2008; Trehin et al., 2021). For post-smolts sampled in the Norwegian Sea, there was a drop in condition factor in the period 2004–2012 and the condition factor remained low thereafter. The drop in condition factor was associated with reduced stomach fullness, indicating poorer prey availability and feeding opportunities during this period (Utne et al., 2021a). A reduced growth of Atlantic salmon from several populations based on scale analyses has also been shown during this period (Jensen et al., 2012; Trehin et al., 2021; Vollset et al., 2022). The observed reduction in stomach fullness, condition factor and individual growth may explain the reduced marine survival after 2004. The marine survival has in general decreased since the 1960s (Parrish et al., 1998) but information about post-smolt size and feeding conditions in the Northeast-Atlantic prior to 1995 is limited. The range of prey species consumed by post-smolts during their first summer in the ocean, and which prey species were the most important food items, have been identified (e.g., Rikardsen et al., 2004; Haugland et al., 2006; Utne et al., 2021a). However, these data have not been used to address how the post-smolt diet may have changed in time and space, and potentially contributed to the reduced condition and growth of Atlantic salmon at sea. Combining knowledge of migratory pathways and distribution of post-smolts with data on the abiotic and biotic conditions along the migration route, make it possible to study how prey availability and other factors affect post-smolts within this geographic region. We hypothesize that the marine feeding conditions for post-smolt in parts of the Northeast Atlantic became poorer in the period 2004–2012, and that this was linked to large-scale ecosystem changes, since there was a synchronous reduction in condition factor, stomach fullness and growth in Atlantic salmon from many European populations.

The main objective of the present study was to investigate if there has been a reduction of post-smolt prey availability within geographic regions along the migratory routes in the Northeast-Atlantic, and if so, to identify the mechanisms causing this reduction. The approach is to estimate (1) geographic and temporal variation in consumption of important prey species and prey groups, (2) the geographic variation in post-smolt stomach fullness in the period 2008–2019 compared to the period 1995–2004, 3) how changes in the marine environment have affected post-smolt feeding conditions. We link data on post-smolt diet in the Northeast Atlantic during 1995–2019 with data on hydrographic conditions, prey abundance and potential competitors.

MATERIALS AND METHODS

Biological Sampling

Atlantic salmon post-smolts were caught in trawl surveys conducted west of Ireland and Scotland, in the northern North Sea, and in the Norwegian Sea in May-August during 1995–2019 (**Figure 1A**). The total sample consisted of 2,572 post-smolts caught during a total of 40 surveys (**Supplementary Table 1**). These include dedicated salmon surveys targeting areas where salmon were known to migrate, surveys mapping the geographic distribution of salmon, and ecosystem surveys targeting other pelagic species but catching salmon post-smolts as bycatch. In all surveys, a pelagic trawl towed at the surface at 3–5 knots (5.6–9.3 km/h) with additional floats was used. Two large floats attached on each side and a float in the center kept the trawl at the surface during towing. More information about surveys objectives, trawling and biological sampling is given by Utne et al. (2021a). Salmon larger than 35 cm before August and larger than 40 cm in August (Gilbey et al., 2021) were excluded from further analyses to ensure that the dataset only included post-smolts.

Fork length to nearest half centimeter and weight to nearest gram were recorded for all sampled post-smolts. Stomachs were removed from the fish on deck and frozen for later analyses of diet. The stomach content was identified to species level when possible, or to closest family if too digested for species identification. Prey identification was based on visual identification of body morphology and species-specific characteristics such as spines, number of legs, pigmentation, etc. The weight of all unique prey groups in each stomach was recorded for all samples. Prey species and groups from each stomach were dried separately at 70°C for more than 24 h, and dry weight was recorded. The feeding ratio (*FR*) is an estimate of the dry weight of the stomach content relative to the fish dry weight. It is a snapshot of the stomach content at the time of sampling. The feeding ratio was calculated following Eq. 1:

$$FR = \frac{100\, m_s}{m_f - m_s} \quad (1)$$

where m_f is the mass (g) of the post-smolt and m_s is the mass (g) of the stomach content. FR_{fish} and FR_{zoo} are equivalent to FR where m_s is the mass of fish or zooplankton in the stomach, respectively.

Regional and Temporal Variation in Diet

To understand spatial and temporal variation in the post-smolt diet, the data sampled along the post-smolt migration routes in the northeast Atlantic region, as identified by Gilbey et al. (2021), were divided into five regions. The diet of post-smolts sampled in each region is presented on an annual basis. The rationale for the separation of subregions was differences in depth (shelf, slope, or deep basin areas), ocean current systems, and dominating water masses. The subregions are: (1) West of Ireland and Scotland (west of 2°W and south of 63°N), where post-smolts migrate along the narrow shelf area dominated by warm Atlantic water flowing northwards. (2) Northern North Sea, which is a shallow shelf area (east of 2°W d south of 62°N). This is the migration pathway for salmon originating from rivers with outlets into the North Sea. Fish from Ireland, western parts of Scotland and countries further south can also migrate through the northwestern part of this area. (3) Southern Norwegian Sea (between 62 and 67°N). The migratory pathway for post-smolts in this region is along the slope on the eastern side of the Norwegian Sea in the warm Atlantic water flowing northwards. (4) Northwestern Norwegian Sea (north of 67°N and west of 5°E). A general pattern is that post-smolts when reaching the Vøring platau at 67°N either migrate northwestward or follow the slope further northeastward, although the migration pattern seems to vary greatly in this region. The northwestward migration starts in a region of the western branch of the Atlantic water, the Norwegian Atlantic Front Current (NwAFC), and continue toward Jan Mayen (**Figure 1B**). (5) Northeastern Norwegian Sea (north of 67°N and east of 5°E). Individuals following the eastern branch of the Atlantic water, the Norwegian Atlantic Slope Current (NwASC), will mainly be distributed in the northeastern Norwegian Sea.

Geographic and Temporal Variation in Stomach Fullness and Consumption of Important Prey

One objective was to identify geographic variation in stomach fullness, here expressed as FR_{zoo} and FR_{fish}, and if these indices changed with time. Secondly, we wanted to identify geographic variation in the probability to consume important prey species. The following prey species/groups were included in the analyses, as they have been identified as important prey groups in earlier studies (Haugland et al., 2006; Utne et al., 2021a): *Ammodytes* spp. larvae (hereafter referred to as sandeel), *Clupea harengus* larvae (hereafter referred to as herring larvae), *Sebastidae* and *Myctophidae* larvae (hereafter referred to as mesopelagic fish larvae), amphipods, euphausiids, and copepods. The number of samples from each year varied, and some years with few or no samples limited the possibility to perform a temporal analysis of geographic differences in feeding ratio or the probability to consume important prey. The data set was therefore aggregated into two time periods for geographical analyses of stomach fullness: 1995–2004 (high condition factor period) and 2008–2019 (low condition factor period) (Utne et al., 2021a). There were no data available for the years 2005–2007. A division into finer time periods was initially tested but rejected due to limited sample size and poor model fit to data for some of the periods.

Geographic interpolated maps of FR_{zoo}, FR_{fish}, and six prey species/groups were produced with generalized additive modeling (GAM) (Hastie and Tibshirani, 1990). This modeling approach interpolates with a smoothing function. Smoothing regression techniques are data-driven and do not force the shape of the response to any parametric form. FR_{fish} and FR_{zoo} had skewed distributions with a high proportion of zero values, and a two-component hurdle model was therefore applied for these response variables. The hurdle model combined two models: (1) A binomial (empty/not empty stomachs) model, and (2) a positive biomass model for the stomach content, for which the data was modeled with a gamma distribution. A Tweedie distribution with log-link was tested for these response variables, but the model fits were not found satisfactory.

For estimating the probability of consuming different prey items, a binomial model was applied, where the response variable was presence/absence of respective prey in the stomachs. From 2012 and onward, all fish larvae were identified to *teleosti* and not to species or family level. Only years with fish larvae identified to species or family level were included in the models for prey presence. In the applied models,

$$r = \alpha + s_1\left(lat_i, lon_i\right) + year + \varepsilon_i \quad (2)$$

r is the response for fish i, s_1 is a two-dimension smoothing term used for latitude and longitude, *year* is included as a random effect variable, and ε is a random normal distributed error term with variance according to the distribution of the response variable. For presence/absence of prey, a logit-link was applied, while a log-link was used for FR_{fish} and FR_{zoo}. The parsimony principle was used to select the model with the lowest Akaike Information Criterion (AIC) (Burnham and Anderson, 2002). GAMs were fitted using the R statistical programming v.4.1.0 environment with package mgcv v. 1.8-35 (Wood, 2011). All model assumptions were visually assessed using Q–Q plots and residual variation vs. fitted values and leverage.

A reduced feeding ratio for post-smolts sampled in the Norwegian Sea in the period 2003–2012 have previously been presented (Utne et al., 2021a) based on the same dataset applied in the analyses presented here. Here we use the data in new analyses to understand the geographic variation in feeding ratio within the Northeast Atlantic, and if this has changed over time. The dataset is also, for the first time, used to explore where the different prey groups are commonly found in post-smolt stomachs.

Linking Post-smolt Feeding to Data on Environmental Conditions and Abundance of Prey and Potential Competitors

The final objective of this study was to understand if changes in post-smolt stomach fullness could be explained by changes in environmental conditions, prey abundance, or interspecific competition. For the Norwegian Sea, there are sufficient data from post-smolt stomach samples, prey abundance and

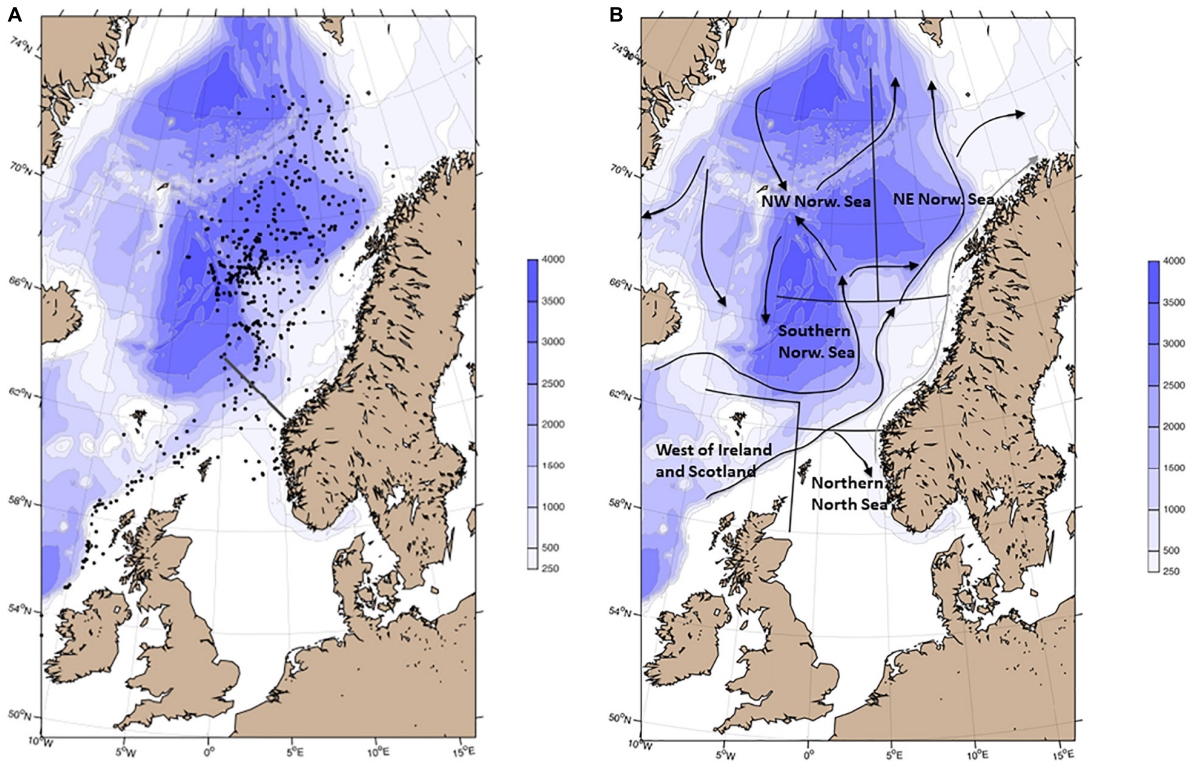


FIGURE 1 | (A) The geographic distribution of sampled post-smolts. Each circle represents a location where post-smolts were sampled, but the number of individuals within each location vary from one to tens of post-smolts. Black solid line off the Norwegian coast around 63°N represents the survey transect measuring hydrography and sampling zooplankton (Svinøy section). **(B)** Map of the study area with the different sub-regions addressed in the analyses, and arrows representing the general currents in the Northeast Atlantic.

environmental data to test this statistically. For the region west of Ireland and Scotland and the northern North Sea, the data are not sufficient to support statistical analyses, but relevant data are presented and evaluated qualitatively.

For the Norwegian Sea ecosystem, historic recruitment of Norwegian-Spring-Spawning Herring (NSSH) for the years 1995–2018 as estimated by stock assessment (ICES, 2020a) was used as a proxy for potential availability of fish larvae available as prey for post-smolts in each year. Standing biomass of zooplankton in May was included as an index of interannual variability in zooplankton abundance. This zooplankton index was calculated from plankton net (WP2) hauls from 200 m depth to the surface at stations with fixed spacing covering the majority of the Norwegian Sea. More information about the zooplankton index is given by ICES (2021b). Mackerel can be a potential competitor for post-smolt prey (Utne et al., 2021b). The spawning stock biomass for Northeast Atlantic mackerel estimated from the analytic assessment (ICES, 2021c) was therefore included in the analyses. Two indices of water circulation for the Norwegian Sea were retrieved from ICES (2021b), which were maximum salinity of the Atlantic Water masses (ATL_{smax}) and proportion of arctic water masses ARC_{prop}. Both indices were measured at a hydrographic transect in the southern Norwegian Sea in May (Svinøy section, **Figure 1A**). The central part of this transect covers the core of the warm and saline Atlantic Water flowing northward in the Norwegian Sea. ARC_{prop} represents the westernmost part of the transect, which is influenced by Arctic Water from the Iceland and Greenland seas (**Figure 1B**). ATL_{smax} is the maximum salinity measured along the transect, while ARC_{prop} is the proportion of the transect with salinity $< 34.9‰$ and water temperature $< 4°C$.

For the region west of Scotland and Ireland, historic recruitment of blue whiting for the years (1995–2018) as estimated by stock assessment (ICES, 2020a) was included in the analyses. Total annual commercial landings were used as a proxy of sandeel abundance, because historic estimates of recruitment or stock size were not available for the regions west Scotland (ICES sandeel region 6a), around Shetland (ICES sandeel region 7), and northern North Sea (ICES sandeel region 5). Total annual commercial landings in these regions give a qualitative representation of sandeel abundance in the years 1995–2018 (ICES, 2020b), with the assumption that the landings reflect stock abundance.

The indices are presented with loess smoothing overlaying the annual point values to show the general trend in temporal development. Loess smoothing is a non-parametric technique that fits a smooth curve through a scatter plot by using local weighted regression, which was done with the R-package "stats" (R Core Team, 2020) using span equal to 0.75 and 2nd degree polynomials.

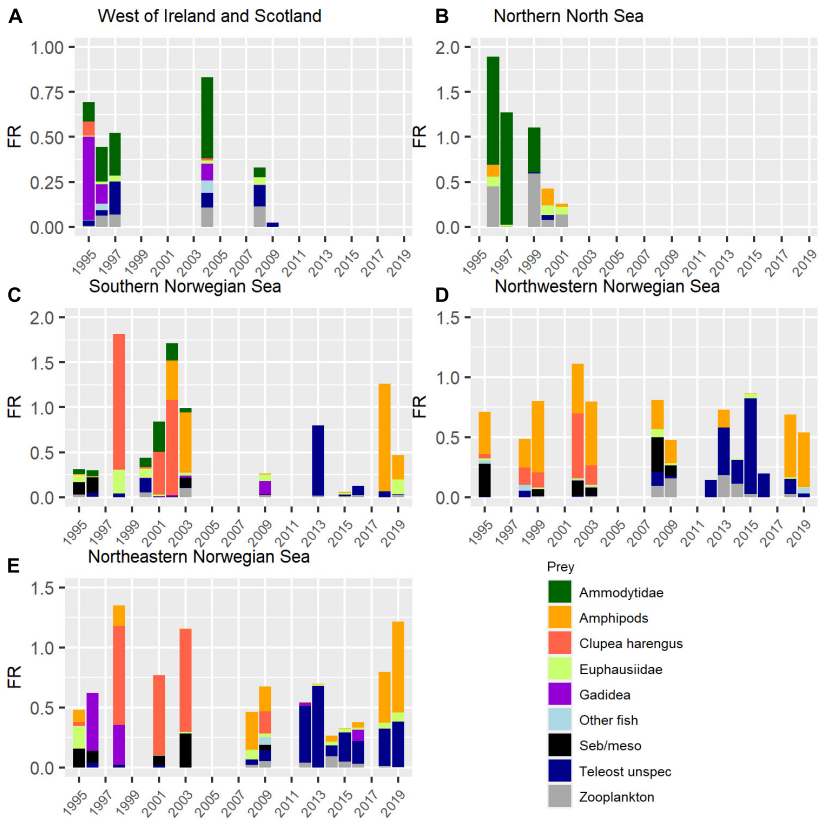


FIGURE 2 | Histograms of annual average FR values for different regions, where each annual value split into prey groups (by weight). The regions are **(A)** West of Ireland and Scotland, **(B)** Northern North Sea, **(C)** Southern Norwegian Sea, **(D)** Northwestern Norwegian Sea, and **(E)** Northeastern Norwegian Sea. The figure was produced with the use of the following R-packages: ggplot2 (Wickham, 2016) and gridExtra (Auguié, 2017).

To test if post-smolt feeding the Norwegian Sea was affected by changes in the environmental variables, a two-step analysis was conducted. In the first part of the analyses, GAMs were applied to estimate annual indices of post-smolt feeding ratio of fish and zooplankton (FR_{fish} and FR_{zoo}). This was necessary to standardize the response variable and eliminate bias from uneven sampling effort. Initial data exploration revealed that the feeding ratios were zero-inflated with a few high values, and a two-step hurdle model was therefore applied. Presence/absence of the response variable was modeled with a binomial distribution with a logit-link. The positive FR observations were modeled with a gamma distribution with a log-link function. The full models prior to model selection takes the form

$$FR_i = \alpha + s_1\left(lat_i, lon_i\right) + s_2\left(fr_i\right) + s_3\left(doy_i\right) + year_i + \varepsilon_i \quad (3)$$

where FR is either FR_{fish} and FR_{zoo}, α is the model intercept, s_1 is a two-dimension smoothing term used for latitude and longitude, s_2 and s_3 are one-dimensional smoothing terms where the number of splines are restricted to 5, *doy* is the day number of the year, *fr* is FR_{fish} when FR_{zoo} is the response variable and FR_{zoo} when FR_{fish} is the response variable, year is modeled with a fixed effect, i represents fish number and ε is a normal distributed random error term. Model fitting was done in R (R Core Team, 2020) using the *mgcv* package (Wood, 2011). Model evaluation followed the general description as described for the geographic interpolation.

In the second part of the analyses, Spearman rank tests were used to calculate the correlation between annual indices of post-smolt feeding and environmental variables.

RESULTS

Regional and Temporal Variation in Post-smolt Diet

A regional presentation of post-smolt diet and stomach fullness (**Figure 2**) shows that sandeel was the most important prey item around the British Isles. In the Norwegian Sea, fish larvae dominated the diet, especially in the southern and eastern region. The proportion of amphipods in the post-smolt diet increased further north and west, and this prey was also important for post-smolts in the Norwegian Sea. Detailed patterns for each region are described in the following.

West of Ireland and Scotland

The dominating prey were sandeel and fish from the cod family (Gadidae) (**Figure 2A**). The years with the lowest FR values were

2008 and 2009, which were the last 2 years with data sampling in the region. In contrast to previous years, gadoids and sandeel were in general absent from the diet these 2 years, even though the small proportion of unidentified fish larvae could belong to these groups.

Northern North Sea

The dominating prey were sandeel larvae and various zooplankton species (**Figure 2B**). Both euphausiids and amphipods were present but did not dominate the diet. The years with the lowest FR values were 2000 and 2001, which were the two last years with data sampling in the region. In contrast to previous years, sandeel or any other fish larvae were not present in the salmon stomachs these 2 years.

Southern Norwegian Sea

The most common prey varied between years, but herring larvae and amphipods dominated the diet in years with high FR in this region (**Figure 2C**). Both these prey species have large interannual variation, varying from close to absent to being the most common prey in the region. Amphipods reappeared in the diet in 2018 and 2019 after being absent during 2008–2016. Larvae of sandeel, mesopelagic fish and fish from the cod family (Gadidae), as well as euphausiids and other zooplankton were also consumed by post-smolts in the southern Norwegian Sea, although the importance of each of these prey groups was relatively small.

Northwestern Norwegian Sea

Amphipods were, as in the southern Norwegian Sea, an important part of post-smolt diet in the Northwestern Norwegian Sea (**Figure 2D**). The exception was the period 2012–2016, when amphipods were absent or a very limited part of the diet in this region. The fish larvae consumed were herring or mesopelagic fish larvae.

Northeastern Norwegian Sea: The diet was dominated by fish larvae in this region (**Figure 2E**). Herring larvae dominated the diet in years with the highest post-smolt feeding ratios (1998, 2001, and 2003). Zooplankton did not dominate the diet in this region, but the strong appearance of amphipods seen further south and west in 2018 and 2019 was also apparent here. Larvae of gadoids or mesopelagic fish were also an important part of the diet.

Geographic Distribution of Prey in Post-smolt Stomachs

Sandeel was part of the diet of post-smolts west of Ireland, around Shetland and in the northern North Sea (**Figure 3A**). Sandeel

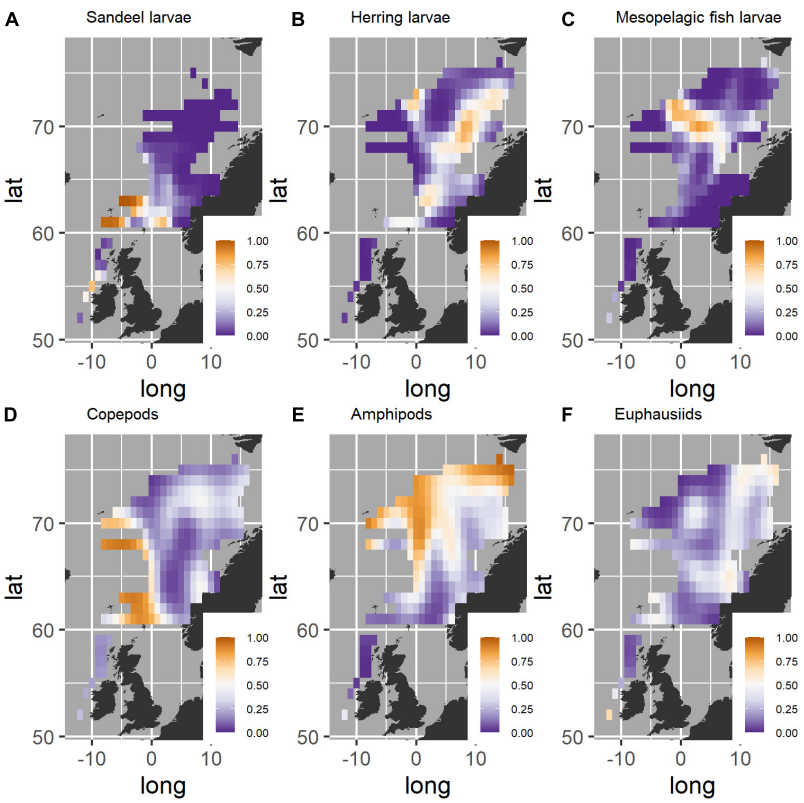


FIGURE 3 | Geographic variation in probability of finding different prey in post-smolt stomachs in areas of the Northeast Atlantic Ocean. A value of 1 indicates that the prey was found in all post-smolt stomachs in the region, while 0 indicates that the prey was not found in any post-smolt stomachs. **(A)** sandeel larvae, **(B)** herring larvae, **(C)** mesopelagic fish larvae, **(D)** copepods, **(E)** amphipods, **(F)** euphausiids. The figure was produced with the use of the following R-packages: ggplot2 (Wickham, 2016) and gridExtra (Auguié, 2017).

larvae were also found in stomachs at the boundary between the North Sea and the southern Norwegian Sea, but not close to the Norwegian coast or further north in the Norwegian Sea.

Herring larvae (**Figure 3B**) were consumed over a large area from west and north of Shetland to the eastern part of the Norwegian Sea off the Norwegian coast from around 62 to 75 °N. The highest probability of finding herring larvae in post-smolt stomachs was in the northeastern part of the Norwegian Sea outside the Norwegian continental and the Barents Sea shelf.

Larvae of mesopelagic fish (**Figure 3C**) were consumed throughout the Norwegian Sea. The probability of finding larvae of mesopelagic fish in post-smolt stomachs was higher in central areas of the Norwegian Sea in the region from the Vøring platau and toward Jan Mayen than in the remaining Norwegian Sea. Larvae of mesopelagic fish were not found in post-smolt stomachs in the North Sea and only to a limited extent west of Ireland and around Scotland.

Copepods were consumed over the entire study area (**Figure 3D**). The region with the highest probability of finding copepods in post-smolts stomachs was in the western part of the Norwegian Sea, where almost all salmon post-smolts had consumed copepods.

Amphipods were consumed over large parts of the Norwegian Sea, but was most commonly found in stomachs sampled in the central, northern and western parts (**Figure 3E**). Amphipods were not consumed west of Ireland and Scotland, and only to a limited extent in the northern North Sea and in the eastern Norwegian Sea.

Euphausiids were consumed over large parts of the sampled region (**Figure 3F**). This includes west of Ireland, north of Scotland and the eastern part of the Norwegian Sea from around 60 °N and up to Svalbard at 76 °N. Euphausiids were also consumed in central parts of the Norwegian Sea. Euphausiids were not found in the stomachs in the northwestern area along the Polar Front between the Lofoten Basin and the Greenland Basin.

Geographic Variation in Stomach Fullness in 1995–2004 Compared to 2008–2019

Fish larvae were consumed by post-smolts over most of the sampled area west of Ireland, north of Scotland, the northern North Sea and throughout the Norwegian Sea during the first time period (1995–2004). The areas with the highest FR_{fish}, with average values well exceeding 1.0, were found west of Ireland, in the northern North Sea, in the southern Norwegian Sea, and in the northeastern part of the Norwegian Sea (**Figure 4A**). In the

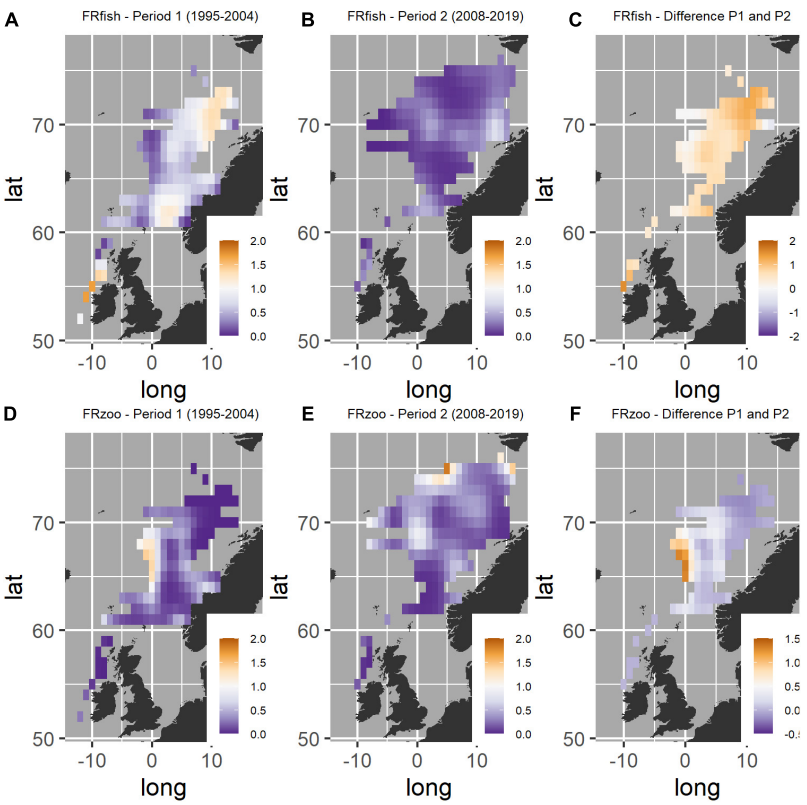


FIGURE 4 | Geographic variation in feeding ratio (FR) estimated by using a hurdle model in areas of the Northeast Atlantic Ocean. **(A)** FR_{fish} in period 1 (1995–2004), **(B)** FR_{fish} in period 2 (2008–2019), **(C)** difference in FR_{fish} between period 1 and 2 where positive values indicate that the FR_{fish} was highest in period 1, **(D)** FR_{zoo} in period 1, **(E)** FR_{zoo} in period 2, and **(F)** difference in FR_{zoo} between period 1 and 2 where positive values indicate higher values in period 1. The figure was produced with the use of the following R-packages: ggplot2 (Wickham, 2016) and gridExtra (Auguié, 2017).

second period (2008–2019), the FR_{fish} was lower than in the first period in all regions, with the largest decrease west of Ireland and in the northeastern Norwegian Sea (**Figures 4B,C**).

Zooplankton were consumed over large parts of the Norwegian Sea. The highest FR_{zoo} values were in the western part of the Norwegian Sea in the first period (1995–2004) (**Figure 4D**), and in the northern Norwegian Sea in the second period (2008–2019) (**Figure 4E**). Comparisons of FR_{zoo} between the two periods were restricted to areas that were sampled in both periods, thereby excluding the northernmost Norwegian Sea in the comparison. There was a pattern with lower values in the second than the first period in the western region of the Norwegian Sea around 64–71°N (**Figure 4F**). For the other regions, the area west of Ireland and the central and eastern Norwegian Sea, there were only minor differences between the two periods, and the difference varied between positive and negative values.

Linking Post-smolt Feeding to Data on Environmental Conditions and Abundance of Prey and Potential Competitors

Post-smolt FR_{fish} in the Norwegian Sea was positively correlated with the extent of Arctic Water (ARC_{prop}), and negatively correlated with the spawning stock biomass of mackerel (**Table 1**). FR_{fish} was not correlated with properties of the Atlantic Water nor to the zooplankton abundance index for the Norwegian Sea. There was a positive correlation between FR_{fish} and herring recruitment strength, although not statistically significant with the selected threshold of 0.05 for the *p*-values ($p = 0.064$, **Table 1**).

Post-smolt FR_{zoo} in the Norwegian Sea was positively correlated with the zooplankton abundance index for the Norwegian Sea (**Table 1**). There was also a significant correlation between FR_{zoo} and the inflow of arctic water masses, although this correlation coefficient was lower than for the zooplankton index. There was no significant correlation between FR_{zoo} and properties of the Atlantic water masses nor to the spawning stock biomass of mackerel.

The probability of finding zooplankton or fish larvae in the post-smolt stomachs, as estimated by using the binomial model, was not correlated to the indices for water masses ARC_{prop} or ATL_{smax}, the plankton index, spawning stock biomass of mackerel or fish larvae indices.

TABLE 1 | Metrics of Spearman's correlations (r-rank correlation coefficient and *p*-value) between post-smolt feeding ratios and environmental variables for the Norwegian Sea.

	FR_{fish}				FR_{zoo}			
	Biomass		**Binomial**		**Biomass**		**Binomial**	
	r	***p***	***r***	***p***	***R***	***p***	***r***	***p***
ARC_{prop}	0.60	0.013	−0.40	0.108	0.51	0.038	−0.02	0.928
ATL_{smax}	0.14	0.599	0.16	0.54	−0.21	0.415	−0.10	0.701
Zoo_May	0.43	0.087	−0.04	0.88	0.60	0.013	−0.30	0.247
R_NSSH	0.48	0.064	0.30	0.25	0.42	0.106	−0.28	0.29
Mac_SSB	−0.73	<0.001	−0.059	0.83	−0.41	0.102	0.32	0.217

ARC_{prop}, is the proportion of Arctic Water; ATL_{smax}, is maximum salinity of the Atlantic Water; Zoo_May, is the zooplankton index based on WP2 hauls in May; R_NSSH, is recruitment of Norwegian Spring Spawning herring; and Mac_SSB, is spawning stock biomass of mackerel.

DISCUSSION

Post-smolt diet and stomach fullness in the Northeast Atlantic changed considerably over the 25-year study period. There was a reduction of fish larvae in the post-smolt stomachs over a large geographic area when comparing the periods 1995–2004 and 2008–2019. We identified the geographic distribution of prey organisms dominating in the post-smolt diet. Sandeel west of Scotland and Ireland and in the northern North Sea, herring in the eastern part of the Norwegian Sea and amphipods in the western part of the Norwegian Sea were particularly important prey species. Reduced proportion of Arctic Water and reduced zooplankton abundance were the major changes affecting post-smolt feeding conditions in the Norwegian Sea. Furthermore, the results indicate that the collapse of several sandeel populations in the Northeast-Atlantic and poor recruitment of NSS-herring since year 2004 have reduced prey availability for post-smolts. The analyses presented here show how these changes have affected salmon feeding conditions by reducing the availability of important prey for salmon, and is an important step further to understand the mechanisms behind reduced marine growth and survival of Atlantic salmon.

Reduced feeding of post-smolts during 2008–2019, as indicated by a reduction of prey in post-smolt stomachs in the Norwegian Sea, was positively correlated with a reduction of Arctic Water in the Norwegian Sea. The large-scale changes to water circulation affected the plankton production and species composition in the Norwegian Sea, and thereby changed the productivity of the ecosystem (Skagseth et al., this issue). These changes in the ecosystem most likely affected the abundance of prey important for salmon through bottom-up processes, as shown in the present study. The findings are furthermore supported by a drop in marine growth for Norwegian salmon occurring simultaneously as the Norwegian Sea ecosystem changed (Vollset et al., 2022). Analogous ecosystem changes have been shown to impact feeding conditions in the Northwest Atlantic Ocean, where capelin is an important prey species for Atlantic salmon. Mills et al. (2013) showed how changing hydrographic conditions in the northwest Atlantic ecosystem in the 1990s propagated to higher trophic levels by affecting species composition and abundance of plankton, as well as the planktivorous fish capelin. A reduction in capelin size and energy density due to the changes in the ecosystem reduced the quality of capelin as prey for salmon (Renkawitz et al., 2015). Previous studies have demonstrated a correlation between reduced return rates of salmon in the northeast Atlantic to large scale oceanographic changes such as the AMO index or the subpolar gyre, or to water temperature or plankton production

south of the Norwegian Sea (e.g., Beaugrand and Reid, 2003, 2012; Friedland et al., 2009; Almodovar et al., 2019). The changes to the plankton community seen in the North Sea and west of Ireland and Scotland (Beaugrand and Reid, 2003, 2012), with a reduction of total copepods and euphausiids, may have continued into the southern Norwegian Sea with the retraction of the inflow of arctic water from the west. There are also studies that show how salmon prey have declined in abundance correlated to changes in water circulation and increased water temperatures. One example is the correlation between primary production, fish recruitment and warmer water in the North Sea in the years 1988–2013 (Capuzzo et al., 2018). Along the Norwegian coast, changes in the water temperature have been linked to lower zooplankton abundance and reduced recruitment of NSSH (Toresen et al., 2019).

Most likely, both global and regional changes in ocean circulation systems and environmental conditions affect salmon feeding conditions, and global and regional changes are often partly correlated. The inflow of Arctic Water into the Norwegian Sea with the East Icelandic Current partly follows the same decadal trend as the subpolar Gyre, which regulates the amount of Arctic Water being transported northwards west of the British Iles (ICES, 2021b). The positive effect of a strong subpolar gyre, which increase the flow of arctic water into the Faroe Iceland ridge, impacts the calanoid copepods in this region (Hatun et al., 2009). Hence, the inflow of Arctic Water into the Norwegian Sea is not only regulated by the East Iceland Current, but also by large scale mixing of Sub-Tropical and Sup-Polar water masses in the Atlantic Ocean. The observed changes in prey availability presented here spans over the period 1995–2019, and no comparable information is available for the years prior to 1995. It is therefore unknown whether the apparent good feeding conditions for post-smolts in the period 1995–2004 are representative for previous decades which had higher return rates of salmon than recent years. However, the East Icelandic Current transporting Arctic Water into the Norwegian sea was unusually strong and cold in the 1960s (Scarnecchia, 1984). Even though the intensity of this current became gradually reduced, the Norwegian Sea was greatly influenced by Arctic Water during the 1970s and 1980s (Dickson and Østerhus, 2007). This indicates that prey availability for post-smolt in the Norwegian Sea could have been high in the decades prior to 1995, even though for instance herring larvae were absent in the period 1960–1982 due to the collapse of NSS-herring stock (ICES, 2020a).

This study showed that reduced abundance of important prey targeted by Atlantic salmon post-smolts has had a negative impact on the feeding conditions for post-smolts in the northeast Atlantic, irrespective of the underlying mechanisms. Sandeel dominated the diet of post-smolts in the late 1990s in several regions, including the area west of Scotland and in the northern North Sea. Sampling west of Scotland in the 1980s also confirmed the importance of sandeel as prey in this region (Morgan et al., 1986). Sandeel larvae became absent in the post-smolt diet in several regions after 2004, which seemed to be linked to a general reduction of the stomach fullness of salmon post-smolts. The decline in sandeel abundance is reflected in a reduction in the sandeel fisheries. The sandeel fishery around Shetland decreased gradually in the early 2000s and came to a full stop in 2003 (**Figures 5A–C**). The sandeel fishery in the eastern part northern North Sea and in the area west of Scotland decreased in the late 1990s, until a stop in 2004. Except for some minor catches in 2007, there have not been catches of sandeel from these regions after 2003 and 2004. There is no indication of increased abundance of sandeel at the traditional important sandeel banks in the Northern North Sea, according to annual surveys (ICES, 2020b).

The disappearance of sandeel larvae available for post-smolts west of Scotland can potentially be compensated by abundant larvae of gadoids in this area in years when gadoid larvae are abundant (**Figure 5D**). The gadoids identified in post-smolts stomachs in this region were most likely blue whiting (*Micromesistius poutassou*), since this species has previously been abundant in post-smolt stomachs (Holst et al., 1996), and because of the geographic overlap between blue whiting larvae (Bailey, 1982) and salmon post-smolts in the region. Recruitment of blue whiting was strong in the years 1995–2004. This was followed by a period of poor recruitment until 2010 and onward, when recruitment again increased (ICES, 2020a). Hence, blue whiting may be important for post-smolt feeding west of Ireland and Scotland in years with strong recruitment, but there is a lack of post-smolt data from this region during the recent years.

The results in this study show that herring larvae were an important part of the post-smolt diet in large parts of the Norwegian Sea, and especially in the northeastern region. This result supports the findings by Haugland et al. (2006), who reported that post-smolt stomach fullness increase in years with strong recruitment of herring. Norwegian spring-spawning herring (NSSH) has a recruitment pattern with occasional very strong year-classes (**Figure 5E**), but in most years the larvae survival is low (Skagseth et al., 2015). This means that the abundance of herring larvae available for post-smolts, and other predators in the ecosystem feeding on herring larvae (Skjoldal et al., 2004), is highly variable between years. There has not been any strong year-classes of herring since 2004 (ICES, 2020a). Poor survival in the first larvae stage, increased predation on the larvae along the Norwegian coast or in the Norwegian Sea, or geographic shifts in spawning locations may have affected the abundance of herring larvae available for post-smolts. There was a clear reduction in zooplankton biomass along the drifts route for NSSH larvae after 2004 (Toresen et al., 2019). This indicates that the poor recruitment is mainly regulated by prey abundance and a potential mismatch between herring larvae and their prey (Toresen et al., 2019). After 2007, the abundance of mackerel has increased in the Norwegian Sea (**Figure 5F**; Nøttestad et al., 2016). Mackerel feed on herring larvae when they have the opportunity (Skaret et al., 2015). The increased abundance of mackerel may also have contributed to reduced survival of herring larvae (Toresen et al., 2019) and therefore contributed to a lower abundance of larvae available for post-smolts.

Competition with mackerel cannot explain the reduction in Atlantic salmon survival during last decades (Utne et al., 2021b), but the negative correlation between mackerel spawning stock biomass and biomass of fish larvae in salmon post-smolt

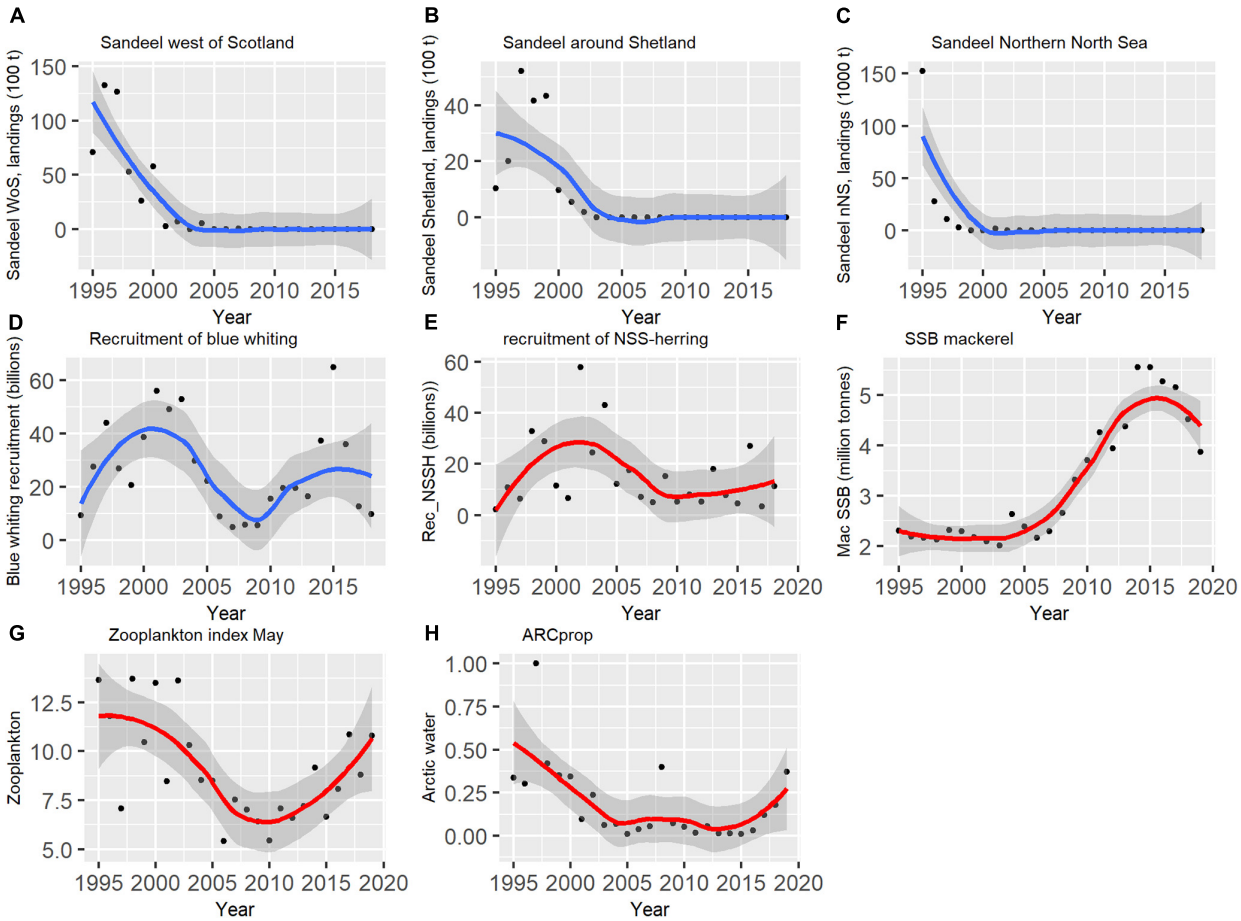


FIGURE 5 | Temporal development of prey abundance and environmental indices potentially important for post-smolts in the Northeast-Atlantic. Indices represented with a blue line is south of the Norwegian Sea, while red lines represent indices for the Norwegian Sea. **(A)** Sandeel landings west of Scotland (woS), **(B)** sandeel landings around Shetland, **(C)** sandeel landings in the northern North Sea, **(D)** recruitment of blue whiting, **(E)** recruitment of Norwegian spring-spawning herring (NSSH), **(F)** spawning stock biomass mackerel **(G)** zooplankton index May, **(H)** index for the proportion of arctic water (ARC_{prop}), and **(I)** salinity of Atlantic water (ATL_{smax}). The figure was produced with the use of the following R-packages: ggplot2 (Wickham, 2016) and cowplot (Wilke, 2020).

stomachs in the present study suggests that competition with mackerel for fish larvae may have a negative effect on post-smolt feeding conditions. However, in the Norwegian Sea there was no indication of a competition between mackerel and Atlantic salmon post-smolts for zooplankton, as there was no correlation between mackerel biomass and the biomass of zooplankton in post-smolt stomachs. This is not surprising, considering the two species mainly target different zooplankton species (Utne et al., 2021b). As an alternative explanation to competition between mackerel and Atlantic salmon post-smolts for fish larvae, the negative correlation between mackerel biomass and biomass of fish larvae in post-smolt stomachs may not be due to competition, but caused by changes in water circulation and environmental conditions affecting both species simultaneously, as the mechanisms affecting mackerel recruitment are not properly understood.

The positive correlation between the Norwegian Sea zooplankton abundance index (**Figure 5G**) and post-smolt stomach fullness of zooplankton shows a direct link between the abundance of zooplankton and post-smolt feeding. Although fish larvae are the preferred prey for post-smolts, a large proportion of the diet is zooplankton (Rikardsen et al., 2004; Utne et al., 2021a). Especially amphipods are an important part of the diet (Utne et al., 2021a), although the results presented here show a large spatial and temporal variation in biomass of amphipods in the diet. The northwestern Norwegian Sea toward the Polar Front is a region where amphipods dominated in post-smolts stomachs, but amphipods were an important part of the diet over a wider geographic area in some years. The variation in biomass of amphipods in post-smolt stomachs probably reflects temporal and spatial variation in amphipod abundance, but the dynamics of amphipods in the Norwegian Sea is not known. The sudden increase of amphipods in the post-smolt diet throughout the Norwegian Sea in 2018 and 2019 coincides with the increased proportion of Arctic Water in the Norwegian Sea (**Figure 5H**). Zooplankton abundance in the sea is normally bottom-up driven, but with potential top-down regulation by pelagic fish (Huse et al., 2012). Water transport, vertical wind

mixing, water temperature and other hydrographic conditions impact zooplankton abundance (Skjoldal et al., 2004; Assmus et al., 2009), often in ways that are not fully understood. In addition, the East Icelandic Current transports copepods into the southwestern Norwegian Sea. Since 2004 there was a sudden drop in the strength of this current, which reduced the transport of copepods into the Norwegian Sea (Kristiansen et al., 2019). This reduced advection of Arctic copepod into the Norwegian Sea may have affected the smolt feeding negatively. This is further supported by the fact that post-smolt in the Southwestern Norwegian Sea had the largest drop in stomach fullness of zooplankton from the years 1995–2004 to 2008–2019.

There has been a period from the early 2000s with less available marine prey for Atlantic salmon post-smolts in a large geographic area in the Northeast Atlantic Ocean. Changes in hydrography and zooplankton abundance in the Norwegian Sea, and recruitment of important fish stocks in the Northeast Atlantic have contributed to the decline in available prey for Atlantic salmon. The effects of this reduction in prey abundance may also have been amplified by increased interspecific competition for fish larvae with mackerel in the 2008–2019 period. The long-term trend in available prey for post-smolts in periods before 1995 is unknown, since we lack data from earlier periods. There may be some recent signals of improved feeding conditions in some regions of the Northeast Atlantic Ocean. A high proportion of Arctic Water into the Norwegian Sea is associated with good post-smolt feeding conditions, and the increased proportion of Arctic Water in 2018 and 2019 compared to the period 2005–2016 may continue due to the temporal autocorrelation in proportions of water masses in the Norwegian Sea. The stop in the sandeel fishery in the early 2000's both in the North Sea and west of Ireland and Scotland also sets the ground for a recovery of sandeel in this region if the environmental conditions turn favorable. Identifying important feeding areas for salmon and making the management decisions necessary to improve and maintain healthy and diverse ecosystems in these areas are important steps toward maintaining Atlantic salmon population. A recovery of reduced Atlantic salmon populations will require healthy and productive natal river systems, and reducing major threats from human activities in coastal areas. However, for this long-distant migrating species, also the marine feeding habitat is of major importance. Knowledge of, and willingness to preserve, marine ecosystems is necessary to ensure healthy Atlantic salmon populations across Europe.

DATA AVAILABILITY STATEMENT

Publicly available datasets were analyzed in this study. This data can be found here: http://metadata.nmdc.no/metadata-api/landingpage/5cc7cbf7d8f56eebaacb5bc8b44dda4d.

AUTHOR CONTRIBUTIONS

KU, VW, and ØS delineated the study. WM and CB sampled parts of the data. VW, ET, WM, and KU retrieved funding for the study. KU analyzed the data. KU, ET, VW, ØS, WM, and CB wrote the manuscript. All authors contributed to the article and approved the submitted version.

FUNDING

This study was funded by the Research Council of Norway as part of project 280308 SeaSalar, and the European Commission under the 7th Framework Program, Grant Agreement no. 212529 (Salsea-Merge).

ACKNOWLEDGMENTS

We thank all people who assisted gathering the data presented, including the skippers and crew onboard the vessels collecting samples.

SUPPLEMENTARY MATERIAL

The Supplementary Material for this article can be found online at: https://www.frontiersin.org/articles/10.3389/fmars.2022.824614/full#supplementary-material

REFERENCES

Almodovar, A., Ayllon, D., Nicola, G. G., Jonsson, B., and Elvira, B. (2019). Climate-driven biophysical changes in feeding and breeding environments explain the decline of southernmost European Atlantic salmon populations. *Can. J. Fish. Aquat. Sci.* 76, 1581–1595. doi: 10.1139/cjfas-2018-0297

Assmus, J., Melle, W., Tjostheim, D., and Edwards, M. (2009). Seasonal cycles and long-term trends of plankton in shelf and oceanic habitats of the Norwegian Sea in relation to environmental variables. *Deep Sea Res. II Top. Stud. Oceanogr.* 56, 1895–1909. doi: 10.1016/j.dsr2.2008.11.004

Auguié, B. (2017). *gridExtra: Miscellaneous Functions for "Grid" Graphics. R Package Version 2.3*.

Bailey, R. S. (1982). The population biology of blue whiting in the North-Atlantic. *Adv. Mar. Biol.* 19, 257–355. doi: 10.1016/B978-0-12-381015-1.00002-2

Beaugrand, G., and Reid, P. C. (2003). Long-term changes in phytoplankton, zooplankton and salmon related to climate. *Glob. Change Biol.* 9, 801–817. doi: 10.1046/j.1365-2486.2003.00632.x

Beaugrand, G., and Reid, P. C. (2012). Relationships between North Atlantic salmon, plankton, and hydroclimatic change in the Northeast Atlantic. *ICES J. Mar. Sci.* 69, 1549–1562. doi: 10.1093/icesjms/fss153

Bradbury, I. R., Lehnert, S. J., Messmer, A., Duffy, S. J., Verspoor, E., Kess, T., et al. (2021). Range-wide genetic assignment confirms long-distance oceanic migration in Atlantic salmon over half a century. *ICES J. Mar. Sci.* 78, 1434–1443. doi: 10.1093/icesjms/fsaa152

Burnham, K. P., and Anderson, D. R. (2002). *Model Selection and Multimodel Inference: A Practical Information-Theoretic Approach*. New York, NY: Springer-Verlag, 488.

Capuzzo, E., Lynam, C. P., Barry, J., Stephens, D., Forster, R. M., Greenwood, N., et al. (2018). A decline in primary production in the North Sea over 25

years, associated with reductions in zooplankton abundance and fish stock recruitment. *Glob. Change Biol.* 24, 352–364. doi: 10.1111/gcb.13916

Dickson, B., and Østerhus, S. (2007). One hundred years in the Norwegian Sea. *Nor. Geogr. Tidsskr.* 61, 56–75. doi: 10.1080/00291950701409256

Forseth, T., Barlaup, B. T., Finstad, B., Fiske, P., Gjoaester, H., Falkegard, M., et al. (2017). The major threats to Atlantic salmon in Norway. *ICES J. Mar. Sci.* 74, 1496–1513. doi: 10.1093/icesjms/fsx020

Friedland, K. D., Hansen, L. P., Dunkley, D. A., and MacLean, J. C. (2000). Linkage between ocean climate, post-smolt growth, and survival of Atlantic salmon (*Salmo salar* L.) in the North Sea area. *ICES J. Mar. Sci.* 57, 419–429. doi: 10.1006/jmsc.1999.0639

Friedland, K. D., MacLean, J. C., Hansen, L. P., Peyronnet, A. J., Karlsson, L., Reddin, D. G., et al. (2009). The recruitment of Atlantic salmon in Europe. *ICES J. Mar. Sci.* 66, 289–304. doi: 10.1093/icesjms/fsn210

Gilbey, J., Utne, K. R., Wennevik, V., Beck, A. C., Kausrud, K., Hindar, K., et al. (2021). The early marine post-smolt distribution of Atlantic salmon in the NE Atlantic: a genetically informed stock-specific synthesis. *Fish Fish.* 22, 1274–1306. doi: 10.1111/faf.12587

Hastie, T. J., and Tibshirani, R. J. (1990). *Generalized Additive Models*. London: Chapman & Hall/CRC, 335.

Hatun, H., Payne, M. R., Beaugrand, G., Reid, P. C., Sando, A. B., Drange, H., et al. (2009). Large bio-geographical shifts in the north-eastern Atlantic Ocean: from the subpolar gyre, *via* plankton, to blue whiting and pilot whales. *Prog. Oceanogr.* 80, 149–162. doi: 10.1016/j.pocean.2009.03.001

Haugland, M., Holst, J. C., Holm, M., and Hansen, L. P. (2006). Feeding of Atlantic salmon (*Salmo salar* L.) post-smolts in the Northeast Atlantic. *ICES J. Mar. Sci.* 63, 1488–1500. doi: 10.1016/j.icesjms.2006.06.004

Holst, J. C., Hansen, L. P., and Holm, M. (1996). *Observations of Abundance, Stock Composition, Body Size and Food of Postsmolts of Atlantic Salmon in the NE Atlantic During Summer: ICES CM Documents;1996/M:4*. Burnaby, BC: ICES, 16.

Huse, G., Holst, J. C., Utne, K., Nøttestad, L., Melle, W., Slotte, A., et al. (2012). Effects of interactions between fish populations on ecosystem dynamics in the Norwegian Sea – results of the INFERNO project Preface. *Mar. Biol. Res.* 8, 415–419. doi: 10.1080/17451000.2011.653372

ICES (2020a). *Working Group on Widely Distributed Stocks (WGWIDE). ICES Document*, Vol. 82. Burnaby, BC: ICES, 1019.

ICES (2020b). *Herring Assessment Working Group for the Area South of 62° N (HAWG)*, Vol. 2. Burnaby, BC: ICES, 1054.

ICES (2021a). Working group on North Atlantic Salmon (WGNAS). *ICES Sci. Rep.* 3:407. doi: 10.17895/ices.pub.7923

ICES (2021b). Working group on the integrated assessments of the Norwegian Sea (WGINOR; outputs from 2020 meeting). *ICES Sci. Rep.* 3:114.

ICES (2021c). Working group on Widely Distributed Stocks (WGWIDE). *ICES Sci. Rep.* 3:874.

Jensen, A. J., Maoileidigh, N. O., Thomas, K., Einarsson, S. M., Haugland, M., Erkinaro, J., et al. (2012). Age and fine-scale marine growth of Atlantic salmon post-smolts in the Northeast Atlantic. *ICES J. Mar. Sci.* 69, 1668–1677. doi: 10.1093/icesjms/fss086

Jonsson, B., and Jonsson, N. (2004). Factors affecting marine production of Atlantic salmon (Salmo salar). *Can. J. Fish. Aquat. Sci.* 61, 2369–2383. doi: 10.1139/f04-215

Jonsson, B., Jonsson, N., and Albretsen, J. (2016). Environmental change influences the life history of salmon Salmo salar in the North Atlantic Ocean. *J. Fish Biol.* 88, 618–637. doi: 10.1111/jfb.12854

Kristiansen, I., Hatun, H., Petursdottir, H., Gislason, A., Broms, C., Melle, W., et al. (2019). Decreased influx of *Calanus* spp. into the south-westem Norwegian Sea since 2003. *Deep Sea Res. I Oceanogr. Res. Pap.* 149:103048. doi: 10.1016/j.dsr.2019.05.008

McCarthy, J. L., Friedland, K. D., and Hansen, L. P. (2008). Monthly indices of the post-smolt growth of Atlantic salmon from the Drammen River, Norway. *J. Fish Biol.* 72, 1572–1588. doi: 10.1111/j.1095-8649.2008.01820.x

Mills, K. E., Pershing, A. J., Sheehan, T. F., and Mountain, D. (2013). Climate and ecosystem linkages explain widespread declines in North American Atlantic salmon populations. *Glob. Change Biol.* 19, 3046–3061. doi: 10.1111/gcb.12298

Morgan, R. I. G., Greenstreet, S. P. R., and Thorpe, J. E. (1986). *First Observations on Distribution, Food and Fish Predators of Postsmolt Atlantic Salmon, Salmo salar, in the Outer Firth of Clyde. ICES C.M., 1986/M: 8*. Burnaby, BC: ICES.

Nøttestad, L., Utne, K. R., Oskarsson, G. J., Jonsson, S. T., Jacobsen, J. A., Tangen, O., et al. (2016). Quantifying changes in abundance, biomass, and spatial distribution of Northeast Atlantic mackerel (Scomber scombrus) in the Nordic seas from 2007 to 2014. *ICES J. Mar. Sci.* 73, 359–373. doi: 10.1093/icesjms/fsv218

Otero, J., Jensen, A. J., L'Abee-Lund, J. H., Stenseth, N. C., Storvik, G. O., and Vollestad, L. A. (2011). Quantifying the ocean, freshwater and human effects on year-to-year variability of one-sea-winter Atlantic Salmon Angled in multiple Norwegian Rivers. *PLoS One* 6:e24005. doi: 10.1371/journal.pone.0024005

Parrish, D. L., Behnke, R. J., Gephard, S. R., McCormick, S. D., and Reeves, G. H. (1998). Why aren't there more Atlantic salmon (*Salmo salar*)? *Can. J. Fish. Aquat. Sci.* 55, 281–287. doi: 10.1139/d98-012

R Core Team (2020). *R: A Language and Environment for Statistical Computing*. Vienna: R Foundation for Statistical Computing.

Renkawitz, M. D., Sheehan, T. F., Dixon, H. J., and Nygaard, R. (2015). Changing trophic structure and energy dynamics in the Northwest Atlantic: implications for Atlantic salmon feeding at West Greenland. *Mar. Ecol. Prog. Ser.* 538, 197–211. doi: 10.3354/meps11470

Rikardsen, A. H., Haugland, M., Bjorn, P. A., Finstad, B., Knudsen, R., Dempson, J. B., et al. (2004). Geographical differences in marine feeding of Atlantic salmon post-smolts in Norwegian fjords. *J. Fish Biol.* 64, 1655–1679. doi: 10.1111/j.0022-1112.2004.00425.x

Rikardsen, A. H., Righton, D., Strom, J. F., Thorstad, E. B., Gargan, P., Sheehan, T., et al. (2021). Redefining the oceanic distribution of Atlantic salmon. *Sci. Rep.* 11:12266. doi: 10.1038/s41598-021-91137-y

Scarnecchia, D. L. (1984). Climatic and oceanic variations affecting yield of Icelandic stocks of Atlantic salmon (*Salmo-Salar*). *Can. J. Fish. Aquat. Sci.* 41, 917–935. doi: 10.1139/f84-107

Skagseth, Ø., Broms, C., Gundersen, K., Hátún, H., Kristiansen, I., Larsen, K. M. H., et al. (this issue). *Arctic and Atlantic waters in the Norwegian Basin, Between Year Variability and Potential Ecosystem Implication.*

Skagseth, O., Slotte, A., Stenevik, E. K., and Nash, R. D. M. (2015). Characteristics of the Norwegian coastal current during years with high recruitment of Norwegian Spring Spawning Herring (*Clupea harengus* L.). *PLoS One* 10:e0144117. doi: 10.1371/journal.pone.0144117

Skaret, G., Bachiller, E., Langoy, H., and Stenevik, E. K. (2015). Mackerel predation on herring larvae during summer feeding in the Norwegian Sea. *ICES J. Mar. Sci.* 72, 2313–2321. doi: 10.1093/icesjms/fsv087

Skjoldal, H. R., Sætre, R., Fernø, A., Misund, O. A., and Røttingen, I. (2004). *The Norwegian Sea Ecosystem*. Trondheim: Tapir Academic Press, 559.

Strøm, J. F., Thorstad, E. B., Chafe, G., Sorbye, S. H., Righton, D., Rikardsen, A. H., et al. (2017). Ocean migration of pop-up satellite archival tagged Atlantic salmon from the Miramichi River in Canada. *ICES J. Mar. Sci.* 74, 1356–1370. doi: 10.1093/icesjms/fsw220

Thorstad, E. B., Bliss, D., Breau, C., Damon-Randall, K., Sundt-Hansen, L. E., Hatfield, E., et al. (2021). Atlantic salmon in a rapidly changing environment-Facing the challenges of reduced marine survival and climate change. *Aquat. Conserv. Mar. Freshw. Ecosyst.* 31, 2654–2665. doi: 10.1002/aqc.3624

Todd, C. D., Hughes, S. L., Marshall, C. T., Maclean, J. C., Lonergan, M. E., and Biuw, E. M. (2008). Detrimental effects of recent ocean surface warming on growth condition of Atlantic salmon. *Global Change Biol.* 14, 958–970. doi: 10.1111/j.1365-2486.2007.01522.x

Toresen, R., Skjoldal, H. R., Vikelao, F., and Martinussen, M. B. (2019). Sudden change in long-term ocean climate fluctuations corresponds with ecosystem alterations and reduced recruitment in Norwegian spring-spawning herring (*Clupea harengus, Clupeidae*). *Fish Fish.* 20, 686–696. doi: 10.1111/faf.12369

Trehin, C., Rivot, E., Lamireau, L., Meslier, L., Besnard, A. L., Gregory, S. D., et al. (2021). Growth during the first summer at sea modulates sex-specific maturation schedule in Atlantic salmon. *Can. J. Fish. Aquat. Sci.* 78, 659–669. doi: 10.1139/cjfas-2020-0236

Utne, K. R., Pauli, B. D., Haugland, M., Jacobsen, J. A., Maoileidigh, N. O., Melle, W., et al. (2021a). Poor feeding opportunities and reduced condition factor for salmon post-smolts in the Northeast Atlantic Ocean. *ICES J. Mar. Sci.* 78, 2844–2857. doi: 10.1093/icesjms/fsab163

Utne, K. R., Thomas, K., Jacobsen, J. A., Fall, J., Maoileidigh, N. O., Broms, C. T., et al. (2021b). Feeding interactions between Atlantic salmon (*Salmo salar*) postsmolts and other planktivorous fish in the Northeast Atlantic. *Can. J. Fish. Aquat. Sci.* 78, 255–268. doi: 10.1139/cjfas-2020-0037

Vollset, K. W., Barlaup, B. T., Mahlum, S., Bjorn, P. A., and Skilbrei, O. T. (2016). Estimating the temporal overlap between post-smolt migration of Atlantic salmon and salmon lice infestation pressure from fish farms. *Aquac. Environ. Interact.* 8, 511–525. doi: 10.3354/aei00195

Vollset, K. W., Urdal, K., Utne, K. R., Thorstad, E. B., Sægrov, H., Raunsgard, A., et al. (2022). Ecological regime shift in the Northeast Atlantic Ocean revealed from the unprecedented reduction in marine growth of Atlantic salmon. *Sci. Adv.* 8. doi: 10.1126/sciadv.abk2542

Wickham, H. (2016). *ggplot2: Elegant Graphics for Data Analysis*. New York, NY: Springer-Verlag. doi: 10.1007/978-3-319-24277-4

Wilke, C. O. (2020). *cowplot: Streamlined Plot Theme and Plot Annotations for 'ggplot2'*.

Wood, S. N. (2011). Fast stable restricted maximum likelihood and marginal likelihood estimation of semiparametric generalized linear models. *J. R. Stat. Soc. Lond. B Stat. Methodol.* 71, 3–36. doi: 10.1111/j.1467-9868.2010.00749.x

Conflict of Interest: The authors declare that the research was conducted in the absence of any commercial or financial relationships that could be construed as a potential conflict of interest.

Publisher's Note: All claims expressed in this article are solely those of the authors and do not necessarily represent those of their affiliated organizations, or those of the publisher, the editors and the reviewers. Any product that may be evaluated in this article, or claim that may be made by its manufacturer, is not guaranteed or endorsed by the publisher.

Copyright © 2022 Utne, Skagseth, Wennevik, Broms, Melle and Thorstad. This is an open-access article distributed under the terms of the Creative Commons Attribution License (CC BY). The use, distribution or reproduction in other forums is permitted, provided the original author(s) and the copyright owner(s) are credited and that the original publication in this journal is cited, in accordance with accepted academic practice. No use, distribution or reproduction is permitted which does not comply with these terms.

frontiers | Frontiers in Marine Science

ORIGINAL RESEARCH
published: 02 May 2022
doi: 10.3389/fmars.2022.831739

Arctic and Atlantic Waters in the Norwegian Basin, Between Year Variability and Potential Ecosystem Implications

Øystein Skagseth[1,2], Cecilie Broms[1], Kjell Gundersen[1,2], Hjálmar Hátún[3], Inga Kristiansen[3], Karin Margretha H. Larsen[3], Kjell Arne Mork[1,2], Hildur Petursdottir[4] and Henrik Søiland[1,2]*

[1] Institute of Marine Research, Bergen, Norway, [2] Bjerknes Centre for Climate Research, Bergen, Norway, [3] Faroe Marine Research Institute, Tórshavn, Faroe Islands, [4] Marine and Freshwater Research Institute, Hafnarfjörður, Iceland

OPEN ACCESS

Edited by:
Gilles Reverdin, Centre National de la Recherche Scientifique (CNRS), France

Reviewed by:
Terry Whitledge, Retired, United States
Jan Marcin Weslawski, Polish Academy of Sciences, Poland
Naomi Penny Holliday, University of Southampton, United Kingdom

***Correspondence:**
Øystein Skagseth
oystein.skagseth@hi.no

Specialty section:
This article was submitted to Ocean Observation, a section of the journal Frontiers in Marine Science

Received: *08 December 2021*
Accepted: *22 March 2022*
Published: *02 May 2022*

Citation:
Skagseth Ø, Broms C, Gundersen K, Hátún H, Kristiansen I, Larsen KMH, Mork KA, Petursdottir H and Søiland H (2022) Arctic and Atlantic Waters in the Norwegian Basin, Between Year Variability and Potential Ecosystem Implications. Front. Mar. Sci. 9:831739. doi: 10.3389/fmars.2022.831739

The ocean climate of the southern Norwegian Sea - the Norwegian Basin - is largely set by the relative amount of Atlantic Water in the eastern and Arctic Water in the western region. Here we utilized hydrographic data from repeated sections, together with annually gridded survey data of the upper 1000 m, to resolve the main hydrographic changes over the period 1995-2019. Based on integrated heat -and freshwater content, we divide into three periods. The first period 1995-2005, denoted Arctic, is characterized by relative fresh and cold Atlantic Water overlaying Arctic Intermediate Water that basically covers the whole Norwegian Basin. Differently, the conditions during the period 2006-2016, denoted Atlantic, are warmer and more saline, and the extent and thickness of Arctic Intermediate Water is greatly reduced. During the most recent period denoted Fresh, 2017-2019, there has been a major freshening of the Atlantic waters, the layer of Arctic Intermediate Water has not recovered, but instead a layer of warmer but relative fresh Arctic Water has expanded. We find that increased abundance of the Arctic zooplankton *Calanus hyperboreus* in the southern and eastern Norwegian Basin coincides with increased extent of Arctic Water. We also note that the overall mesozooplankton biomass in the Norwegian Basin is significantly higher during periods of relative high amount of Arctic Water. Furthermore, we show that both nitrate and silicate winter (pre-bloom) concentrations are significantly higher in the Arctic Water compared to Atlantic Water, and that there is a reduction in nutrients from the Arctic period compared subsequent Atlantic and Fresh periods. Since these nutrients can be interpreted as the potential for new production, changes in the influx of western Arctic waters are expected to have a bottom-up effect on the Norwegian Sea. Hence, this study indicates that the amount of Arctic waters and their concentration of nutrients and zooplankton are more important for the Norwegian Basin ecosystem functioning rather than the temperature of the Atlantic waters.

Keywords: Arctic water, Atlantic water, nutrients variations, zooplankton, Norwegain basin, water masses

INTRODUCTION

The southern Norwegian Sea - the Norwegian Basin - is a confluence area of warm and saline Atlantic Water from the south and relative fresher and colder Arctic waters from the west (Helland-Hansen and Nansen, 1909; **Figure 1**). Over the last 60 years, there have been marked changes in the hydrographic conditions in the Norwegian Basin. During the 1960s to the 1990s, the Norwegian Basin experienced a cooling and freshening mainly because of increased supply of Arctic Water from the East Icelandic Current (EIC, Blindheim et al., 2000). The Norwegian Sea started to warm and become more saline from the mid-1990s due to advection of warmer inflowing Atlantic Water (Skagseth and Mork, 2012), associated with circulation changes in the North Atlantic (Häkkinen and Rhines, 2004; Hátún et al., 2005). The warming continued until mid-2000s when the Norwegian Basin remained in a relatively warm and saline state (e.g., Mork et al., 2019). During the recent years, a major freshening of the Norwegian Basin has been reported (Mork et al., 2019; Holliday et al., 2020). In this paper we investigate these major hydrographic changes and discuss some potential ecosystem effects in the Norwegian Basin over the period 1995-2019.

To understand the causes of variability in the Norwegian Basin it is necessary to consider the relative contribution of Atlantic and Arctic waters as well as changes in the local ocean to atmosphere heat loss (Mork et al., 2019). Variability in the Atlantic inflow waters to the Norwegian Basin are related to atmospheric driven circulation changes in the North Atlantic sub-tropical and sub-polar gyres (Eden and Willebrand, 2001; Marshall et al., 2001; Häkkinen and Rhines, 2004). Numerous studies have reported that hydrographic anomalies propagate

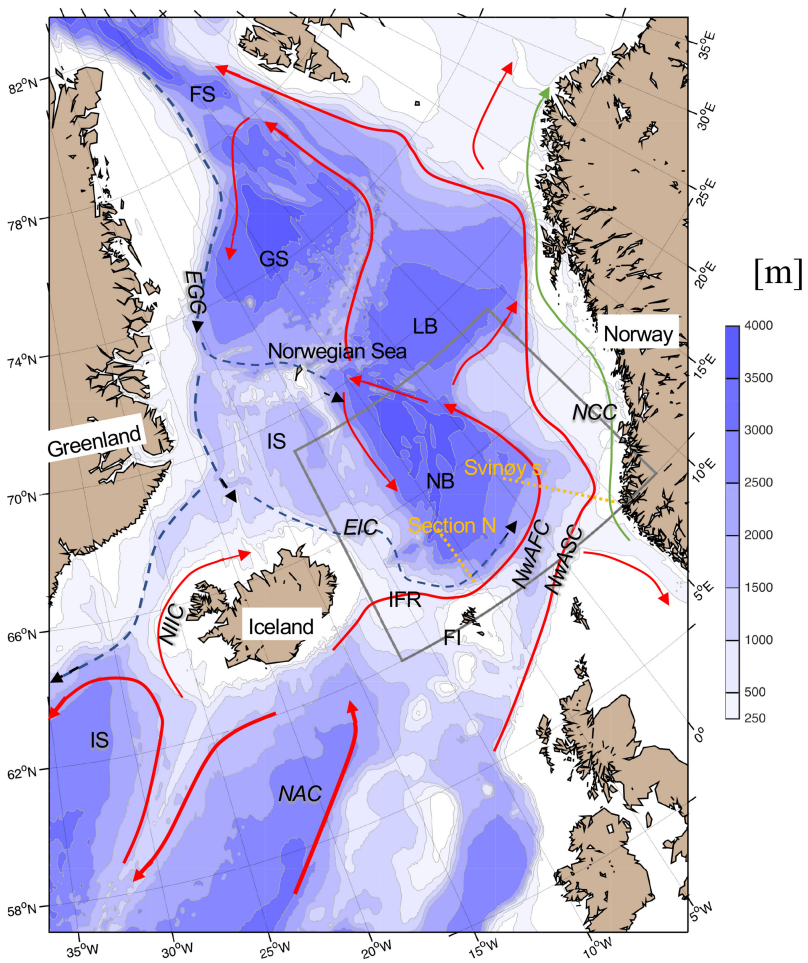


FIGURE 1 | Map of the investigation area including schematic of the major currents associated with Atlantic Water in red, Arctic and Polar Water in black dashed, and freshwater boundary current in green. Yellow dashed lines show position of the repeated section used in this study; the Section N and the Svinøy section. The square shows the area used to calculate integrated quantities for the Norwegian Basin. North Atlantic Current, (NAC); Irminger Sea, (IS); North Icelandic Irminger Current, (NIIC); East Icelandic Current, (EIC); Iceland-Faroe Ridge, (IFR); Faroe Islands, (FI); Norwegian Atlantic Slope Current, (NwASC); Norwegian Atlantic Front Current, (NwAFC); Norwegian Coastal Current, (NCC); East Greenland Current, (EGC); Norwegian Basin, (NB); Lofoten Basin, (LB); Iceland Sea, (IS); Greenland Sea, (GS) and Fram Strait, (FS). Color show water depth in meters.

with the North Atlantic Current toward (Dickson et al., 1988; Krahman et al., 2001; Hátún et al., 2005; Holliday et al., 2008) and through the Norwegian Sea (Helland-Hansen and Nansen, 1909; Furevik, 2001; Chafik et al., 2015; Broome and Nilsson, 2018; Asbjørnsen et al., 2019). However, less focus has been on the Arctic flow from the west.

Arctic Water enters the Norwegian Basin from the Iceland and Greenland Seas. Mixing of Atlantic type water from the North Icelandic Irminger Current and waters from the East Greenland Current forms so-called North Icelandic Winter Water (Stefansson, 1962). This water type is a source to the EIC (Macrander et al., 2014). It is further transformed while flowing along the northern slope of the Iceland Faroes Ridge where it is denoted Modified East Icelandic Water (MEIW; Read and Pollard, 1992). MEIW contributes to the Arctic Intermediate Water (AIW) in the Norwegian Sea (Blindheim et al., 2000). However, the main sources of AIW are from further north in the Iceland Sea and from the Greenland Sea (Blindheim, 1990). These waters flow southward following the general cyclonic circulation along the western slope of the Norwegian Basin (Søiland et al., 2008; Voet et al., 2010) and contribute to the AIW in the Norwegian Sea (Blindheim, 1990; Blindheim et al., 2000; Mork and Blindheim, 2000; Jeansson et al., 2017).

The characteristics of the Atlantic and Arctic source waters also cause hydrographic variability in the Norwegian Basin. The most striking event is the "Great Salinity Anomaly" in the 1970s that propagated from the Arctic with the East Greenland Current into the North Atlantic and finally returned into the Norwegian Sea in the late 1970s (Dickson et al., 1988). Another example is the warmer and more saline Atlantic inflow after 2000 (Hátún et al., 2005; Hansen et al., 2015), which propagated north through the Nordic Seas and whereof a part thereafter recirculated in the Fram Strait. This increased the upper salinity in the Greenland and Iceland Seas, and hence changed the properties of the Arctic waters that subsequently enter the Norwegian Sea at depth (Lauvset et al., 2018). While such indirect changes may be more difficult to track, they are potentially more predictable due to their longer time scale.

In terms of integrated heat and freshwater content in the Norwegian Basin, there are three distinct multi–year periods during the years 1995 to 2019 (Mork et al., 2019; **Figure 2**). The first period, 1995-2005 (hereafter termed the Arctic period), is a transition period from cold and fresh "Arctic" condition to warmer and more saline "Atlantic" condition. This transition has been related to a switch from a relative strong to weak sub-polar gyre of the North Atlantic from 1995 to 1996 (Häkkinen and Rhines, 2004). Hátún et al. (2005) attributed the effect of this weakening gyre to more saline and warmer Atlantic Water around the Faroes, which is the southern entrance to the Norwegian Basin. In the second period from 2006-2016 (here termed the Atlantic period), the Norwegian Basin remained in a relatively warm and saline state. During this period the atmospheric forcing represented by the NAO-index did not show consistent deviation from the climatology. The third period includes the recent years 2017-2019 (termed the Fresh period), where there has been a notable freshening, but only minor reduction in heat content (Mork et al., 2019). This can partly be related to the "anomalous freshening" in the Northeast Atlantic in 2014-2015 that, with a time-lag of a few years, has propagated with the main circulation into the Norwegian Basin (Holliday et al., 2020), although with anomalous low ocean to atmosphere cooling over the Norwegian Basin (Mork et al., 2019).

In the Norwegian Basin, changes in the hydrographic conditions may affect the biological production in numerous ways (see Skjoldal, 2004 for a comprehensive review). It is a highly productive area and home of large commercial fish stocks that rely on zooplankton as prey during spring and summer. The seasonal cycle in light, and thus primary production, is pronounced and zooplankton represent the primary transfer of energy from nutrients and phytoplankton production to zooplankton and fish (Melle et al., 2014). As such, the overall abundance of zooplankton is important for the energy transfer across trophic levels.

The large arctic copepod, *Calanus hyperboreus* dominates the zooplankton biomass within the Iceland and Greenland Seas

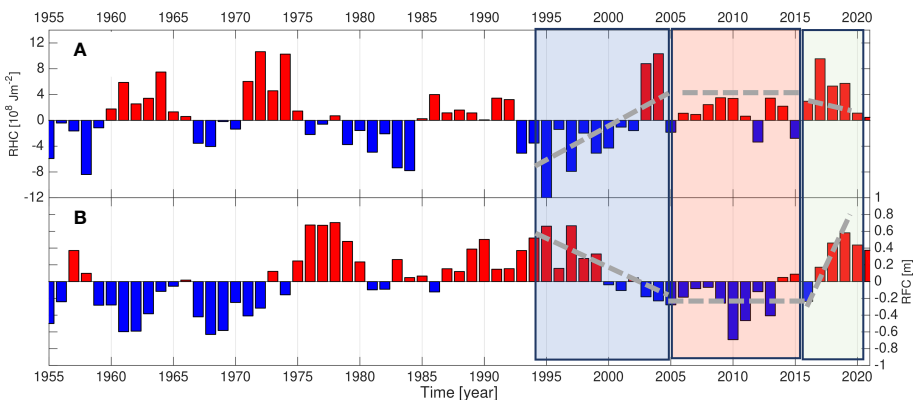


FIGURE 2 | **(A, B)** Time series of Relative Heat Content (RHC) and Relative Freshwater Content (RFC) in the Norwegian Basin (after Mork et al., 2014).

(Wiborg, 1954; Hirche, 1997; Astthorsson and Gislason, 2003; Gislason, 2018; Strand et al., 2020). The expatriate, *C. hyperboreus*, from the Iceland and Greenland Seas have been used as a tracer of Arctic Water variability in the southern Norwegian Basin (Wiborg, 1954; Kristiansen et al., 2019).

In this study, we explore the hydrographic variability within the Norwegian Basin from 1995 to 2019, with particular emphasis on the Arctic influx from the west and relate the contrasting hydrographic states to the pre-bloom (winter) nutrient concentrations and to the total zooplankton biomass in May. Furthermore, we investigate the abundance of the expatriate, *C. hyperboreus*, within the eastern Norwegian Basin to determine whether its traceability can also be detected within this region.

DATA AND METHODS

Data

We utilize hydrographic data from several sources. To describe the variability in the cyclonic circulation in the southern and eastern Norwegian Basin, we use two repeated hydrographic sections (**Figure 1**). Extending northwards from the Faroes, the Section N was initiated in 1988 by the Faroe Marine Research Institute (FAMRI) (Larsen et al., 2012). Typically, it has been occupied four times a year on 14 fixed stations, with some modification since the work started. The Svinøy section extends northwestward from the Norwegian coast and has been regularly operated since the mid 1970s by the Institute of Marine Research (IMR), typically four to five times a year, with 17 fixed stations (**Figure 1**).

To describe the annual 3-D hydrographic variability from 1995 to 2019, we combined data sets from ICES (International Council for the Exploration of the Sea), PINRO (Polar Research Institute of Marine Fisheries and Oceanography, Russia), and the Argo Global Data Assembly Centre in France (Argo, 2000) (Mork et al., 2019). Data are from spring, between 15 April and 15 June, that coincide with the Northeast Atlantic Pelagic Ecosystem Surveys that include CTD stations every 60 nautical miles to a maximum depths of 1000 m. All hydrographic data are corrected for the climatological seasonal trend (Skagseth and Mork, 2012). The number of CTD profiles for the Norwegian Basin for each year varies from 50 to 150. For each year, at 5 m depth interval, the observations were interpolated using objective analysis on a grid with intervals of 0.5° and 0.25° in the zonal and meridional directions, respectively.

We used nutrient data collected on the repeated hydrographic surveys along Svinøy section by IMR (Gundersen et al., 2021). Here, we use nitrate and silicate data from standard depths 10, 30, 50, 70, 100, 200, 500, 800, 1000, 1500, 2000 m. Only winter data (January-March) are used, to avoid the effect of nutrient consumption by primary production (Baggøien et al., 2012). Here we contrast the depth-mean distributions for the Arctic (1995-2005), the Atlantic (2006-2016), and the Fresh (2017-2019) periods. Nutrient observations in the Section N started in 2013 and are therefore not included in this study.

The zooplankton biomass was sampled at the ICES co-ordinated IESNS (International Ecosystem Survey in Nordic Sea) ecosystem surveys by several countries and vessels, covering the Norwegian Sea and adjacent areas (ICES, 2021a; ICES, 2021b). In order to have comparable geographical coverage of the southern Norwegian Sea every year, the area reported in the present paper is bounded by the longitudes 8°W and 12°E and latitudes 62°N and 70°N. The zooplankton have been sampled as standard since 1995, and sampling was carried out from the end of April until the beginning of June. All zooplankton biomass samples were collected by vertical hauls with WP2 nets with 0.25m^2 mouth area (Fraser, 1966) and mesh-size of 200 μm, except from the Norwegian vessels which used the modified mesh-size of 180 μm. The nets were hauled from 200 m to the surface or from the bottom whenever bottom depth is less than 200 m. The wet zooplankton samples were oven-dried at ~ 60°C for at least 24 h and data are presented as gram dry weight per m^2. Due to avoidance of larger zooplankton when sampling with WP2, the dry weight presented is considered to represent the mesozooplankton biomass.

C. hyperboreus was sampled at Section N and at the Svinøy section. The zooplankton time-series at Section N started in 1993, however no data are available for 1996, 1998 and 2006. The zooplankton time-series from the Svinøy secion started in 1995. Only the five northernmost stations along Section N, which are always north of the Iceland-Faroe Front (Kristiansen et al., 2016), and thus influenced by Arctic waters, are included in this paper. In the Svinøy section only the three westernmost stations are used and are thus in comparable waters as Section N. In Section N the data are during the period 10-27 May, in the Svinøy section from 17 April to 17 May. By using data from this period of the season, the analysis are refined to the overwintering generations, which makes the between-year abundances comparable. Zooplankton samples at both sections were collected by vertical hauls with WP2 nets with 0.25m^2 mouth area (Fraser, 1966), and mesh-size 200 μm (Section N) and 180 μm (Svinøy section). Sampling was conducted from 50 m depth to the surface at the Section N, and from 200 m depth to the surface at the Svinøy section. All samples were preserved with 4% formaldehyde on board. In the laboratory, the samples were divided into subsamples with a plankton splitter, and an aliquot of around 200 to 300 animals from each sample was identified and counted. For the Svinøy section, *C. hyperboreus* has been identified to copepodite stages. The copepodite stage IV, V, and adult females and males were used in the present analysis and younger stages were omitted because these younger stages have great fluctuations in abundance during the growth season (Gislason, 2018). The older stages will in addition represent the overwintering stages (Hirche, 1997; Astthorsson and Gislason, 2003; Broms et al., 2009; Gislason, 2018). At Section N, *C. hyperboreus* has not been identified to copepodite stages and thus all stages are included. However, stages younger than CIII have very seldom been observed in the samples (pers.com. I. Kristiansen, Faroe Marine Research Institute) and we therefore interpret these data as overwintering stages. The data are presented as abundance per m^3.

Methods

To show the focused period herein (1995-2019) in a longer time perspective updated series over the period 1955-2021 of heat and freshwater are presented (Mork et al., 2014). At each grid point from the gridded hydrography, the heat and freshwater contents were calculated above the depth of the specific volume anomaly equals to 2.1×10^{-7} m^3 kg^{-1} (denoted here as s21). The surface s21 corresponds approximately to the surface σ_t = 27.9 that is close to the lower depth of the Atlantic layer in the Norwegian Basin (Mork and Blindheim, 2000; Rossby et al., 2009). Local time averaged temperature and salinity at the s21 surface were used as reference values. Relative heat and freshwater contents were calculated by removing the temporal averages before integrating over the Norwegian Basin (see Mork et al., 2014 for details). We do not have the full access to the Russian hydrographic data used in Mork et al. (2014) before 1995. However, a comparison of the estimated relative heat and freshwater contents using the s21 or the 1000 dbar surfaces as reference yield qualitatively similar results (not shown).

From the gridded hydrography we construct maps showing the depth-mean isohalines for two vertical layers 50-200 m and 300-800 for the three periods defined above (**Figure 5**). The volumetric census is made for Temperature-Salinity classes of 0.1°C by 0.01, respectively, (**Figure 6**) and confined to the area limited by 62-69°N and 12°W to 8°E and depth range 0-1000 m (see area in **Figure 1**). We use *in-situ* temperature throughout the manuscript. In the upper 1000 m considered here, the difference between temperature and potential temperature is less than 0.1°C. This would not affect the results. For salinity we use the traditional practical salinity unit to simplify comparison with earlier studies.

Nutrient concentrations are presented with median and 95% confidence interval (**Figure 7**). We contrast the depth-mean distributions for the Arctic, Atlantic and Fresh periods. We include mean estimates for three stations over the continental slope in Atlantic Water and for the three westernmost station representing Arctic Water (see **Figure 3**).

The zooplankton biomass estimates (**Figure 8**) are based on a bootstrapping method. For each year, we draw from the observations series of length equal to the number of samples with replacement. This procedure is repeated 1000 times from which median and the 95% confidence interval is presented. The main assumption behind this method is statistical stationarity within the area.

RESULTS

Three Contrasting Periods

As a starting point, we investigate the integrated heat and freshwater content (Mork et al., 2014) in the Norwegian Basin (**Figure 2**). Three periods are defined: *i)* 1995-2005, Arctic - associated with a transition from cold/fresh to warm and saline, *ii)* 2006-2016, Atlantic - a generally consistent warm and saline period, and *iii)* 2017-2019, Fresh - a period that show record strong freshening while temperatures remained high.

Variable Water Mass Composition – Hydrographic Sections

We utilize the Section N (**Figure 3**) and the Svinøy section (**Figure 4**) to illustrate the variable distribution of water masses in the inflow region to the Norwegian Basin. During the Arctic period there was a several hundred-meter-thick layer of AIW at both sections. Common for both sections, there have been large changes in the Arctic Intermediate layer, with an almost total loss of AIW (S < 34.9 and -0.5°C < T< 1.0°C) from the Arctic period (**Figures 4A**, **5A**) to the subsequent Atlantic period (**Figures 4B**, **5B**). AIW, defined by the above TS criteria, has not re-appeared at either of these sections. At Section N section there are some minor traces of low salinity Arctic water MEIW/AIW (S < 34.9 and 1.0°C < T <4°C) during the Fresh period 2017-2019, but this is not observed in the Svinøy section (**Figures 4C**, **5C**). A curious observation, at both sections, is a remarkable close resemblance between the 35 isohaline and the 4°C isotherm in the Atlantic inflow domain during the first two decades (1995-2005 and 2006-2016, **Figures 3A, B** and **4A, B**). However, during the Fresh period the 35 isohaline is closer to the 6°C isotherm in the Section N (**Figure 3C**), and this is also observed downstream in the Svinøy section, but only for the Norwegian Atlantic Front Current west of 1.25°E (**Figure 4C**). At the eastern part of the section, the 35 isohaline still resembles the 4°C isotherm fairly well.

Horizontal Maps of Salinity

The depth-mean salinity maps illustrate some marked differences between the upper layer (50-200 m) that include the MEIW and intermediate layer (300-800 m) that contain the AIW (**Figure 5**). For the 50-200 m layer, the 34.9 isohaline typically align with the shelf slope bordering the Iceland Sea and the Norwegian Basin (**Figure 5A**). However, during the Fresh period a tongue of the 34.9 isohaline extends into the southern Norwegian Basin. For the 35 isohaline we find that this extends farthest west for the Atlantic period, and farthest east for the Fresh period, and with the largest differences in the interior Norwegian Basin. For the 300-800 m layer the substantial eastward extent of the 34.9 isohaline into the Norwegian is limited to the Arctic period (**Figure 5B**). The 35 isohaline is confined to the eastern shelf break of the Norwegian Basin, slightly more westward during the Atlantic period, before turning west and encircling the deep Atlantic Water in the Lofoten Basin.

Volumetric TS Plots

Finally, the volumetric TS-plots illustrate the major changes in the water masses during the three defined periods in the Norwegian Basin (**Figure 6**). In the climatology, all water classes during the period 1995-2019 are included. The most prominent feature is the broad distribution in TS-space ranging from warm and saline Atlantic Water (35.2-35.3, 6-8°C) that is cooled and freshened in the Norwegian Sea and Arctic, to finally Norwegian Sea Deep Water (NSDW) with salinity of 34.91 and T below 0°C (**Figure 6A**). AIW and MEIW are characterized by lower salinities due to Polar (or Arctic) influence. The surface water, located in a band of temperature about 8°C and salinties from 34.4 to 35 is remnants of the Norwegian Coastal Current.

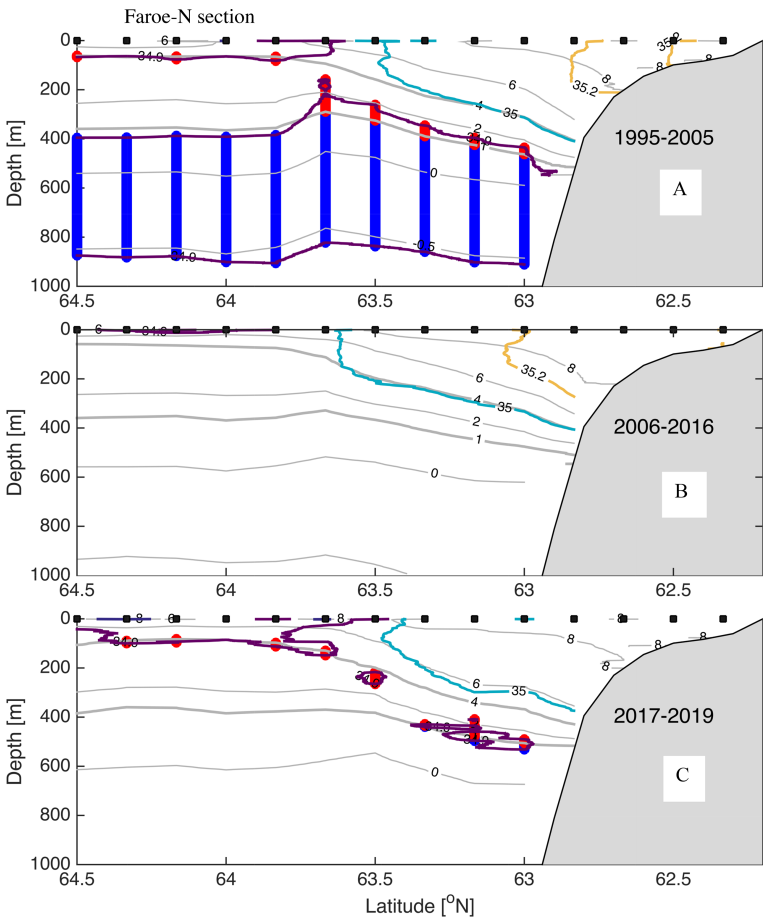


FIGURE 3 | **(A–C)** Mean temperature and salinity for the Section N section for the periods **(A)** 1995-2005, **(B)** 2006-2016, and **(C)** 2017-2019. Colors are for salinity showing 34.9 (purple), 35.0 (light blue) and 35.2 (yellow) isohalines, and gray show isotherms -0.5, 0,1,.,8°C. Thick vertical lines indicate Arctic Intermediate Water (blue) and Modified East Icelandic Water (red). Black squares show positions of the stations.

Compared to the climatology the distribution during the sub-periods discussed here is more confined (compare **Figure 6A** and **Figures 6B–D**). As such, the period 1995-2005 distributes as a relative confined anomalous positive band of Atlantic Water TS-classes (**Figure 6B**) seen as a red band (positive) between blue bands (negative) both on the saline and fresh side. Another marked feature is the positive anomaly of the relative cold and fresh AIW (-0.5 < T < 1°C , S<34.9). During the following period 2006-2016 the Atlantic Water classes are anomalously warm and especially saline, and the AIW is greatly reduced (**Figure 6C**). During 2017-2019 large changes have occurred, which are different from the two previous decades (**Figure 6D**). First, the Atlantic Waters have become anomalous fresh exceeding by far the two previous decades. Second, the AIW indicate a further decrease, and instead the fresher and warmer MEIW (T in the range [1-4] °C and S < 34.9) has again become more dominant.

Pre-Bloom (Winter) Nutrients

Given the stark changes especially in the AIW, but also the MEIW, it is of interest to investigate if these changes also are associated with changes in the nutrient concentrations. We used pre-bloom (winter) data (Jan-Mar) from the Svinøy section and from the same periods hitherto discussed: 1995-2005, 2006-2016, and 2017-2019. Near-surface nutrient concentrations in the north-western part of the section (**Figures 7C, D**) west of the Norwegian Atlantic Front Current (**Figure 1**) are generally higher than in the eastern part of the section (**Figures 7A, B**) in the Norwegian Atlantic Slope Current. Binned over the defined periods, both nitrate and silicate concentrations were higher during the Arctic compared to the subsequent Atlantic and Fresh periods (**Figure 7**). The decline is most apparent in near-surface waters (0-200/500m) and most pronounced for silicate concentrations. In deeper waters (2000-2500 m) there is little difference between the two periods.

Zooplankton

The large hydrographic changes are likely to impact the zooplankton abundances and species composition through nutrient driven influence on primary production or by direct lateral influxes of animals from the west (Kristiansen et al., 2019). To explore such ecosystem effects, we investigate the coinciding

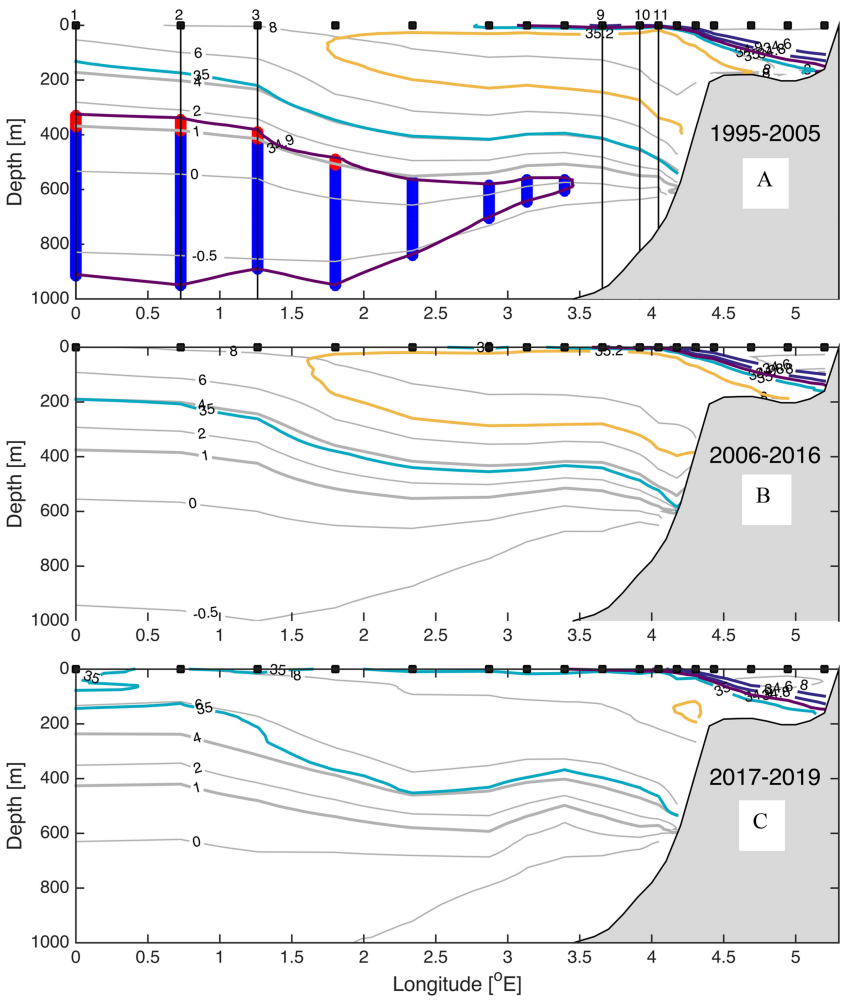


FIGURE 4 | **(A–C)** Mean temperature and salinity for the Svinøy section for the periods **(A)** 1995-2005, **(B)** 2006-2016, and **(C)** 2017-2019. Colors are for salinity showing 34.9 (purple), 35.0 (light blue) and 35.2 (yellow) isohalines, and gray show isotherms -0.5, 0, 1,., 8°C. Vertical lines show nutrient data used in **Figures 8**, **9** stations 1-3 represent the western edge of the Norwegian Atlantic Front Current, and stations 9-11 represent the "core" Atlantic water. Thick vertical lines indicate Arctic Intermediate Water (blue) and Modified East Icelandic Water (red). Black squares show positions of the stations.

changes in mesozooplankton biomass in the upper 200 meters of the Norwegian Basin, sampled in May (**Figure 8**). The mesozooplankton biomass index represents a larger area covering the southern Norwegian Sea, including the Norwegian Basin and adjacent areas (**Figure 1**). The biomass is mainly represented by *Calanus finmarchicus* within the Norwegian Sea in the productive season, and the seasonal time-window of sampling will mainly represent the overwintering generation of *C. finmarchicus* (Skjoldal et al., 2004; Broms and Melle, 2007; Broms et al., 2009; Bagøien et al., 2012; Strand et al., 2020). The biomass showed high values in the first part of the time-series, from 1995 to mid-2000s. Thereafter, the biomass was largely reduced and reached a minimum around 2010. The period after mid-2000s can be regarded as a period with lower biomass, however an increase towards the end of the time-series is observed. When relating the mesozooplankton biomass to the three identified time-periods, the Arctic period has a mean of 10 g m^{-2}, the Atlantic period has a mean of 6.4 g m^{-2}, and the Fresh period have a mean of 9.5 g m^{-2}.

In contrast to *C. finmarchicus*, *C. hyperboreus* does not reproduce in the Norwegian Basin (Wiborg, 1954), and its relative abundance can therefore be used as indicator of advection of Arctic waters from the Greenland and Iceland Seas. We here show that the previously demonstrated water mass, MEIW, and *C. hyperboreus* are advected to the Section N (Kristiansen et al., 2019), and extend further east to the Svinøy Section (**Figure 9**). Further more, the increased influx of water from the west during the recent Fresh period (**Figure 5A**) coincided with increased abundances of *C. hyperboreus*, at both sections, although not to the levels of the first decade. The variability of *C. hyperboreus* thus tends to follow that of the overall biomass (**Figure 8**) with maximum values in the Atlantic period, followed by low values and some years virtually absent in the Atlantic period, and finally a relative increase in the most recent Fresh period.

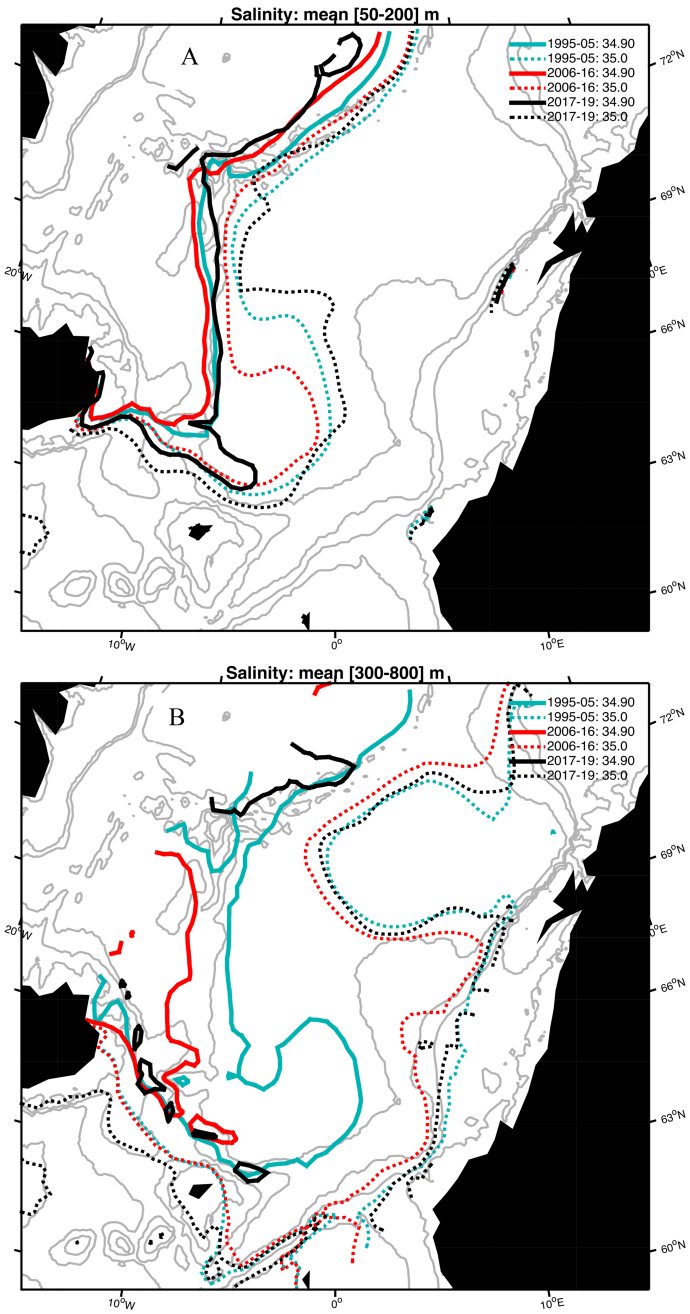


FIGURE 5 | **(A, B)** Depth-mean salinity over the depth range **(A)** 50-200m, and **(B)** 300-800m for the three periods 1995-2005, 2006-2016, and 2017-2019. Isohalines included are 34.9 (solid) and 35.0 (dashed).

DISCUSSION

Our analysis showed that the Norwegian Basin the three defined multi-annual periods turned out to have distinct differences in nutrients, and for both zooplankton biomass and species. In the Arctic period, 1995 to 2005, the Atlantic inflow was relative fresh and cold, and the observations show a pronounced layer of AIW, relative high nutrients and maximum values for zooplankton biomass and *C. hyperboreus* abundance. During the subsequent Atlantic period, 2006-2016, the Atlantic waters were relatively warm and saline, the layer of AIW almost disappeared, the level of nutrients was relatively low, and there was significant decrease in both in *C. hyperboreus* and zooplankton biomass. During the most recent Fresh period, 2017-2019, the Atlantic Water became less saline but still relative warm. There was still little evidence of AIW but increased presence of MEIW. During this period the

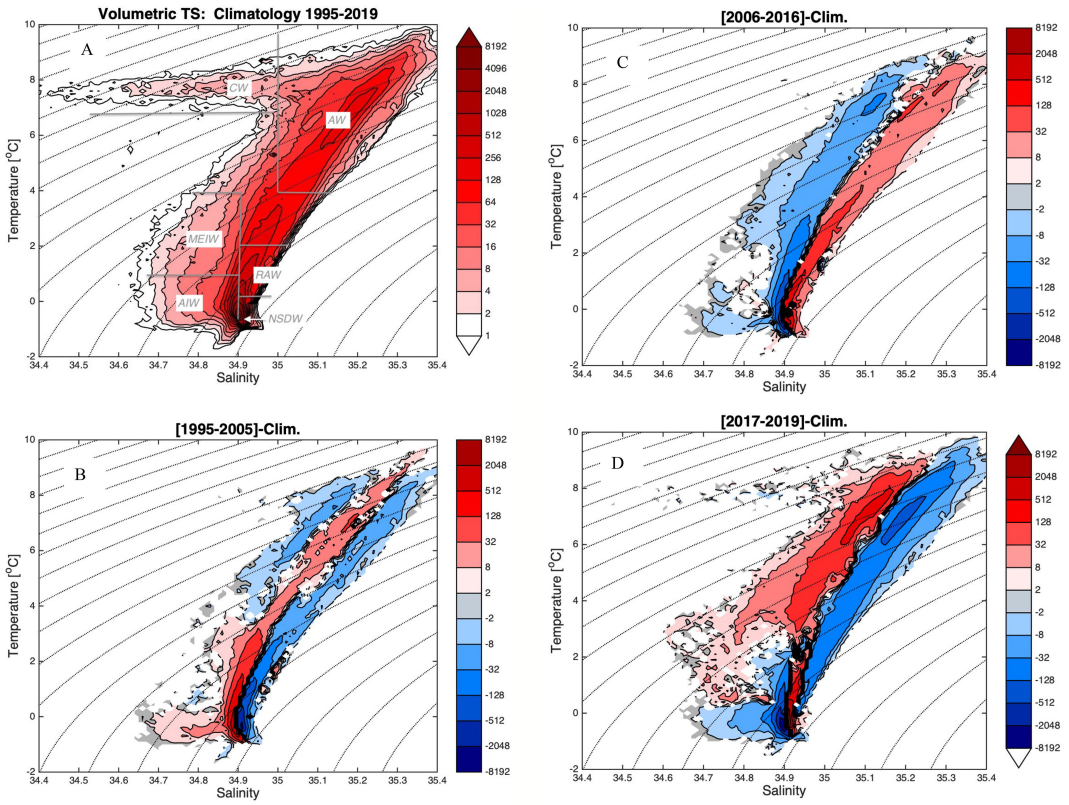


FIGURE 6 | **(A–D)** Volumetric TS-plots for the Norwegian Basin. **(A)** Climatology 1995-2019 including schematic distribution of water masses discussed, **(B)** difference mean 1995-2005 and the climatology, **(C)** difference mean 2006-2016 and climatology, and **(D)** difference mean 2017-2019 and climatology. The values represent number of grid points 0.5° longitude x 0.25° latitude over 5 m depth. The color scale is log 2. In difference plots b-d red colors are positive and blue colors are negative. Data include the depth layers 0-1000m and the area is limited by 62 and 69°N and 12°W and 8°E (see area **Figure 1**). Dashed lines are isopycnal lines. Abbreviations for water masses includes Atlantic Water (AW), Return Atlantic Water (RAW), Artic Intermediate Water (AIW), Modified East Icelandic Water (MEIW), Norwegian Sea Deep Water (NSDW) and Coastal Water (CW).

nutrients remained at the level of the Atlantic period, but there was a relative increase in zooplankton biomass and *C. hyperboreus*. We first discuss the cause of the observed changes and proceed with potential effects on the ecosystem.

A major change during the study period (1995-2019) is the decrease of the AIW, defined with salinity less than 34.9 and temperatures between -0.5 and +1.0 °C (Swift and Aagaard, 1981; Blindheim, 1990; Jeansson et al., 2017), from the Arctic to the Atlantic period (**Figures 3**–**6**). A possible cause of this reduction is the increasing salinity of the Norwegian Atlantic Current into the early 2000s. This water partly turns southward in the Fram Strait as Return Atlantic Water, causing increase in the surface salinity in the Greenland Sea, leading to more saline and hence deeper winter convection (Lauvset et al., 2018). A possible interpretation could be that a more saline AIW vintage, that does not meet previous TS definition replaced the classical AIW type. However, the volumetric plots show that the AIW layer is largely reduced during the two latter periods and that this insulating layer between the Atlantic Water and the NSDW basically vanished. Another prominent feature is the MEIW that is transported with the East Icelandic Current into the southwestern Norwegian Basin and then follows the general cyclonic circulation (Meincke, 1978; Blindheim, 1990; Søiland et al., 2008; Semper et al., 2020; Hátún et al., 2021). According to the spatial maps of MEIW (**Figure 5A**), there is a tongue of the 34.9 isohaline that extend anomalous eastward in the southern Norwegian Sea during the period Fresh.

Related to the changes in the Arctic Water two partially related mechanisms are at play. First, the fueling of zooplankton *via* the EIC (Wiborg, 1954; Kristiansen et al., 2022). Kristiansen et al. (2019) found a coinciding decrease of MEIW and *C. hyperboreus* abundance at Section N in the early 2000s but an increase of *C. hyperboreus* since 2017 within the southwestern Norwegian Sea (Kristiansen et al., 2022). This paper shows that the increase in *C. hyperboreus* abundance with increasing Arctic Waters can also be traced to the eastern part of the Norwegian Basin (**Figure 9**). This mechanism is likely important during the Arctic and Fresh periods, but less so during the Atlantic period. Second, the generally higher level of *C. hyperboreus* during the Arctic period indicate advection from regions of higher concentration. Such areas are found further north in the Iceland and Greeland Seas (Wiborg, 1954; Hirche, 1997). Thus, the elevated abundance of *C. hyperborus* during the Arctic period is in accordance with increased inflow of AIW from

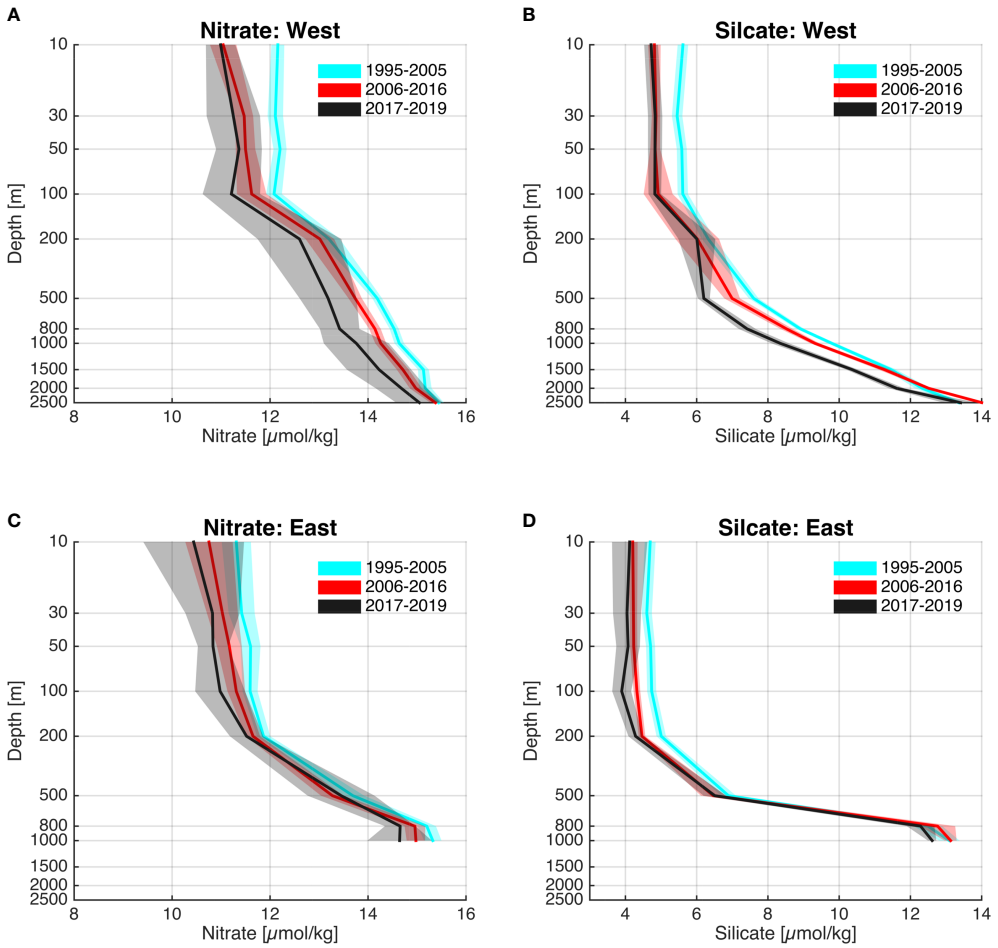


FIGURE 7 | **(A–D)** Time-mean depth profiles of nutrients in the Svinøy section showing **(A)** nitrate, and **(B)** silicate from the stations 1-3, and **(C)** nitrate and **(D)** silicate from the stations 9-11. The legend shows the periods 1995-2005 (magenta), 2006-2016 (red), and 2017-2019 (black). Data are from months January-March. The shaded areas show the 95% confidence interval. The positions of the stations are indicated in **Figure 4A**.

the Greenland and Iceland Seas. This also applies to the overall mesozooplankton biomass within the Norwegian Basin since the abundance of *C. hyperboreus* and mesozooplankton biomass co-vary, which suggests that other zooplankton species are also advected eastwards with the Arctic waters.

However, our results show a significant reduction in the amount of winter nutrients contrasting the Arctic to the subsequent Atlantic and Fresh periods. This can be interpreted as a reduction in the potential for new production that correspond to the major changes in ocean climate. Note that the elevated levels of nutrients extend to intermediate depths, thus annual upper ocean winter refueling of nutrients could simply be explained by local enhanced winter mixing.

Macronutrient concentrations, and silicate in particular, are generally higher in Arctic surface waters (**Figure 7**). New production is determined as the seasonal drop in NO3 concentrations, from a uniform depth profile of concentrations in winter to unexploitable levels below detection in summer. Therefore, we propose that if the observed lower original winter concentrations continue its downward trend (Hátún et al., 2017; Gundersen et al., 2021) the region will generate less seasonal new production overall. Additionally, diatom growth is only competitive to other phytoplankton at silicate concentrations >2 umol/L (Furnas, 1990; Egge and Aksnes, 1992). Diatoms will therefore lose their competitive edge at lower silicate concentrations in surface waters in developing spring blooms. Diatoms are considered one of the main staples for dominant zooplankton groups in the Norwegian Sea, and zooplankton growth is highly dependent on the timing and magnitude of the spring bloom (Melle et al., 2004; Eiane and Tande, 2009). Also, clearance and ingestion rates for, *C. finmarchicus* are at a peak during diatom spring blooms in the Norwegian Sea (Meyer-Harms et al., 1999). Therefore, silicate concentrations in surface waters, which showed a decline in the last number of decades (Rey, 2012; Hátún et al., 2017; Gundersen et al., 2021) may have impacted the amounts of diatoms available for major groups of zooplankton in these waters. Juvenile fish of commercial stocks in the Norwegian Sea (e.g. herring and cod) are strongly dependent on successful zooplankton growth and reproduction

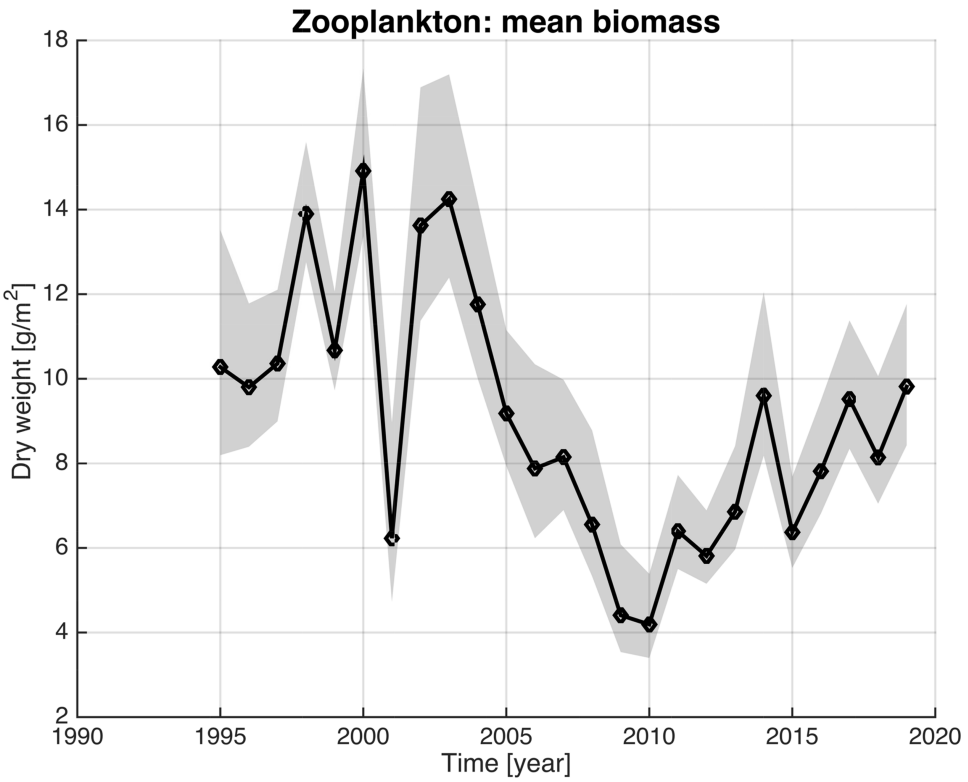


FIGURE 8 | Median zooplankton biomass in the Norwegian Basin in May. The mean number of observations per year is 93. Solid line shows the median and the gray band represents the 95% confidence interval.

each year (Skjoldal, 2004; Gjøsæther, 2009). Therefore, lower initial silicate concentrations at the onset of the spring bloom season may lead to weaker diatom blooms and hence, less successful growth and survival of zooplankton and fish larvae in these oceans. However, zooplankton diets are diverse (Meyer-Harms et al., 1999) and hence, not solely dependent on diatom growth and development. Therefore, we propose that the magnitude and longevity of the spring bloom, determined by the total amount of available nitrate in surface waters at the onset of the spring bloom, may play an equally important role in determining the seasonal magnitude of new production available for zooplankton growth and development in these waters.

Changes in temperature can affect the growth rates (Campbell et al., 2001), length of growth season (Strand et al., 2020), and distribution of *C. finmarchicus,* and thus potentially influence on the zooplankton biomass and production. An extension of suitable habitats for *C. finmarchicus* have been observed in Arctic areas and related to temperature and retreat of the ice-edge (Aarflot et al., 2018; Moller and Nilsen, 2020; Tarling et al., 2022). The ability of *C. finmarchicus* to complete its life cycle is found to increase with temperature at the entrance to the Arctic (Tarling et al., 2022). The optimum temperature window for older copepodite stages of *C. finmarchicus* (CV and adults) based on distribution and abundance data is 6–11°C (Helaouet and Beaugrand, 2007). In the Norwegian Sea, *C. finmarchicus* occupy waters with surface temperatures from 0 to 13°C, with the highest abundance occurring between 5 and 9°C (Strand et al., 2020). Since the upper-ocean temperature during the three considered periods are all basically within these optimal windows, temperature may not be a major driver of ecosystem change in the Norwegian Basin during the present climate conditions.

While beyond the scope of this work, recent studies indicate that the here discussed contrasting periods in the Norwegian Basin have also affected fish (Eliasen et al., 2021; Kristiansen et al., 2022; Utne et al., 2022). The reduction of Arctic Water in the Norwegian Sea in the early 2000s resulted in reduced feeding of post-smolts of salmon (Utne et al., 2022), drop in marine growth of Norwegian salmon (Vollset et al., 2022), and in a marked shift of the herring feeding migration towards East Icelandic Current (Eliasen et al., 2021; Kristiansen et al., 2022). These results are in accordance with the results of this paper linking changes in the ocean climate to plankton production and species composition in the Norwegian Sea, and thereby changed productivity of the ecosystem. We acknowledge that we in this paper have not included data of phytoplankton which are needed to bridge proposed link from nutrients to zooplankton. Inclusion of such data would, however, add new uncertainties and for further details on primary production we refer to the paper of Silva et al. (this issue).

The suggested link between the relative amount of Arctic to Atlantic Water masses, lateral influx of nutrients and arctic

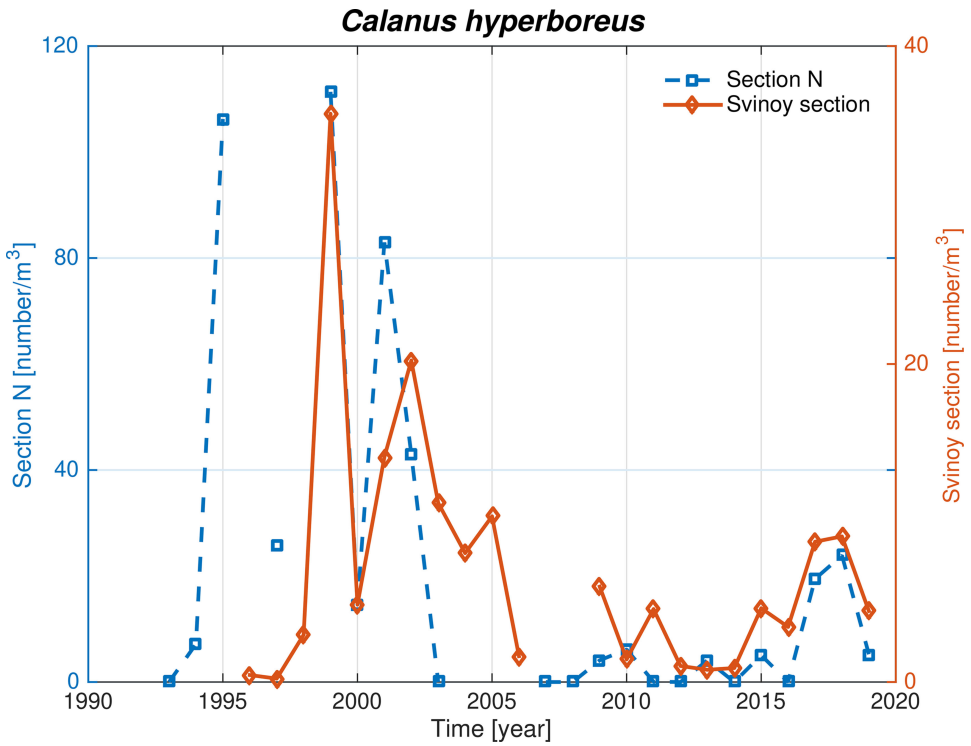


FIGURE 9 | *Calanus hyperboreus* at the Section N (blue) and Svinøy section (red) during spring.

zooplankton, and zooplankton likely growth provide a potential for making ecosystem predictions. While atmospheric forcing which drive regional circulation and water mass modification, are basically unpredictable, the memory in terms of advected water masses may provide a forecast horizon on the order of several years.

CONCLUDING REMARKS

We investigate the major oceanographic changes of the Norwegian Basin over the period 1995 to 2019 and potential impacts on marine ecosystems. Limited evidence supports that temperature drive ecosystem changes, while changing nutrients levels in connection to water masses may play a stronger role. We find that nutrient concentrations are generally higher in Arctic waters, compared to Atlantic waters, and that during the Arctic period (1995-2005) nutrients were significantly higher compared to the subsequent Atlantic period (2006-2016), and Fresh period, (2017-2019). We have not investigated primary production per se but note that high level of nutrients and zooplankton abundance tend to be synchronized in the Norwegian Basin. During the Arctic period, and partly during the Fresh period, the observations indicate increased amount of arctic zooplankton that are advected from the Iceland – and Greenland seas into the Norwegian Basin. Since these large and nutritious arctic zooplankton are preferred food for large fish stock (e.g. Norwegian spring spawning herring), these shifts likely have major impacts on fish stock dynamics, and therefore also on the fisheries and economies.

DATA AVAILABILITY STATEMENT

The raw data supporting the conclusions of this article will be made available by the authors, without undue reservation.

AUTHOR CONTRIBUTIONS

All authors contributed to the article and approved the submitted version.

FUNDING

This study was carried out as part of the project "Sustainable multispecies harvest from the Norwegian Sea and adjacent ecosystems" funded by the Research Council of Norway (project number 299554). Data collection along Section N received support from the European Framework Programs under grant agreement numbers GA212643 (THOR), and 308299 (NACLIM) and from the Danish Ministry of Climate, Energy and Utilities through its climate support program to the Arctic (FARMON projects). The Argo data were collected and made freely available by the International Argo Program and the national programs that contribute to it. (https://argo.ucsd.edu, https://www.ocean-ops.org). The Argo Program is part of the Global Ocean Observing System. This study was supported by the Institute of Marine Research project "Monitoring of the environment and plankton condition in the Norwegian Sea" and the Research Council of Norway (NorArgo2, #269753).

ACKNOWLEDGMENTS

We thank all Captains and crew, the Plankton Chemistry and the Zooplankton Laboratories at IMR, the Environmental Department and the Pelagic Department at FAMRI, the Zooplankton Laboratory at MFRI (Marine and Freshwater Institute Iceland) for all shipboard collections and sample analysis over the years.

REFERENCES

Aarflot, J. M., Skjoldal, H. R., Dalpadado, P., and Skern-Mauritzen, M. (2018). Contribution of Calanus Species to the Mesozooplankton Biomass in the Barents Sea. *ICES J. Marine Sci.* 75, 2342–2354. doi: 10.1093/icesjms/fsx221

Argo (2000). *Argo Float Data and Metadata From Global Data Assembly Centre (Argo GDAC)* (SEANOE). doi: 10.17882/42182

Asbjørnsen, H., Årthun, M., Skagseth, Ø., and Eldevik, T. (2019). Mechanisms of Ocean Heat Anomalies in the Norwegian Sea. *J. Geophys. Res. Oceans* 124, 3908–2923. doi: 10.1029/2018JC014649

Astthorsson, O. S., and Gislason, A. (2003). Seasonal Variations in Abundance, Development and Vertical Distribution of *Calanus finmarchicus*, C. hyperboreus and *C. glacialis* in the East Icelandic Current. *J. Plankton Res.* 25, 843–854. doi: 10.1093/plankt/25.7.843

Bagøien, E., Melle, W., and Kaartvedt, S. (2012). Seasonal Development of Mixed Layer Depths, Nutrients, Chlorophyll and *Calanus finmarchicus* in the Norwegian Sea – A Basin-Scale Habitat Comparison. *Progr. Oceanography* 103, 58–79. doi: 10.1016/j.pocean.2012.04.014

Blindheim, J. (1990). Arctic Intermediate Water in the Norwegian Sea. *Deep Sea Res.* 37 (9), 1475–1489. doi: 10.1016/0198-0149(90)90138-L

Blindheim, J., Borovkov, V., Hansen, B., Malmberg, S. A., Turrell, W. R., and Østerhus, S. (2000). Upper Layer Cooling and Freshening in the Norwegian Sea in Relation to Atmospheric Forcing. *Deep Sea Res. I* 47, 655–680. doi: 10.1016/S0967-0637(99)00070-9

Broms, C., and Melle, W. (2007). Seasonal Development of Calanus Finmarchicus in Relation to Phytoplankton Bloom Dynamics in the Norwegian Sea. *Deep Sea Res. Part II* 54, 2760–2775. doi: 10.1016/j.dsr2.2007.08.021

Broms, C., Melle, W., and Kaartvedt, S. (2009). Oceanic Distribution and Life Cycle of Calanus Species in the Norwegian Sea and Adjacent Waters. *Deep Sea Res. Part II-Top. Stud. Oceanogr.* 56, 1910–1921. doi: 10.1016/j.dsr2.2008.11.005

Broomé, S., and Nilsson, J. (2018). Shear Dispersion and Delayed Propagation of Temperature Anomalies Along the Norwegian Atlantic Slope Current. *Tellus* 70A, 1–13. doi: 10.1080/16000870.2018.1453215

Campbell, R. G., Wagner, M. M., Teegarden, G. J., Boudreau, C. A., and Durbin, E. G. (2001). Growth and Development Rates of the Copepod Calanus Finmarchicus Reared in the Laboratory. *Marine Ecol. Prog. Ser.* 221, 161–183. doi: 10.3354/meps221161

Chafik, L., Nilsson, J., Skagseth, Ø., and Lundberg, P. (2015). On the Flow of Atlantic Water and Temperature Anomalies in the Nordic Seas Toward the Arctic Ocean. *J. Geophys. Res. Oceans* 120, 7897–7918. doi: 10.1002/2015JC011012

Dickson, R. R., Meincke, J., Malmberg, S.-A., and Lee, A. J. (1988). The "Great Salinity Anomaly" in the Northern North Atlantic 1968-82. *Prog. Oceanogr.* 20, 103–151. doi: 10.1016/0079-6611(88)90049-3

Eden, C., and Willebrand, J. (2001). Mechanism of Interannual to Decadal Variability of the North Atlantic Circulation. *J. Clim.* 14, 2266–2280. doi: 10.1175/1520-0442(2001)014<2266:MOITDV>2.0.CO;2

Egge, J., and Aksnes, D. (1992). Silicate as Regulating Nutrient in Phytoplankton Competition. *Mar. Ecol. Prog. Ser.* 83, 281–289. doi: 10.3354/meps083281

Eiane, K., and Tande, K. S. (2009). "Meso and Microzooplankton," in *Ecosystem Barents Sea* (Trondheim: Tapir Academic Press), vol. 587 . Eds. E. Sakshaug, G. Johnsen and K. Kovac, pp, 209–234.

Eliasen, S. K., Homrum, E.Í., Jacobsen, J. A., Kristiansen, I., Óskarsson, G. J., Salthaug, A., et al. (2021). Spatial Distribution of Different Age Groups of Herring in Norwegian Sea, May 1996-2020. *Front. Mar. Sci.* 8. doi: 10.3389/fmars.2021.778725

Fraser, J. H. (1966). Zooplankton Sampling. *Nature* 211, 915–916. doi: 10.1038/211915a0

Furevik, T. (2001). Annual and Interannual Variability of Atlantic Water Temperatures in the Norwegian and Barents Seas: 1980–1996. *Deep Sea Res. I* 48 (2), 383–404. doi: 10.1016/S0967-0637(00)00050-9

Furnas, M. J. (1990). *In Situ* Growth Rates of Marine Phytoplankton: Approaches to Measurement, Community and Species Growth Rate. *J. Plankton Res.* 12, 1117–1151. doi: 10.1093/plankt/12.6.1117

Gislason, A. (2018). Life Cycles and Seasonal Vertical Distribution of Copepods in the Iceland Sea. *Polar Biol.* 41, 2575–2589. doi: 10.1007/s00300-018-2392-4

Gjøsæther, H. (2009). "Commercial Fisheries (Fish, Seafood and Marine Mammals)," in *Ecosystem Barents Sea* (Trondheim: Tapir Academic Press), vol. 587 . Eds. E. Sakshaug, G. Johnsen and K. Kovac, 373–414.

Gundersen, K., Lien, V. S., Møgster, J. S., Nilsen, J.E.Ø., and Vindenes, H. (2021). "Declining Silicate and Nitrate Concentrations in the Northern North Atlantic," in *Copernicus Marine Service Ocean State Report, Issue 5, Journal of Operational Oceanography*, vol. 14:sup1, s23–s31. doi: 10.1080/1755876X.2021.1946240

Häkkinen, S., and Rhines, P. B. (2004). Decline of Subpolar North Atlantic Circulation During the 1990s. *Science* 304, 555–559. doi: 10.1126/science.1094917

Hansen, B., Larsen, K. M. H., Hátún, H., Kristiansen, R., Mortensen, E., and Østerhus, S. (2015). Transport of Volume, Heat, and Salt Towards the Arctic in the Faroe Current 1993–2013. *Ocean Sci.* 11, 743–757. doi: 10.5194/os-11-743-2015

Hátún, H., Azetsu-Scott, K., Somavilla, R., Rey, F., Johnson, C., Mathis, M., et al. (2017). The Subpolar Gyre Regulates Silicate Concentrations in the North Atlantic. *Sci. Rep.* 7. doi: 10.1038/s41598-017-14837-4

Hátún, H., Chafik, L., and Larsen, K. M. H. (2021). The Norwegian Sea Gyre - A Regulator of Iceland-Scotland Ridge Exchanges. *Front. Mar. Sci.* doi: 10.3389/fmars.2021.694614

Hátún, H., Sandø, A. B., Drange, H., Hansen, B., and Valdimarsson, H. (2005). Influence of the Atlantic Subpolar Gyre on the Thermohaline Circulation. *Science* 309, 1841–1844. doi: 10.1126/science.1114777

Helaouet, P., and Beaugrand, G. (2007). Macroecology of *Calanus Finmarchicus* and C. Helgolandicus in the North Atlantic Ocean and Adjacent Seas. *Mar. Ecol. Progr. Ser.* 345, 147–165. doi: 10.3354/meps06775

Helland-Hansen, B., and Nansen, F. (1909). *The Norwegian Sea: Its Physical Oceanography Based Upon the Norwegian Researches 1900–1904.* (Bergen: A/S John Griegs Boktrykkeri) 390 pp.

Hirche, H.-J. (1997). "Life Cycle of the Copepod Calanus Hyperboreus at the Greenland Sea," in *Mar. Biol*, vol. 128. , 607–618.

Holliday, N. P., Bersch, M., Berx, B., Chafik, L., Cunningham, S., Florindo-López, C., et al. (2020). Ocean Circulation Causes the Largest Freshening Event for 120 Years in Eastern Subpolar North Atlantic. *Nat. Com.* 11, 585. doi: 10.1038/s41467-020-14474-y

Holliday, N. P., Hughes, S. L., Bacon, S., Beszczynska-Möller, A., Hansen, B., Lavin, A., et al. (2008). Reversal of the 1960s to 1990s Freshening Trend in the Northeast North Atlantic and Nordic Seas. *Geophys. Res. Lett.* 35, L03614. doi: 10.1029/2007GL032675

ICES (2021a). Working Group of International Pelagic Surveys (WGIPS). *ICES Sci. Rep.* 3 (40), 481. doi: 10.17895/ices.pub.8055

ICES (2021b). Working Group on the Integrated Assessments of the Norwegian Sea (WGINOR; Outputs From 2020 Meeting). *ICES Sci. Rep.* 3 (35), 114. doi: 10.17895/ices.pub.8021

Jeansson, E., Olsen, A., and Jutterstrøm, S. (2017). Arctic Intermediate Water in the Nordic Sea–2009. *Deep Sea Res. Part1* 128, 82–97. doi: 10.1016/j.dsr.2017.08.013

Krahman, G., Visbeck, M., and Reverdin, G. (2001). Formation and Propagation of Temperature Anomalies Along the North Atlantic Current. *J. Phys. Oceanogr.* 31, 1287–1303. doi: 10.1175/1520-0485(2001)031<1287:FAPOTA>2.0.CO;2

Kristiansen, I., Gaard, E., Hátún, H., Jonasdottir, S., and Ferreira, A. S. A. (2016). Persistent Shift of *Calanus* Spp. In the Southwestern Norwegian Sea Since 2003, Linked to Ocean Climate. *ICES J. Mar. Sci.* 73, 1319–1329. doi: 10.1093/icesjms/fsv222

Kristiansen, I., Hátún, H., Jacobsen, J. A., Eliasen, S. K., Petursdottir, H., and Gaard, E. (2022). Spatial Variability of the Feeding Conditions for the Norwegian Spring Spawning Herring in May. *Front. Mar. Sci.* doi: 10.3389/fmars.2022.823006

Kristiansen, I., Hátún, H., Petursdottir, H., Gislason, A., Broms, C., Melle, W., et al. (2019). Decreased Influx of *Calanus* Spp. Into the South-Western Norwegian Sea Since 2003. *Deep Sea Res. Part I: Oceanographic Res. Papers* 149, 103048. doi: 10.1016/j.dsr.2019.05.008

Larsen, K. M. H., Hátún, H., Hansen, B., and Kristiansen, R. (2012). Atlantic Water in The Faroe Area: Sources and Variability. *ICES J. Marine Sci.* 69, 802–808. doi: 10.1093/icesjms/fss028

Lauvset, S. K., Brakstad, A., Våge, K., Olsen, A., Jeansson, E., and Mork, K. A. (2018). Continued Warming, Salinification and Oxygenation of the Greenland Sea Gyre. *Tellus* 70A, 1–9. doi: 10.1080/16000870.2018.1476434

Møller, E. F., and Nielsen, T. G. (2020). Borealization of Arctic Zooplankton—Smaller and Less Fat Zooplankton Species in Disko Bay, Western Greenland. *Limnol. Oceanogr.* 65, 1175–1188. doi: 10.1002/lno.11380

Macrander, A., Valdimarsson, H., and Jónsson, S. (2014). Improved Transport Estimate of the East Icelandic Current 2002–2012. *J. Geophys. Res. Oceans* 119, 3407–3424. doi: 10.1002/2013JC009517

Marshall, J., Kushner, Y., Battisti, D., Chang, P., Czaja, A., Dickson, R., et al. (2001). North Atlantic Climate Variability: Phenomena, Impacts and Mechanisms. *Int. J. Climatol.* 21, 1863–1898. doi: 10.1002/joc.693

Meincke, J. (1978). On the Distribution of Low Salinity Intermediate Waters Around the Faroes. *Dtsch. Hydrogr. Zeitschrift* 31, 50–64. doi: 10.1007/BF02226000

Melle, W., Ellertsen, B., and Skjodal, H. R. (2004). "Zooplankton: The Link to Higher Trophic Levels," in *The Norwegian Sea Ecosystem* Trondheim: Tapir Academic Press. Ed. H. R. Skjoldal (Tapir, Trondheim, Norway: Tapir Academic Press), 209–234.

Melle, W., Runge, J., Head, E., Plourde, S., Castellani, C., Licandro, P., et al. (2014). The North Atlantic Ocean as Habitat for *Calanus finmarchicus*: Environmental Factors and Life History Traits. *Prog. Oceanogr.* 129, 244–284. doi: 10.1016/j.pocean.2014.04.026

Meyer-Harms, B., Irigoien, X., Head, R., and Harris, R. (1999). Selective Feeding on Natural Phytoplankton by Calanus Finmarchicus Before, During, and After the 1997 Spring Bloom in the Norwegian Sea. *Limnol. Oceanogr.* 44, 154–165. doi: 10.4319/lo.1999.44.1.0154

Mork, K. A., and Blindheim, J. (2000). Variations in the Atlantic Inflow to the Nordic Sea–1996. *Deep Sea Res. I* 47, 1035–1057. doi: 10.1016/S0967-0637(99)00091-6

Mork, K. A., Skagseth, Ø., Ivshin, V., Ozhigin, V., Hughes, S. L., and Valdimarsson, H. (2014). Advective and Atmospheric Forced Changes in Heat and Fresh Water Content in the Norwegian Se–2010. *Geophys. Res. Lett.* 41, 6221–6228. doi: 10.1002/2014GL061038

Mork, K. A., Skagseth, Ø., and Søiland, H. (2019). Recent Warming and Freshening of the Norwegian Sea Observed by Argo Data. *J. Clim* 32 (12), 3695–3705. doi: 10.1175/JCLI-D-18-0591.1

Read, J. F., and Pollard, R. T. (1992). Water Masses in the Region of the Iceland Faeroes Front. *J. Phys. Oceanogr.* 22, 1365–1378. doi: 10.1175/1520-0485(1992)

Rey, F. (2012). Declining Silicate Concentrations in the Norwegian and Barents Seas. – *ICES J. Mar. Sci.* 69, 208–212. doi: 10.1093/icesjms/fss007

Rossby, T., Ozhigin, V., Ivshin, V., and Bacon, S. (2009). An Isopycnal View of the Nordic Seas Hydrography With Focus on Properties of the Lofoten Basin. *Deep Sea Res. Part I* 56 (11), 1955–1971. doi: 10.1016/j.dsr.2009.07.005

Søiland, H., Prater, M. D., and Rossby, T. (2008). Rigid Topographic Control of Currents in the Nordic Seas. *Geophys. Res. Lett.* 35, 1–5. doi: 10.1029/2008GL034846

Semper, S., Pickart, R. S., Våge, K., Larsen, K. M., Hátún, H., and Hansen, B. (2020). The Iceland-Faroe Slope Jet: A Conduit for Dense Water Toward the Faroe Bank Channel Overflow. *Nat. Com.* 11, 5390. doi: 10.1038/s41467-020-19049-5

Skagseth, Ø., and Mork, K. A. (2012). Heat Content in the Norwegian Se–2010. *ICES J. Mar. Sci.* 69, 826–832. doi: 10.1093/icesjms/fss026

Skjoldal, H. R. (2004). *The Norwegian Sea Ecosystem* (Trondheim: Tapir Academic Press), 559 pp.

Stefansson, U. (1962). *North Atlantic Waters* Vol. 3 (Rit. Fiskideildar), 269 pp.

Strand, E., Bagøien, E., Edwards, M., Broms, C., and Klevjer, T. (2020). Spatial Distributions and Seasonality of Four *Calanus* Species in the Northeast Atlantic. *Prog. Oceanogr* 185, 102344. doi: 10.1016/j.pocean.2020.102344

Swift, J. H., and Aagaard, K. (1981). Seasonal Transitions and Water Mass Formation in the Iceland and Greenland Seas. *Deep Sea Res.* 28, 1107–1129. doi: 10.1016/0198-0149(81)90050-9

Tarling, G. A., Freer, J. J., Banas, N. S., Belcher, A., Blackwell, M., Castellani, C., et al. (2022). Can a Key Boreal *Calanus* Copepod Species Now Complete its Life-Cycle in the Arctic? Evidence and Implications for Arctic Food-Webs. *Ambio* 51 (2), 333–344. doi: 10.1007/s13280-021-01667-y

Utne, K. R., Skagseth, Ø., Wennevik, V., Broms, C. T., Melle, W., and Thorstad, E. B. (2022). Impacts of a Changing Ecosystem on the Feeding and Feeding Conditions for Atlantic Salmon During the First Months at Sea. *Front. Mar. Sci.* 9, 824614. doi: 10.3389/fmars.2022.824614

Voet, G., Quadfasel, D., Mork, K. A., and Søiland, H. (2010). The Mid-Depth Circulation of the Nordic Seas Derived From Profiling Float Observations. *Tellus* 62A, 516–529. doi: 10.1111/j.1600-0870.2010.00444.x

Vollset, K. W., Urdal, K., Utne, K. R., Thorstad, E. B., Sægrov, H., Raunsgard, A., et al. (2022). Ecological Regime Shift in the North-East Atlantic Revealed From the Unprecedented Reduction in Marine Growth of Atlantic Salmon. *Sci. Adv.* 8, eabk2542.

Wiborg, K. F. (1954). *Investigations on Zooplankton in Coastal and Offshore Waters of Western and Northwestern Norway. Report on Norwegian Fishery and Marine Investigations*. (Bergen, Norway: A/S John Griegs Boktrykkeri), Vol. XI. 1.

Conflict of Interest: The authors declare that the research was conducted in the absence of any commercial or financial relationships that could be construed as a potential conflict of interest.

Publisher's Note: All claims expressed in this article are solely those of the authors and do not necessarily represent those of their affiliated organizations, or those of the publisher, the editors and the reviewers. Any product that may be evaluated in this article, or claim that may be made by its manufacturer, is not guaranteed or endorsed by the publisher.

Copyright © 2022 Skagseth, Broms, Gundersen, Hátún, Kristiansen, Larsen, Mork, Petursdottir and Søiland. This is an open-access article distributed under the terms of the Creative Commons Attribution License (CC BY). The use, distribution or reproduction in other forums is permitted, provided the original author(s) and the copyright owner(s) are credited and that the original publication in this journal is cited, in accordance with accepted academic practice. No use, distribution or reproduction is permitted which does not comply with these terms.

frontiers | Frontiers in Marine Science

ORIGINAL RESEARCH
published: 19 May 2022
doi: 10.3389/fmars.2022.779335

Temporal Variability of Co-Occurring *Calanus finmarchicus* and *C. helgolandicus* in Skagerrak

Tone Falkenhaug, Cecilie Broms, Espen Bagøien and Nikolaos Nikolioudakis*

Institute of Marine Research (IMR), Bergen, Norway

The congeneric copepods *Calanus finmarchicus* and *C. helgolandicus* co-occur in the northern North Sea and Skagerrak where they play important roles as prey for higher trophic levels. This study analyses a 26-year time series (1994-2019) with a ~ two-week temporal resolution for *Calanus* spp. at a fixed monitoring station in Skagerrak, off southern Norway. Seasonal variation, inter-annual variability and long-term trends for the two species were examined. Strong differences in the species-specific seasonality were revealed, with *C. finmarchicus* dominating in spring and *C. helgolandicus* in autumn. The seasonal peak of *C. finmarchicus* was associated with relatively low temperatures (6-8°C) and high chlorophyll *a* concentration, while *C. helgolandicus* displayed its seasonal maximum at higher temperatures (11-16°C). *C. finmarchicus* was found to produce one dominant annual generation (in spring), but two or more generations are considered likely. Contrasting long-term trends in abundances were found for the two species, suggesting that their population sizes were affected by different mechanisms. The abundance of *C. helgolandicus* showed an increasing trend over the time period studied, apart from the last years. The abundance of *C. finmarchicus* was more variable and displayed no unidirectional long-term trends over the time series. The study revealed a shift in the phenology of *Calanus* spp. over the last 25 years at this site. Since 1994 the timing of the annual peaks in both *C. finmarchicus* and *C. helgolandicus* have advanced by about one month. Moreover, the seasonal pattern of *C. helgolandicus*, switched from a unimodal to a bimodal pattern around 2002, with a small additional peak also appearing in spring. The results suggest that the proximity to the Norwegian Trench influences the demography and abundance of *C. finmarchicus* in this coastal area, both as a gateway for the advective supply, as well as a habitat for local overwintering.

Keywords: *Calanus*, time-series, trends, seasonal variations, phenology, demography, Skagerrak, North Sea

OPEN ACCESS

Edited by:
Teresa Sofia Giesta da Silva, Marine and Freshwater Research Institute, Iceland

Reviewed by:
Frederic Maps, Laval University, Canada
Hjálmar Hátún, Faroe Marine Research Institute (FAMRI), Faro Islands

****Correspondence:***
Tone Falkenhaug
tone.falkenhaug@hi.no

Specialty section:
This article was submitted to Marine Ecosystem Ecology, a section of the journal Frontiers in Marine Science

Received: *18 September 2021*
Accepted: *05 April 2022*
Published: *19 May 2022*

Citation:
Falkenhaug T, Broms C, Bagøien E and Nikolioudakis N (2022) Temporal Variability of Co-Occurring Calanus finmarchicus and C. helgolandicus in Skagerrak. Front. Mar. Sci. 9:779335. doi: 10.3389/fmars.2022.779335

INTRODUCTION

Calanoid copepods of the genus *Calanus* spp. are major components of the zooplankton in the Northeast Atlantic Ocean and shelf seas (Conover, 1988; Melle et al., 2014). Two of the species in this ecologically important "*Calanus* complex" (Bonnet et al., 2005; Falk-Petersen et al., 2009), are the cold-boreal *Calanus finmarchicus* (Gunnerus, 1770) and the warm-temperate *C. helgolandicus* (Claus, 1863).

The distributional range of *C. finmarchicus* covers parts of the sub-polar North Atlantic, from eastern Canada to the Nordic Seas and the North Sea (Jaschnov, 1970; Helaouët et al., 2011; Melle et al., 2014; Strand et al., 2020). This species is observed at least in the temperature range 0 - 14°C, but with highest concentrations between 5 - 9°C (Jónasdóttir and Koski, 2011; Strand et al., 2020). *C. helgolandicus* (Claus, 1863) is associated with shelf areas along the eastern Atlantic. It has a more southerly distribution, mainly from the Mediterranean to the North Sea (40° - 60°N; Helaouët and Beaugrand, 2007), and typically occupies habitats with temperatures between 9° and 20°C (Bonnet et al., 2005).

The northern North Sea and Skagerrak is a shelf ecosystem with a wide-open boundary to the North Atlantic. This region represents a transition zone, where the biogeographic distributions of *C. finmarchicus* and *C. helgolandicus* overlap. In this part of the North Sea, *C. finmarchicus* is close to the southern limit of its geographical distribution while *C. helgolandicus* is close to its northern limit (Wilson et al., 2016; Strand et al., 2020), and both species are thus expected to be sensitive to small variations in environmental variables. These two *Calanus* species dominate the zooplankton abundance in this area, where they can make up 90% of the mesozooplankton biomass (Krause et al., 2003; Bonnet et al., 2005), and are key prey for early-life stages and adults of commercially important fish species such as cod, herring and lesser sandeel (Munk and Nielsen, 1994; Arnott and Ruxton, 2002; Heath, 2007; van Deurs et al., 2009). Over the last five decades, extensive changes in the zooplankton communities in the North-East Atlantic and on the European shelves have taken place. These changes have likely been driven by increased ocean temperatures, and include a biogeographical shift for several copepod species, with a poleward extension of warm-water species associated with a decrease in the number of cold-water species (Beaugrand et al., 2002). As a result, the abundance of *C. finmarchicus* has declined by 70% in the North Sea since 1970, concurrent with an apparent increase in the abundance of *C. helgolandicus* (Fromentin and Planque, 1996; Planque and Taylor, 1998).

Whereas long-term changes in zooplankton abundance in the North Sea have been thoroughly studied, potential changes in seasonal cycles and phenology have received less attention. *C. finmarchicus* has generally been considered to have a predominantly one-year life cycle throughout most of its geographic range (e.g. Heath et al., 2000; Melle et al., 2014 and references therein). However, the importance of a second generation has received more attention in recent studies (e.g. Strand et al., 2020; Skjoldal et al., 2021) and as many as three generations can develop in the southern North Sea (Fransz et al., 1991; Hirche et al., 2001). Regardless of the number of generations, the seasonal cycle of *C. finmarchicus* is characterized by a strong annual peak occurring in spring, potentially followed by smaller secondary peaks in summer and fall (Planque and Fromentin, 1996). In contrast, *C. helgolandicus* typically has multiple generations each year and its seasonality varies with latitude (Bonnet et al., 2005). In the Mediterranean, the annual peak in *C. helgolandicus* occurs in spring, whereas in the North Sea and Northeast Atlantic the peak is displayed in autumn (Planque and Fromentin, 1996; Bonnet et al., 2005). Long-term changes in abundance as well as the seasonal cycle and phenology of *C. finmarchicus* and *C. helgolandicus* may have consequences for the North Sea and Skagerrak ecosystems. Several studies from this area have linked fish recruitment not only to the abundance, but also to the seasonality of the *Calanus* species that serve as important prey (Beaugrand et al., 2003; Johannessen et al., 2012; Durant et al., 2013).

The present study is based on a time series from Arendal Station 2, located in the northern Skagerrak, where *Calanus* spp. have been sampled with high temporal resolution from 1994 to 2019. The timeseries from this station is of interest for several reasons. First, even though long-term changes in abundances of *Calanus* species in the North Sea have been thoroughly described, this has mainly been based on the high-quality data from the Continuous Plankton Recorder (CPR, Batten et al., 2003; Richardson et al., 2006). However, these CPR-results have been criticized due to the sampling being confined within a narrow depth interval around ~ 7 m depth while observations suggest that *C. finmarchicus* and *C. helgolandicus* occupy different depths (Jónasdóttir and Koski, 2011). Changes in vertical distributions of the two species in parallel with changes in water temperatures, will not be captured by the sampling method of CPR, and may instead be interpreted as changes in abundance. The present study covers a larger part of the water column and may thus avoid biases due to changes in vertical distributions of the populations. In addition, our study presents data from a part of the North Sea where the CPR coverage is sparse and where few long-term monitoring data on zooplankton exist. This study may thus complement our understanding of the long-term changes of the most important zooplankton species in an area under pressure from human activities and climate change. Second, the high temporal resolution is well suited to examine the seasonal patterns of the species and to evaluate whether there have been changes in phenology during the last 26 years. Potential phenological changes within this area could represent valuable information regarding as to how these two species may respond to climate changes, knowledge that could prove useful also for other geographical areas.

This study aims at establishing for the first time the seasonal cycles and long-term trends in abundance for each of the congeneric copepods *C. finmarchicus* and *C. helgolandicus* in the northern Skagerrak. This includes a description and comparison of the demography and number of generations for the two co-occurring sibling species. We also explore potential changes in phenology throughout the studied period. The following research questions are addressed:

- Can distinct cohorts of the congeneric *C. finmarchicus* and *C. helgolandicus* be identified and followed at the study site?
- If so, how many generations do each of the species produce annually in the area?
- Do the species phenologies overlap during the productive season?
- Is there a clear trend in the phenology and abundances of both species during the last 26 years?

MATERIALS AND METHODS

Study Site

This study is based on high frequency time-series data from 1994 to 2019 obtained from the Arendal Station 2 which is located in the northern Skagerrak, 1 nautical mile offshore at 75 m depth (58°23′N 8°49′E, **Figures 1** and **2**). The monitoring station is operated by the Institute of Marine Research in Norway. The Skagerrak is part of the north-west European Shelf and forms a transition area between the Baltic Sea and the North Sea proper. While the North Sea is a shallow shelf area, with an average depth of approximately 80 m, Skagerrak has as a mean depth of 200 m. The Skagerrak is directly connected to the Norwegian Sea *via* the Norwegian Trench, which extends southward from the Norwegian Sea and follows the Norwegian coastline into the center of Skagerrak where it reaches a maximum depth of 710 m. The predominant circulation in Skagerrak is anti-clockwise and is influenced by three main water masses of different origin. Warm, saline Atlantic water (salinity >35) enters the North Sea from the north and follows the western slope of the Norwegian Trench into Skagerrak, as the Norwegian Trench Atlantic Inflow (NTI; Furnes et al., 1986). Waters from the southern North Sea (Jutland Current, salinity < 34) carry relatively cold and fresh water along the west coast of Denmark and mixes with brackish water from the Baltic Sea, forming the Norwegian Coastal Current (NCC). The NCC flows along the Norwegian coast, transporting water out and northward from the Skagerrak and North Sea. Most of the water entering the North Sea shelf flows through Skagerrak before leaving, and many of the hydrographic events taking place in the North Sea will thus be reflected in this region. The coastal area of northern Skagerrak is strongly influenced by the brackish NCC and the outflow of freshwater from rivers, and the hydrographic conditions at the Arendal Station 2 are characterized by strong seasonal cycles in both salinity and temperature (Sætre et al., 2003; Albretsen et al., 2012). The site is influenced by relatively fresh coastal waters (25–32) in the upper 30 m and by more saline Skagerrak and North Sea water (32–35) deeper in the water-column. Surface water temperature ranges from 0°C to 20°C, with the annual minimum in March and maximum in August. The freshwater outflow combined with thermal heating results in the development of a pronounced pycnocline at 15-20 m from March to October. However, wind driven coastal upwelling is common along the coast, which may bring high salinity Atlantic

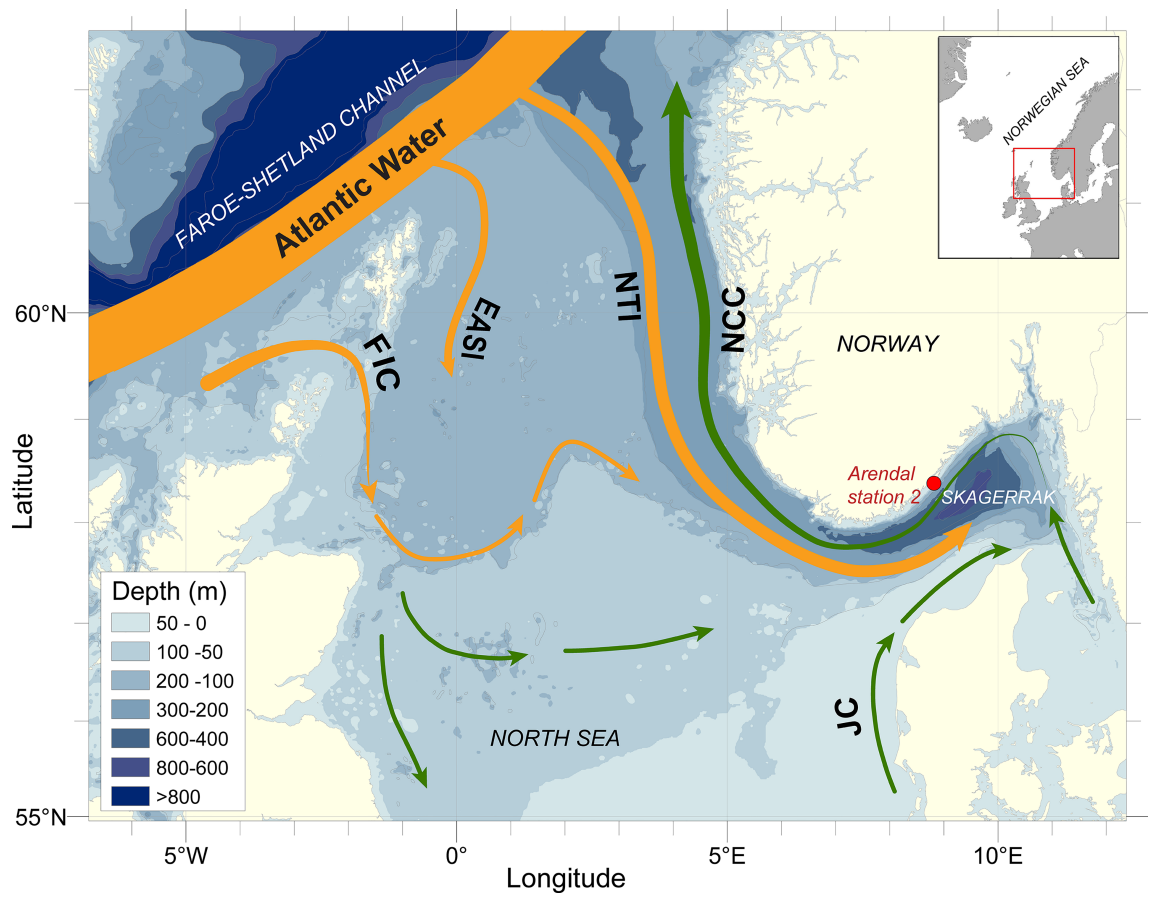


FIGURE 1 | North Sea and Skagerrak with main currents and location of Arendal Station 2 monitoring site. NTI: Norwegian Trench Atlantic Inflow; NCC, Norwegian Coastal Current; ESAI, East Shetland Atlantic Inflow; FIC, Fair Isle Current; JC, Jutland Current. Inset map shows the location of the Skagerrak area relative to adjacent seas.

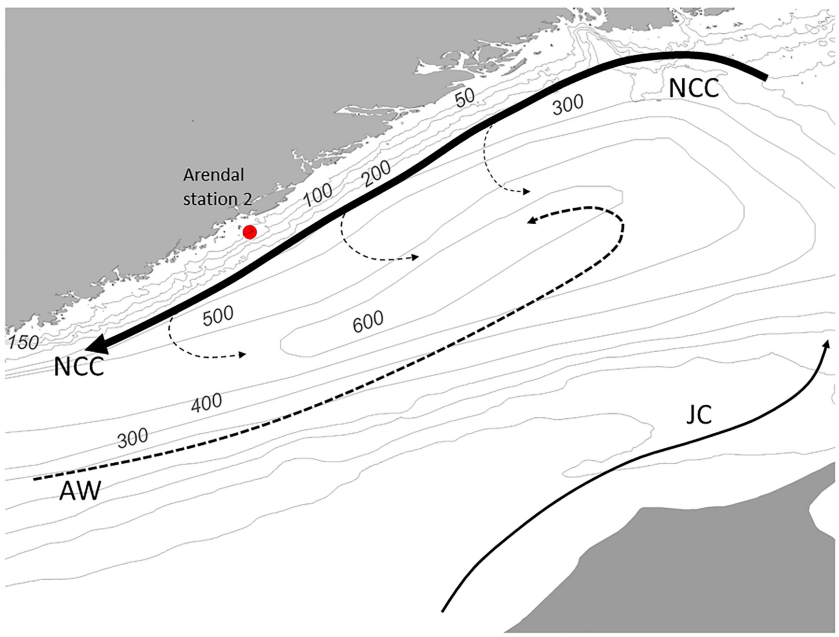


FIGURE 2 | Local bathymetry and prevailing circulation systems in Skagerrak. NCC, Norwegian Coastal Current; AW, Atlantic water; JC, Jutland Current.

water to the surface. A detailed description of the current system and hydrography in the North Sea-Skagerrak is given by Otto et al. (1990), Rohde (1996) and Sætre et al. (2003). A spring phytoplankton bloom, dominated by diatoms, usually starts between February and April and typically lasts for 2-4 weeks. Chlorophyll values are generally low during summer, followed by a smaller autumn bloom of dinoflagellates in August–September (Dahl and Johannessen, 1998; Dahl et al., 2005).

Data Collection

Plankton at the Arendal sampling site has generally been monitored once to twice a month since 1994. Zooplankton was sampled by vertical hauls from 50 m to the surface, using a standard WP2 net (specified in UNESCO, 1968) with mesh-size 180 µm. Each sample was split into two equal parts with a Motoda splitter (Motoda, 1959). One half of the sample was preserved in 4% borax buffered formaldehyde-seawater solution for species identification and enumeration, and the other half used for biomass measurements (not presented here). *Calanus* spp. were enumerated and identified to copepodite stage. In order to determine the proportions of *C. finmarchicus* and *C. helgolandicus* in the samples, 20 individuals of *Calanus* for each of the copepodite stages CV, CVI females and CVI males were identified to species according to Fleminger and Hulseman (1977). CV and female CVI of the two species were discriminated based on the morphology and teeth of the basipod of the fifth pair of swimming legs. Male CVI were identified on the basis of the relative lengths of the endopod and exopod of the fifth leg. The reliability of discriminating *C. finmarchicus* and *C. helgolandicus* as CV and CVI copepodites by morphology has been confirmed by molecular methods (Lindeque et al., 2006). The abundance of each species was obtained by multiplying the total number of *Calanus* spp. within each developmental stage, by the stage-specific proportions. Copepodite stages CI-IV were counted, but for these stages the two species cannot be separated morphologically (Frost, 1974; Fleminger and Hulsemann, 1977).

Time Series Analysis

Sampling for *Calanus* was generally carried out once to twice a month (irregular intervals). To regularize the time series, data for the different developmental stages, sexes and species of *Calanus* spp., were averaged to monthly values for each year. When no sampling took place within a month, data for the month were imputed using the mean of the preceding and following month. For the different stage-resolved monthly time series, 12 to 18 missing values were imputed, which represents 4-6% of the 300 monthly values. If zero counts of individuals were found in the sample(s) of a month for each of the time series, these were not imputed, retaining the zero count observations. Subsequently, three more time series were created by aggregating (i) copepodite stages CI to IV for *Calanus* spp. ('*Calanus* spp. I-IV. I-IV'), (ii) stages CV, CVI male and CVI female for *Calanus finmarchicus* ('*C.fin* V-VI') and (iii) stage CV, CVI male and CVI female for *Calanus helgolandicus* ('*C.hel* V-VI'). These three aggregated time series are the ones for which long term trends and periodicities are explored in the present study. Throughout the 1994-2019 study period, for each of the time series, the percentage of zero counts was 1.33%, 1.67% and 2.67 for *Calanus* spp. I-IV, *C.fin* V-VI and *C.hel* V-VI, respectively.

Each of the three time-series was subjected to Seasonal and Trend decomposition using Loess (STL) (Cleveland et al., 1990). STL was selected over other methods as it allows the seasonal component to change over time and the smoothness of the

trend-cycle to be user-defined. A preliminary examination of the data revealed that the seasonal component was not constant over time. A 5-year window for the trend smoother was chosen, while the seasonal window was set to 12 months, thus allowing for variable amplitude and/or timing of the seasonal cycle. The selected 5-year trend smoother captured relatively well the long-term changes observed in the abundance of each aggregated time-series. Wider smoother-windows (e.g., 10 years) were tested, but led to over-smoothing, thus missing patterns with evident high/low abundance values, whereas lower values (e.g., 1 year) led to a very wiggly smoother from which long-term trends could not be easily discerned.

A Generalised Additive Model (GAM) (Hastie and Tibshirani, 1990; Wood, 2017) was used to evaluate potential changes in the seasonal patterns and abundance of the two species throughout the study period, for each of the three time series. The Tweedie distribution was chosen for its ability to handle zero values in the dataset through the parameter p which defines the model distribution. When $1<p<2$, the model is a Poisson mixture of Gamma distributions. Let Y(t) be the observed abundance of the copepods in the studied time series. We assume that:

$$Yi \sim Tw_p(\mu_i, \phi), \quad (1)$$

where ϕ is the dispersion parameter and the mean μ_i is linked to the linear predictor through a known link function g,

$$g(\mu_i) = \beta X_i \quad (2)$$

where X_i is a vector of covariates and β is a vector of unknown regression parameters. GAM fitting was done by setting the family argument to 'tw' for automatic estimation of the parameter p and generalized cross validation (GCV) was used to determine the optimal model fit. A tensor product smoother using 'Month' and 'Year' was applied to the abundance of each time series. All analysis was carried out in R 4.1.1 (R Core Team, 2021). For the STL decomposition and the GAM fitting the 'fable' (0.3.1, O'Hara-Wild et al., 2021) and 'mgcv' (Wood, 2017) packages were used, respectively. GAM plots were created using the 'ggplot2' (Wickham, 2016) and 'mgcViz' (Fasiolo et al., 2020) packages.

RESULTS

Calanus spp. Seasonal Cycles

The seasonal variation in abundance of *Calanus* spp. was pronounced, and differences in the seasonal dynamics between *Calanus finmarchicus* and *C. helgolandicus* were evident. In **Figures 3** and **4**, data from all years have been pooled and thus show the general seasonal patterns over the period studied. Due to pooling of data for all years, between-year differences in timing must be assumed to result in a wider distribution than would be the case for any single year

Young *Calanus* copepodites of stages CI-III generally appeared in late February (**Figure 3A**). These stages displayed a marked pulse that peaked from mid-March to mid-April (medians of ~ 3350-8000 ind. m^{-2}, for the upper 50 m) and was strongly reduced by early May. This pulse of young copepodites belonging to the new generation of the year (G1) was well timed with the spring phytoplankton bloom, which occurred before the temperature in upper waters showed any notable increase. Still, the peak of these young copepodites showed a slight delay of about two weeks compared to the phytoplankton peak (**Figure 3A**).

Calanus finmarchicus of stage CV and adults (pooled) showed increasing numbers already from the beginning of January, a peak during mid-April to mid-May (~ 2500-3200 ind. m^{-2}), and thereafter decreasing numbers (**Figure 3B**). Still, these older stages of *C. finmarchicus* remained present in moderate concentrations until early autumn. The overall distribution of these stages indicates that the older part of the *C. finmarchicus* population reached its peak about one month after the phytoplankton bloom had collapsed, and the population started to decrease about 4 months before the temperature had reached its maximum.

Calanus helgolandicus of stage CV and adults (pooled) were present throughout the year, though with their main occurrence during July-November with a long-lasting peak from about August to October (medians of ~ 1100-2400 ind. m^{-2}, **Figure 3C**). The seasonal population distribution of older stages of *C. helgolandicus* mirrored the seasonal temperature cycle, with the highest abundances occurring when temperature was peaking. The highest abundance was at least one month delayed relative to the autumn phytoplankton bloom. Moderate increases of *C. helgolandicus*, however, were also noted in April-May when water-temperature was far lower (5-8°C).

Demography

Adult females of *Calanus finmarchicus* were practically absent from the station in winter until early January (**Figure 4**). Following a further modest increase in late January, the number of females rose markedly until reaching the annual maximum in late March (median of ~ 600 ind. m^{-2}). Some variability in the spring abundances of adult females was evident, and in early May the concentrations were almost at the same level as in late March. Whether the spring distribution for abundance of *C. finmarchicus* adult females represents one single but somewhat irregular peak, or a composite of more peaks with differing timing is not clear (**Figure 4**). From mid-May the numbers decreased, and from July and for the rest of the year the levels were low (< 80 ind. m^{-2}), except for a small increase in August. The seasonal development of the generations is carefully reviewed in the "Discussion" section.

Adult males of *C. finmarchicus* were present in low numbers at the station as early as January. Even if the medians were unchanged during January and February (8 ind. m^{-2}), some years had higher abundances of males towards the end of February. (**Figure 4**). Thereafter the abundances generally remained at zero ind. m^{-2} or a very low level until March. The annual maximum of adult males occurred in the first half of May (median of 45 ind. m^{-2}) (**Figure 4**). Male abundances then decreased, and remained

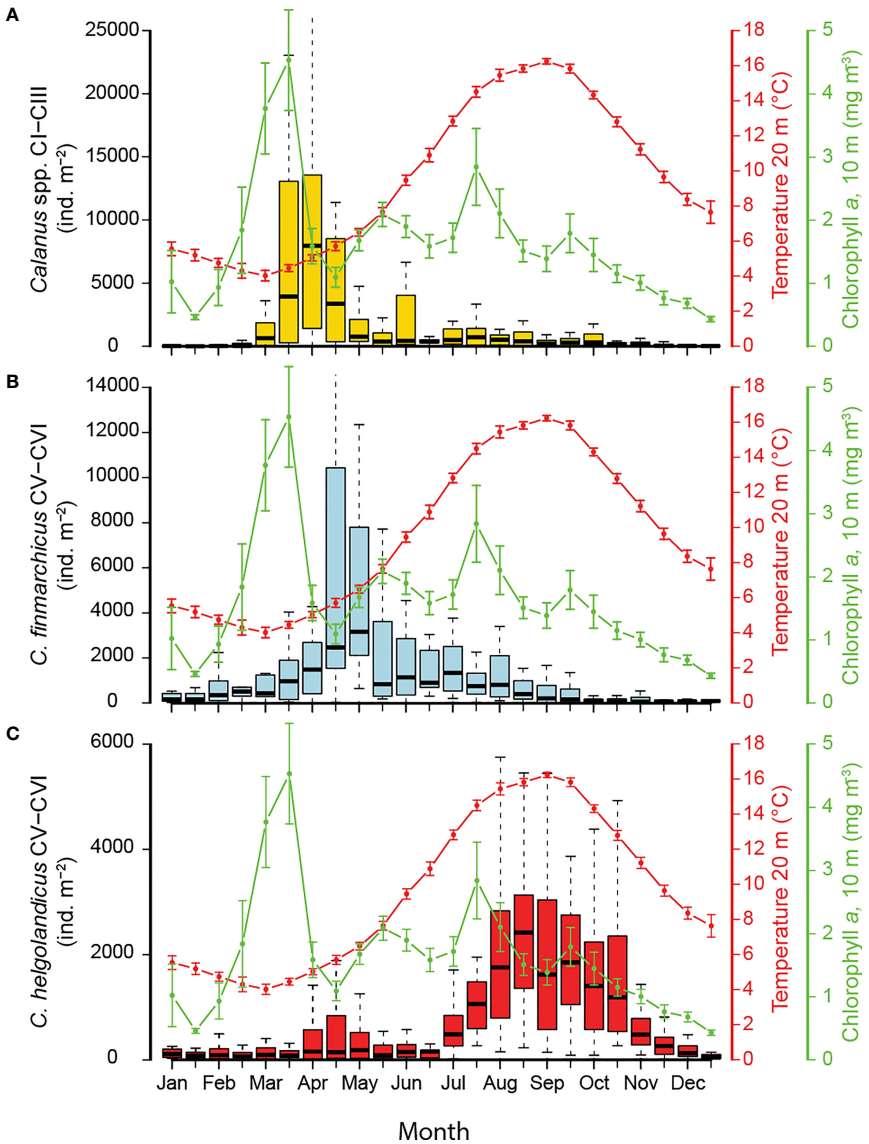


FIGURE 3 | Seasonal pattern in abundances at 0-50 m depth of **(A)** *Calanus* spp. CI-CIII **(B)**, *C. finmarchicus* CV-VI and **(C)** *C. helgolandicus* CV-VI. Lower and upper edges of boxes represent the 25 and 75 percentiles, and the horizontal lines the medians. Extreme observations outside the range of the whiskers are not shown. Seasonal variation in temperature (20 m, mean and standard error, SE) and Chl-*a* (10 m, mean and SE) on right axis. Data on temperature and Chl-a were obtained from the Norwegian Coastal Monitoring Programme.

at lower levels until mid-August, indicating a small new peak in July-early August. From October and for the rest of the year, *C. finmarchicus* adult males were practically absent.

C. finmarchicus copepodites of stage CV occurred in two annual peaks, the first peak very pronounced while the second peak far more subtle (**Figure 4**). CV were present in low numbers in winter (< 90 ind. m^{-2} during early September – mid April), their numbers thereafter increased rapidly to the annual maximum in early May (median of ~ 2700 ind. m^{-2}). Abundances then fell abruptly to lower levels, thereafter increasing very slowly to reach a minor second peak in early July (median of ~1200 ind. m^{-2}).

C. helgolandicus CV and adults displayed a rather synchronous seasonal pattern at the station. The species was present throughout the year and observed in low and variable numbers from January to July, with somewhat elevated occurrences of CV during April - early May being the most noticeable feature during the first half of the year (**Figures 3** and **4**). A simultaneous and strong increase in abundance of all three stages occurred from July to late August. *C. helgolandicus* CV reached its annual maximum (~1350 ind. m^{-2}) in late August and showed elevated abundances until December. The peaks for adults occurred during August-September, followed by decreasing numbers, and low levels in November and December.

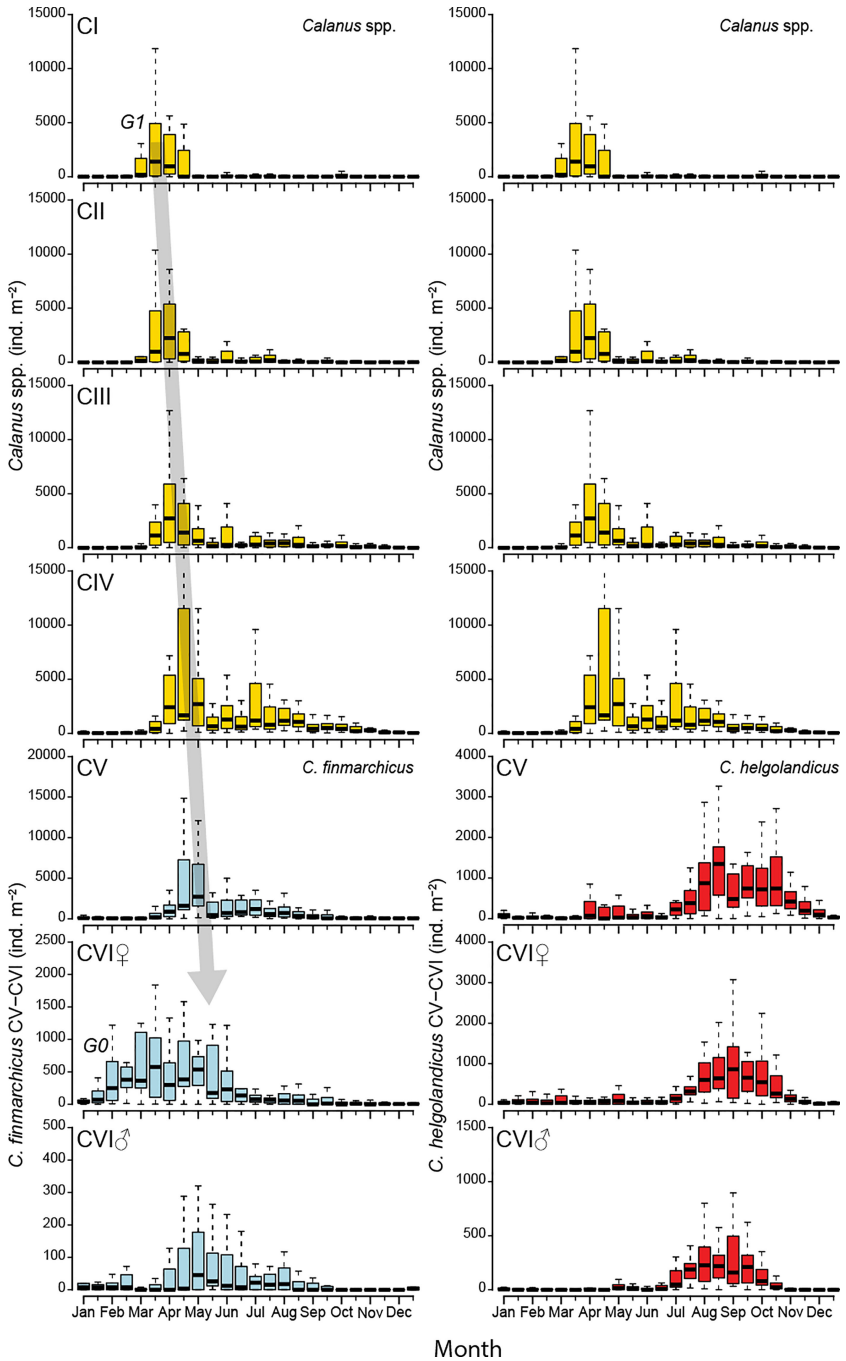


FIGURE 4 | Boxplots of abundances of *Calanus* spp CI-IV (yellow), *C. finmarchicus* CV-VI (blue) and *C. helgolandicus* CV-VI (red) versus two-week period. Lower and upper edges of boxes represent the 25 and 75 percentiles, and the horizontal lines the medians. Extreme observations outside the range of the whiskers are not shown. Copepodite stages CI-IV were not identified to species but are included in both left- and right-hand panels to aid elucidation of stage and generation cycles for each species. The shadowed arrow indicates our suggested first new generation of *C. finmarchicus* of the year, G1; G0, overwintering population.

Calanus spp. stages CI-IV were present in low numbers during late December - late February (medians < 80 ind. m^{-2} of CI-IV pooled) (**Figure 4**). A strong increase in the abundance of CI occurred in early March, and the annual maximum for this stage was reached in the last half of March. Copepodite stages CII-III showed slightly delayed patterns compared to that of CI, with abundances peaking in the first half of April. Copepodite stages CI-III were present in variable though lower numbers also later in the season, but without showing clear and consistent secondary peaks. The seasonal pattern for stage CIV was similar

to the patterns for CI-CIII, but with a little delay. Maximum abundances of stage CIV occurred in early April – early May. CIV also displayed considerable levels later in the year, with a rather wide secondary peak around July.

Interannual Trends in Abundance

The decomposition of the three aggregated *Calanus* time series (i.e., *Calanus* spp. stages CI-CIV, *C. finmarchicus* CV-VI and *C. helgolandicus* CV-VI) into trend and seasonal components is shown in **Figure 5**. Bars at the left side of each panel represent the relative scales of the components. The variation in size of the grey bars stems from the different scales of the respective plots; if the y-axis of each plot were set to the same range, the grey bars would have the same size. The short bar in the seasonal plots indicates that for all three time series, the seasonal cycle is explaining more of the observed variation in the data than the trend component (longer bars in the trend plots). The residuals (lowermost panels) show that there is substantial variation in the time series that is not explained by either the seasonal nor the long-term trend component (similar size to the grey bar of the 'Data' plot).

For *Calanus* spp. stages CI-IV no unidirectional trend was found. A period with high abundances was observed between 2003 and 2012, with a slight decrease in the middle of this period (**Figure 5A**, second panel). A few years with relatively high

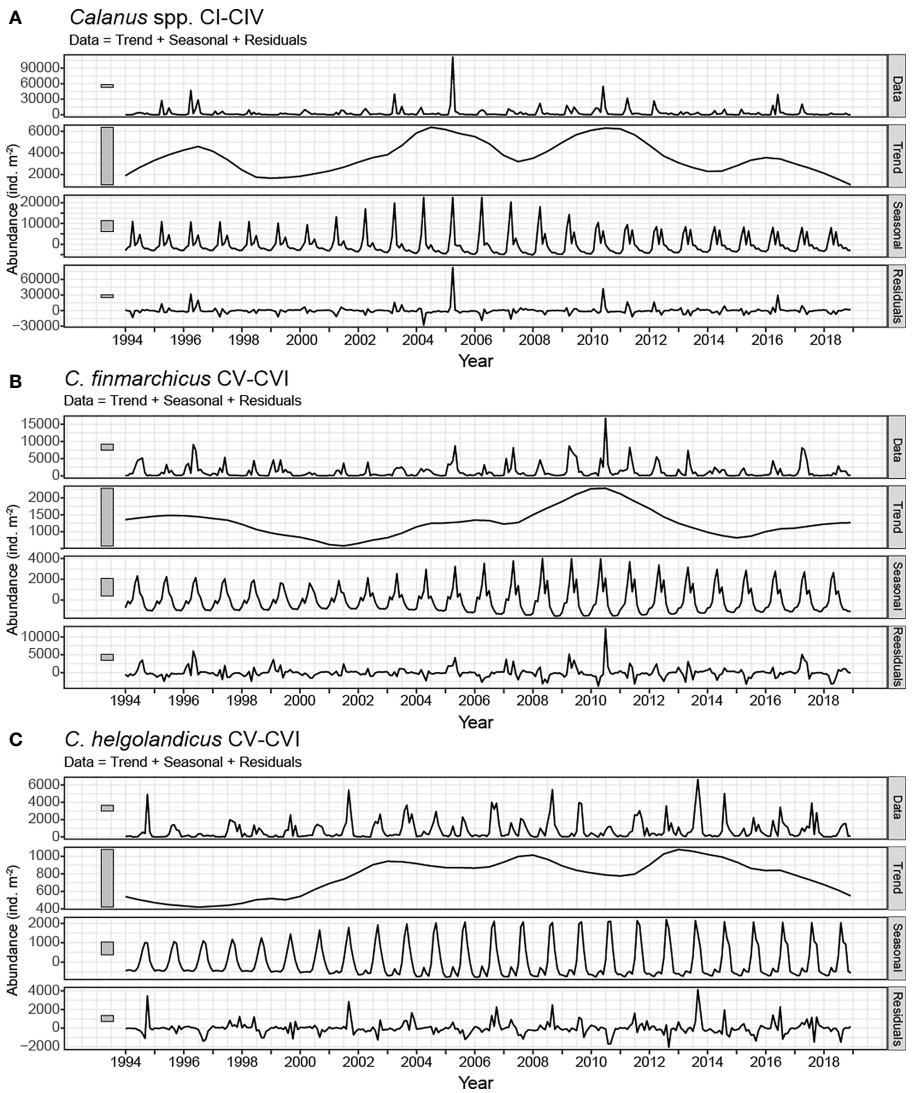


FIGURE 5 | Seasonal and Trend time series decomposition using Loess with a 5-year trend window and 12-month seasonal window for the abundance of **(A)** *Calanus* spp. CI-IV, **(B)** *C. finmarchicus* CV-VI and **(C)** *C. helgolandicus* CV-VI. For each of the three time series shown **(A–C)**, five sub-panels are presented. Original data are presented in the uppermost panels as monthly average abundances (Data). The Loess trend-cycle component (Trend) captures the interannual variability. The seasonal component (Season) shows the within-year variability throughout time. In the lowermost panel for each time series, the component representing the remainder is shown (Residuals), which is what is left after subtraction of the seasonal and the trend/cycle components from the original monthly abundances. Grey bars to the left of each panel show the relative scales of contribution of each component.

abundances were also observed at the beginning of the time series, whereas in the last decade the trend was generally decreasing.

Nor did we observe any unidirectional long-term trend for the abundance of *C. finmarchicus* CV-VI (**Figure 5B**, second panel). However, strong interannual variability was observed, with alternating periods of low and high densities. A period with high abundances was observed around 2009-2011, while much lower values were observed around the years 2001 and 2015. The annual abundances as represented by the trend for *C. finmarchicus* varied by a factor of 5 between high (~ 2010) and low (~2001) periods.

C. helgolandicus CV-VI (**Figure 5C**, second panel) had low abundance at the beginning of the time period. The population showed a marked increase from 2000 to 2003 and remained at a high level until 2014. The very last years, the levels decreased.

Interannual Variation in Seasonality

The seasonal trend-decomposition revealed that the seasonal component in all three time-series varied over time (**Figure 5**). *Calanus* spp. CI-IV (**Figure 5A**, third panel) showed a regular seasonal pattern, however with a period of higher amplitudes during 2002-2008. Since 2008 the amplitude of the peaks has declined. In *C. finmarchicus* CV-VI (**Figure 5B**, third panel) the spring peak dominated throughout the time series, however with varying amplitude. The variation in the amplitude mirrored the interannual trend in abundance, suggesting that the trend in *C. finmarchicus* is mainly related to variations in the spring abundances. In *C. helgolandicus* (CV-VI) one single annual peak was observed during the first years of the time-series (**Figure 5C**, third panel). However, since 2002 a bimodal seasonal pattern emerged, with a small spring peak, and a stronger peak later in the year with increasing amplitude.

Figure 6 shows the modelled seasonal dynamics over the years carried out with the GAM. This makes it possible to examine if there have been interannual changes in phenology and abundance during the time-period. The model suggests that there were two annual peaks in *Calanus* spp. CI-IV (deviance explained = 56.4%, **Figures 6A, B**). The seasonal timing of the spring peak has been consistent over the years, regularly occurring in mid-March. In contrast, the model suggests that the timing of the secondary peak has advanced by one month during 1994-2018, moving from July to June (**Figure 6A**).

One strong annual peak in *C. finmarchicus* CV-VI was predicted by the fitted model (deviance explained = 61.5%),

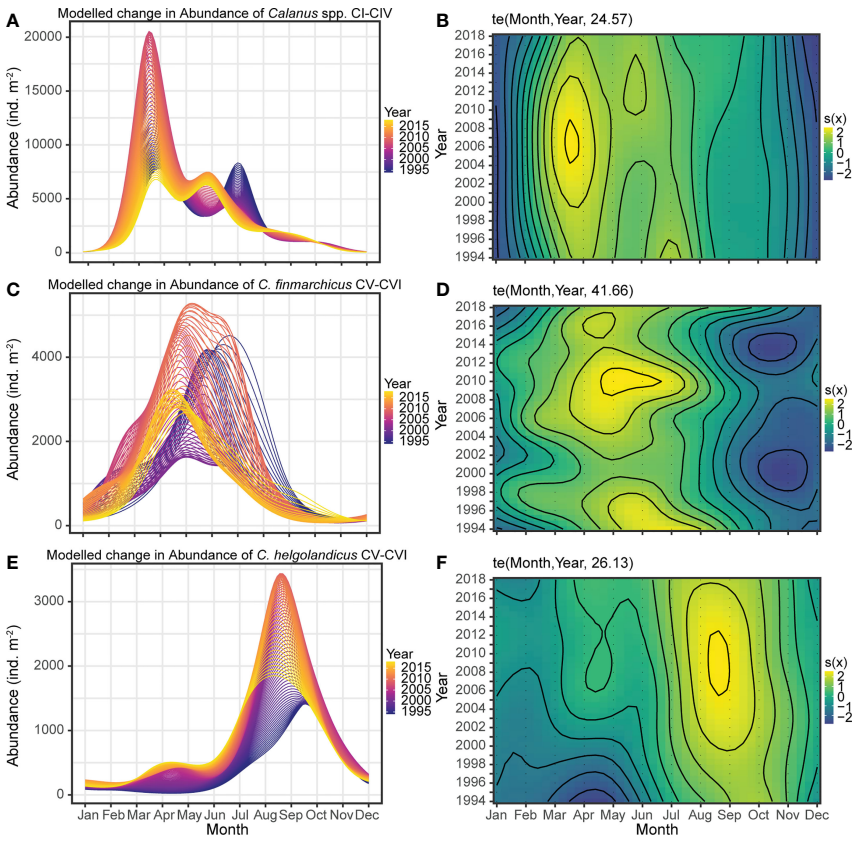


FIGURE 6 | Modelled abundance of *Calanus* spp. stages CI-IV **(A)**, *C. finmarchicus* CV-VI **(C)**, and *C. helgolandicus* CV-VI **(E)** showing the within year variation throughout the study period. Model predictions are based on a tensor product smoother for the Month x Year interaction. Each line represents a year shown in a color gradient for better visualization. The smoother is also shown in the two-dimensional plane, with contours and color gradient denoting the intensity of the smoother effect, **(B, D, F)** for the three time series respectively.

with large interannual variability in abundances (**Figures 6C, D**). The fitted model suggests a gradual change in the timing of the annual peak in *C. finmarchicus* CV-VI, which has advanced by about one month during the time series.

A strong annual peak in *C. helgolandicus* CV-VI in autumn (August-September) was predicted by the model (deviance explained = 63.4%), with increasing abundances over the years (**Figures 6E, F**). Concurrent with the increasing abundances, the model indicates an earlier timing of the autumn peak over time, suggesting an advancement from mid-September to mid-August. Moreover, the model suggests that the seasonality of *C. helgolandicus* has changed from a unimodal to a bimodal pattern. In the early years of the time series, one single annual peak of *C. helgolandicus* was found, whereas after around 2002 an additional small peak appeared, occurring in mid-April. This is also evident from the time-series decomposition model shown in **Figure 5C**.

DISCUSSION

This study presents the first in-depth description of the seasonal and interannual variability of *Calanus finmarchicus* and *C. helgolandicus* in northern Skagerrak. The two species co-occurred at this location throughout the year, but their seasonal maxima were separated in time. The annual peak in CV-VI of *C. finmarchicus* occurred in April-May in association with the phytoplankton spring bloom. In contrast, the same stages of *C. helgolandicus* had its annual maximum in August-September, well matched in time with the annual maxima in temperature, and also concurring with the late summer peak in chlorophyll. Similar to this finding, previous studies have demonstrated that in areas where the two species co-occur, they tend to be separated in time (Planque and Fromentin, 1996; Wilson et al., 2015). This has been interpreted as thermal niche differentiation between the two species, related to cooler temperatures earlier in the year and warmer temperatures later in the year (Helaouët and Beaugrand, 2007). In the present study, the annual maximum abundances of *C. finmarchicus* occurred at water temperatures 6-8°C while the peak in *C. helgolandicus* was found at 11-16°C. This is in agreement with previous observations of peak abundances of *C. finmarchicus* and *C. helgolandicus* at 0-9°C and 13-17°C respectively (Bonnet et al., 2005). Temperature has been found to be the most important factor influencing both spatial distributions and seasonality in both species (Planque and Fromentin, 1996; Montero et al., 2021). *C. finmarchicus* develops faster than *C. helgolandicus* at temperatures below 12°C, whereas *C. helgolandicus* develops faster than *C. finmarchicus* at temperatures above 13°C (Wilson et al., 2015). Based on model results, Møller et al. (2012) suggested that a temperature increase to above 11°C would trigger a shift from a *C. finmarchicus* to a *C. helgolandicus* dominated system. In line with this, we observed a seasonal shift at the Arendal station from *C. finmarchicus* to *C. helgolandicus* when temperatures reached 11°C in June. The seasonal variation in populations is not only related to temperature and food, but also to ocean circulation (Speirs et al., 2004). Young copepodites of *C. finmarchicus* have been shown to be transported into the North Sea from the north in surface layers during spring (Heath et al., 1999; Madden et al., 1999) while diapausing individuals enter the area during winter *via* the deep Norwegian Trench Atlantic Inflow (Gao et al., 2021; **Figure 1**). Furthermore, advective transport from warmer regions of the southern North Sea may contribute to the observed peak in *C. helgolandicus* (Planque and Fromentin, 1996; Wilson et al., 2016).

When co-occurring in time, the two species may also be separated in terms of their vertical distributions (Williams, 1985; Jonasdottir and Koski, 2011; Lindegren et al., 2020). Our data are based on depth-integrated samples from 50 m to the surface, and no information on vertical distributions are available from this site. Abundances of *C. finmarchicus* decreased to low numbers in July when surface temperatures reached >12°C. During the summer months it is likely that the species stayed below the thermocline where temperatures rarely exceeded 14°C. It is therefore possible that sampling from the uppermost 50 m may have caused some underestimation of the *C. finmarchicus* abundance during the later part of the year. Predation and descent to overwintering depths further off-shore may also contribute to the abrupt decline in July. Nevertheless, the observed seasonal cycle of *C. finmarchicus* at the Arendal station concurs with other studies from the northern North Sea where *C. finmarchicus* were found to start the descent for diapause in July and to be completely absent from the surface waters by September (Jonasdottir et al., 2005).

The here observed presence and increasing abundance of *C. finmarchicus* adults in January and February is in accordance with the timing of the termination of the overwintering period reported from the Northeast Atlantic (Østvedt, 1955; Melle et al., 2014). As younger copepodite stages were absent this early in the year, we suggest that *C. finmarchicus* adults present in January and February belong to the overwintering population (G0). The first individuals of the *Calanus* spp. CI peak in March and are probably the offspring from the adults of the overwintering generation observed in January/February, thus representing the first generation (G1) of *C. finmarchicus*. The further development of this first cohort is reflected in our data by the increase in *C. finmarchicus* CV and adults in April-May (**Figure 4**), which we believe also represent the first generation G1. This interpretation is supported by the expected developmental time of the different copepodite stages of *C. finmarchicus* (Corkett et al., 1986). At temperatures between 3.5 and 4°C (February-March), the estimated developmental times from eggs to CI are 26-28 days, suggesting that the first cohort of CI observed in early March were spawned in early February. The expected development time to CV is 55-60 days which agrees with the observed increase of CV in April.

Copepodite stages CI-IV were not identified to species in this study. However, based on the very low numbers of *C. helgolandicus* in early spring as well as the match in time with the following developmental stages, we interpret the majority of young copepodites observed March-April to be *C. finmarchicus*, while the second peak in July is a mixture of both species.

The timing of G1 at the Arendal station agrees well with previous studies from Skagerrak coastal water area (Båmstedt, 2000; Bagøien et al., 2000) but seems to be slightly earlier than reported for the Coastal Water further north off western Norway (Broms and Melle, 2007; Bagøien et al., 2012). We observed that stage CI started to increase markedly in early March, while stages CII and CIII showed the first strong increases about two weeks later in late March. In the Norwegian Coastal Current further north (62 - 70°N), the first strong increase in abundance of copepodites CI was observed from April, and the abundances of stages CI-III remained high until mid-June (Bagøien et al., 2012). Previous studies from coastal waters of northern Norway, have also reported the first generation of young copepodites to appear in April (Falkenhaug et al., 1997; Skreslet et al., 2000; Skjoldal et al., 2021). We conclude that the youngest copepodites of the G1 generation at the Arendal station (58°23′N) increase about one month earlier than has been reported for the coastal waters in the more northerly regions (north of 62°N). Broms and Melle (2007); Bagøien et al. (2012) and Skjoldal et al. (2021), all noted that young *C. finmarchicus* copepodites of the G1 generation had an earlier timing in coastal water compared to Atlantic Water, which was related to the earlier onset of the spring phytoplankton bloom in the stratified coastal waters (Bagøien et al., 2012). A possible explanation for the earlier timing of *C. finmarchicus* CI of G1 in Skagerrak coastal waters, compared to locations further north, is the earlier onset of the spring phytoplankton bloom at lower latitudes (Vikebø et al., 2012).

Our results suggest that *C. finmarchicus* produces one dominant annual generation (G1) at the Arendal station. The minor peak in CV observed in early July, and the increases in males and females in July-August may represent a smaller second generation (G2). Even if our data don't show clear indications of more generations after that, more than two generations cannot be discarded. The first generation (G1) can be followed as one discrete cohort, while subsequent generation(s) were less clear. Considering the strong advective environment at the Arendal sampling site, the observation of a discrete G1 generation of *C. finmarchicus* is surprising. It has been suggested that discrete generations of *C. finmarchicus* are only produced in semi-enclosed localities (Aksnes and Magnesen, 1983) or at sites in close proximity to overwintering sites (Heath et al., 2000; Maar et al., 2013; Melle et al., 2014). In contrast, at locations more distant from overwintering sites, advective processes will lead to mixing of cohorts (Speirs et al., 2004), which hampers the interpretation of generations. *C. finmarchicus* is believed not to overwinter in the North Sea - Skagerrak in substantial numbers (Fransz et al., 1991; Heath et al., 1999; Madden et al., 1999). Nevertheless, overwintering aggregations are known to exist in the Norwegian Trench (Rees, 1949; Krause et al., 2003; Heath et al., 2004). Moreover, the Norwegian Trench is the major route of inflowing *C. finmarchicus* from the Norwegian Sea, (Backhaus et al., 1994; Heath et al., 1999; Gao et al., 2021) and diapausing *C. finmarchicus* are advected to the North Sea and Skagerrak by a deep inflow of Atlantic water, mainly during winter and early spring (Gao et al., 2021). The Arendal station is located on the northern slope of the Norwegian Trench which reaches its maximum depth (700 m) 40 km southeast of the monitoring station (**Figure 2**). The time for the appearance of the overwintering population (G0) in upper layers at the Arendal station was similar to what has been reported from other regions in the Norwegian Sea. We suggest that the proximity to the overwintering site in the Norwegian Trench enables the early spring invasion of G0 in February to this coastal area, and further that the observed spring cohort G1 of *C. finmarchicus* is the offspring of the overwintering stock originating from the Norwegian Trench.

C. finmarchicus has been found to complete 2-3 generations in the North Sea and Skagerrak (Båmstedt, 2000; Krause et al., 2003). We observed a small increase in CI-III in June-July, and somewhat elevated levels in *C. finmarchicus* CV and adults in July and August which may indicate a second generation (G2) of *C. finmarchicus*. However, the CI-III at this time of the year is likely a mixture of *C. finmarchicus* and *C. helgolandicus*. Moreover, Skagerrak is an advective system and some of the observed CV and adults may have been advected from the northern North Sea, or from nearby fjords. Females of G1 can continue to produce eggs for a month or more, and the developmental times of each stage will vary in relation to temperature and food availability (cf. Corkett et al., 1986). As a result, the secondary generations will be less synchronous and difficult to separate as cohorts.

For *C. helgolandicus*, the distinction of generations is less clear. A small increase in *Calanus* spp. CI-IV in July was followed by a peak in *C. helgolandicus* CV in late August, approximately two weeks prior to the annual peak in adults. Young copepodites were not identified to species, and the secondary peak in CI-CIV is probably a mixture of both *C. finmarchicus* and *C. helgolandicus*. The July peak in CI-CIV may represent a single cohort, indicating local production of *C. helgolandicus* in the area. Local populations of *C. helgolandicus* has been documented previously in Skagerrak and adjoining fjords (Bagøien et al., 2000; Jonasdottir et al., 2005). Yet, the large overlap in timing of the copepodite stages and adults strongly suggests that the population is also subject to advective transport from other areas, and there is probably considerable generational 'smearing' from both local and various up-stream locations. *C. helgolandicus* CV and adults were present all year at the Arendal site, although in low numbers during winter. It is generally believed that *C. helgolandicus* does not enter diapause but rather feed actively through winter (Williams and Conway, 1984; Bonnet et al., 2005). However, the overwintering behavior of this species remains unresolved (Wilson et al., 2015), as *C. helgolandicus* has been found to enter diapause in some locations (Hirche, 1983).

Interannual Trends

The Arendal time series revealed strong interannual variability in the abundances of *C. finmarchicus* and *C. helgolandicus*, however with clear interspecific differences in their temporal patterns. This suggests that the population sizes of the two species are affected by different mechanisms, as has previously been shown by Montero et al., (2021). While a generally

increasing trend, apart from the very latest years with decreasing levels, was observed for *C. helgolandicus*, no unidirectional long-term trend was detected in *C. finmarchichus*. In fact, the abundance of *C. finmarchicus* has, based on expectations that this species is decreasing in the North Sea and Skagerrak area and retreating northwards (Beaugrand et al., 2002; Chust et al., 2014), remained surprisingly unchanged over time. However, intermittent shorter periods with high and low abundances were observed.

The lack of a consistent long-term trend in *C. finmarchicus* at this monitoring site is in contrast with previous studies based on CPR data, showing a long-term decrease in occurrences of this species in the North Sea during the last decades. Since the 1960s the biomass of *C. finmarchicus* has declined by 70% in the North Sea (Fromentin and Planque, 1996; Reid et al., 2003) which has been related to rising temperatures. The most dramatic reduction in *C. finmarchicus* occurred in the late 1980's, often referred to as the North Sea regime shift (Beaugrand, 2004; Alvarez-Fernandez et al., 2012). The Arendal time series was initiated after the major decline of *Calanus* in the North Sea, and the abundances at this site prior to the 1980's are not known. A reduction in the *C. finmarchicus* population at this site may thus have taken place prior to the initiation of the time-series presented here, which may explain why no consistent long-term decline was observed. If so, we might speculate that *C. finmarchicus* now is at a lower level at this site compared to the decades before the present time series.

A period with high abundances of *C. finmarchicus* was observed around 2009-2011. Comparing our data with the CPR data for the relevant standard area (B1) reveals similar patterns for *C. finmarchicus* in years after 1994 (Montero et al., 2021) with peak abundances in 2010. Similarly, a period with a higher ratio of *C. finmarchicus* to *C. helgolandicus* was reported from the North Atlantic CPR data during 2009-2011, which was related to years of low winter North Atlantic Oscillation index (NAO; Edwards et al., 2014). Indeed, the period of high abundances of *C. finmarchicus* reported here coincides with a period of strong negative NAO index in winters 2009/2010 and 2010/2011, reflected in below average SST in the NE Atlantic (González-Pola et al., 2020).

C. finmarchicus populations in the North Sea are not self-sustained and are highly dependent on the inflow from the Norwegian Sea (Heath et al., 1999; Gao et al., 2021). Variability in *C. finmarchicus* abundances in the North Sea have previously been linked to the NAO (Fromentin and Planque, 1996) which again is correlated with the inflow of water to the North Sea and the Skagerrak (Winther and Johannessen, 2006; Hjøllo et al., 2009). In the late 1980's, this relationship broke down, which was explained by a decline in the overwintering stock in the southern Norwegian Sea and the Faroe Shetland Channel, and a northward shift of the species as a result of ocean warming (Heath et al., 1999; Reid et al., 2003). In the southern Norwegian Sea, a reduction in the abundance of *C. finmarchicus* and *C. hyperboreus* have been observed after 2003, and the abundances have remained at lower levels since then (Kristiansen et al., 2019; Skagseth et al., 2022). These changes have been attributed to reduced inflow of subarctic and arctic waters into the Norwegian Sea from west, which in turn has been linked to changes in the North Atlantic subpolar gyre (Kristiansen et al., 2019; Skagseth et al., 2022). However, the underlying mechanisms for the variations in *C. finmarchicus* population size in the North Sea and Skagerrak are still poorly understood and both large scale physical processes as well as local drivers need to be considered (Papworth et al., 2016). Recent studies suggest that the decoupling of NAO in the late 1980's mainly occurred in western areas, while in the northeastern North Sea the fluctuations in *C. finmarchicus* remain related to NAO (Montero et al., 2021). In agreement with this, Gao et al. (2021) concluded that the inflow of *C. finmarchicus* biomass into the North Sea through the Norwegian Trench, accounted for 41% of the biomass in the North Sea and thus is a strong driver for the interannual variability of this species. Furthermore, Maar et al. (2013) suggested that the annual abundance of *C. finmarchicus* in the North Sea is sensitive to the degree of overwintering within the North Sea, because it allows individuals of this species to utilize the spring bloom more efficiently and independently of the timing and amount of oceanic inflow. It has also been suggested that the inflow of *C. finmarchicus* through the Norwegian Trench can facilitate favorable nursing conditions to the spring spawning North Sea cod (Huserbråten et al., 2018). The Norwegian Trench is thus of significance both as a gateway for the transport of *Calanus* to the area (Gao et al., 2021), as well as a habitat for local overwintering (Heath et al., 2004).

An increasing trend in the abundance of *C. helgolandicus* at the Arendal station was found until about 2013, being especially pronounced during 2000-2003. This is in accordance with numerous studies based on CPR data, reporting that this species has become more abundant and widely distributed in the North Sea over the past 50 years (Fromentin and Planque, 1996; Beaugrand, et al., 2002; Reid et al., 2003; Chust et al., 2014). Similar observations have been made at fixed point monitoring stations around the North Sea: At Helgoland (southern North Sea), *C. helgolandicus* has been increasing since the 1980's, while in waters off Stonehaven (Scotland) an increase was not observed until 1999 (Bonnet et al., 2005). In contrast, Maud et al. (2015) found no temporal change in the abundance of *C. helgolandicus* at the Plymouth L4 site (English Channel) during 1988-2012. This suggests spatial differences in the dynamics of *C. helgolandicus* within the North Sea, implying that the species is more sensitive to environmental changes nearer the edge of its geographical range (Helaouët et al., 2013; Maar et al., 2013). The expansion of *C. helgolandicus* in the North Sea has been attributed to increased oceanic temperatures due to climate change (Reygondeau and Beaugrand, 2011) and temperature has been considered as the main factor affecting growth and population dynamics in *C. helgolandicus* (Møller et al., 2012; Montero et al., 2021). Sea temperatures in Skagerrak have increased by 1 C° since 1990 (Albretsen, 2012). We suspect that higher water temperatures have contributed to the increase in *C. helgolandicus* at this site.

Phenology

The present study indicates a shift in the phenology of *Calanus* spp. during the last 25 years at the northern Skagerrak study site.

Since 1994 the annual autumn peak of *Calanus* spp. CI-IV seems to have advanced by about one month. In contrast, we observed no changes in the seasonal timing of the spring peak in *Calanus* spp. CI-IV. It should be kept in mind that the copepodite stages CI-IV were not identified to species, and the autumn peak was probably a mixture of both species.

Moreover, the models suggest an earlier timing of the annual peaks for both *C. finmarchicus* CV-VI and *C. helgolandicus* CV-VI. This is in line with studies reporting a shift towards earlier seasonal timing in a number of zooplankton taxa in the North Sea during the last decades (Edwards and Richardson, 2004; Mackas et al., 2012; Reygondeau et al., 2015). These changes have been related to rising temperatures, suggesting that plankton tend to follow an 'earlier when warmer' strategy (Mackas et al., 2012). Also, in the more northern Norwegian Sea, a small change in the timing of *C. finmarchicus* has been observed, where the spring peak was suggested to occur four days earlier (Dupont et al., 2017). The phenology of *C. finmarchicus* is strongly correlated with temperature (Mackas et al., 2012), and in the central North Sea the seasonal peak of this species has advanced by 10 days during 1958-2002 (Edwards and Richardson, 2004; Bonnet et al., 2005). Similarly, at Helgoland (southern North Sea), *C. helgolandicus* has shifted to an earlier timing by at least 1 month during the years 1975-2006 (Mackas et al., 2012). An earlier seasonal timing in *Calanus* species has been related to shorter development time with increasing temperatures (Cook et al., 2007) or to variations in the duration of the spring phytoplankton bloom (Aßmus et al., 2009).

Variations in timing and phenology of *Calanus* spp. may also be caused by advection of cohorts from other areas (Espinasse et al., 2018). The Arendal sampling site is located in a highly advective system, with a large degree of temporal variation (Rodhe, 1996). Consequently, advective supply of *Calanus* spp. to the site is expected to play an essential role in contributing to the observed temporal variations. However, despite the high temporal variability, spatial homogeneity has been documented for the area (Dahl and Johannessen, 1998). The observations made at the Arendal sampling site can thus be considered as representative for a larger area of the Skagerrak.

An important result of his study is the appearance of a small spring peak in *C. helgolandicus* at the Arendal station. The fitted models suggest a change in the seasonal pattern of *C. helgolandicus*, switching from a unimodal to a bimodal pattern around year 2002, when a small spring peak emerged. A similar change in the seasonality of *C. helgolandicus* has been described from other regions of the North Sea. Beare and McKenzie (1999) observed a change from one to two annual peaks in *C. helgolandicus* in the northern North Sea, where a small spring peak occurred during 1980-1999. In the western North Sea (Stonehaven time series), a small spring peak in *C. helgolandicus* developed during the late 1980's (Bonnet et al., 2005; Wilson et al., 2015). Strand et al. (2020) reported spring occurrences of *C. helgolandicus* along a section in the northeastern North Sea based on CPR data from 2008-2016. Our study not only supports these findings, but also reveals that this spring peak appeared around the year 2002. We suggest that *C. helgolandicus* in the northeastern North Sea is approaching a seasonality reported as typical in more southerly areas (Bonnet et al., 2005).

The seasonal cycle of *C. helgolandicus* is mainly driven by the temperature regime, and different cycles have been observed for different areas (Bonnet et al., 2005). In warmer regions (southern North Sea and the Mediterranean), the peak in annual abundance occurs earlier in the year compared to the northern North Sea which is considered to be related to optimal temperature for fecundity and hatching (Bonnet et al., 2005; Wilson et al., 2016). Surprisingly, the small spring peak for *C. helgolandicus* at the Arendal station occurs in April-May when temperatures are below 8°C. Experimental studies suggest that *C. helgolandicus* is not able to develop from eggs to adults at these temperatures (Bonnet et al., 2009; Møller et al., 2012). The presence of *C. helgolandicus* at these low temperatures may indicate an adaption to lower temperatures as were suggested by Møller et al. (2012). However, the occurrence of *C. helgolandicus* in spring may also be explained by advective transport of spring populations from more southern and warmer regions in the North Sea. Analysis of possible relationships between the population dynamics and environmental conditions is outside the scope of this study. Whether the observed shifts in phenology is a response to changes in local conditions, or to large scale variations in advective processes will be addressed in future studies.

In order to reveal possible mechanisms behind phenological changes in the *Calanus* sibling species, further studies should consider detailed demographic data and multiple phenological indices. Moreover, extended sampling to full ocean depth, including the deeper areas of the Norwegian Trench, would provide a more complete picture of the *Calanus* populations in this area.

The observed changes in annual abundance and phenology of *Calanus* spp. at the Arendal station mainly took place around the years 2000 – 2005. During the same period a regime shift was identified in the North Sea (late 1990's - early 2000's; Alvarez-Fernandez et al., 2012; Beaugrand et al., 2014). Furthermore, several studies have suggested that major shifts took place in the coastal waters of the Norwegian Skagerrak in the early 2000's, including a shift in stoichiometry (Frigstad et al., 2013), a change in the macroalgae community (Moy and Christie, 2012), and recruitment failure of coastal gadoid species (Johannessen et al., 2012). Even though this station is located at the shelf off the Norwegian coast and may thus not be representative for the larger North Sea, it might represent zooplankton changes that have taken place in Skagerrak and along the south coast of Norway. The present time-series may thus be more relevant indices, potentially explaining recruitment variability and failure in coastal fish populations, among others the decline in coastal cod populations (ICES, 2021).

CONCLUSIONS

This study presents the first comparative description of phenology and long-term variability of two co-occurring, congeneric species of *Calanus* in northern Skagerrak. The

study demonstrates that both species produce more than one generation at this site, but only the first generation of *C. finmarchicus* could be followed as a single cohort. The phenologies of the two species were found to be separated in time, with *C. finmarchicus* dominating in spring and *C. helgolandicus* in autumn. Here we provide evidence that the phenologies of both *Calanus* species have changed over the last 25 years at this site. Since 1994 the timing of the annual peaks for older stages of both C. *finmarchicus* and *C. helgolandicus* have advanced by about one month. Moreover, the seasonal pattern of *C. helgolandicus*, has switched from a unimodal to a bimodal pattern, with a small additional peak also appearing in spring. Our results revealed a generally increasing trend in the abundance of *C. helgolandicus* at this site. In contrast, the abundance of *C. finmarchicus* was variable with no unidirectional long-term trend over the last 25 years.

We propose that the phenologies of the two species are separated in time due to different temperature preferences, which supports the occurrence of environmental niche separation between closely related copepod species. However, the observed changes in phenology of *C. helgolandicus* suggests that the species is approaching a seasonality reported as typical in more southerly areas, indicating an ability for species to adapt to changing environments. Variations in the timing of these ecologically important copepods, may have implications for higher trophic levels such as the survival of early life stages of fish. Our findings suggests that the proximity to the Norwegian Trench enables the early spring invasion of the overwintering population of *C. finmarchicus* to the Skagerrak coastal area. We therefore conclude that the Norwegian Trench influences the demography and the abundance of *C. finmarchicus* in this coastal area, both as a gateway for the advective supply, and as a habitat for local overwintering. The contrasting long term trends in abundances of the two species suggest that the population sizes of *C. finmarchicus* and *C. helgolandicus* are affected by different drivers, which underlines that both large-scale climatic processes as well as local biological drivers should be considered in order to understand the complex underlying mechanisms behind the variability.

DATA AVAILABILITY STATEMENT

The original contributions presented in the study are included in the article/supplementary material. Further inquiries can be directed to the corresponding author.

AUTHOR CONTRIBUTIONS

TF, CB, and EB were responsible for writing the manuscript. TF and EB compiled and organized the database. NN performed the time series analysis. EB, NN, and TF made figures and maps. All co-authors contributed substantially to the interpretation of the data and writing of the manuscript and gave final approval for publication.

FUNDING

This study was supported by the "CoastRisk" project (No. 299554/F40) and the "Sustainable harvesting in the Norwegian Sea and adjacent ecosystems" project (No. 299554), both funded by the Research Council of Norway (RCN). An earlier part of this study was supported by the RCN through projects RECNOR (No. 178 679/S40) and ECCO (No. 200508). The monitoring at Arendal Station 2 is operated by the Institute of Marine Research, partly funded by the Norwegian Environment Agency.

ACKNOWLEDGMENTS

We thank the many colleagues at the IMR Flødevigen Research Station who have been collecting and processing samples from Arendal Station 2 since 1994. Special thanks to Lena Omli for establishing the zooplankton time-series. We thank Lena Omli, Signe Johannessen, Jon Rønning and Gaston Aguirre for enumeration and species identifications of *Calanus*. The authors are grateful to Dr. Maud Alix for assistance with the figures. We also thank the referees for their constructive reviews that helped to improve the final version of the manuscript.

REFERENCES

Aßmus, J., Melle, W., Tjøstheim, D., and Edwards, M. (2009). Seasonal Cycles and Long-Term Trends of Plankton in Shelf and Oceanic Habitats of the Norwegian Sea in Relation to Environmental Variables. *Deep. Sea. Res. (Part. II. Top. Stud. Oceanogr.)* 56, 1895–1909. doi: 10.1016/j.dsr2.2008.11.004

Aksnes, D. L., and Magnesen, T. (1983). Distribution, Development, and Production of *Calanus Finmarchicus* (Gunnerus) in Lindåspollene, Western Norway 1979. *Sarsia* 68, 195–207. doi: 10.1080/00364827.1983.10420572

Albretsen, J., Aure, J., Sætre, R., and Danielssen, D. S. (2012). Climatic Variability in the Skagerrak and Coastal Waters of Norway. *ICES. J. Mar. Sci.* 69, 758–763. doi: 10.1093/icesjms/fsr187

Alvarez-Fernandez, S., Lindeboom, H., and Meesters, E. (2012). Temporal Changes in Plankton of the North Sea: Community Shifts and Environmental Drivers. *Mar. Ecol. Prog. Ser.* 462, 21–38. doi: 10.3354/meps09817

Arnott, S. A., and Ruxton, G. D. (2002). Sandeel Recruitment in the North Sea: Demographic, Climatic and Trophic Effects. *Mar. Ecol. Prog. Ser.* 238, 199–210. doi: 10.3354/meps238199

Backhaus, J. O., Harms, I. H., Krause, M., and Heath, M. R. (1994). An Hypothesis Concerning the Space-Time Succession of *Calanus Finmarchicus* in the Northern North Sea. *ICES. J. Mar. Sci.* 54, 169–180. doi: 10.1006/jmsc.1994.1018

Bagøien, E., Kaartvedt, S., and Øverås, S. (2000). Seasonal Vertical Migrations of *Calanus* Spp. In Oslofjorden. *Sarsia* 85, 299–311. doi: 10.1080/00364827.2000.10414581

Bagøien, E., Melle, W., and Kaartvedt, S. (2012). Seasonal Development of Mixed Layer Depths, Nutrients, Chlorophyll and *Calanus Finmarchicus* in the Norwegian Sea - A Basin-Scale Habitat Comparison. *Prog. Oceanogr.* 103, 58–79. doi: 10.1016/j.pocean.2012.04.014

Båmstedt, U. (2000). Life Cycle, Seasonal Vertical Distribution and Feeding of *Calanus Finmarchicus* in Skagerrak Coastal Water. *Mar. Biol.* 137, 279–289. doi: 10.1007/s002270000337

Batten, S. D., Clark, R., Flinkman, J., Hays, G. C., John, E., John, A. W. G., et al. (2003). CPR Sampling: The Technical Background, Materials and Methods, Consistency and Comparability. *Prog. Oceanogr.* 58, 193–215. doi: 10.1016/j.pocean.2003.08.004

Beare, D., and McKenzie, E. (1999). Temporal Patterns in the Surface Abundance of *Calanus Finmarchicus* and *C. Helgolandicus* in the Northern North Sea 1958–1996 Inferred From Continuous Plankton Recorder Data. *Mar. Ecol. Prog. Ser.* 190, 241–251. doi: 10.3354/meps190241

Beaugrand, G. (2004). The North Sea Regime Shift: Evidence, Causes, Mechanisms and Consequences. *Prog. Oceanogr.* 60, 245–262. doi: 10.1016/j.pocean.2004.02.018

Beaugrand, G., Brander, K. M., Lindley, J. A., Souissi, S., and Reid, P. C. (2003). Plankton Effect on Cod Recruitment in the North Sea. *Nature* 426, 661–664. doi: 10.1038/nature02164

Beaugrand, G., Harlay, X., and Edwards, M. (2014). Detecting Plankton Shifts in the North Sea: A New Abrupt Ecosystem Shift Between 1996 and 2003. *Mar. Ecol. Prog. Ser.* 502, 85–104. doi: 10.3354/meps10693

Beaugrand, G., Reid, P. C., Ibanez, F., Lindley, J. A., and Edwards, M. (2002). Reorganization of North Atlantic Marine Copepod Biodiversity and Climate. *Science* 296, 1692–1693. doi: 10.1126/science.1071329

Bonnet, D., Harris, R. P., Yebra, L., Guilhaumon, F., Conway, D. V. P., and Hirst, A. G. (2009). Temperature Effects on *Calanus Helgolandicus* (Copepoda: Calanoida) Development Time and Egg Production. *J. Plankton. Res.* 31, 31–44. doi: 10.1093/plankt/fbn099

Bonnet, D., Richardson, A., Harris, R., Hirst, A., Beaugrand, G., Edwards, M., et al. (2005). An Overview of *Calanus Helgolandicus* Ecology in European Waters. *Prog. Oceanogr.* 65, 1–53. doi: 10.1016/j.pocean.2005.02.002

Broms, C., and Melle, W. (2007). Seasonal Development of *Calanus Finmarchicus* in Relation to Phytoplankton Bloom Dynamics in the Norwegian Sea. *Deep. Sea. Res. II.* 54, 2760–2775. doi: 10.1016/j.dsr2.2007.08.021

Chust, G., Castellani, C., Licandro, P., Ibaibarriaga, L., Sagarminaga, Y., and Irigoien, X. (2014). Are *Calanus* Spp. Shifting Poleward in the North Atlantic? A Habitat Modelling Approach. *ICES. J. Mar. Sci.* 71, 241–253. doi: 10.1093/icesjms/fst147

Cleveland, R. B., Cleveland, W. S., McRae, J. E., and Terpenning, I. J. (1990). STL: A Seasonal-Trend Decomposition Procedure Based on Loess. *J. Off. Stat* 6 (1), 3–33.

Conover, R. J. (1988). Comparative Life Histories in the Genera *Calanus* and *Neocalanus* in High Latitudes of the Northern Hemisphere. *Hydrobiologia* 167/168, 127–142. doi: 10.1007/BF00026299

Cook, K. B., Bunker, A., Hay, S., Hirst, A. G., and Speirs, D. C. (2007). Naupliar Development Times and Survival of the Copepods *Calanus Helgolandicus* and *Calanus Finmarchicus* in Relation to Food and Temperature. *J. Plankton. Res.* 29, 757–767. doi: 10.1093/plankt/fbm056

Corkett, C. J., McLaren, I. A., and Sevigny, J. M. (1986). The Rearing of the Marine Calanoid Copepods *Calanus Finmarchicus* (Gunnerus), *C. Glacialis* Jashnov and *C. Hyperboreus* Kroyer With Comment on the Equiproportional Rule. *Syllogeus* 58, 539–546.

Dahl, E., Bagøien, E., Edvardsen, B., and Stenseth, N. C. (2005). The Dynamics of *Chrysochromulina* Species in the Skagerrak in Relation to Environmental Conditions. *J. Sea. Res.* 54, 15–24. doi: 10.1016/j.seares.2005.02.004

Dahl, E., and Johannessen, T. (1998). Temporal and Spatial Variability of Phytoplankton and Chlorophyll a: Lessons From the South Coast of Norway and the Skagerrak. *J. Mat. Sci.* 55, 680–687. doi: 10.1006/JMSC.1998.0401

Dupont, N., Bagøien, E., and Melle, W. (2017). Inter-Annual Variability in Spring Abundance of Adult *Calanus finmarchicus* From the Overwintering Population in the Southeastern Norwegian Sea. *Prog. Oceanogr.* 152, 75–85. doi: 10.1016/j.pocean.2017.02.004

Durant, J. M., Hjermann, D.Ø., Falkenhaug, T., Gifford, D. J., Naustvoll, L. J., Sullivan, B. K., et al. (2013). Extension of the Match-Mismatch Hypothesis to Predator-Controlled Systems. *Mar. Ecol. Prog. Ser.* 474, 43–52. doi: 10.3354/meps10089

Edwards, M., Helaouët, P., Johns, D. G., Batten, S., Beaugrand, G., Chiba, S., et al. (2014). "Global Marine Ecological Status Report: Results From the Global CPR Survey 2012/2013," in *SAHFOS Technical Report*, vol. 10. (Plymouth, U.K: Sir Alister Hardy Foundation for Ocean Science), 1–37.

Edwards, M., and Richardson, A. (2004). Impact of Climate Change on Marine Pelagic Phenology and Trophic Mismatch. *Nature* 430, 881–884. doi: 10.1038/nature02808

Espinasse, M., Halsband, C., Varpe, Ø., Gislason, A., Gudmundsson, K., Falk-Petersen, S., et al. (2018). Interannual Phenological Variability in Two North-East Atlantic Populations of. *Calanus. Finmarchicus. Mar. Biol. Res.* 14 (7), 752–767. doi: 10.1080/17451000.2018.1506135

Falkenhaug, T., Tande, K., and Timonin, A. (1997). Spatio-Temporal Variations in the Copepod Community in Malangen, Northern Norway. *J. Plankton. Res.* 19, 449–468. doi: 10.1093/plankt/19.4.449

Falk-Petersen, S., Mayzaud, P., Kattner, G., and Sargent, J. R. (2009). Lipids and Life Strategy of Arctic *Calanus*. *Mar. Biol. Res.* 5, 18–39. doi: 10.1080/17451000802512267

Fasiolo, M., Nedellec, R., Goude, Y., and Wood, S. N. (2020). Scalable Visualization Methods for Modern Generalized Additive Models. *J. Comput. Graph. Stat.* 29 (1), 78–86. doi: 10.1080/10618600.2019.1629942

Fleminger, A., and Hulsemann, K. (1977). Geographical Range and Taxonomic Divergence in North Atlantic *Calanus* (*C. Helgolandicus, C. Finmarchicus* and *C. Glacialis*). *Mar. Biol.* 40, 233–248. doi: 10.1007/BF00390879

Fransz, H. G., Colebrook, J. M., Gamble, J. C., and Krause, M. (1991). The Zooplankton of the North Sea. *Neth. J. Sea. Res.* 28, 1–52. doi: 10.1016/0077-7579(91)90003-j

Frigstad, H., Andersen, T., Hessen, D. O., Jeansson, E., Skogen, M., Naustvoll, L. J., et al. (2013). Long-Term Trends in Carbon, Nutrients and Stoichiometry in Norwegian Coastal Waters: Evidence of a Regime Shift. *Prog. Oceanogr.* 111, 113–124. doi: 10.1016/j.pocean.2013.01.006

Fromentin, J. M., and Planque, B. (1996). *Calanus* and Environment in the Eastern North Atlantic. II. Influence of the North Atlantic Oscillation on *C. Finmarchicus* and *C. Helgolandicus*. *Mar. Ecol. Prog. Ser.* 134, 111–118. doi: 10.3354/meps134111

Frost, B. W. (1974). *Calanus Marshallae*, a New Species of Calanoid Copepod Closely Allied to the Sibling Species *C. Finmarchicus* and *C. Glacialis*. *Mar. Biol.* 26, 77–99. doi: 10.1007/BF00389089

Furnes, G. K., Hackett, B., and Sætre, R. (1986). Retroflection of Atlantic Water in the Norwegian Trench. *Deep. Sea. Res. Part A. Oceanogr. Res. Pap.* 33, 247–265. doi: 10.1016/0198-0149(86)90121-4

Gao, S., Hjøllo, S. S., Falkenhaug, T., Strand, E., Edwards, M., and Skogen, M. (2021). Overwintering Distribution, Inflow Patterns and Sustainability of *Calanus Finmarchicus* in the North Sea. *Prog. Oceanogr.* 194, 102567. doi: 10.1016/j.pocean.2021.102567

González-Pola, C., Larsen, K. M. H., Fratantoni, P., and Beszczynska-Möller, A. (2020). ICES Report on Ocean Climate 2019. *ICES. Coop. Res. Rep.* 350, 136. doi: 10.17895/ices.pub.7537

Hastie, T. J., and Tibshirani, R. J. (1990). *Generalized Additive Models* (Boca Raton: Chapman & Hall/CRC), 392.

Heath, M. R. (2007). The Consumption of Zooplankton by Early Life Stages of Fish in the North Sea. *ICES. J. Mar. Sci.* 64, 1650–1663. doi: 10.1093/icesjms/fsm156

Heath, M. R., Astthorsson, O. S., Dunn, J., Ellertsen, B., Gaard, E., Gislason, A., et al. (2000). Comparative Analysis of *Calanus Finmarchicus* Demography at Locations Around the Northeast Atlantic. *ICES. J. Mar. Sci.* 57, 1562–1580. doi: 10.1006/jmsc.2000.0950

Heath, M. R., Backhaus, J. O., Richardson, K., McKenzie, E., Slagstad, D., Beare, D., et al. (1999). Climate Fluctuations and the Spring Invasion of the North Sea by *Calanus Finmarchicus*. *Fish. Oceanogr.* 8, 163–176. doi: 10.1046/j.1365-2419.1999.00008.x

Heath, M. R., Boyle, P. R., Gislason, A., Gurney, W. S. C., Hay, S. J., Head, E. J. H., et al. (2004). Comparative Ecology of Overwintering *Calanus Finmarchicus* in the Northern North Atlantic, and Implications for Life Cycle Patterns. *ICES. J. Mar. Sci.* 61 (4), 698–708. doi: 10.1016/j.icesjms.2004.03.013

Helaouët, P., and Beaugrand, G. (2007). Macroecology of *Calanus Finmarchicus* and *C. Helgolandicus* in the North Atlantic Ocean and Adjacent Seas. *Mar. Ecol. Prog. Ser.* 345, 147–165. doi: 10.3354/meps06775

Helaouët, P., Beaugrand, G., and Reid, P. C. (2011). Macrophysiology of *Calanus Finmarchicus* in the North Atlantic Ocean. *Prog. Oceanogr.* 91, 217–228. doi: 10.1016/j.pocean.2010.11.003

Helaouët, P., Beaugrand, G., and Edwards, M. (2013). Understanding Long-Term Changes in Species Abundance Using a Niche-Based Approach. *PloS One* 8, e79186. doi: 10.1371/journal.pone.0079186

Hirche, H. J. (1983). Overwintering of *C. Finmarchicus* and *C. Helgolandicus*. *Mar. Ecol. Prog. Ser.* 11, 281–290. doi: 10.3354/meps011281

Hirche, H. J., Brey, T., and Niehoff, B. (2001). A High-Frequency Time Series at Ocean Weather Ship Station M (Norwegian Sea): Population Dynamics of *Calanus Finmarchicus*. *Mar. Ecol. Prog. Ser.* 219, 205–219. doi: 10.3354/meps219205

Hjøllo, S. S., Skogen, M. D., and Svendsen, E. (2009). Exploring Currents and Heat Within the North Sea Using a Numerical Model. *J. Mar. Syst.* 78, 180–192. doi: 10.1016/j.jmarsys.2009.06.001

Huserbråten, M. B. O., Moland, E., and Albretsen, J. (2018). Cod at Drift in the North Sea. *Prog. Oceanogr.* 167, 116–124. doi: 10.1016/j.pocean.2018.07.005

ICES (2021). Report of the Working Group on the Assessment of Demersal Stocks in the North Sea and Skagerrak (WGNSSK). *ICES. Sci. Rep.* 3 (66), 988. doi: 10.17895/ices.pub.8211

Jaschnov, W. A. (1970). Distribution of *Calanus* Species in the Seas of the Northern Hemisphere. *Internat. Rev. Der. Gesamt. Hydrobiol. Und. Hydrograph.* 55, 197–212. doi: 10.1002/iroh.19700550203

Johannessen, T., Dahl, E., Falkenhaug, T., and Naustvoll, L. J. (2012). Concurrent Recruitment Failure in Gadoids and Changes in the Plankton Community Along the Norwegian Skagerrak Coast After 2002. *ICES* 69, 795–801. doi: 10.1093/icesjms/fsr194

Jónasdóttir, S. H., and Koski, M. (2011). Biological Processes in the North Sea: Comparison of *Calanus Helgolandicus* and *Calanus Finmarchicus* Vertical Distribution and Production. *J. Plankton. Res.* 33, 85–103. doi: 10.1093/plankt/fbq085

Jonasdottir, S. H., Trung, N., Hansen, F., and Gärtner, S. (2005). Egg Production and Hatching Success in the Calanoid Copepods *Calanus Helgolandicus* and *Calanus Finmarchicus* in the North Sea From March to September 2001. *J. Plankton. Res.* 27, 1239–1259. doi: 10.1093/plankt/fbi091

Krause, M., Fock, H., Greve, W., and Winkler, G. (2003). North Sea Zooplankton: A Review. *Senckenb. Marit.* 33, 71–204. doi: 10.1007/BF03043048

Kristiansen, I., Hjalmar, H., Petursdottir, H., Gislason, A., Broms, C., Melle, W., et al. (2019). Decreased Influx of Calanus Spp. Into the Southwestern Norwegian Sea Since 2003. *Deep. Sea. Res. Part I.* 149, 103048. doi: 10.1016/j.dsr.2019.05.008

Lindegren, M., Thomas, M. K., Jónasdóttir, S., Nielsen, T. G., and Munk, P. (2020). Environmental Niche Separation Promotes Coexistence Among Ecologically Similar Zooplankton Species—North Sea Copepods as a Case Study. *Limnol. Oceanogr.* 65, 545–556. doi: 10.1002/lno.11322

Lindeque, P. K., Hay, S. J., Heath, M. R., Ingvarsdottir, A., Rasmussen, J., Smerdon, G. R., et al. (2006). Integrating Conventional Microscopy and Molecular Analysis to Analyse the Abundance and Distribution of Four *Calanus* Congeners in the North Atlantic. *J. Plankton. Res.* 2, 221–238. doi: 10.1007/BF03043048

Møller, E. F., Maar, M., Jónasdóttir, S. H., Gissel Nielsen, T., and Tönnesson, K. (2012). The Effect of Changes in Temperature and Food on the Development of *Calanus Finmarchicus* and *Calanus Helgolandicus* Populations. *Limnol. Oceanogr.* 57, 211–220. doi: 10.4319/lo.2012.57.1.0211

Maar, M., Møller, E. F., Gürkan, Z., Jonasdottir, S. H., and Nielsen, T. G. (2013). Sensitivity of *Calanus* Spp. Copepods to Environmental Changes in the North Sea Using Life-Stage Structured Models. *Prog. Oceanogr.* 111, 24–37. doi: 10.1016/j.pocean.2012.10.004

Mackas, D. L., Greve, W., Edwards, M., Chiba, S., Tadokoro, K., Eloire, D., et al. (2012). Changing Zooplankton Seasonality in a Changing Ocean: Comparing Time Series of Zooplankton Phenology. *Prog. Oceanogr.* 97–100, 31–62. doi: 10.1016/j.pocean.2011.11.005

Madden, H., Beare, D., Heath, M. R., Fraser, J. G., and Gallego, A. (1999). The Spring/Early Summer Distribution of *Calanus* Spp. In the Northern North Sea and Adjacent Areas. *Fish. Oceanogr.* 8, 138–152. doi: 10.1046/j.1365-2419.1999.00006.x

Maud, J. L., Atkinson, A., Hirst, A. G., Lindeque, P. K., Widdicombe, C. E., Harmer, R. A., et al. (2015). How Does *Calanus Helgolandicus* Maintain Its Population in a Variable Environment? Analysis of a 25-Year Time Series From the English Channel. *Prog. Oceanogr.* 137, 513–523. doi: 10.1016/j.pocean.2015.04.028

Melle, W., Runge, J., Head, E., Plourde, S., Castellani, C., Licandro, P., et al. (2014). The North Atlantic Ocean as Habitat for *Calanus Finmarchicus*: Environmental Factors and Life History Traits. *Prog. Oceanogr.* 129, 244–284. doi: 10.1016/j.pocean.2014.04.026

Montero, J. T., Lima, M., Estay, S. A., and Rezende, E. L. (2021). Spatial and Temporal Shift in the Factors Affecting the Population Dynamics of *Calanus* Copepods in the North Sea. *Glob. Change. Biol.* 27, 576–586. doi: 10.1111/gcb.15394

Motoda, S. (1959). Devices of Simple Plankton Apparatus. *Mem. Fac. Fish. Hokkaido. Univ.* 7, 73–94.

Moy, F. E., and Christie, H. (2012). Large-Scale Shift From Sugar Kelp (*Saccharina Latissima*) to Ephemeral Algae Along the South and West Coast of Norway. *Mar. Biol. Res.* 8 (4), 309–321. doi: 10.1080/17451000.2011.637561

Munk, P., and Nielsen, T. (1994). Trophodynamics of the Plankton Community at Dogger Bank: Predatory Impact by Larval Fish. *J. Plankton. Res.* 16, 1225–1245. doi: 10.1093/plankt/16.9.1225

O'Hara-Wild, M., Hyndman, R., Wang, E., and Caceres, G. (2021). *Fable: Forecasting Models for Tidy Time Series* (R package version 0.3.1). Available at: https://CRAN.R-project.org/package=fable.

Østvedt, O. J. (1955). Zooplankton Investigations From Weather-Ship M in the Norwegian Sea 1948–49. *Hvalrådets. Skrift.* 40, 1–93.

Otto, L., Zimmerman, J. T. F., Furnes, G. K., Mork, M., Sætre, R., and Becker, G. (1990). Review of the Physical Oceanography of the North Sea. *Neth. J. Sea. Res.* 26, 161– 238. doi: 10.1016/0077-7579(90)90091-T

Papworth, D. J., Marini, S., and Conversi, A. (2016). A Novel, Unbiased Analysis Approach for Investigating Population Dynamics: A Case Study on *Calanus Finmarchicus* and Its Decline in the North Sea. *PloS One* 11 (7), e0158230. doi: 10.1371/journal.pone.0158230

Planque, B., and Fromentin, J. M. (1996). *Calanus* and Environment in the Eastern North Atlantic. I. Spatial and Temporal Patterns of C. Finmarchicus and *C. Helgolandicus*. *Mar. Ecol. Prog. Ser.* 134, 101–109. doi: 10.3354/meps134101

Planque, B., and Taylor, A. H. (1998). Long-Term Changes In Zooplankton and the Climate of the North Atlantic. *ICES J. Mar. Sci.* 55, 644–654. doi: 10.3354/meps134101

R Core Team (2021). *R: A Language and Environment for Statistical Computing* (Vienna, Austria: R Foundation for Statistical Computing). Available at: https://www.R-project.org/.

Rees, C. B. (1949). Continuous Plankton Records: The Distribution of *Calanus Finmarchicus* (Gunn.) and Its Two Forms in the North Sea. *Hull. Bull. Mar. Ecol.* 2, 215–275.

Reid, P. C., Edwards, M., Beaugrand, G., Skogen, M., and Stevens, D. (2003). Periodic Changes in the Zooplankton of the North Sea During the Twentieth Century Linked to Oceanic Inflow. *Fish. Oceanogr.* 12, 260–269. doi: 10.1046/j.1365-2419.2003.00252.x

Reygondeau, G., and Beaugrand, G. (2011). Future Climate-Driven Shifts in Distribution of *Calanus Finmarchicus*. *Global Change Biol.* 17, 756–766. doi: 10.1111/j.1365-2486.2010.02310.x

Reygondeau, G., Molinero, J. C., Coombs, S., MacKenzie, B. R., and Bonnet, D. (2015). Progressive Changes in the Western English Channel Foster a Reorganization in the Plankton Food Web. *Prog. Oceanogr.* 137, 524–532. doi: 10.1016/j.pocean.2015.04.025

Richardson, A. J., Walne, A. W., John, A. W. G., Jonas, T. D., Lindley, J. A., Sims, D. W., et al. (2006). Using Continuous Plankton Recorder Data. *Prog. Oceanogr.* 68, 27–74. doi: 10.1016/j.pocean.2005.09.011

Rodhe, J. (1996). On the Dynamics of the Large-Scale Circulation of the Skagerrak. *J. Sea. Res.* 35, 23–38. doi: 10.1016/S1385-1101(96)90731-5

Sætre, R., Aure, J., and Danielsen, D. S. (2003). Long-Term Hydrographic Variability Patterns Off the Norwegian Coast and in the Skagerrak. *ICES. Mar. Sci. Symp.* 219, 150–159.

Skjoldal, H. R., Aarflot, J. M., Bagøien, E., Skagseth, Ø., Rønning, J., and Lien, V. S. (2021). Seasonal and Interannual Variability in Abundance and Population Development of *Calanus Finmarchicus* at the Western Entrance to the Barents Se-2019. *Prog. Oceanogr.* 195, 102574. doi: 10.1016/j.pocean.2021.102574

Skreslet, S., Olsen, K., Mohus, Å., and Tande, K. S. (2000). Stage-Specific Habitats of *Calanus Finmarchicus* and *Calanus Helgolandicus* in a Stratified Northern Norwegian Fjord. *ICES. J. Mar. Sci.* 57, 1656–1663. doi: 10.1006/jmsc.2000.0968

Speirs, D. C., Gurney, W. S. C., Holmes, S. J., Heath, M. R., Wood, S. N., and Clarke, E. D. (2004). Understanding Demography in an Advective Environment: Modelling *Calanus Finmarchicus* in the Norwegian Sea. *J. Anim. Ecol.* 73, 897–910. doi: 10.1111/j.0021-8790.2004.00857.x

Strand, E., Bagøien, E., Edwards, M., Broms, C., and Klevjer, T. (2020). Spatial Distributions and Seasonality of Four *Calanus* Species in the Northeast Atlantic. *Prog. Oceanogr.* 185, 102344. doi: 10.1016/j.pocean.2020.102344

UNESCO. (1968). "UNESCO Zooplankton Sampling. Part I and Part II," in *Monographs on Oceanographic Methodology*. Eds. D. J. Tranter and J. H. Fraser (Paris: UNESCO), 174.

van Deurs, M., van Hal, R., Tomczak, M. T., Jonasdottir, S. H., and Dolmer, P. (2009). Recruitment of Lesser Sandeel *Ammodytes Marinus* in Relation to Density Dependence and Zooplankton Composition. *Mar. Ecol. Prog. Ser.* 381, 249–258. doi: 10.3354/meps07960

Vikebø, F. B., Korosov, A., Stenevik, E. K., Husebø, Å., and Slotte, A. (2012). Spatio-Temporal Overlap of Hatching in Norwegian Spring-Spawning Herring and the Spring Phytoplankton Bloom at Available Spawning Substrata. *ICES. J. Mar. Sci.* 69, 1298–1302. doi: 10.1093/icesjms/fss083

Wickham, H. (2016). *Ggplot2: Elegant Graphics for Data Analysis* Vol. 2016 (New York:Springer-Verlag New York.). doi: 10.1007/978-0-387-98141-3

Williams, R. (1985). Vertical Distribution of *Calanus Finmarchicus* and *C. Helgolandicus* in Relation to the Development of the Seasonal Thermocline in the Celtic Sea. *Mar. Biol.* 86, 145–149. doi: 10.1007/BF00399020

Williams, R., and Conway, D. V. P. (1984). Vertical Distribution, and Seasonal and Diurnal Migration of *Calanus Helgolandicus* in the Celtic Sea. *Mar. Biol.* 79, 63–73. doi: 10.1007/BF00404986

Wilson, R. J., Heath, M. R., and Speirs, D. C. (2016). Spatial Modeling of *Calanus Finmarchicus* and *Calanus Helgolandicus*: Parameter Differences Explain Differences in Biogeography. *Front. Mar. Sci.* 3, 157. doi: 10.3389/fmars.2016.00157

Wilson, R. J., Speirs, D. C., and Heath, M. R. (2015). On the Surprising Lack of Differences Between Two Congeneric Calanoid Copepod Species, *Calanus Finmarchicus* and *C. Helgolandicus*. *Prog. Oceanogr.* 134, 413–431. doi: 10.1016/j.pocean.2014.12.008

Winther, N. G., and Johannessen, J. A. (2006). North Sea Circulation: Atlantic Inflow and Its Destination. *J. Geophys. Res.* 111, C12018. doi: 10.1029/2005JC003310

Wood, S. N. (2017). *Mgcv: Mixed GAM Computation Vehicle With GCV/AIC/REML Smoothness Estimation*. Available at: https://cran.r-project.org/web/packages/mgcv/index.html.

Conflict of Interest: The authors declare that the research was conducted in the absence of any commercial or financial relationships that could be construed as a potential conflict of interest.

Publisher's Note: All claims expressed in this article are solely those of the authors and do not necessarily represent those of their affiliated organizations, or those of the publisher, the editors and the reviewers. Any product that may be evaluated in this article, or claim that may be made by its manufacturer, is not guaranteed or endorsed by the publisher.

Copyright © 2022 Falkenhaug, Broms, Bagøien and Nikolioudakis. This is an open-access article distributed under the terms of the Creative Commons Attribution License (CC BY). The use, distribution or reproduction in other forums is permitted, provided the original author(s) and the copyright owner(s) are credited and that the original publication in this journal is cited, in accordance with accepted academic practice. No use, distribution or reproduction is permitted which does not comply with these terms.

frontiers | Frontiers in Marine Science

ORIGINAL RESEARCH
published: 06 June 2022
doi: 10.3389/fmars.2022.818507

Prevalence of *Kudoa thyrsites* (Myxozoa, Multivalvulida) in Atlantic Mackerel, *Scomber scombrus* L., in the Vicinity of the Faroe Islands

*Dánjal Petur Højgaard**, *Eydna í Homrum* and *Ian Salter**

Faroe Marine Research Institute, Tórshavn, Faroe Islands

OPEN ACCESS

Edited by:
Teresa Sofia Giesta da Silva, Marine and Freshwater Research Institute, Iceland

Reviewed by:
Teunis Jansen, Technical University of Denmark, Denmark
Simon Jones, Department of Fisheries and Oceans, Canada

***Correspondence:**
Ian Salter
ians@hav.fo
Dánjal Petur Højgaard
danjalpeturh@gmail.com

Specialty section:
This article was submitted to Marine Ecosystem Ecology, a section of the journal Frontiers in Marine Science

Received: *19 November 2021*
Accepted: *02 May 2022*
Published: *06 June 2022*

Citation:
Højgaard DP, í Homrum E and Salter I (2022) The Prevalence of Kudoa thyrsites (Myxozoa, Multivalvulida) in Atlantic Mackerel, Scomber scombrus *L., in the Vicinity of Faroe Islands. Front. Mar. Sci. 9:818507. doi: 10.3389/fmars.2022.818507*

Atlantic mackerel *Scomber scombrus* is an important migratory fish in Faroese waters and the Northeast Atlantic at large. Similar to other fish species from marine environments, mackerel can be infected by the myxozoan parasite *Kudoa thyrsites*, leading to myoliquefaction that renders the fish commercially unviable. Despite the ecological and economic significance of *K. thyrsites* as a parasite, little is known regarding its prevalence in the Faroese mackerel fishery. Prior to analysing field samples, we examined 104 samples of Atlantic mackerel selected from a Faroese processing plant on the basis of visible soft-tissue. Using microscope smears we observed *K. thyrsites* in 98% of the soft-tissue mackerel specimens and a direct comparison with qPCR demonstrated strong agreement between the two techniques ($\Phi = 0.429$, $p<0.01$; Fisher's exact test). We used qPCR to analyze a total of 594 Atlantic mackerel specimens, collected from Faroese fishing grounds during 2017 and 2018. Overall prevalence was 4.1% (95% confidence interval; 2.5-5.7%) and ranged from 0-14% at different locations. Infection by *K. thyrsites* was documented in fish as young as 2 years (195g) and up to 14 years (615g) of age. A logistic regression model indicated the odds of infection were statistically associated with sampling location and month, but not gender, age, weight or length, although a Chi-squared test on age categories showed the oldest fish (>10 years) had highest prevalence (10.8%, CI: 4.2-17.5%). In order to investigate potential infection pathways we performed qPCR analysis on eDNA in water samples collected from the Faroese Plateau. However, we found no molecular evidence for *K. thyrsites* spores in Faroese plankton assemblages. Our data support the prevailing hypothesis that both the alternating invertebrate host and infection of Atlantic mackerel by *K. thyrsites* occurs in more southern waters.

Keywords: *Kudoa thyrsites*, Atlantic mackerel, Faroe Islands, myoliquification, FAMEOS, Faroese Marine Ecosystem Observing Study, eDNA

INTRODUCTION

Fish infected with myxosporidia from the family *Kudoidae* (Meglitsch, 1947) show myoliquefaction, more commonly referred to as soft-tissue. The mechanism for this phenomenon has been linked to proteases, like cathepsin, which are released by the pre-sporogenic plasmodia into host muscle tissue (Henning et al., 2013). The post mortem drop in muscle pH boosts the activity of the cathepsin enzyme (Levsen, 2015) leading to further decomposition. Notably, the presence of parasite-derived proteases in fresh and frozen/thawed commercial fish species can render the filet unfit for consumption, leading to significant economic losses.

The number of documented species in the genus *Kudoa* has increased from 44 (Moran et al., 1999a) to close to 100 (Levsen, 2015). Myoliquefaction of numerous fish species occurs in association with the genus *Kudoa* across a broad range of environments. In particular, *K. thyrsite*s exhibits a global distribution (Whipps and Kent, 2006) and has been reported in 18 different fish families, comprising 9 orders (Henning et al., 2013), it is thus of major concern for both capture fisheries and aquaculture. It has been reported in northeast Pacific Hake (*Merluccius productus*) (King et al., 2012), Mediterranean silver scabbardfish (*Lepidopus caudatus*) (Kovaleva et al., 1979; Giulietti et al., 2019) and Atlantic mackerel (*Scomber scombrus*) (Levsen et al., 2008). Aquaculture of Atlantic salmon (*Salmo salar*) in British Columbia, Canada has suffered financial losses due to *K. thyrsites* infection (St-Hilaire et al., 1997a, St-Hilaire et al., 1998; Moran et al., 1999b). More recently, *K. islandica* has been identified in spotted wolfish (*Anarchicas minor*), Atlantic lumpfish (*Anarhichas lupus*) and lumpsucker (*Cyclopterus lumpus*) in the North Atlantic (Kristmundsson and Freeman, 2014). Additionally, *K. islandica* has been found in reared lumpsucker in Norway (Alarcon et al., 2015). Currently, there are no documented cases of *K. thyrsites* or *K. islandica* in Faroese aquaculture.

Atlantic mackerel is an economically important species for the Faroe Islands, and in the Northeast Atlantic at large. Previous work has developed our understanding of mackerel in regards to feeding preferences (Langøy et al., 2012; Bachiller et al., 2016), distribution of spatial biomass (Nøttestad et al., 2016) and recent patterns of geographical expansion (Ólafsdóttir et al., 2019). Earlier work in the northern North Sea found up to 8.9% of mackerel exhibiting "soft flesh" phenomenon in association with *K. thyrsites* spores in muscle tissue (Levsen et al., 2008). Annual surveys of mackerel have documented prevalence of post-mortem myoliquefaction at 0.6-3.1% (n=2500) and have observed significantly lower prevalence in medium (400-600g) compared to large-sized (>600g) mackerel (Levsen, 2015, Giulietti et al. 2022).

Kudoa thyrsites is classified as a multivalvulid myxosporidia (Myxozoa) (Lom and Dyková, 2006), an obligate parasite that alternates between invertebrate and vertebrate hosts (Kent et al., 2001; Americus et al., 2020). The general biology of Myxozoa displays bi-phasic life cycles that alternate between myxospores and actinospores and is well characterized in fresh water myxozoans (Yokoyama, 2003). Actinospores are released from an invertebrate host and may attach and enter a fish host, resulting in the development of a plasmodium (Lom and Dyková, 2006; Okamura et al., 2015). The skin, fins, gills and buccal cavity have all been demonstrated as portals of entry for actinospores (triactynomyxon) of *Myxobolus cerebralis* (El-Matbouli et al., 1995). The release of myxospores can occur when the fish host is alive, through the egestion of phagocytosed spores as observed in common Carp (*Cyprinus carpio*) (Ogawa et al., 1992). In *Kudoa* spp., it has been suggested that post-mortem myoliquefaction may serve to facilitate myxospore release (Langdon, 1991). Most actinosporeans have been reported to infect oligochaetes (Kent et al., 2001), although polychaetes, sipunculids, bryozoans and cephalopods have been described as invertebrate hosts for myxozoans (Yokoyama, 2003). The invertebrate host for *K. thyrsites* infection in mackerel is unknown. Infections in aquaculture are known from exposure to infected seawater (Moran et al., 1999c; Jones et al., 2012) and PCR-based analysis of raw seawater from infection hotspots detects *K. thyrsites* year round (Jones et al., 2016).

In recent years, quality control procedures used at land-based fish processing plants in the Faroes have identified soft-flesh in the mackerel fishery as an economically significant problem. However, the prevalence of *K. thyrsites* infection in Faroese fishing grounds remains currently uncharacterised. The specific objectives of the present study were (i) compare detection of *K. thyrsites* with microscopic and molecular techniques as the causative agent of post-mortem myoliquefaction, (ii) determine overall prevalence and spatio-temporal variability of *K. thyrsites* in the commercial Faroese fishery and (iii) examine the potential occurrence of *K. thyrsites* in water samples in Faroese waters.

MATERIAL AND METHODS

Sampling of Muscle Tissue

Selected Soft-Flesh Mackerel Specimens From Production Plant

A total of 104 mackerel were obtained from a land-based commercial production plant in the Faroe Islands (Varðin Pelagic, Tvøroyri). The samples originated from the production line in August-November 2015 and were selected on the basis of those specimens that exhibited evidence of post-mortem myoliquefaction (i.e. "soft mackerel"). All samples were stored at -20°C at the Faroe Marine Research Institute until further analysis.

Mackerel Specimens From Faroese Fishery

A total of 584 mackerel were sampled from commercial trawlers and during two research trips of the Faroe Marine Research Institute during 2017 (#184) and 2018 (#400). Samples were collected from different locations from the Faroese fishery, both in Faroese and British territorial waters (**Figure 1**). Full details of the region and time of year samples were collected are documented in **Tables 1**, **2**. The biological parameters sampled were pinched-tail-length (Hansen et al., 2018), ungutted weight, sex, sexual maturity and age (as inferred from annual growth

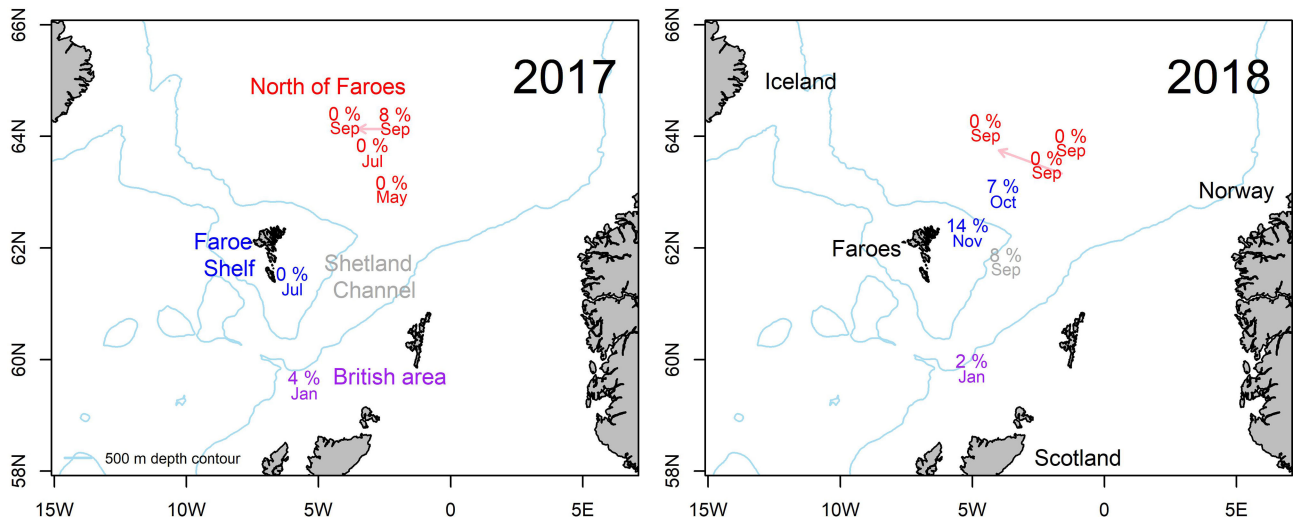


FIGURE 1 | Map of the study area documenting sample locations. Prevalence of *Kudoa* thyrsites in Atlantic mackerel in 2017 (left) and 2018 (right). Month of capture and prevalence of infection is shown. Arrows indicate displacement of text label for plotting clarity. Text colours correspond to different sampling regions: North of Faroes (Red), Faroe Shelf (Blue), Shetland Channel (grey) and British Area (purple).

TABLE 1 | Prevalence of *Kudoa thyrsites* infection in Atlantic mackerel samples collected during 2017 and 2018.

Date	Sampling area	No. Of fish	Infected Mackerel	Prevalence %
29/01/2017	British Area	25	1	4
05/05/2017	North of Faroes	22	0	0
06/07/2017	The Faroe Shelf	20	0	0
11/07/2017	North of Faroes	18	0	0
15/09/2017	North of Faroes	50	0	0
18/09/2017	North of Faroes	50	4	8
16/01/2018	British Area	50	1	2
16/09/2018	North of Faroes	50	0	0
20/09/2018	North of Faroes	50	0	0
23/09/2018	North of Faroes	50	0	0
28/09/2018	Shetland Channel	50	4	0
09/10/2018	The Faroe Shelf	50	3	8
09/10/2018	The Faroe Shelf	50	4	6
08/11/2018	The Faroe Shelf	50	7	8

TABLE 2 | Contingency table of methodological comparison between microscope smears and qPCR.

	qPCR - positive	qPCR - negative
Microscope - positive	94	8
Microscope - negative	0	2

increments of the otoliths). All samples were stored at -20°C prior to further analysis.

Analysis of *K. thyrsites* Infection

The 104 soft-flesh samples obtained from the factory processing plant were analysed using both microscope smears and qPCR detection. The 594 field samples of mackerel from the wild fishery were analysed with qPCR. Positive molecular detections were verified by microscope smears of archived muscle samples.

Microscope Smears

Specimens were defrosted at room temperature and muscle samples extracted (approx. 1.5 cm deep) from both the left and right side of the anterior dorsal fin. Muscle smears were prepared and examined by light microscopy (Optica DM-20) at 400x magnification. An approximately 1mm x 1mm piece was extracted from each muscle sample with a scalpel (chopping of muscle fibres) and forceps and used to prepare microscope wet-smears (St-Hilaire et al., 1997a; Giulietti et al., 2022). Muscle samples were subsequently stored at -20°C for molecular analysis. The left side was used for sample preparation and the right-side as a sample archive. One-hour searches were conducted on each smear for the detection of *K. thyrsites* spores, which were recorded photographically (**Figures 2**, **3**). The selected smears were preserved by mounting in glycerol-gelatin (Berland, 2005). Samples were classified as infected or not-infected depending on the detection of *K. thyrsites* spores. *K. thyrsites* were clearly identified by their morphology, specifically the presence of one enlarged polar capsule (**Figure 3**), which are evenly sized in the recently documented *K. islandica* (Kristmundsson and Freeman, 2014).

qPCR Detection

The three muscle tissue replicates (approx. 200 mm^3) were extracted separately using a HotSHOT DNA preparation based on a previously published method (Truett et al., 2000). In brief, 50 µL of alkaline lysis buffer (25 mM NaOH, 0.2 mM disodium EDTA, pH 12) was added to a sterile 200 µL PCR tube. The muscle sub-samples were added to the tube and mashed with a sterile spatula. The lysis solution was incubated in a PCR

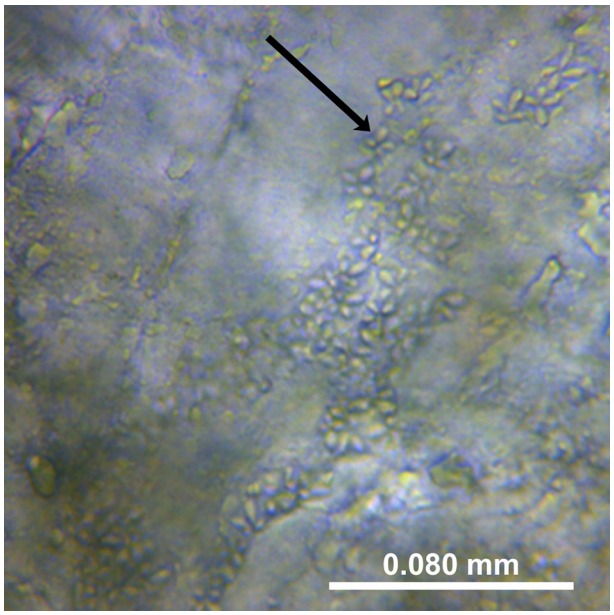


FIGURE 2 | A photo from a wet smear of Kudoa thyrsites spores from the soft mackerels examined. The muscle is partially degraded by the cathepsin enzyme; magnification 400x.

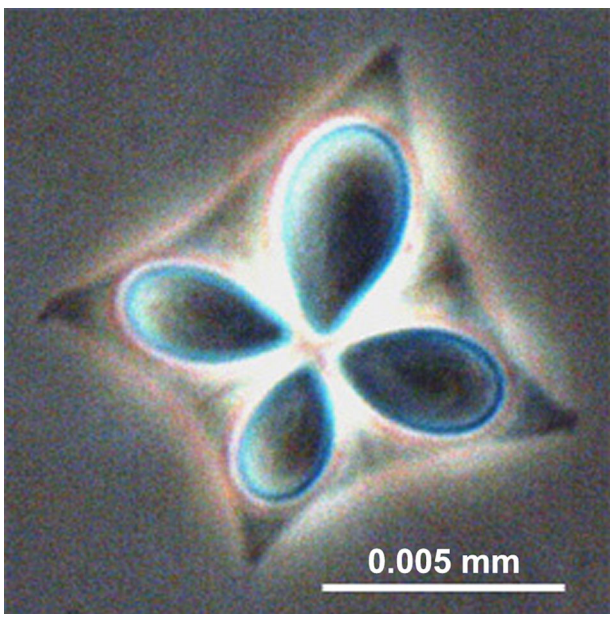


FIGURE 3 | A single spore of Kudoa thyrsites with four nematocysts (polar capsules) clearly visible. (phase contrast. Levsen, 2015).

machine preheated to 95°C for 30 min. and cooled at 4°C. Subsequently 50 µL of neutralization buffer (40 mM Tris-HCl, pH 5) was added to the tube, which was vortexed and incubated for 10-15 min. The tube was centrifuged to collect cellular debris and the supernatant removed and diluted 1:10 with nuclease-free water for subsequent PCR reactions.

Presence/absence tests were performed on the diluted lysates based on a previously published method validated for *K. thyrsites* (Funk et al., 2007). Each reaction well contained 4µL of QuantiTect, 0.25 µL of *Kudoa* Probe, 0.4 µL of *Kudoa* Primer-F, 0.4 µL of *Kudoa* Primer-R and 2.95 µL of nuclease-free water. 2 µL of DNA template was added to bring the reaction volume to 10 µL. Samples were 1:10 dilutions of the HotSHOT lysate. *Kudoa* Probe: VIC-TATCGCGAGAGCCGC-MGB. *Kudoa* F-primer: TGGCGGCCAAATCTAGGTT. *Kudoa* R-primer: GACCGCACACAAGAAGTTAATCC. Positive controls were included in each plate run that were obtained from a previous analysis of visibly infected tissue that yielded consistent amplification in PCR runs. The negative control replaced DNA templates with 2µL of nuclease-free water. Reactions were carried out in 96-well plates using an Applied Biosystems StepONE Plus realtime PCR platform. Samples were analysed in triplicate, corresponding to the three muscle sub-sample tissues extracted independently. The amplification profile was 50°C for 2 mins and 95°C for 15 mins then 45 cycles of 94°C for 15 s and 60°C for 1 min. The Ct value was defined as 20 times the standard deviation of the baseline fluorescent signal. Samples were classified as positive for *K. thyrsites*, if more than 1 of the 3 subsamples exhibited positive amplification.

Plankton Samples Collected From Faroe Plateau

Water Column Sampling

Water column samples were collected on the Faroese Shelf from January through to December (2018) with weekly to biweekly resolution (61.9703 °N. 6.8805 °W) as part of the Faroese Marine Ecosystem Observing (FAMEOS) program. Approximately 9 L of sample water were collected in acid-washed carboys following thorough rinsing (four times) with sample water. Seawater samples were collected using a pump (6m) from a land-based sampling facility connected to the fjord. The depth of the fjord is 18m and is well-mixed throughout the year due to tidal currents. A sample volume of 1.5 L replicate was collected onto 0.2 µm sterivex filters (Millipore; #SVGP01050) using a peristaltic pump and silicon tubing. Between each sampling event, the silicon tubing was stored in a solution of 10% v/v HCl. Prior to sampling, the tubing was flushed with 5 volumes of distilled water and 1 L of sample water prior to connecting sterivex tubing. Upon completion of the filtration the Sterivex filters were capped and stored at -80°C until extraction.

DNA was extracted directly from the Sterivex cartridges using a modified protocol of the Qiagen Dneasy Blood and Tissue Kit (Qiagen, #69504). Sterivex cartridges were removed from the freezer and allowed to defrost at room temperature for 20 min. A final check on residual volume was performed by expunging air through the Sterivex cartridge with a 50mL sterile syringe. The male nipple of the Sterivex cartridge was flame sealed and extraction reagents were added directly inside of the cartridge using sterile filter pipette tips. Extraction proceeded according to the manufacturer's instructions with the following modifications.

A volume of 720 µL of buffer ATL and 80 µL of proteinase K was added directly to the interior of the Sterivex cartridge. The female inlet was capped with a male luer-lock cap. The Sterivex cartridges were then placed in a rotary spinner and incubated at 56°C for 2 h. The cartridges were rotated 90° around their central axis every 30 min to ensure even coverage of the filter roll with extraction solution. The lysis solution was removed from the Sterivex cartridge using a sterile 3 mL luer-lock syringe and transferred to sterile DNase-free 2mL Eppendorf tubes. The Eppendorfs were pulse vortexed (10 s) and spun down in a mini-centrifuge. Subsequently, 600 µL of extraction solution was transferred to a clean 2 mL Eppendorf tube, followed by 600 µL of buffer AL solution. These Eppendorf tubes were pulse vortexed (10 s) to mix and centrifuged. Taking each Eppendorf in turn, 600 µL of ethanol was added followed by pulse-vortexing and centrifugation. This extraction solution was added to the Qiagen DNEasy Blood and Tissue kit spin columns in 3x ~ 600 µL aliquots. The spin column procedure followed the manufacturers instructions. DNA was eluted from the spin column in 120 µL of nuclease-free water following an incubation period of 5 min at 37°C. The flow-through from the first elution step was pipetted back onto the column for a second elution under identical conditions.

DNA concentrations in the extracts were measured with a Qubit Fluorometer and Qubit dsDNA HS assay (Q32854). Following the manufacturer's instructions, DNA extracts were frozen at −20°C until further processing (Salter et al., 2019). Presence-absence tests for *K. thyrsites* were carried out according to the qPCR protocol described in section 2.2.2. Single filter replicates were analysed in triplicate on non-diluted DNA extractions. Inhibition controls were carried out on seawater samples using a commercially available assay (Techne TKIT06035). An Applied Biosystems StepOnePLUS realtime PCR platform was used for amplification. DNA extract aliquots (40 µL) were spiked with 5 µL of control template. Each PCR reaction mixture of 20 µL contained 5 µL sample (including control template), 10 µL of 2X qPCR mastermix (TKITMM01), 2 µL of control primer/probe (TaqMan hydrolysis probe) and 3 µL of nuclease-free seawater. Template and primer/probe sequences are proprietary (Techne). PCR reactions were performed under thermocycler conditions of 2 mins at 95°C and 50 cycles of 10 s at 95°C and 60 s at 60°C. Fluorogenic data was collected through the VIC channel. Inhibition was tested for in four technical PCR replicates of each sample. A comparison of Ct values between samples including internal control template and nuclease-free seawater with internal control template was used to diagnose inhibition, where a Ct shift of >3 was considered as inhibitory (Salter et al., 2019). Inhibition was not detected in any of the seawater samples.

Statistical Analysis

Mean-Square Contingency Coefficient (Φ)

Statistical agreement between the visual and molecular detection methods was determined from binomial presence-absence data and calculated from mean square contingency coefficients (e.g. Salter et al., 2019), a metric commonly referred to as Φ (Cheetham and Hazel, 1969). Visual and molecular detection rates were treated as binary variables (1 = presence and 0 = absence). The two independent detection methods were compared in a 2x2 contingency table. The phi coefficient (Φ) was calculated according to Equation 1 and can be considered as analytically equivalent to the Pearson's product moment correlation taking values that range from -1 (negatively correlated) to 1 (positively correlated).

$$\phi = [(ad) - (bc)]\sqrt{(a+b)(c+d)(a+c)(b+d)} \quad (1)$$

where a = presence-presence, b=presence-absence, c=absence-presence and d= absence-absence.

Chi-Squared and Fisher's Exact Tests

Following the recommendation of (Rósza et al., 2000) we define prevalence as the proportion of examined individuals that tested positive for *K. thyrsites*. Statistical comparisons of prevalence were based on the analysis of 2x(n) contingency tables, where rows represented the binomial categories of infected or not infected and (n) the number of columns representing categorical descriptor variables (e.g. year, age class). If all cells of the contingency table had expected frequencies >5 we used a Chi-squared test, if this assumption was not met, and or the contingency table was 2x2, we used a Fisher's exact test, significance level,$\alpha = 0.05$.

Logistic Regression (Generalised Linear Model)

Statistical analyses were run in the R environment (RStudio Team, 2020) using base R and the aod package (Lesnoff and Lancelot, 2019). We used a logistic regression to model the odds of infection as a binomial outcome from a linear combination of the following predictor variables: latitude (location), time (month), age (year class), size (weight) and gender (M/F). Predictor variables were continuous, except for gender, which was included as a binary variable. Model fit was measured by examining if the model including predictor variables fits significantly better than a null model (intercept only). The test statistic compares the residual deviance of the two model versions from distributed Chi-squared values with degrees of freedom equal to the number of predictor variables in the fitted model. The statistical significance of model coefficients was examined from Chi-squared tests, significance level,$\kappa\alpha = 0.05$.

Prevalence Confidence Intervals

Prevalence data are presented with 95% confidence intervals, calculated according to the following Equation 2:

$$p' - Z_\alpha \sqrt{\frac{p'q'}{n}} \leq p \geq p' + Z_\alpha \sqrt{\frac{p'q'}{n}} \quad (2)$$

where p' = x/n, x = samples positive for *K. thyrsites*, n = number of samples, q' = 1-p', $\alpha = 0.05$, $Z_\alpha = 1.96$

Welch Two Sample t-Test

The inter-annual differences between length and age parameters of the sampled mackerel were determined using a Welch two sample t-test to account for unequal sample size/variance in 2017 and 2018.

RESULTS

Detection of Infections in Soft-Flesh Specimens From Factory Processing

A total of 104 soft-flesh samples obtained from the factory processing plant in 2015 were examined both by microscope smears and qPCR (**Table 2**). The proportion of *K. thyrsites* spores (**Figure 2**) was 98% from microscope smears compared to 90% from qPCR. No samples scored positive by qPCR and negative by microscopy. In some cases it was possible to observe multiple spores in the soft-flesh mackerel specimens (**Figure 3**). The mean square contingency co-efficient calculated from the 2x2 contingency table was 0.43. A Fisher's exact test also demonstrated a significant association ($p<0.001$) of detection outcome from the two methodological approaches.

Prevalence in Faroese Commercial Fishery

The mackerel sampled in 2017-2018 ranged from 2-14 years (**Figure 4A**) corresponding to a length range of 28.1-41.1 cm (**Figure 4B**) and weights of 190-660g (data not shown). Fish 5 years and older dominated in both 2017 (median = 6 years) and 2018 (median = 8 years). The size at age was also comparable between 2017 and 2018 (**Figure 4C**). Welch's two-sample t-test showed that on average mackerel sampled in 2017 were significantly younger ($p<0.001$) and smaller ($p<0.01$) than in 2018.

The overall prevalence of *K. thyrsites* detected by qPCR was 4.1% (95% confidence interval (CI): 2.5-5.7%). Prevalence was higher in 2018 (4.8%, CI: 2.7-6.8%) compared to 2017 (2.7%, CI: 0.4-5.1%) but the overlapping confidence intervals as well as a Chi-squared test indicated there was no significant association between sampling year and overall prevalence ($p>0.05$). The range in the proportion of fish infected was 0-14%, with the maximum value measured on the Faroese shelf in October 2018 (**Figure 1** and **Table 1**). Positive PCR detection of *K. thyrsites* was detected in fish as young as 2 years (29.8 cm and 195g) and up to 14 years (40 cm and 595g). Two of the 24 positive PCR samples were negative for the presence of *K. thyrsites* spores when examined under the microscope.

A logistic regression model was used to test if the odds of prevalence could be explained by a linear combination of the following predictor variables: latitude, month, weight, age and gender. Model fit was tested by examining the residual deviance for the model including predictors with a null model (intercept only). Residual deviance was 180 on 578 degrees of freedom and null deviance was 200 on 583 degrees of freedom. The distributed Chi-squared value on 5 degrees of freedom (number of predictor variables) was 20.13, corresponding to significance level of $p<0.005$. The logistic regression model including predictor variables thus had a statistically significant better fit than a null model. The coefficients within the model and their statistical significance were as follows: latitude (-0.67, $p<0.01$), month (0.39, $p<0.001$), age (0.18, $p>0.05$), weight (-0.001, $p>0.05$) and gender (0.32, $p>0.05$). Consequently, only geographical location and month were significant predictor variables. The negative co-efficient for latitude (°N) indicates a decrease in the log odds of prevalence moving northward, whilst the positive coefficient for month indicates an increase in the log odds of prevalence later in the year.

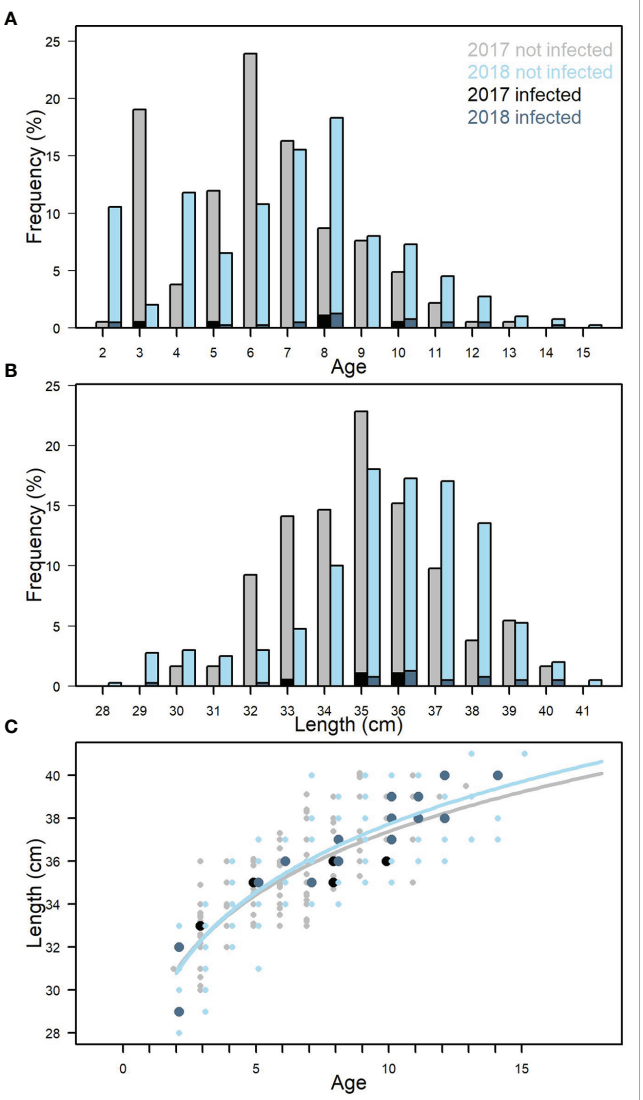


FIGURE 4 | Age distribution for all samples from 2017 and 2018 **(A)**. Length distribution for all samples from 2017 and 2018 **(B)**. Length-weight relationship for all samples. 2017 and 2018 **(C)**. Black and dark blue indicate fish infected with *Kudoa thyrsites*.

Sampling locations were classified into different regions within the study area (see **Tables 1**, **2**). The Faroese shelf had highest prevalence (8.2%, CI: 4.1-12.4%, n=170), followed by the British Area (2.7%, CI: 0-6.3%, n=75) and the Northern area (1.4%, CI: 1.4% 0-2.7%, n=289). A Chi-squared test of the 2x3 contingency table showed that prevalence was significantly associated with region ($p<0.05$). Since age was only just outside statistical significance in the logistic regression, we also examined differences categorically. The oldest fish (>10 years) had the highest prevalence (10.8%, CI: 4.2-17.5%, n= 83), followed by

medium (6-9 years) fish (3.1%, CI: 1.2-5.0%, n=322) and young (2-5 years) fish (2.8%, CI: 0.4-5.2%). A Chi-squared test on the contingency table showed a significant association between age category and prevalence ($p<0.01$).

Seawater Analyses

Water column samples were analysed from the Faroese shelf spanning a full seasonal cycle from February-November in 2018 (**Table 3**). During the year, temperature ranged from 6.2-10.5°C, peaking in September. Pre-bloom chlorophyll (chl < 1 μg L^{-1}) nitrate concentrations were 11.6 ± 0.4 μmol L^{-1} and drawn down to 3.6 μmol L^{-1} on 5th June corresponding to a first phytoplankton bloom peaking at 3.7 μg chl L^{-1}. A second larger phytoplankton bloom (6.6 μg chl L^{-1}) occurred on 21st August, followed by a rapid decline. DNA was successfully extracted from every sample and extract concentrations ranged from 1.2-8.4 ng μL^{-1} (average = 5.4 ng μL^{-1}). All samples successfully amplified for a PCR inhibition control with Ct scores ranging from 23.16 ± 0.14 to 24.12 ± 0.17, which in all cases deviated <3 Ct from a negative control (nuclease-free water) spiked with a control template. None of the water samples were positive for *K. thyrsites*.

DISCUSSION

Prevalence of *K. thyrsites* in Faroese Fishery

K. thyrsites was confirmed as the causative agent of myoliquefaction of Atlantic Mackerel within the Faroese wild fishery. Investigations of myoliquefaction in various fish species in Icelandic waters have identified *K. islandica* as the causative agent (Kristmundsson and Freeman, 2014), although it has not yet been identified in Atlantic mackerel. The morphology of *K. thyrsites* and *K. islandica* is quite distinct, where the former has one enlarged polar capsule, clearly visible in our samples (**Figure 3**). The vast majority of specimens obtained from a factory processing plant tested positive for *K. thyrsites* using both microscope smears and PCR. There was good statistical agreement between the two techniques, enabling us to apply qPCR to a large number of (>500) natural samples. It is unclear why we could not observe spores in a small fraction of the samples. There is some anecdotal evidence of spores disappearing in soft-flesh mackerel specimens (Levsen, personal communication), which could be related to spatial heterogeneity within the muscle sample itself. The focus of the present study was not to describe the intensity of infection. However, it is possible that quantifying variation of intensity across regions or age categories, along with manual muscle texture testing (Levsen et al., 2008) could explain some of the small discrepancies in detection. Future work integrating prevalence, intensity and muscle texture of *K. thyrsites* infected mackerel, and other *Kuoda* genera, is generally required (Giulietti et al. 2022).

There was spatial and temporal variability evident in the prevalence of *K. thyrsites* in mackerel comprising the Faroese wild fishery. Logistic regression modelling showed that both more northerly latitudes and later sampling months increased the log odds of detecting prevalence. Different regions were also statistically associated with *K. thyrsites*, with the shallow Faroese shelf environment displaying highest prevalence. Previous studies in the Northern North Sea have also documented temporal variability of *K. thyrsites* in mackerel (Levsen et al., 2008), including inter-annual differences (Levsen, 2015). Although our prevalence estimates are similar to those reported in the North Sea, we did not detect statistically significant inter-annual variability.

Separating spatial and temporal variability in migratory fish such as Atlantic mackerel remains challenging. For example in

TABLE 3 | Biogeochemical characteristics of Faroese shelf waters during eDNA survey of *K. thyrsites*.

Date *dd/mm/yyyy*	Temperature *°C*	Nitrate *μmol L^{-1}*	Chlorophyll *μg L^{-1}*	Inhibition Control (Ct)	*Kudoa Thyrsites*
20/02/18	6.23	11.76	0.25	23.42 ± 0.08	A
20/03/18	6.19	11.58	0.3	23.39 ± 0.14	A
03/04/18	6.32	11.03	1.07	23.43 ± 0.18	A
10/04/18	6.19	9.47	2.01	23.32 ± 0.04	A
17/04/18	6.51	9.46	1.95	23.27 ± 0.24	A
01/05/18	6.95	8.07	1.46	23.16 ± 0.15	A
22/05/18	7.6	4.88	2.2	23.23 ± 0.16	A
05/06/18	8.38	3.6	3.71	23.21 ± 0.08	A
21/06/18	8.77	6.55	0.84	23.26 ± 0.15	A
10/07/18	9.4	7.22	0.95	23.41 ± 0.05	A
24/07/18	9.79	*n.d.*	0.73	23.24 ± 0.18	A
31/07/18	10.09	6.93	*n.d.*	23.79 ± 0.77	A
21/08/18	10.39	*n.d.*	6.64	23.37 ± 0.18	A
04/09/18	10.45	7.54	0.76	23.72 ± 0.10	A
18/09/18	10.37	7.75	0.71	23.75 ± 0.19	A
16/10/18	9.6	8.73	0.48	24.12 ± 0.17	A
13/11/18	8.85	10.11	0.21	23.92 ± 0.14	A
27/11/18	8.52	10.68	0.14	23.94 ± 0.16	A

Presence or absence (P/A) of K. thyrsites was determined by qPCR. Inhibition Control is an independent assay of DNA extracts to confirm absence of K. thyrsites is not caused by qPCR inhibition from environmental samples (see Materials and Methods). Four technical PCR replicates were analysed for each sample and data are reported as the mean Ct scores ± 1 standard deviation. n.d. denoted missing data.

our dataset, the observed prevalence in the British Area is associated with sampling in January. However, the Faroese shelf and the area north of the Faroe islands both had sample coverage during September and October, with notably higher prevalence observed on the Faroese shelf. Specific factors that influence regional patterns of infection could be related to water mass properties characterising different oceanographic regimes. For example there are notable differences in temperature and salinity properties that comprise different water masses found to the north of the Faroe Islands, as well as there is variability in the relative composition of water masses among years (Hátún and Chafik, 2021). All of the samples collected north of Faroes are from an environment influenced by relatively cold Norwegian North Atlantic Water, while those on The Faroe Shelf are from an environment characterised by warmer and more saline waters.

Prevalence of *K. thyrsites* in mackerel was evident across the entire range of age classes sampled in the Faroese wild fishery. Prevalence was highest in larger and older fish (>10 years) and is consistent with studies from the North sea (Levsen, 2015). However, notably we also detected *K. thyrsites* in two and three year old fish, clearly demonstrating the potential for infection in younger adults. Presumably the likelihood of parasite-host encounters scale as a function of age, although migratory patterns into potentially infective areas may also contribute. Traditional stock migration patterns have shown that spawning occurs in the southern areas (close to Spain, France and Ireland) from February-July. Adult mackerel (>2-3 years) distribute to the north during the feeding migration phase in summer and can be found in an area extending from Gibraltar (36°N) up to Svalbard (78°N) to the areas east of Greenland (Jansen et al., 2016; Nøttestad et al., 2016). In late autumn the mackerel return towards the wintering areas around Shetland Isles and stay there during winter. In January the mackerel start their southward migration to the spawning grounds (Jansen et al., 2012) and we detected infection in January in the British area. Interestingly, no *K. thyrsites* was detected in mackerel from the Faroese Shelf late spring/early summer (May and July). The spatial and temporal patterns observed in our data appear to suggest that mackerel migrating into Faroese fishing grounds become infected in other areas. Our observations need to be interpreted cautiously within the context of the sampling regime. Further research is required to fully elucidate spatial and temporal patterns in the occurrence of infection.

Non-Detection of *K. thyrsites* in Seawater Samples

In the current study we did not detect the presence of *K. thyrsites* in Faroese shelf seawater samples. Although it is challenging to conclude absence from non-detection in PCR-assays, it seems unlikely that extraction or inhibition of seawater samples could adequately explain the ubiquitous non-detection observed in our study. In all samples tested, DNA concentrations in extracts were reasonably high and an independent extraction control confirmed there was no PCR-inhibition of seawater samples used in the present study. Furthermore, specific multiplex inhibition controls for quantitative PCR of Atlantic cod (*Gadus morhua*) using the same extraction method has not revealed any specific inhibition of seawater samples collected on the Faroese shelf (Salter et al., 2019). Failure of the extraction methodology to specifically extract DNA from the *K. thyrsites* target also seems unlikely. The Qiagen extraction kit used in this study includes a vigorous bead-beating step that has been applied previously to successfully extract *K. thyrsites* rDNA from seawater filters (Jones et al., 2016). The seawater samples used in this study were obtained from an archive of a coastal environmental DNA monitoring program (FAMEOS) and so spiking parallel water samples with the possible range of un-envisaged targets was not feasible. However, future studies targeting *K. thyrsites* in natural seawater samples may consider the addition of spores as an additional control measure.

The non-detection of *K. thyrsites* in annual seawater samples from the Faroese shelf support a hypothesis that Atlantic mackerel are not locally exposed to the parasite (**Table 3**). This is further supported by the circumstantial observation that *K. thyrsites* has not currently been observed in farmed Atlantic Salmon on the Faroese shelf, unlike other areas (St-Hilaire et al., 1997a; St-Hilaire et al., 1997b; St-Hilaire et al., 1997c; St-Hilaire et al., 1998; Moran et al., 1999b). The Faroese shelf is the shallowest environment in our survey area and corresponds to the highest prevalence of *K. thyrsites* (**Table 1**). Considering that practically all known life-cycles of myxosporeans involve annelid worms as an alternate host (Yokoyama, 2003), tight pelagic-benthic coupling on a tidally-mixed shelf might be considered to promote encounter rates between actinospores and migratory fish hosts. It is clear from seawater screening close to aquaculture facilities suffering from *Kudoa* spp. infections that myxospores can be detected in seawater samples and UV irradiation of raw seawater reduces infection (Jones et al., 2016). A seawater study of *K. yasunagai* in infected aquaculture areas appears to suggest some seasonality of myxospore abundances that were linked to water temperature and ecology of the alternate invertebrate host (Ishimaru et al., 2014). Our seawater survey covered the typical annual temperature range of the Faroese shelf and growth and decline of phytoplankton blooms that might influence invertebrate ecology. To the best of our knowledge our seawater survey is the first attempt to detect *K. thyrsite* myxospores in seawater samples in association with wild fish infections. One unexplored infection pathway is through feeding. In particular, sampling regimes that target intensive feeding in Southern spawning areas (Jansen et al., 2021) may help identify infection pathways occurring in Atlantic mackerel prior to their northward migration.

CONCLUSIONS

In the present study, we have investigated the prevalence of *K. thyrsites* in Atlantic mackerel in the Faroese fishery. Examination of soft-flesh (myoliquefaction) specimens obtained from a Faroese processing factory demonstrated *K. thyrsites* as the causative agent. We found excellent agreement between

microscope smears and PCR detection of *K. thyrsites*, allowing us to apply more rapid molecular detection methods on a large number (>500) of mackerel specimens caught from the wild Faroese fishery. We observed infection across the entire age range (2-14 years) of mackerel and statistical analyses indicated spatial and temporal, but not inter-annual, variability in prevalence. Highest prevalence was observed on the relatively shallow, tidally mixed Faroese shelf. It was not possible to detect *K. thyrsites* spores in seawater samples from the Faroese shelf, despite sampling across the entire range of biogeochemical conditions occurring throughout the year. Taken together, with the absence of *K. thyrsites* infection in farmed salmon on the Faroese shelf, our data support the hypothesis that infection likely occurs in southern spawning areas and infected fish migrate north into the Faroese fishery. Future work investigating fish and water column samples in these southern areas could help resolve the spatial and temporal dynamics of *K. thyrsites* prevalence in Atlantic mackerel.

DATA AVAILABILITY STATEMENT

The original contributions presented in the study are included in the article/supplementary material. Further inquiries can be directed to the corresponding author.

ETHICS STATEMENT

The samples were taken on sea onboard fishery or research vessels. The fish was cooled in RSW seawater onboard and later frozen on land. Thus all sampling occurred from already dead fish.

AUTHOR CONTRIBUTIONS

DH and IS developed the main ideas. EH constructed the maps and histograms. IS and DH wrote the manuscript with feed-back from EH. All authors approved the submitted version.

FUNDING

This work was funded by Fiskivinnugransking (Fisheries Research Fund of the Faroe Islands Grant number 16/00632) and Felagið Nótaskip (Faroese Pelagic Organisation), Faroe Islands. We thank them sincerely for making this work possible. The collection of environmental DNA samples from coastal time-series was financially supported through the FAMEOS project (Granskingarráðið).

ACKNOWLEDGMENTS

The samples of soft mackerel came from Varðin Pelagic. Tvøroyri and the samples 2017-2018 were provided by research vessel "Magnus Heinason" and different commercial pelagic fishery vessels. Initial qPCR-analysis (the 2015 sample of soft mackerel) was done by Dr. Jonhard Eysturskarð; the PCR-analysis of the 2017-18 samples and stomach was done at Inova by Fiskaaling. Otolith work was done by the staff of Havstovan. Dr. Jan A. Jacobsen commented on the manuscript and assistant Dagunn H.J. Clementsen helped with the figures. The authors are grateful for the excellent effort of all the crew and staff involved. We acknowledge the provision of DNA archive samples from the genomic observatory FAMEOS (Faroese Marine Ecosystem Monitoring Study) (PI: Ian Salter).

REFERENCES

Alarcon, C. R., Lee, H., Goodarzi, H., Halberg, N., and Tavazoie, S. F. (2015). N6-Methyladenosine Marks Primary microRNAs for Processing. *Nature* 519, 482–485. doi: 10.1038/nature14281

Americus, B., Lotan, T., Bartholomew, J. L., and Atkinson, S. D. (2020). A Comparison of the Structure and Function of Nematocysts in Free-Living and Parasitic Cnidarians (Myxozoa). *Int. J. Parasitol.* 50, 763–769. doi: 10.1016/j.ijpara.2020.04.012

Bachiller, E., Skaret, G., Nøttestad, L., and Slotte, A. (2016). Feeding Ecology of Northeast Atlantic Mackerel, Norwegian Spring-Spawning Herring and Blue Whiting in the Norwegian Sea. *PloS One* 11 (2), e0149238. doi: 10.1371/journal.pone.0149238

Berland, B. (2005). *Whole Mounts* (Malaysia: Occasional Publication No. 1. Institute of Oceanography Kustem), 1–54.

Cheetham, A. H., and Hazel, H. E. (1969). Binary (Presence–Absence) Similarity Coefficients. *Paleontology.* 43, 1130–1136.

El-Matbouli, M., Hoffmann, R. W., and Mandok, C. (1995). Light and Electron Microscopic Observations on the Route of Thetriactinomyxon-Sporoplasm of Myxobolus Cerebralis Fromepidermis Into Rainbow Trout Cartilage. *J. Fish. Biol.* 46, 919–935. doi: 10.1111/j.1095-8649.1995.tb01397.x

Funk, V. A., Rapp, M., Sojonky, K., Jones, S., Robinson, J., and Falkenberg and Miller, K. M. (2007). Development and Validation of an RNA- and DNAbased Quantitative PCR Assay for Determination of *Kudoa Thyrsites* Infection Levels in Atlantic Salmon *Salmo Salar*. *Dis. Aquat. Org.* 75, 239–249. doi: 10.3354/dao075239

Giulietti, L., Karlsbakk, E., Cipriani, P., Bao, M., Storesund, J. E., Marathe, N. P., et al. (2022). Long-Term Investigation of the 'Soft Flesh' Condition in Northeast Atlantic Mackerel Induced by the Myxosporean Parasite *Kudoa Thyrsites* (Cnidaria, Myxozoa): Temporal Trends and New Molecular Epidemiological Observations. *Fish. Res.* 248, 106221. doi: 10.1016/j.fishres.2021.106221

Giulietti, L., Mattiucci, S., Paoletti, M., Grevskott, D. H., Bao, M., Cipriani, P., et al. (2019). Morphological and Molecular Identification of a New *Kudoa Thyrsites* Isolate in Mediterranean Silver Scabbardfish *Lepidopus Caudatus*. *Dis. Aquat. Org.* 132, 125–134. doi: 10.3354/dao03316

Hansen, F. T., Burns, F., Post, S., Thygesen, U. H., and Jansen, T. (2018). Length Measurement Methods of Atlantic Mackerel (*Scomber Scombrus*) and Atlantic Horse Mackerel (*Trachurus Trachurus*) – Current Practice, Conversion Keys and Recommendations. *Fish. Res.* 205, 57–64. doi: 10.1016/j.fishres.2018.04.002

Hátún, H., and Chafik, L. (2021). And Larsen, KThe Norwegian Sea Gyre – A Regulator of Iceland-Scotland Ridge Exchanges. *Front. Mar. Sci.* 8, 1–15. doi: 10.3389/fmars.2021.694614

Henning, S. S., Hoffmann, L. C., and Manley, M. (2013). A Review of *Kudoa*-Induced Myoliquefaction of Marine Fish Species in South Africa and Other Countries. *S. Afr. J. Sci.* 109, 1–5. doi: 10.1590/sajs.2013/20120003

Ishimaru, K., Matsuura, T., Tsunemoto, K., and Shirakashi, S. (2014). Seasonal Monitoring of *Kudoa Yasunagai* From Seawater and Aquaculture Water Using Quantitative PCR. *Dis. Aquat. Org.* 108, 45–52. doi: 10.3354/dao02702

Jansen, T., Campbell, A., Kelly, C. J., Hátún, H., and Payne, M. R. (2012). Migration and Fisheries of North East Atlantic Mackerel (*Scomber Scombrus*) in Autumn and Winter. *PloS One* 7, 1–9. doi: 10.1371/journal.pone.0051541

Jansen, T., Post, S., Kristiansen, T., Oskarsson, G. J., Boje, J., MacKenzie, B. R., et al. (2016). Ocean Warming Expands Habitat of a Rich Natural Resource and Benefits a National Economy. *Ecol. Appl.* 26, 2021–2032. doi: 10.1002/eap.1384

Jansen, T., Slotte, A., dos Santos Schmidt, T. C., Sparrevohn, C. R., Jacobsen, J. A., and Kjesbu, O. S. (2021). Bioenergetics of Egg Production in Northeast Atlantic Mackerel Changes the Perception of Fecundity Type and Annual Trends in Spawning Stock Biomass. *Prog. Ocean.*, 16, 198. doi: 10.1016/j.pocean.2021.102658

Jones, S. R. M., Cho, S., Nguyen, J., and Mahony, M. (2016). Acquired Resistance to *Kudoa Thyrsites* in Atlantic Salmon Salmo Salar Following Recovery From a Primary Infection With the Parasite. *Aquaculture* 451, 457–462. doi: 10.1016/j.aquaculture.2015.10.002

Jones, S. R. M., Forster, I., Liao, X., and Ikonomou, M. G. (2012). Dietary Nicarbazin Reduces Prevalence and Severity of *Kudoa Thyrsites* (Myxosporea: Multivalvulida) in Atlantic Salmon *Salmo Salar* Post-Smolts. *Aquaculture* 342-343, 1–6. doi: 10.1016/j.aquaculture.2012.01.033

Kent, M. L., Andree, K. B., Bartholomew, J. L., El-Matbouli, M., Desser, S. S., Devlin, R. H., et al. (2001). Recent Advances in Our Knowledge of the Myxozoa. *J. Eukaryot. Microbiol.* 48, 395–413. doi: 10.1111/j.1550-7408.2001.tb00173.x

King, J. R., McFarlane, G. A., Jones, S. R. M., Gilmore, S. R., and Abbott, C. L. (2012). Stock Delineation of Migratory and Resident Pacific Hake in Canadian Waters. *Fish. Res.* 114, 19–30. doi: 10.1016/j.fishres.2010.12.024

Kovaleva, A. A., Shulman, S. S., and Yakovlev, V. N. (1979). Myxosporidians of the Genus Kudoa (Myxosporidia. Multivalvulea) From the Atlantic Ocean Basin. *Trudy. Zool. Inst. Akad. Nauk. SSSR.* 78, 42–64).

Kristmundsson, Á., and Freeman, M. A. (2014). Negative Effects of *Kudoa Islandica* N. Sp. (Myxosporea: Kudoidae) on Aquaculture and Wild Fisheries in Iceland. *Int. J. Parasitol.* 3 (2) 135–146. doi: 10.1016/j.ijppaw.2014.06.001

Langøy, H., Nøttestad, L., Skaret, G., Broms, C., and Fernö, A. (2012). Overlap in Distribution and Diets of Atlantic Mackerel (*Scomber Scombrus*), Norwegian Spring- Spawning Herring (*Clupea Harengus*) and Blue Whiting (*Micromesistius Poutassou*) in the Norwegian Sea During Late Summer. *Mar. Biol. Res.* 8, 442–460. doi: 10.1080/17451000.2011.642803

Langdon, J. S. (1991). Myoliquefaction Post-Mortem ('Milkyflesh') Due to *Kudoa Thyrsites* (Gilchrist) (Myxosporea:Multivalvulida) in Mahi Mahi, *Coryphaena Hippurus L. J.Fish. Dis.* 14, 45–54. doi: 10.1111/j.1365-2761.1991.tb00575.x

Lesnoff, M., and Lancelot, R. (2019) *R Package Aod: Analysis of Overdispersed Data, Version 1.3.1*. Available at: https://CRAN.R-project.org/package=aod.

Levsen, A. (2015). A Review of Kudoa Species (Myxozoa. Multivalvulida) Affecting Seafood Quality. With Emphasis on *K. Thyrsites* in Atlantic Mackerel (*Scomber Scombrus*). *J. Fish. Sci. Tech.*, 3–9. Nha Thrang University.

Levsen, A., Jørgensen, A., and Mo, T. A. (2008). Occurrence of Postmortem Myoliquefactive Kudoosis in Atlantic Mackerel. *Scombrus Scombrus* L. From the North Sea. *J. Fish. Dis.* 31, 601–611.

Lom, J., and Dyková, I. (2006). Myxozoan Genera: Definition and Notes on Taxonomy, Life-Cycle Terminology and Pathogenic Species. *Fol. Parasit.* 53, 1–36. doi: 10.14411/fp.2006.001

Meglitsch, P. A (1947). Studies on Myxosporidia from the Beaufort Region. II. Observations on Kudoa clupeidae (Hahn), gen. nov. *J. Parasitol.*. 33 (3), 271–277.

Moran, J. W. D., Margolis, L., Webster, J. M., and Kent, M. L. (1999a). Development of *Kudoa Thyrsites* (Myxozoa: Myxosporidia) in Netpen-Reared Atlantic Salmon Determined by Light Microscopy and a Polymerase Chain Reaction Test. *Dis. Aquat. Org.* 37, 185–193. doi: 10.3354/dao037185

Moran, J. W. D., Whitaker, D. J., and Kent, M. L. (1999b). A Review of the Myxosporean Genus *Kudoa* Meglitsch, (1947) and its Impact on the International Aquaculture Industry and Commercial Fisheries. *Aquac.* 172 (1-2), 163–196. doi: 10.1016/S0044-8486(98)00437-2

Moran, J. D. W., Whitaker, D. J., and Kent, M. L. (1999c). Natural and Laboratory Transmission of the Marine Myxozoan Parasite *Kudoa Thyrsites* to Atlantic Salmon. *J. Aquatulture Anim. Health* 11, 110–115. doi: 10.1577/1548-8667(1999)011<0110:NALTOT>2.0.CO;2

Nøttestad, L., Utne, K. R., Óskarsson, G. J., Jónsson, S. T., Jacobsen, J. A., Tangen, Ø., et al. (2016). Quantifying Changes in Abundance. Biomass. And Spatial Distribution of Northeast Atlantic Mackerel (*Scomber Scombrus*) in the Nordic Seas From 2007 to 2014. *ICES. J. Mar. Sci.* 73 (2), 359–373. doi: 10.1093/icesjms/fsv218

Ogawa, K., Delgahapitiya, K. P., and T. and Wakabayashi, H. (1992). Histological Studies on the Host Response to Myxobolus Artus Akhmerov 1960 (Myxozoa: Myxobolidae) Infection in the Skeletal Muscle of Carp, Cyprinus Carpio L. *J. Fish. Biol.* 41, 363–371. doi: 10.1111/j.1095-8649.1992.tb02665.x

Okamura, B., Gruhl, A., and Bartholomew, J. L. (2015). "An Introduction to Myxozoan Evolution, Ecology and Development," in *Myxozoan Evolution, Ecology and Development*, 1–20. Switzerland: Springer Link International

Ólafsdóttir, A. H., Utne, K. R., Jacobsen, J. A., Jansen, T., Óskarsson, G. J., Nøttestad, L., et al. (2019). Geographical Expansion of Northeast Atlantic Mackerel (*Scomber Scombrus*) in the Nordic Seas From 2007 to 2016 was Primarily Driven by Stock Size and Constrained by Low Temperatures. *Deep-Sea. Res. Part II.* 159, 152–168. doi: 10.1016/j.dsr2.2018.05.023

Rósza, L., Reiczigel, J., and Majoros, G. (2000). Quantifying Parasites in Samples of Hosts. *J. Parasitol.* 86, 228–232. doi: 10.1645/0022-3395(2000)086[0228:QPISOH]2.0.CO;2

RStudio Team (2020). *RStudio: Integrated Development for R. RStudio* (Boston, MA: PBC).

Salter, I., Eliasen, S., Joensen, M., Kristiansen, R., Steingrund, P., and Vestergaard, P. (2019). Quantitative Environmental DNA Survey Maps Regional Biomass of Atlantic Cod in Oceanic Waters. *Nat. Commun. Bio*. 2, 461–470. doi: 10.1038/s42003-019-0696-8

St-Hilaire, S., Hill, M., Kent, M. L., Whitaker, D. J., and Ribble, C. (1997b). A Comparative Study of Muscle Texture and Intensity of *Kudoa Thyrsites* Infection in Farm-Reared Atlantic Salmon. *Salmo Salar. On* the Pacific Coast of Canada. *Dis. Aquat. Org.* 31, 221–225. doi: 10.3354/dao031221

St-Hilaire, S., Ribble, C., Whitaker, D. J., and Kent, M. L. (1997a). Evaluation of a Nondestructive Diagnostic Test for Kudoa Thyrsites in Farmed Atlantic Salmon (*Salmo Salar*). *Aquac.* 156, 139–144. doi: 10.1016/S0044-8486(97)00081-1

St-Hilaire, S., Ribble, C., Whitaker, D. J., and Kent, M. L. (1997c). Prevalence of *Kudoa Thyrsites* Sexually Mature and Immature Pen-Reared In Atlantic Salmon (*Salmo Salar*) in British Columbia .Canada. *Aquaculture* 162, 69–77. doi: 10.1016/S0044-8486(98)00208-7

St-Hilaire, S., Ribble, C., Whitaker, D. J., and Kent, M. L. (1998). Prevalence of *Kudoa Thyrsites* in Sexually Mature and Immature Pen-Reared Atlantic Salmon (Salmo Salar) in British Columbia, Canada. *Aquaculture* 162, 69–77. doi: 10.1016/S0044-8486(98)00208-7

Truett, G. E., Heeger, P., Mynatt, R. L., Walker, J. A., and Warman, M. L. (2000). Preparation of PCR-Quality Mouse Genomic DNA Wit Hot Sodium Hydroxide and Tris (HotSHOT). *Biotechniques.* 29 (1), 52–54. doi: 10.2144/00291bm09

Whipps, C. M., and Kent, M. L. (2006). Phylogeography of the Cosmopolitan Marine Parasite *Kudoa Thyrsites* (Myxozoa: Myxosporea). *J. Eukaryot Microbiol.* 53, 364–373. doi: 10.1111/j.1550-7408.2006.00114.x

Yokoyama, H. (2003). A Review: Gaps in Our Knowledge on Myxozoan Parasites of Fishes. *Fish. Path.* 38 (4), 125–136s. doi: 10.3147/jsfp.38.125

Conflict of Interest: The authors declare that the research was conducted in the absence of any commercial or financial relationships that could be construed as a potential conflict of interest.

Publisher's Note: All claims expressed in this article are solely those of the authors and do not necessarily represent those of their affiliated organizations, or those of the publisher, the editors and the reviewers. Any product that may be evaluated in this article, or claim that may be made by its manufacturer, is not guaranteed or endorsed by the publisher.

Copyright © 2022 Højgaard, í Homrum and Salter. This is an open-access article distributed under the terms of the Creative Commons Attribution License (CC BY). The use, distribution or reproduction in other forums is permitted, provided the original author(s) and the copyright owner(s) are credited and that the original publication in this journal is cited, in accordance with accepted academic practice. No use, distribution or reproduction is permitted which does not comply with these terms.

frontiers | Frontiers in Marine Science

TYPE Original Research
PUBLISHED 29 August 2022
DOI 10.3389/fmars.2022.822343

Check for updates

OPEN ACCESS

EDITED BY
Peter Grønkjær,
Aarhus University, Denmark

REVIEWED BY
Jens Tang Christensen,
Aarhus University, Denmark
William Gerald Ambrose Jr.,
Coastal Carolina University,
United States

*CORRESPONDENCE
Petur Steingrund
peturs@hav.fo

SPECIALTY SECTION
This article was submitted to Marine Ecosystem Ecology, a section of the journal Frontiers in Marine Science

RECEIVED 25 November 2021
ACCEPTED 08 August 2022
PUBLISHED 29 August 2022

CITATION
Matras U, Salter I, Larsen KMH, Gaard E and Steingrund P (2022) Relationship between plankton dynamics and growth of the long-lived clam *Arctica islandica* on the Faroe shelf.
Front. Mar. Sci. 9:822343.
doi: 10.3389/fmars.2022.822343

COPYRIGHT
© 2022 Matras, Salter, Larsen, Gaard and Steingrund. This is an open-access article distributed under the terms of the Creative Commons Attribution License (CC BY). The use, distribution or reproduction in other forums is permitted, provided the original author(s) and the copyright owner(s) are credited and that the original publication in this journal is cited, in accordance with accepted academic practice. No use, distribution or reproduction is permitted which does not comply with these terms.

Relationship between plankton dynamics and growth of the long-lived clam *Arctica islandica* on the Faroe shelf

Una Matras[1,2], Ian Salter[1], Karin Margretha H. Larsen[1], Eilif Gaard[1] and Petur Steingrund[1]*

[1]Faroe Marine Research Institute, Tórshavn, Faroe Islands, [2]Glasir, Tórshavn College, Tórshavn, Faroe Islands

Marine ecosystem dynamics can vary on timescales ranging from months to centuries, but many observational data are limited to just a few decades. The bivalve *Arctica islandica* may live up to five centuries depositing annual growth increments in its shells which can serve as an indicator for ecosystem productivity. In the present study, 154 specimens of *A. islandica* were collected on the Faroe Shelf and standardised annual growth increments for 143 of them – 44 from coastal stations and 99 from shelf stations – were compared with climatic, oceanographic and biological variables. *A. islandica* growth from coastal and shelf stations was not correlated with basin-scale climate indices (the AMO index, the NAO index, the AO index or the subpolar gyre index) or, more locally, with windspeed or sea surface temperature on the Faroe Shelf. For the shelf stations there was a significant negative correlation between *A. islandica* growth and the volume transport of the Faroe Current flowing just north of Faroe Islands (r = -0.62). There was a weak nonsignificant positive correlation with an index of primary production on the Faroe Shelf (r = 0.31) and a strong negative correlation with a zooplankton biomass index in mid-summer (r = -0.76). There was also a strong positive correlation between *A. islandica* growth and the biomass of the bottom-feeding fish species *Melanogrammus aeglefinus* two years later (r = 0.62). These results seem to suggest that *A. islandica* growth may represent the amount of fresh phytoplankton that reaches the near-bottom water layers and could probably be regarded as a proxy for the strength of pelagic-benthic coupling that is modulated through phytoplankton-zooplankton interactions in the overlying water. Our results highlight the potential for *A. islandica* to serve as a long-term proxy for linking variability in pelagic ecosystem dynamics to demersal fish stocks.

KEYWORDS

***Calanus finmarchicus*, faroe shelf, bottom feeding fish, phytoplankton, zooplankton, *Arctica islandica* growth, ocean currents**

Introduction

Indications from fish stock dynamics demonstrate centennial-scale variations in marine ecosystem dynamics and highlight that statistical correlations based on short time-series may be an artefact of the observational period e.g. Myers (1998). The Norwegian spring spawning herring (*Clupea harengus*) (Nakken, 2008; Sætersdal, 2008), along with the Bohuslän herring, have been observed for several centuries and demonstrate transitions between warm periods with good herring catches and cool periods with virtually no catches (Alheit and Hagen, 1997; Toresen and Østvedt, 2000; Nakken, 2008), although stock collapse in the 1960's has been partially attributed to intense fishing pressure (Dragesund et al., 2008). Atlantic cod (*Gadus morhua*) (Kurlansky, 1998; see also Nakken, 2008) is another example. One of the largest cod stocks was the Northern cod off Newfoundland, Canada (Robichaud and Rose, 2004) and was fished for over 500 years until it collapsed in the beginning of the 1990s, following intensive fishing since the 1950s (Drinkwater, 2002; Rose, 2005). Although regarded as a classical example of overfishing long-term variability in environmental factors (*e.g.* low temperatures) were also responsible (Drinkwater, 2002). There are also indications of ecosystem variability of the Faroe shelf with evidence of long-term variations in cod stock size since 1860s (ICES, 2016), haddock (*Melanogrammus aeglefinus*) stock size since 1920s (ICES, 2016) and catches of pilot whales (*Globicephala melas*) since 1709 (Hátún et al., 2009). Cod and haddock biomasses were exceptionally low since 2006 (ICES, 2021) and seabirds declined much in abundance in the 1970-1980s (Gaard et al., 2002). Although fish catch statistics are available from 1903 (www.ices.dk), and stock assessments of a select fish species extend back to the first half of the 20th century, most stock assessments and survey data only extend back to the 1980's. Therefore methods that can serve as indicators over longer timescales are warranted. Investigating the growth dynamics of the long-lived clam, *Arctica islandica*, represents one such possibility. *A. islandica* feeds on phytoplankton and deposits annual growth rings that can serve as an indicator for marine producitivity (Witbaard et al., 2003). Phytoplankton are at the base of the marine foodweb and temporal and spatial variability in plankton characteristics is a useful framework to address larger-scale ecosystem dynamics.

Previous studies on the Faroese shelf have observed positive correlations between phytoplankton production and higher trophic levels, including cod production (Steingrund and Gaard, 2005). It is likely such connections are mediated through the abundance of key prey items, such as sandeels, an important food for cod (Rae, 1967; Sørensen, 2021), which are also positively correlated with phytoplankton production (Eliasen et al., 2011). However, after 2005 cod production on the Faroe Shelf decreased in relation to phytoplankton production (ICES, 2021), corresponding to higher summer zooplankton abundances (ICES, 2021). It has been hypothesised previously (Witbaard et al., 2003) that zooplankton dynamics can mediate demersal fish production through enhanced grazing activity, which reduces the downward flux of phytoplankton to the sediments. The surface export of certain phytoplankton functional types, *e.g.* diatom resting spores, can transport significant amounts of labile carbon to the sediments (Salter et al., 2007; Salter et al., 2012; Rembauville et al., 2016) and influence the growth of benthic organisms through the provision of energy rich compounds (Wolff et al., 2011; Rembauville et al., 2018). Hence, bottom feeding fish like cod and haddock (Sørensen, 2021) may be expected to be negatively affected by high zooplankton concentrations, but this needs to be substantiated further.

The ocean quahog (*Arctica islandica* L.) is a long-lived (up to 500 years, Butler et al., 2013) bivalve mollusc, which inhabits the continental shelves in the North Atlantic Ocean including the Faroe Shelf (Bonitz et al., 2018). It feeds on phytoplankton (Ballesta-Artero et al., 2017) in the vicinity of the seafloor (Witbaard et al., 2003) and grows continuously throughout its life depositing annual growth increments (see e.g. Scourse et al., 2006). The width of these annual growth rings represents an archive of the feeding conditions of the animal during its life. Similar features can be seen in other bivalves as well (Witbaard et al., 2005; Reynolds et al., 2017). The rings are normally very distinct because the animal only feeds during the spring/summer (April to August) and presumably rests buried in the sediment during the rest of the year. There tends to be a high degree of synchronization in growth between individuals on specific sites (Schöne et al., 2003a), but there might be large differences in growth between adjacent sites (Witbaard, 1996) although a common signal may be discernible for distances up to at least 80 km (Butler et al., 2009). Large differences between individual shells may be observed in changing environments and complex hydrography (Epplé et al., 2006).

Several studies show such growth chronologies for various locations in the North Atlantic, e.g., Witbaard et al. (2003) and Bonitz et al. (2018). The *A. islandica* growth chronologies from different sites in the NE Atlantic are apparently weakly correlated and do not necessarily correlate with the same local or regional drivers. The *A. islandica* growth near the Isle of Man correlated positively with seawater temperature, but was also influenced by stratification (Butler et al., 2010). The *A. islandica* growth in northern Norway also correlated positively with sea surface temperature (Mette et al., 2016). A positive correlation between *A. islandica* growth and the winter NAO index (high temperature, high NAO index), was observed at sites in the North Sea and on the Norwegian coast (Schöne et al., 2003a). A positive relationship between phytoplankton production and *A. islandica* growth was reported for the Faroe Shelf (Bonitz et al., 2018). At a site on the north coast of Iceland, no single

environmental driver was discernible (Butler et al., 2013). On the other hand, negative correlations between *A. islandica* growth and temperature was observed in the North Sea, since cold winters reflected nutrient enrichment (Schöne et al., 2003b). A negative relationship between *A. islandica* growth and sediment suspension was observed in the North Sea (Witbaard et al., 2005). Also, a negative correlation was found between *A. islandica* growth and the abundance of zooplankton, although no relationship was found for phytoplankton (Witbaard et al., 2003).

The above studies indicate that local conditions may affect the *A. islandica* growth, but such shortcomings may be overcome by increasing the sampling area. A study compiled growth time series of *A. islandica* and *G. glycymeris* from eight locations west of Scotland/England to construct a composite index of bivalve growth that reflected a common environmental driver, in this case anomalies in sea surface temperature (Reynolds et al., 2017). Results can also be improved by taking other variables into account. Another study in northern Norway combined *A. islandica* growth with an oxygen isotope record and in this way obtained a closer relationship with large-scale North Atlantic sea surface temperatures (Mette et al., 2016).

The Faroe Plateau is located approximately mid-way between Iceland and Scotland (Figure 1). Deep Norwegian Sea Water dominates below 500 m, whereas the shallower water masses are dominated by Atlantic water from the North Atlantic Current, which basically flows in a north-easterly direction past the Faroes (Hansen and Østerhus, 2000). The Faroe Shelf is a much smaller area inside the 100-130 m contour that is characterised by strong tidal currents, which make the water column nearly homogeneous with regards to temperature and salinity (Hansen and Meincke, 1984; Gaard et al., 1998; Hansen et al., 1998; Larsen et al., 2008). The tidal currents also induce a clockwise residual circulation around the islands (Gaard and Hansen, 2000; Larsen et al., 2008) that contributes in maintaining a persistent tidal front (Gaard et al., 1998; Larsen et al., 2009) separating the Faroe Shelf from the outer offshore surroundings. The annual variability in the magnitude of the primary production on the Faroe Shelf is not fully understood, but the primary production tends to be higher in cold years (Gaard, 2003) and the onset of the spring bloom depends on hydrographic conditions (Eliasen et al., 2016; Eliasen et al., 2019), see also Eliasen et al. (2017a); Eliasen et al. (2017b). The shelf ecosystem has its own planktonic community that in terms of species composition and production is different from the surrounding oceanic environment (Gaard, 1996; Gaard et al., 1998; Gaard, 1999; Gaard, 2000). A rich benthic fauna and forage fish, such as sandeels, Norway pout and blue whiting support the local cod, haddock and saithe stocks (Steingrund and Gaard, 2005; Steingrund et al., 2009; ICES, 2021), which are vital to the local economy.

There has already been conducted a study of *A. islandica* growth on the Faroe Shelf (Bonitz et al., 2018) that was based on results from two locations. In the present study a large number of *A. islandica* specimens (154) have been sampled from seven sites on the Faroe Shelf and in coastal waters. The objective of the present study is to explore the potential to use *A. islandica* growth as a long-term ecosystem indicator by comparing with various atmospheric and oceanographic features and, more locally, with the plankton characteristics on the Faroe Shelf as well as biomass metrics of selected fish species. We hypothesize that the *A. islandica* growth will be negatively correlated with zooplankton biomass and positively correlated with bottom-feeding fish like flatfish and haddock (*Melanogrammus aeglefinus*) (Sørensen, 2021).

Materials and methods

Sampling of Arctica islandica

The specimens of *Arctica islandica* from the sites V, O, H (Figure 1) were collected by divers during spring 2010 (Table 1). The shells from site K were caught as bycatch on longlines in June 2011 by Faroese fishermen, just north of the island of Kalsoy. The shells from sites N and S were caught on longlines during the summer 2014 and 2015, respectively. The shells from site E (east) were collected as bycatch in a dredge fishery for *Aequipecten opercularis* in December 2012 and they were dead specimens unlike the specimens from the other sites that were alive when sampled. Since they were not overgrown with organisms and both shells were attached it was assumed that they had died during late summer or autumn 2012 due to the dredging activity. This growth ring was disregarded because it might not have been complete and the last valid growth ring was therefore for 2011. A. *islandica* siphons are sometimes observed in the dredged catch (U. Matras, personal observation) and the shells might have died because they could no longer feed without siphons and/or avoid predation by starfish. It is unlikely that the shells had been buried in the sediments for years (and therefore had avoided biofouling) because the dredge was designed to capture *Aequipecten opercularis* that are epibenthic. Also the shells showed no signs of black coloration due to iron sulfides that would be expected if they had been buried deeply in the sediments. Since most *A. islandica* shells in the dredged catch were either overgrown or detached we believe that setting the terminal year for site E to 2011 is the best we can do.

Samples were frozen and later thawed to determine the biometric characteristics of the individuals. Shell length (longest anterior-posterior dimension), height (deepest dorsoventral dimension) and width (widest lateral dimension) were measured with vernier callipers to the nearest 0.1 mm, and the wet meat weight was determined to the nearest 0.1 g. Dry shell weights were measured to the nearest 0.1 g.

10.3389/fmars.2022.822343

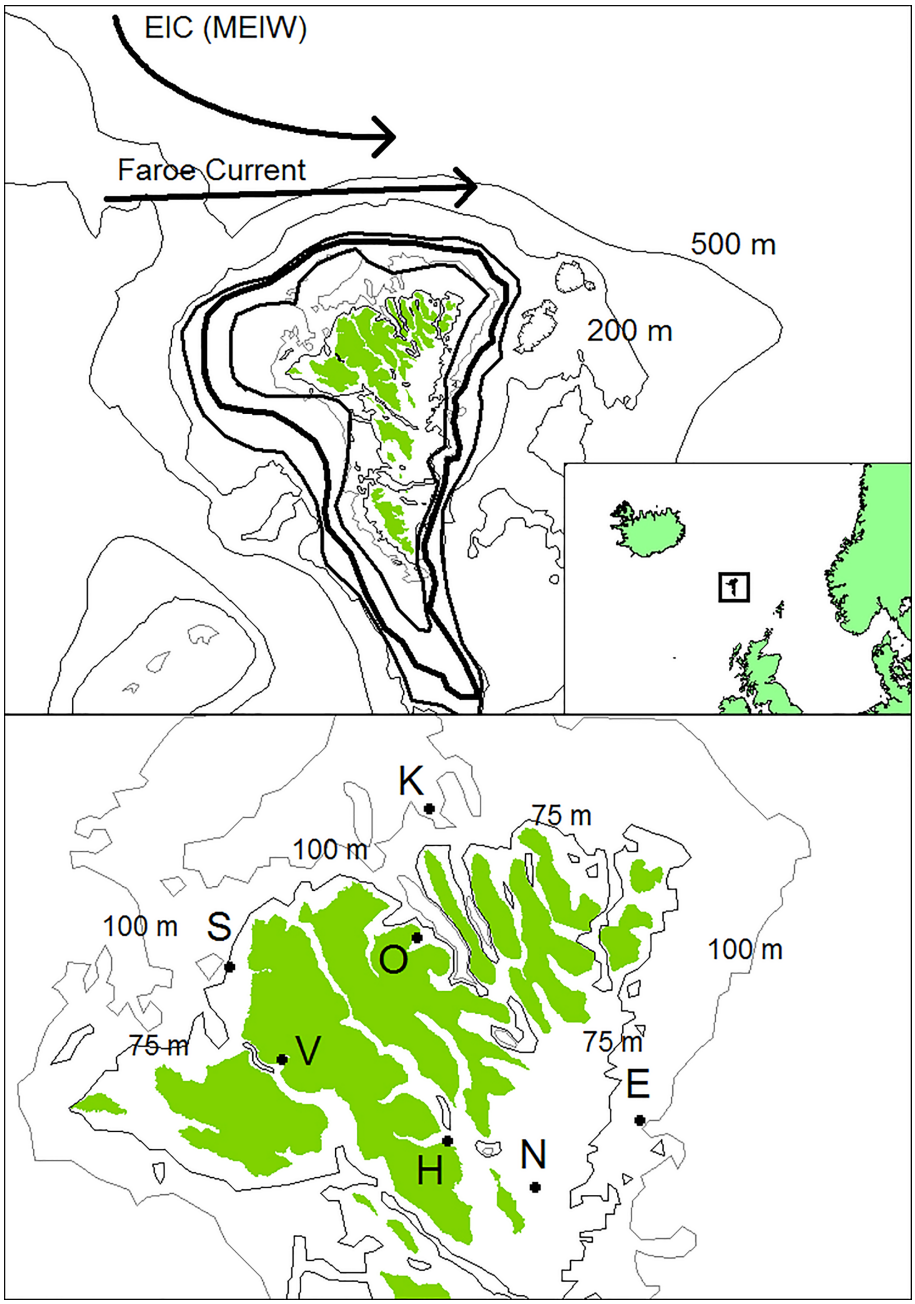


FIGURE 1
Locations of the sites where the *A. islandica* specimens were collected. The position of the tidal front (+/- 1 SD) is indicated by thick lines (based on Larsen et al., 2009). The location of the Faroe Current and the East Icelandic Current (EIC) or Modified East Icelandic Water (MEIW) is also shown. Thin lines show 75, 100, 200 and 500 m depth contours.

Age determination

The procedure used for age determination was the "Acetate Peel Method" as developed by Ropes (1987). The left valve of a pair was selected for sectioning since it has a single prominent tooth in the hinge. The tooth contains annuli useful in confirming counts made in the valve portion. Each valve was marked on the ventral margin at a point from the posterior end equal to one-third of the valve length. This oriented sectioning through the umbo and parallel to the broadest tooth surface (Figure 2). The valve was oriented with the tooth toward the front of the saw machine and was positioned to cut from the

TABLE 1 Description of the *Arctica islandica* sample locations (sites) as well as number of shells sampled (N) and used in the study (N2) and time span in years of the oldest individual for each site. The true age is 15 years older than the depicted age.

Site	Name	Lat	Lon	Depth (m)	Date	Met.	N	N2	Start	End
K	Kallur	62°25' N	6°48' W	80-110	15. July 2011	LL	46	42	1727	2010
E	East	62°04' N	6°20' W	100	1. Dec. 2012	DR	30	28	1613	2011
S	Saksun	62°15' N	7°17' W	70	10. July 2015	LL	45	40	1860	2014
N	Nólsoy	62°00' N	6°35' W	42-62	8. May 2014	LL	24	24	1849	2014
V	Vestmanna	62°09' N	7°10' W	Ca. 25	5. Feb. 2010	DI	11	8	1862	2009
O	Oyndarfjørður	62°16' N	6°51' W	15-22	19. May 2010	DI	7	7	1947	2009
H	Hvítanes	62°03' N	6°47' W	20-28	21. May 2010	DI	5	5	1841	2009

The method used for collecting the shells included longlining (LL), dredging (DR) and diving (DI).

mark on the ventral margin through the middle of the tooth, or immediately beside the posterior edge of the tooth.

The cut valves that included the hinge tooth were embedded in an epoxy resin. The mixed epoxy was poured into folio moulds to a depth of about half to one cm. When lowering the valve into the epoxy, the cut surface was pressed down onto the mould bottom to force out bubbles. After an overnight hardening period, the embedded valves were removed from the moulds.

A grinding machine was used to obtain a flat, smooth surface on the embedded cut surfaces of the valves. Five successively finer grits (180, 500, 600, 800 and 1200) of carbide paper were used for grinding and polishing the surface. Most of the grinding was done with the coarse grit paper to remove epoxy and to expose the broadest area of the tooth; the finer grits were used to minimize scratches from the coarser grit papers.

After polishing the code numbers for each valve were engraved into the epoxy. These numbers were automatically transcribed onto the acetate peel during the next step. The polished block face was then placed in or flooded with a solution of citric acid and hydrochloric acid (in the proportion 0.625% and 0.75%) for one to two minutes, depending on the size of the shell, to etch the valve surfaces and subsequently rinsed in distilled water, taking care not to damage the etched surfaces. The block was left to dry for at least an hour or until the next day.

Acetate peels of type TACPHAN N 882 GL 50 MICRON were made by supporting the etched block with the surfaces uppermost and level. Acetone was pipetted onto the specimen and had to flood completely without bubbles for a successful peel. An acetate sheet was laid over the surface. After at least a one-hour drying period, the acetate sheet was peeled off and put

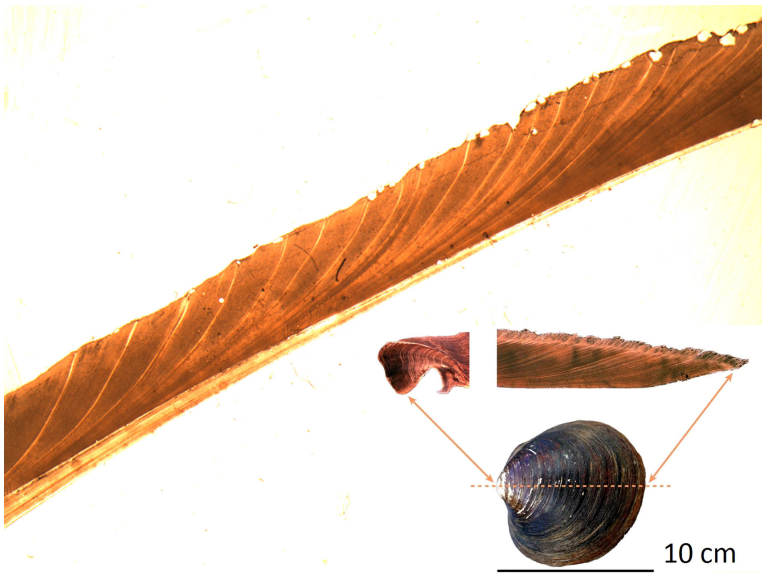


FIGURE 2
Photograph of the growth rings of a part of a typical *A. islandica* shell on the Faroe Shelf.

between two object glasses for examination. Examination of the acetate peel was carried out under a light stereomicroscope Leica M80 and the image was digitized with the Camera Q Imaging, Retiga 2000R, FAST 1394. Annual growth increment widths were measured with the software Image-Pro Plus, Version 7.0 for Windows™.

Detrending

A detrending procedure was applied to the raw growth data. The width of the growth rings of *A. islandica* increases over the first five-ten years of life and decreases thereafter with increasing age (Stott et al., 2010). In order to extract year-to-year variations in growth rate it is necessary to remove the ontogenetic growth trend. This can either be done by fitting growth curves to each individual or estimating a common growth curve for all shells in a particular area, *i.e.*, a regional curve (RCS: regional curve standardization). This latter approach has the advantage to better reflect long-term changes in growth and is used in this study. The large number of shells makes such an approach feasible. It may be difficult to fit growth curves to the whole life of the shells and the first 15 rings were therefore excluded, *i.e.*, all shells were 15 years older than the number of rings presented in the results. We used the program ARSTAN (Cook and Krusic, 2007), version 44h2 for Windows XP™ to estimate the regional growth curves and the residuals (measurements divided by the regional curve), see also Cook (1985). This program was originally developed for tree-ring analyses and commonly used for *A. islandica*, *e.g.* Bonitz et al. (2018). In the individual detrending procedure we used option 1, *i.e.*, a negative exponential function: growth index = a*exp(-b(t))+k, where a, b, and k (positive) were fitted constants and t denoted growth ring number. For shells where this function did not work, the Hugershoff growth function was used, see below. In the regional detrending we used the Hugershoff growth equation, *i.e.*, growth index = $a(t+p)^b$*exp(-c(t+p))+k, where a, b, c, p and k were fitted constants and t denoted growth ring number with a potential offset with the integer p.

Cross-dating

In cases when a few tens of shells are evaluated a cross-dating procedure is normally performed where false or missing rings are identified by comparing with other shells. Also, starting with live-caught shells (with known end year) and matching dead shells (with unknown end year) to the growth pattern of live-caught shells, long term growth chronologies are constructed (see Bonitz et al., 2018). In this study the end year was known for all shells because they were either collected alive or assumed to be dead the previous year. Although other published studies have reported high correlations between the growth of individual shells (Schöne et al., 2003a) this appeared to be much more diffuse in our material leaving it difficult to identify years with unusually wide or narrow bands (marker years) (Butler et al., 2009). Preliminary results from the COFECHA program (Cook and Holmes, 1986) suggested that there was no simple way to match the growth of individual shells to each other without excluding many shells from the material and/or deleting or adding a number of growth rings for individual shells. This selection process may be difficult to perform based on growth rings alone in the absence of absolutely dated growth years. However, the high number of shells was considered to represent an alternative way to detect a common signal even though the correlation between individual shells was low and this procedure was followed in this study. The technique of increasing the number of observations in order to get higher representativeness and higher precision is a fundamental principle in statistics (*e.g.* Motulsky, 2018).

Construction and validation of growth indices

In order to take potential effects of seawater depth into account the material was split up into coastal sites (NVOH) and shelf sites (KES). The pooled data for the shelf sites and coastal sites were treated by the ARSTAN program. The program estimated the regional curves for these two sites and the Hugershoff growth equation was used because initial analyses suggested that this growth function never became negative or showed erroneous results. We did not use data adaptive growth functions such as splines, since these functions may just follow the data and not detect important signals, in this case deviations from the general trend. The ratio of the individual growth increments in relation to the expected ontogenetic growth (from the RCS curve) was used as the growth index. The robust (bi-weight) procedure was used in order to avoid the unwanted effects of potential outliers and the program also provided bootstrapped confidence intervals for the growth indices. The standard (std) growth index was used with no variance stabilization. We also quantified the differences in growth between the individual *A. islandica* sites in an eastward (clockwise) direction. This could be done by averaging sites E and N and subtracting the average of sites S and K. However, this procedure would require the existence of all four data points in order to be calculated and the time series would end in 2010. Instead we assigned the S-K-E-N sites the x-values of 1, 2, 3 and 4, respectively, and the y-values of the *A. islandica* growth and calculated the slope of the regression line (y versus x). This was done for each year separately. For example, a positive slope showed that sites E and N grew faster than sites S and K. The benefit of this approach was that the time series could be extended to 2013 although the last three data points were associated with higher uncertainty.

When evaluating the robustness of the *A. islandica* growth indices we used the method presented by Stott et al. (2010), which is based on references presented in the paper. Stott et al. (2010) used the Expressed Population Signal (EPS), which is a signal-to-total variance ratio: EPS = nr/(nr+(1-r)), where r is the average correlation coefficient of all combinations of growth series for individual shells and n is the number of shells covering a specified time interval. The ARSTAN program also provided the EPS values.

The regional curve standardization (RCS) procedure is normally regarded to preserve the long term, decadal or centennial, variability in the growth time series of *A. islandica* (*e.g.*, Butler et al., 2013). However, in cases where slowly growing individuals attain the oldest ages the growth time series may show an increasing growth trend over time as confirmed by preliminary investigations of the material. The problem was partly avoided by excluding the 11 oldest individuals (born prior to 1825).

Environmental data

Sea surface temperature and the tidal front

A data series of sea surface temperature, extending from 1914 to 1969 and 1991 to 2014 was obtained from two coastal stations as presented in Larsen et al., 2008 (their Figure 8A). For the analysis herein, only the April to August seasonal mean was selected since the growth of *A. islandica* in Faroese waters is restricted to this period (Bonitz et al., 2018).

To determine the hydrographic environment at the *A. islandica* sites, we estimated location and variance of the tidal front based on Larsen et al. (2009). They used seven years of underway SST data from R/V Magnus Heinason, 65 Towed Temperature Wire sections and available CTD data from several years on the Faroe Shelf (including standard hydrographic sections crossing the shelf) to determine the typical location and variation of the front. The findings of Larsen et al. (2009) compared well with a more recent analysis by Eliasen et al. (2017a) using near-surface satellite chlorophyll data.

NAO index

North Atlantic Oscillation (NAO) Index Data were obtained from the Climate Analysis Section, NCAR, Boulder, USA, Hurrel and Deser (2009) (updated regularly). Accessed 22 November 2021.

AO index

The Arctic Oscillation index was obtained as an ncep analysis product and obtained from the website:

https://www.cpc.ncep.noaa.gov/products/precip/CWlink/daily_ao_index/monthly.ao.index.b50.current.ascii.table on 14. February 2022. The average of all twelve months was used.

AMO index

The Atlantic Multidecadal Oscillation index (Trenberth et al., 2021), unsmoothed from the Kaplan SST V2, calculated at NOAA PSL1, http://www.psl.noaa.gov/data/timeseries/AMO/, was downloaded 9. March 2022. The average of all twelve months was used.

Subpolar gyre index

The subpolar gyre index, based on satellite altimetry, was taken from Hátún and Chafik (2018) with updates and extended back to 1960 with a linear regression 1994-2003 against the data in Hátún et al. (2005).

Windspeed data

Windspeed data for the Faroe Shelf (lon = -7.5 dec. deg. lat = 61.9033 dec. deg) was obtained from 'http://www.esrl.noaa.gov/psd/data/gridded/data.ncep.reanalysis.html'. Dataset_title = 'NCEP-NCAR Reanalysis 1'. Title = 'mean daily NMC reanalysis (1948)'. Description = 'Data is from NMC initialized reanalysis (4x/day). It consists of T62 variables interpolated to pressure surfaces from model (sigma) surfaces.' The average of all twelve months was used.

Faroe current volume transport

As an indicator of the strength of the North Atlantic drift, we use data for the Faroe Current volume transport. The Faroe Current is the largest of three Atlantic inflow branches towards the Nordic seas and volume transport is monitored just north of the Faroe Shelf (Hansen et al., 2015; Østerhus et al., 2019). The volume transport estimate is based on a combination of *in situ* Acoustic Doppler Current Profiler measurements (initiated in 1997), hydrographic observations and satellite altimetry sea level anomaly (since 1993) as described in Hansen et al. (2015).

Phytoplankton

An annual index of accumulated new primary production was based on nitrate drawdown in Faroese shelf waters from winter level to late June 1990-2014 plus a calculated mean net influx of nutrients into the shelf water (Gaard and Hansen, 2000; Gaard, 2003; Steingrund and Gaard, 2005).

Zooplankton

Zooplankton was collected annually during the second half of June 1990-2014 as part of monitoring activity at FAMRI. The sampling was conducted on vertical hauls from 50 m depth to the surface using WP-2 nets with a mesh size of 200 µm. The towing speed was 0.3–0.5 m s-1. Zooplankton biomass was determined by drying at ~60°C until a constant weight was attained. The time series for zooplankton biomass represents an average over 20-25 stations that were distributed throughout the shelf inside the 100 m bottom depth contour (Jacobsen et al., 2019).

Fish data

Long term fish data for fish feeding on bottom organisms were obtained from commercial biomass and landings data. A long-term, 1914-2017, biomass time series of haddock (*Melanogrammus aeglefinus* L) was obtained from ICES (2016) with updates in ICES (2021). Landing data for European plaice (*Pleuronectes platessa*, L) and lemon sole (*Microstomus kitt*, L) was obtained from ICES catch statistics (www.ices.dk). Taking the geometric mean of these catches was assumed to preserve the time development for each species better than adding the catches. The years associated with war periods plus some years after were removed in order to avoid effects of extremely low fishing pressure and its effect on catch and stock size.

Statistics

We used simple linear regression to analyze the relationship between *A. islandica* growth (y) and various variables (x). In one case we used multiple regression since we had two x-variables. When analyzing whether two variables, which themselves are time series, are correlated, autocorrelation could be taken into account. We used the "modified Chelton method" proposed by Pyper and Peterman (1998) that has a procedure to calculate the "effective" number of degrees of freedom as outlined in equations 1-3.

$$r_{XX}(j) = [N/(N-j)]\sum_{t=1}^{N-j}\left[\left(\sum_{t=1}^{N-j}X_t - X_{arit}\right)\left(X_{t+j} - X_{arit}\right)\right]/\sum_{t=1}^{N}\left(\sum_{t=1}^{N-j}X_t - X_{arit}\right)^2, \quad (1)$$

where $r_{XX}(j)$ is the autocorrelation coefficient of time series X at lag j, N is the sample size (number of years), and X_{arit} is the aritmetric mean of time series X. The same formula was used to calculate $r_{YY}(j)$.

$$1/N^* = 1/N + (2/N)\sum_{j=1}^{N/5} r_{XX}(j)r_{YY}(j), \quad (2)$$

where N* is the "effective" number of degrees of freedom and N/5 is rounded down to the nearest integer.

$$r_{crit} = \sqrt{\left[\left(t^2_{\alpha,N^*-2}\right)/\left(t^2_{\alpha,N^*-2} + N^* - 2\right)\right]}, \quad (3)$$

The effect of autocorrelation on the statistics is a matter of which assumptions are made. If it is assumed that the values for the years are independent of each other traditional regressions can be made. If it is assumed that the high (low) values of adjacent years are somehow connected the regression needs to take autocorrelation into account and reduce the effective number of data points and increase the corresponding p-values. Potential biological or oceanographic mechanisms may still be valid even though they cannot be demonstrated statistically due to a high autocorrelation, see discussion about cod recruitment in Canadian waters (Drinkwater, 2002).

Results

Construction of *A. islandica* growth indices

Growth bands were easily identified in most of the shells (Figure 2). The shells generally grew slower with increasing age (Figure S1) and removing this ontogenetic trend (Figure S2) provides a relative annual growth index, herafter termed '*A. islandica* growth' or just 'growth' for each of the sites (Figure 1). Annual growth at sites in closest proximity correlated weakly positively with each other (R = 0.20-0.45) and distant sites weakly negatively (R = -0.14) in a clockwise direction around Faroe Islands: S-K-E-VOH-N (Tables S1–S4, Figure S3). Importantly, there was a systematic pattern in the differences between sites (see procedure in methods). The eastern sites (E and N) grew faster than the western sites (S and K) when the volume transport of the Faroe Current was larger than normal (Figure 3). In order to account for this spatial signal and also to take water depth into account we pooled coastal sites (NVOH) and shelf sites (KES) (Table 1). The shelf sites were mostly located inside the tidal front, although site E was close to the boundary of the tidal front and therefore may have experienced variable hydrographic conditions as the tidal front moves closer to (away from) the shore on a range of time scales (fortnightly to annual) (Figure 1).

There was a low correlation between the growth of individuals as measured by an average coefficient of correlation (R-bar) of 0.02 to 0.12 (Figures 4; S4, S5). However, the large number of shells gave sufficiently high EPS values for the shelf sites from c. 1935 to 2014 as judged by the (default) 50 year moving window of EPS in Figure 4. Removing the 11 oldest shells increased the EPS values prior to 1898 and this might have been related to the revision of the regional curve standardization (RCS), see Figures S6–S8. If the E series was omitted due to the slightly uncertain end point of the series (it was assumed to be one year prior to year of capture based on the appearance of the shells) the EPS values became negative prior to 1906 (not shown) indicating the E series could not be removed from the material.

Based on the EPS values, the shelf *A. islandica* growth index was sufficiently accurate from c. 1873 (25 years before 1898) to 2014 although the EPS values were lower and varied between 0.55 and 0.75 from 1899 to 1933. The coastal *A. islandica* growth index had a nearly sufficiently high EPS value back to c. 1959 and consequently a reliable growth index from c. 1934 (25 years before 1959). These conclusions seem to be justified by considering the 95% confidence intervals of the two growth indices (Figure 5). The shelf and coastal *A. islandica* growth indices were also weakly positively correlated with each other (Figure 6). Accepting lower EPS values for the coastal *A. islandica* growth index and extending it back to 1873 increased the R-squared from 0.17 to 0.23.

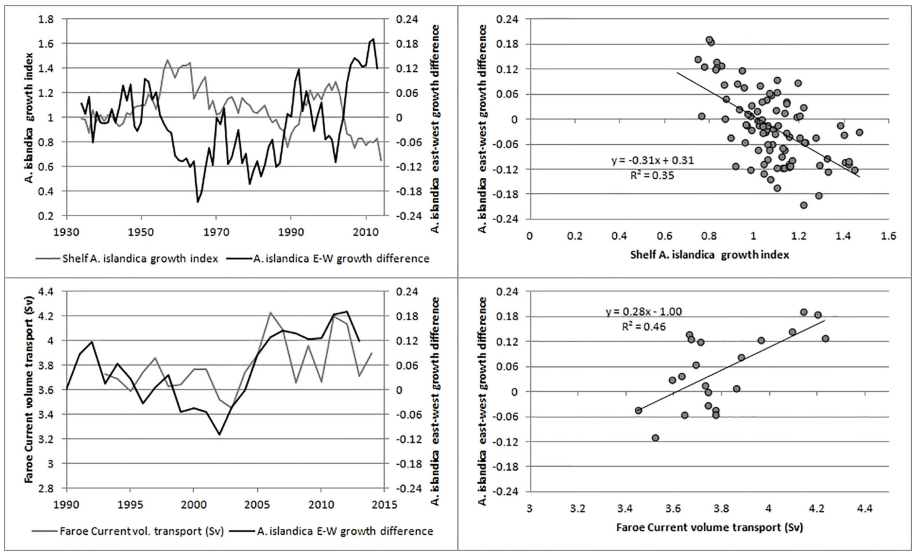


FIGURE 3
The difference in growth of *A. islandica* between eastern (E, N) and western sites (S, K). The sites were arranged in an eastward direction as the sequence S-K-E-N with x-coordinates 1 to 4 and y-coordinates equal to the *A.islandica* growth. The difference in growth between eastern and western sites was, for each year separately, quantified as the slope of the regression line between y and x. Upper: compared with the shelf *A. islandica* growth index (sites KES). Lower: compared with the Faroe Current volume transport.

Omitting the years from 2010 to 2013 increased it to 0.28 (Figure 5). Applying two different detrending methods, a negative exponential function applied on each individual versus a common regional growth curve, gave very similar results for the shelf *A. islandica* growth index, see Figure S9, indicating a robustness to detrending methods. In summary, both the coastal and shelf *A. islandica* growth indices show similar overall trends: slow growth periods in 1870-90s, 1930s, 1980s and rapid growth periods in 1900-10s, 1950-60s and 2000s.

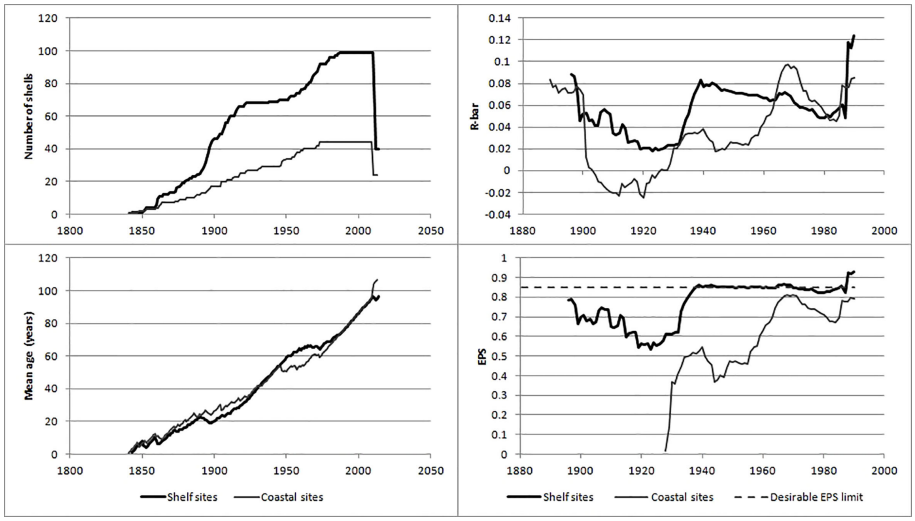


FIGURE 4
Statistics associated with the shelf and coastal *A. islandica* growth indices. Upper left: the number of shells as basis for the indices, lower left: the corresponding mean age for the shells, upper right: the average correlation coefficients for moving 50-year windows, lower right: the corresponding Expressed Population Signal, EPS. The true age is 15 years older than the 'mean age'.

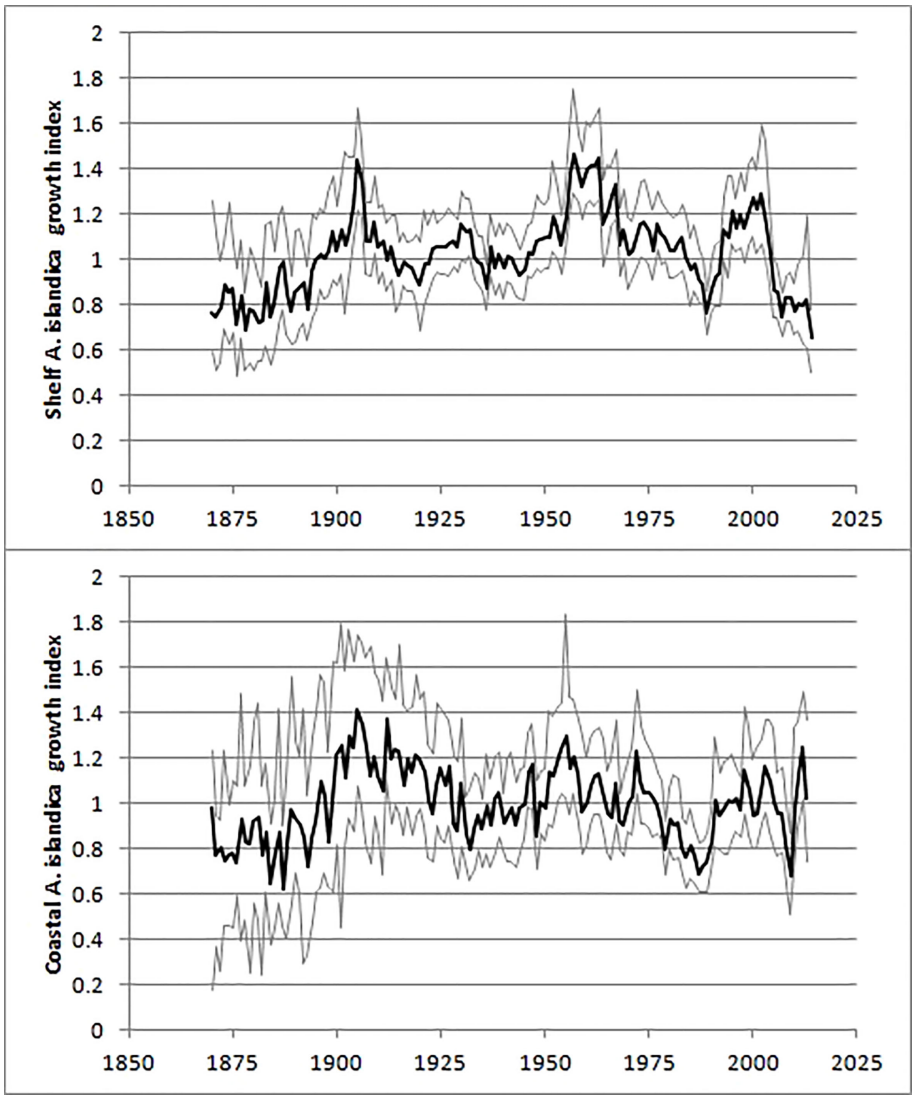


FIGURE 5
The shelf (upper) and coastal (lower) *A. islandica* growth index. Thin lines indicate the bootstrapped 95% confidence intervals.

Since the shells were live collected the end year in the time series was known and the construction of the *A. islandica* growth indices could be done without the traditional cross-dating procedure. Identifying and correcting potential age reading errors on the basis of years with unusual rapid or slow growth was not feasible in this study since such years occurred in a non-systematic way (Figures S4, S5). For the site E, where the shells were collected dead and assumed to have had the last valid growth ring the previous year (2011), we checked this assumption by shifting the whole series back in time and got the highest correlation with other shells when the end year was set to 2011 (assuming that 2012 was not an option because that growth ring was probably not complete), see Table S7. Investigating series E in more detail we applied the program COFECHA. Results suggested that there were only two shells that consistently over a more than 100 year time period showed a shift (of -4 and -2 years, respectively) in the growth compared with the growth of the other shells in the KES series. Both these shells were among the eleven old shells that were excluded from the material for other reasons.

We compared our shelf *A. islandica* growth index with the growth chronology presented in Bonitz et al. (2018) that was based on shells sampled from partly the same area and where the cross-dating technique was applied. The latter chronology was based on the negative exponential detrending method that was applied for each individual shell (option 4 in the ARSTAN program) and was consequently compared with a version of KES that was detrended in the same way. There was a positive correlation between the shelf *A.*

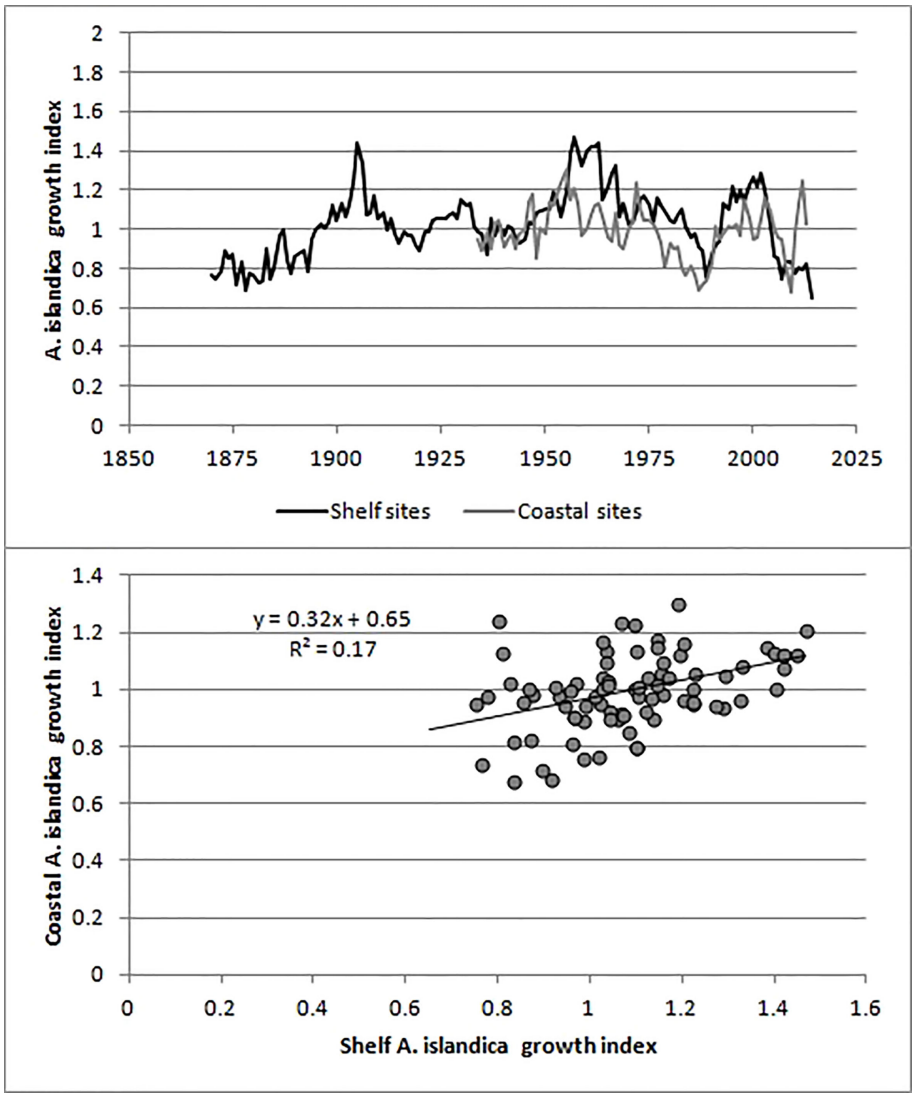


FIGURE 6
Comparison of the shelf and coastal *A. islandica* growth indices.

islandica growth index and the chronology presented in Bonitz et al. (2018), see Figure S10.

Comparison of *A. islandica growth* indices with other variables

There was no significant correlation between neither the shelf nor coastal *A. islandica* growth indices and large scale climatic indices such as NAO, AMO, AO or the gyre index (Table 2). This also applied to some of the more local variables such as sea-surface temperature on the Faroe Shelf as well as windspeed (Table 2). However, a negative correlation between the volume transport of the Faroe Current, that flows eastwards just north of Faroe Islands, and the shelf *A. islandica* growth index was observed (Table 2). There was a weak positive correlation between the shelf *A. islandica* growth index and an index of primary production on the Faroe Shelf although the statistical test (the Modified Chelton Method) showed the unexpected feature by having a higher N and lower p-value when autocorrelation was taken into account (Table 2; Figure 7). There was a strong negative correlation between the shelf *A. islandica* growth index and an index of zooplankton biomass/concentration in June/July on the Faroe Shelf (Table 2; Figure 7) although this relationship became insignificant when the strong autocorrelation was taken into account.

There was a strong positive correlation between the shelf *A. islandica* growth index and the biomass of haddock lagged by two

TABLE 2 Results from regression analyses between *A. islandica* growth indices from shelf sites (KES) or coastal sites (NVOH) and a variety of variables.

Variable	Shelf *A. islandica*					Coastal *A. islandica*				
	R	p*	p	N*	N	R	p*	p	N*	N
Arctic oscillation	-0.29	0.08	**0.02**	38.0	65	-0.06	0.71	0.64	41.2	64
AMO	-0.13	0.54	0.12	24.3	142	0.22	0.34	**0.046**	20.4	80
Subpolar gyre index	-0.25	0.46	0.06	10.7	55	0.26	0.36	0.059	14.4	54
NAO Jan-March	-0.11	0.34	0.20	78.7	142	-0.15	0.30	0.17	46.5	80
NAO April-June	-0.05	0.63	0.52	77.2	141	0.12	0.24	0.29	96.4	80
Temperat. (Ap-Aug)	-0.15	0.56	0.21	18.2	76	-0.07	0.71	0.60	29.1	55
Windspeed (Ap-Aug)	-0.27	0.052	0.03	53.6	67	-0.14	0.35	0.28	50.3	66
FC volume transport	-0.62	**0.02**	**0.002**	14.2	22	-0.06	0.83	0.79	14.5	21
FC heat transport	-0.73	0.08	**0.000**	6.8	22	-0.08	0.76	0.75	18.7	21
A. isl. E-W difference	-0.60	**0.016**	**0.000**	15.7	80	0.23	0.31	**0.044**	22.4	80
Primary production	0.31	**0.045**	0.13	42.1	25	-0.22	0.45	0.31	14.3	24
Zooplankton	-0.76	0.07	**0.000**	6.2	24	0.14	0.54	0.52	20.8	23
Haddock, y+2	0.68	**0.003**	**0.000**	16.8	84	0.31	0.14	**0.004**	23.9	83
Lemon sole, y+2	0.34	0.13	**0.001**	20.9	92	0.04	0.86	0.73	25.8	91
Plaice, y+2	0.17	0.48	0.11	20.3	92	-0.28	0.19	0.01	22.9	91
Gm lem. plaice, y+2	0.46	**0.03**	**0.000**	21.8	92	-0.10	0.62	0.35	27.9	91

The abiotic variables included climate indices, sea surface temperature, windspeed, Faroe Current volume or heat transport. The biotic variables included plankton characteristics and biomass metrics of bottom feeding fish such as the biomass of haddock and the commercial catch of flatfish such as lemon sole and plaice and their geometric mean. The biomass metrics were lagged by 2 years to account for the time it takes for an effect to be manifested in the biomass. Also, the difference in growth of *A. islandica* sites in an eastward direction was investigated, see text. When serial autocorrelation (*) was taken into account the p-values tended to be higher and the adjusted number of years (N*) lower, although two exceptions are indicated by squares. P-values less than 0.05 are indicated with a bold font.

years (Table 2; Figure 8) and this also applied to the coastal *A. islandica* growth index (Table 2). There was a positive, but insignificant correlation between the shelf *A. islandica* growth index and catch of lemon sole or plaice, but a much stronger correlation for a combination of them (Table 2; Figure 8). This correlation was weaker for the coastal *A. islandica* growth index (Table 2).

Discussion

The main finding of the present study is a long-term *A. islandica* growth index for the Faroe Shelf that may reflect the amount of fresh phytoplankton that reaches the near-bottom water layers and could probably be regarded as a proxy for the strength of pelagic-benthic coupling that is modulated through phytoplankton-zooplankton interactions in the overlying water. The *A. islandica* growth index appears to capture vital aspects of benthic production on the Faroe Shelf as represented by biomasses or catches of commercial bottom-feeding fish species. Through a detailed comparison with oceanographic and biological variables we propose potential mechanisms linking pelagic and benthic productivity on the Faroe Shelf.

The potential of *A. islandica* as an ecosystem indicator

A. islandica growth indices were not correlated with basin-scale climate indices (NAO, AO, AMO, SPG, Table 2). The strength of the North Atlantic subpolar gyre has been linked to a primary productivity index on the Faroe Shelf ecosystem (Jacobsen et al., 2019), but was not correlated with *A. islandica* growth indices (Table 2). On the other hand, we found a negative correlation between the volume transport of the Faroe Current (used as a proxy for the North Atlantic drift) and the shelf *A. islandica* growth index (Table 2). Relationships between ocean currents and *A. islandica* growth have been found for the North Sea (Witbaard, 1996). Looking even more locally, the Faroe Shelf sea surface temperature, which is representative for the water mass inside the tidal front (excluding local anomalies within fjords), exhibited a weak negative relationship with the shelf *A. islandica* growth index (Table 2; Figure 7).

No correlation was observed between the shelf *A. islandica* growth index and the primary production index on the Faroe Shelf (Table 2; Figure 7) even though the statistical test (the modified Chelton method) apparently provided a spurious positive relationship when autocorrelation was taken into account. The lack of correlation between primary production and *A. islandica* growth is in line with some studies (Witbaard, 1996), but in contrast with other studies linking primary productivity to growth of *A. islandica* (Bonitz et al., 2018) and knowing that *A. islandica* feeds on fresh phytoplankton (Witbaard et al., 2003). Recalling the negative relationship with temperature, this might appear somewhat counter-intuitive since there are examples of observed positive

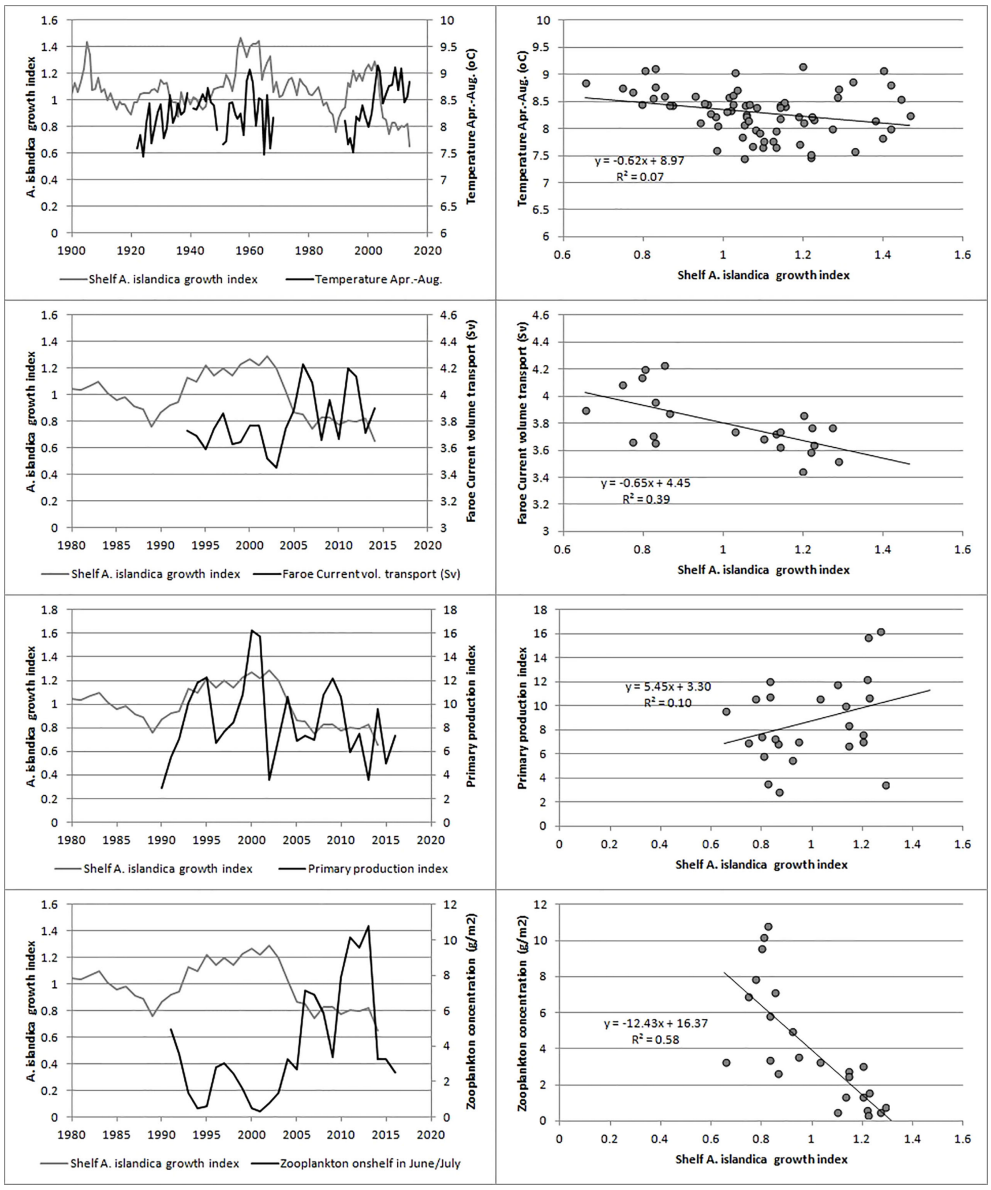


FIGURE 7
Relationship between the shelf A. islandica growth index and environmental factors shown as time series and as scatterplots. Top: sea surface temperature during April to August, upper middle: Faroe Current volume transport, lower middle: index of primary production on the Faroe Shelf, bottom: index of zooplankton biomass on the Faroe Shelf.

relationships with temperature (Butler et al. (2010); Reynolds et al. (2017); Poitevin et al. (2019)), but it may partially be caused by a negative relationship between temperature and primary production on the Faroe Shelf (Gaard, 2003). The effect of primary production may not be absent, however. There was a strong negative correlation between zooplankton biomass in June/July and the shelf *A. islandica* growth index (Table 2; Figure 7) although insignificant when autocorrelation was taken into account. A similar inverse relationship between *A. islandica* growth and zooplankton biomass has been observed in the North Sea (Witbaard et al., 2003). As mentioned earlier, Witbaard et al. (2003) suggested that zooplankton can reduce the downward flux of phytoplankton to the sediments and hinder shell growth. On the shallow and well-mixed Faroese shelf the preferential feeding of zooplankton on energy rich plankton functional types may modulate the relationship between primary production indices and growth indices of *A. islandica*. Analysis of long-term plankton datasets could address these links.

If, as suggested above, *A. islandica* growth integrates the amount of primary production and degree of pelagic-benthic

10.3389/fmars.2022.822343

coupling on the Faroese shelf, then it is possible to hypothesize that population dynamics of bottom-feeding fish display some temporal coherence with *A. islandica* growth. Haddock and flatfish, in this case lemon sole and plaice, have been fished for more than a century in Faroese waters and commercial catch records and/or biomass estimates are available. We observed a positive correlation between the shelf *A. islandica* growth index and the biomass or catch of these bottom-feeding fish species on the Faroe Plateau, although not statistically significant in all cases (Table 2). There appeared to be a time lag of this effect of two years indicating that food availability acted on year class strength and/or individual growth of young fish as observed for the relationship between primary production and cod production (Steingrund and Gaard, 2005). Overall the findings from the present study suggest that the growth of *A. islandica* from well mixed areas inside the tidal front reflects the amount of productivity reaching the benthic environment. This appears to be influenced by zooplankton biomass in addition to total

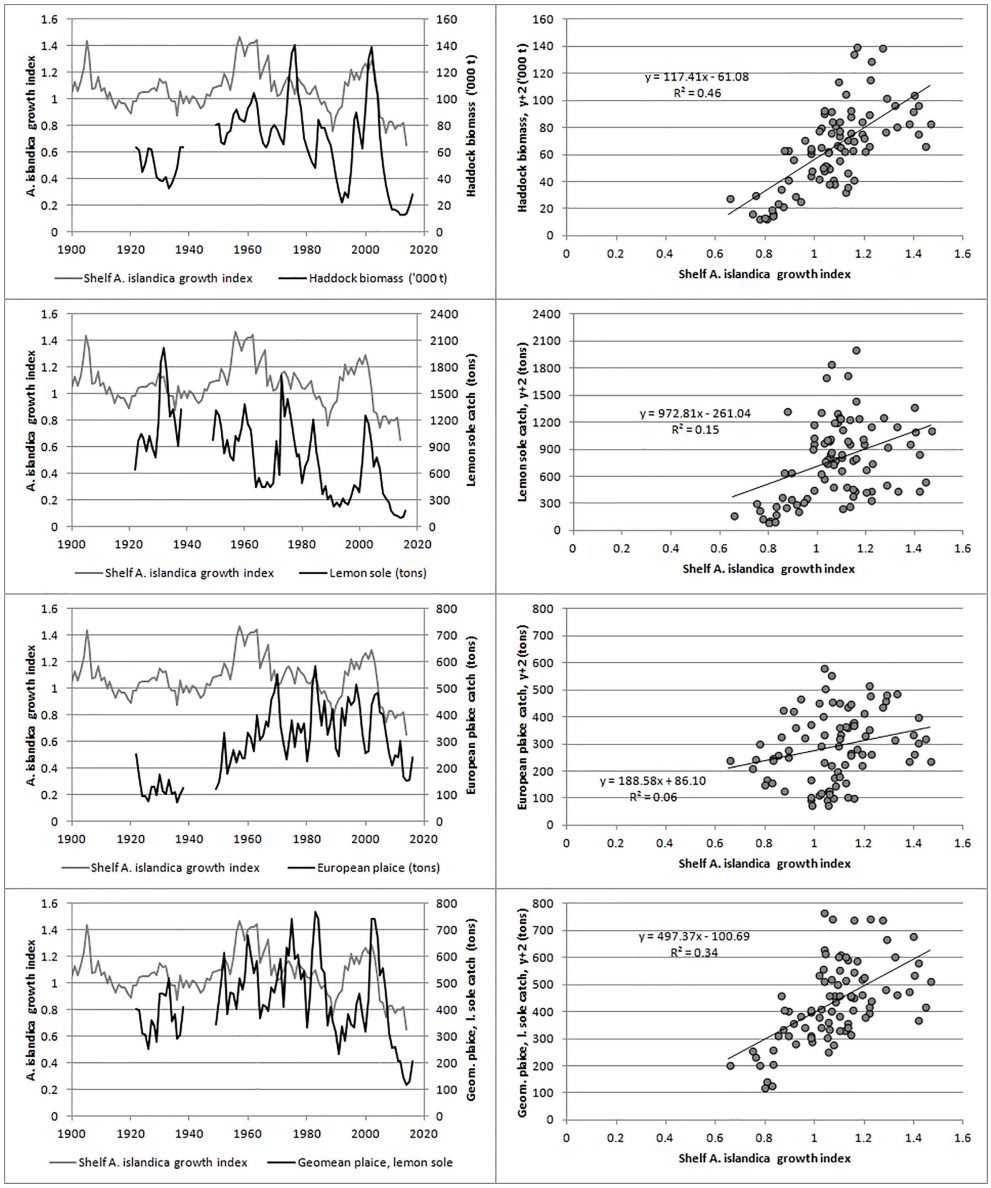


FIGURE 8
Relationship between the shelf A. islandica growth index and measures of bottom feeding fish on Faroe Plateau shown as time series and as scatterplots with a lag of two years (y+2). Top: haddock biomass, upper middle: catch of lemon sole, lower middle: catch of European plaice, bottom: geometric mean of the catches of lemon sole and plaice.

phytoplankton production in the upper layers. Although the coastal *A. islandica* growth index was positively correlated with the shelf *A. islandica* growth index, the relationships with temperature, plankton or bottom-feeding fish were less clear. This discrepancy may be explained by enhanced local variability characterising the near-shore areas or that other processes were involved. The combined evidence of having a mechanism that is backed up by phytoplankton, zooplankton and fish data, although not significant in all cases or for all settings, leads us to conclude that the shelf *A. islandica* growth index may be regarded as a long-term proxy for the phytoplankton productivity that specifically fuels the benthic environment on the Faroe Shelf.

Long-term changes in the ecosystem

Both *A. islandica* growth indices (Figure 5) show that the benthic productivity of the Faroe Shelf ecosystem has fluctuated in periods with a periodicity of around 50 years. There were peaks around years 1900, 1960 and 2000 and lows in 1880, 1930, 1990 and 2010. The exceptionally low biomass of haddock during 1990-1994 and 2006-2016 was associated with exceptionally poor shell growth c. two years before (Figure 8) strongly indicating that environmental factors, here most likely the amount of fresh phytoplankton that reaches the benthic environment, were involved in the near-collapse of the Faroe haddock stock. This may also be the case for Faroe Plateau cod that has shown a very similar variation in stock size since the 1960s (ICES, 2021). Similar arguments apply to flatfish, although catches without information about fishing effort may not necessarily reflect productivity of fish. Our study underpins the importance of long-term ecosystem studies and also provides a starting point for future studies to separate the effects of overfishing from the effects of environmental variability in Faroese waters.

Ecological processes on the Faroe Shelf

The *A. islandica* growth may add an important piece of information to the understanding of ecological processes on the Faroe Shelf as depicted tentatively in Figure 9 and is the result of former and current research. The ecosystem on the Faroe Shelf is fuelled by the local primary production as well as input of zooplankton from abroad. Briefly, ocean currents advect adult Calanus spp. onto Faroe Shelf in March-April and, boosted by the primary production, Calanus eggs and nauplii form the diet and determine the abundance of fish larvae on the Shelf (Eliasen et al., 2011; Jacobsen et al., 2019). The fish larvae grow in size and shift to prey on adult zooplankton (Calanus spp. and neritic zooplankton) to such a degree that there is a negative correlation between fish juveniles and zooplankton in summer (late June) (Jacobsen et al., 2019), which in turn may reduce the amount of fresh phytoplankton that reaches the near-bottom water and therefore hamper the *A. islandica* growth. The relationships depicted in Figure 9 might not apply to all time periods back in time or into the future. If, for example, the amount of Calanus that is advected from the SW Norwegian Sea or elsewhere was or becomes substantially higher than currently observed, or if the amount of fish juveniles was or becomes much lower (e.g., reduced by some predators), fish juveniles (and adult sandeels) might not be able to graze down zooplankton in summer and this would reduce or even flip the correlations between *A. islandica* and many of the variables in Figure 9.

Returning to the negative correlation between shelf *A. islandica* growth and the strength of the Faroe Current, we here want to add a possible effect of the East Icelandic Current, which advects large amounts of zooplankton and runs adjacent and beneath the Faroe Current. Including a measure of Modified East Icelandic Water, MEIW (observed on the same monitoring section as the Faroe Current; Kristiansen et al., 2019, with updates for 2018-19) as an additional variable to the Faroe Current model, improved the model considerably and left both variables highly significant ($R = 0.81$, both p-values < 0.001, $N = 22$). The model indicated that a strong East Icelandic Current, as measured by MEIW north of Faroe Islands, had a positive effect on the shelf *A. islandica* growth index while the strength of the Faroe Current had a negative effect. This can be interpreted according to Figure 9: zooplankton is advected with the East Icelandic Current (Kristiansen et al., 2019) close to the Faroe Shelf but the Faroe Current may sweep the zooplankton eastwards so that it to a lesser extent enters the Faroe Shelf or in a more easterly location. If this zooplankton influx occurs in April-May and consists of adult or subadult Calanus species it would represent an important food source for fish juveniles (Jacobsen et al., 2019) and boost the fish juveniles in the down-grazing of zooplankton during mid-summer and increase the amount of fresh phytoplankton that reaches the benthic environment. The low (high) *A. islandica* growth on the shelf and the relatively more rapid (slow) growth in the easterly locations (Table 2; Figure 3) when the Faroe Current is strong (weak) is consistent with this hypothesis.

Many aspects in Figure 9 as well as alternative aspects could be addressed in the future, for example that nutrients are advected with the currents onto the Faroe Shelf. Also, the *A. islandica* age reading could be compared or calibrated with analyses of elements in the shells (Marali et al., 2017). The effect of salmon aquaculture or other human activities on shell growth could also be investigated.

Construction of *A. islandica* growth indices

Here we return to the methodical part of the construction of the *A. islandica* growth indices. After removing the ontogenetic

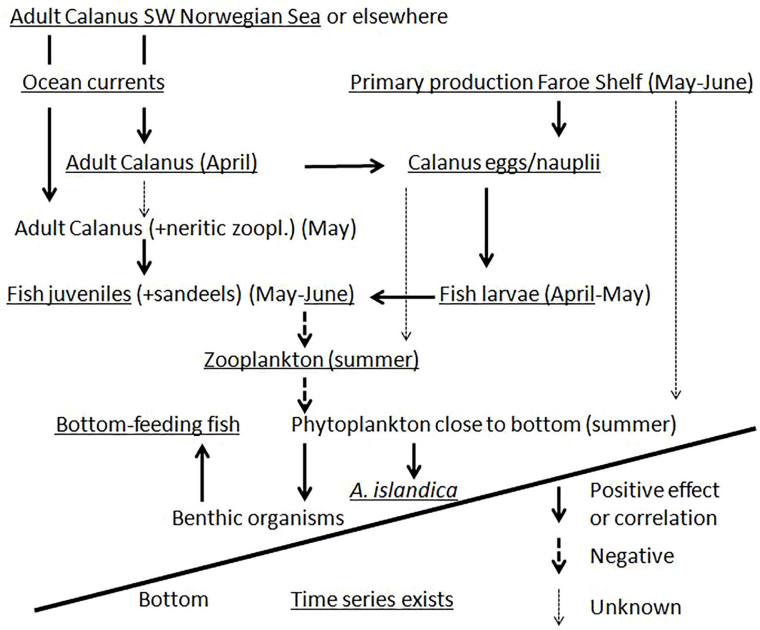


FIGURE 9
Simplified schematic presentation of ecological processes on the Faroe Shelf. Note that this is not a complete description of all ecological linkages but is meant to clarify the ecological processes discussed in the current study.

trend, see next paragraph, narrow and wide growth rings ('marker years') were observed to occur frequently, but usually not the same years, see Figure S5. There was an extremely low inter-correlation between the growth of individual shells (Table S5; Figure 4), as in Epplé et al. (2006). One reason could be variable local conditions induced by strong tidal currents. This made it impossible to correct for potential age reading errors on the basis of the growth pattern of other shells. In order to detect the faint signal among the large noise in the data, we maximised the number of observations by including all shells as basis for the growth index – for shallow and deep areas, respectively. In this way we got sufficiently high precision (high EPS values) due to the statistical principle of gaining precision and representativeness by letting the number of observations be large (Motulsky, 2018). This approach may in principle include random or irrelevant variation and it may be argued that it is better to work with few shells that are strongly correlated (*e.g.* Schöne et al., 2003a). There were clusters of shells that correlated positively with each other (see Table S7) and could potentially represent a starting point when constructing the growth index. Problem was that the same applied to other clusters of shells that showed different growth patterns. In the absence of absolutely dated growth rings it was unknown which cluster represented the variability of potential environmental drivers. Our only option at this point was to include as many shells as possible where random noise is cancelled out. The shelf *A. islandica* growth index was correlated with various environmental drivers indicating that this approach was successful, but there is certainly scope for improvements in future studies.

To remove the ontogenetic trend in growth various growth functions can be fitted to these data that are either applied on an individual basis or to all shells in a region (RCS standardization) where it is assumed that the shells have the same expected growth with increasing age. Fitting growth curves to individual shells has the advantage to take individual variation into account but the disadvantage that long term variability, *i.e*, on the same scale as the age of the individuals, may not be adequately quantified (Butler et al., 2013). In this study we used the RCS standardization. However, since very old shells may also be those with the slowest growth they may cause the *A. islandica* growth index to show an increasing growth over time. Therefore, the eleven oldest shells were not used in this study.

Even though EPS values are widely used to evaluate the quality and length of the *A. islandica* growth indices our results show that confidence intervals should also be used. The EPS values for the shelf *A. islandica* growth were around the desired limit of 0.85 after 1940. However, the confidence intervals were as wide as 0.3 (Figures 5; S11) showing that many years were not statistically different from each other. Hence, for our material more weight should be put on the overall and long-term time development rather than individual years.

Given these considerations the shelf *A. islandica* growth index appears to be of high quality and robust with regards to

settings of the detrending method. Applying growth functions on individual shells gave a very similar result compared with the RCS method, see Figure S9. The positive correlation between the shelf *A. islandica* growth index and the growth chronology presented in Bonitz et al. (2018), see Figure S10, lends further support. It also suggests that the two methods of either applying a cross-dating procedure on few live caught and fossil shells or omitting the cross-dating procedure on many live caught shells may complement each other. Hence, the labour demanding process of cross-dating may be omitted by just examining a large enough number of live-caught shells.

Data availability statement

The data supporting the conclusions of this article will be made available by the authors, without undue reservation.

Ethics statement

Specific ethical review and approval were not needed for this monitoring because the samples were taken from scientific research trips and from commercial catches, which do not fall under the national or EU legislation regarding animal welfare.

Author contributions

UM and PS developed the main idea. UM undertook the Arctica preparations and age readings while PS performed the other data preparations and analyses. PS wrote the manuscript with feedback from UM, EG, KL, and IS. All authors approved the submitted version.

Funding

The research was funded by the Faroe Marine Research Institute, Faroese Research Council, and Faroese Fisheries Research Fund. The Faroe Current data collection received support from the European Framework Programs under grant agreement numbers GA212643 (THOR), and 308299 (NACLIM) and from the Danish Ministry of Climate, Energy and Utilities through its climate support program to the Arctic (FARMON projects).

Acknowledgments

We want to thank the divers and fishermen that kindly provided the ocean quahog shells. Without their help and efforts this work would not be possible. We also want to thank three anonymous referees for comments and suggested improvements on earlier versions of the manuscript.

Conflict of interest

The authors declare that the research was conducted in the absence of any commercial or financial relationships that could be construed as a potential conflict of interest.

Publisher's note

All claims expressed in this article are solely those of the authors and do not necessarily represent those of their affiliated organizations, or those of the publisher, the editors and the reviewers. Any product that may be evaluated in this article, or claim that may be made by its manufacturer, is not guaranteed or endorsed by the publisher.

Supplementary material

The Supplementary Material for this article can be found online at: https://www.frontiersin.org/articles/10.3389/fmars.2022.822343/full#supplementary-material

References

Alheit, J., and Hagen, E. (1997). Long-term climate forcing of European herring and sardine populations. *Fish. Oceanogr.* 6 (2), 130–139. doi: 10.1046/j.1365-2419.1997.00035.x

Ballesta-Artero, I., Witbaard, R., Carroll, M. L., and van der Meer, J. (2017). 2017 Environmental factors regulating gaping activity of the bivalve arctica islandica in northern Norway. *Mar. Biol.* 164, 116. doi: 10.1007/s00227-017-3144-7

Bonitz, F. G. W., Andersson, C., Trofimora, T., and Hátún, H. (2018). Links between phytoplankton dynamics and shell growth of arctica islandica on the faroe shelf. *J. Mar. Syst.* 179, 72–87. doi: 10.1016/j.jmarsys.2017.11.005

Butler, P. G., Richardson, C. A., Scourse, J. D., Wanamaker, A. D.Jr., Shammon, T. M., and Bennell, J. D. (2010). Marine climate in the Irish Sea: Analysis of a 489-year marine master chronology derived from growth increments in the shell of the clam arctica islandica. *Quaternary Sci. Rev.* 29 (2010), 1614–1632. doi: 10.1016/j.quascirev.2009.07.010

Butler, P. G., Richardson, C. A., Scourse, J. D., Witbaard, R., Schöne, B. R., Fraser, N. M., et al. (2009). Accurate increment identification and the spatial extent of the common signal in five arctica islandica chronologies from the fladen ground, northern north Sea. *Paleoceanography* 24, PA2210. doi: 10.1029/2008PA001715

Butler, P. G., Wanamaker, A. D.Jr., Scourse, J. D., Richardson, C. A., and Reynolds, D. J. (2013). Variability of marine climate on the north icelandic shelf in a 1357-year proxy archive based on growth increments in the bivalve arctica islandica. *Palaeogeogr. Palaeocl.* 373, 141–151. doi: 10.1016/j.palaeo.2012.01.016

Cook, E. R. (1985). A time series analysis approach to tree ring standardization. Dissertation thesis (University of Arizona, Tucson), 171 pp.

Cook, E. R., and Holmes, R. L. (1986). "User manual for program ARSTAN," in *Tree-ring chronologies of Western north America: California, Eastern Oregon and northern great basin with procedures used in the chronology development work including users man- uals for computer programs COFECHA and ARSTAN*. Eds. R. L. Holmes, R. K. Adams and H. C. Fritts (Tucson, AZ: Laboratory of Tree-Ring Research, University of Arizona), 50–65.

Cook, E. R., and Krusic, P. J. (2007). *ARSTAN — a tree-ring standardization program based on detrending and autoregressive time series modeling, with interactive graphics* (Palisades, NY: Tree-Ring Laboratory, Lamont Doherty Earth Observatory of Columbia University).

Dragesund, O., Østvedt, O. J., and Toresen, R. (2008). "Norwegian Spring-spawning herring: history of fisheries, biology and stock assessment," in *Norwegian Spring-spawning herring and northeast Arctic cod, 100 years of research and management*. Ed. O. Nakken (Trondheim: Tapir Academic Press), 177 p, ISBN

Drinkwater, K. F. (2002). A review of the role of climate variability in the decline of northern cod. *American Fisheries Society Symposium*, Vol. 32, 113–130.

Eliasen, S. K., Hansen, B., Larsen, K. M. H., and Hátún, H. (2016). The exchange of water between the faroe shelf and the surrounding waters and its effect on the primary production. *J. Mar. Syst.* 153, 1–9. doi: 10.1016/j.jmarsys.2015.08.004

Eliasen, S. K., Hátún, H., Larsen, K. M. H., Hansen, B., and Rasmussen, T. A. S. (2017a). Phenologically distinct phytoplankton regions on the faroe shelf - identified by satellite data, in-situ observations and model. *J. Mar. Sys.* 169, 99–110. doi: 10.1016/j.jmarsys.2017.01.015

Eliasen, S. K., Hátún, H., Larsen, K. M. H., and Jacobsen, S. (2017b). Faroe shelf bloom phenology – the importance of ocean-to-shelf silicate fluxes. *Cont. Shelf Res.* 143, 43–53. doi: 10.1016/j.csr.2017.06.004

Eliasen, S. K., Hátún, H., Larsen, K. M. H., Vang, H. B. M., and Rasmussen, T. A. S. (2019). The faroe shelf spring bloom onset explained by a 'Critical volume hypothesis'. *J. Mar. Syst.* 194, 91–101. doi: 10.1016/j.jmarsys.2019.02.005

Eliasen, K., Reinert, J., Gaard, E., Hansen, B., Jacobsen, J. A., Grønkjær, P., et al. (2011). Sandeel as a link between primary production and higher trophic levels on the faroe shelf. *Mar. Ecol. Prog. Ser.* 438, 185–194. doi: 10.3354/meps09301

Epplé, V. M., Brey, T., Witbaard, R., Kuhnert, H., and Pätzold, J. (2006). Sclerochronological records of arctica islandica from the inner German bight. *Holocene* 16 (5), 763–769. doi: 10.1191/0959683606hl970rr

Gaard, E. (1996). Phytoplankton community structure on the faroe shelf. *Fróðskaparrit* 44, 95–106.

Gaard, E. (1999). The zooplankton community structure in relation to its biological and physical environment on the faroe shelf 1989-1997. *J. Plankton Res.* 21, 1133–1152. doi: 10.1093/plankt/21.6.1133

Gaard, E. (2000). Seasonal abundance and development of calanus finmarchicus in relation to phytoplankton and hydrography on the faroe shelf. *ICES J. Mar. Sci.* 57, 1605–1611. doi: 10.1006/jmsc.2000.0963

Gaard, E. (2003). Plankton variability on the faroe shelf during the 1990s. ICES marine science symposia. *ICES J. Mar. Sci.* 219, 182–189.

Gaard, E., and Hansen, B. (2000). Variations in the advection of calanus finmarchicus onto the faroe shelf. *ICES J. Mar. Sci.* 57, 1612–1618. doi: 10.1006/jmsc.2000.0962

Gaard, E., Hansen, B., and Heinesen, S. P. (1998). Phytoplankton variability on the faroe shelf. *ICES J. Mar. Sci.* 55, 688–696. doi: 10.1006/jmsc.1998.0373

Gaard, E., Hansen, B., Olsen, B., and Reinert, J. (2002). Ecological features and recent trends in physical environment, plankton, fish and sea birds in the faroe plateau ecosystem. In K Sherman and H-R Skjoldal Eds. *Large Marine Ecosystems of the North Atlantic*. Elsevier, pp. 245–265. doi: 10.1016/S1570-0461(02)80060-X

Hansen, B., and Østerhus, S. (2000). North Atlantic - Nordic seas exchanges. *Prog. Oceanography* 45, 109–208. doi: 10.1016/S0079-6611(99)00052-X

Hansen, B., Larsen, K. M. H., Hátún, H., Kristiansen, R., Mortensen, E., and Østerhus, S. (2015). Transport of volume, heat, and salt towards the Arctic in the faroe current 1993–2013. *Ocean Sci.* 11, 743–757. doi: 10.5194/os-11-743-2015

Hansen, B., and Meincke, J. (1984). Long-term coastal sea surface temperature observations at the faroe islands. *Rapports et procès-verbaux des réunions*, vol. 185. (du Conseil International pour l'Exploration de la Mer), 162–169.

Hansen, B., Steffánsson, U., and Svendsen, E. (1998). Iceland, Faroe and Norwegian coasts. *Sea* 11, 733–758.

Hátún, H., and Chafik, L. (2018). On the recent ambiguity of the north Atlantic subpolar gyre index. *J. Geophys. Res. Oceans* 123, 5072–5076. doi: 10.1029/2018JC014101

Hátún, H., Payne, M. R., Beaugrand, P. C., Reid, P. C., Sandø, A. B., Drange, H., et al. (2009). Large Bio-geographical shifts in the north-eastern Atlantic ocean: From the subpolar gyre, *via* plankton, to blue whiting and pilot whales. *Prog. Oceanography* 80 (2009), 149–162. doi: 10.1016/j.pocean.2009.03.001

Hátún, H., Sandø, A. B., Drange, H., Hansen, B., and Valdimarsson, H. (2005). Influence of the Atlantic subpolar gyre on the thermohaline circulation. *Science* 309, 1841–1844. doi: 10.1126/science.1114777

Hurrel, J. W., and Deser, C. (2009). North Atlantic climate variability: The role of the north Atlantic oscillation. *J. Mar. Syst.* 78 (2009), 28–41. doi: 10.1016/j.jmarsys.2008.11.026

ICES (2016). *Report of the north-Western working group (NWWG), 27 April–4 ma* (Copenhagen: ICES Headquarters).

ICES (2021). *ICES scientific reports* Vol. 3 (Copenhagen: Northwestern Working Group NWWG), 556 p. doi: 10.17895/ices.pub.8186

Jacobsen, S., Gaard, E., Hátún, H., Steingrund, P., Larsen K.M.H. Reinert, J., Ólavsdóttir, S. R., et al. (2019). Environmentally driven ecological fluctuations on the faroe shelf revealed by fish juvenile surveys. *Front. Mar. Sci.* 6. doi: 10.3389/fmars.2019.00559

Kristiansen, I., Hátún, H., Petursdottir, H., Gislason, A., Broms, C., Melle, W., et al. (2019). Decreased influx of calanus spp. into the south-western Norwegian Sea since 2003. *Deep-Sea Res. Part I* 149, 103048. doi: 10.1016/j.dsr.2019.05.008

Kurlansky, M. (1998). *Cod, a biography of the fish that changed the world*. (Jonathan Cape, Random House: 20 Vauxhall Bridge Road, London SW1V 2SA), 294 p, ISBN: .

Larsen, K. M. L., Hansen, B., and Svendsen, H. (2008). Faroe shelf water. *Continental shelf Res.* 28, 1754–1768. doi: 10.1016/j.csr.2008.04.006

Larsen, K. M. L., Hansen, B., and Svendsen, H. (2009). Faroe shelf front: properties and exchange. *J. Mar. Syst.* 78 (2009), 9–17. doi: 10.1016/j.jmarsys.2009.02.003

Marali, S., Schöne, B. R., Merz-Kraus, R., Griffin, S. M., Wanamaker, A., Matras, U., et al. (2017). Ba/Ca ratios in shells of arctica islandica-potential environmental proxy and crossdating tool. *Palaeogeography Palaeoclimatology Palaeoecol.* 465 (2017), 347–361. doi: 10.1016/j.palaeo.2015.12.018

Mette, M. J., Wanamaker, A. D.Jr., Carroll, M. L., Ambrose, W. G.Jr., and Retelle, M. J. (2016). Linking large-scale climate variability with arctica islandica shell growth and geochemistry in northern Norway. *Limnol. Oceanogr* 61, 748–764. doi: 10.1002/lno.10252

Motulsky, H. (2018). *Intuitive biostatistics: A nonmatematical guide to statistical thinking. 4th ed.* (New York: Oxford University Press).

Myers, R. A. (1998). When do recruitment – environmental correlations work? *Rev. Fish Biol. Fisheries* 8, 285–305. doi: 10.1023/A:1008828730759

Nakken, O. (2008). *Norwegian Spring-spawning herring and northeast Arctic cod, 100 years of research and management*. Ed. O. Nakken (Trondheim: Tapir Academic Press), 177 p, ISBN: .

Poitevin, P., Thébault, J., Siebert, V., Donnet, S., Archambault, P., Doré, J., et al. (2019). Growth response of arctica islandica to north Atlantic oceanographic conditions since 1850. *Front. Mar. Sci.* 6. doi: 10.3389/fmars.2019.00483

Pyper, B. J., and Peterman, R. M. (1998). Comparison of methods to account for autocorrelation in correlation analyses of fish data. *Canadien J. Fisheries Aquat. Sci.* 55, 2127–2140. doi: 10.1139/f98-104

Rae, B. B. (1967). The food of cod on faroese grounds. *Mar. Res.* 6, 1–23.

Rembauville, M., Blain, S., Manno, C., Tarling, G., Thompson, A., Wolff, G. A., et al. (2018). The role of diatom resting spores for pelagic-benthic coupling in the southern ocean. *Biogeosciences*. 15, 3071–3084. doi: 10.5194/bg-15-3071-2018

Rembauville, M., Manno, C., Tarling, G. A., Blain, S., and Salter, I. (2016). Strong contribution of diatom resting spores to deep sea carbon export fluxes in the naturally iron-fertilized waters downstream of south Georgia. *Deep-Sea Res. Part I* 115, 22–35. doi: 10.1016/j.dsr.2016.05.002

Reynolds, D. J., Richardson, C. A., Scourse, J. D., Butler, P. G., Hollyman, P., Román-González, A., et al. (2017). Reconstructing north Atlantic marine climate variability using an absolutely-dated sclerochronological network. *Palaeogeography Palaeoclimatology Palaeoecol.* 465 (2017), 347–361. doi: 10.1016/j.palaeo.2016.08.006

Robichaud, D., and Rose, G. A. (2004). Stock structure and range in Atlantic cod (Gadus morhua): inference from 100 years of tagging. *Fish Fish.* 5, 185–214. doi: 10.1111/j.1467-2679.2004.00141.x

Ropes, J. W. (1987). *Preparation of acetate peels of valves from the ocean quahog, arctica islandica, for age determinations* Vol. 50 (Woods Hole: NOAA/National Marine Fisheries Service).

Rose, G. A. (2004). Reconciling overfishing and climate change with stock dynamics of Atlantic cod (Gadus morhua) over 500 years. *Can. J. Fish. Aquat. Sci.* 61, 1553–1557. doi: 10.1139/F04-173

Sørensen, B. L. (2021). Growth and spatial distribution of cod and haddock on the Faroe Plateau and relationship with the amount of forage fish. Biology thesis (University of Copenhagen, Faculty of Science, Department of Biology, Copenhagen), 74 p.

Sætersdal, G. (2008). "From fisheries research to fisheries science 1900-1940: tracing the footsteps of Johan hjort in Bergen and ICES," in *Norwegian Spring-spawning herring and northeast Arctic cod, 100 years of research and management*. Ed. O. Nakken (Trondheim: Tapir Academic Press), 177 p.

Salter, I., Kemp, A. E. S., Moore, C. M., Lampitt, R., Wolff, G. A., and Holtvoeth, J. (2012). Diatom resting spore ecology drives enhanced carbon export from a naturally iron fertilized bloom in the southern ocean. *Global Biogeochemical Cycles* 26, GB1014. doi: 10.1029/2010GB003977

Salter, I., Lampitt, R., Sanders, R., Poulton, A., Kemp, A., Boorman, B., et al. (2007). Estimating carbon, silica, and diatom export from a naturally fertilised phytoplankton bloom in the southern ocean using PELAGRA: A novel drifting sediment trap. *Deep-Sea Res. Part II* 54 (18-20), 2233–2259. doi: 10.1016/j.dsr2.2007.06.008

Schöne, B. R., Kröncke, I., Houk, S. D., and Castro, A. D. F. (2003b). The cornucopia of chilly winters: ocean quahog (Arctica islandica l., Mollusca) master chronology reveals bottom water nutrient enrichment during colder winters (North Sea). *Senckenbergiana maritima* 32, 1–13. doi: 10.1007/BF03043092

Schöne, B. R., Oschmann, W., Rössler, J., Castro, A. D. F., Houk, S. D., Kröncke, I., et al. (2003a). North Atlantic oscillation dynamics recorded in shells of a long-lived bivalve mollusk. *Geology* 31 (12), 1037–1040. doi: 10.1130/G20013.1

Scourse, J. D., Richardson, C. A., Forsythe, G., Harris, I., Heinemeier, J., Fraser, N., et al. (2006). First cross-matched floating chronology from the marine fossil record: data from growth lines of the long-lived bivalve mollusc arctica islandica. *Holocene* 16, 967–974. doi: 10.1177/0959683606hl987rp

Steingrund, P., Clementsen, D. H., and Mouritsen, R. (2009). Higher food abundance reduces the catchability of cod (Gadus morhua) to longlines on the faroe plateau. *Fisheries Res.* 100, 230–239. doi: 10.1016/j.fishres.2009.08.002

Steingrund, P., and Gaard, E. (2005). Relationship between phytoplankton production and cod production on the faroe shelf. *ICES J. Mar. Sci.* 62, 163–176. doi: 10.1016/j.icesjms.2004.08.019

Stott, K. J., Austin, W. E. N., Sayer, M. D. J., Weidman, C. R., Cage, A. G., and Wilson, R. J. S. (2010). The potential of arctica islandica growth records to reconstruct coastal climate in north west Scotland,UK. *Quaternary Sci. Rev.* 29, 1602–1613. doi: 10.1016/j.quascirev.2009.06.016

Toresen, R., and Østvedt, O. J. (2000). Variation in abundance of Norwegian spring-spawning herring(Clupea harengus, clupeidae) throughout the 20th century and the influence of climatic fluctuations. *Fish Fisheries* 1, 231–256. doi: 10.1046/j.1467-2979.2000.00022.x

Trenberth, K., Zhang, R.National Center for Atmospheric Research Staff (2021) *"The climate data guide: Atlantic multi-decadal oscillation (AMO).".* Available at: https://climatedataguide.ucar.edu/climate-data/atlantic-multi-decadal-oscillation-amo.

Witbaard, R. (1996). Growth variations in arctica islandica l. (Mollusca): a reflection of hydrography-related food supply. *ICES J. Mar. Sci.* 53, 981–987. doi: 10.1006/jmsc.1996.0122

Witbaard, R., Duineveld, G. C. A., Amaro, T., and Bergman, M. J. N. (2005). Growth trends in three bivalve species indicate climate forcing on the benthic ecosystem in the southeastern north Sea. *Climate Res.* 30, 29–38. doi: 10.3354/cr030029

Witbaard, R., Jansma, E., and Sass Klaassen, U. (2003). Copepods link quahog growth to climate. *J. Sea Res.* 50, 77–83. doi: 10.1016/S1385-1101(03)00040-6

Wolff, G., Billet, D., Holtvoeth, J., Bett, B., Fitzgeorge-Balfour, T., Fisher, E., et al. (2011). Natural iron fertilisation and the impact of enhanced carbon export on deep-sea ecosystems. *PLoS One* 6 (6), e20697. doi: 10.1371/journal.pone.0020697

Østerhus, S., Woodgate, R., Valdimarsson, H., Turrell, B., de Steur, L., Quadfasel, D., et al. (2019). Arctic Mediterranean Exchanges: a consistent volume budget and trends in transports from two decades of observations. *Ocean Sci.* 15, 379–399. doi: 10.5194/os-15-379-2019

frontiers | Frontiers in Marine Science

TYPE Original Research
PUBLISHED 13 October 2022
DOI 10.3389/fmars.2022.803171

Check for updates

OPEN ACCESS

EDITED BY
Ibon Galparsoro,
Technological Centre Expert in Marine and Food Innovation (AZTI), Spain

REVIEWED BY
Dmitry Lajus,
Saint Petersburg State University, Russia
Peter Grønkjær,
Aarhus University, Denmark

*CORRESPONDENCE
Eydna í Homrum
eydnap@hav.fo

SPECIALTY SECTION
This article was submitted to Marine Ecosystem Ecology, a section of the journal Frontiers in Marine Science

RECEIVED 27 October 2021
ACCEPTED 22 September 2022
PUBLISHED 13 October 2022

CITATION
Homrum Eí, Óskarsson GJ, Ono K, Hølleland S and Slotte A (2022) Changes towards stable good somatic condition and increased gonad investment of Norwegian spring-spawning herring (*Clupea harengus*) after 2005 are linked to extended feeding period.
Front. Mar. Sci. 9:803171.
doi: 10.3389/fmars.2022.803171

COPYRIGHT
© 2022 Homrum, Óskarsson, Ono, Hølleland and Slotte. This is an open-access article distributed under the terms of the Creative Commons Attribution License (CC BY). The use, distribution or reproduction in other forums is permitted, provided the original author(s) and the copyright owner(s) are credited and that the original publication in this journal is cited, in accordance with accepted academic practice. No use, distribution or reproduction is permitted which does not comply with these terms.

Changes towards stable good somatic condition and increased gonad investment of Norwegian spring-spawning herring (*Clupea harengus*) after 2005 are linked to extended feeding period

Eydna í Homrum[1]*, Guðmundur J. Óskarsson[2], Kotaro Ono[3], Sondre Hølleland[3] and Aril Slotte[3]

[1]Faroe Marine Research Institute, Tórshavn, Faroe Islands, [2]Marine and Freshwater Research Institute, Hafnafjörður, Iceland, [3]Institute of Marine Research, Bergen, Norway

Norwegian spring spawning herring (*Clupea harengus*) migrate from spawning areas on the Norwegian shelf in February-March to feeding areas in the Norwegian Sea in April-August, returning to wintering areas in northern Norwegian waters from September onwards when feeding ceases. After around 2005 the Norwegian Sea has become warmer and here we address recent changes in migration, somatic condition and gonad development of herring related to these changes. Analyses were based on combined Norwegian, Icelandic and Faroese data on fishery (~81% of total commercial catch) and biological parameters from an extensive material of individual fish (n = 310749) during the period 1994-2019. Fishery data demonstrated large-scale changes in herring distribution over the study period. This was further supported by spatiotemporal modelling of body growth, somatic condition, gonad development and concurrent centre of gravity changes of the sampled fish. After 2005 the population showed a clear tendency of being distributed farther south-westwards in the Norwegian Sea during feeding and returning to wintering areas later in the year. This tendency increased with age, and with body length and somatic condition within age groups. Moreover, the somatic condition increased for all age groups from the early 2000s towards stable high levels after 2005, mainly due to extra weight gained from extended feeding into the autumn. Length at age decreased continuously during 2003-2010 for all age groups, suggesting impact of density dependent limiting factors but also that the environmental shift may have led to immediate poorer feeding conditions early in the year. Hence, extra energy from extended autumn feeding was rather invested into gonad weights tending to increase over the study period. Mechanisms behind the observed changes are likely linked to spatial and seasonal changes in zooplankton abundance. Overall, zooplankton production possibilities along the frontal areas in the south-western part of the

Norwegian Sea have likely increased after the general environmental shift. This also includes a change towards increased probabilities of an additional second generation of some copepods developing in warmer waters, facilitating a prolonged feeding period for herring.

KEYWORDS

Norwegian spring spawning herring, Norwegian Sea, somatic condition, gonad development, distribution changes, extended feeding period, body growth

Introduction

The migratory Norwegian spring spawning herring (*Clupea harengus*) (hereafter herring) is the world's largest herring stock (Hay et al., 2001) with high economical value for several countries (Bjørndal et al., 2004). Over the last century the stock has shown large fluctuations related to variable recruitment (Figure 1A) (Devold, 1963; Ottersen et al., 2013). This, combined with overexploitation resulted in a full stock collapse in the late 1960s and a rebuilding period following strict management regimes (Toresen and Østvedt, 2000). After the recruitment of the strong 1983 year-class (Røttingen, 1990) the stock has stabilized again at high levels and is currently sustaining one of the largest fisheries in the North East Atlantic (Figure 1A).

The herring have a triangular migration pattern between spawning areas on the Norwegian shelf (Figure 2) in February-March, feeding in the Norwegian Sea in April-August and a returning to oceanic or coastal wintering in Norwegian waters from September onwards (Devold, 1963; Dragesund et al., 1997; Holst et al., 2002). The exact position and timing – particularly for the wintering areas – varies periodically.

The main feeding area in the Norwegian Sea and adjacent areas is composed of several water masses and ocean currents (Figure 2). The central Norwegian Sea is dominated by relatively warm Atlantic water (Hansen and Østerhus, 2000). The Norwegian Sea has become warmer since the mid-1990s, stabilizing at high heat content after 2005 (Figure 1B). This recent warm state is a result of increased temperatures in the Atlantic inflow from the north-eastern Atlantic and reduced heat losses to the atmosphere over this region (Hátún et al., 2005; Asbjørnsen et al., 2019; Mork et al., 2019). The Norwegian Sea Gyre (NSG) is a system of counter-clockwise currents; to the south the NSG is bordered by the Faroe Current and to the east by the colder East Icelandic Current. Contrasting periods with strong and weak NSG have also revealed oceanographic changes in the feeding area, which are likely to affect the ecosystem (Hátún et al., 2021) and higher trophic levels, such as herring.

Mechanisms behind the spatiotemporal dynamics in herring distribution are far from fully understood, but one important factor is the size of the stock. Density dependent effects are typically important during the feeding season, with the tendency to utilize larger areas in the Norwegian Sea at high stock levels (Holst et al., 2002; Eliasen et al., 2021). Another important factor affecting spatial distribution is the age structure in the stock. Shifts in wintering areas generally occur when large incoming year classes are recruiting to the spawning stock in the Norwegian Sea from their nursery areas in the Barents Sea (Huse et al., 2010).

Migration distance is observed to be size dependent both during feeding (Nøttestad et al., 1999; Eliasen et al., 2021) and spawning migration (Slotte, 1999b; Slotte and Fiksen, 2000) where the largest herring migrate farthest. The migration of a year class may, therefore, change over times as it grows, and in general be extended when the stock is dominated by old fish. For shifts in feeding areas, however, Eliasen et al. (2021) demonstrated that during the period 1999-2004, herring of all ages simultaneously shifted the feeding area northwards, indicating that this shift as well as the subsequent southward shift was governed by the environment rather than incoming year classes.

During the feeding season, the largest and oldest, experienced fish tend to migrate towards the productive areas along the cold Jan Mayen front, between the Iceland Sea and the Norwegian sea (Misund et al., 1997; Nøttestad et al., 2007; Melle et al., 2020; Eliasen et al., 2021). This pattern was also evident prior to the stock collapse (Jakobsson, 1968; Dragesund et al., 1997; Holst et al., 2002).

The Jan Mayen front has been identified as an important transitional zone in both zooplankton biomass, abundance and diversity, changing significantly across the front (Melle et al., 2020). Both prey abundance and stomach content of herring was higher on the western, colder side of the front (Melle et al., 2020; Kristiansen et al., 2022), where *Calanus hyperboreus* was important part of the diet. On the Atlantic side, the herring mainly fed on overwintering stages of *Calanus finmarchicus*, i.e. before the development of the new generation of the year, and the phenology of *C. finmarchicus* appears to be an important driver of the herring feeding migration (Broms et al., 2012; Melle et al., 2020).

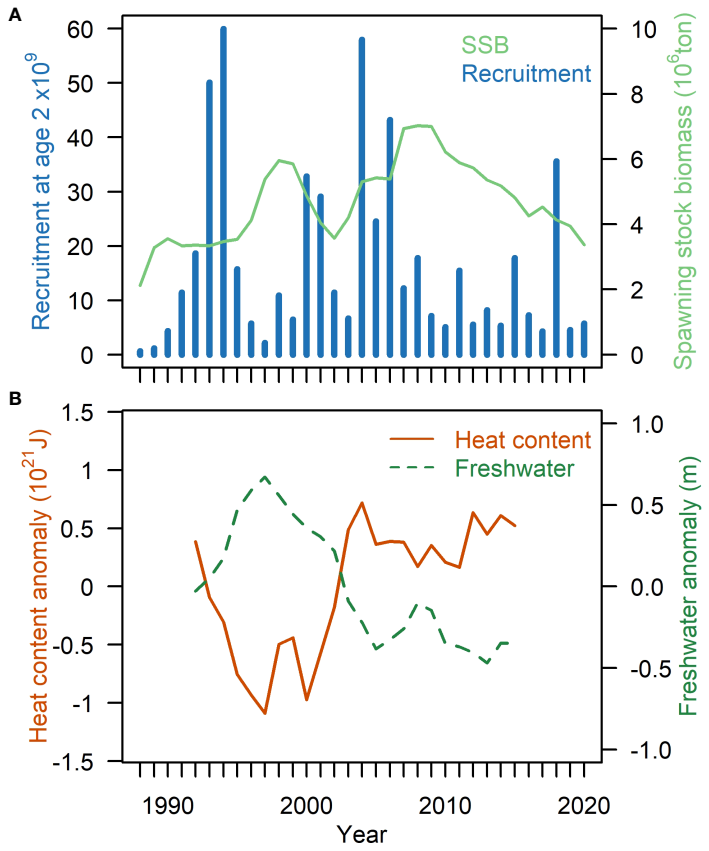


FIGURE 1
(A) Spawning stock biomass (SSB) and recruitment at age 2 of Norwegian spring-spawning herring (source: ICES advice 2021). **(B)** Heat content anomaly (brown solid) and freshwater anomaly (green stippled) in the Norwegian Sea from surface to 400m depth 1992-2015. Redrawn with permission and data from Asbjørnsen et al., 2019 based on ECCOv4 data.

The warming of the Norwegian Sea would in general be expected to be positive for individual growth of a species like herring, which is at the northerly distributional range (Rose, 2005). Herring exhibits temperature dependent growth (Husebø et al., 2007; Brunel and Collas, 2010; Hunter et al., 2019), given that the feeding conditions and competition for prey also are favourable. Herring growth is suggested to be linked to the biomass of zooplankton in the Norwegian Sea in May (Huse et al., 2012; dos Santos Schmidt et al., 2020), and the most recent updated ecosystem review (ICES, 2021a) reports a general increase in zooplankton biomass in the area both during spring and summer since 2010.

Recent research has, however, demonstrated a clear change in the timing and seasonality of zooplankton production in this ecosystem (Kristiansen et al., 2016; Strand et al., 2020; Skjoldal et al., 2021). While previously there was thought to be only one generation of *C. finmarchicus*, Strand et al. (2020) found two generations of *C. finmarchicus* across the central Norwegian Sea 2008-2016, where the second generation was observed in September-October. Around 2003 a sudden shift was observed north of the Iceland – Faroe front, after which two generations of *C. finmarchicus* were produced (Kristiansen et al., 2016). This change in phenology was linked to changes in water mass distribution (Kristiansen et al., 2019) where colder water masses retracted westward, which in turn lead to an increase of individuals from the Norwegian Basin. Consequently, an earlier reproduction enabled the species to produce two generations after 2003 leading to increased abundance in September. Similar shifts have been observed at the western entrance to the Barents Sea (Skjoldal et al., 2021). There the warming resulted in a shifted phenology after 2005 with evidence for a second generation leading to increased summer abundance of *C. finmarchicus*. Also on the western side of the Atlantic peak abundance of *Pseudocalnaus* sp. has shifted from spring to summer, thus becoming available as prey to herring in the autumn months since the mid 2000s (Wilson et al., 2018).

These changes in phenology of *C. finmarchicus* may be of significant importance for herring that potentially could experience high prey availability in the Norwegian Sea in autumn. At that time of the year, herring were historically

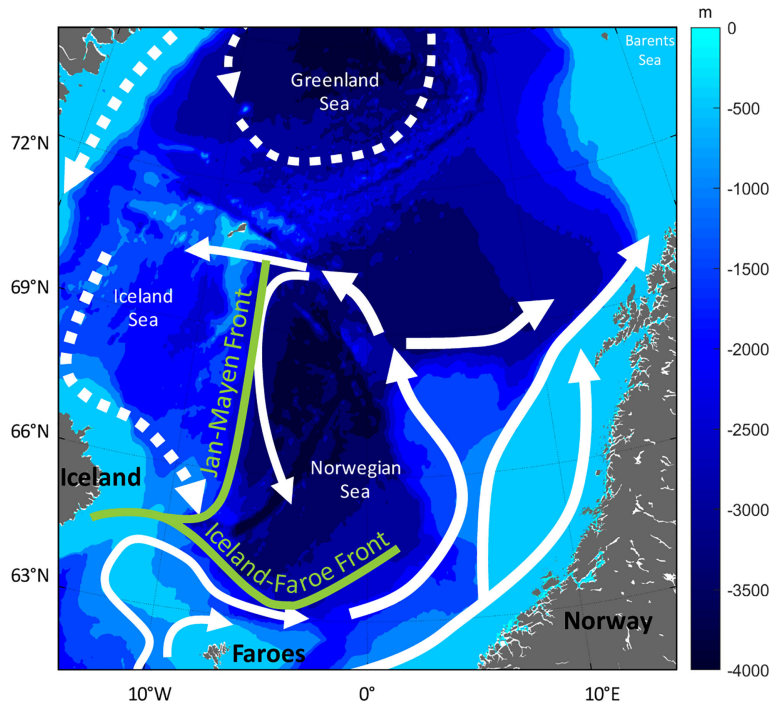


FIGURE 2
Map of the Norwegian Sea and surrounding waters. Map overlaid with bottom depth and main currents (white arrows, dotted currents are cold water masses) and main fronts (green colour).

already settled at wintering grounds with empty stomachs using stored energy to develop gonads (Slotte, 1999a).

Herring growth has been linked to density dependent effects (slowest growth at highest abundance) as well as environmental factors (Husebø et al., 2007; Brunel and Collas, 2010; dos Santos Schmidt et al., 2020). dos Santos Schmidt et al. (2020) found that weight at age tended to decrease from 1994 to lowest levels in 1997, increasing again and stabilizing at high levels in 2005-2014. It was noteworthy that growth in terms of total body length at age tended to cease, whereas both the total body weight and gonad weight at length remained at high levels after 2005. They concluded that growth in terms of body length likely decreased in warmer waters in the Norwegian Sea ecosystem under stiff prey intra- and inter-specific competition to support increased condition and investment into reproduction, yielding higher fecundity. dos Santos Schmidt et al. (2020) focused on early overwintering (October – November) and pre-spawning (February), and therefore lacked spatio-temporal information – particularly during the feeding period.

Herring feeding starts already in April, and it remains unsolved where and when herring gains the weight over the feeding season before they arrive at the wintering grounds in autumn. It also remains unsolved how the herring actually allocates energy between body growth (in terms of length), somatic weight, and gonad weight over the feeding season. Especially the gonad development is a process that could influence body growth. Body growth ceases quickly in herring following first maturation (Engelhard and Heino, 2004a; Engelhard and Heino, 2004b), but it is also likely that maturation processes of adult herring may affect body growth directly, as has been demonstrated for other teleost species (Bhatta et al., 2012). For herring, depending heavily on energy reserves for gonad development (Slotte, 1999a), it is therefore likely that body growth of the herring may cease when the onset of maturation and gonad building starts in July (dos Santos Schmidt et al., 2017). To summarize, growth in length is hypothesized to be related to feeding opportunities in early summer, before maturation of gonads sets on. Somatic weight and gonad weight, on the other hand, are hypothesized to be related to feeding opportunities throughout the feeding season, also after onset of gonad maturation.

Given the recent evidence of increased abundance of a second generation of *C. finmarchicus* well into the autumn, this provides opportunity for herring to extend their feeding period and gain more energy to invest into gonad development even after onset of maturation and increase the migration potential during the spawning season (Slotte, 1999a). In fact, the international fisheries in recent years have demonstrated that herring are distributed all the way from Iceland across the Norwegian Sea to Norwegian coastal waters into late

November (ICES, 2021b), clearly indicating a delayed migration eastwards to the wintering areas.

The main objective of the current study was to explore whether spatiotemporal dynamics in distribution of the herring stock and concurrent length at age, somatic condition levels and gonad development changed when the Norwegian Sea had warmed around 2005 and *C. finmarchicus* became available as prey during autumn. Explicitly, we test the hypothesis that warming of the Norwegian Sea with extended zooplankton reproduction season and more generations of *C. finmarchicus*, has prolonged the herring feeding period. Furthermore, that the extended feeding period has led to improved gonadal conditions and increased spawning migration potential rather than body growth in terms of length.

Data and methods

The data used are national official landings statistics and biological parameters of adult herring sampled from both commercial landings and surveys from Norway, Faroes and Iceland. Temporally, the data span from 1994 to 2019 and all months of the year (Figure S1). The underlying data material is believed to cover the adult herring stock (generally, ages 4 and older) well in terms of describing potential spatiotemporal changes.

Landings statistics and biological samples from the commercial fleet

Two sources of fisheries dependent data have been used. Firstly, official landings statistics, which have been used to describe the seasonal and spatial development of the fisheries in the study period. Secondly, biological samples of individual fish from commercial landings.

The data from the commercial fleet do not reflect the entire distribution area of herring (Figure 3), but they provide the necessary information for the spatial aspects of the research questions. Norway, Faroes and Iceland have taken on average 81% of the herring catches since 1994 with a relatively constant proportion over these years. This further supports the significance of these data.

The landings statistics used in this study are the Norwegian, Faroese and Icelandic official landings of herring from 1994 to 2019. The landings have been aggregated in 5-year periods (except the first period, which covers six years), annual quarter and statistical rectangle (0.5° latitude, 1° longitude). These aggregations have been made to describe the seasonal and interannual development of the spatial patterns of the herring fisheries in one Figure (4 by 5 panels).

Samples from commercial catches were either frozen at sea and sent to the research institutes or collected at the landing sites; in both cases, the samples were analysed at the national research institutes. The sampling strategy for individual fish was simple random sampling. Sample size was generally 25-50 fish. Commercial samples were mainly taken by purse seine or pelagic trawl.

Biological samples from survey catches

The survey data used were biological samples of individual fish.

Spatially, the survey data cover the distribution area of adult herring (Figure 3). The spawning survey is confined to the spawning area of herring along the Norwegian coast, whereas the internationally coordinated ecosystem surveys in the Nordic Seas (ICES, 2021b) cover the entire adult feeding area in the Nordic Seas.

Biological samples from survey catches were taken randomly on board pelagic trawl vessels. Samples generally consisted of 25-100 fish or as many as the catch allowed. Samples were analysed immediately after being caught. Age was sometimes determined on the vessel and sometimes once back on land.

Biological parameters

The biological material analysed in the present study was collected from survey samples and samples from commercial landings. The biological parameters recorded were total length (cut to the nearest cm below), whole body weight (including guts), sex, sexual maturity (stage 1-8; 1-2 = immature, 3-5 = maturing, 6 = spawning, 7 = spent, 8 = resting), gonad weights (note that Norwegian gonad weights were available for all years, whereas Icelandic and Faroese only from 2005 onwards), stomach content (only the Norwegian data; the information used here is stomach empty or non-empty) and age determination, which was based on either scales (Norwegian and Icelandic) or otoliths (Faroese – and to some extent Norwegian and Icelandic).

The focus of the study was the main habitat of the adult stock in the Norwegian Sea. Therefore, samples west of 22°E were used, excluding the main nursery area of the Barents Sea. Moreover, only herring at ages 3 and older were used in the study, some of which were still immature herring having left the nursery areas 1-2 years prior to first spawning. For statistical modelling all fish aged 10 and older were merged into a 10+ group. In total, 310749 age determined herring fulfilled these criteria (Table 1) and after filtering for the relevant seasons, n_{length} = 167430 and n_{weight} = 166340 remained (Table 2). Herring containing information on stomach fullness were $n_{stomach}$ = 211548. For analyses of gonad weight (n_{gonad} = 62216; Table 2) some extra filtering was conducted to remove fish, which may have been mis-staged as immature fish during the subjective gonad staging, as the point here was to focus only on maturing fish. Firstly, only herring aged 4-10+ in maturation

10.3389/fmars.2022.803171

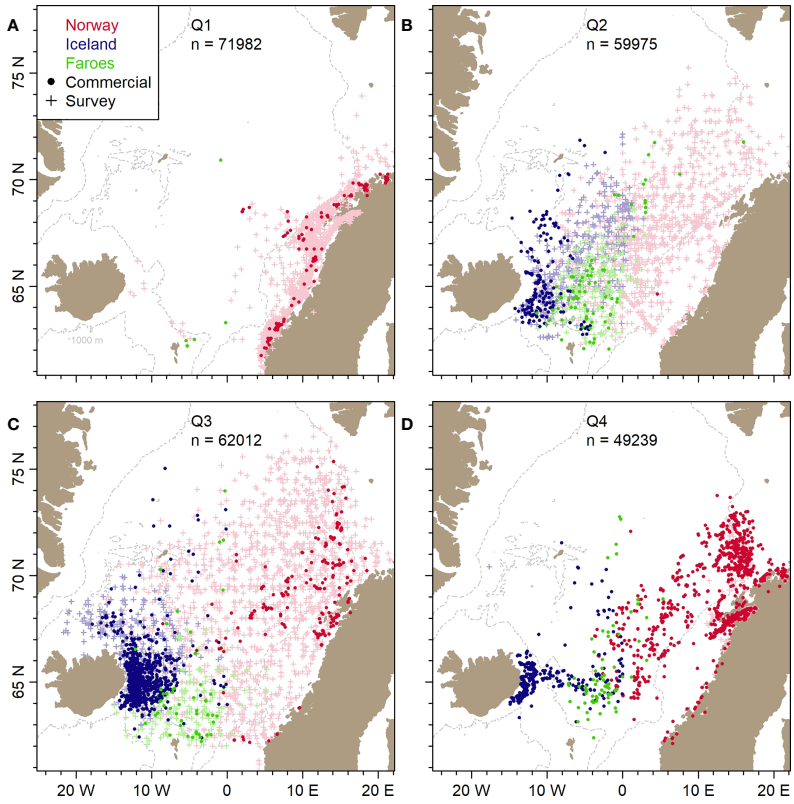


FIGURE 3
Study area. Positions of all Norwegian (red), Icelandic (blue) and Faroese (green) samples of herring from scientific surveys (+) and commercial catches (•) included in the present study for the period 1994-2019. The panels **(A–D)** represent annual Quarters 1-4.

stages 3-5 were included. Secondly, for fish in maturation stage 3 (early maturing) those with gonadosomatic index (GSI)< 1.25% (GSI=gonad weight/total weight*100) were excluded. Thirdly, for fish in maturation stages 4-5 (late maturing) those with GSI< 2.5% were excluded. The thresholds 1.25% and 2.5% GSI were chosen because fish with lower GSI did not realistically reflect fish in maturity stages 3 and 4-5 respectively; this assessment was based on visual inspection of scatter plots of gonad weight against fish weight (not shown).

Model description

In order to track herring distribution as well as temporal and seasonal changes in age-based body size, weight, and gonad weight in the Norwegian Sea, we fitted spatiotemporal distribution models for each response variable (body size, weight, and gonad weight) separately for each age group 3-10+ and season (May, July, Sep-Oct and Nov-Dec) for the period 1994-2019. Coordinates in latitude and longitude were transformed to the EPSG:32630 coordinate system before the analysis in order to preserve distances as much as possible (though, no single projection system will be able to preserve distance perfectly with such a large geographical extent).

A total of five covariates were explored in the analysis depending on the response variable analysed (Table 3): the year, total body length, sex, Fulton K (K=100 x weight in g/(length in cm)^3), and day of the year;

$$\mu_a(i) = \sum_{j=1}^{p} \beta_a(j) X_a(i,j) + \epsilon_a(s_i, t_i), \quad for \quad \begin{matrix} a = 1,\ldots, A, \\ i = 1,\ldots, n_a, \end{matrix}$$

$$\epsilon_a(\cdot, t_i) \sim \mathrm{MVN}(0, \Sigma_t),$$

$$Y_a(i) \sim f(\mu_a, \sigma_a, \theta_a),$$

where $\mu_a(i)$ is the expected response (body size, weight, and gonad weight) for individual i (total of n_a observations) of age-season group a (total of A age-season groups). X_a is the design matrix of covariates included in the model for age-season group a, β is the matrix of covariate effects to be estimated. The index j is an indicator of the covariate number and goes from 1 to p. $\epsilon_a(s_i,t_i)$ is the spatio-temporal random effect value for location s_i, time t_i, and age-season group a that follows a multivariate normal distribution (MVN) with a Matérn covariance structure Σ_t approximated by the stochastic partial

differential equation (spde) approach of Lindgren et al. (2011).

TABLE 1 Number of biological samples by year, with information on age, older than 2 year and west of 22°E.

	Number of biological samples	
Year	Condition and gonad weight	Stomach fullness
1994	12683	11937
1995	22712	21752
1996	22809	19164
1997	19579	15945
1998	18515	15474
1999	15140	13635
2000	9262	8375
2001	8473	7899
2002	6635	6196
2003	7606	6478
2004	5114	4498
2005	11609	8250
2006	9603	7291
2007	12048	7118
2008	9949	4240
2009	11180	4518
2010	14706	6877
2011	10860	3776
2012	11943	5262
2013	11020	4543
2014	7690	3784
2015	7600	3860
2016	10766	5395
2017	11694	6445
2018	10163	2022
2019	11390	6814
Total	310749	211548

For analyses regarding condition and gonad weight, further filtering was done (see text).

The covariance structure Σ_t is the same for all years. The generic function f is the chosen probability density function to model the response variable Y_a with the corresponding dispersion parameter σ_a and distribution specific parameter θ_a. This f is selected individually for each age-season group, and response variable, based on model selection and chosen among normal, log-normal, skewed-normal, gamma, tweedie, and student-t distributions (Table S.01). All models were fitted using R (R Core Team, 2021) (code available at https://github.com/holleland/spatiotemporalDynamicsNSSH) and TMB (Kristensen et al., 2016).

For each combination of age-season group, initial selection of covariates was based on visual exploration of the relationship between the five covariates and the response variable (Zuur et al., 2010). All continuous variables were included in the model using thin-plate regression splines as implemented by default in GAM (Wood, 2003; Wood, 2011). From the above model, further adjustments (choice of likelihood function and covariates) were made *via* residual diagnostics (Q-Q plot as in Hartig (2020) and plot of residuals *vs*. covariates) until the model showed a reasonable fit (i.e. no signs of under/overdispersion, multimodality, etc) (Supplementary zip). The model configuration was built step-by-step based on best fit for each combination of age and season. Therefore, there was not a predefined list of alternate models, on which for example an AIC-selection could be based on. AIC is otherwise a commonly used criterion for selecting models. Gear effects were not included in the models; when plotted against different gear types (3 general categories), final model residuals did not show any major pattern (Supplementary zip), supporting our approach.

As expected, fish weight and gonad weight increased with increasing fish length (Figure S2 and S3) and this topic was not further explored in this paper. We presented the effect of covariates on the response variable by plotting their marginal effect i.e. the effect of a variable based on the median values for

TABLE 2 Number of fish in each combination of age and season for body length, somatic condition (weight) and gonad weight modelling.

	Body length				Somatic condition (weight)				Gonad weight	
age	May	Jul	Sep-Oct	Nov-Dec	May	Jul	Sep-Oct	Nov-Dec	Sep-Oct	Nov-Dec
3	2402	2857	603	2828	2376	2857	603	2828		
4	5112	3531	2106	6987	5112	3531	2106	6987	2007	6758
5	8407	3494	3346	7351	7343	3494	3346	7351	3209	6422
6	9583	5057	4169	5944	9583	5057	4169	5944	3895	5337
7	8471	4891	3980	4357	8471	4891	3980	4357	3605	3936
8	6557	4934	3410	3401	6557	4934	3410	3401	3170	3167
9	4457	4438	2949	2380	4457	4438	2949	2380	2864	2304
10+	12341	10186	8854	7198	13190	10186	8854	7198	8492	7050
Total	58179	39388	29417	40446	57089	39388	29417	40446	27242	34974

all other covariates included in the final models (Table 3). Therefore, variation in length within age groups could be interpreted as *length at age*, whereas variation in weight and gonad weights within age groups could be interpreted as variation in *somatic condition* and *gonad development per sex*, respectively. Here on, these terms were used when describing the model results. Note also, that somatic condition and length at age did not differ with sex, and therefore sex was not used as covariate in the model for these parameters (Table 3). However, the gonad development was different between females and males; model predictions were shown for females.

To illustrate spatial variations in body growth, somatic condition and gonad development, we mapped the modelled spatiotemporal random effect of herring for each age, season and year (see example for age 7 herring in Figure S4–S6) across the prediction area. The prediction area was delimited by the convex hull of the data points used in each model. For the autumn months the prediction area boundaries were manually adjusted based on the distribution of the fisheries. The spatiotemporal effect can be interpreted as the deviation in the modelled response due to geographical location from an *average fish* with median values for all covariates. To summarize these maps, we calculated a weighted centre of gravity (CG) for positive (above average) and negative (below average) spatiotemporal deviations by season, age and year, weighted by the magnitude of the effect. The calculations of CG for below- and above-average spots are detailed below for each year t, where lon_i and lat_i are the longitude and latitude associated with predicted grid cell i out of totally n_{area} cells and $d_i^{a,t}$ is 1 if $\varepsilon_a(s_i,t) > 0$ and 0 otherwise.

$$\begin{cases} \text{CG}^{\text{lon}}_{\text{above}}(a,t) = \frac{1}{\sum_{j=1}^{n_{area}} d_j^{a,t} \left|\epsilon_a(s_j,t)\right|} \sum_{i=1}^{n_{area}} d_i^{a,t} \ \text{lon}_i \ |\epsilon_a(s_i,t)|, \\ \text{CG}^{\text{lat}}_{\text{above}}(a,t) = \frac{1}{\sum_{j=1}^{n_{area}} d_j^{a,t} \left|\epsilon_a(s_j,t)\right|} \sum_{i=1}^{n_{area}} d_i^{a,t} \ \text{lat}_i \ |\epsilon_a(s_i,t)|, \end{cases}$$

$$\begin{cases} \text{CG}^{\text{lon}}_{\text{below}}(a,t) = \frac{1}{\sum_{j=1}^{n_{area}} \left(1-d_j^{a,t}\right) \left|\varepsilon_a(s_j,t)\right|} \sum_{i=1}^{n_{area}} (1-d_i^{a,t}) \ \text{lon}_i \ |\varepsilon_a(s_i,t)|, \\ \text{CG}^{\text{lat}}_{\text{below}}(a,t) = \frac{1}{\sum_{j=1}^{n_{area}} \left(1-d_j^{a,t}\right) \left|\varepsilon_a(s_j,t)\right|} \sum_{i=1}^{n_{area}} (1-d_i^{a,t}) \ \text{lat}_i \ |\varepsilon_a(s_i,t)|, \end{cases}$$

To easier spot trends, we averaged across adjacent age groups and smoothed the temporal trajectories of the CGs across years by a 3-year moving average.

Raw data summaries on weight and length

Raw data summaries on body weight, gonad weights and length were used to supplement the model outputs with regards to marginal effects of the covariate year. There were two main motives to do so. Firstly, it was done to describe the seasonal development in all months and secondly, to highlight the overall differences between the periods [1994-2004] and [2005-2019]. In order to allow comparing weights among seasons and years, the body weight and gonad weight material was standardised to only include fish of length 33 cm, which was the modal value for length in the full dataset. Length, which is more affected by density dependence, was standardised to average length of age 6 per year. Only years with data for at least 8 months were used to produce 3-month running averages before taking averages over the periods [1994-2004] and [2005-2019]. Herring at 33 cm and six years old are representative for sexually mature herring.

Feeding activity and fisheries' location in August-September

Subjective data on stomach fullness were analysed to give a simple description of the relationship between proportion of non-feeding herring (empty stomachs) and how southerly the targeted herring fishery was in August-September. The season August-September was chosen, because in these months in the early years in the study period the entire stock had already migrated to the wintering areas. In the latest years there has been no fishery in the traditional northern wintering areas in August-September. The latitudinal location of the herring fisheries was used as proxy for a position on a south-western – north-eastern axis. A more southerly position indicated herring still being in the south-western feeding areas. The relationship was tested by linear regression.

Note, that information on stomach fullness was only available for the Norwegian material, which rarely are

TABLE 3 List of covariates included in the final models.

Response variable	Season	Formula (R notation)
Body length	All seasons	~ year
Body weight	July	~ year + s3(log.length, k=3)
Body weight	Except July	~ year + s3(length, k=5)
Gonad weight	Sep-Oct	~ year + sex + s3(length, k=3) + s3(fultonK, k=3) + s3(dayofyear, k=3)
Gonad weight	Except Sep-Oct	~ year + sex + s3(log.length, k=3) + s3(fultonK, k=3) + s3(dayofyear, k=3)

obtained from the western part of the study area off Iceland. Therefore, stomach fullness data are not representative for the whole stock throughout the year, but they are used here as an indication of feeding activity in the stock in August-September. Landings were, however, represented by the combined Faroese, Icelandic and Norwegian catches, because in later years the Norwegian catches have been very low in August-September, and therefore the catch area was not estimated to be representative of a targeted herring fishery.

All figures and analyses for this paper were produced using R (R Core Team, 2021), except Figure 2, which was produced using MatLab.

Results

Large scale changes in fishery

Over the period 1994-2019 large-scale changes in the herring fishery in the Norwegian Sea were observed with a shift in both timing and distribution showing a main tendency to occur progressively later in the year and further to the southwest (Figure 4).

The fishery in the main spawning period in first quarter has been quite stable and consistently conducted along the Norwegian coast since 1994 constituting between 27% and 37% of the total annual herring fishery.

Early in the feeding season in second quarter there has been large variability in the herring fishery. The first years, there was a significant (24%) fishery in the central Norwegian Sea extending towards the Iceland-Faroe ridge. In the period 2000-2004 there was still a large fishery, but the fishery had moved farther north in the Norwegian Sea. Since around 2005, the fishery again was closer to the Iceland-Faroe ridge, but only small quantities were taken and in the latest years it was less than 1% of the annual catches.

In third quarter the fishery constituted between 10% and 22% of the total annual landings, with highest percentages in the period 2005-2014. In the earlier years the vast majority of the catches were taken in northern Norway, but gradually over the years the main fishery in the third quarter moved first to the Norwegian Sea and then southwest to the Icelandic shelf edge from around 2005.

In the fourth quarter the relative catches increased persistently from 31% in the mid-1990s to 63% in the latest years. Further, the fisheries in fourth quarter started shifting westward from around 2005, i.e. from the Norwegian coast to also be in the oceanic waters off the Norwegian shelf, then into the central Norwegian Sea and the Icelandic shelf edge in later years.

Changes in modelled somatic condition

In the early part of the time-series, herring generally reached maximum somatic condition (weight at age) in July or September-October and then weight decreased over the autumn months (Figures 5D–F). This pattern changed around 2005, after which herring continued to add weight into the autumn months.

The modelled somatic condition varied much interannually during the first ten years of the study period, which started with a decline in weight in September-October of all age groups from 1994 to 1997. This was followed by a general but variable increase until around 2005, after which the September-October weights were both higher and more stable than before 2005.

The weight addition after 2005 in September-October was seen across all age groups, but for the oldest herring the maximum weight was even maintained into November-December (Figure 5F). This was a gradual shift where the older the fish got the higher the November-December weights tended to be (Figures 5D–F, S7 middle row).

The difference in somatic condition between May and December was generally higher after 2005 than in earlier years. The raw data summaries of body weight at 33 cm supported the model results (Figure 6A). In both periods, herring started after spawning with the same initial weight, but it developed differently over the rest of the season clearly being higher from September onwards in the period after 2005 and was maintained until spawning.

Changes in modelled gonad development of females

Modelled gonad weight in September-October was generally more variable in the earlier part of the study period than in the latest years (Figures 5G–I). The weight addition from September-October to November-December was larger after 2005. This pattern was increasing with age (Figures 5G–I, and S7 bottom row).

The highest gonad weights in November-December were reached when the somatic condition in the same months was high (Figures 5F, I). The male gonads (testes) had also added more weight in winter in the recent years as compared to the earlier period (Figure 6C). The autumn/winter weights were higher for males than for females (Figures 6B, C).

The gonad weights of maturing herring of both sexes were also clearly higher in the period 2005 and later than in the earlier period (Figures 6B, C), and the difference between the two periods was evident over all months October-January, from early maturing until the pre-spawning stages.

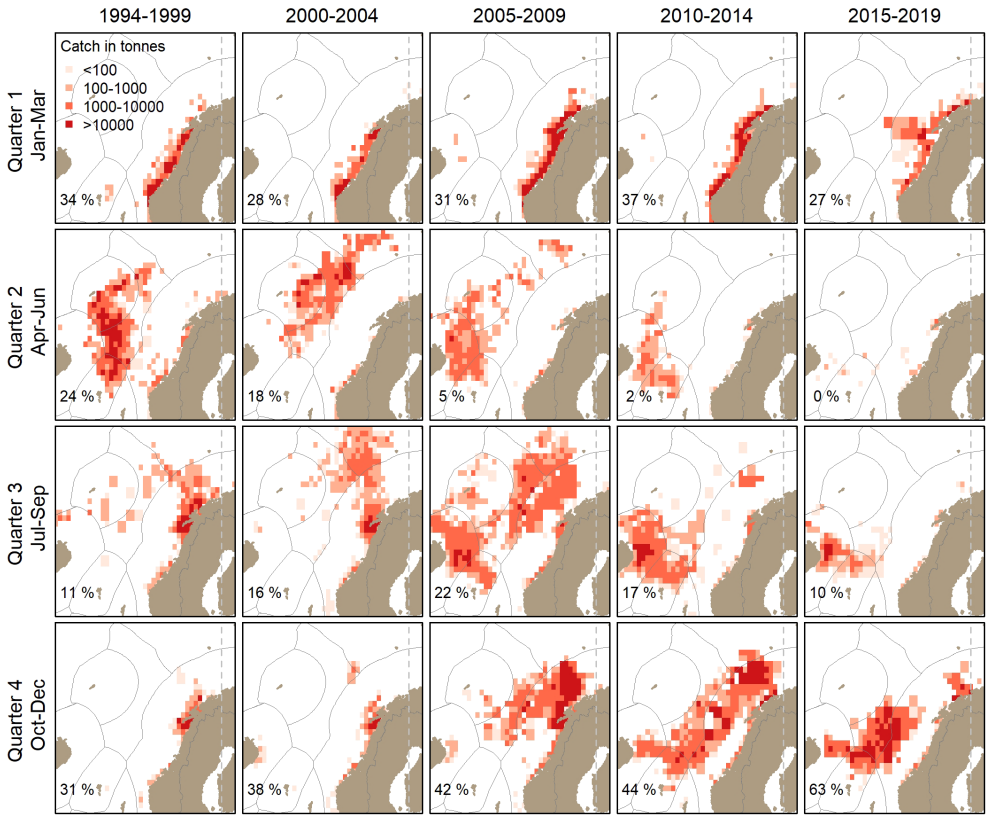


FIGURE 4
The Norwegian spring-spawning herring fisheries of the Norwegian, Icelandic and Faroese fleets by quarter of the year in five-year intervals over the study period 1994-2019. Data are shown as sum of landings within a statistical rectangle (0.5° latitude, 1° longitude). Grey lines indicate national exclusive economic zones. In bottom left corner is given the percentage of the quarterly catch in relation to all year in the given period.

Changes in modelled length at age

The temporal trend in modelled length at age showed large variability in the earlier part of the study period (Figures 5A–C). For lengths of older fish, the large variability ceased around 2005, after which there were some years with generally small lengths. There was, however, a year-class effect, where minimum length occurred first for the younger fish and then gradually later for the older ages. These minima in lengths some years after 2005 concurred with stable high weights after 2005.

The youngest fish grew most in length from May to July (Figures 5A and S7 top row) and in some years until September-October. With increasing age, the length addition over the feeding period was not discernible with our modelling approach. The raw data summaries (Figure 6D) supplemented with the results that six year old herring, which were largely sexually mature, had on average added most of the length before July. There was no significant difference between the periods [1994-2004] and [2005-2019], but in the period after 2005 there were indications that length was added further into autumn as compared to the period before 2005.

Modelled centre of gravity

The centre of gravity of the sampled herring showed that the whole population tended to move in the south-western direction after 2005 for all seasons analysed, regardless of whether the body length, weight and gonad weight was above or below average (Figure 7, Figures S8-10).

The tendency of being distributed to the south-western area increased with age and for body length and somatic condition within ages for all seasons. In July, an exception was older herring below average length and somatic condition, which in later years were shifted in a south-eastward direction; this was possibly an artefact of North Sea herring being sampled.

Contrastingly to the general pattern of length and somatic condition, the herring with above average gonad weights in

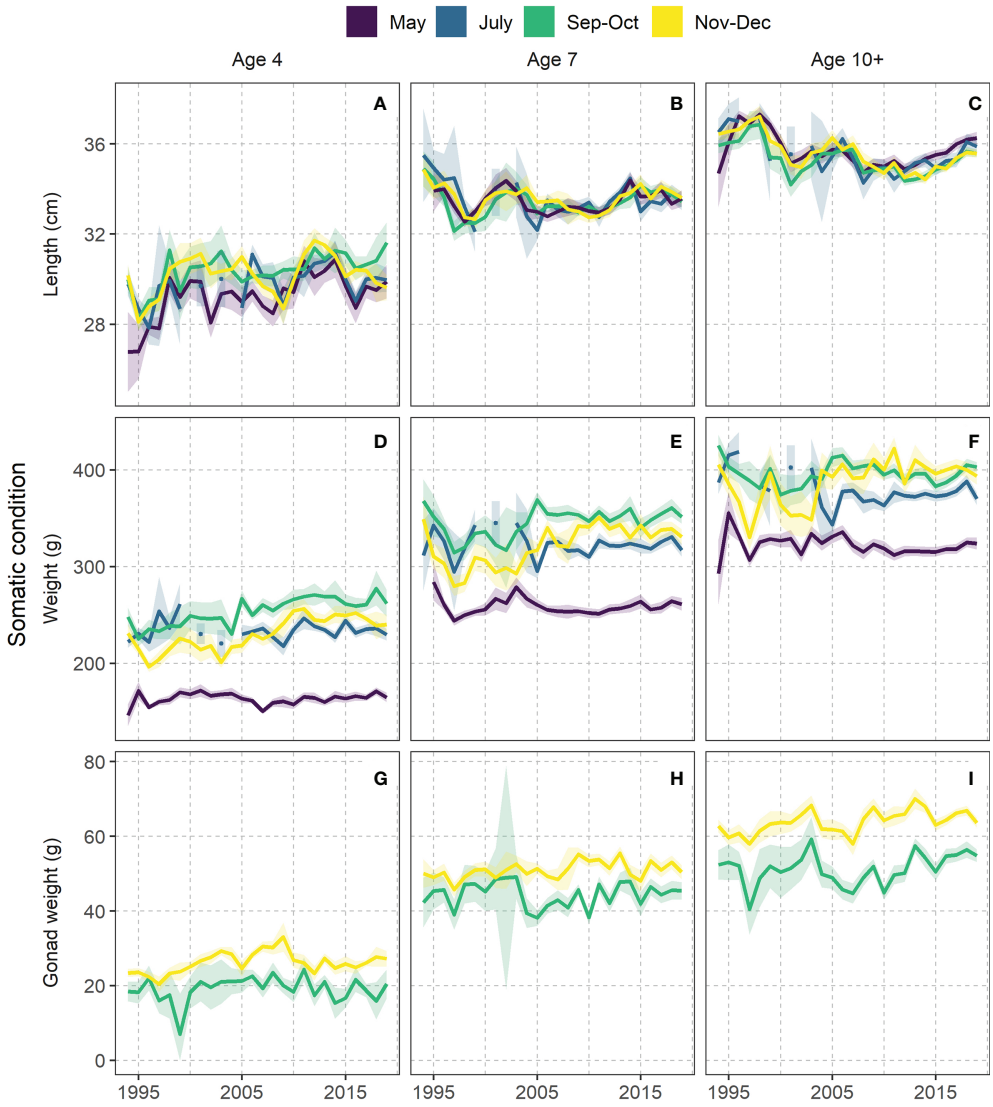


FIGURE 5
Marginal effects of sampling year and season on length at age **(A–C)**, somatic condition **(D–F)** and gonad development **(G–I)** from the spatiotemporal model. Presented for ages 4, 7 and 10+ (age 10 and older). All covariates except year were fixed at their median observed values and spatial effect set to zero. For detailed depictions including all ages, see Figure S6A-C.

September-October were found farther east than those with below average gonad weight (Figure 7, bottom row).

In November-December there were no apparent differences between below and above locations in any of the investigated parameters.

There were also indications that in the latest years of the study period, the above and below average fish were distributed in the same area. This pattern was clearest for older fish in September-October.

During the period 1997-2005, there was an opposite tendency in the population, towards moving in the north-eastern direction in May and July. This was linked with the much more eastern distribution in autumn (September-October, November-December) during this period.

Feeding activity and fisheries' location in August-September

There was a significant linear relationship (R2 = 0.44; p = 0.0004) between the proportion of non-feeding herring in August-September, based on Norwegian samples, and the latitudinal centre of gravity of the commercial herring fishery of the combined fleets of Norway, Iceland and Faroes (Figure 8).

10.3389/fmars.2022.803171

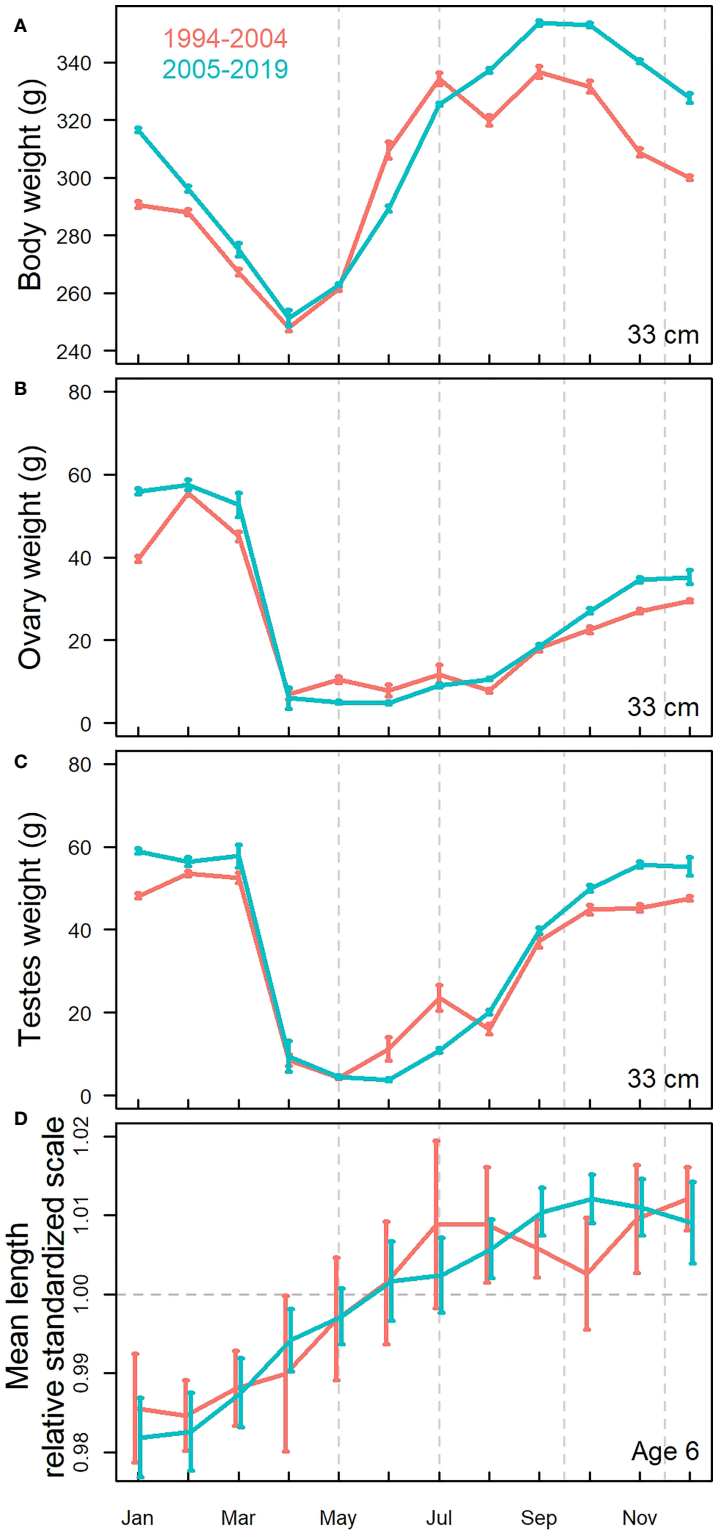


FIGURE 6
Seasonal variation based on raw data summaries showing monthly development in **(A)** weight (standardized at 33cm length) and gonad weight (standardized at 33 cm length) for **(B)** females (ovaries) and **(C)** males (testes) and **(D)** standardized mean length compared between the periods before (red) and after (green) 2005. The error bars indicate 95% confidence intervals of the means.

The proportion of non-feeding herring (empty stomachs) was lowest when the fishery was most southerly (and in reality south-westerly (Figure 4, Jul-Sep)). The development over time showed that there was a shift around 2010, after which the fisheries were more southerly and lower proportions of non-feeding herring.

Discussion

Over the study period the herring population showed a clear tendency of being distributed progressively farther in the south-western part of the Nordic Seas during the feeding period. This tendency increased with age, and length and somatic condition within age groups. Herring also had an increasingly delayed return to wintering areas farther east in Norwegian coastal and offshore waters. Furthermore, there was a clear change in somatic condition towards stable high levels after 2005 as well as increased gonad investment. Herring length at age also stabilized around 2005, but at relatively small sizes. The identified changes were most notable for the oldest fish (10 years and older). The described changes in the biological parameters of herring were concurrent with marked oceanographic changes and with a phenological shift in the zooplankton community.

Extended feeding period

Our hypothesis, that herring had extended their feeding period into autumn, was supported by spatiotemporal modelling. After 2005, the weight gain between July and September-October was higher than before 2005. The additional full-year data added that herring started after spawning with the same initial weight both before and after 2005, but the weight addition was larger after 2005, particularly from September onwards and the somatic weight remained high until spawning.

The feeding activity investigations also supported the prolonged feeding hypothesis, but here in terms of a spatial relationship. When the fishery in August – September was in a south-westerly position the proportion of empty stomachs was low. That is, when the herring was distributed towards southwest it was most likely still feeding during early autumn.

South-westward shift in distribution

The change towards a more south-westward feeding distribution of herring after 2005 is likely linked to both spatial differences in prey distribution and prolonged prey availability. History has shown that herring migrations after spawning at the Norwegian coast typically has been in the western direction towards areas north of Faroes and further west into north-east Icelandic waters (Dragesund et al., 1997; Eliasen et al., 2021). The current south-western distribution of herring in the feeding season (Eliasen et al., 2021) is similar to the feeding distribution prior to the stock-collapse in the 1960s (Dragesund et al., 1997).

The south-western areas are in general very productive with high prey availability for herring (Kristiansen et al., 2016; Kristiansen et al., 2019; Melle et al., 2020; Kristiansen et al., 2021). The high stomach fullness west of the Jan Mayen front (Melle et al., 2020) illustrates the importance of these frontal areas in the annual migrations of herring. Further, the south-western autumn fisheries have in the latest years congregated near the East-Icelandic shelf edge, indicating that productivity has been high in this area also late in autumn. The observed fishing patterns for herring can to some extent reflect behaviour of the fishing fleets caused by e.g. fisheries management and changes in agreements among the fishing parties to this stock. Such artefacts are, however, not explaining sufficiently the observed south-westward changes in the fishing pattern after 2005, because all nations - also those not hampered by regulations - changed the fishing pattern in the south western direction.

The shift in distribution towards the southwest after 2005 was seen over all months studied, which indicates that prey availabilities may have been higher near Iceland, compared to other parts of the Nordic Seas during the entire feeding period. The analyses of centre of gravity showed a more south-westward distribution of herring with above average somatic condition in May and July. However, herring with above as well as below average somatic condition followed the same change in migration pattern. They basically all tended to shift distribution in same south-western direction over the study period, likely a result of aggregating more in the productive frontal areas in southwest. This tendency of shifting distribution towards southwest increased with increasing age, and length within age groups in accordance with the size dependent migration hypothesis (Nøttestad et al., 1999; Eliasen et al., 2021). The size dependent migration hypothesis provides an alternative explanation to the superior somatic condition observed in the southwestern region, which may apply particularly early in the feeding season.

It is, however, to be noted that the migration patterns have shifted quite suddenly in the opposite direction as well. A detailed study on the acoustic abundance of herring in May showed that during the period 1999-2004 the herring feeding area was shifted northwards (Eliasen et al., 2021). This northward shift was also evident in the centre of gravity in the biological samples and in the fisheries dynamics during spring and summer 2000-2004 demonstrated in the present study.

This northward shift in the feeding area happened after a period with rapid declining somatic condition during 1994-1997

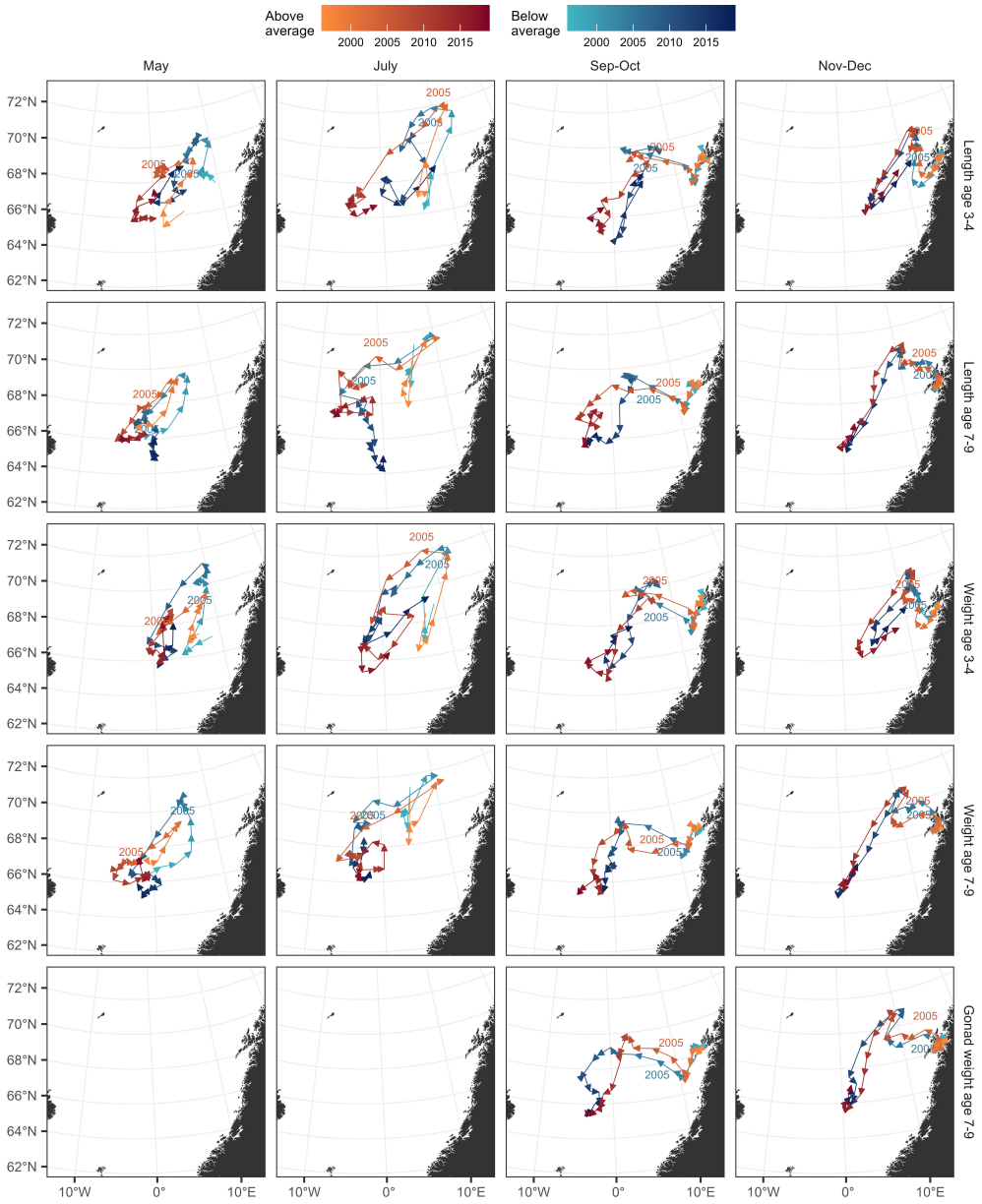


FIGURE 7
Modelled spatiotemporal changes in centre of gravity (CG) for ages 3-4 and 7-9 for length, weight and gonad weight (horizontally) and season (vertically). The variations in CG are shown split between two groups of herring having body length, fish weight and gonad weight either above (red) or below (blue) average. For detailed depictions including all ages, see Figures S8A-C.

to lowest levels over the time series in the present study, which also influenced the reproductive potential through atresia in the herring with poorest condition (Óskarsson et al., 2002). Hence, this major drop in somatic condition in 1997 and the following north eastward shift in feeding distribution suggest that the areas along the fronts in the south-western part of the Norwegian Sea were less productive or otherwise inhabitable in the late 1990s, as discussed by Eliasen et al. (2021).

Somatic condition and gonad development

The spatiotemporal modelling demonstrated that the extra energy gained from improved feeding conditions in combination with extended feeding period was reflected in the gonad investment of the herring, with gonad weights being higher after 2005. The main indication of the increased gonad

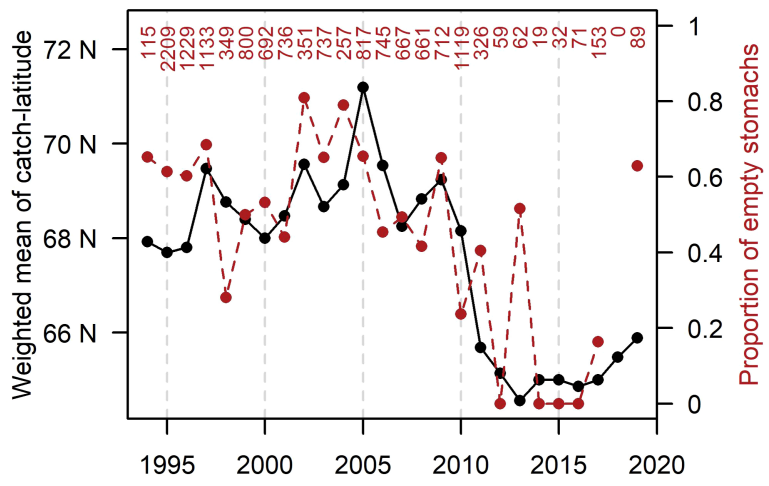


FIGURE 8
Interannual development of weighted average catch latitude (from combined Norwegian, Faroese and Icelandic fleets) and proportion of empty stomachs (based on Norwegian samples) in August-September. Number of fish analysed for stomach fullness per year is indicated at the top.

investment after 2005 was the increase in gonad weight between the early (September-October) and late (November-December) autumn, which was tightly linked to somatic condition and age. The oldest fish were able to maintain high somatic condition until late autumn and had the largest increase in gonad weights from early to late autumn. This is again likely linked to the fact that the oldest herring with the highest migration potential, in accordance with the size dependent migration hypothesis (Nøttestad et al., 1999; Eliasen et al., 2021), in fact were the ones migrating farthest west and gaining most from the extended period with available prey.

Both the change towards better somatic condition and higher gonad weights supported the previous results from dos Santos Schmidt et al. (2020). They further noted different trends for condition and body growth in terms of length. They specifically linked the differences in allocation of energy to condition and gonad investment versus body growth, to the warming of the Norwegian Sea, herring stock size and inter-specific competition from mackerel (*Scomber scombrus*).

Mackerel has large diet overlap with herring (Prokopchuk and Sentyabov, 2006; Langøy et al., 2012; Bachiller et al., 2016; Óskarsson et al., 2016). In addition to diet overlap, dos Santos Schmidt et al. (2020) argued that the mackerel became more widely distributed in the Nordic Seas after the turn of the century (Olafsdottir et al., 2019), which lead to herring and mackerel occupying overlapping habitats as well (Huse et al., 2012; Utne and Huse, 2012). Similarly, herring abundance has been shown to affect growth of North East Atlantic mackerel (Ólafsdóttir et al., 2016). Our results suggested that, overall, the somatic condition and reproductive investment of herring did not decrease during this period of inter-species overlap with mackerel. This suggests that herring has adapted to the changed conditions, both oceanographic changes and inter-specific competition by utilizing the available resources further into the autumn months.

The finding, that reduced herring body growth in terms of length was concurrent with increasing somatic condition and investment into fecundity (dos Santos Schmidt et al., 2020) may in fact be linked with this postponed timing in energy gain over the growth season. Our study demonstrated that, on average, body growth in terms of length of sexually mature herring ceased during summer around July when onset of maturation normally is occurring (dos Santos Schmidt et al., 2017). Under such conditions where energy is gained late in the season and maturation processes already have started, allocation to body length may be prevented by the internal hormonal control, leaving more as reserves for spawning migration and gonad building. This has been shown for other teleost species (Bhatta et al., 2012). Whereas the final allocation into fecundity appears to be related to available energy, the onset of maturation does not appear to have changed throughout the study period. This is consistent with the onset of maturation being governed by other factors such as genetics and photoperiod (Han et al., 2020; dos Santos Schmidt et al., 2022).

Possible links to oceanography and lower trophic levels

In the early 1990s the central Norwegian Sea was cooling with minimum heat content around the turn of the century (Asbjørnsen et al., 2019). After the mid-1990s, the north Atlantic subpolar gyre

declined markedly, resulting in much increased temperatures and salinities in the Atlantic inflows from the north eastern Atlantic into the Nordic Seas (Hátún et al., 2005). Advective time lags of these hydrographic anomalies, in addition to reduced regional ocean heat losses to the atmosphere led to a marked warming in the central Norwegian Sea after 2002 (Asbjørnsen et al., 2019; Mork et al., 2019). Around the turn of the century, the dynamics of the Norwegian Sea Gyre also exhibited large variations (Hátún et al., 2021) first towards a strong gyre in 1999-2000 and then towards a weak gyre in 2002-2003. Such shifts in oceanographic conditions may in turn affect herring.

The warmer environment after 2005 may have improved the herring growth potential as it has been shown to increase with temperature (Brunel and Collas, 2010; Hunter et al., 2019), given high availability of prey.

The herring feeding migration is to large degree governed by the production of its preferred prey *C. finmarchicus*, which has a seasonal development linked to dynamics in the phytoplankton blooms (Broms and Melle, 2007). The interannual variability in the primary production in the Norwegian Sea is mainly driven by the transport of nutrients into the area from neighbouring waters. This is a possible mechanism for how climate can be an important driver for the availability of biological material in the food web (Skogen et al., 2007; Skagseth et al., 2022). In their updated ecosystem review, ICES (2021a) state that annual primary production in the Norwegian Sea has ended later in the year and been higher during the period 2013-2019 compared to 2005-2012, likely caused by increased inflow of cold and fresh water that has higher nutrient concentrations.

The variability in the Norwegian Sea Gyre is linked to the input of colder East Icelandic water into the Norwegian Sea. This, in turn, governs the relative contribution of both *C. hyperboreus* and large overwingering stages of *C. finmarchicus*, which are both important as prey to herring early in the feeding season (Kristiansen et al., 2019; Kristiansen et al., 2022). The influx of subarctic waters from the Iceland Sea is also a key nutrient source for the Norwegian Sea (Skagseth et al., 2022).

The meso-zooplankton biomass, as observed during the international ecosystem survey in the Norwegian Sea (IESNS) from late April to early June, is frequently used as a biomass index of lower trophic levels. Zooplankton biomass based on this index has also been suggested to explain growth conditions for herring (Huse et al., 2012; dos Santos Schmidt et al., 2020).

After being at relatively stable high levels 1995-2003 the zooplankton biomass index showed a dramatic drop during years 2003-2010, followed by a slow increasing trend until today, when levels again are comparable to the period prior to 2003 (ICES, 2021a). The observed trend is similar in all regions with some years lag in the colder areas off northeast Iceland and the Jan Mayen Front.

The observed changes in both body growth and somatic condition of herring in May tended to follow the same trend as the zooplankton biomass index, both of which were based on data overlapping in time and space. However, despite this apparent match between zooplankton abundance in May and the concurrent body growth and somatic condition, one may conclude from the present results that poor feeding conditions early in the feeding period are not necessarily detrimental for the herring's potential to gain weight over the feeding period.

Our results support a prolonged feeding period after 2005. It remains, however, unsolved what type of prey the herring fed on to be able to gain condition in autumn. A second generation of *C. finmarchicus* developing in late summer-autumn (Kristiansen et al., 2016; Strand et al., 2020; Skjoldal et al., 2021), which could sustain prolonged feeding opportunities for herring far into the autumn, is a reasonable explanation. But it cannot be excluded that other types of prey have been even more important.

Previous studies of herring diet have shown that they may shift to bigger prey like amphipods and euphausiids in July-August (Dalpadado et al., 2000; Bachiller et al., 2016; Óskarsson et al., 2016), especially in the western areas in more Arctic waters. These taxa may, however, also be important predators of *C. finmarchicus* copepodites (Melle et al., 2004; Skjoldal et al., 2004) taking advantage of a second generation of prey in autumn themselves.

Conclusion and outlook

Here we have demonstrated that the Norwegian spring-spawning herring have extended the feeding period in the south western part of the feeding area in the Nordic Seas. By doing so, they have managed to gain weight into the autumn months and thereby also enhance allocation of energy into gonads. Our results indicate that the somatic condition and available energy for gonad development and migrations is likely of higher importance for herring than length at age. Our results demonstrate that there are processes in the ecosystem in the Nordic Seas from May to late autumn that enhance the pre-spawning condition and reproductive investment of this stock, even though it has less effect on body growth in terms of length. The good pre-spawning condition and reproductive investment in later years has, however, not manifested itself in generally improved recruitment to the herring stock (Figure 1).

The timing of both primary production (Skogen et al., 2007; ICES, 2021a) and zooplankton production (Kristiansen et al., 2016; Strand et al., 2020; Skjoldal et al., 2021) may shift to such a degree that an index measured at the same time every year may not fully grasp actual fluctuations in the production.

The Norwegian Sea is clearly a dynamic region affected by varying oceanographic features linked to climatic changes (Asbjørnsen et al., 2019; Mork et al., 2019; Hátún et al., 2021) that can alter such important seasonal processes. We have only briefly touched on the potential effects that climate variability may have on important seasonal dynamics in the ecosystem and resources therein. Future monitoring and studies should therefore also focus on processes happening later in the year. Specifically, we encourage studies on zooplankton and further diet investigations of herring and other main predators on zooplankton in the Norwegian Sea in the autumn months.

Data availability statement

Inquiries regarding data availability can be directed to the corresponding author.

Ethics statement

Ethical review and approval was not required for the animal study because samples were taken from commercial catches and from scientific research trips. No specific ethical review and approval were needed for this monitoring.

Author contributions

EH, AS, and GÓ developed the main ideas. All authors structured the framework for the modelling and analyses. KO was the main responsible for model analyses of condition and gonad development and wrote the corresponding sections in the article with contributions from SH. EH compiled all data and analysed data with regards to fisheries dynamics and feeding. EH and AS wrote the manuscript, with feed-back from GÓ, KO, and SH. All authors contributed to the article and approved the submitted version.

Funding

This study was partly funded by the project "Sustainable multi-species harvest from the Norwegian Sea and adjacent ecosystems" the Research Council of Norway (project number 299554).

Acknowledgments

Thanks to four reviewers for input to improve the manuscript.

Conflict of interest

The authors declare that the research was conducted in the absence of any commercial or financial relationships that could be construed as a potential conflict of interest.

Publisher's note

All claims expressed in this article are solely those of the authors and do not necessarily represent those of their affiliated organizations, or those of the publisher, the editors and the reviewers. Any product that may be evaluated in this article, or claim that may be made by its manufacturer, is not guaranteed or endorsed by the publisher.

Supplementary material

The Supplementary Material for this article can be found online at: https://www.frontiersin.org/articles/10.3389/fmars.2022.803171/full#supplementary-material

SUPPLEMENTARY FIGURE 1
Positions of all Norwegian, Icelandic and Faroese samples of herring included in the present study for the period 1994-2019 presented by month. The colour of the points indicates year of sampling as shown in legend.

SUPPLEMENTARY FIGURE 2
Marginal effects of fish length and season on weight at age. All covariates (sampling year, Fulton K, sex and day-of-year) except fish length were fixed at their median observed values and spatial effect was set to zero. Box plot of fish lengths by age and season shown on the top for each age.

SUPPLEMENTARY FIGURE 3
Marginal effect of fish length and season on gonad weight at age. All covariates (sampling year, Fulton K, sex and day-of-year) except fish length were fixed at their median observed values and spatial effect was set to zero. Box plot of fish lengths by age and season shown on the top for each age.

SUPPLEMENTARY FIGURE 4
Example of mapped modelled below average spots (blue) and above average spots (red) of length at age of herring for age 7, for selected years in May, July, September-October and November-December.

SUPPLEMENTARY FIGURE 5
Example of mapped modelled below average spots (blue) and above average (red) of somatic condition of herring for age 7, for selected years in May, July, September-October and November-December.

SUPPLEMENTARY FIGURE 6
Example of mapped modelled below average spots (blue) and above average (red) of gonad development of herring for age 7, for selected years in September-October and November-December.

SUPPLEMENTARY FIGURE 7
Marginal effects of sampling year and season on length at age, somatic condition and gonad development for all age groups 3-10+. All covariates (sampling year, Fulton K, sex and day-of-year) except year were fixed at

their median observed values and spatial effect was set to zero. Box plot of fish lengths by age and season shown on the top for each age.

SUPPLEMENTARY FIGURE 8
Modelled spatiotemporal changes in centre of gravity (CG) of length at age for all ages 3-10+ (vertically) and season (horizontally). The variations in CG are shown split between two groups of herring having body length, fish weight and gonad weight either above (red) or below (blue) average.

SUPPLEMENTARY FIGURE 9
Modelled spatiotemporal changes in centre of gravity (CG) of somatic condition for all ages 3-10+ (vertically) and season (horizontally). The variations in CG are shown split between two groups of herring having body length, fish weight and gonad weight either above (red) or below (blue) average.

SUPPLEMENTARY FIGURE 10
Modelled spatiotemporal changes in centre of gravity (CG) of gonad development for all ages 3-10+ (vertically) and season (horizontally). The variations in CG are shown split between two groups of herring having body length, fish weight and gonad weight either above (red) or below (blue) average.

Supplementary zip-file with figures showing residual checks for fish weight and gonad weight modelling and gear (three general groups).

References

Asbjørnsen, H., Årthun, M., Skagseth, Ø, and Eldevik, T. (2019). Mechanisms of ocean heat anomalies in the Norwegian Sea. *J. Geophys. Res. Ocean* 124, 2908–2923. doi: 10.1029/2018JC014649

Bachiller, E., Skaret, G., Nøttestad, L., and Slotte, A. (2016). Feeding ecology of northeast Atlantic mackerel, Norwegian spring-spawning herring and blue whiting in the Norwegian Sea. *PloS One* 11, 1–25. doi: 10.1371/journal.pone.0149238

Bhatta, S., Iwai, T., Miura, C., Higuchi, M., Shimizu-Yamaguchi, S., Fukada, H., et al. (2012). Gonads directly regulate growth in teleosts. *Proc. Natl. Acad. Sci. U. S. A.* 109, 11408–11412. doi: 10.1073/pnas.1118704109

Bjørndal, T., Gordon, D. V., Kaitala, V., and Lindroos, M. (2004). International management strategies for a straddling fish stock: A bio-economic simulation model of the Norwegian spring-spawning herring fishery. *Environ. Resour. Econ.* 29, 435–457. doi: 10.1007/s10640-004-1045-y

Broms, C., and Melle, W. (2007). Seasonal development of calanus finmarchicus in relation to phytoplankton bloom dynamics in the Norwegian Sea. *Deep Res. Part II Top. Stud. Oceanogr.* 54, 2760–2775. doi: 10.1016/j.dsr2.2007.08.021

Broms, C., Melle, W., and Horne, J. K. (2012). Navigation mechanisms of herring during feeding migration: The role of ecological gradients on an oceanic scale. *Mar. Biol. Res.* 8, 461–474. doi: 10.1080/17451000.2011.640689

Brunel, T., and Collas, M. D. (2010). Effects of temperature and population density on von bertalanffy growth parameters in Atlantic herring: A macro-ecological analysis. *Mar. Ecol. Prog. Ser.* 405, 15–28. doi: 10.3354/meps08491

Dalpadado, P., Ellertsen, B., Melle, W., and Dommasnes, A. (2000). Food and feeding conditions of Norwegian spring-spawning herring (Clupea harengus) through its feeding migrations. *ICES J. Mar. Sci.* 57, 843–857. doi: 10.1006/jmsc.2000.0573

Devold, F. (1963). The life history of the atlanto-scandian herring. rapp. proc.-verb. des reun. *Cons. Int. Explor. Mer.* 154, 98–108.

dos Santos Schmidt, T. C., Berg, F., Folkvord, A., Pires, A. M. A., Komyakova, V., Tiedemann, M., et al. (2022). Is it possible to photoperiod manipulate spawning time in planktivorous fish? A long-term experiment on Atlantic herring. *J. Exp. Mar. Bio. Ecol.* 552, 1–10. doi: 10.1016/j.jembe.2022.151737

dos Santos Schmidt, T. C., Devine, J. A., Slotte, A., Claireaux, M., Johannessen, A., Enberg, K., et al. (2020). Environmental stressors may cause unpredicted, notably lagged life-history responses in adults of the planktivorous Atlantic herring. *Prog. Oceanogr.* 181, 14. doi: 10.1016/j.pocean.2019.102257

dos Santos Schmidt, T. C., Slotte, A., Kennedy, J., Sundby, S., Johannessen, A., Óskarsson, G. J., et al. (2017). Oogenesis and reproductive investment of Atlantic herring are functions of not only present but long-ago environmental influences as well. *Proc. Natl. Acad. Sci.* 114, 2634–2639. doi: 10.1073/pnas.1700349114

Dragesund, O., Johannessen, A., and Ulltang, Ø. (1997). Variation in migration and abundace of Norwegian spring spawning herring (Clupea harengus l.). *Sarsia* 82, 97–105. doi: 10.1080/00364827.1997.10413643

Eliasen, S. K., Homrum, E., Jacobsen, J. A., Kristiansen, I., Óskarsson, G. J., Salthaug, A., et al. (2021). Spatial distribution of different age groups of herring in Norwegian Sea, may 1996–2020. *Front. Mar. Sci.* 8. doi: 10.3389/fmars.2021.778725

Engelhard, G. H., and Heino, M. (2004a). Maturity changes in Norwegian spring-spawning herring before, during, and after a major population collapse. *Fish. Res.* 66, 299–310. doi: 10.1016/S0165-7836(03)00195-4

Engelhard, G. H., and Heino, M. (2004b). Maturity changes in Norwegian spring-spawning herring clupea harengus: compensatory or evolutionary responses? *Mar. Ecol. Prog. Ser.* 272, 245–256. doi: 10.3354/meps272245

Hansen, B., and Østerhus, S. (2000). North Atlantic–Nordic seas exchanges. *Prog. Oceanogr.* 45, 109–208. doi: 10.1016/S0079-6611(99)00052-X

Hartig, F. (2022). DHARMa: Residual diagnostics for hierarchical (Multi-level / mixed) regression models. R package version 0.4.6. Available at: https://CRAN.R-project.org/package=DHARMa.

Hátún, H., Chafik, L., and Larsen, K. M. H. (2021). The Norwegian Sea gyre – a regulator of Iceland-Scotland ridge exchanges. *Front. Mar. Sci.* 8. doi: 10.3389/fmars.2021.694614

Hátún, H., Sandø, A. B., Drange, H., Hansen, B., and Valdimarsson, H. (2005). Influence of the Atlantic subpolar gyre on the thermohaline circulation. *Science* 309, 1841–1844. doi: 10.1126/science.1114777

Han, F., Jamsandekar, M., Pettersson, M. E., Su, L., Fuentes-Pardo, A. P., Davis, B. W., et al. (2020). Ecological adaptation in atlantic herring is associated with large shifts in allele frequencies at hundreds of LOCI. *Elife* 9, 1–20. doi: 10.7554/ELIFE.61076

Hay, D. E., Toresen, R., Stephenson, R., Thompson, M., Claytor, R., Funk, F., et al. (2001). "Taking stock: An inventory and review of world herring stocks in 2000," in *Expectations for a new millenium*. Ed. F. Funk (Fairbanks: Alaska Sea Grant College Program), 381–454.

Holst, J. C., Dragesund, O., Hamre, J., Misund, O. A., and Ostvedt, O. J. (2002). Fifty years of herring migrations in the Norwegian Sea. *ICES Mar. Sci. Symp.* 215, 352–360. doi: 10.17895/ices.pub.8874

Hunter, A., Speirs, D. C., and Heath, M. R. (2019). Population density and temperature correlate with long-term trends in somatic growth rates and maturation schedules of herring and sprat. *PloS One* 14, 1–22. doi: 10.1371/journal.pone.0212176

Husebø, Å., Slotte, A., and Stenevik, E. K. (2007). Growth of juvenile Norwegian spring-spawning herring in relation to latitudinal and interannual differences in temperature and fish density in their coastal and fjord nursery areas. *ICES J. Mar. Sci.* 64, 1161–1172. doi: 10.1093/icesjms/fsm081

Huse, G., Fernö, A., and Holst, J. C. (2010). Establishment of new wintering areas in herring co-occurs with peaks in the "first time/repeat spawner" ratio. *Mar. Ecol. Prog. Ser.* 409, 189–198. doi: 10.3354/meps08620

Huse, G., Holst, J. C., Utne, K., Nøttestad, L., Melle, W., Slotte, A., et al. (2012). Effects of interactions between fish populations on ecosystem dynamics in the Norwegian Sea - results of the INFERNO project. *Mar. Biol. Res.* 8, 37–41. doi: 10.1080/17451000.2011.653372

ICES (2021a). Norwegian Sea ecoregion – Ecosystem overview. in: *ICES Advice: Ecosystem Overviews*. Report. (Copenhagen: International Council for the Exploration of the Sea). doi: 10.17895/ices.advice.8188

ICES (2021b). Working group on widely distributed stocks (WGWIDE). *ICES Sci. Rep.* 3, 874. doi: 10.17895/ices.pub.8298

Jakobsson, J. (1968). Herring migrations east of Iceland during the summer and autumn 1966 and 1967. *Fisk. Skr. Ser. Havundersøgelser* 15, 17–22.

Kristensen, K., Nielsen, A., Berg, C. W., Skaug, H., and Bell, B. (2016). TMB: Automatic differentiation and Laplace approximation. *J. Stat. Softw.* 70, 1–21. doi: 10.18637/jss.v070.i05

Kristiansen, I., Gaard, E., Hátún, H., Jónasdóttir, S. H., and Ferreira, A. S. A. (2016). Persistent shift of calanus spp. in the southwestern Norwegian Sea since 2003, linked to ocean climate. *ICES J. Mar. Sci.* 73, 1319–1329. doi: 10.1038/278097a0

Kristiansen, I., Hátún, H., Petursdottir, H., Gislason, A., Broms, C., Melle, W., et al. (2019). Decreased influx of calanus spp. into the south-western Norwegian

Sea since 2003. *Deep Res. Part I. Oceanogr. Res. Pap.* 149, 103048. doi: 10.1016/j.dsr.2019.05.008

Kristiansen, I., Jónasdóttir, S. H., Gaard, E., Eliasen, S. K., and Hátún, H. (2021). Seasonal variations in population dynamics of calanus finmarchicus in relation to environmental conditions in the southwestern Norwegian Sea. *Deep Res. Part I. Oceanogr. Res. Pap.* 171, 1–12. doi: 10.1016/j.dsr.2021.103508

Kristiansen, I., Hátún, H., Jacobsen, J. A., Eliasen, S. K., Petursdottir, H., and Gaard, E. (2022). Spatial Variability of the Feeding Conditions for the Norwegian Spring Spawning Herring in May. *Front. Mar. Sci.* 9, 1–14. doi: 10.3389/fmars.2022.823006

Langøy, H., Nøttestad, L., Skaret, G., Broms, C., and Fernö, A. (2012). Overlap in distribution and diets of Atlantic mackerel (scomber scombrus), Norwegian spring- spawning herring (clupea harengus) and blue whiting (micromesistius poutassou) in the Norwegian Sea during late summer. *Mar. Biol. Res.* 8, 442–460. doi: 10.1080/17451000.2011.642803

Lindgren, F., Rue, H., and Lindström, J. (2011). An explicit link between Gaussian fields and Gaussian Markov random fields: The SPDE approach. *J. R. Stat. Soc Ser. B.* 73, 423–498. doi: 10.1111/j.1467-9868.2011.00777.x

Melle, W., Ellertsen, B., and Skjoldal, H. R. (2004). "Zooplankton: The link to higher trophic levels," in *The Norwegian Sea ecosystem*. Ed. H. R. Skjoldal (Trondheim: Tapir Academic), 137–202.

Melle, W., Klevjer, T., Strand, E., Wiebe, P. H., Slotte, A., and Huse, G. (2020). Fine-scale observations of physical and biological environment along a herring feeding migration route. *Deep Res. Part II Top. Stud. Oceanogr.* 180, 1–19. doi: 10.1016/j.dsr2.2020.104845

Misund, O. A., Melle, W., and Fernö, A. (1997). Migration behaviour of Norwegian spring spawning herring when entering the cold front in the Norwegian Sea. *Sarsia* 82, 107–112. doi: 10.1080/00364827.1997.10413644

Mork, K. A., Skagseth, Ø., and Søiland, H. (2019). Recent warming and freshening of the Norwegian Sea observed by argo data. *J. Clim.* 32, 3695–3705. doi: 10.1175/JCLI-D-18-0591.1

Nøttestad, L., Giske, J., Holst, J. C., and Huse, G. (1999). A length-based hypothesis for feeding migrations in pelagic fish. *Can. J. Fish. Aquat. Sci.* 56, 26–34. doi: 10.1139/cjfas-56-s1-26

Nøttestad, L., Misund, O. A., Melle, W., Hoddevik Ulvestad, B. K., and Orvik, K. A. (2007). Herring at the Arctic front: Influence of temperature and prey on their spatio-temporal distribution and migration. *Mar. Ecol.* 28, 123–133. doi: 10.1111/j.1439-0485.2007.00182.x

Olafsdottir, A. H., Rong, K., Arge, J., Jansen, T., Óskarsson, G. J., Nøttestad, L., et al. (2019). Geographical expansion of northeast Atlantic mackerel (scomber scombrus) in the Nordic seas from 2007 to 2016 was primarily driven by stock size and constrained by low temperatures. *Deep Res. Part II* 159, 152–168. doi: 10.1016/j.dsr2.2018.05.023

Ólafsdóttir, A. H., Slotte, A., Jacobsen, J. A., Óskarsson, G. J., Utne, K. R., and Nøttestad, L. (2016). Changes in weight-at-length and size-at-age of mature northeast Atlantic mackerel (Scomber scombrus) from 1984 to 2013: effects of mackerel stock size and herring (Clupea harengus) stock size. *ICES J. Mar. Sci.* 73, 1255–1265. doi: 10.1093/icesjms/fsv142

Óskarsson, G. J., Gudmundsdottir, A., Sveinbjörnsson, S., and Sigurðsson, Þ. (2016). Feeding ecology of mackerel and dietary overlap with herring in icelandic waters. *Mar. Biol. Res.* 12, 16–29. doi: 10.1080/17451000.2015.1073327

Óskarsson, G. J., Kjesbu, O. S., and Slotte, A. (2002). Predictions of realised fecundity and spawning time in Norwegian spring-spawning herring (Clupea harengus). *J. Sea Res.* 48, 59–79. doi: 10.1016/S1385-1101(02)00135-1

Ottersen, G., Stige, L. C., Durant, J. M., Chan, K. S., Rouyer, T., Drinkwater, K. F., et al. (2013). Temporal shifts in recruitment dynamics of north Atlantic fish stocks: Effects of spawning stock and temperature. *Mar. Ecol. Prog. Ser.* 480, 205–225. doi: 10.3354/meps10249

Prokopchuk, I., and Sentyabov, E. (2006). Diets of herring, mackerel, and blue whiting in the Norwegian Sea in relation to calanus finmarchicus distribution and temperature conditions. *ICES J. Mar. Sci.* 63, 117–127. doi: 10.1016/j.icesjms.2005.08.005

Røttingen, I. (1990). "The 1983 year class of Norwegian spring spawning herring as juveniles and recruit spawners," in *Proceedings of fourth soviet-Norwegian symposium*. Ed. T. Monstad (Bergen: Institute of Marine Research), 165–203.

R Core Team (2021). *R: A language and environment for statistical computing* (Vienna, Austria: R Foundation for Statistical Computing). Available at: https://www.R-project.org/.

Rose, G. A. (2005). On distributional responses of north Atlantic fish to climate change. *ICES J. Mar. Sci.* 62, 1360–1374. doi: 10.1016/j.icesjms.2005.05.007

Skagseth, Ø., Broms, C., Gundersen, K., Hátún, H., Kristiansen, I., and Larsen, K. M. H. (2022). Arctic and Atlantic Waters in the Norwegian Basin, Between Year Variability and Potential Ecosystem Implications. *Front. Mar. Sci.* 9, 1–14. doi: 10.3389/fmars.2022.831739

Skjoldal, H. R., Aarflot, J. M., Bagøien, E., Skagseth, Ø., Rønning, J., and Lien, V. S. (2021). Seasonal and interannual variability in abundance and population development of calanus finmarchicus at the western entrance to the barents Sea 1995–2019. *Prog. Oceanogr.* 195, 1–20. doi: 10.1016/j.pocean.2021.102574

Skjoldal, H. R., Dalpadado, P., and Dommasnes, A. (2004). "Food webs and trophic interactions," in *The Norwegian Sea ecosystem*. Ed. H. R. Skjoldal (Trondheim: Tapir Academic), 447–506.

Skogen, M. D., Budgell, W. P., and Rey, F. (2007). Interannual variability in Nordic seas primary production. *ICES J. Mar. Sci.* 64, 889–898. doi: 10.1093/icesjms/fsm063

Slotte, A. (1999a). Differential utilization of energy during wintering and spawning migration in Norwegian spring-spawning herring. *J. Fish. Biol.* 54, 338–355. doi: 10.1006/jfbi.1998.0868

Slotte, A. (1999b). Effects of fish length and condition on spawning migration in Norwegian spring spawning herring (Clupea harengus l. *Sarsia* 84, 111–127. doi: 10.1080/00364827.1999.10420439

Slotte, A., and Fiksen, Ø (2000). State-dependent spawning migration in Norwegian spring-spawning herring. *J. Fish. Biol.* 56, 138–162. doi: 10.1006/jfbi.1999.1145

Strand, E., Bagøien, E., Edwards, M., Broms, C., and Klevjer, T. (2020). Spatial distributions and seasonality of four calanus species in the northeast Atlantic. *Prog. Oceanogr.* 185, 102344. doi: 10.1016/j.pocean.2020.102344

Toresen, R., and Østvedt, O. J. (2000). Variation in abundance of Norwegian spring-spawning herring (Clupea harengus, clupeidae) throughout the 20th century and the influence of climatic fluctuations. *Fish. Fish.* 1, 231–256. doi: 10.1111/j.1467-2979.2000.00022.x

Utne, K. R., and Huse, G. (2012). Estimating the horizontal and temporal overlap of pelagic fish distribution in the Norwegian Sea using individual-based modelling. *Mar. Biol. Res.* 8, 548–567. doi: 10.1080/17451000.2011.639781

Wilson, C. J., Murphy, H. M., Bourne, C., Pepin, P., and Robert, D. (2018). Feeding ecology of autumn-spawned Atlantic herring (Clupea harengus) larvae in trinity bay, Newfoundland: Is recruitment linked to main prey availability? *J. Plankton Res.* 40, 255–268. doi: 10.1093/plankt/fby003

Wood, S. N. (2003). Thin plate regression splines. *J. R. Stat. Soc Ser. B. Stat. Methodol.* 65, 95–114. doi: 10.1111/1467-9868.00374

Wood, S. N. (2011). Fast stable restricted maximum likelihood and marginal likelihood estimation of semiparametric generalized linear models. *J. R. Stat. Soc Ser. B. Stat. Methodol.* 73, 3–36. doi: 10.1111/j.1467-9868.2010.00749.x

Zuur, A. F., Ieno, E. N., and Elphick, C. S. (2010). A protocol for data exploration to avoid common statistical problems. *Methods Ecol. Evol.* 1, 3–14. doi: 10.1111/j.2041-210X.2009.00001.x

Advantages of publishing in Frontiers

OPEN ACCESS
Articles are free to read for greatest visibility and readership

FAST PUBLICATION
Around 90 days from submission to decision

HIGH QUALITY PEER-REVIEW
Rigorous, collaborative, and constructive peer-review

TRANSPARENT PEER-REVIEW
Editors and reviewers acknowledged by name on published articles

Frontiers
Avenue du Tribunal-Fédéral 34
1005 Lausanne | Switzerland

Visit us: www.frontiersin.org
Contact us: frontiersin.org/about/contact

REPRODUCIBILITY OF RESEARCH
Support open data and methods to enhance research reproducibility

DIGITAL PUBLISHING
Articles designed for optimal readership across devices

FOLLOW US
@frontiersin

IMPACT METRICS
Advanced article metrics track visibility across digital media

EXTENSIVE PROMOTION
Marketing and promotion of impactful research

LOOP RESEARCH NETWORK
Our network increases your article's readership